1,2,4-Triazoliums: Applications in Biocatalysis, Organocatalysis and Stable Radical Synthesis

JACOB MURRAY

1,2,4-Triazoliums: Applications in Biocatalysis, Organocatalysis and Stable Radical Synthesis

Jacob Murray

A thesis submitted in partial fulfilment of the requirements for the degree of Doctor of Philosophy

Department of Chemistry

Durham University

November 2022

Declaration

The work described in this thesis was carried out at the Department of Chemistry, Durham University, between October 2019 and October 2022, under the supervision of Prof. AnnMarie O'Donoghue. The material contained has not been previously submitted for a degree at this or any other university. All work has been carried out by the author unless otherwise indicated.

J. Murray

Copyright

Abstract

Herein we report the exploration of carbenes derived from 1,2,4-triazoliums in the novel rearrangement reaction to stable Blatter radicals, biocatalysis and organocatalysis.

Nitron is an intriguing 1,2,4-triazolium, with a C(5)-N-anilino substituent which permits establishment of a tautomeric equilibrium between the C(3) and C(5)-N positions. This work continues from our initial report of the unusual rearrangement of Nitron to Blatter radicals. The synthesis of Nitron was revisited and contemporary synthetic strategies were employed to enhance isolated yields and scope. Evaluating the series of Nitron derivatives for propensity to form Blatter radicals enabled the isolation of seven new radicals and implicated the role of the carbenic tautomer in the initial hydrolytic ring opening step. Evaluation of the tautomeric equilibrium was performed by spectrophotometric determination of C(5)-NH pK_a values and NMR spectroscopic kinetic monitoring of C(3)-H/D exchange. A 10-fold drop in carbene proportion at equilibrium when Nitron is substituted with a 4-$F_3CC_6H_4$ group at the C(5)-N-anilino position was attributed to stabilisation of the formal N^- charge in the zwitterionic form. The experimental evidence supports a faster ring opening from the carbene tautomer compared to the zwitterion.

Owing to the growing interest in stable organic diradicals, a range of synthetic strategies was explored to couple Blatter radicals. The intolerance of radical character to synthetic conditions and cross-reactivity of the ring and exocyclic nitrogen positions complicated this coupling. A synthetic strategy to a coupled di-Nitron was developed and evaluation for di-radical formation provided circumstantial evidence. The lack of a C(3)-H for carbene formation appears to limit hydrolytic ring opening. Future work could explore conditions to promote hydrolytic ring opening at the 1,2,4-triazolium C(3)-position.

The use of heterocyclic azolium-derived carbenes for organocatalysis originated from the mechanistic evaluation of thiamine (pyrophosphate, TPP) (a thiazolium) as a cofactor in TPP-dependent enzymes. Since this discovery, the field of NHC organocatalysis has grown exponentially, with chemists developing catalysts centred about the more acidic 1,2,4-triazolium scaffold. We report the first synthesis of a 1,2,4-triazolium replica of TPP in attempt to improve the yield, selectivity and scope of TPP-dependent biocatalytic

transformations. Kinetic evaluation of H/D exchange of TPP and the isolated 1,2,4-triazolium mimic using NMR spectroscopy permitted estimation of C(2/3)-H pK_a values and showed a ~1.5 unit decrease for 1,2,4-triazolium mimics in comparison to thiamine.

Initial evaluation of 1,2,4-triazolium mimics focussed on model benzoin condensation reactions, in the absence of enzyme. An approximate 10-fold enhancement in rates of initial hydroxyaryl adduct were determined through kinetic monitoring. Assessment of the 1,2,4-triazolium mimic as a cofactor was performed with TPP-dependent enzymes pyruvate decarboxylase from *Saccharomyces cerevisiae* and pyruvate oxidase from *Aerococcus sp.* via spectrophotometric coupled assays and direct NMR spectroscopic analysis. Loss of enzyme activity in the presence of the cofactor mimic was observed implying that binding to the active site occurred but the mimic was less active. This decreased activity was thought to be due to a conformational discrepancy within the active site. Future work will screen a greater range of more tolerant TPP-dependent enzymes to fully explore compatibility of the 1,2,4-triazolium mimic.

Complementary studies evaluated the hydrolytic stability of TPP by ^{31}P NMR spectroscopy in a series of deuterated buffers from p*D* 0-13. Under physiological conditions (p*D* 4-7) TPP is very stable with minimal hydrolysis of the pyrophosphate over several months ($t_{1/2}$ = 300-500 days). Under acidic conditions (p*D* < 3), hydrolysis of the pyrophosphate becomes more prevalent ($t_{1/2}$ down to 2 days). Above p*D* 8, hydrolysis of the pyrophosphate group is negligible, but cleavage of the methylene linker occurs.

Finally, 1,2,4-triazoliums isolated within these projects were evaluated as catalysts to the benzoin condensation, a key NHC organocatalysed transformation. Intriguingly, Nitron derivatives showed no propensity for catalysis, despite showing similar rates constants for H/D-exchange as other commonly employed 1,2,4-triazolium catalysts. This result was unexpected and attributed to the unusual chemical nature of carbenes derived from Nitron derivatives. The evaluation of more sustainable reaction conditions for NHC organocatalysis led to the observation that rate enhancements were observed when the benzoin condensation was performed under aqueous conditions with a more traditional 1,2,4-triazolium catalyst. This observation paves the way for significant future work to develop an understanding of NHC-organocatalysed transformations in water.

Acknowledgements

First and foremost, I would like to thank my supervisor, AnnMarie O'Donoghue, for all her guidance and support over the past three years, particularly through the challenging COVID lockdowns. Thanks also to David Hodgson for his support and advice, particularly relating to the development of phosphorylation techniques.

Within the AMOD group I would like to thank Josh Rawlinson and Matthew Smith for their support over the years and help with proof reading. I would particularly like to single out Jiayun (Estelle) Zhu for being the best Post-Doc a group could ask for. Her help throughout the past three years has been invaluable.

Within the wider Chemistry Department in Durham, I would like to thank Carlotta Pagli and Robyn Poulton from the DRWH group for sharing in the pain that is phosphorylation chemistry. Thanks also to the analytical services in the Department for all their help throughout the three years, most notably Dr Juan Aguilar-Malavia and Dr Dmitrii Yufit for support in NMR spectroscopy and X-ray crystallography, respectively.

Last, but not least, I would like to thank my family, friends and particularly Lucy for all their support through the highs and lows of the past three years.

Table of Contents

Abbreviations

AMP	Adenosine Monophosphate	**NHC**	N-Heterocyclic Carbene
ADP	Adenosine Diphosphate	**NMR**	Nuclear Magnetic Resonance
ATP	Adenosine Triphosphate	**O-DNP**	Overhauser Dynamic Nuclear Polarisation
BAL	Benzaldehyde Lyase	**[Ox]**	Oxidation
BFD	Benzoyl Formate Decarboxylase	**PAC**	Phenylacetyl Carbinol
CED	Cumulative Energy Demand	**PDC**	Pyruvate Decarboxylase
CoA	Coenzyme A	**PLP**	Pyridoxal Phosphate
CV	Cyclic Voltammetry	**POx**	Pyruvate Oxidase
DCM	Dichloromethane	**PQQ**	Pyrroloquinoline Quinone
DES	Deep Eutectic Solvent	**REDOX**	Reduction/Oxidation
DMF	Dimethylformamide	**RT**	Room Temperature
DMSO	Dimethyl sulfoxide	**S**	Spin Quantum Number
EDG	Electron Donating Group	**SAM**	S-Adenosyl Methionine
ee	Enantiomeric Excess	**$ScCO_2$**	Supercritical CO_2
EHS	Environmental Health and Safety	**S_N1**	Unimolecular Nucleophilic Substitution
EWG	Electron Withdrawing Group	**S_N2**	Bimolecular Nucleophilic Substitution
EPR	Electron Paramagnetic Resonance	**SOMO**	Singly Occupied Molecular Orbital
$E^{ox}_{1/2}$	Half-Cell Oxidation Potential	**TEA**	Triethylamine
$E^{ox}_{1/2}$	Half-Cell Reduction Potential	**TEAA**	Triethylammonium Acetate
FAD	Flavin Adenine Dinucleotide	**TEAB**	Triethylammonium Bicarbonate
FMN	Flavin Mononucleotide	**THF**	Tetrahydrofuran
HEPES	4-(2-Hydroxyethyl) piperazine-1-ethanesulfonic acid	**TLC**	Thin Layer Chromatography
HFCC	Hyperfine Coupling Constants	**TMACl**	Tetramethylammonium Chloride
HMBC	Heteronuclear Multiple-Bond Coherence	**TMP**	Thiamine Monophosphate
HOMO	Highest Occupied Molecular Orbital	**TOYE**	Thermophilic Old Yellow Enzyme
HRMS	High Resolution Mass Spectrometry	**TPP**	Thiamine Pyrophosphate
IC_{50}	Half Maximal Inhibitory Concentration	**$t_{1/2}$**	Half-Life
IL	Ionic Liquid	**UV-Vis**	Ultra Violet-Visible
IPA	Isopropyl Alcohol	**XRD**	X-Ray Diffraction
IS	Internal Standard	**2-MeTHF**	2-methyltetrahydrofuran
LCA	Life Cycle Assessment	**σ**	Hammett Substituent Constant
LC-MS	Liquid Chromatography-Mass Spectrometry		
LUMO	Lowest Unoccupied Molecular Orbital		
MES	2-(N-morpholino) ethanesulfonic acid		
MRI	Magnetic Resonance Imaging		
NAD	Nicotinamide adenine dinucleotide		

1. Introduction

1.0. Foreword

This thesis focusses on stable N-heterocyclic carbenes (NHCs) and Blatter type-radicals, a class of stable organic radical. The link in common throughout the work presented is the use of 1,2,4-triazolium precursors to access both NHCs and Blatter radicals. Carbenes formed from 1,2,4-triazoliums are explored in the Nitron to Blatter radical rearrangement (Chapter 2), in chemomimetic biocatalysis (Chapter 3) and organocatalysis (Chapter 4). This introductory chapter briefly explores the chemical nature of stable carbenes and organic radicals. An overview of synthetic strategies to access azolium ions is also presented, as key to Chapters 2-4 is the development of synthetic strategies to new and under-explored 1,2,4-triazolium scaffolds.

1.1. Stable Carbenes

A carbene is a divalent, uncharged carbon species with six valence electrons of which four are involved in bonding and two remain non-bonding, centred on the carbon. The non-bonding electrons can be paired in a single orbital (singlet carbene) or unpaired in different orbitals (triplet carbene). Depending on the hybridisation at carbon, carbenes are either linear or bent in geometry.[1]

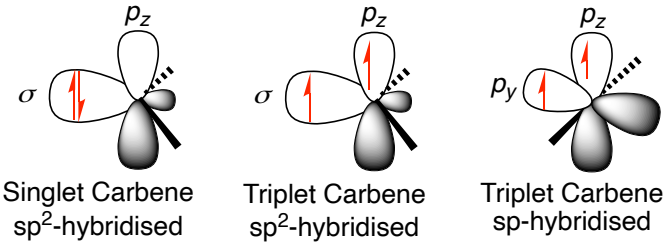

Figure 1.1.1. Orbital representations of a singlet carbene and the bent and linear forms of triplet carbenes.

Ground-state multiplicity of carbenes dictates their reactivity, with singlet carbenes being ambiphilic in nature and triplet carbenes having diradical character. Multiplicity is determined by the relative energies of the σ and p_z-orbitals. Typically, the most stable electron configuration occurs when electrons possess the same spins in different orbitals (Hunds' Rule of maximum spin multiplicity); however, where there is a large σ-p_z energy difference, electron pairing is more favourable. The electronic nature of substituents can alter the σ-p_z energy gap and determine the reactive nature of the carbene. Electron withdrawing groups inductively stabilise the σ orbital, increasing the σ-p_z energy gap, favouring singlet carbene character; whereas, electron donating groups have been found to inductively destabilise the σ orbital, having the opposite effect and favouring triplet

carbenes. As formation of triplet carbenes results in an overall destabilising effect, often bulky substituents are required to stabilise these reactive species.[1]

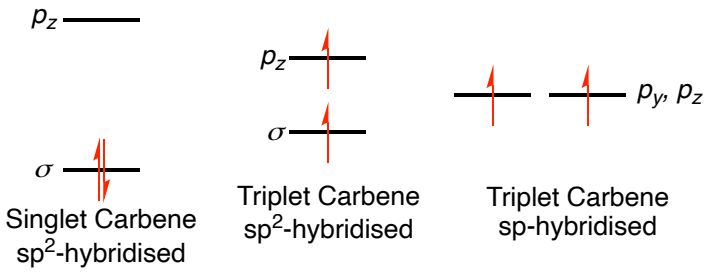

Figure 1.1.2. Relative orbital energies of singlet and triplet carbenes.

Despite the majority of carbenes being highly reactive intermediates, there are a selection of more stable examples. Stabilisation of singlet carbenes is achieved with heteroatoms such as NR_2, OR, SR or F, providing both σ-withdrawing and π-donating stabilising effects (Figure 1.1.3).[1]

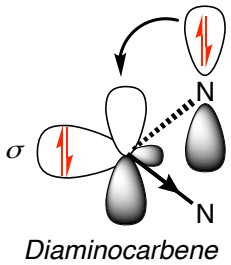

Figure 1.1.3. Stable carbenes such as a diamino carbene are stabilised by inductive withdrawing effects and mesomeric effects.

The earliest reported attempts to isolate a carbene were by Wanzlick *et al.* in 1960 who heated 1,3- diphenylimidazolin-2-ylidene (**1**) under vacuum, eliminating chloroform to generate carbene (**2**). However, the carbene in this case was not isolated and instead dimerised forming tetraaminoalkene (**3**) (Scheme 1.1.1). Carbene character was confirmed through the trapping of electrophiles.[2] It wasn't until 1988 that the first stable carbene, a phosphinosilyl carbene (**4**), was isolated by Bertrand and co-workers (Figure 1.1.4).[3] This is an example of a push-pull carbene with groups of differing electron density, a concept revisited when considering the stability of persistent radicals. It is important to highlight that although this compound has carbene character it is thought to exist more in its phosphoacetylene form.[1, 3]

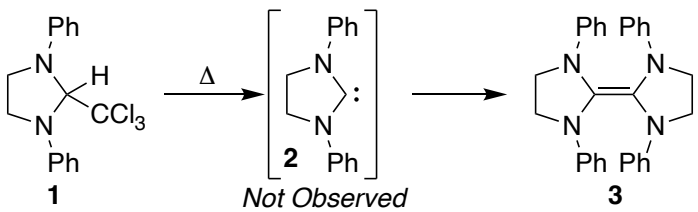

Scheme 1.1.1. First attempted isolation of a stable carbene. Instead, a dimerised product formed, which was proposed to proceed via the carbene.

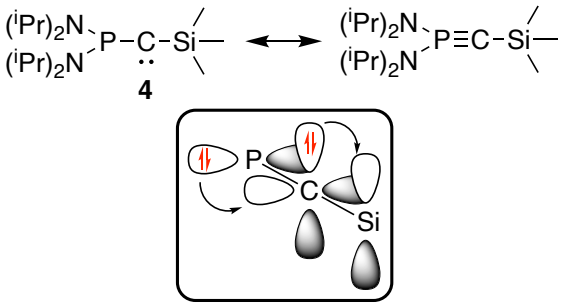

Figure 1.1.4. The first reported carbene, a phosphinosilyl carbene **4**, reported by Bertrand *et al*.

Heterocyclic azolium ions have been found to display singlet carbene character upon deprotonation at the C(2/3)-H positions (Figure 1.1.5).[4] These have been grouped into a class of carbenes called N-heterocyclic carbenes (NHCs), which now encompasses a range of N-heterocycles. Figure 1.1.5 highlights a selection of NHCs: thiamine (**5**), a thiazolium which inspired the field of NHC organocatalysis, is central to Chapter 3; Nitron (**6**), the topic of Chapter 2, is an unusual class of 1,2,4 triazolium with a C(5)-phenylamino substituent. Other 1,2,4-triazoliums such as (**7**) have been developed as more advanced asymmetric organocatalysts, diamidocarbenes (**8**) are a class of 6-membered ring carbene; finally, bis-amino cyclopropeniums (BACS) (**9**) have more recently gained interest for intriguing orthogonal behaviour.[1, 5] Our group is particularly interested in organocatalytic applications of NHCs, focussing on fundamental physical organic properties and mechanisms underpinning reactivity.[6-9]

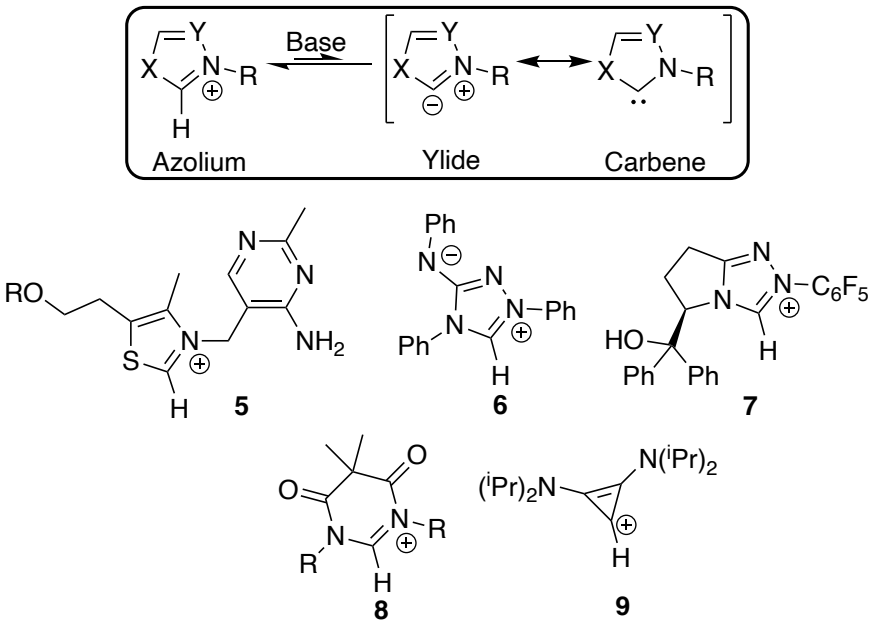

Figure 1.1.5. Top: The typical generation of a carbene from an azolium ion by base-deprotonation of the C-H; Bottom: A small selection of NHC precursors, C-H deprotonation yields the carbene. Examples include a thiazolium, thiamine (**5**); a 1,2,4-triazolium, Nitron (**6**); a chiral 1,2,4-triazolium (**7**), used typically as an organocatalyst; a diamidocarbene precursor (**8**) and a BAC (**9**).

1.2. Stable Organic Radicals

As with carbenes, stable organic radicals have intriguing properties owing to their unusual electronic nature. Since the first report of a stable organic radical, the triphenylmethyl radical (**10**), by Gomberg in 1900 the field of persistent organic radicals has gained steady momentum.[10] A selection has emerged including analogues of (**10**) such as polychlorotriphenylmethyl (**11**), nitroxide (**12**), (oxo)verdazyl (**13**), and phenalenyl (**14**) radicals to name but a few (Figure 1.2.1).[11, 12] Chapter 2 discusses a relatively less-well known class of stable organic radical, Blatter radicals (**15**), shown in Figure 1.2.1 as the C(3)-Ph parent compound. Interest in open-shell organic systems has grown due to the unusual properties exhibited with respect to their closed-shell equivalents, including magneto- and photochemical applications. In particular, developing new metal-free, molecular magnetic materials is an expanding area of research.[11]

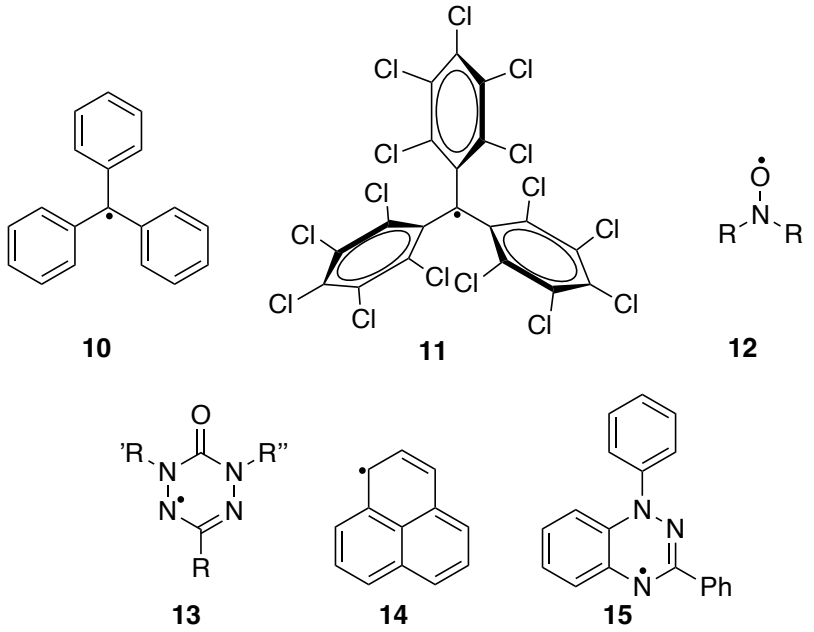

Figure 1.2.1. A selection of persistent organic radicals: triphenylmethyl radical (**10**) was the first reported stable radical, the polychlorotriphenylmethyl radical (**11**) was designed to improve the stability versus (**10**), nitroxide (**12**), oxoverdazyl (**13**), phenylalenyl (**14**) and the parent Blatter radical (**15**), which is central to Chapter 2.

Radicals are characterised by the presence of a singly occupied molecular orbital (SOMO) and, in the majority of circumstances, are highly reactive due to the tendency to form closed-shell species via a variety of processes including recombination and disproportionation.[11] The peculiarity of persistent organic radicals with regards to stability helps explain their relative rarity within organic chemistry.[12] The stabilisation of persistent organic radicals is elucidated by a combination of steric and electronic factors.[13] These lower the reactivity of the radical by shielding its centre and reducing

the energy of the SOMO. When considering radicals (**10**) and (**11**), the steric hindrance at the centre is large and hence protects the radical centre from attack. However, for radical **10**, it is still the case that dimerization may occur (**16**) (Figure 1.2.2) reducing its half-life.[11, 14] As such, functionalisation of the phenyl rings as in radical (**11**) has been explored to further stabilise the radical; this particular species is highly stable due to the vast bulk. Radical (**11**) is so bulky that the phenyl groups cannot readily slip past each other and it exists in *P*- and *M*-atropoisomeric forms, with an interconversion energy in the region of 23 kcal mol^{-1}.[11]

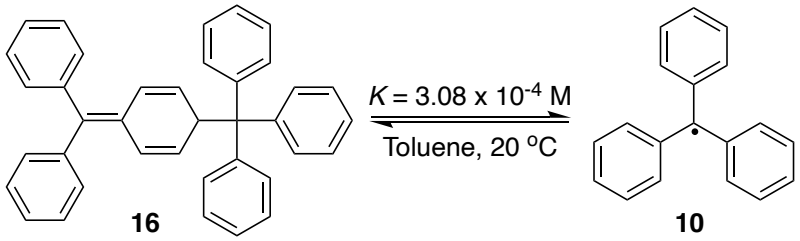

Figure 1.2.2. Dimerization of the triphenylmethyl radical (**10**); the equilibrium constant is reported at 20 °C in toluene.

Electron-donating groups (EDGs) and electron-withdrawing groups (EWGs) may also incur a stabilising effect. As seen in Figure 1.2.3, interaction with an empty antibonding orbital (π^*) or filled bonding orbital (n) reduces the overall electron energy.[13] Alternatively, electronic stabilisation may be considered as the ability of substituents to delocalise the radical centre, as is the case for phenalenyl radicals (**14**). A combination of EDGs and EWGs within a single species greatly enhances stability, referred to as the captodative effect. Many persistent radicals capitalise upon this, for example 1-alkyl-4-(carboalkoxy)pyridinyl (**17**) radicals which have a noticeable push-pull effect (Figure 1.2.4).[13, 15]

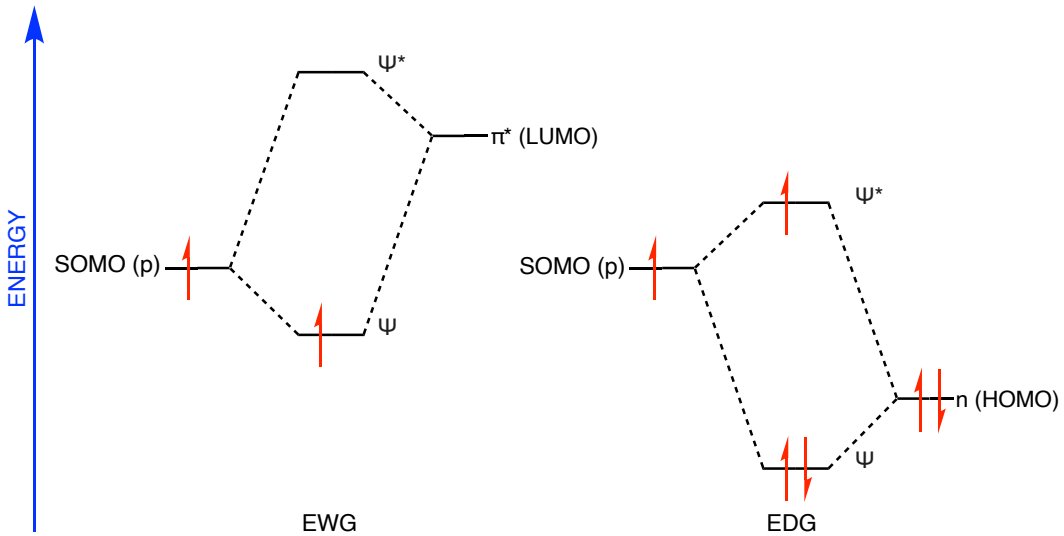

Figure 1.2.3. A stepwise perturbation approach explaining the electronic stabilisation of persistent radicals by electron-donating and withdrawing groups. These groups lower electron energy and hence stabilise the SOMO.

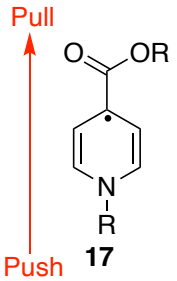

Figure 1.2.4. The 1-alkyl-4-(carboalkoxy)pyridinyl (**17**) radical, which displays the captodative effect.

The presence of a SOMO within an organic species makes characterisation much more complicated. Primarily this is due to the paramagnetic broadening of signals within nuclear magnetic resonance (NMR) spectroscopy under normal experimental techniques.[16] A variety of alternative techniques are utilised, including cyclic voltammetry (CV) and electron paramagnetic resonance (EPR) spectroscopy. CV is a popular tool in the field of persistent radicals, used to probe the reversible single electron oxidation and reduction processes.[17] Figure 1.2.5 depicts a CV spectrum of radical (**10**), characteristic of the majority of persistent radicals. As seen, two reversible electrochemical events exist corresponding to the oxidation and reduction of the radical.

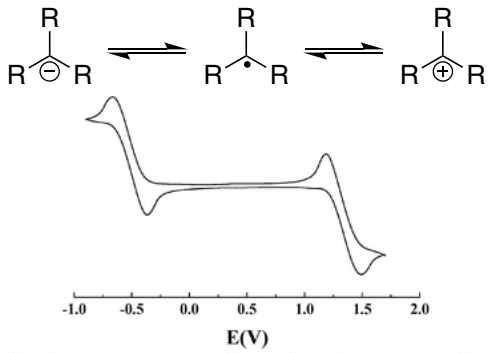

Figure 1.2.5. CV spectrum of radical (**11**) (R = pentachlorophenyl) corresponding to single electron oxidation and reduction of the species. Adapted from Ref. 11 with permission from The Royal Society of Chemistry.

EPR spectroscopy follows the same principles as NMR spectroscopy, probing the interaction of magnetic dipoles with an applied magnetic field and electromagnetic radiation. Where EPR spectroscopy differs is that it is concerned with electron as opposed to nuclear spin states. Whereas many chemical components possess the properties of a nuclear magnetic dipole, electron magnetic dipoles only exist within species with unpaired electrons. Radical species are characterised as open-shell and therefore possess an electron magnetic dipole moment and are well suited to study by EPR spectroscopy. Moreover, it is common for open-shell organic species to contain only a single unpaired electron, corresponding to a total spin quantum number, S = ½. This makes characterisation much simpler compared to transition metal complexes where typically S > ½.[18]

Perhaps the most important information obtained from EPR is the electron-nuclear hyperfine coupling between the unpaired electron and the surrounding nuclei. This consists of isotropic and anisotropic parts, with the isotropic share referring to through-bond interactions. These correlate to a probability of finding the electron spins at the position of a particular nucleus. Within the persistent radical field this is useful for determining the presence of stabilising atoms within the molecule. EPR spectral outputs are complex and non-trivial to interpret, depending on the magnitude and relative orientation of all magnetic tensors with respect to each other and the applied field. Essential simulations allow for determination of these tensors and information retrieval from the spectra.[18]

Figure 1.2.6 shows the EPR spectrum of the α-nitronyl nitroxide radical (**18**). It consists of a 1:2:3:2:1 signal of 5 lines, characteristic of the coupling of a single electron to two equivalent nitrogen atoms. In other words, these two nitrogen atoms contribute to the stabilising effect of radical (**18**).[11, 18]

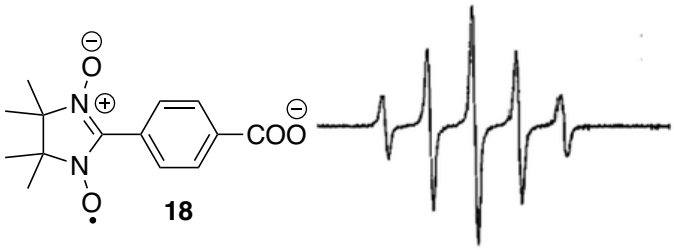

Figure 1.2.6. An α-nitronyl nitroxide radical (**18**) and its EPR spectrum. Adapted from Ref. 11 with permission from The Royal Society of Chemistry.

1.3. General Syntheses of Azoliums

Chapters 2-4 all consider synthetic strategies to new and under-explored 1,2,4-triazolium scaffolds. There are many synthetic strategies to access the full spectrum of heterocyclic azolium ions. General synthetic strategies to thiazoliums and 1,2,4-triazoliums are discussed below.

Aspects of thiazolium ion syntheses can be applied to the synthesis of 1,2,4-triazoliums. Thiazoliums are typically synthesised by a selection of methods (Scheme 1.3.1). Condensation of thioformamides (**19**) with an α-chloroketone yields the desired salts in good yields; however, this strategy requires the isolation of precursor thioformamides.[19]

An alternative approach is to synthesise the precursor thiones (**20**) by reaction of an α-bromoketone with carbon disulphide and sodium hydroxide. Subsequent treatment with hydrogen peroxide and acetic acid yields the thiazolium which can be precipitated by counterion exchange.[20] This latter approach is the most commonly employed method to isolate a broad range of functionalised thiazolium salts.

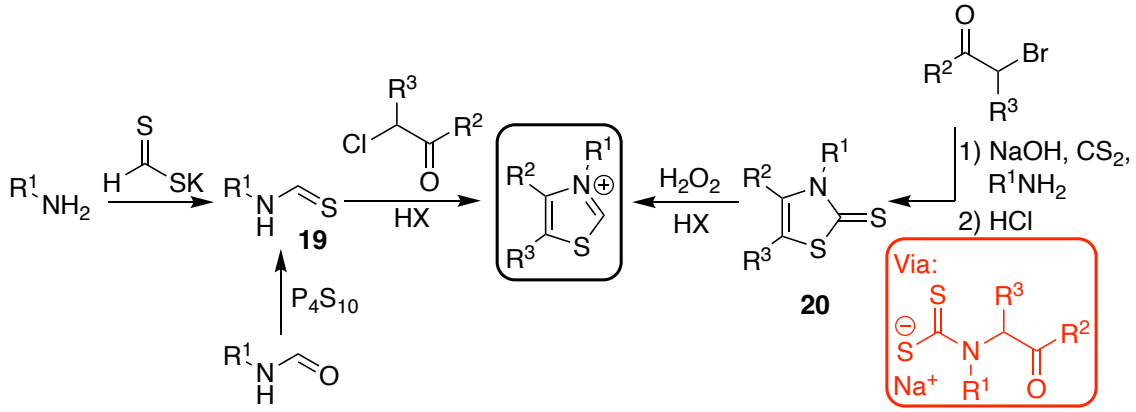

Scheme 1.3.1. General synthetic strategies to thiazoliums either via thioformamides or thiones.

1,2,4-Triazolium salts have experienced increased attention owing to preferential catalytic properties. As such, a broader range of synthetic strategies exist to access these azolium ions, which all typically involve two aspects: initial synthesis of an amidrazone (**21**), followed by cyclisation to an azolium ion. Amidrazones are synthesised through activation of a precursor amide by treatment with either trimethyloxonium tetrafluoroborate or thionyl chloride (Scheme 1.3.2). Subsequent reaction with an aryl hydrazine yields the target amidrazones as their protonated salts. Ring closure can be achieved via a selection of processes, to isolate either the azolium directly or by initial synthesis of a thione and then oxidation to the azolium. Direct methods to isolate the azolium include treatment with chloromethyl methyl ether, chloromethyl pivalate and silver triflate or trialkyl orthoformates. The latter is by far the most favourable approach as it is a significantly less hazardous reagent than the alternative approaches and requires no further reagents.[19]

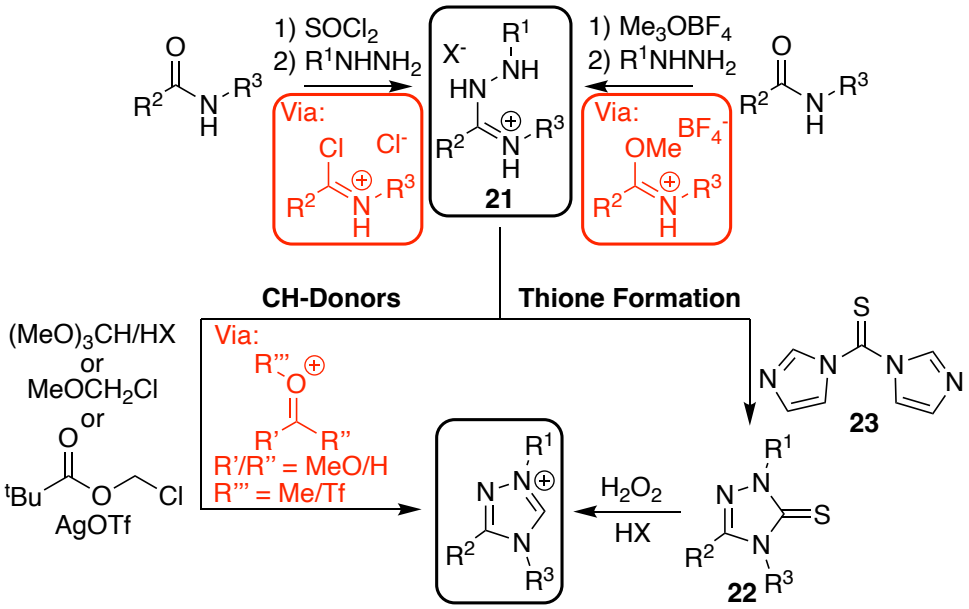

Scheme 1.3.2. General synthetic strategies to 1,2,4-triazoliums typically involve synthesis of an amidrazone, followed by ring closure to form a thione or reaction directly to the azolium with a CH-donor reagent.

In the case of some 1,2,4-triazoliums, particularly those with electron withdrawing N-aryl substituents, the approaches discussed above do not always proceed successfully. An alternative synthetic strategy, similar to the preparation of thiazoliums, is to first isolate the precursor thione (**22**). This can be installed through the use of a bis-imidazole thiourea (**23**). As with the thiazoliums, treatment with hydrogen peroxide gives the azolium which can be precipitated by anion exchange from the acetic acid solvent.

1.4. Aims

This thesis is split into three areas of research, all focussed around 1,2,4-triazoliums and N-heterocyclic carbenes. Chapter 2 explores an unusual rearrangement from Nitron (**6**) to C(3)-amido (**24**) and C(3)-amino (**25**) Blatter radicals, first reported by our group in 2017 (Figure 1.4.1).[21] Initially, we sought to determine the scope of this newly reported rearrangement, by altering the N-aryl substituents on Nitron and exploring reaction to form radicals. Prior to our recent work, only the synthesis of parent Nitron (**6**) was reported. Zwitterionic Nitron exists in a tautomeric equilibrium (K^T) with a carbenic form. This work also aimed to better understand the relevance of this tautomerisation in the formation of Blatter-type radicals.[22] Finally, within the field of stable organic radicals, the synthesis of diradicals is receiving significant attention due to their intriguing and potentially useful properties. Chapter 2 explores the synthesis of diradicals from C(3)-amido and -amino Blatter radicals.

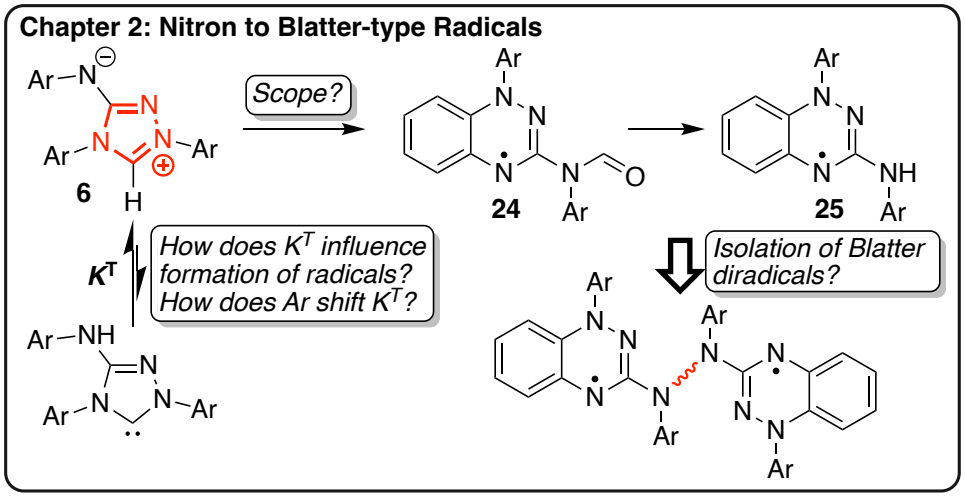

Figure 1.4.1. Schematic outline of the key areas of exploration in Chapter 2.

Chapter 3 explores the design, synthesis and initial biocatalytic evaluation of a novel enzyme cofactor mimic of thiamine pyrophosphate (TPP) (**5{PP}**), with a 1,2,4-triazolium core (**26{PP}**) (Figure 1.4.2). Enzymes work in tandem with cofactors which are typically small organic compounds (some containing metals) with catalytic activity of their own. Many organocatalysts used within chemical synthesis are based upon these cofactors. Chemical intuition has led to structural changes to cofactor scaffolds which improve the outcome of organocatalytic reactions (yield, selectivity, turnover). One key example is thiamine (**5**), a thiazolium which was initially used in C-C bond forming transformations. This chapter seeks to explore whether a 1,2,4-triazolium mimic of TPP

is compatible with TPP-dependent enzymes and whether reaction rates, scope and selectivity can be enhanced in biocatalytic transformations.

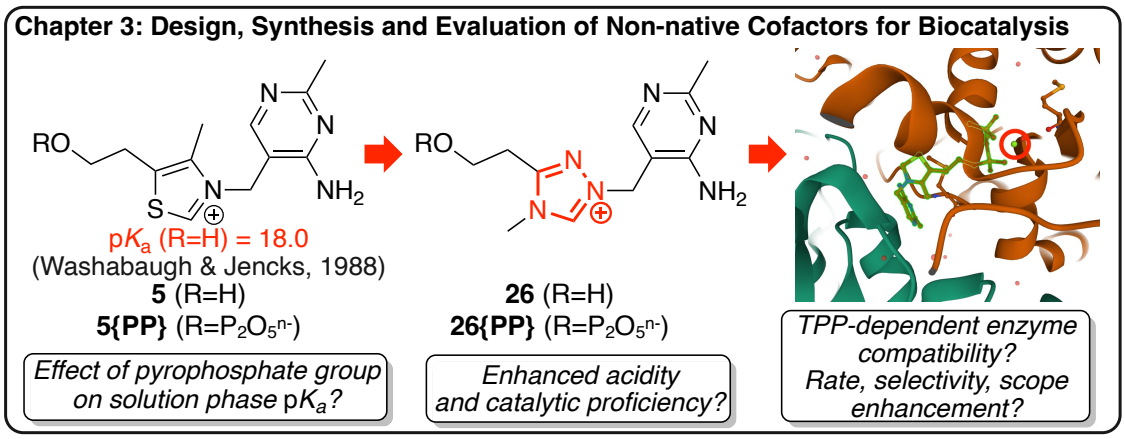

Figure 1.4.2. Schematic outline of the key areas of exploration in Chapter 3.

As with all aspects of human life, the chemical industry is receiving increased scrutiny with respect to environmental impact and sustainability. Organocatalysis is an inherently more sustainable concept, reducing energy requirements for difficult chemical transformations and negating the use of toxic metal catalysts. However, many organocatalysed processes rely heavily on non-sustainable, environmentally hazardous solvents (e.g. DCM/THF). The focus of Chapter 4 is NHC-organocatalysis with a focus on sustainability (Figure 1.4.3). The 1,2,4-triazolium scaffolds (Nitrons (**6**), N-Aryl thiamine mimics (**27**)) explored in Chapters 2 and 3 are evaluated as potential organocatalysts. Interestingly, despite previous studies highlighting the carbenic nature of Nitron, there has been no reports to date of applications in organocatalysis. These are initial studies and further work is required.

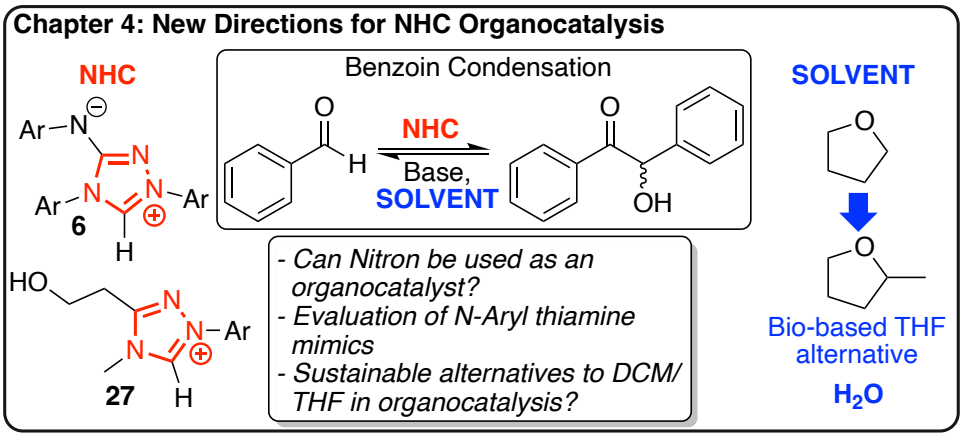

Figure 1.4.3. Schematic outline of the key areas of exploration in Chapter 4.

1.5. References

1. D. Bourissou, O. Guerret, F. P. Gabbaï and G. Bertrand, *Chem. Rev.*, 2000, **100**, 39-92.
2. H. W. Wanzlick, *Angew. Chem. Int. Ed.*, 1962, **1**, 75-80.
3. A. Igau, H. Grutzmacher, A. Baceiredo and G. Bertrand, *J. Am. Chem. Soc.*, 1988, **110**, 6463-6466.
4. D. M. Flanigan, F. Romanov-Michailidis, N. A. White and T. Rovis, *Chem. Rev.*, 2015, **115**, 9307-9387.
5. R. M. Wilson and T. H. Lambert, *Acc. Chem. Res.*, 2022, **55**, 3057-3069.
6. C. J. Collett, R. S. Massey, O. R. Maguire, A. S. Batsanov, A. C. O'Donoghue and A. D. Smith, *Chem. Sci.*, 2013, **4**.
7. E. M. Higgins, J. A. Sherwood, A. G. Lindsay, J. Armstrong, R. S. Massey, R. W. Alder and A. C. O'Donoghue, *Chem. Comm.*, 2011, **47**, 1559-1561.
8. R. S. Massey, C. J. Collett, A. G. Lindsay, A. D. Smith and A. C. O'Donoghue, *J. Am. Chem. Soc.*, 2012, **134**, 20421-20432.
9. C. J. Collett, R. S. Massey, J. E. Taylor, O. R. Maguire, A. C. O'Donoghue and A. D. Smith, *Angew. Chem. Int. Ed.*, 2015, **54**, 6887-6892.
10. M. Gomberg, *J. Am. Chem. Soc.*, 1900, **22**, 757-771.
11. I. Ratera and J. Veciana, *Chem. Soc. Rev.*, 2012, **41**, 303-349.
12. B. D. Koivisto and R. G. Hicks, *Coord. Chem. Rev.*, 2005, **249**, 2612-2630.
13. H. G. Viehe, Z. Janousek, R. Merenyi and L. Stella, *Acc. Chem. Res.*, 1985, **18**, 148-154.
14. T. H. Colle, P. S. Glaspie and E. S. Lewis, *J. Org. Chem.*, 1978, **43**, 2722-2725.
15. R. Sustmann and H.-G. Korth, in *Advances in Physical Organic Chemistry*, ed. D. Bethell, Academic Press, 1990, vol. 26, pp. 131-178.
16. F. Rastrelli and A. Bagno, *Chem. Eur. J.*, 2009, **15**, 7990-8004.
17. N. Elgrishi, K. J. Rountree, B. D. McCarthy, E. S. Rountree, T. T. Eisenhart and J. L. Dempsey, *J. Chem. Ed.*, 2017, **95**, 197-206.
18. M. M. Roessler and E. Salvadori, *Chem. Soc. Rev.*, 2018, **47**, 2534-2553.
19. L. Benhamou, E. Chardon, G. Lavigne, S. Bellemin-Laponnaz and V. Cesar, *Chem. Rev.*, 2011, **111**, 2705-2733.
20. I. Piel, M. D. Pawelczyk, K. Hirano, R. Fröhlich and F. Glorius, *Eur. J. Org. Chem.*, 2011, **2011**, 5475-5484.
21. J. A. Grant, Z. Lu, D. E. Tucker, B. M. Hockin, D. S. Yufit, M. A. Fox, R. Kataky, V. Chechik and A. C. O'Donoghue, *Nat. Commun.*, 2017, **8**, 15088.
22. C. Färber, M. Leibold, C. Bruhn, M. Maurer and U. Siemeling, *Chem. Comm.*, 2012, **48**, 227-229.

2. From Nitron to Stable Blatter-Type Radicals

2.0. Foreword

Since the first report of the Nitron (**6**) to Blatter-type radical (**25**) rearrangement by our group in 2017, there has been little further exploration. Nevertheless, these novel radicals are gaining interest within the stable organic radical field. The evaluation of this transformation first required the synthesis of a broader range of Nitron derivatives as highlighted in Chapter 2.2. Nitron exists in tautomeric equilibrium between a zwitterion and a carbene, and it is unknown how this influences the formation of Blatter-type radicals. Chapter 2.3 explores both the scope of the Nitron to Blatter-type rearrangement, the influence of Nitron tautomerisation and the effect of the N-substituents on the position of this equilibrium. In recent years, organic diradicals (stable organic radicals coupled via a linker) have received significant attention due to their intriguing electronic properties and applications. Chapter 2.4 highlights the initial explorations of coupling these novel amido- and amino- Blatter radicals into di-radical species. Chapter 2 begins with a discussion of previous work into Blatter radicals including synthetic routes, functionalisation, properties and applications (Chapter 2.1).

2.1. Introduction

Blatter radicals (**15**), or benzotriazinyl radicals, are an under explored class of persistent organic radicals, named after their discoverer (Figure 2.1.1).[23] Although first reported in the late 1960s, synthetic adversity has limited the exploration of this class of radical.[24] However, in recent times a systematic screening of syntheses by Koutentis *et al.* and further discoveries by other parties have made evaluation more viable.[25-28] Blatter radicals are characterised by a SOMO with the majority of the radical character centred about the *N*(4) atom (Figure 2.1.1). They also have a fused aryl ring and further functionalisation at the *N*(1) and *C*(3) positions, usually in the form of aryl groups, but can also be further derivatised.[23, 25-28] These characteristics account for the stability of this class of persistent radical as well as the intriguing properties.

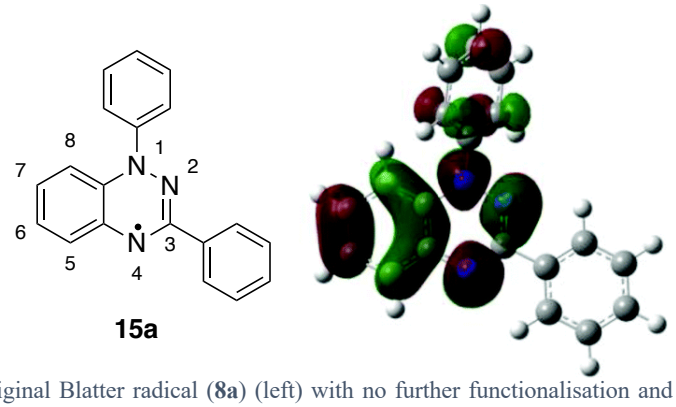

Figure 2.1.1. The original Blatter radical (**8a**) (left) with no further functionalisation and the SOMO of radical **8a** (right) calculated using UDFT with the hybrid B3LYP method and triple-ζ basis set 6-311+G(d,p) the green and red colours refer to positive and negative phases of the SOMO respectively. Adapted from Ref. 16 with permission from the Centre National de la Recherche Scientifique (CNRS) and The Royal Society of Chemistry.

Stability may be rationalised through the delocalisation of the radical about the molecule. Computational studies using spin polarised density functional theory (UDFT) with the hybrid B3LYP method and triple-ζ basis set 6-311+G(d,p) highlight the SOMO and the delocalisation of the radical centre (Figure 2.1.1).[29] As seen, there is a significant amount of SOMO character on the fused nitrogen atoms within the heterocycle as well as within the fused aryl ring.

The bulky, non-fused aryl groups also help provide some steric hindrance to the radical centre. These aryl groups are too bulky to be co-planar to the fused-ring system due to unfavourable interactions between hydrogens on the rings. The *N*(1) aryl group has a large torsion angle of ~50° and this strongly affects the solid-state packing.[30] They form

an ordered, π-slip-stacked arrangement, helping to account for their bulk magnetic properties (Figure 2.1.2).[31]

Figure 2.1.2. Molecular packing of Blatter radical (**15a**). Reprinted by permission from Copyright Clearance Center: [Springer Nature] [Russian Journal of General Chemistry] [A. T. Gubaidullin, B. I. Buzykin, I. A. Litvinov and N. G. Gazetdinova, Russ. J. Gen. Chem., 2004, 74, 1015–1020] (Molecular and Crystal Structure of a Superstable Free Radical, 1,3-Diphenyl-1,4-dihydro-1,2,4-benzotriazin-4-yl, A. T. Gubaidullin et al), [COPYRIGHT] (2020)

Characterisation of Blatter radicals via NMR spectroscopy is non-trivial due to the paramagnetic broadening of signals. Typically Blatter radicals are characterised by cyclic voltammetry and EPR spectroscopy, for example Figure 2.1.3 radical (**15b,** C(7)-F functionalised). The cyclic voltammogram was obtained using a glassy carbon disk as working electrode, Pt wire as counter electrode and a Ag/AgCl (1 M KCl) reference. The concentration of radical was 1 mM in DCM, with an $^{n}Bu_4NPF_6$ (0.1 M) electrolyte and ferrocene was used as the internal reference.[28] The CV spectrum shows two electrochemical events, corresponding to oxidation at positive, $E_{1/2}^{ox}$ = 0.288 V, and reduction at negative, $E_{1/2}^{red}$ = -0.864 V, electrode potential. Varying substituents on the Blatter radicals affects variation in their reduction and oxidation (REDOX) stability and CV may be used to probe this. The EPR spectrum consists of 7 peaks, consistent with a radical centre coupled to three ring nitrogen-14 atoms. The EPR spectrum in this case is for a Blatter radical functionalised in the *C*(7) position with a fluorine atom; however, the appearance is analogous to a more traditional Blatter radical.[28]

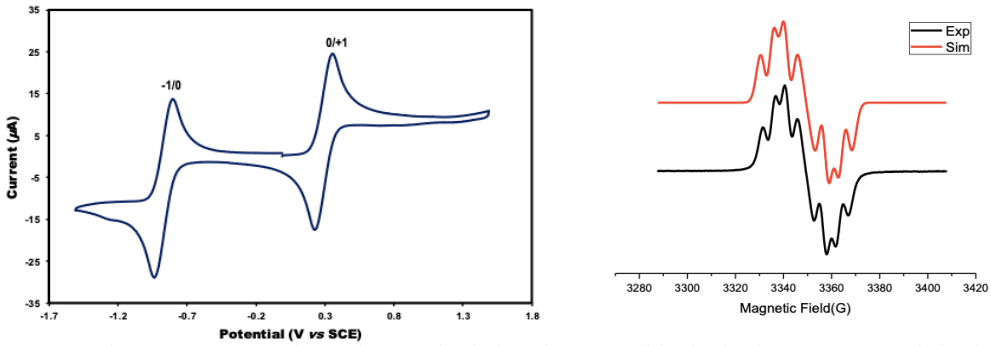

Figure 2.1.3. Left - a CV spectrum for a Blatter radical, denoting reversible single electron REDOX behaviour. Right - an EPR spectrum for-Blatter radical with a fluorine group in the C(7) position (**15b**) showing a 7-line spectrum consistent with radical coupling to 3 nitrogen centres. Adapted with permission from A. C. Savva, S. I. Mirallai, G. A. Zissimou, A. A. Berezin, M. Demetriades, A. Kourtellaris, C. P. Constantinides, C. Nicolaides, T. Trypiniotis and P. A. Koutentis, J. Org. Chem., 2017, **82**, 7564–7575.. Copyright 2020 American Chemical Society.

2.1.1. The Synthesis and Reactions of Blatter Radicals

Historic Syntheses

Benzotriazinyl radicals were first reported by Blatter *et al.* in 1968 with the original analogue (**15a**) where R = Ph.[23] This synthesis (Scheme 2.1.1) alluded to an unusual electrocyclisation of a triazabutadiene species (**28**), characteristic of many synthetic routes to Blatter radicals. This results in the formation of a 1,2,4-benzotriazine intermediate (**29**), which upon treatment with base yields the desired radical (**15a**). The original synthesis provided the initial evidence of this class of open-shell organic molecule; however, suffered major drawbacks with regards to synthesis and purification prompting further synthetic exploration.

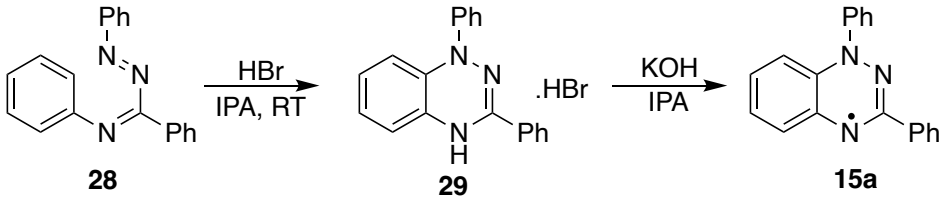

Scheme 2.1.1. The original reported synthesis of the parent Blatter radical (**15a**) developed by Blatter *et al.*.

Until recently the most common synthetic route to Blatter radicals was the oxidative cyclisation of amidrazones (**30**) via a triazabutadiene (**28**) intermediate, Scheme 2.1.2, as developed by Neugebauer *et al*. in the late 1970s.[32] The outcomes of this pathway are strongly affected by the purity of the initial amidrazone (**30**), which is difficult to synthesise and purify.[26, 33] To exploit the intriguing properties expressed by Blatter radicals, more facile routes to Blatter radicals were required.

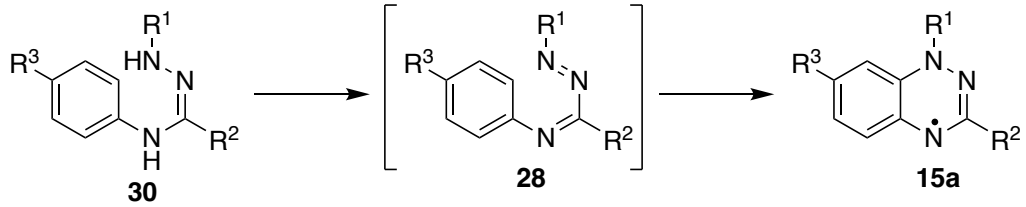

Scheme 2.1.2. Neugebauer's classical Blatter radical synthesis.

Recent Advances in Blatter Radical Synthesis

Within the original publication by Blatter *et al.*, an alternate pathway to the target molecule (**15a**) was mentioned.[23] More recent work has capitalised upon this and refined the synthetic strategy (Scheme 2.1.3). *N'*-(het)arylhydrazides (**31**) are readily synthesised from the corresponding hydrazides and 1-halo-nitroarenes, followed by reduction and cyclodehydration to radicals **15**. This useful synthetic strategy towards the Blatter radical avoids the need to isolate or purify the troublesome amidrazone intermediate (**30**); however, the versatility is limited by the poor scope for functionalisation.[26, 33] Although the reduction and cyclodehydration steps appear to be high yielding for a range of substrates, the reaction between the 1-halo-2-nitroarene and the hydrazide has a narrow substituent tolerance, limited to more electron withdrawing substituents. Yields ranging from 85 % to 17 % for the more electron-withdrawing CF_3 substituents at R^1 and R^3, thus the broad practicality of this synthetic strategy is limited.[26]

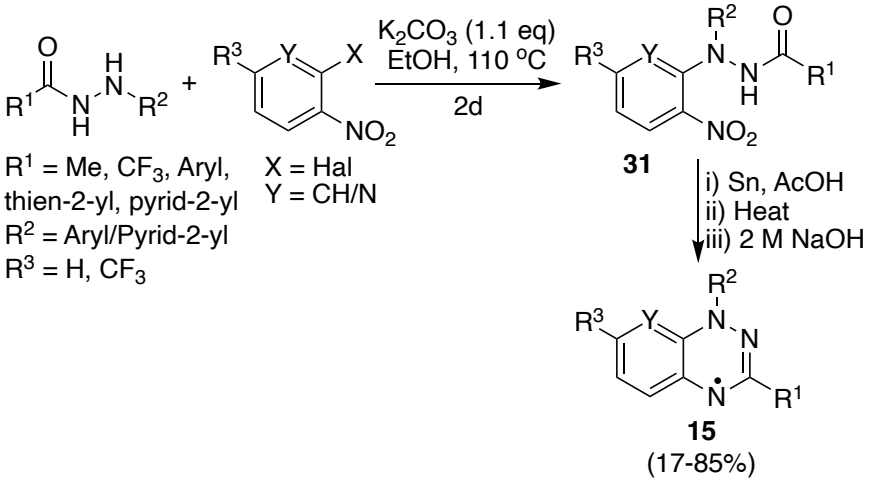

Scheme 2.1.3. Blatter radical (**15**) synthesis via an N'-(het)arylhydrazide (**31**) species, as alluded to in Blatter's original paper.

Another more recent advance has been the development of a synthetic route via Aza-Wittig chemistry (Scheme 2.1.4).[28] Again, this is advantageous as it avoids the isolation or purification of the problematic amidrazone (**30**).[33] This work builds on that of Huisgen *et al.* from 1969 which took N-(4-methoxyphenyl)iminophosphorane (**34**) and diphenylnitrylimine (**35**) and obtained a methoxy-substituted radical in a low yield of 5.5 % (Scheme 2.1.5).[34] In this work, instead of the diphenylnitrylimine (**32**), 1-(het)aroyl-2-diazenes (**33**) were utilised to much greater success. The synthetic route did however fail to yield a methoxy substituted Blatter radical at the *C*(7) position and instead returned the corresponding benzotriazinone (**36**).[13] This could be due to the electron-donating substituent destabilising the SOMO of the radical with respect to oxidation.

Retrospectively, Huisgen's low yields could tentatively be attributed to the use of the methoxy-substituted iminophosphorane leading to formation of the benzotriazinone.

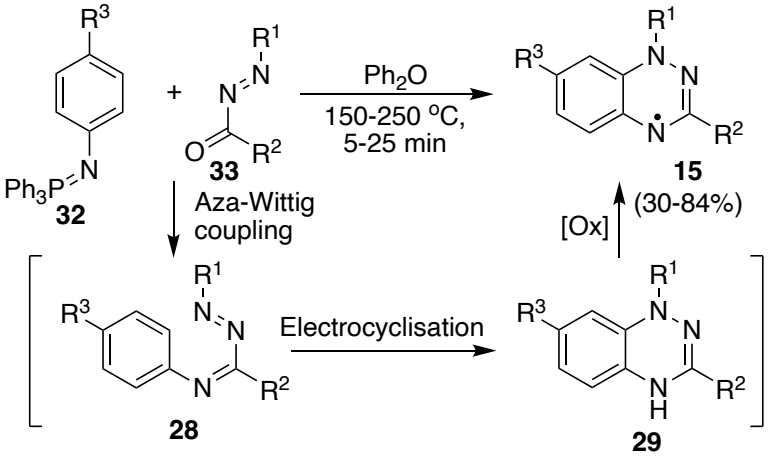

Scheme 2.1.4. Synthetic route to Blatter radicals (**15**) via Aza-Wittig Chemistry.

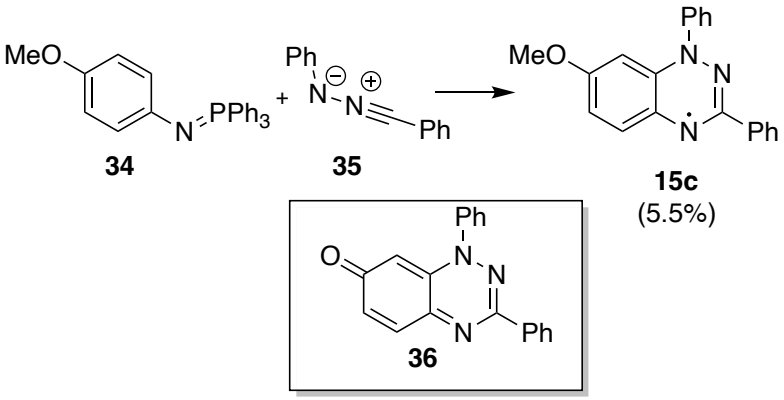

Scheme 2.1.5. Huisgen's original Blatter radical synthesis, which yielded the target radical in low yields. Insert: the benzotriazinone oxidised product obtained when trying to obtain a methoxy-substuted Blatter radical in Scheme 2.1.4. This could be a contributing factor to the low yields witnessed by Huisgen.

Blatter radicals can also be synthesised with a variety of substituents at the *C*(3) position, via the corresponding benzotriazine (**37**) (Scheme 2.1.6). This conversion provided varying degrees of success, from no yield of the target radical in the cases of R = NHPh, CN or $PO(OEt)_2$ to moderate yields when R = S^{t}Bu, CCPh or CF_3.[35] However, it should be noted that these yields do not account for the species being 'analytically pure' and yields after purification were significantly lower. Moreover, the authors of this study elude to the fact that the precursor benzotriazines are not readily available and therefore must also be synthesised. Upon further exploration of the literature, it is found that the benzotriazines can be synthesised relatively easily, in moderate yields (Scheme 2.1.7).[36] However, this is still multistep, and proceeds via diazonium chemistry, which generally suffers from drawbacks with regards to safety.[37] Nonetheless, this conversion is particularly interesting as the *C*(3) position may be varied and could behave as a scaffold

for the coupling of Blatter radicals to other molecules, including biomolecules and other radicals.

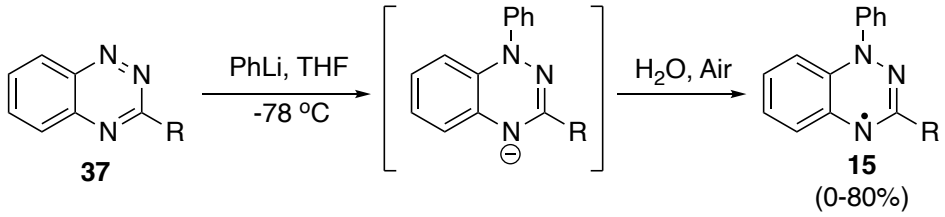

Scheme 2.1.6. Synthesis of C(3) functionalised Blatter radicals from benzotriazines.

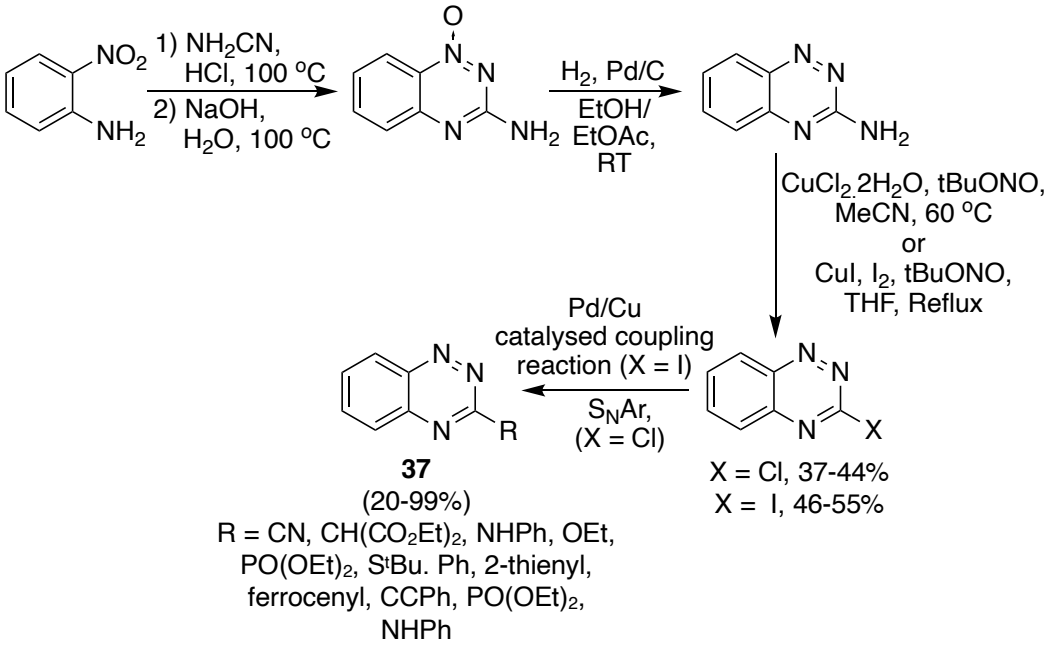

Scheme 2.1.7. Synthesis of benzotriazines (**37**) for the development of C(3) functionalised derivatives of Blatter radicals (**15**) (Scheme 2.1.6).

The final synthetic route discussed, and the one of most interest with regards to this work, is that of an unusual rearrangement of Nitron (**6**) (Scheme 2.1.8). Nitron, a common N-heterocycle utilised in the detection of nitrates and perchlorates, has been found to hydrolytically ring open and re-cyclise to an amido-Blatter radical (**24**).[21, 38, 39] Mechanistically, it is proposed that following ring-opening to the amido-substituted amidrazone (*Z*)-(**38**), isomerism yields (*E*)-(**38**), the intermediate in more typical Blatter radical syntheses. Blatter radicals could then form in one of two processes as shown in Scheme 2.1.8.[21] As with the syntheses discussed above this avoids direct isolation of the amidrazone which is beneficial with regard to obtaining higher yields.[28, 33] Interestingly the Nitron zwitterion is in tautomeric equilibrium with a stable carbene which could have implications in this unusual rearrangement to Blatter radicals.

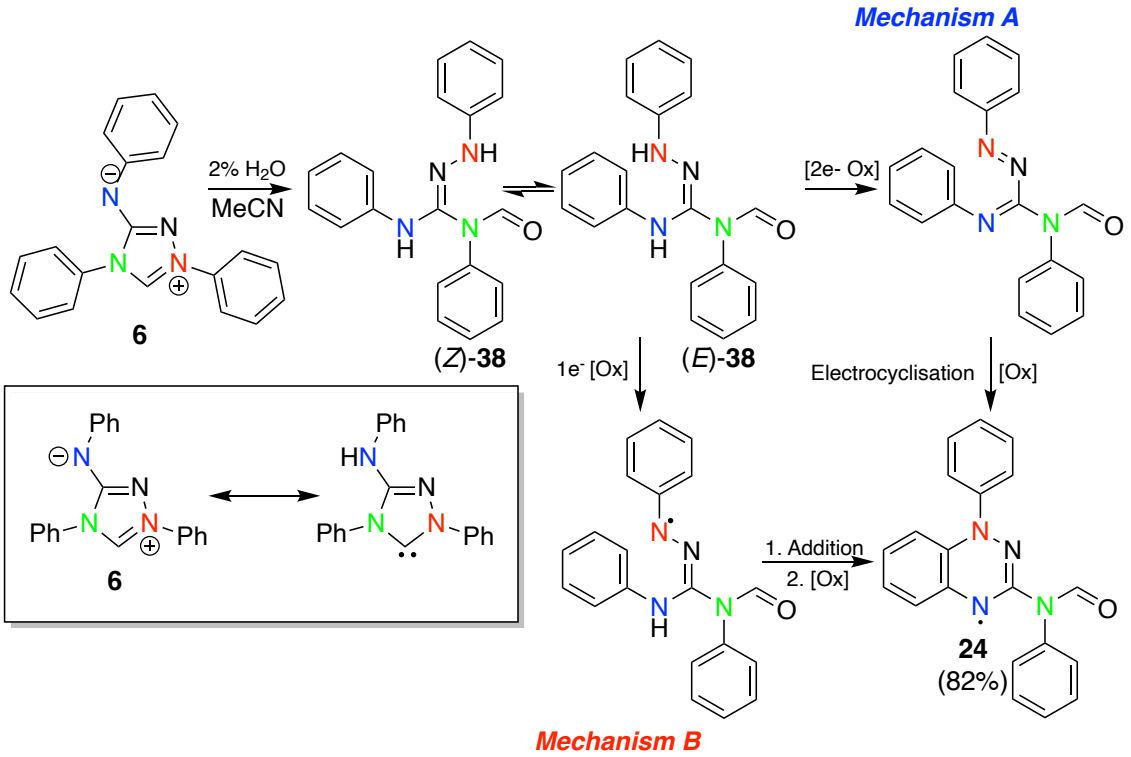

Scheme 2.1.8. The Nitron (**6**) to amido-Blatter radical (**24**) rearrangement via in situ amidrazone formation (**38**), isomerisation, cyclisation and oxidation. There are two potential mechanisms for this to occur. Insert shows the tautomerisation of Nitron.

This route to a novel analogue of the parent Blatter radical (**15**) is particularly interesting as the amido group provides a new handle for synthetic manipulation. So far, the amido group has been hydrolysed to an amino group (**25**) (Scheme 2.1.9) however, future exploration of this will hopefully develop further chemistries.

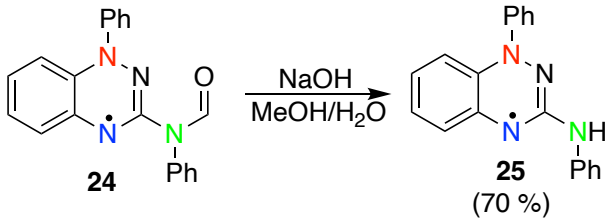

Scheme 2.1.9. Hydrolysis of the amido-Blatter radical (**24**) to the amino-Blatter radical (**25**).

The ease of this conversion and high yields of radical obtained are particularly advantageous; however, as of yet, the synthetic diversity of this rearrangement is untested. Moreover, despite this rearrangement being straightforward, the synthesis of Nitron is more complex. Section 2.2 discusses the development of a more straightforward synthetic strategy to Nitron and further derivatisation. Section 2.3 further explores the Nitron to Blatter-type radical conversion in greater detail, with a particular focus on the role of the initial tautomerisation of Nitron.

Reactions and Post-synthetic Modifications of Blatter Radicals

The inherent stability of Blatter radicals makes them apposite for a variety of post-synthetic modifications. In doing so, the scope for Blatter radical use within areas such as biologics, materials, electronics and photonics becomes greater. Post-synthetic translations have, in general, focussed on modification via protecting group chemistry as well as cross-couplings.[24, 27, 40] With regards to protecting group chemistry, a selection of hydroxyl group transformations have been enacted, providing access to a wider range of analogues (e.g. Scheme 2.1.10).[24] These transformations provide access to a wider span of Blatter radical derivatives; however, it should be noted that the radical chosen with the trifluoromethyl group in the C(7)-position is described as a 'super-stable' radical. This is because the CF_3 group stabilises the SOMO, whilst also blocking oxidation of the radical, which usually occurs at this position (Scheme 2.1.5).[41] This raises the question as to whether the CF_3 group provides greater tolerance to the reaction conditions, and whether a species without the CF_3 would survive the reactions to the same extent.

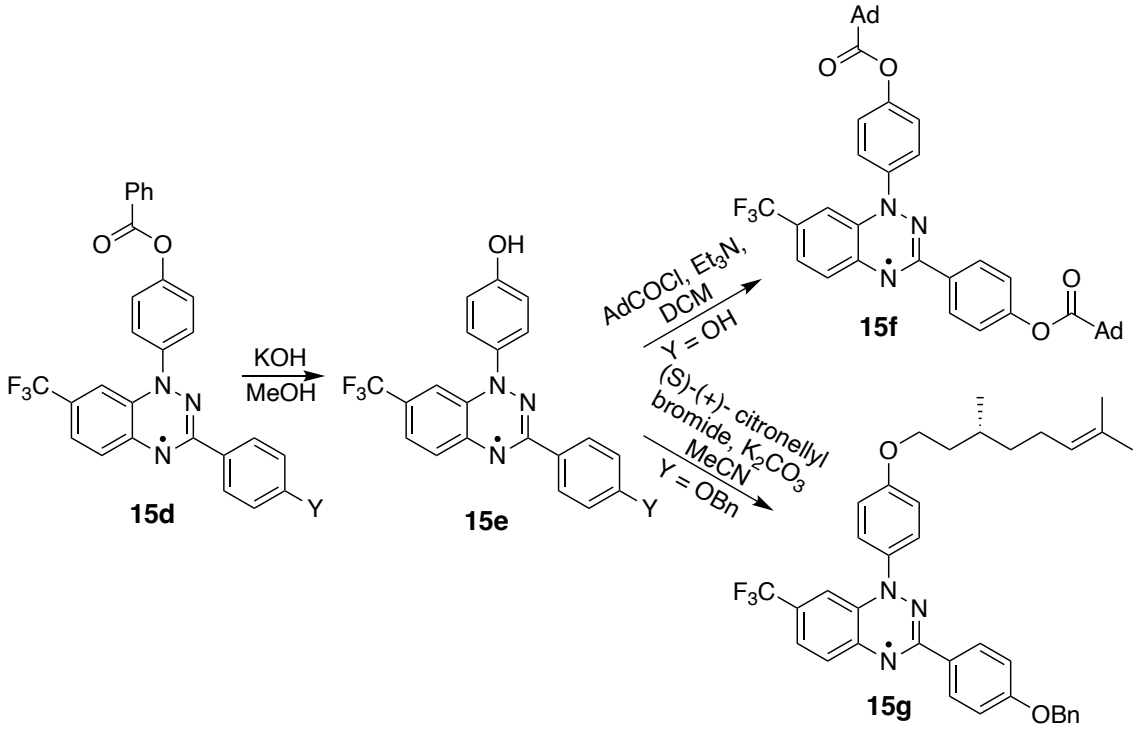

Scheme 2.1.10. Exploration of the post synthetic modifications of Blatter radicals through the use of protecting group chemistry.

Iodo-substituted Blatter radicals (**15h**) have been implicated in cross-coupling reactions to further derivatise Blatter radicals (Scheme 2.1.11), providing access to **15i**.[24, 40] With further modification this is particularly interesting as it could conceivably be used to incorporate a radical species into a polymer backbone. Intriguingly with this species, reaction occurs at direct positions with responsibility for SOMO stabilisation (Figure 2.1.1).[29] Nevertheless, the radical character remains intact demonstrating the superior stability of Blatter radicals.

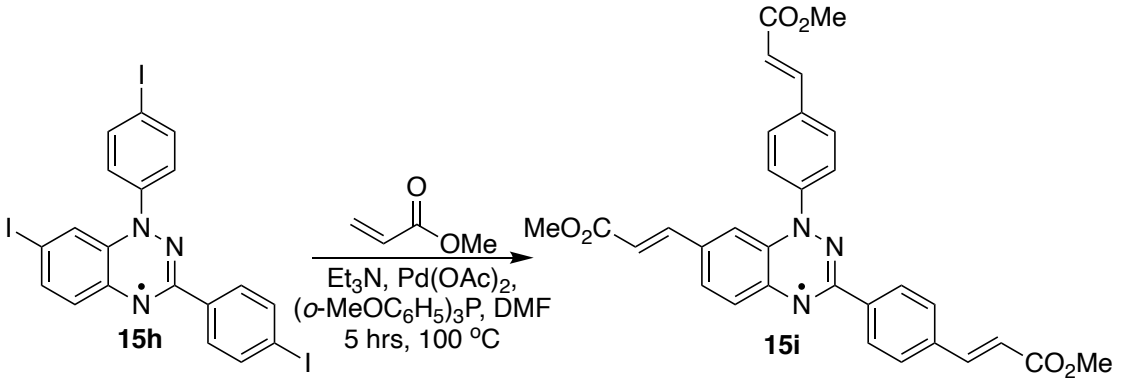

Scheme 2.1.11. Cross coupling of an iodo-substituted Blatter radical (**15h**) with methyl acrylate to a methyl acrylate-substituted Blatter radical (**15i**).

Blatter radicals (**15**) may partake in a reductive ring contraction in the presence of zinc and acid, known as Barton's reductive ring contraction (Scheme 2.1.12).[42, 43] Recent work by Koutentis *et al*. has optimised this, reducing the equivalents of zinc and time required. This transformation gives access to a variety of benzimidazoles (**39**), significant moieties within the pharmaceutical sector which find use as anticancer agents, antivirals, anti-HIV species and more.[44, 45] Mechanistically, the transformation is believed to exhibit a reductive ring opening, followed by recyclization and loss of ammonia. Despite the existence of many more versatile, straightforward synthetic routes to benzimidazoles, this transformation is still of interest.

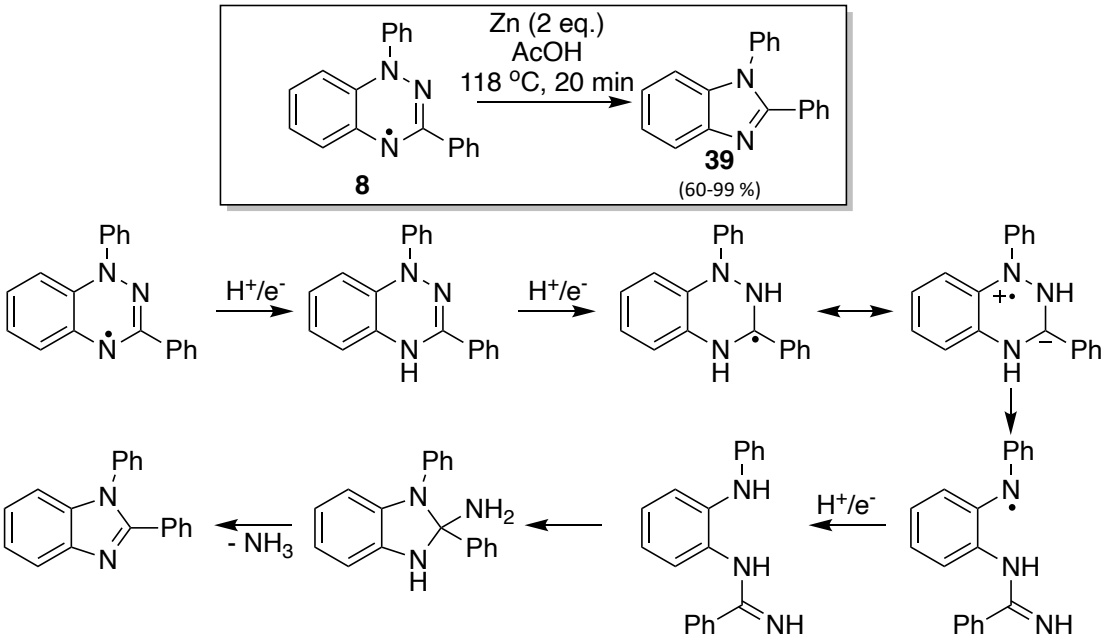

Scheme 2.1.12. Barton's ring contraction of the parent Blatter radical (**8**) with insert showing the refined conditions as developed by Koutentis et al.

Through considered functionalisation and post-synthetic modification of Blatter radicals (**15**), planar radicals can be obtained (Scheme 2.1.13).[46] Planarity alters the solid-state packing of Blatter radicals and hence the bulk magnetic properties. Moreover, the planarization also allows for further spin delocalisation due to greater π overlap between rings.[30, 46] Synthetically, these species were obtained via a benzotriazine (**37a**) which was then coupled to a further aryl ring by a sulphur (**37b**) or oxygen (**37c**). Finally, the planar Blatter radical (**40**) was formed in low yields via treatment with ^{t}BuLi and oxidation in air.[46]

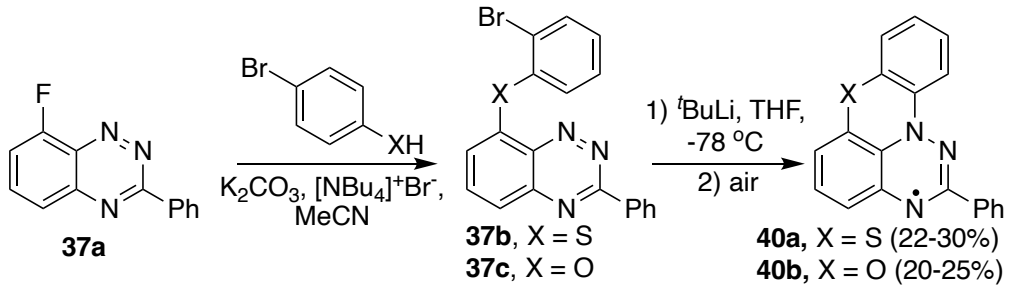

Scheme 2.1.13. Synthesis of a planar Blatter radical (**40**), where X = S or O, from benzotriazines (**37**).

Planar Blatter radicals may also be obtained in higher yields through radical, Pschorr-type cyclisation processes (Scheme 2.1.14), as opposed to the anionic process described in Scheme 2.1.13. Access to the pre-cyclised species is similar to that in Scheme 2.1.13 but with sodium hydride used as a slightly more forcing base. The important aspect of this synthesis is the requirement of an amino, or acetylated amino group, ortho to the

phenolic carbon. This then undergoes a diazotisation to provide the radical centre, which couples at the *N*(1) position.[30, 47]

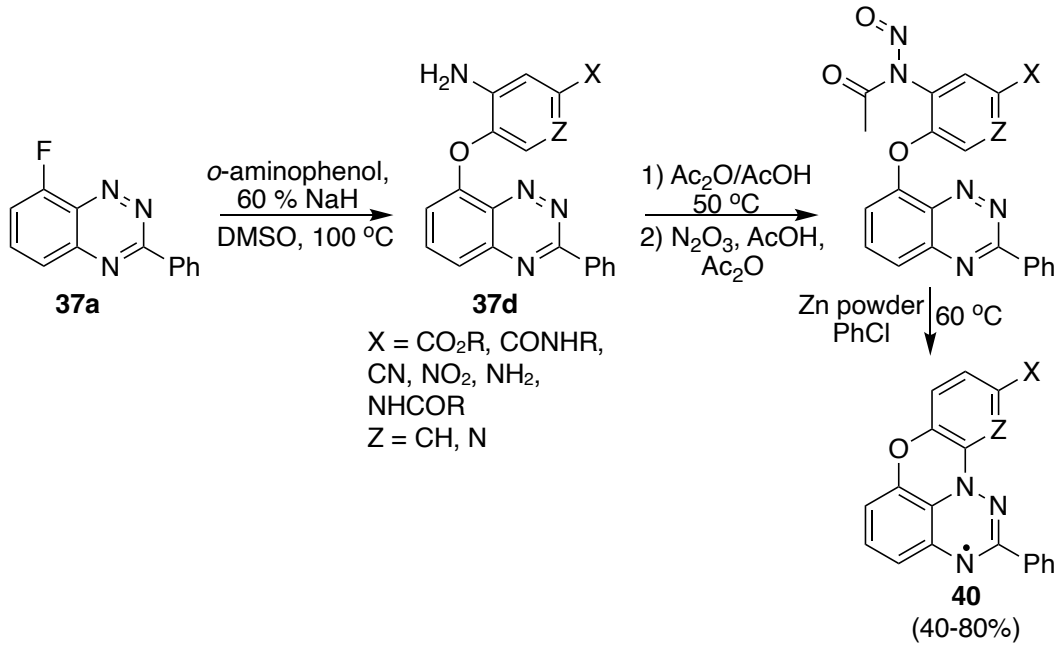

Scheme 2.1.14. Synthesis of planar Blatter radicals via a Pschorr-type radical cyclisation.

2.1.2. Properties of Blatter Radicals

Growing interest in persistent radicals is in the main attributed to the magnetic properties arising from the paramagnetic nature of open-shell molecules.[11, 12] Less discussed are the photochemical properties of persistent radicals, which in general are poor due to fast, non-radiative relaxation of the S_1 state which quenches emission. Nonetheless, there are some known examples, of which Blatter radicals are one.[29, 48, 49]

Photochemical Properties of Persistent Radicals

In general, radicals do not show fluorescent properties, attributed to rapid S_1 relaxation as well as a tendency to photodegrade upon excitation; as such, many have found uses as profluorescent moieties.[29, 49, 50] Profluorescence refers to regaining of fluorescent properties of the radical upon reformation of a closed-shell species. For example, verdazyl radicals (**13**) have been used as profluorescent radical probes to detect radical species. In their open-shell state, these are non-fluorescent due to quenching of emission; however, upon recombination with a radical species, open-shell character is lost and fluorescence is switched on (Figure 2.1.4).[49]

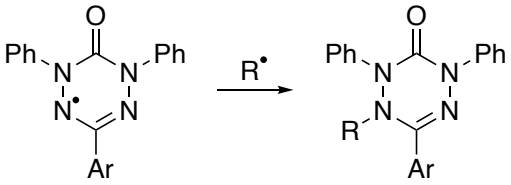

Figure 2.1.4. The use of profluorescent verdazyl radicals (**13**) as radical probes. Fluorescence is regained upon recombination and loss of radical character.

Despite this, there still exists radical species with photochemical properties. Furthermore, those species which are fluorescent should be expected to have higher quantum yields than their closed-shell partners as there is no propensity for intersystem crossing or charge recombination.[29, 51] The polychlorotriphenylmethyl radical (**11**) has been found to be photoreactive and undergoes a light-induced ring closure to a perchlorophenylfluorenyl (**41**) species (Figure 2.1.5). Product **41** still has radical character as proven by EPR studies. Conversion was found only to occur in solution, with the rate-determining step being hydrogen abstraction from the solvent.[37] Although this conversion is interesting it limits the use of radical **2** in applications such as open-shell electronics as these require photochemical robustness.

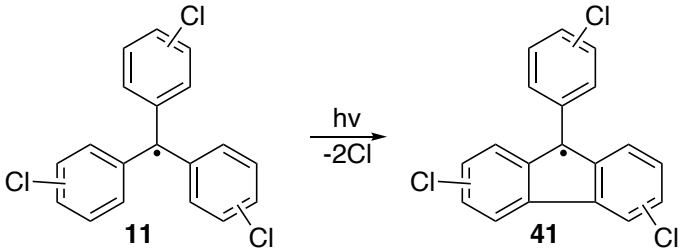

Figure 2.1.5. Photochemical ring closure of radical **11**. This limits its usefulness in photochemical applications.

Another interesting open-shell organic species is the (3,5-dichloro-4-pyridyl)bis(2,4,6-trichlorophenyl)methyl radical (**42**), which is based upon radical (**10**) (Figure 2.1.6). This is photoluminescent and has the highest fluorescent quantum yields observed for an open-shell molecule of 0.81 when recorded in a matrix of diethyl ether, isopentane and ethanol at 77 K.[50] The advantage of radical (**42**) is that it provides enhanced stability, but also that the pyridyl groups provide scope for a reversible proton response, allowing for tuning of the emission wavelength. Fluorescent quantum yields in this case are highest in more apolar environments, at lower temperatures, due to the increased rigidity of the environment. This is supported by the encapsulation in a rigid poly(methyl methacrylate) (PMMA) film, which at room temperature enhanced the quantum yield by 10-fold with respect to solution.[40]

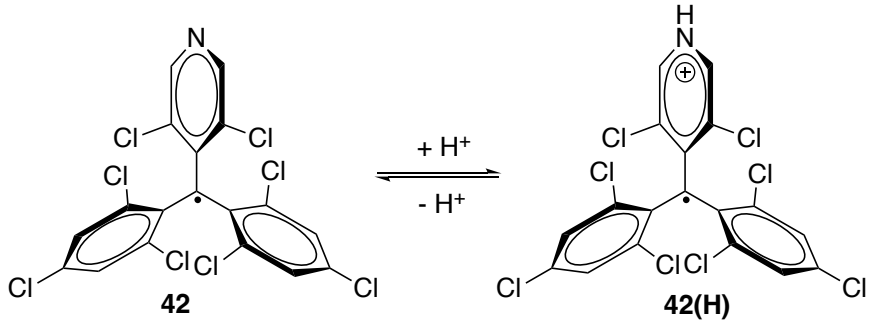

Figure 2.1.6. The (3,5-dichloro-4-pyridyl)bis(2,4,6-trichlorophenyl)methyl radical (**42**) which has the highest reported fluorescence quantum yield for an open shell molecule. It also takes advantage of a pyridine nitrogen which can be used to tune the photochemical properties.

Photochemistry of Blatter Radicals

Shown in Figure 2.1.7 is the absorption spectrum for the parent Blatter radical (**15a**) in a variety of solvents, normalised with respect to the most prominent transition at 272 nm. This transition was assigned to the SOMO-1 to lowest unoccupied molecular orbital (LUMO) transition which appears as a benzenoid to quinoidal transition facilitated by the coplanarity of the fused rings. With regards to the SOMO-LUMO transition, this transition is particularly weak and found at about 550 nm, characterised by a Laporte forbidden π-π* transition.[29]

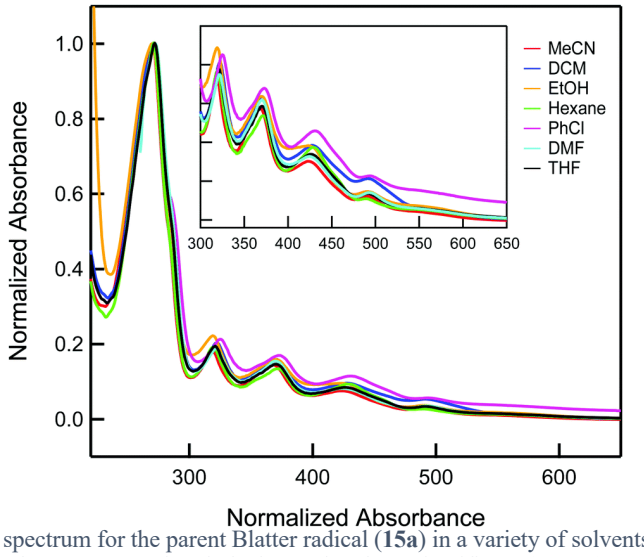

Figure 2.1.7. Absorbance spectrum for the parent Blatter radical (**15a**) in a variety of solvents. Reproduced from Ref. 29 with permission from the Centre National de la Recherche Scientifique (CNRS) and The Royal Society of Chemistry.

Of greater relevance are the photoluminescence properties of the Blatter radical (**15a**) and Figure 2.1.8 shows the emission spectrum in a selection of solvents for excitation at 490 nm. The emission when in DCM is much broader in comparison to other solvents, where vibronic structure has been resolved. Moreover, in DCM the emission experiences a blue shift in comparison to the other solvents used which has been attributed to ground state solute aggregation due to limited solvation by solvents other than DCM.[29]

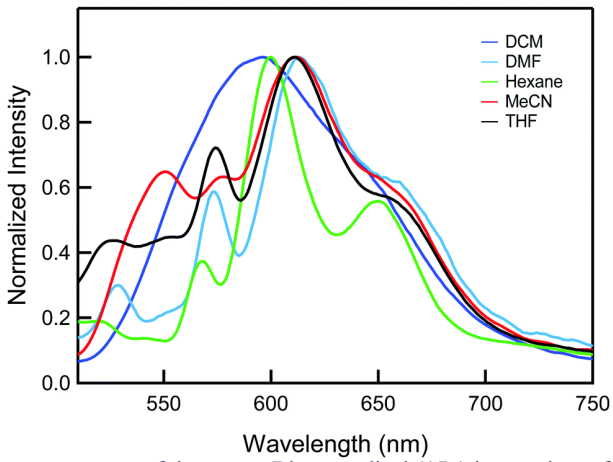

Figure 2.1.8. The fluorescence spectrum of the parent Blatter radical (**15a**) in a variety of solvents. Reproduced from Ref. 29 with permission from the Centre National de la Recherche Scientifique (CNRS) and The Royal Society of Chemistry.

The emission properties were not just investigated at 490 nm excitation, but a range of wavelengths. In particular, excitation at ~370 nm was curious as emission was very broad, spanning the visible spectrum and therefore being classed as pure white light.[29] There are very few reports of white-light emission from a single molecule and the majority are combinations of chromophores or metal complexes with mixed ligands.[51, 52] Blatter radicals (**15**) are particularly interesting, despite the very low quantum yield, as further functionalisation could improve upon this. The emission properties of the Blatter radical were studied within a PMMA film at a variety of concentrations of radical. Increasing the radical concentration was found to decrease the fluorescence intensity for wavelengths greater that ~500 nm. This could be attributed to aggregation of the radical leading to fluorescence quenching, supported by the fact that the spectra more resemble solution phase spectra at lower radical:PMMA ratios.[29]

Magnetochemistry of Persistent Radicals

The paramagnetic nature of persistent radicals results in intriguing bulk magnetic properties. Consequently, organic magnetic materials have been of keen interest for a considerable period of time. Development, however, has been hindered due to the difficulty in obtaining stable radicals at room temperature with the desired properties. Recent advances, coupled with a drive to develop more sustainable materials, could see the replacement of traditional magnetic materials with greener organics.[11, 53]

As organic species contain only relatively light elements, the magnetic behaviour is solely determined by the isotropic magnetic exchange interactions. All anisotropic contributors

to magnetic exchange, as well as spin-orbit and hyperfine interactions may be considered negligible. As such, they can be thought to behave magnetically isotropically, and be described by an effective spin Hamiltonian at zero applied magnetic field (Equation 2.1.1, J_{ij} is the effective exchange interaction and S is the total spin quantum number for magnetic centres i and j).[11]

$$H = -2\sum J_{ij} S_i S_j \qquad \textbf{Equation 2.1.1}$$

Within Equation 2.1.1, J_{ij} describes the effective exchange parameter, with a positive value corresponding to a parallel spin alignment in the ground-state known as ferromagnetism. A negative value for J_{ij} corresponds to an antiparallel alignment in the ground-state, giving rise to antiferromagnetism. At high temperatures, open-shell organics behave paramagnetically with no spin order; however, as temperature decreases the thermal energy becomes comparable to the magnetic exchange interactions, allowing for spin ordering.[11]

Ferromagnetic interactions only arise from orthogonal arrangement, with an overlap integral of zero between two SOMOs of each interacting radical centre. Antiferromagnetic interactions are observed when the overlap integral is non-zero for non-degenerate SOMOs. These interactions have been shown to take place between discrete molecules as well as within molecules where multiple spin centres have been coupled together. Intermolecular, through-space, interactions have been found to depend mainly on the isotropic exchange interactions between the SOMOs of the nearest adjacent molecules. If these interactions can be assembled correctly in three-dimensions, bulk magnetic properties can be obtained.[11]

Intramolecular coupling of radical species is much more studied within the field of organic molecular materials. In part this is due to the greater control over the interactions of open-shell centres. When coupling two open-shell, high energy, orthogonal orbitals in close proximity, the tendency is for the species to adopt a high-spin triplet state to lower the electron energy, in accordance with Hund's rule. The magnetic properties are however determined not by this, but by the symmetry and topology of the SOMO orbitals. It has been found that in general, radicals linked as *meta*-substituents on a benzene ring

form ferromagnetic interactions, whereas radicals linked as *para*-substituents on a benzene ring have a tendency to form antiferromagnetic interactions; for example, the verdazyl-diradicals as seen in Figure 2.1.9. EPR experiments at 77 K indicate a triplet state, suggesting that even at low temperatures, interaction is possible to form a thermally accessible triplet electron state. It should be noted that only weak interactions between radical centres were found for these species.[11, 12]

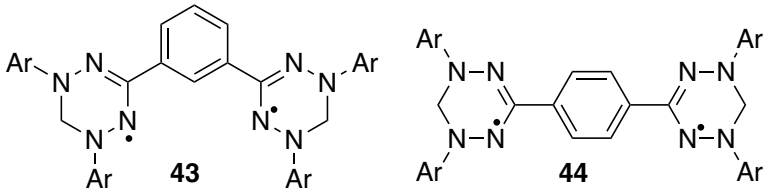

Figure 2.1.9. Verdazyl diradicals coupled through benzene via meta- and para- interactions, altering the magnetic properties.

Magnetochemistry of Blatter Radicals

The magnetochemistry of single-radical centred molecules is dependent upon solid-state structure (Figure 2.1.2). The molecular structure of a Blatter radical is not planar and instead the two phenyl groups are forced out of the plane by the unfavourable steric interactions of these groups with the ring.[30] In the solid-state this leads to a π-slip stacked packing arrangement, which allows the triazinyl centres to be in close proximity, permitting the transfer of magnetic information.[41]

Intermolecular magnetic coupling of Blatter radicals has been well explored and the parent Blatter radical (**15a**) shows antiferromagnetic ordering at low temperature.[54] The Weiss constant of -2.2 K indicates a very weak antiferromagnetic interaction and poor communication between molecules. In the initial magnetic studies, a derivative of (**15**) with a chlorine in the *C*(7)-position was also explored and found to have far more interesting magnetic properties. It exhibited a broad maximum in its magnetic susceptibility at 142 K corresponding to short range, low dimensional antiferromagnetic ordering with strong communication between molecules. This behaviour was attributed to a Heisenberg exchange-coupled alternating linear chain model. The strong interaction was postulated to be due to the formation of radical pairs which are closely packed, within the van der Waals' distance.[54]

The so-called 'super-stable radical' (**15j**) was explored due to the increased stability with respect to oxidation and therefore greater propensity for use in novel materials. Packing of this in the solid-state is depicted in Figure 2.1.10 and shows a slippage angle of 27.8°. It was found that this radical followed Curie-Weiss behaviour down to 10 K with a Weiss constant of +1.41 K, suggesting weak ferromagnetic interactions. The behaviour was attributed to a 1D Heisenberg ferromagnetic model along the direction of the close, molecular π-stacking. This example is of interest as it displays ferromagnetic ordering as opposed to antiferromagnetic as seen for other Blatter radical species; however, it has been found that weak antiferromagnetic interactions between the stacks quench the bulk ferromagnetism.[41] Therefore, further work is required to develop magnetic materials from single molecule Blatter radicals.

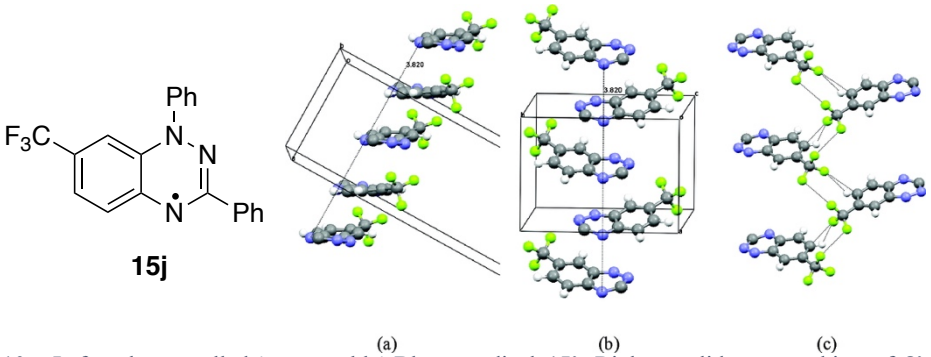

Figure 2.1.10. Left - the so-called 'super-stable' Blatter radical **15j**. Right - solid-state packing of **8i** along the crystallographic a axis, showing the π-slippage. Adapted with permission from C. P. Constantinides, P. A. Koutentis, H. Krassos, J. M. Rawson and A. J. Tasiopoulos, *J. Org. Chem.*, 2011, **76**, 2798–2806. Copyright 2020 American Chemical Society.

2.1.3. Applications of Blatter Radicals

Electronics

A pressure-sensitive 2D tetracyanoquinodimethane (TCNQ) salt of a Blatter radical (**15a**) was reported in the 1990s; however, Blatter radicals in electronics have witnessed a greater surge of interest only in recent years. The compound in question was a solid with semiconducting properties and an 'unusual' dependence of conductivity with respect to pressure at ~2 kbar. The solid-state structure (Figure 2.1.11) consists of a set of two TCNQ dimers separated by a skewed TCNQ molecule. The lack of discrete stacks of TCNQ leads to the formation of layers of Blatter radicals between these TCNQ dimers. Figure 2.1.11 shows the dependence of conductivity on pressure for the semiconductor. As seen, increasing the pressure enhances the conductivity attributed to an increase in orbital overlap, reducing the band gap of the material to zero.[53]

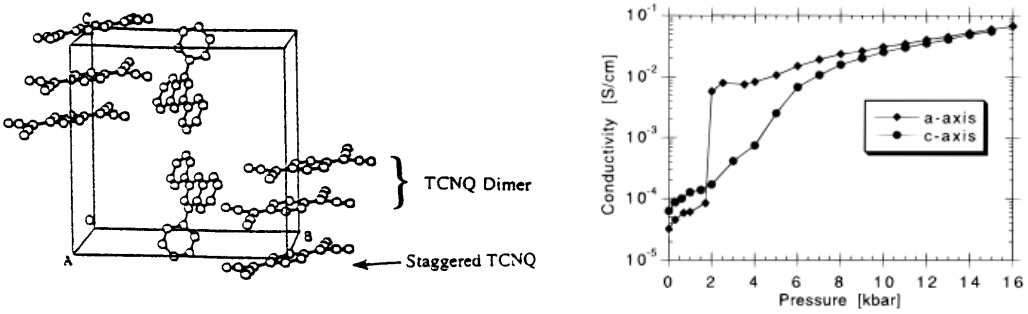

Figure 2.1.11. Left – solid-state packing of the TCNQ dimers, separated by a staggered TCNQ molecule and with layers of Blatter radical (**15a**) between the TCNQ layers. Adapted with permission from K. A. Hutchison, G. Srdanov, R. Menon, J. C. P. Gabriel, B. Knight and F. Wudl, *J. Am. Chem. Soc.*, 1996, **118**, 13081–13082. Copyright 2020 American Chemical Society.

More recent work has described a pyrene-fused Blatter radical as a quantum bit, referring to a unit of quantum information in quantum computing. The radical was deposited on copper beryllium plates, with the copper behaving as a good conductor and beryllium as the dopant. The quantum coherence time, the lifetime of the superposition state, which correlates to the time available for a quantum calculation, was similar to that of other molecular systems. The application of Blatter radicals to quantum computing extends way beyond the realms of organic chemistry, demonstrating the importance of open-shell molecules to current and future technologies.[54]

Metal Complexes

Blatter radicals provide advantages as open-shell ligands due to their greatly enhanced air and moisture stabilities. The first reported Blatter radical, designed specifically for metal complex coordination, was a C(3)-pyridyl variant (**15k**) (Figure 2.1.12). Copper(II) hexafluoroacetylacetonate dihydrate ($Cu(hfac)_2.2H_2O$) was used to provide a coordination centre, owing to copper's azaphilicity. The crystal structure of compound (**45**) (Cu(**15k**)$hfac_2$) showed a Jahn-Teller distorted complex, with the radical bound to the complex in a bipyridyl ligand-type fashion. The magnetic properties of this complex were explored, and it was found to display ferromagnetic coupling between the copper(II) centre and the radical ligand. At lower temperatures, further antiferromagnetic couplings arose due to interaction of neighbouring radical centres. The ferromagnetic copper(II)-radical interactions determined here are larger than those observed for the copper(II)-verdazyl radical type complex which has also been explored. This was attributed to the larger Jahn-Teller distortion for the bonds coupled to the verdazyl radical, increasing the metal-radical distance.[55]

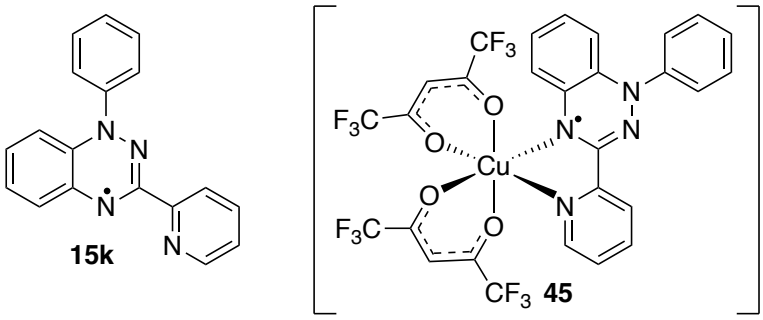

Figure 2.1.12. The pyridyl Blatter radical (**15k**) and the copper complex formed from this (**45**).

Further studies of radical **15k** have formed manganese(II), iron(II), cobalt(II) and nickel(II) metal complexes. It was found that Mn(II) and Fe(II) couple antiferromagnetically to the radical centres, whereas Ni(II) and Cu(II) couple ferromagnetically. The interaction for Co(II) was difficult to determine experimentally and theoretically. Observations were explained by consideration of the pseudo-octahedral metal centres: the SOMO of the Blatter radical may be considered as a π-type ligand. Mn(II) and Fe(II) have non-orthogonal (non-zero) orbital overlap with the π-system of the radical and their own t_{2g}. As mentioned previously, the requirement for ferromagnetism is orthogonality of interacting spins, and a lack of orthogonality results in antiferromagnetism.[2] With regards to Ni(II) and Cu(II), unpaired electrons are located within the e_g orbital, which has an orthogonal (zero) overlap integral with the π-type ligand.[55,56]

Biological Efficacy

The biological efficacy of Blatter radicals is poorly explored, and work within our group is progressing this area. The oxidation product of a benzotriazinyl radical (**36**) has however been explored for its anti-cancer properties. Access to the benzotriazinone requires forcing conditions of 10 equivalents of MnO_2 but can provide high yields (Scheme 2.1.15). The cytotoxicity of (**36**) was similar to that of pleurotin (**46**), a naturally occurring antibiotic and anti-cancer agent. The Blatter radicals in this case are pyridyl-substituted as this has been reported to alter cytotoxicity against some cancer cell lines. As well as the oxidation product, precursor Blatter radicals were also explored. Anti-cancer activity of all substrates was attributed to the inhibition of thioredoxin reductase (TrxR), which catalyse NADPH-dependent reduction of the protein thioredoxin. TrxRs, a class of selenium containing enzymes, have roles in cell growth and transformation, protection against oxidative damage and the recycling of ascorbate.[57,58]

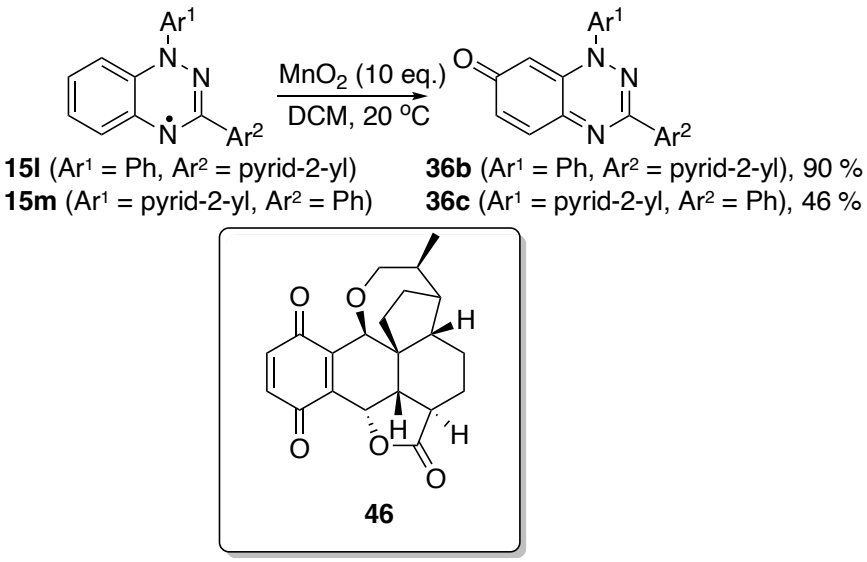

Scheme 2.1.15. Oxidation of Blatter radicals (**15**) to benzotriazinones (**36**), which have been shown to be good anticancer agents. Insert shows pleurotin (**46**).

Radicals exhibited similar cytotoxicity towards breast and prostate cell lines however were 13 and 105 times less active than the benzotriazinone products respectively. Nevertheless, both showed promising cytotoxicity against breast (MCF-7) and prostate (DU-145) cancer cell lines (Table 2.1.1). In particular, cytotoxicity against the DU-145 cell line was promising and merits further exploration. Compounds were compared to TEMPO (**12**), which in these conditions, against these two cancer cell lines proved to be very non-toxic.[55]

Table 2.1.1. Summary of the IC_{50} values of a selection of radicals and benzotriazinones, summarised in Scheme 2.1.15, against breast (MCF-7) and prostate cancer (DU-145).

Compound	IC_{50} DU-145 / μM	IC_{50} MCF-7 / μM
TEMPO (12)	151.400 ± 0.03	>999
15l	3.140 ± 0.179	34.740 ± 6.236
15m	3.177 ± 0.154	26.415 ± 2.538
36a	0.245 ± 0.003	0.303 ± 0.009
36b	0.241 ± 0.011	0.277 ± 0.002

Benzotriazinyl radicals have also been implicated in the mode of action of Tirapazamine (**47**), a stage-III clinical trial, hypoxic tumour selective anti-cancer agent (Scheme 2.1.16). Rapidly growing tumours become depleted in oxygen as their growth surpasses blood supply. Within normal tissue, typical pO_2 values are in the range of 40-60 mmHg, compared to tumorous tissue with pO_2 around 10 mmHg. With regards to typical therapies, this creates problems as hypoxic tumours become less susceptible to radiation and other cancer drugs. This is typically due to the disorganised nature of blood vessels

about the tumour, disrupting delivery of cancer drugs; moreover, oxygen is required to ensure DNA damage is permanent. Such issues have led to the search for hypoxia-selective anticancer drugs such as Tirapazamine (**47**).[56, 57]

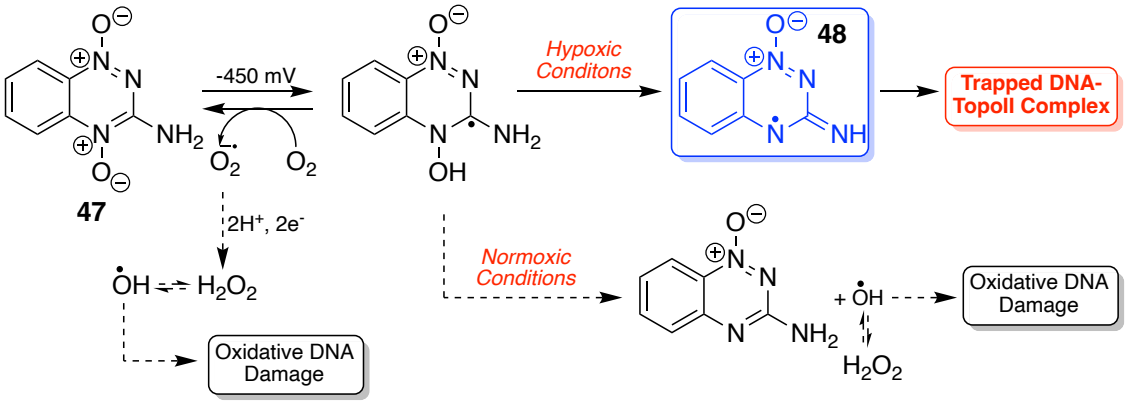

Scheme 2.1.16. Summary of the mechanism of action under hypoxic conditions, also shown is the proposed mechanism under normoxic conditions.

Tirapazamine (**47**), another 1,2,4-benzotriazine, is structurally comparable to a Blatter radical, particularly the amido- (**24**) and amino- (**25**) Blatter radicals derived from Nitron (**6**). Its mode of action is thought to be inhibition of DNA-replication, with DNA-Topoisomerase II (TopoII) adducts being the implicated source. The key intermediate thought to be responsible for formation of this adduct is the benzotriazinyl radical (**48**) highlighted in Scheme 2.1.16. Blatter radicals, although structurally different, perhaps could behave similar to Tirapazamine (**47**) and therefore warrant exploration in medicinal applications.[59]

2.1.4. Conclusions

Blatter radicals are an interesting class of persistent organic radical owing to their excellent stabilities, electrochemical properties and solid-state magnetochemistry. Interest and application has significantly increased in the past 20 years due, particularly due to synthetic developments which have improved access and increased the scope of Blatter radical derivatives.

Our group recently reported the unusual rearrangement of Nitron to Blatter radicals, which occurs spontaneously in acetonitrile. The remainder of this chapter discusses further exploration of this intriguing reaction.

2.2. Synthesis of Nitron Derivatives

2.2.1. Foreword

The following section highlights the development of an updated synthesis of Nitron (**6**), with less reliance on hazardous reagents and improved isolated yields. The synthetic strategy is fully evaluated including key by-products and the scope explored by varying the three aryl groups of Nitron (**6**). All Nitron derivatives were fully characterised and, where possible, crystal structures obtained. The conversion of the range of Nitron derivatives to Blatter radicals (**24**) was explored (Chapter 2.3) and potential application as organocatalysts also evaluated (Chapter 3).

2.2.2. Introduction

Nitron (**6a**), 1,4-diphenyl-3-phenylamino-1,2,4-triazolium inner salt, is a 1,2,4-triazolium which has traditionally been used in the detection of nitrates and perchlorates. Recently, it has received greater interest owing to the discovery of the unusual Nitron to Blatter radical rearrangement, as highlighted within Chapter 2.1.[21] The lack of attention until recently has meant that very little investigation has been completed into the synthesis and further derivatisation of Nitron. Traditionally, Nitron (**6a**) has been synthesised as highlighted in Scheme 2.2.1 where 1,3-diphenyl thiourea (**49a**) is first de-sulphurised with lead tetroxide to give a carbodiimide (**50a**). Subsequent reaction with phenyl hydrazine yields an amidrazone (**51a**) which is ring-closed by initial treatment with formaldehyde (**52a**) and oxidation with sodium nitrite and acetic acid.[58] There are various drawbacks to this synthesis: the current solvents used include benzene, which has been phased out due to its hazard profile; lead tetroxide is environmentally hazardous, with difficult disposal protocols; the final oxidation step is overly harsh, leading to over oxidation and decomposition of the triazolium; finally, there have been more recent developments in the synthesis of 1,2,4-triazoliums which can effect ring closure in a single, more high yielding step.[19] Some of these synthetic strategies are highlighted within Chapter 1.

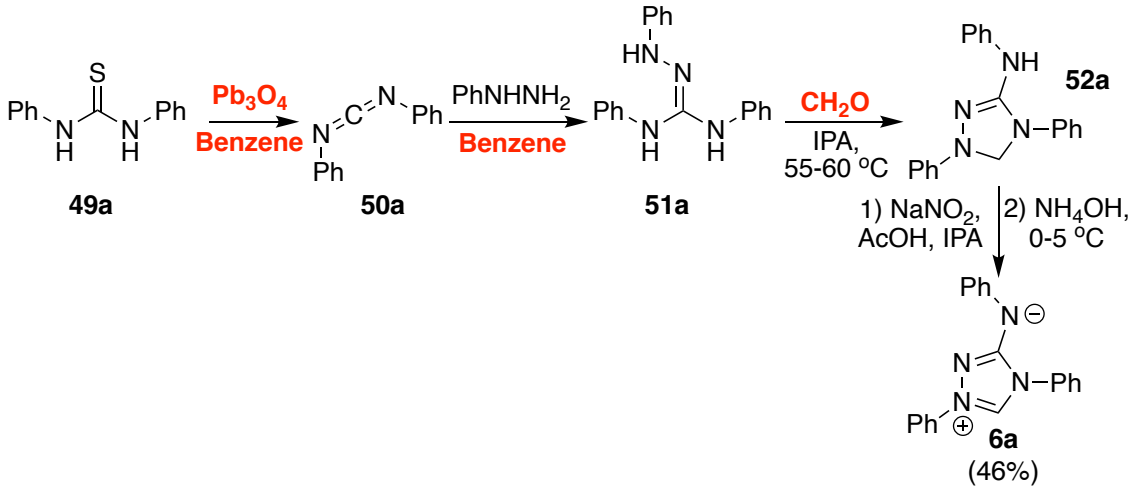

Scheme 2.2.1. Previously reported synthetic route to Nitron (**6a**) starting from 1,3-diphenylthiourea, with hazardous reagents, for which viable replacements will be explored, highlighted in **red**.

Nitron (**6a**) has traditionally seen application in nitrate and perchlorate detection. Nitrate and perchlorate salts are common by-products of human activities, with nitrate a key fertiliser in agriculture and perchlorates being found in the manufacture of rocket fuels, pyrotechnics, lubricating oils and more. Invariably, these environmentally hazardous salts have permeated into groundwater, rivers and soils.[59] Quantification is challenging but Nitron (**6a**) can be used in spectrophotometric or potentiometric titrations owing to the formation of highly insoluble salts with nitrate and perchlorate.[60] Nitron is an orange-yellow solid (as its zwitterion), giving a bright yellow solution when dissolved. In its protonated, cationic form, a white solid and colourless solution are formed.

Nitron (**6a**) is a 1,2,4-triazolium which may undergo C(3)-H deprotonation of a 1,2,4-triazolylidene although the C(3)-H pK_a is unknown. The potential for formation of an N-heterocyclic carbene has underpinned additional applications for Nitron beyond gravimetric analysis, including exploration as both a ligand in organometallic chemistry and in organocatalysis. As a ligand, a series of catalytically relevant Nitron-metal complexes have been synthesised and explored in typical metal-catalysed reactions. Iridium complexes were explored in some useful metal catalysed reactions including the dehydration of formic acid, the hydrosilylation of carbonyl compounds, the transfer hydrogenation of ketones and the hydrocoupling of hydrosilanes and alcohols. Turnover frequencies were comparable to other NHC-iridium catalysts highlighting the potential applications of these ligands.[61] No further derivatives of Nitron were explored as metal ligands, highlighting a potential area for growth in this field.

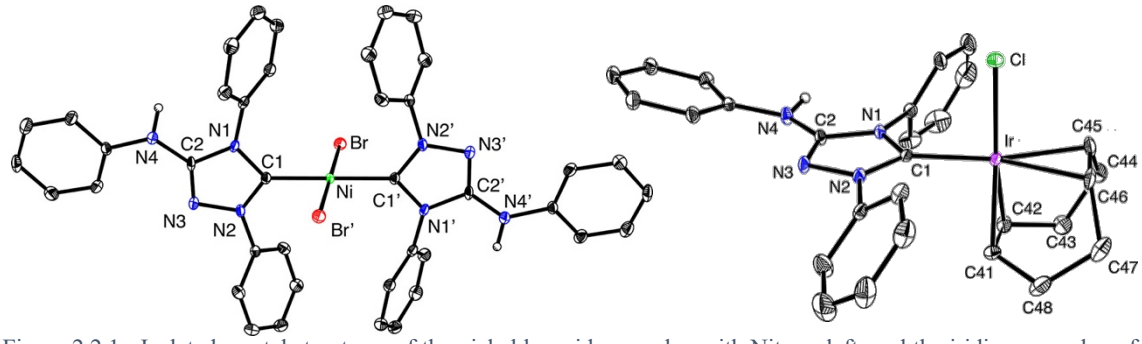

Figure 2.2.1. Isolated crystal structures of the nickel bromide complex with Nitron, left, and the iridium complex of Nitron, right, with COD ligand also present.[61] Reprinted with permission from P. J. Quinlivan, A. Loo, D. G. Shlian, J. Martinez and G. Parkin, Organometallics, 2021, 40, 166-183. Copyright 2022 American Chemical Society.

Our group's initial interest stemmed from our general interest in triazolium ions as organocatalysts. Under catalytically relevant conditions, ring opening to both the triazabutadiene (**53**) and amido-Blatter radical (**24a**) were observed. It was hoped that in exploring further derivatives of Nitron, we could understand the Nitron (**6**) to Blatter radical (**24**) reaction in more detail. Furthermore, Nitron derivatives with lower propensities for Blatter radical formation could be potentially useful organocatalysts.

This chapter highlights the development of a more contemporary synthetic strategy to Nitron (**6**). Each step of the original parent Nitron synthesis is critically analysed, outlining the key by-products observed and isolated along with strategies to avoid these and isolate the desired pure compounds.

2.2.3. Synthetic Route Development

Accessing Amidrazones

Amidrazones (**30**/**51**) are common intermediates in the synthesis of many 1,2,4-triazoliums such as those used for organocatalysis.[62-64] The difference in the case of the synthesis of Nitron (**6**) is the extra, exocyclic aniline which can be included by starting from substituted (thio)ureas as opposed to amides. Initial exploration of the amidrazone (**51**) synthesis attempted to activate the leaving group ability of the oxygen by reaction with either trimethyloxonium tetrafluoroborate or thionyl chloride. Both syntheses are commonplace in traditional routes to 1,2,4-triazoliums (Scheme 2.2.2).[63, 64]

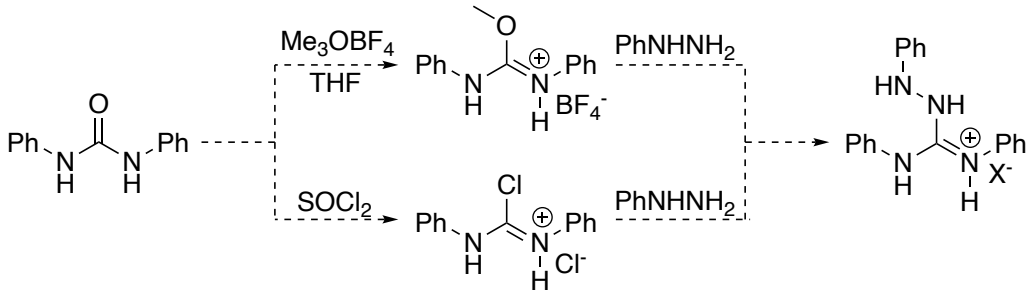

Scheme 2.2.2. Attempted syntheses of amidrazones via typical 1,2,4-triazolium synthesis chemistry, activating the carbonyl-oxygen as a leaving group with either trimethyloxonium tetrafluoroborate or thionyl chloride. Both reactions failed to proceed suggesting the extra nitrogen in this case greatly complicates the reactivity.

Neither approach was successful, attributed to the presence of the extra nitrogen atom altering the reactivity at the carbonyl oxygen. With regards to methylation of the urea at oxygen, it could be considered that one of the nitrogen atoms would be preferentially methylated in competition with the carbonyl oxygen due to a higher local 'concentration'. Moreover, in the case of amides, this nitrogen is deactivated due to donation into the σ^*_{CO} bond whereas for ureas, the deactivation is lower due to the presence of 2 nitrogen atoms. In the case of the thionyl chloride reaction, it was not so clear why it did not proceed; however, the important conclusions to be drawn are that these substituted ureas do not react in the same way as the amides.

Traditionally, Nitron (**6a**) is synthesised via a carbodiimide (**50a**) (Scheme 2.2.1), more typically linked with peptide coupling chemistry. Within the original synthesis, lead tetroxide is used as the desulphurising reagent however this utilises heavy metals which are difficult to handle and environmentally toxic.[21] In a bid to improve upon this, a selection of other desulphurisation techniques were explored, using iodine as the key reagent (Scheme 2.2.3).[65] Initially, the synthetic route highlighted in Scheme 2.2.3 (a) was attempted, using iodine in tandem with triphenylphosphine to synthesise the carbodiimides from ureas or thioureas. It was found that that these reactions worked well however by TLC were found not reach to complete conversion. Moreover, the triphenylphosphine oxide formed was very difficult to remove and made isolation of the desired carbodiimide difficult.

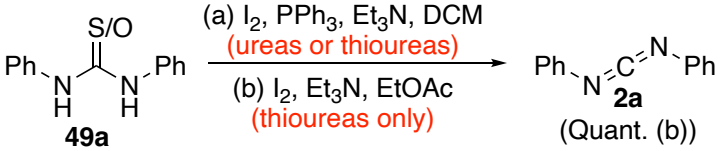

Scheme 2.2.3. Different conditions explored for the synthesis of carbodiimides. Approach (a) benefitted from also being applicable to ureas but suffered from drawbacks in reduced yields and purification complications. Conditions for (b) were only applicable to thioureas however gave quantitative yields, short reaction times and more straightforward isolation.

An alternative method (Scheme 2.2.3 (b)), only for thioureas (**49**), was attempted which was very similar but did not require triphenylphosphine.[66] This was found to be significantly better, showing complete conversion in under 2 hours to the desired carbodiimides (**50**). Initially water was excluded from the work up to avoid the formation of ureas from the carbodiimide. Removal of residual iodine was attempted by filtration through both silica and activated carbon but, neither proved successful. Eventually a 10 % aqueous thiosulphate wash was attempted and yielded the best results with limited urea formation. It is proposed that the particularly greasy, hydrophobic nature of the carbodiimides (**50**), owing to their highly symmetrical nature, decreases the electrophilicity towards water in these cases. Within the characterisation for the carbodiimide, it was noticed that another product was present which consisted of a unimer (**53**) (a monomer carbodiimide unit, activated by a free aniline) of m/z = 288, followed by subsequent repeat units of increasing m/z of 194. It has been reported that carbodiimides, in particular those with pendant aromatics, are susceptible to polymerisation.[67] Polymer by-product could be easily removed by dissolving the crude carbodiimide in hexane, leaving insoluble polymer, and filtering through a celite plug. A silica plug or column were not appropriate as it was also reported that carbodiimides are not stable on silica.[67]

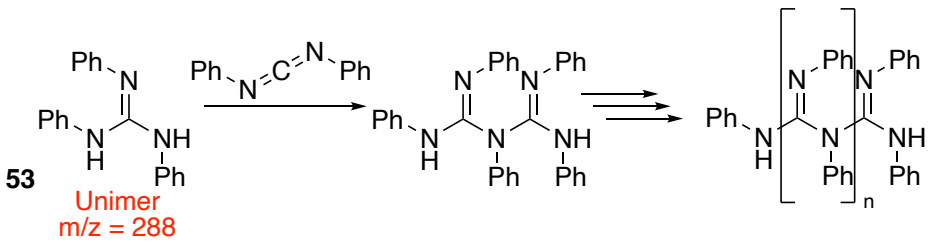

Scheme 2.2.4. Polymerisation of the diphenyl carbodiimide. Initial unimer formation requires free aniline present in solution suggesting some initial carbodiimide decomposition. Evidence for polymerisation was found by both LC-MS and high resolution MS.

Reaction of phenylhydrazine with carbodiimides (**50**) was not altered significantly from the traditional synthesis apart from changing the solvent to toluene in place of benzene (Scheme 2.2.5). It was also found that it was important to carry out the reaction under argon and degas the solvent due to the oxidative instability of amidrazones (**51**) with respect to their corresponding triazabutadienes (**54**). Although it is feasible for the triazabutadienes (**54**) to react in the final ring closing step, their reactivity was much diminished when considering the secondary amine-like character of the nitrogen in the amidrazone (**51**) in comparison to the imine-like nitrogen of the triazabutadiene (**54**).

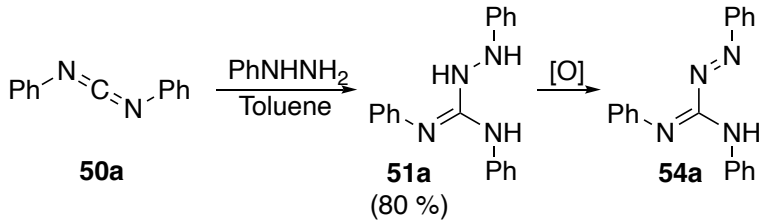

Scheme 2.2.5. Synthesis of amidrazones from carbodiimides (**50**) is in general straightforward. Amidrazones (**51**) are oxidatively unstable, readily forming triazabutadienes (**54**) in air.

When initially exploring the synthesis of amidrazones (**51**), diphenyl thiourea (**49a**) and di-*p*-tolyl thiourea (**49b**) were chosen as the derivatives of interest. When attempting to isolate the tolyl-functionalised amidrazone an alternative by-product, herein denoted as an N^5-adduct, was isolated in moderate yields (**55b**) (Scheme 2.2.6). Mechanistically, it is suggested that a molecule of amidrazone can react with a second carbodiimide and cyclise with the loss of *p*-toluidine. This was found to also occur for the parent, phenyl amidrazone however to a much less significant extent. The tolyl-carbodiimide (**50b**) has significantly less electrophilic character at the central carbon, owing to the donating effects of the para-methyl groups. This has the effect of slowing reactivity enough for competitive reaction of the formed amidrazone with the slow reacting carbodiimide, to form significant amounts of this N^5-adduct. There have been previous reports of these heterocycles which date back to the late 1800s and early 1900s however there have been no reports since this time; these will be explored further in at the end of this chapter in greater detail.[68]

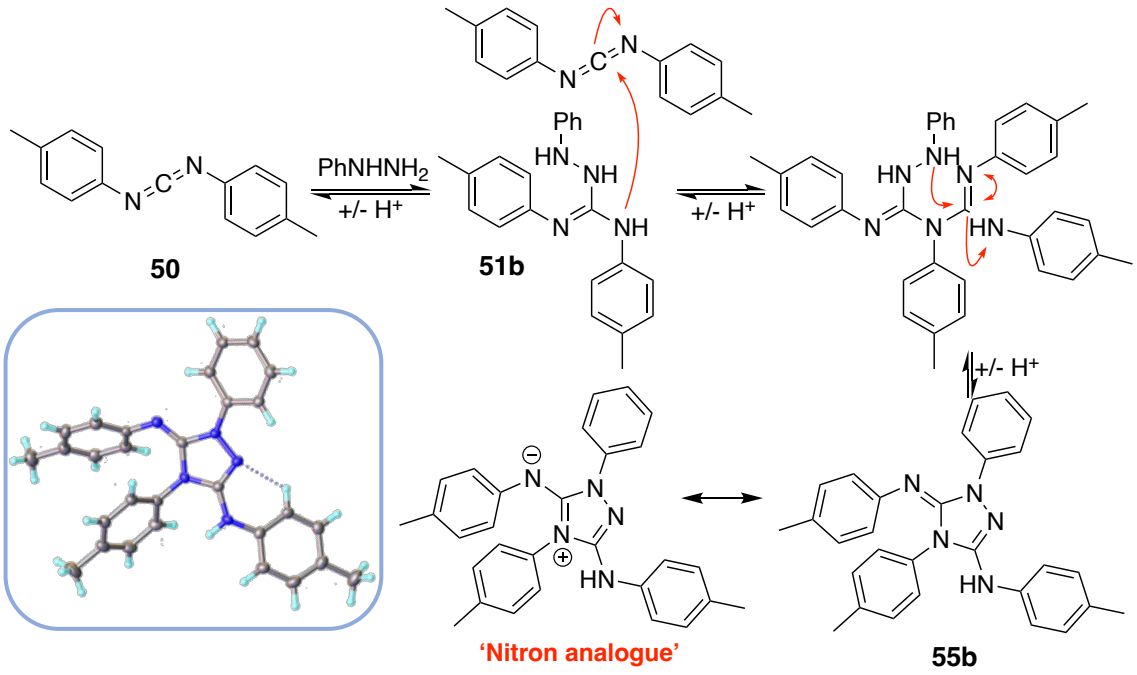

Scheme 2.2.6. Proposed mechanism for the synthesis of N-heterocyclic by-product from the amidrazone synthesis. This by-product can be considered as a Nitron derivative with an extra aniline at the carbenic position. Inset shows the isolated X-ray crystal structure of this interesting by-product.

N^5-adduct (**55**) can be considered as a Nitron derivative with an extra aniline group at the carbenic position. As such, a small amount was stirred in acetonitrile and monitored for formation of the corresponding radical (Scheme 2.2.7). As might be expected, the C(3) position in this case is less susceptible to hydrolytic ring opening owing to the electron donating nitrogen reducing electrophilicity and no option for carbene tautomer formation as for the parent Nitron (**6a**).

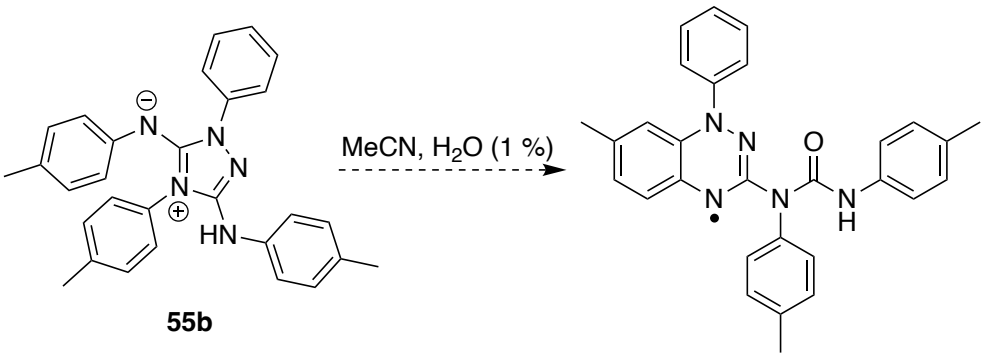

55b

Scheme 2.2.7. Proposed radical formation from N-heterocyclic by-product (**55b**). This experiment, as could be predicted, was unsuccessful.

Inserting the carbenic unit

There exists a significant number of methods for inserting the carbenic unit of a 1,2,4-triazolium.[19] The traditional method for Nitron synthesis consists of reaction with formaldehyde to first form a triazole, followed by subsequent oxidation with sodium nitrite to form the triazolium (Scheme 2.2.1).[58] This method works well however there have been more recent developments which could transform this two-step process into a single, more high yielding step.

One of the more favourable approaches to the ring closing of 1,2,4-triazoliums is the use of trialkyl orthoformates (Scheme 2.2.8 (a)). These comparatively less hazardous reagents give straightforward access to triazoliums under acidic conditions at reflux. Initial attempts using trialkyl orthoformates for the synthesis of Nitron (**6a**), however, proved unsuccessful with either no catalytic acid or a small amount of hydrochloric acid added. As this ring closing approach was not proving successful, two alternative methods were also explored. Chloromethyl pivalate and silver triflate were found to lead to the desired heterocycle however also resulted in significant by-products (Scheme 2.2.8 (b)). Isolation of the desired Nitron was found to be particularly difficult and so alternative reactions were explored. Chloromethyl methyl ether (MOM-Cl) is another well used reagent for the synthesis of triazoliums (Scheme 2.2.8 (c)). Again, ring closing appeared

successful however, the high reactivity of MOM-Cl caused a significant number of by-products to form, such as methylation on the exocyclic amino group.

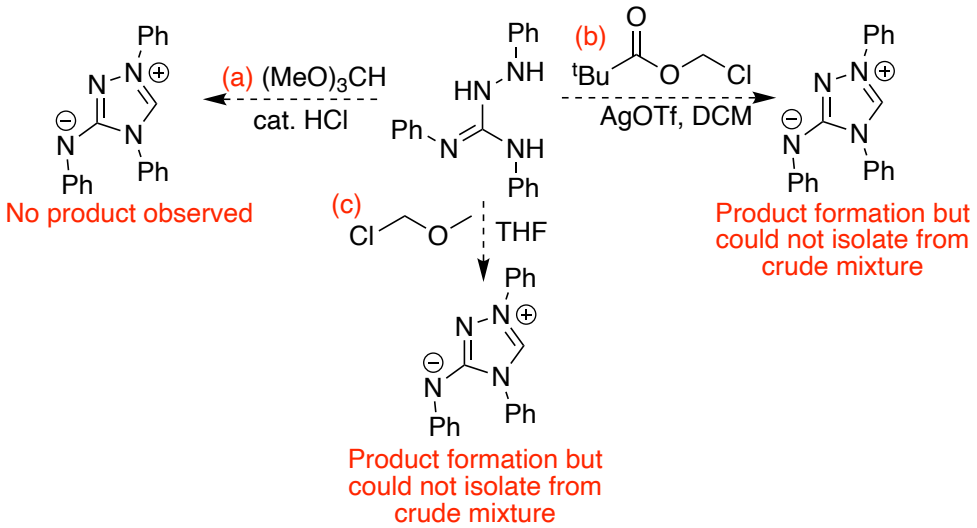

Scheme 2.2.8. Initial attempted ring closures of amidrazones to form Nitron. (a) trimethyl orthoformate at reflux with catalytic HCl proved unsuccessful; (b) use of chloromethyl pivalate and silver triflate was successful however was a messy reaction and it was not possible to isolate the desired Nitron; (c) chloromethyl methyl ether also appeared successful but as an effective methylating reagent also caused significant by-product formation which could not be purified.

As a final attempt, the use of trimethyl orthoformate was revisited with weaker acid, ammonium tetrafluoroborate, in a stoichiometric amount. Pleasingly, this was found to yield complete conversion to the desired Nitron-tetrafluoroborate salt, which precipitated from the reaction mixture upon cooling. This white salt could be readily converted to the characteristic yellow zwitterionic form by a straightforward bicarbonate wash to give the desired Nitron in a good yield (Scheme 2.2.9).

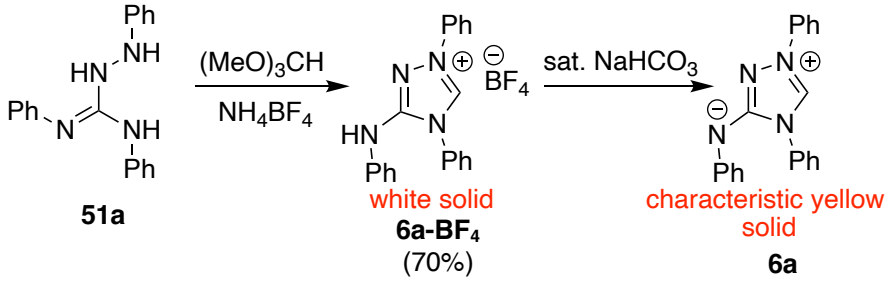

Scheme 2.2.9. Final conditions determined for the ring closure of the parent amidrazone to form the all phenyl substituted Nitron.

Exploring the Scope of the Developed Synthetic Strategy

Scheme 2.2.10 highlights the developed synthetic route to Nitron, in which a yield of 65 % was obtained for the parent Nitron (**6a**). This compares favourably to the literature route to Nitron (~40 %), whilst using significantly less hazardous, 'greener' reagents. To fully explore the scope and attempt to obtain new Blatter radical derivatives, a selection of different aromatic substituents were explored. Table 2.2.1 summarises the derivatives

explored, and the final yields obtained for each of the Nitron (**6**) analogues. Here, the substituent Ar^1 is delivered via the aryl hydrazine, and Ar^2 and Ar^3 via the initial thiourea.

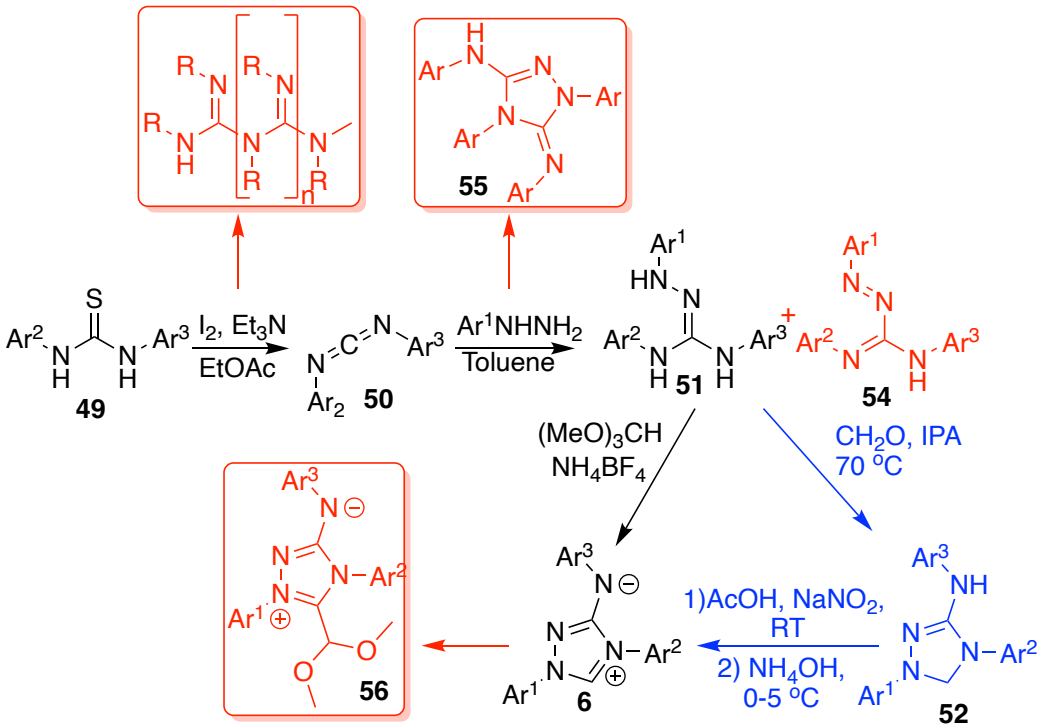

Scheme 2.2.10. Developed synthetic route to Nitron (**6a**, Ar^1=Ar^2=Ar^3=Ph) from *N,N'*-diphenyl thiourea which uses more modern techniques for both the desulphurisation and ring closing steps.

Table 2.2.1. Summary of the Nitron derivatives explored in this project where Ar^1, Ar^2 and Ar^3 assignments are those in Scheme 2.2.10. Also shown are the convergent yields of those derivatives which could be synthesised.

Derivative	Ar^1	Ar^2	Ar^3	Yield / %
6a	Ph	Ph	Ph	65
6b	Ph	4-$CH_3C_6H_4$	4-$CH_3C_6H_4$	16
6c	Ph	4-$F_3CC_6H_4$	4-$F_3CC_6H_4$	55
6d	Ph	4-$EtOC_6H_4$	4-$EtOC_6H_4$	31
6e	Ph	4-$EtOC_6H_4$	4-$F_3CC_6H_4$	-[a]
6f	4-$MeOC_6H_4$	Ph	Ph	50
6g	4-FC_6H_4	Ph	Ph	55
6h	4-$F_3CC_6H_4$	Ph	Ph	-[a]
6i	4-NCC_6H_4	Ph	Ph	50
6j	4-$F_3CC_6H_4$	4-$F_3CC_6H_4$	4-$F_3CC_6H_4$	30
6k	4-$MeOC_6H_4$	4-$EtOC_6H_4$	4-$EtOC_6H_4$	-[a]
6l	4-$F_3CC_6H_4$	4-$EtOC_6H_4$	4-$EtOC_6H_4$	-[a]
6m	4-$MeOC_6H_4$	4-$F_3CC_6H_4$	4-$F_3CC_6H_4$	47

[a] Nitron derivatives not isolated, see text for discussion.

The initial derivative explored alongside the parent Nitron was the tolyl-substituted Nitron (**6b**). Isolation of the desired Nitron in this case was difficult (≤15 % yield). The

main reason for this was that the key product isolated from the amidrazone forming step was the N-heterocyclic by-product (**55b**). A range of different conditions were explored using different solvents, temperatures and concentrations of reagents in an attempt to isolate the amidrazone as the major product, with little success. As mentioned, the reduced electrophilicity of the carbodiimide was presumed to be the cause. Derivative **6c** (Ar^1=Ph, Ar^2=Ar^3=4-$F_3CC_6H_4$) was synthesised readily from the commercially available thiourea. In this case, very little of the N-heterocyclic by-product (**55c**) was observed by LC-MS, supporting the theory that the electrophilicity of the carbodiimide dictates the product outcome. The final product could again be isolated as the tetrafluoroborate salt, and the zwitterionic form after a subsequent saturated sodium bicarbonate wash.

Synthesis of derivatives **6d** (Ar^1=Ph, Ar^2=Ar^3=4-$EtOC_6H_4$) and **6e** (Ar^1=Ph, Ar^2 = 4-$CF_3C_6H_4$, Ar^3=4-$EtOC_6H_4$) required initial synthesis of the respective thioureas (**49**). These were readily accessed in quantitative yields by stirring the respective aryl isothiocyanates with substituted anilines in acetonitrile (Scheme 2.2.11).[69] Obtaining Nitron derivative **6d** was significantly more challenging due to the decreased oxidative stability of the amidrazone. As stated, all amidrazones readily form triazabutadiene in air and, as might be predicted, the electron donating effect of the *p*-ethoxy groups increase the ease of oxidation by raising the energy of the HOMO. There was also significant N-heterocyclic by-product formation in this case owing to the decreased electrophilicity of the carbodiimide. Nevertheless, the Nitron derivative (**6d**) could be synthesised by quick handling of the triazabutadiene. Subsequent purification was complicated again by the instability of the Nitron derivative, this was evidenced by a rapid colour change during attempted recrystallisation. It was however found that in isolating as the protonated tetrafluoroborate salt, stability and isolated yields were vastly improved.

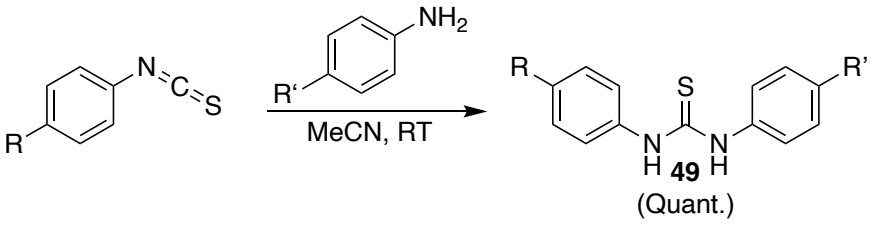

Scheme 2.2.11. Synthesis of commercially unavailable thioureas by reaction of more readily available aryl isothiocyanates with substituted anilines.[69]

As might be envisaged for **6e** (**6e'** Ar^1 = Ph, Ar^2 = 4-$EtOC_6H_4$, Ar^3 = 4-$CF_3C_6H_4$; **6e''** Ar^1 = Ph Ar^2 = 4-$CF_3C_6H_4$, Ar^3 = 4-$EtOC_6H_4$), synthesis was complicated by the formation of two structural isomers of the final Nitron derivative (Figure 2.2.2). Alongside this, the amidrazone could not be purified from the N-heterocyclic by-product (**55e**) which formed in significant amounts. As such, isolation of the desired Nitron was not possible at all for this molecule. It had been predicted that of the two isomers, **6e'** would be most favourably formed due to the negative charge aligning with the electron-withdrawing 4-CF_3 group and the positive charge with the 4-ethoxy group (Figure 2.2.2). This did not appear to be the case and the absolute product outcome could not be determined due to the synthetic difficulties.

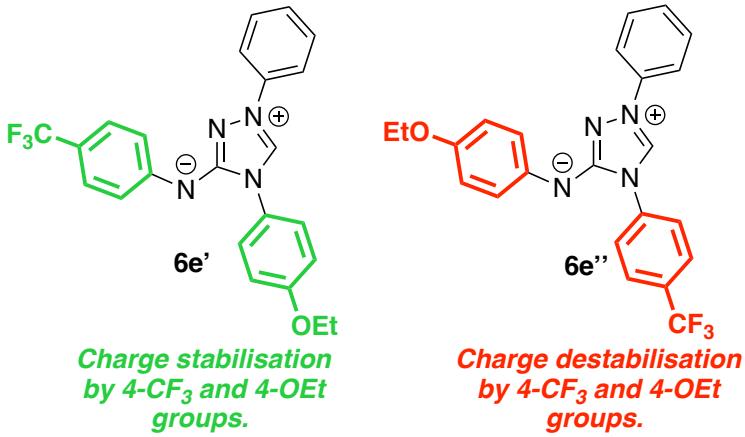

Figure 2.2.2. The two structural isomers of **6e**, of which **6e'** would be predicted to be the more favoured isomer.

A selection of derivatives utilised diphenyl thiourea (**49a**) to deliver Ar^2=Ar^3=Ph, as with the parent Nitron, but used different aryl hydrazines to modify Ar^1. Three of the derivatives were electron withdrawing in nature: **6g** (Ar^1 = 4-FC_6H_4; σ_p = 0.06); **6h** (Ar^1 = 4-$CF_3C_6H_4$; σ_p = 0.54); **6i** (Ar^1 = 4-CNC_6H_4; σ_p = 0.66).[70] Derivative **6g** is only mildly withdrawing in nature and so the amidrazone was very easy to isolate pure and carry through to the final Nitron. Both **6h** and **6i** have significantly larger Hammett values implying greater electron withdrawing character and saw significantly greater amounts of the N-heterocyclic by-product formed. This suggests, rationally, that by-product formation is not just determined by the electrophilicity of the carbodiimide but also the nucleophilicity of the corresponding aryl hydrazine.

The lipophilic nature of the trifluoromethyl group of derivative **6h** meant that purification of the amidrazone from the N-heterocycle was not possible so this route was abandoned. Alternatively, derivative **6i** was much easier to isolate pure as the N-heterocycle but, it

was insoluble in all solvents explored. This allowed purification of the amidrazone by recrystallisation and hot filtration from isopropanol. Finally, ring closure to the Nitron analogue was straightforward however isolation as the tetrafluoroborate salt was required due to significant ring opening occurring upon washing with saturated bicarbonate solution. Ring opening was evidenced by a colour change from yellow to red, characteristic of triazabutadiene formation and confirmed by LC-MS analysis.

A hydrazine with an electron donating aryl substituent was also explored in derivative **6f** (Ar^1=4-$MeOC_6H_4$, Ar^2=Ar^3=Ph). Synthesis was generally straightforward, with triethylamine added at the amidrazone step, to account for the hydrochloride salt of the hydrazine. Oxidative stability in this case was poorer than for the corresponding Nitron derivatives with electron withdrawing Ar^1 (**6g-i**) but, isolation of the final triazolium in good yields was relatively straightforward.

Formation of derivative **6j** involved a different challenge to previously explored Nitron derivatives. The amidrazone was easy to synthesise and isolate, with minimal N-heterocyclic by-product. Presumably, the enhanced electrophilicity of the carbodiimide in this case offsets the diminished nucleophilicity of the aryl hydrazine. Subsequent reaction with trimethyl orthoformate was complicated by the greatly increased acidity of the final Nitron. This allowed the formed Nitron derivative to react further with another equivalent of trimethyl orthoformate to give the adduct (**56**) (Scheme 2.2.12). Adduct and Nitron derivative were inseparable by all attempted purification techniques and so an alternative technique was required. Orthoformate adducts of 1,2,4-triazoliums have not been previously reported however work within our group is exploring the isolation and potential applications of these species, obtained from different starting amidrazones. In this work, isolation of the adducts was non-trivial and so none were fully characterised or explored further.

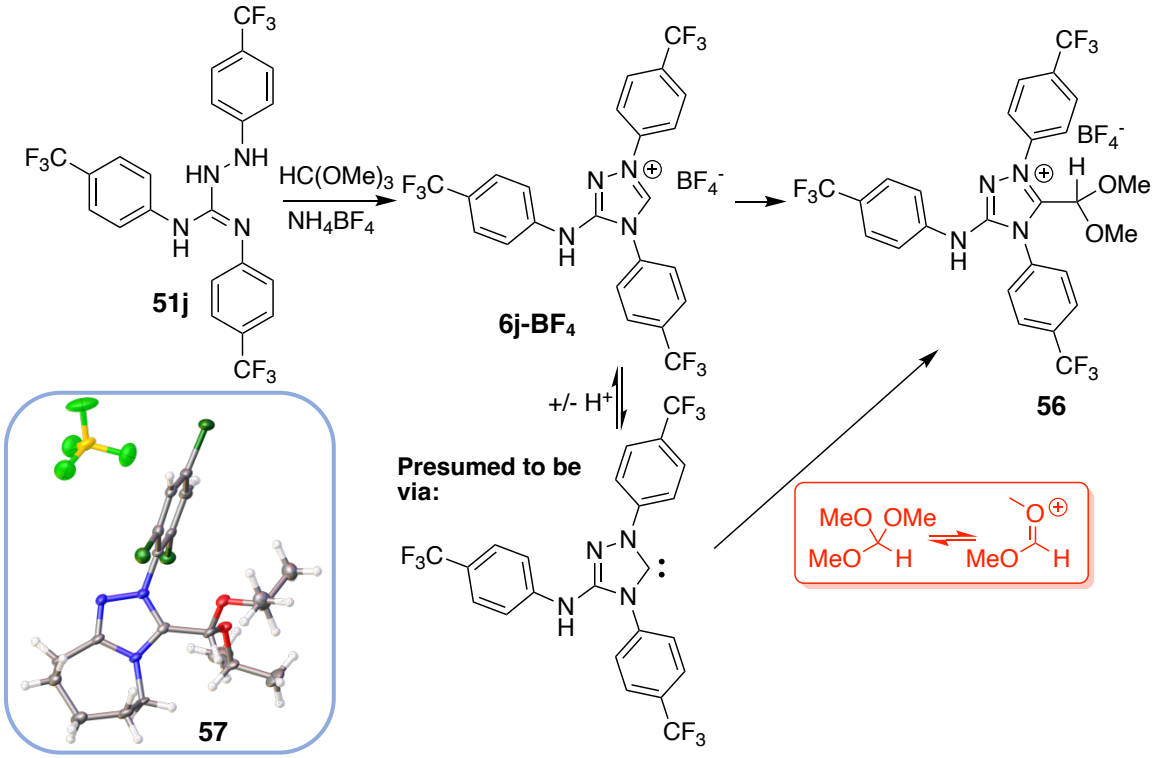

Scheme 2.2.12. Formation of trimethyl orthoformate adducts from the more acidic synthesised Nitron derivative. Inset shows a previously isolated alkyl orthoformate adduct of a different 1,2,4-triazolium (**57**).

The traditional route to Nitron tackles the final ring closure via a two-step process: reaction with formaldehyde to give the triazole (**52**) and oxidation with sodium nitrite to give the triazolium (**6a**). Derivatives **6j** and **6m** were synthesised via this route, relatively successfully (Scheme 2.2.13). Reaction with formaldehyde yielded a triazole which readily precipitated from the reaction mixture. For both derivatives, it was found that the oxidation conditions used in the traditional Nitron synthesis were too harsh, giving over-oxidation and other side reactions. This included the proposed formation of the green, amino-Blatter radicals as highlighted in the literature review. The conditions were altered to remove the isopropyl alcohol completely and use acetic acid as the solvent in a room temperature oxidation. This gave a clean, quantitative conversion from the triazoles (**52**) to the 1,2,4-triazoliums (**6**).

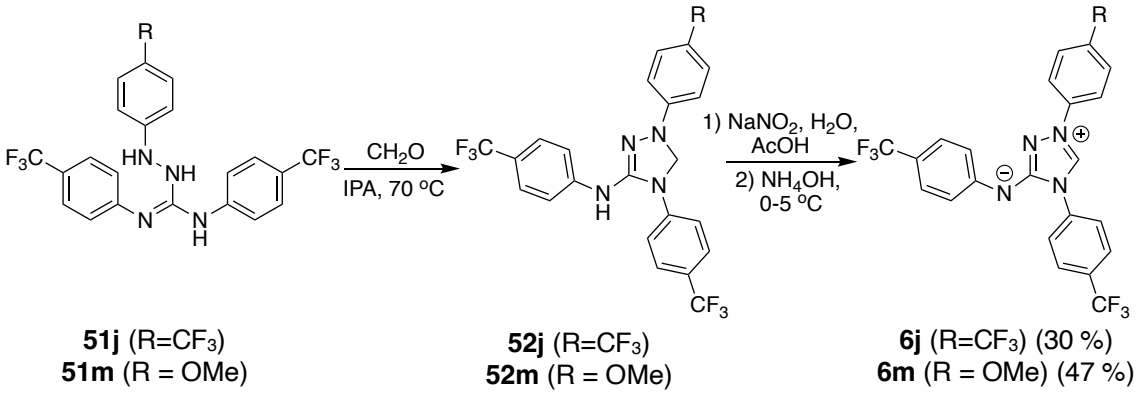

51j (R=CF_3)
51m (R = OMe)

52j (R=CF_3)
52m (R = OMe)

6j (R=CF_3) (30 %)
6m (R = OMe) (47 %)

Scheme 2.2.13. Alternative route to Nitron derivatives **6j** (R=CF_3) and **6m** (R=OMe) using formaldehyde to cyclise followed by oxidation with sodium nitrite in acetic acid.

The final Nitron derivatives of interest were **6k** and **6l** but synthesis of these proved very difficult for reasons discussed previously. The synthesis of derivative **6k** suffered from significant oxidative instability at the amidrazone step on account of the increased donation into the HOMO. This made isolation of the amidrazone very difficult and a crude mixture was isolated. The subsequent ring closure with both trimethyl orthoformate and formaldehyde routes was not successful. As might be envisaged with **6l**, the amidrazone did not form as the major product and instead the N-heterocyclic by-product (**55l**) was the major observed product. This is a consequence of the carbodiimide and aryl hydrazine being the most deactivated electrophile and nucleophile, respectively, of those explored.

All Nitron derivatives (**6**) were fully characterised using standard techniques including NMR spectroscopy and mass spectrometry. Where possible X-ray diffraction crystal structures were also obtained and these are summarised in Figure 2.2.3. Typically, suitable crystals were formed as the tetrafluoroborate salts by slow evaporation of solutes from methanol. A selection of bond lengths and angles, and torsion angles are highlighted in Table 2.2.2. N(2)-aryl groups are all very close to planarity, this maximises orbital overlap, providing a conjugative stabilising effect. N(4)-dihedral angles are typically much larger and this is likely to avoid steric clashes with the exocyclic N-aryl group. The exceptions to this are compound **6f**, with R^1 = OMe, and the zwitterionic structure **6m**. It could be that the electron donating group destabilises this structure and that an increase in planarity at N(4) provides more stabilisation, outcompeting the destabilising effect of the steric clash. The zwitterionic structure has the most planar structure overall, most likely because the NH is no longer present allowing a more planar conformation to be

adopted, enhancing orbital overlap. It is typically difficult to isolate crystals suitable for XRD analysis of the zwitterions. It would be intriguing to analyse a crystal structure of the zwitterionic Nitron and determine how the phenyl group orientates itself in this case. Computational studies (B3LYP; 3-21g) suggest a twist of 22.4º for the zwitterionic form in comparison to the twist of 118.4º in the tetrafluoroborate salt form, implying the out of plane twist is a steric effect (Figure 2.2.4). When considering the cationic N-protonated Nitron in computational studies at the same level of theory, an estimate of 81.7º was determined for the out of plane twist. The difficulty in producing crystals of the zwitterionic form of Nitron could stem from this shift in phenyl twist, altering the packing in the crystal lattice. Moreover, the colour shift from white solid to yellow solid upon formation of the zwitterion could be due to the increased conjugation upon shift to a more planar structure.

Bond angles about the carbenic position N(2)-C(3)-N(4) (NCN) have recently been related to the C(3)-H acidity of a range of fused 1,2,4-triazoliums, typically used in NHC-organocatalysis.[71] It has been found that as the internal NCN bond angle increases, the values for k_{DO} decrease, reflective of a decrease in C(3)-H acidity. In the case of these Nitron derivatives, the change is small but appears to follow this trend, with electron withdrawing groups (CN/F) giving the smallest bond angles. Section 2.3 explores the kinetic acidities of these Nitron derivatives in more detail.

Finally, the C(5)-N bond lengths were explored showing in particular a significant decrease for the zwitterionic structure. This is likely due to the increase in double bond character upon formation of the anionic nitrogen, which readily conjugates into the 1,2,4-triazolium ring. Other compounds do not appear to show a significant trend.

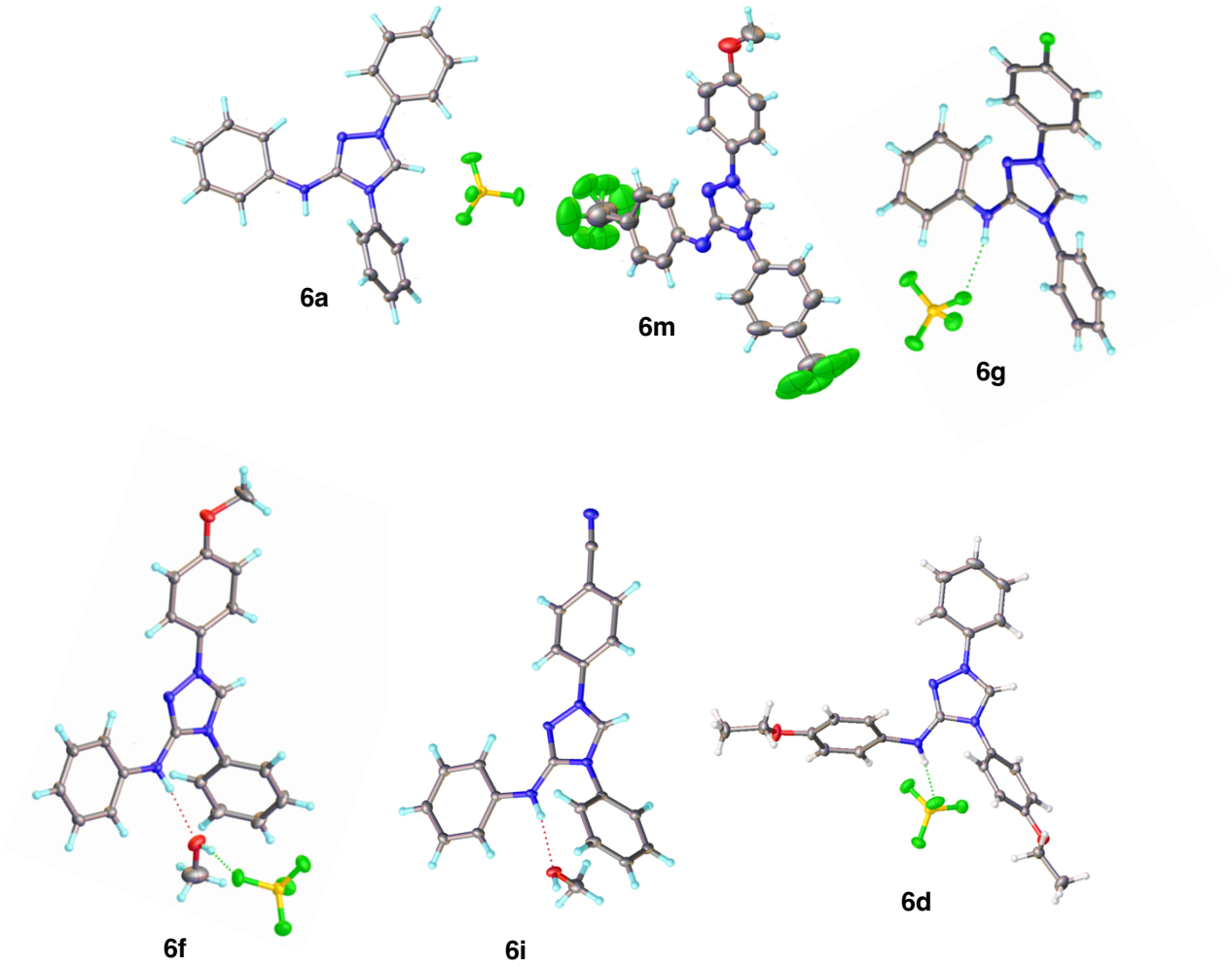

Figure 2.2.3. Crystal structures of various Nitron derivatives discussed above, determined by single crystal XRD, used to structurally compare the effect of substituents on key bond angles, lengths and dihedral angles.

Table 2.2.2. Summary of some of the key dihedral angles, bond lengths and bond angles determine from XRD crystal structures of various Nitron derivatives. Atom numbering follows IUPAC convention for labelling of 1,2,4-triazoliums.

Structure	R^1	R^2	Counterion	N(2)-Dihedral Angle / °	N(4)-Dihedral Angle / °	N(2)-Ph Bond Length / Å	N(4)-NPh Bond Length /Å	N(2)-C(3)-N(4) Bond Angle / °	C(5)-N Bond Length /Å
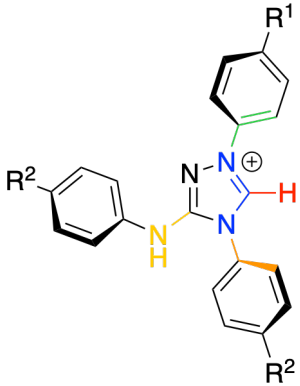	H	H	BF_4^-	-5.168	118.402	1.433	1.444	107.61	1.347
	F	H	BF_4^-	-8.884	104.417	1.432	1.446	107.24	1.355
	CN	H	BF_4^-	-4.779	108.879	1.431	1.446	107.13	1.343
	OMe	H	BF_4^-	-5.161	55.890[a]	1.433	1.439	107.26	1.346
	OMe	*CF_3*	*Zwitterion*	*-3.663*	*35.523*	*1.429*	*1.427*	*108.8*	*1.313*
	H	OEt	BF_4^-	-8.284	110.673	1.433	1.445	107.51	1.353

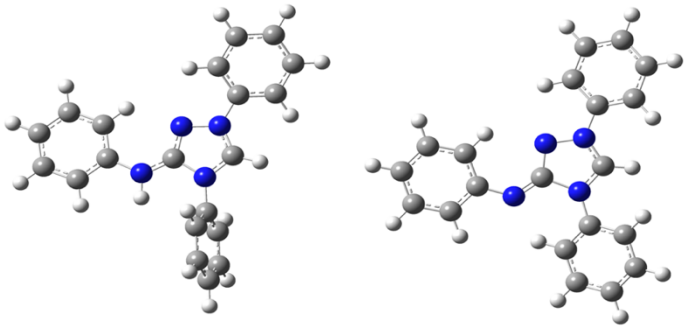

2.2.4. N^5 Adduct Syntheses

As mentioned, during the synthesis of the Nitron derivatives, a new class of compounds was discovered, labelled N^5-adducts. Mechanistically, this was proposed to proceed according to Scheme 2.2.6. The synthetic strategy to amidrazones could be readily altered to instead isolate N^5-adducts by reducing the molar equivalents of aryl hydrazine added. In doing so, excess carbodiimide is present in solution and results in further reaction to the cyclised products (Scheme 2.2.14). A range of aryl hydrazines were explored and these are summarised in Table 2.2.3. Isolated yields were typically very good and compounds precipitated directly from the reaction media with minimal purification required. If necessary, recrystallisation from isopropanol can be used as an effective purification strategy.

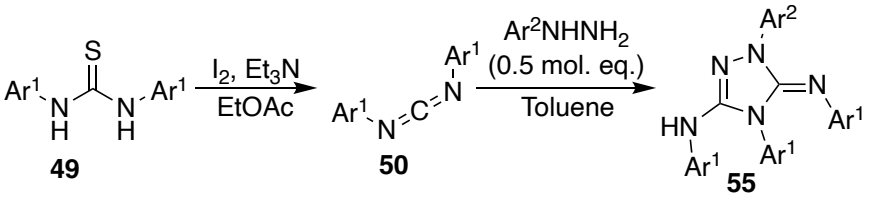

Scheme 2.2.14. Altered synthesis to isolate N^5-adducts in high yields from thioureas and aryl hydrazines.

Table 2.2.3. Isolated yields of a selection of N^5-adducts using the synthetic procedure shown in Scheme 2.2.14.

Derivative	Ar^1	Ar^2	Yield[a] / %
55a	Ph	Ph	57
55b	4-$H_3CC_6H_4$	Ph	34
55c	Ph	4-$F_3CC_6H_4$	41
55d	Ph	4-NCC_6H_4	37
55e	4-$EtOC_6H_4$	Ph	66
55f	4-$F_3CC_6H_4$	Ph	63

[a]Yield over two steps, from the thiourea.

These adducts have an intriguing structure, with a high nitrogen content. It is hoped future work can explore properties and applications of these N^5-adducts in more detail.

2.2.5. Conclusions

To summarise, Scheme 2.2.1 highlights the improved synthetic route developed to access Nitron (**6**) and derivatives. The key by-products, which are observed at each step, are highlighted in red and the alternative ring closing procedure using formaldehyde is shown in blue. Throughout the synthetic work, it became very apparent that the ease of synthesis and isolation of a pure amidrazone (**51**) underpins the success of the entire route. It is

possible to circumvent this issue via the formaldehyde ring closing route; however, for some derivatives it is a case that synthesis is not possible via this route because amidrazone formation was outcompeted by oxidation to triazabutadienes and cyclisation to N^5-adducts. This work has focussed solely on *para*-substituted aromatic derivatives and a selection of *ortho*- and *meta*-substituted could also be explored.

Nitron derivatives are an interesting class of 1,2,4-triazolium owing to the exocyclic anilino group and applications of these will be explored in the subsequent chapters.

2.3. Exploring the Nitron to Blatter Radical Rearrangement

2.3.1. Foreword

The following section highlights the exploration of the Nitron (**6**) to Blatter radical (**24**) conversion for the selection of Nitron derivatives discussed in Chapter 2.2. Radicals are difficult to characterise owing to a lack of NMR signal; however, proof of structure and radical character was attempted through elemental analysis, XRD, cyclic voltammetry and EPR spectroscopy.

2.3.2. Introduction

Whilst probing the potential application of Nitron (**6a**) as a N-heterocyclic carbene organocatalyst, the unusual rearrangement of Nitron to amido-Blatter radicals (**24**) was discovered to occur in wet acetonitrile (Scheme 2.1.8).[21] Mechanistically, it was proposed that initial ring-opening by adventitious water leads to formation of a N-formyl amidrazone (**38**). Subsequent isomerisation to the required (*E*)-isomer gives a structure which can readily form Blatter-type radicals. Final ring closure and oxidation could feasibly occur via two pathways: two-electron oxidation to the triazabutadiene and electrocyclization to the radical, as is believed to be the case in other synthetic strategies to Blatter radicals (Mechanism A); alternatively, a single-electron oxidation to form a N-hydrazonyl radical followed by an intramolecular radical addition and further oxidation (Mechanism B).[21, 23, 28, 72, 73]

In our initial report only a small selection of derivatives were explored (**6a**, **6n**, **6o**, **6p**, **6q**) with a selection of C(3)-functionalised Nitrons explored in the conversion (Scheme 2.3.1). Synthetic challenges to access further Nitron derivatives had until this point limited the exploration. These derivatives were found to proceed through to radicals (**24a**, **24n**, **24o**, **24p**, **24q**) as with the parent Nitron; however, the yields and ease of reaction were not as good with both mild base and oxidant required to force the reactions in the case of C(3)-functionalised Nitrons.

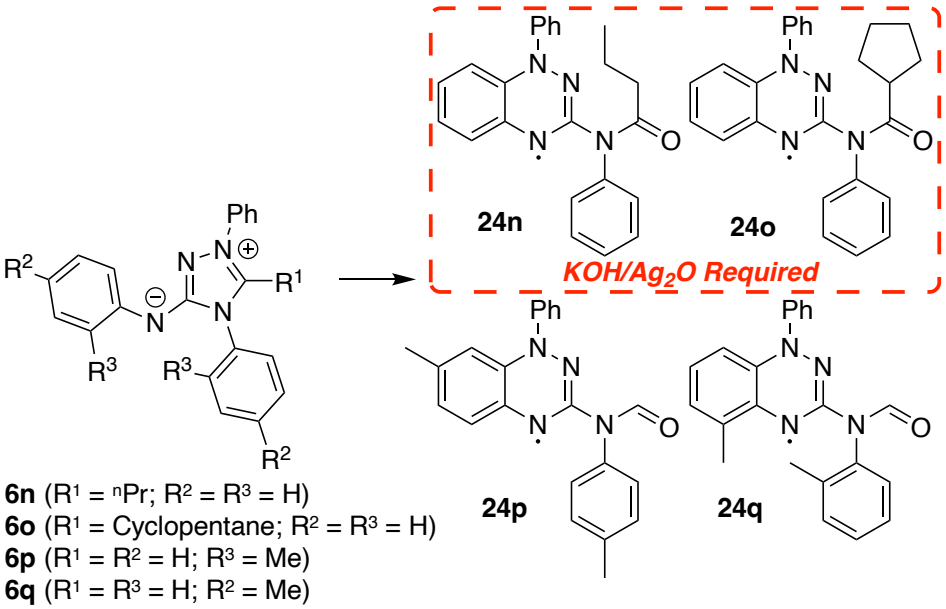

Scheme 2.3.1. Further Nitron derivatives explored as part of the initial project. Conversion to Blatter radicals was not as clean and, for reaction of **6n** and **6o**, required extra oxidant and base to accelerate the reactions; yields were significantly poorer as a result.

Despite the many applications of Blatter radicals (**15**), as highlighted within Chapter 2.1, these novel amido- and amino- Blatter radicals (**24**/**25**) have not yet been fully explored. Recently, these Blatter-type radicals have been shown to be very effective, switchable polarising agents for increasing NMR signal intensity.[74] Insensitivity of NMR nuclei can be overcome through hyperpolarisation by species with unpaired electrons. Similar to the use of contrast agents within MRI, the radical species enhance relaxation times and therefore increase signal intensity through the use of microwave-promoted transfer of spin polarisation. Through space, polarisation interactions are governed by the Overhauser Effect and this leads to the use of Overhauser dynamic nuclear polarisation (O-DNP). Stable radicals are typically used as the polarising reagents; however, a key limitation is the presence of unpaired electrons in the hyperpolarised solution, rapidly accelerating nuclear spin relaxation to thermal equilibrium. A key solution is to be able to 'switch-off' the unpaired electrons upon polarisation to prevent this rapid relaxation and electrochemistry can provide this switching. Blatter-type radicals (**24**/**25**) have been shown to have relatively narrow potential windows, with both oxidation and reduction processes occurring within a -1.4 - 0.7 V potential window. In comparison, TEMPOL (**12b**), another stable radical often used for O-DNP, presents only a single oxidation potential in this region. This should enhance both the ease and stability of the Blatter-type radicals to electrochemical switching.

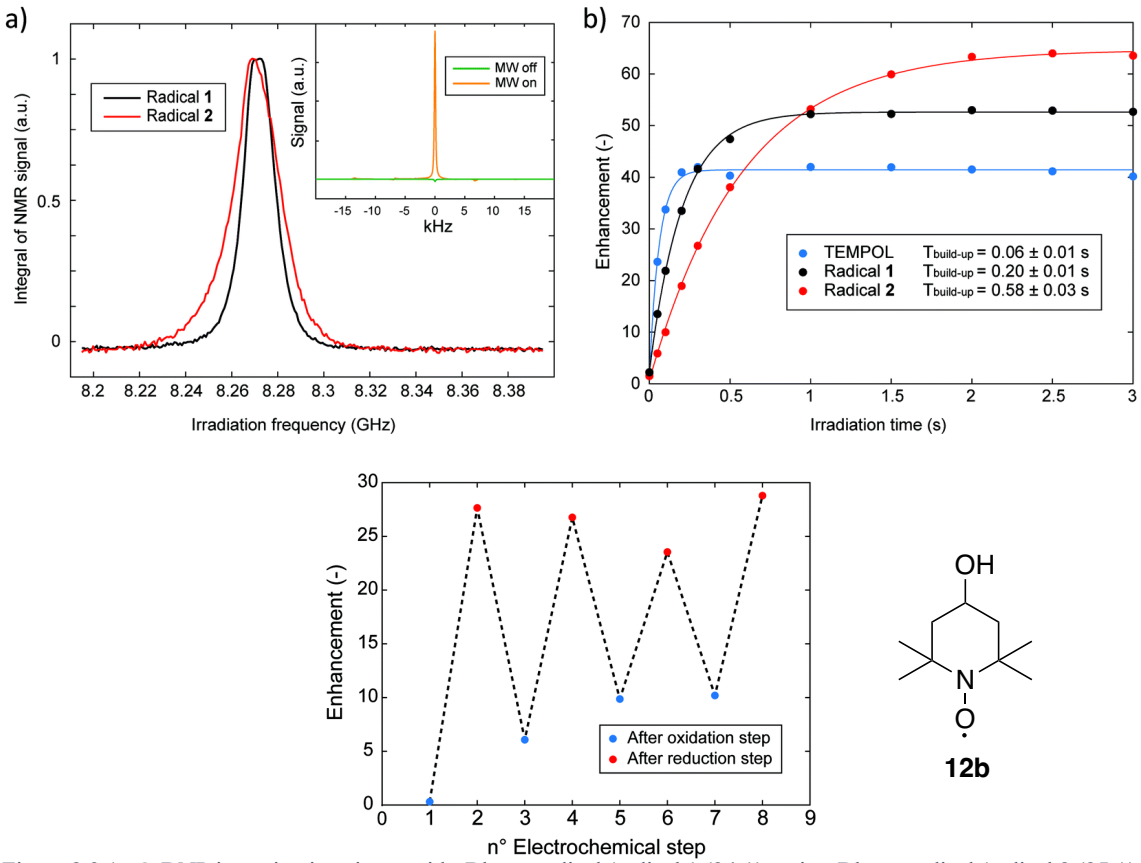

Figure 2.3.1. O-DNP investigations into amido-Blatter radical (radical 1 (**24a**)) amino-Blatter radical (radical 2 (**25a**)) in comparison to TEMPOL (**12b**) a common O-DNP additive. (a) highlights the effect of polarisation with microwave irradiation on the NMR signal in the presence of the radicals; (b) highlights the improved enhancement for Blatter radicals (**24a**/**25a**) in comparison to TEMPOL (**12b**) with the amino radical appearing to show a different polarisation mechanism; (c) highlights the stability of Blatter radicals (**25a**) to being electrochemically switched on/off and the use of this in the enhancement of NMR signals. Figure reproduced from: F. Saenz, M. Tamski, J. Milani, C. Roussel, H. Frauenrath and J.-P. Ansermet, *Chem. Comm.*, 2022, **58**, 689-692.

Exploring these radicals as O-DNP agents it was found that NMR signal intensity could be greatly enhanced, with amido- and amino-Blatter radicals (**24a**/**25a**) showing higher absolute signal enhancements than the TEMPOL (**12b**) radical. The switchable nature of the Blatter radicals was further explored and it was found that they were stable over multiple cycles (Figure 2.3.2 (c)). Oxidation became increasingly difficult over time but, this was likely due electrode fouling, highlighting an issue with the experiment set up, not the radical.

These novel amido- and amino-Blatter radicals (**24**/**25**) are slowly gaining interest due to ease of synthesis and their intriguing properties. So far, the library of various C(3)-amino and amido Blatter radicals has been limited to the N-Ph parent radical and a small selection functionalised at the N-formyl group. In general, this has been due to the lack of commercially available Nitron derivatives (**6**) and the outdated nature of the synthetic strategy to Nitrons. With the development of a new synthetic strategy to Nitron (**6a**) and

significant exploration into derivatisation, as highlighted in Chapter 2.2, the versatility of the Nitron to Blatter radical conversion can be fully explored.

2.3.3. Isolation and Characterisation of New Blatter-type Radicals

A key aim of this study was to explore the scope of the Nitron (**6**) to amido- and amino-Blatter radical (**24/25**) conversion. The parent Nitron (**6a**) has been found to cleanly convert to Blatter radical in wet acetonitrile over 3 days, in excellent yield (82%). Although the conversion timescale is relatively slow, the great simplicity of the method is attractive. As with the parent Nitron, all new derivatives (**6b-m**) were placed in wet acetonitrile and stirred at room temperature (Scheme 2.3.2). Radical formation was monitored using LC-MS as the analytical technique, before probing radical character through NMR and EPR spectroscopy and CV. Table 2.3.1 summarises these results and shows in general that the Nitron (**6**) to Blatter radical (**24**) conversion is sensitive to functionalisation. It was found that functionalisation on the N(1) position (highlighted red), did not greatly impact radical formation, allowing a selection to be isolated. Moreover, the inclusion of electron donating groups at the R^1/R^2 positions also permitted radical formation; however, these reactions did not proceed as cleanly. This was perhaps due to instability of the radical product owing to the increase in SOMO energy from the lone pair donation. Nitron derivatives with *p*-CF_3 substitution at the R^1/R^2 (**6c, 6i, 6l**) position were very stable in solution showing no apparent degradation to any product over a week and slowly hydrolysing over subsequent weeks to triazabutadienes. Previous work in our group has shown that non-N-formylated triazabutadienes (**54**) are stable and do not undergo oxidative electrocyclization. Selective formylation of the desired nitrogen has not proved possible, highlighting the advantages of the Nitron to Blatter radical rearrangement for successful derivatives. Although attempted, complex product mixtures were obtained with minimal evidence of radical formation. This is likely owing to the multiple nucleophilic N-sites where formylation could occur.

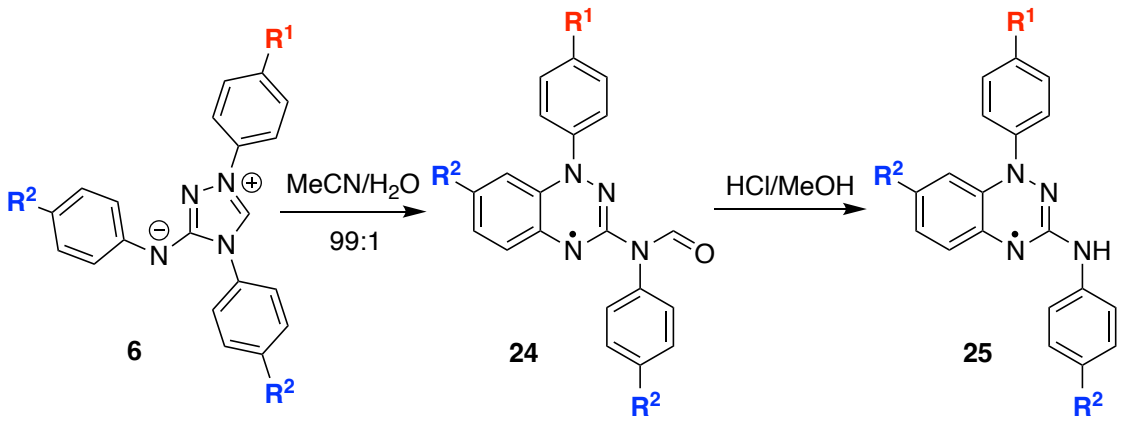

Scheme 2.3.2. Synthesis of Blatter radicals (**24**) from derivatives of Nitron (**6**), and subsequent hydrolysis to amino Blatter radicals (**25**). Table 2.3.1 summarises the explored derivatives.

Table 2.3.1. Summary of the Blatter radical syntheses explored in this work including yields and reaction times.

Derivative	R^1	R^2	Radical (24)?	Time (days)	Yield (24) / %	Yield (25) / %
6a	H	H	Yes (**24a**)	3	82	87
6b[a]	H	Me	No	-	-	-
6c	H	CF_3	No	-	-	-
6d	H	OEt	Yes (**24d**)	3	41	-
6f	MeO	H	Yes (**24f**)	7-10	45	76
6g	F	H	Yes (**24g**)	3-5	75	88
6i	CN	H	Yes (**24i**)	3-5	60	80
6j	CF_3	CF_3	No	-	-	-
6m	OMe	CF_3	No	-	-	-

[a]Nitron derivative substituted with R^2 = Me had been reported previously and isolation of a Blatter radical in this case was likely complicated by the diminished isolated yields (< 15 %, Chapter 2.2).

For those derivatives which failed to form radicals simply by stirring in wet acetonitrile, alternative conditions were explored. These particularly focussed on increasing the rate of hydrolysis of the 1,2,4-triazolium by increasing p*H* of the solution, whilst also increasing the rate of oxidation of the N-formyl triazabutadiene (**38**, Scheme 2.1.8). Previous work had shown that use of mild sodium hydroxide and silver(I) oxide oxidant could aid radical formation, despite these conditions also causing significant by-product formation. Nitron derivative **6c** was chosen as it was easiest to synthesise and one of the first derivatives to be explored in the Nitron to Blatter radical conversion. A selection of oxidative procedures were explored, including the use of electrochemistry. With the derivatives discussed here, however, this was unsuccessful and merely increased the conversion to the unreactive N-anilino triazabutadiene (**54c**). A range of other oxidants were explored in this conversion alongside electrochemical oxidations. Unfortunately, in enhancing the rate of zwitterionic ring opening by using hydroxide solutions, the rate of hydrolysis (or de-formylation) of the N-formyl triazabutadiene is also increased

significantly. This essentially shuts down Blatter radical formation as the non-formylated triazabutadienes do not react to radicals. As such, this approach to isolate these novel radicals was not explored any further.

Table 2.3.2. Summary of the conditions screened for radical formation of the Nitron derivatives which do not show spontaneous radical conversion under the conditions of acetonitrile/water (98:2).

Solvent	Oxidant	Derivatives Explored	Time	Major Product by LC-MS
MeCN/H_2O (98:2)	None	All	3 days-3 months	(**6a, d, f, g, i**) BR (**6c, j, m**) Nitron (**6b**) Triazabutadiene
MeCN/H_2O (98:2)	AgO	**6c, j, m**	1 month	Nitron/triazabutadiene
MeCN/H_2O (98:2)	MnO	**6c, j, m**	1 month	Nitron/triazabutadiene
MeCN/H_2O (98:2)	Pd/C	**6c, j, m**	1 month	Nitron/triazabutadiene
MeCN/H_2O (98:2)	Graphite Electrode	**6c**	< 4 hrs	Nitron/triazabutadiene
MeCN/0.5 M NaOH (98:2)	None	**6c, j, m**	1 month	Triazabutadiene
MeCN/0.5 M NaOH (98:2)	AgO	**6c, j, m**	1 month	Triazabutadiene
MeCN/0.5 M NaOH (98:2)	MnO	**6c, j, m**	1 month	Triazabutadiene
MeCN/0.5 M NaOH (98:2)	Pd/C	**6c, j, m**	1 month	Triazabutadiene
MeCN/0.5 M NaOH (98:2)	Graphite Electrode	**6c**	< 4 hrs	Triazabutadiene
DCM/H_2O (98:2)	None	**6c**	2 weeks	Nitron
MeCN/H_2O_2 (98:2)	H_2O_2	**6c**	1 day	Triazabutadiene

Isolated radicals were initially characterised by NMR spectroscopy and broadened spectra were obtained. Subsequently, reversible oxidation and reduction processes were probed via cyclic voltammetry in acetonitrile with a tetrabutylammonium hexafluorophosphate electrolyte, with platinum electrodes (Figure 2.3.2). Values were further compared to the parent Blatter radical (**15a**), which was synthesised according to Scheme 2.3.3.[35, 63] Table 2.3.3 summarises the half-wave oxidation and reduction potentials for the isolated radicals with respect to the ferrocene half-wave potential. Amido-Blatter radicals see significant overlap with the ferrocene internal standard and so decamethylferrocene was used. Decamethylferrocene has a half-wave potential of 0.50 V in comparison to ferrocene.[21]

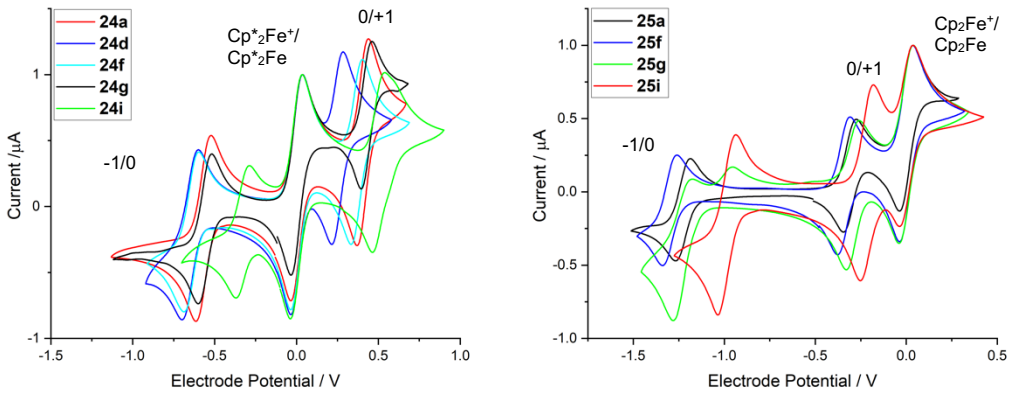

Figure 2.3.2. Left: Cyclic voltammograms of isolated amido Blatter radicals (**24**) compared to decamethylferrocene in acetonitrile, with tetrabutylammonium hexafluorophosphate electrolyte and a scan rate of 50 mV s^{-1}. Right: Cyclic voltammograms of isolated amino Blatter radicals (**25**) compared to ferrocene in acetonitrile, with tetrabutylammonium hexafluorophosphate electrolyte and a scan rate of 50 mV s^{-1}.

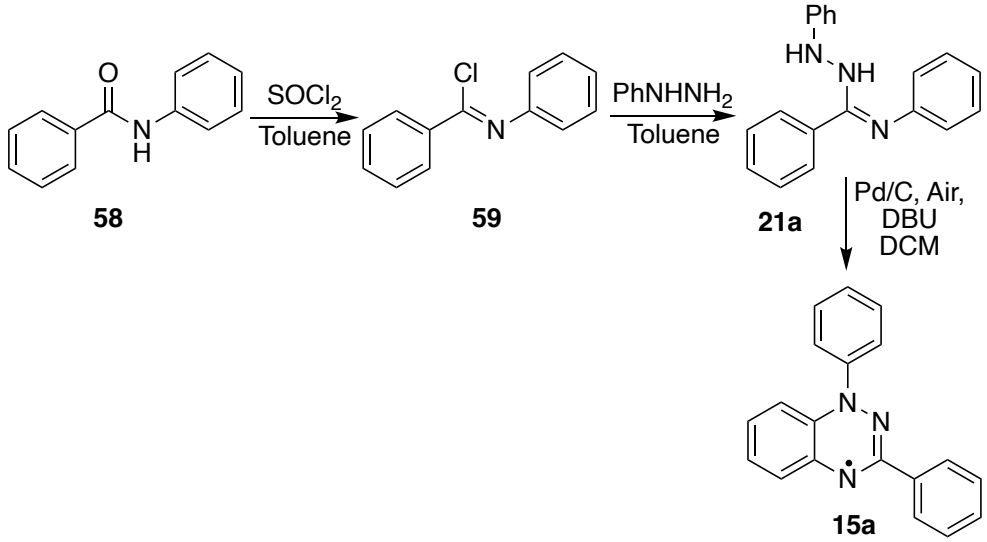

Scheme 2.3.3. Synthesis of the parent Blatter radical via amidrazone synthesis and subsequent oxidation to the Blatter radical.

Table 2.3.3. Summary of the half-wave oxidation and reduction potentials of isolated radicals vs the ferrocene/ferrocenium half-wave potential.

Radical	$E^{0/+1}_{1/2}$ / V	$E^{0/-1}_{1/2}$ / V	ΔE / V
24a	-0.096	-1.07	0.97
24d	-0.25	-1.15	0.90
24f	-0.13	-1.14	1.01
24g	-0.073	-1.06	0.99
24i	0.0017	-0.83	0.83
25a	-0.31	-1.23	0.92
25f	-0.34	-1.30	0.96
25g	-	-	-
25i	-0.22	-0.99	0.77
15	-0.18	-1.25	1.07

Exploring the cyclic voltammetry data, typically the amino radicals have smaller values for ΔE than the amido Blatter radicals by up to 0.1 V. Interestingly, derivative **24/25i**, substituted with the pCN group gives the smallest values for ΔE for both the amido and amino Blatter radical. These small values for ΔE arise from moderately higher oxidation potentials and significantly higher reduction potentials. This significantly higher reduction potential can be rationalised by inductive stabilisation of the benzotriazinyl anion formed in this case, considering the large Hammett-σ value of the cyano group of 0.66.[70] Interestingly, radicals with smaller values of ΔE have been shown to be particularly useful as dynamic nuclear polarisation agents in NMR.[74] This radical derivative could be particularly useful in these studies. As would be anticipated, the inclusion of electron donating groups at the N(1)-position or the fused ring decrease the reduction potential as the anionic form is disfavoured. Conversely, the oxidation potentials for these derivatives, forming the cationic form, are much lower, highlighting the stabilising effect of these electron donating groups. Finally, in comparison to the parent, C(3)-phenyl Blatter radical (**15a**), all have significantly smaller ΔE values, highlighting the potential advantages of these new Blatter radical functionalities.

Anomalous behaviour was observed in the cyclic voltammogram for the *p*-F amino Blatter radical (**25g**). The oxidation component appeared normal when forming the benzotriazinyl cation. During reduction it appeared instead to undergo a two-electron reduction in one process; however, upon oxidising back to the neutral radical it appeared to lose these electrons in two consecutive one electron processes (Figure 2.3.3). One possibility is that at this potential an electron adds to both the radical centre and to the fluorobenzene ring forming a radical anion. The non-symmetrical behaviour could be due to a conformational change upon formation of the radical anion, altering the oxidation potentials.

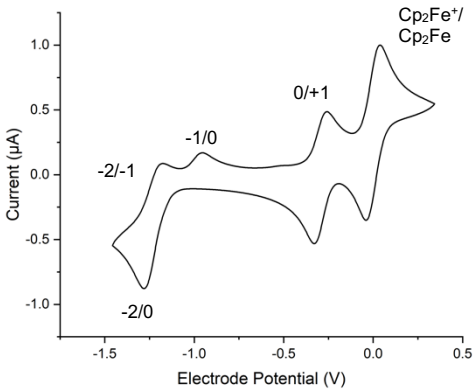

Figure 2.3.3. Unusual electrochemical behaviour of radical **25g** exhibiting normal oxidation behaviour (1e$^-$ process) but an unusual 2-electron reduction, followed by sequential 1-electron oxidation processes to return to the radical.

To further characterise the radicals, electron paramagnetic resonance (EPR) spectroscopy was explored. EPR spectra were acquired by Dr Victor Chechik in the University of York. Typically data matched that previously isolated on the amido- and amino- Blatter radicals (**24a**/**25a**). Simulated and experimental spectra were in good agreement and it was found that including the fourth, exocyclic nitrogen atom within the simulation gave a moderate improvement in the fit. This moderate fit improvement could highlight a small amount of radical character delocalised on this exocyclic nitrogen. Hyperfine coupling constants give an indication of the location of spin density across the radicals (Table 2.3.4).

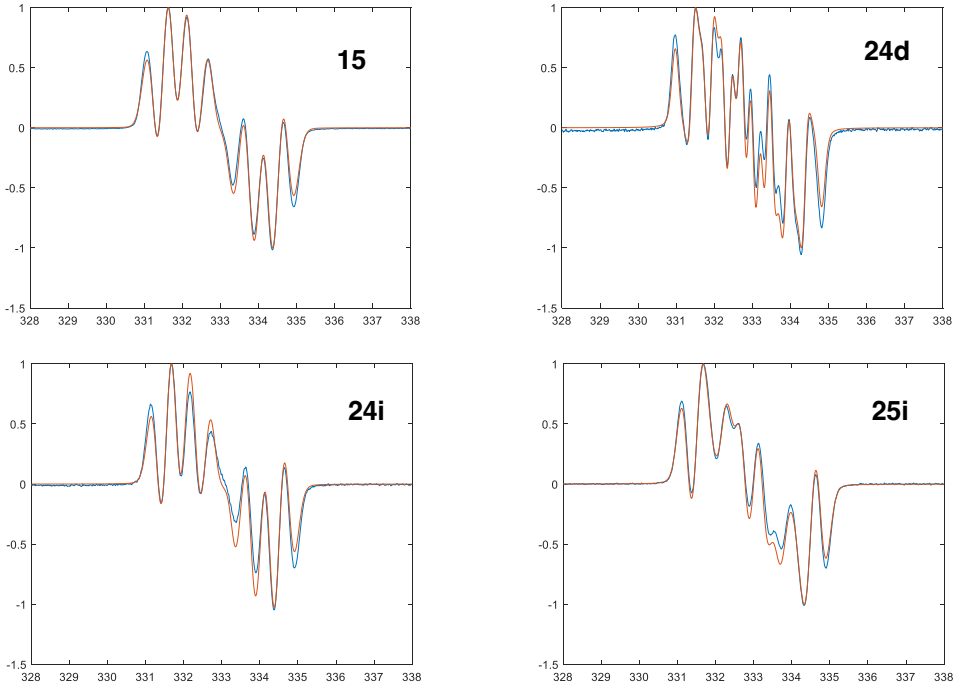

Figure 2.3.4. Representative EPR Spectra for amido and amino Blatter radicals, blue lines are experimental spectra and orange lines are simulated spectra. Top left: parent radical (**15**); Top Right: pOEt Amido Blatter radical (**24d**); Bottom Left: pCN Amido Blatter radical (**24i**); Bottom Right: pCN Amino Blatter radical (**25i**).

Table 2.3.4. Summary of the hyperfine coupling constants for the isolated radicals, giving insight into the delocalisation of radical character across the 3 (or 4) nitrogen atoms.

Compound	a_N1 / Gauss	a_N2 / Gauss	a_N3 / Gauss	a_N4 / Gauss
15	7.55	5.22	4.78	0.72[a]
24a	8.04	5.10	4.63	0.98
24d	7.31	5.29	4.73	1.31
24f	8.18	5.06	4.49	1.00
24g	7.58	5.56	4.31	1.06
24i	7.38	4.69	5.18	0.56
25a	7.94	5.76	4.26	0.72
25f	8.13	5.65	4.13	1.13
25g	7.93	5.76	4.25	0.88
25i	7.25	5.81	4.30	0.76

[a]In this case it is an exocyclic phenyl, compound **15** does not have an exocyclic nitrogen.

Hyperfine coupling constants show that radical character at N(1), N(2), N(3), and N(4) (numbering as in Figure 2.3.5) does not vary substantially with substituents. Electron donating substituents (**24d**, **24g**, **25 g**) appear to reduce the radical localisation at N(1), whilst increasing the contribution of N(2). This can be attributed to a destabilisation of N(1) by these donating substituents, where N(2) is less affected (more remote). Radicals **24i** and **25i** with strongly withdrawing cyano-substituents at N(3) greatly increase radical contribution of these positions due to the stabilising effects. The same trend is not observed for the fluoro-substituted radicals (**24f/25f**) which show very similar values to the unsubstituted N-Ph radicals (**24a/25a**).

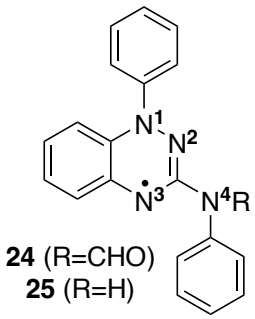

Figure 2.3.5. Amido (R=CHO, **24**) and amino (R=H. **25**) Blatter radical numbering references for hyperfine coupling constants discussed in Table 2.3.4 and Table 2.3.5.

To provide further insight into the EPR studies, computationally derived SOMOs and spin density plots were determined for a selection of the radicals using the UB3LYP/6-311+g(d,p) level of theory. These had previously been calculated for the parent Blatter radical (**15**) and the unfunctionalized amido- and amino Blatter Radicals (Figure 2.3.6, Table 2.3.5). Despite adding a fourth nitrogen to the fitting of the EPR spectra increasing the simulation quality in comparison to experimental data, the computationally derived

spin densities do predict minimal radical character at N(4). Increasing the number of terms in any simulation typically improves the overall fit compared to experimental data. It is important to determine the chemical implications of this and in this case it appears not to be a chemical effect but purely an improved mathematical fit. Values for both % SOMO contribution and the EPR hyperfine constants (EPR-II) show a similar predicted trend to that observed in the experimental data (Table 2.3.4): changes are small but correlated to electron donating destabilisation and electron withdrawing stabilisation.

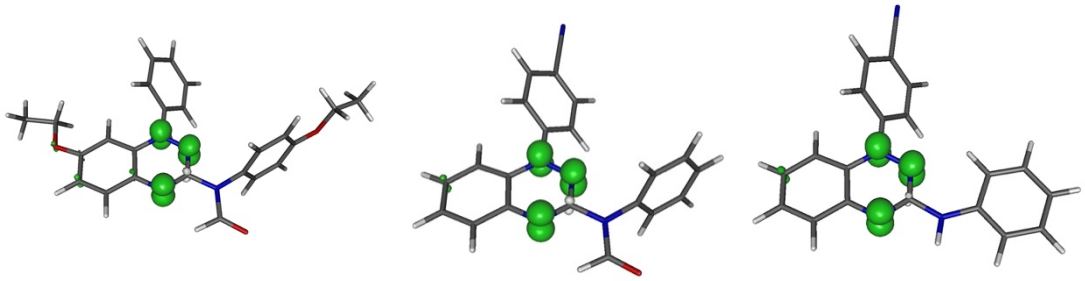

Figure 2.3.6. Computed spin density representations for amido Blatter radicals (**24d** and **24**i) and amino Blatter radical (**25i**) showing density mainly localised on the 3 ring nitrogen atoms. Determined with the UB3LYP/6-311+g(d,p) level of theory.

Table 2.3.5. Summary of the % SOMO contributions, electron spin, and hyperfine coupling constants (HFCCs) for parent radical (**15**), amido Blatter radicals (**24a, 24d, 24i**) and amino Blatter radicals (**25a, 25i**) determined by computational chemistry using the UB3LYP/6-311+g(d,p) level of theory.

Compound	Atom	SOMO / %	Spin / e	HFCC / Gauss	EPR-II / Gauss
15[a]	N(1)	18	0.22	4.43	5.31
	N(2)	20	0.37	3.27	4.11
	N(3)	18	0.32	3.51	4.36
24a[a]	N(1)	18	0.23	4.77	5.70
	N(2)	21	0.46	3.47	4.32
	N(3)	17	0.32	3.16	4.35
	N(4)	1	0.01	-0.17	-0.20
24d	N(1)	16	0.22	4.26	5.09
	N(2)	18	0.33	3.19	4.00
	N(3)	18	0.31	3.18	4.22
	N(4)	0	0.00	-0.26	-0.32
24i	N(1)	16	0.22	4.28	5.01
	N(2)	21	0.35	3.21	4.04
	N(3)	17	0.30	3.25	4.02
	N(4)	0	0	-0.29	-0.33
25a[a]	N(1)	18	0.26	4.70	5.62
	N(2)	19	0.33	3.28	4.16
	N(3)	18	0.30	3.27	4.05
	N(4)	0	-0.02	-0.47	-0.53
25i	N(1)	17	0.23	4.13	4.95
	N(2)	19	0.33	3.26	4.12
	N(3)	18	0.31	3.31	4.09
	N(4)	0	-0.02	-0.48	-0.55

[a]Values previously reported.[21]

Finally, where possible, new Blatter radicals were crystallised and characterised using X-ray crystallography. Figure 2.3.7 summarises the isolated crystal structures and Table 2.3.6 compares some of the key bond lengths and angles within the Blatter radicals. Comparing amido- (**24a**, **f**) to amino- (**25a**, **f**) Blatter radicals both the N(1) and C(3) dihedral angles become more planar. This could be due to the loss of the formyl group, allowing a more planar N-phenyl conformation or perhaps due to an increased conjugation required for stabilisation. The C(3)-NPh bond lengths also decrease from amido- to amino- radicals, consistent with an increase in conjugation from the N-Ph onto the benzotriazinyl ring. In considering the exocyclic nitrogen lone pair of electrons, upon de-formylation, this is more readily available for conjugation into the benzotriazinyl ring, consistent with a shorter C(3)-N bond length and greater planarity of this N-aryl substituent.

There is also an increased N(3)-bond angle for the amino-Blatter radicals, perhaps attributed to greater s-orbital character at nitrogen and a greater stabilising effect. These N(3)-bond angles are close to trigonal planar, with the amino-Blatter radicals being closest to this angle. A more trigonal planar radical centre should be reflected in lower propensity to form the anion upon reduction as this conformation destabilises anionic charges. The cyclic voltammetry data (Table 2.3.3) reflects these small changes in N(3)-bond angle, with more negative reduction potentials for amino radicals, which have more trigonal planar N(3)-bond angles. This trend is also observed with regards to substituent effects where, for example, the pCN substituted amido radical (**24i**) has the highest reduction potential and also the least trigonal planer N(3)-bond angle of the amido radicals.

In considering substituent effects on the radical XRD crystal structures there appears to be no clear trend observed for N(1) or C(3)-dihedral angles, although the changes are large. Interestingly, the largest differences are observed for the pCN-substituted radical (**24i**) which also has the smallest ΔE determined by cyclic voltammetry. There is a clear trend for N(1)-Ph bond lengths, which decrease for more electron withdrawing derivatives as would be expected. Similar observations can be made of the C=N bond which decreases for electron withdrawing groups. Finally, the fused-ring dihedral angles reflect a greater planarity for amino-Blatter radicals and therefore greater delocalisation

of electrons across the benzotriazinyl scaffold. This can again be related to the loss of a formyl and therefore a greater contribution to stabilisation from the central structure.

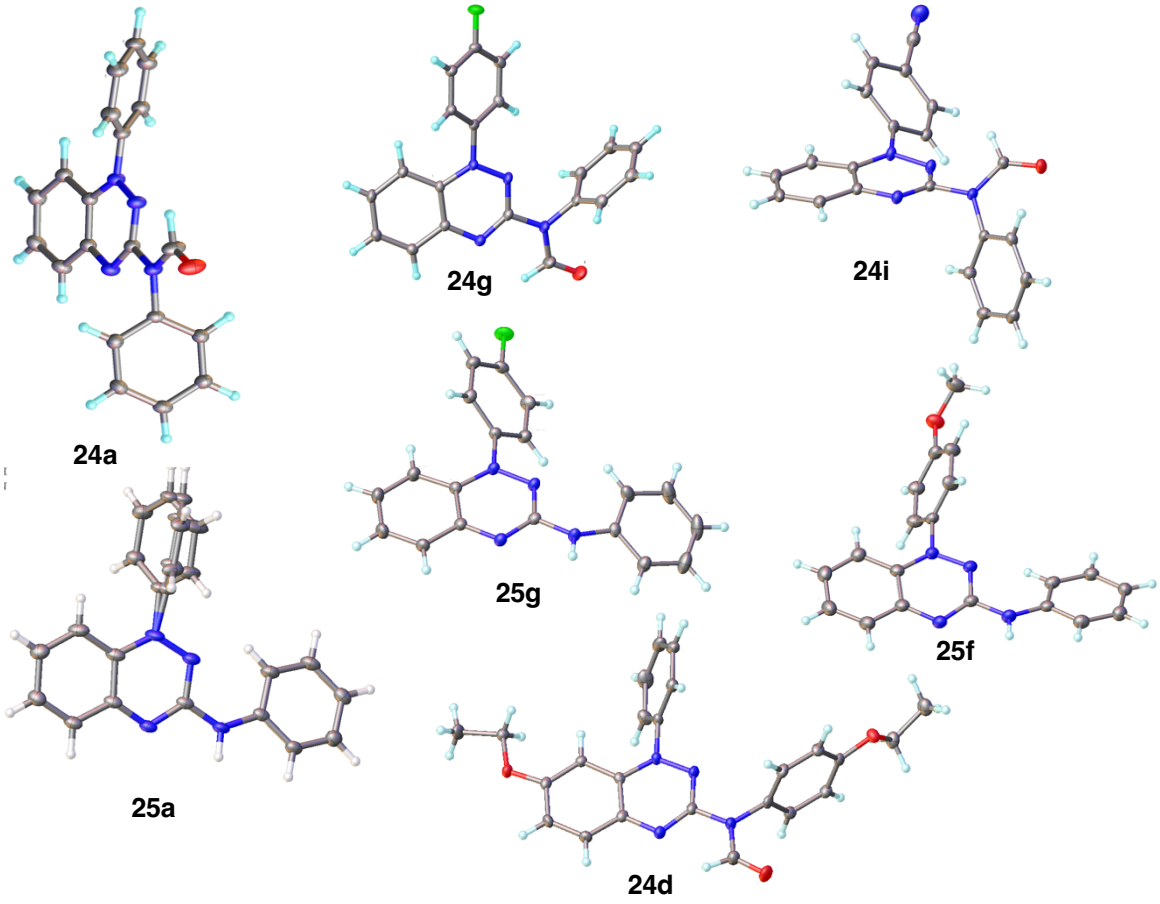

Figure 2.3.7. Summary of the structures determined by X-ray crystallography for Blatter radicals isolated in this project. Crystals suitable for XRD analysis were typically obtained by slow evaporation of methanol solvent containing radical solutes.

Table 2.3.6. Summary of key dihedral angles, bond angles and lengths for amido- (**24**) and amino- (**25**) Blatter radicals.

Structure	R^1	R^2	N(1)-Dihedral Angle / °	C(3)-Dihedral Angle / °	N(1)-Ph Length /Å	C(3)-NPh Length /Å	N(3) Bond Angle / °	Fused Ring Dihedral Angle / °	C=N Length /Å
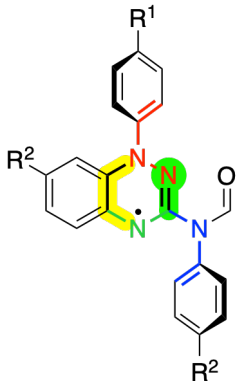	H	H	35.535	92.434	1.428	1.417	114.47	-3.793	1.336
	F	H	31.765	83.329	1.427	1.414	114.14	-2.007	1.326
	CN	H	35.457	41.015	1.425	1.421	114.03	-2.747	1.323
	H	OEt	120.805	89.198	1.435	1.416	114.72	0.165	1.335
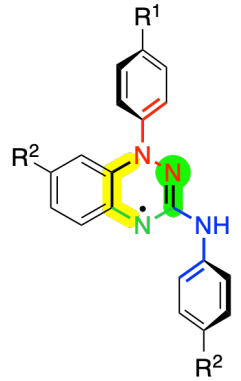	H	H	76.812	-9.260	1.446	1.370	115.30	-0.587	1.343
	F	H	52.764	-3.523	1.434	1.373	115.33	-1.458	1.342
	MeO	H	129.743	-12.798	1.439	1.372	115.32	-2.711	1.341

2.3.4. The Role of Nitron Tautomerism

The trends observed in radical formation can be discussed according to Figure 2.3.8. Changing the Ar^1 substituent seems to have limited effect on the radical formation, and this is likely due to a small Ar^1 effect on the electrophilicity of the N-formyl groups of (**38**). In the case of electron-withdrawing groups at Ar^2, the N-formyl group has significantly enhanced electrophilicity, accelerating hydrolysis of this group to N-anilino triazabutadienes (**54**) as opposed to electrocyclization to the desired radicals (**24**). As mentioned above, these non-formylated triazabutadienes (**54**) are very stable and do not undergo oxidative electrocyclization directly to amino-Blatter radicals (**25**). Ring opening for the electron-withdrawing Nitron derivatives (**6c**, **6j**, **6m**) is particularly slow, which limits the formation of the N-formyl triazabutadiene (**38**) further. In the case of introducing electron donating groups at these positions, the rate of ring opening appears much faster. Moreover, the electrophilicity of the N-formyl carbon is vastly reduced which slows the rate of hydrolysis significantly allowing electrocyclization to the Blatter radical (**24**) to occur.

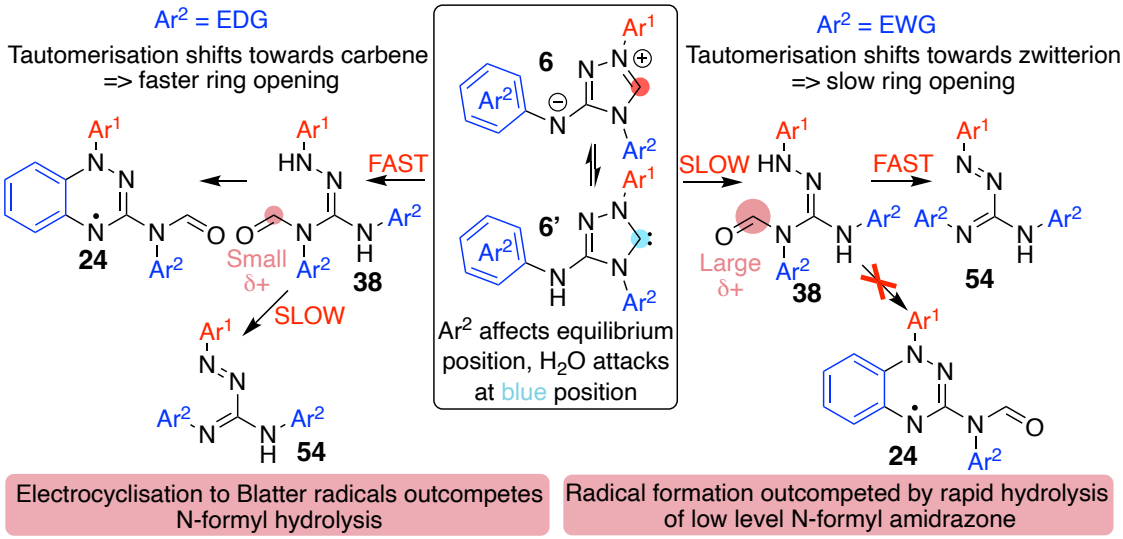

Figure 2.3.8. The observed trend in radical formation suggests it is the 1,2,4-triazolyl-ylidene which is more susceptible to ring opening than the 1,2,4-triazolium as electron donating groups at Ar^2 favour ring opening. Once ring opening occurs, the formation of radical is dependent on the hydrolytic stability of the N-formyl group. If fast hydrolysis to the triazabutadiene occurs, radical is not formed; however, if it is slower, electrocyclization can readily occur to yield the desired radicals.

The observed trends for triazolium ring opening, with electron-withdrawing groups slowing and electron donating groups enhancing ring opening appear initially counterintuitive. It would be anticipated that electron withdrawing groups enhance the electrophilicity of the C(3)-position of the triazolium (**6**) and increase the rate of ring opening. This observed influence of substituents led us to consider the role of tautomerisation in hydrolytic ring opening. 1,2,4-Triazoliums form singlet carbenes with

an empty p-orbital, to which a nucleophile like water could attack, potentially facilitating hydrolysis at this position. Introduction of electron directing groups at Ar^2 will also influence the position of the zwitterion-carbene tautomer of Nitron derivatives (**6**) and alter rates of ring opening. Although both **6** and **6'** tautomers are formally neutral, less electronic and bond reorganisation is needed upon attack of water for **6'** hence activation barriers could be lower in this case. Electron withdrawing *p*CF_3 groups will greatly stabilise the exocyclic negatively charged N atom, shifting the equilibrium in favour of the zwitterion; *p*OEt groups will decrease the stability of this negative charge, shifting the equilibrium in favour of the carbenic tautomer. Increasing concentrations of **6'** by introducing electron donating substituents could increase the rate of hydrolytic ring opening.

In collaboration with Tom Richardson, a 4th Year MChem student, further investigations into the mechanism of ring opening explored the effects of methylation of the exocyclic amino group. Treating Nitron (**6a**) with trimethyloxonium tetrafluoroborate in anhydrous DCM readily enabled this methylation (**60a**) in good yield (43%). Purification was possible by recrystallisation or column chromatography (Scheme 2.3.4). Interestingly, methylation of the exocyclic amino group vastly slowed ring opening of Nitron (**60a**) to the point that no reaction was seen over the space of 2 weeks, in comparison to Nitron (**6a**) which spontaneously ring opens and cyclizes within 3 days (Figure 2.3.9). This can be explained through shutting down the tautomerism to the carbene which appears to be the most readily hydrolysed species in solution. Otherwise, the position of N-methylation is too remote to have a significant steric or electronic effect on ring opening at the C(3)-position. This provides further evidence that the ring opening via the carbenic tautomer is faster relative to the zwitterionic form.

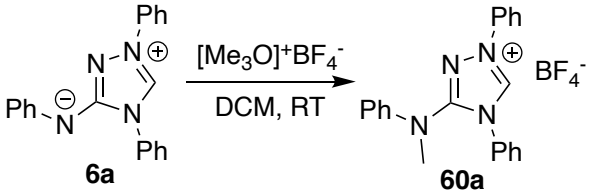

Scheme 2.3.4. Synthesis of methylated-Nitron (**60a**) using trimethyloxonium tetrafluoroborate, in good yield. Methylation switches off the Nitron tautomerisation and hence allows exploration of the effect of this tautomerisation on ring opening.

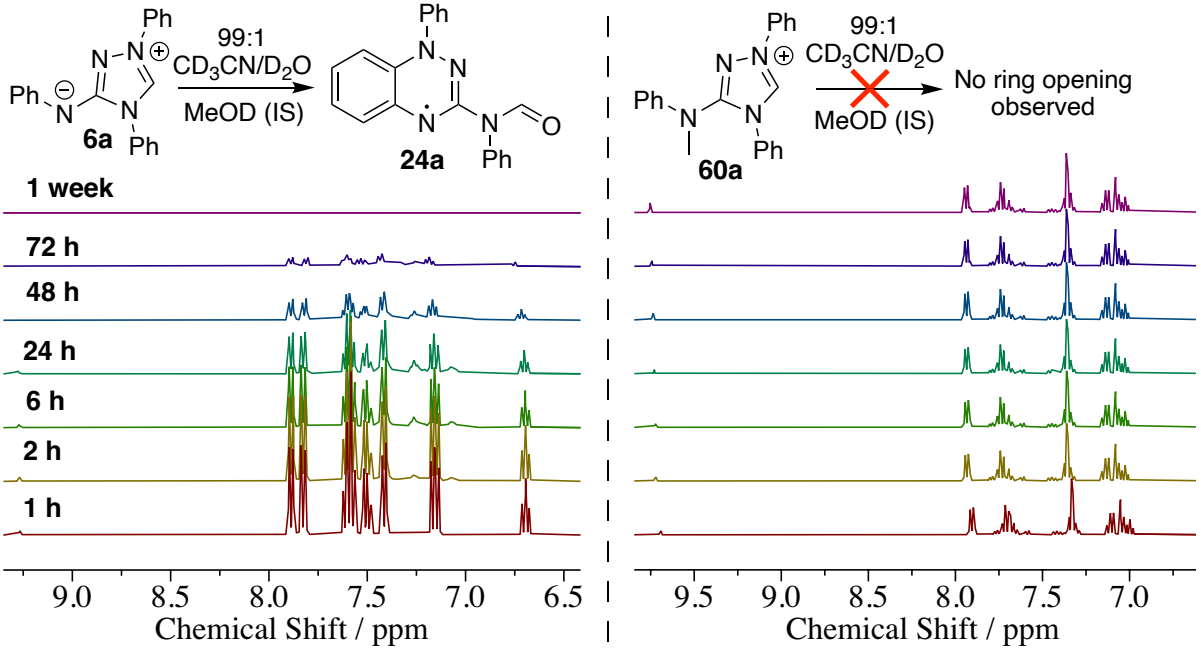

Figure 2.3.9. ^{1}H NMR spectroscopy studies on the ring opening of Nitron and methylated Nitron showing ring opening and radical formation within 3 days for Nitron (**6a**) however no change in NMR signal for the methylated Nitron (**60a**) over the time frame. This suggests that the loss of tautomerism greatly influences the hydrolytic stability.

To give further insight into the effect of the electron directing groups on the tautomerisation, exocyclic nitrogen pK_a values were measured and C(3)-H acidities estimated for a selection of the derivatives. Using these values, an estimate for pK^T, the tautomeric equilibrium constant between carbenic and zwitterionic forms can be estimated (Equation 2.3.1).

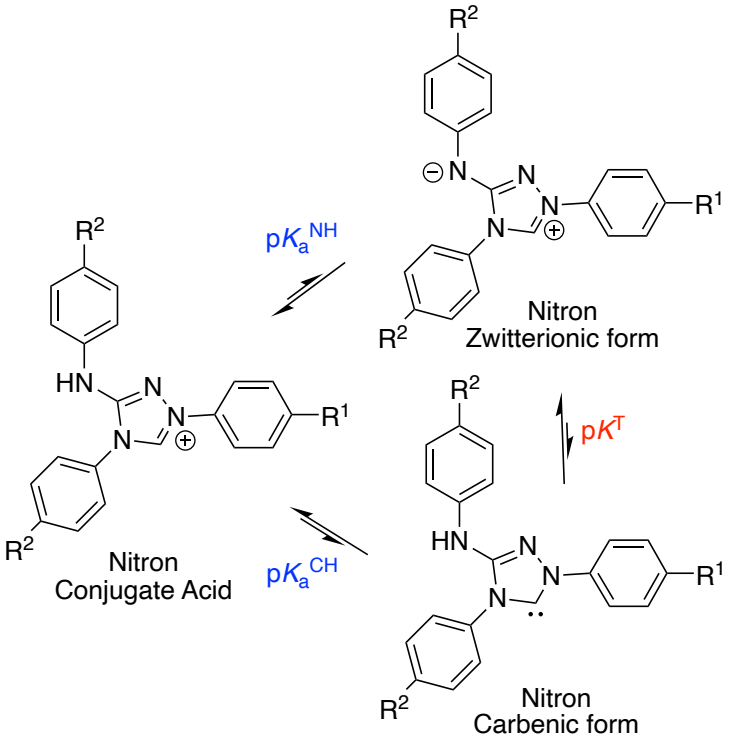

Figure 2.3.10. Thermodynamic cycle for proton dynamics at Nitron which can be manipulated through knowledge of the exocyclic nitrogen pK_a^{NH} and the C(3)-H pK_a^{CH} to estimate values for pK_T, the tautomeric equilibrium.

$$pK^T = pK_a^{CH} - pK_a^{NH} \qquad \textbf{Equation 2.3.1}$$

Nitrogen pK_a values were determined using a reliable spectrophotometric titration method. Substrates were dissolved in acetonitrile and added to buffers (0.1 M, I = 0.3 M) at 0.01 mM concentrations. Absorbance was measured across the p*H* range and plotted to give the absorbance-wavelength plots in Figure 2.3.11, for Nitron derivative (**6d**) (Appendix 7.1.1 for Nitron derivatives (**6a**, **6c**)). These plots were fit to Equation 2.3.2, derived as shown (Equations 2.3.3-2.3.7), where A_{obs} is the observed absorbance, A_{max} is the maximum absorbance (at which substrate is either fully protonated/deprotonated), A_{min} is the minimum absorbance (at which substrate is either fully protonated/deprotonated), p*H* is that of the buffer used and K_a is the acid dissociation constant for the substrate. At the chosen analytical wavelength of 360 nm, the absorbance increases with p*H*, thus A_{max} reflects fully deprotonated substrate and A_{min} the fully protonated form. This gives a value for pK_a^{obs} (Equation 2.3.8) (Table 2.3.7); p*H* values were recorded in aqueous solution whereas A_{obs} values were recorded in 30 % v/v acetonitrile to solubilise the non-polar substrates. In principle, these absorbance changes could result from CH or NH dissociation. Given that CH pK_as are predicted to be above p*H* 14 (*vide infra*) and the large observed effect of Ar[2], the pK_a^{obs} values can be assigned to NH.

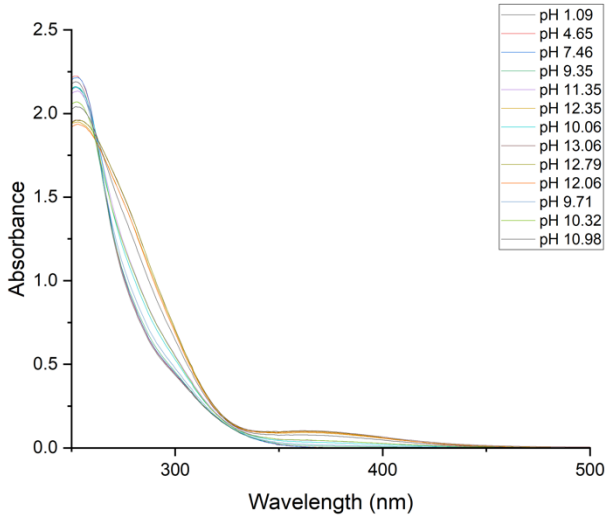

Figure 2.3.11. UV-Vis absorbance spectra collected for Nitron derivative (**6d**) across the p*H* range 1-13, change of absorbance at 360 nm was used to estimate the exocyclic nitrogen pK_a using Equations 2.3.2-2.3.7, as plotted in Figure 2.3.12.

$$A_{obs} = \frac{A_{min}.10^{-pH} + A_{max}.K_a}{10^{-pH} + K_a} \qquad \textbf{Equation 2.3.2}$$

$$K_a = \frac{[H^+][A^-]}{[HA]} \qquad \textbf{Equation 2.3.3}$$

$$[H^+] = 10^{-pH} \qquad \textbf{Equation 2.3.4}$$

$$[HA] \propto A_{max} - A_{obs} \ (360\ \text{nm}) \qquad \textbf{Equation 2.3.5}$$

$$[A^-] \propto A_{obs} - A_{min} \ (360\ \text{nm}) \qquad \textbf{Equation 2.3.6}$$

$$K_a = \frac{10^{-pH}(A_{max} - A_{obs})}{(A_{obs} - A_{min})} \qquad \textbf{Equation 2.3.7}$$

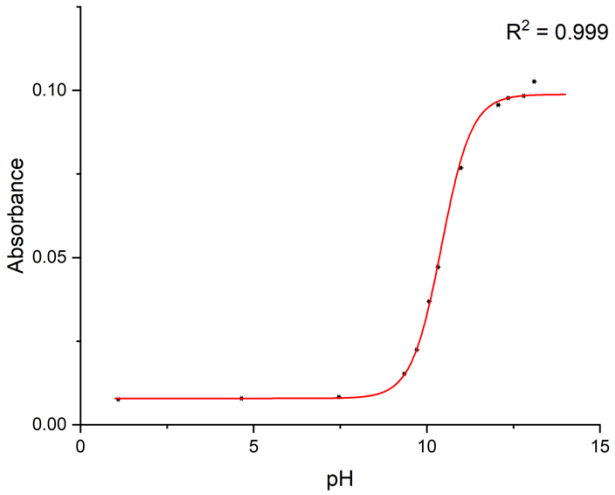

Figure 2.3.12. Plot of p*H* vs Absorbance at 360 nm for derivative **6d**. The solid line shows the fit of reaction data to Equation 2.3.2 to determine a value for K_a and therefore pK_a, according to Equation 2.3.8.

$$pK_a = -log_{10}K_a \qquad \textbf{Equation 2.3.8}$$

Table 2.3.7. Summary of the K_a and pK_a values determined for the three explored Nitron derivatives with different substituent on Ar^2 (**6a**, **6c**, **6d**). Significant shifts in the observed pK_a can be attributed to the electron donating/withdrawing substituent effects on N-anion stability.

Derivative	Ar^1	Ar^2	K_a /×10^{-10} M	p$K_a^{NH(obs)}$
6a	Ph	Ph	1.66	9.78 ± 0.04
6c	Ph	4-$CF_3C_6H_4$	14.1	8.85 ± 0.03
6d	Ph	4-$EtOC_6H_4$	0.398	10.4 ± 0.02

Values for the exocyclic p$K_a^{NH(obs)}$ are similar to those of substituted phenols and have similar substituent effects on pK_a. Phenol has a pK_a of 9.98 with *para*-methoxyphenol at 10.21 and *para*-nitrophenol at 7.15.[75] Phenolic pK_as are typically substantially lower than those of anilines ($PhNH_2$ → $PhNH^-$, pK_a > 30) owing to the higher electronegativity of oxygen. The cationic heterocycle of Nitron in this case further enhances NH acidity such that the phenol OH and Nitron NH are similar. The 2 pK_a unit difference between

derivatives **6c** and **6d** suggests there would be a likely significant shift in the tautomeric equilibrium of the zwitterionic and carbenic forms. This adds to the hypothesis that this tautomerisation is key to the Nitron to Blatter radical rearrangement.

Values for pK_a^{CH} can be estimated using a kinetic method to monitor hydrogen-deuterium exchange at a range of buffer p*D* values. The background theory to this approach is discussed in greater detail in Chapter 3.3.4. Typically, H/D exchange is monitored via ^{1}H NMR spectroscopy over a range of p*D* values from 0-6 and values for k_{ex} (the first-order rate constant of exchange) manipulated to estimate a carbon acid pK_a. Nitron derivatives have been found to ring open above p*D* values of 3-4 and so instead H/D exchange was monitored at a single p*D* of 1.09 and compared to previous results to estimate pK_a^{CH} values. In doing so, ring opening of the Nitron derivatives is supressed and reliable rate constant estimates can be generated (like methylation, protonation suppresses ring opening). Furthermore, based on spectrophotometric studies, the Nitron derivatives will be in the conjugate acid form at p*D* 0-6 thus H/D exchange occurs on the cationic conjugate acid. Proton transfer at nitrogen is diffusion controlled at all p*H*s in aqueous solution whereas proton transfer at carbon is slower. This permits analysis of proton transfer at carbon in isolation.

Substrates were dissolved in MeCN-d_3 and added to 0.1 M DCl (30% v/v MeCN-d_3), recording the time of mixing, with a tetramethylammonium chloride (TMACl) internal standard. Decay of the C(3)-H peak was monitored over 6-48 hrs at 25 °C via ^{1}H NMR spectroscopy with parameters described in the experimental section. Fraction of substrate, F(S), can be determined according to Equation 2.3.9 where A_{CH} refers to the integral of the C(3)-H position and A_{IS} to the integral of the TMACl peak. The benefit of this is that absolute concentrations of substrates need not be known. A plot of F(S) against time shows a first order, exponential decay (Figure 2.3.13 for derivative **6i**, Appendix 7.1.2 for **6a-6m**) and a plot of ln[F(S)] against time gives a straight-line (Figure 2.3.14). Table 2.3.8 summarises the k_{ex} values determined at two different proportions of MeCN-d_3 owing to the need to solubilise less polar derivatives. Also highlighted are values previously reported under very similar experimental conditions for another 1,2,4-triazolium scaffold (**61**).[76]

$$F(S) = \frac{(A_{CH}/A_{IS})_t}{(A_{CH}/A_{IS})_0} \qquad \textbf{Equation 2.3.9}$$

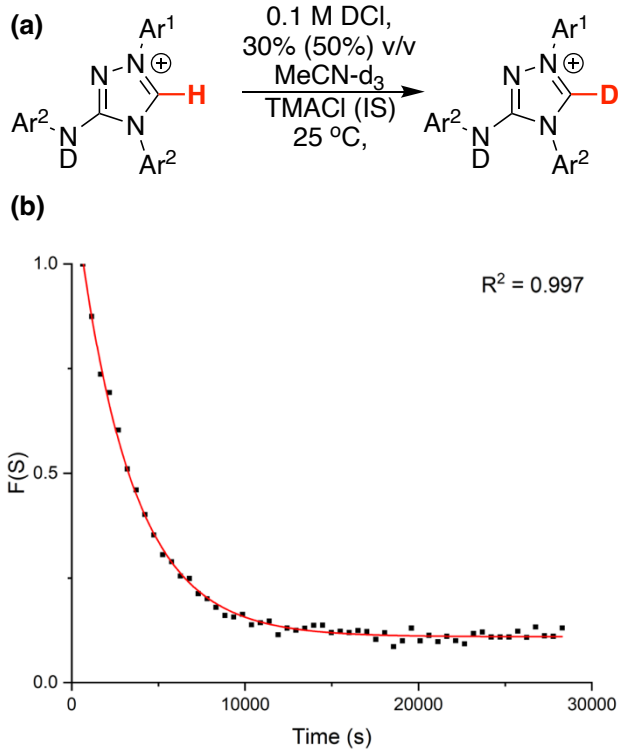

Figure 2.3.13. (a) C(3)-H exchange of Nitron derivatives in 0.1 M DCl, with 30% or 50% v/v MeCN-d_3 at 25 °C with a TMACl internal standard, monitored by ^{1}H NMR spectroscopy. (b) Plot of F(S) against time for the decay of the C(3)-H peak of Nitron derivative **6i** in 0.1 M DCl (30% v/v MeCN-d_3) at 25 °C displaying an excellent fit ($R^2 = 0.997$) to a first-order decay.

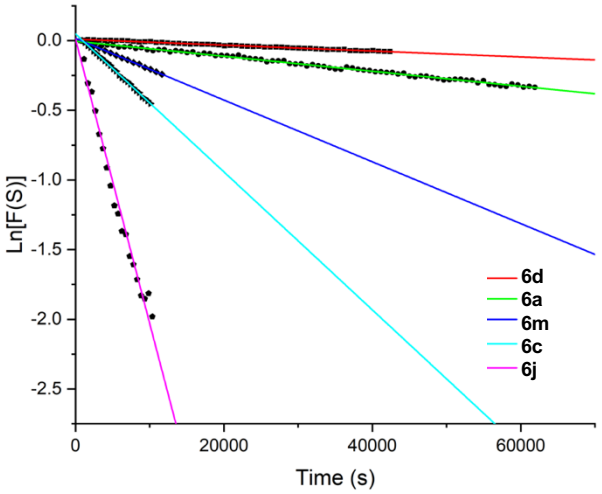

Figure 2.3.14. Plots of ln[F(S)] against time for a selection of Nitron derivatives (**6**) in 0.1 M DCl (30% v/v MeCN-d_3) at 25 °C, giving linear plots from which the gradient was used as an estimate for the first-order rate constant for H/D exchange, k_{ex}.

Table 2.3.8. Summary of the estimates determined for the rate of H/D exchange at the C(3)-position of various Nitron derivatives (**6**) in 0.1 M DCl solution at 25 °C. Also shown are results previously reported for H/D exchange on another 1,2,4-triazolium scaffold (**61**), for which pK_a values were subsequently estimated.

Compound		Ar^1	Ar^2	k_{ex} in 30% MeCN / $\times 10^{-6}$ s^{-1}	k_{ex} in 50% MeCN / $\times 10^{-6}$ s^{-1}	pK_a^{CH} 30% (50%) v/v MeCN
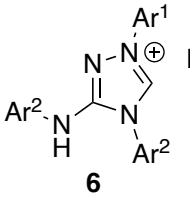 6	**6a**	Ph	Ph	6.39 ± 0.01	5.38 ± 0.05	17.8[a] (17.9)
	6d	Ph	4-$EtOC_6H_4$	3.01 ± 0.02	2.12 ± 0.03	18.1[a] (18.3)
	6c	Ph	4-$F_3CC_6H_4$	33.7 ± 1.5[c]	49.5 ± 0.3	17.1[a] (16.9)
	6i	4-NCC_6H_4	Ph	61.3 ± 0.2	-	16.8
	6g	4-FC_6H_4	Ph	7.27 ± 0.01	-	17.7[a]
	6m	4-$MeOC_6H_4$	4-$F_3CC_6H_4$	-	22.2 ± 0.2	(17.3)
	6j	4-$F_3CC_6H_4$	4-$F_3CC_6H_4$	-	204 ± 6.5	(16.3)
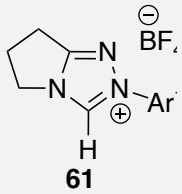 61	**61a**	Ph	-	0.899	-	17.6[b]
	61b	C_6F_5	-	121	-	17.3[b]

[a]Values determined from by single point analysis at pD 1.09. Accuracy is much lower than for values determined by multipoint analysis. [b]Values determined for p$K_a^{CH(obs)}$ from exploration of H/D-exchange across the pD region 0-6 from Massey *et al.* 2012.[76] The theory to this is covered in Section 3.3.4.[c]This value is lower than anticipated which is thought to be due to experimental error from poor substrate solubility.

Experimental k_{ex} values show that for compounds with similar substitution patterns (**6a** and **61a**), Nitron (**6a**) is approximately 7-fold more kinetically acidic. This is not reflected in the determined pK_a^{CH} values highlighting the limitations of this single point analysis in comparison to the typical multipoint least squares fit analysis. The determined k_{ex} values also a similar trend with respect to substitution, with more electron withdrawing substituents increasing k_{ex}. Finally, the highest value for k_{ex} of ~ 2×10^{-4} s^{-1} for compound **6j** is even faster than the N-C_6F_5 triazolium (**61b**), which is the fastest observed previously.

Estimates for C(3)-H and NH pK_a values can be used in Equation 2.3.1 to estimate values for pK^T, the tautomeric equilibrium between zwitterionic and carbenic forms of Nitron (**6**). Estimates for this are summarised in Table 2.3.9, alongside the calculated % free carbene in solution.

Table 2.3.9. Summary of experimentally determined pK^T values estimated using Equation 2.3.1, which were used to estimate the proportion of the carbenic tautomer of Nitron derivatives at present in solution at pH 7.

Derivative	Ar^1	Ar^2	p$K_a^{NH(obs)}$	p$K_a^{CH(obs)}$	pK^T (Approx.)[a]	Free Carbene[b] / $\times 10^{-6}$%
6a	Ph	Ph	9.78 ± 0.04	~17.8	7.9	1.3
6c	Ph	4-$CF_3C_6H_4$	8.85 ± 0.03	~17.1	8.3	0.5
6d	Ph	4-$EtOC_6H_4$	10.4 ± 0.02	~18.1	7.7	2.0

[a]pK^T determined according to Equation 2.3.1. [b]Free carbene determined as $10^{-pK^T} \times 100$.

Values for pK^T are independently influenced by changes of acidity at both the C(3)-H and exocyclic NH. NH pK_as will be more influenced by changes in Ar^1 than Ar^2 thus substituent effects on the C(3)-H acidity are more modest in comparison to the changes on NH. If a constant pK_a^{CH} is considered whilst lowering pK_a^{NH} it can be shown that the zwitterion is favoured (pK^T increases). Conversely, if a constant pK_a^{NH} is considered, lowering the pK_a^{CH} favours formation of the carbene (increases pK^T). This trend has been observed synthetically, where Ar^2 has been kept constant as phenyl and Ar^1 changed, with electron withdrawing groups decreasing pK_a^{CH} and proceeding to radical formation. The estimates for pK^T imply only modest changes in the proportion of free carbene present in solution; however, these changes do reflect the observed trend in rates/tendency to form radical. Moreover, in considering traditional NHCs, such as **61a** (Ar^1 = Ph) and **61b** (Ar^1 = C_6F_5), where % free carbene can be estimated as ~ 3.2×10^{-7} % at pH 7 by considering values of pK_a^{CH} of ~17.5. This shows that proportionally, for equal concentrations of Nitron versus a standard NHC, there would be approximately four times as much of the Nitron carbene in solution at pH 7. This can also be reflected in the hydrolytic stability, with traditional 1,2,4-triazoliums being significantly more stable in solution than Nitron.

Alongside experimental exploration of the effect of the tautomerisation of Nitron derivatives on ring opening, computational studies were carried out by Dr Mark Fox. Using the B3LYP/6-311+G(d,p) level of theory, estimates for % free carbene at equilibrium could be estimated in the gas phase and in acetonitrile at room temperature (Table 2.3.10). These estimates were based on the relative energies of carbene and zwitterion as determined through computational calculations in the different media. These computational values differ from the experimental values above which were determined for an aqueous, protic environments; however, they are likely closer to the true values under the experimental conditions in 98:2 acetonitrile. Importantly, they again

highlight a significant drop in % carbenic tautomer for the CF_3-functionalised Nitron derivative in comparison to parent Nitron.

Table 2.3.10. Computed % carbenic tautomer proportions for Nitron derivatives **6a** and **6c** in both the gas phase and with solvent set to acetonitrile determined with the B3LYP/6-311+G(d,p) level of theory. Determined by Dr. Mark Fox.

Derivative	Ar^1	Ar^2	Gas phase Carbene Proportion / %	Solution phase (MeCN) Carbene Proportion / %
6a	Ph	Ph	0.0018	1.74
6c	Ph	4-$CF_3C_6H_4$	0.000025	0.01

2.3.5. Conclusions

This chapter has explored the Nitron (**6**) to Blatter radical (**24**) rearrangement in significant detail, isolating seven new Blatter radicals (**24**/**25**) in good yields. For those Nitron derivatives which did not react to form Blatter radicals, a significant number of alternative conditions were screened using a spread of oxidants, bases and solvents; however, no radicals were isolated under these explored conditions. Isolated radicals were characterised using cyclic voltammetry, EPR spectroscopy and, where possible, X-ray crystallography. Key properties were discussed in relation to their functionalisation.

This project has led to significantly greater mechanistic understanding of the Nitron (**6**) to Blatter radical (**24**) rearrangement, in particular the role of tautomerisation of Nitron. Functionalisation of Nitron can significantly shift the position of the tautomeric equilibrium, with electron withdrawing groups on the exocyclic N-aryl disfavouring carbene formation. These experimentally and computationally determined trends provide greater insight into the novel Nitron to Blatter radical rearrangement.

2.4. Exploration of Blatter Diradical Syntheses

2.4.1. Foreword

This section highlights the attempted syntheses of Blatter-type diradicals via various techniques. Although generally these syntheses proved unsuccessful, they highlight some interesting synthetic strategies to novel organic heterocycles. It is hoped that this section could spark future projects aimed at isolating Blatter-type diradicals via this route.

2.4.2. Introduction

As mentioned in Chapter 2.1 diradical species are of particular interest in the development of new, functional materials. However, diradicals with the correct high-spin properties, thermal robustness, persistence at room temperature and ferromagnetism are still rare. Blatter-type diradicals may provide access to novel organic magnetic materials which have the ideal properties for assimilation into real-world applications. They have been used so far in organic field-effect transistors, photodetectors, organic light emitting diodes (OLEDs) and organic photovoltaics. Suitability has been attributed to their good charge transport, chemical stability and appropriate band gaps.[77] A selection of homo- and hetero- Blatter-type radicals are discussed below followed by recent efforts within this project to develop a new series of Blatter diradicals.

The first example of a diradical based upon Blatter radicals is shown in Scheme 2.4.1.[78] The structure involves two Blatter radicals (**15**), fused together via a fluorenyl linker. Synthesis of this diradical (**63**), via species **62**, is relatively cumbersome and low yielding; however, it is an elegant technique for attaching two radical centres to the central fluorene moiety. This example is particularly interesting due to the unique generation of room temperature quintet states in the solid phase. It is more common to observe a triplet state at room temperature in accordance with Hund's rule.[2] Evidence for such a state was obtained by EPR spectroscopy, in which solution phase showed the appearance of 2 non-interacting doublet states (S = ½) . Solid-state measurements, however, showed the apparent interaction to form the intermolecular quintet state ($\Delta M_s = \pm 2$) could be attributed to the formation of a 'very tight' and ordered dimer.[78]

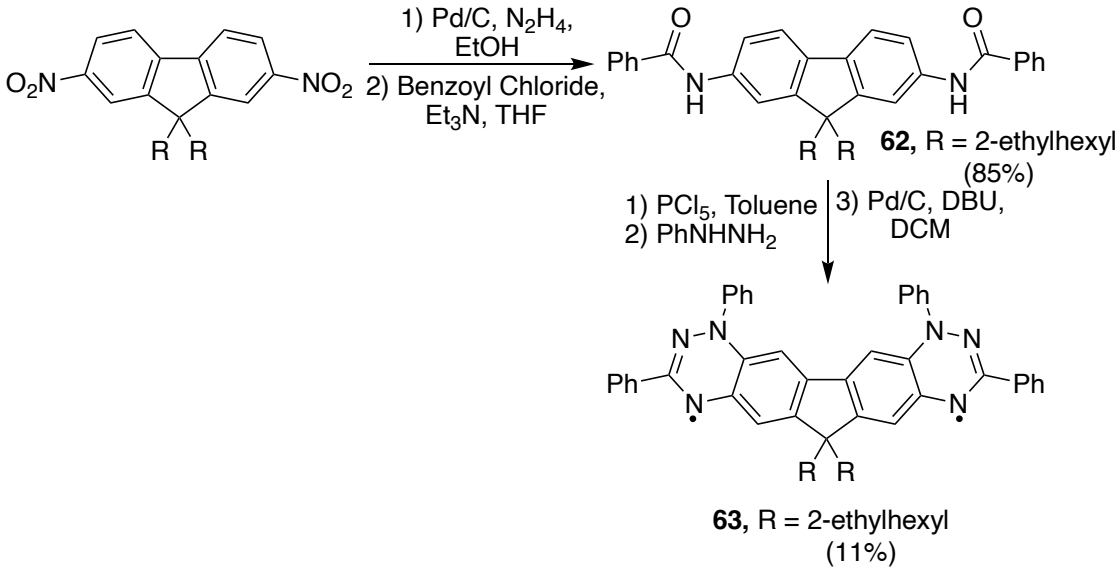

Scheme 2.4.1: Synthesis of the first reported Blatter diradical (**63**) which shows an unusual quintet spin state in the solid-state.

Computationally, it was suggested that the ground state for a discrete diradical of **63** should be a triplet, with a small value for $\Delta E_{S\text{-}T}$ of 1.0 kcal mol^{-1}. For diradical dimers, the intramolecular singlet state (Type I) was found to be 123 meV higher than the intermolecular singlet state (Type II) (Figure 2.4.1). Furthermore, the intermolecular quintet state (Type III) was found to be only 2 meV higher in energy than Type II, allowing for thermal population. The effective magnetic moment decreased at 300 K with increasing field strength. This was attributed to the through-space interaction of dimers, such that the quintet states may order antiferromagnetically. This can only be attributed to a quintet state and the fact that this state is slightly higher in energy results in the depopulation at lower temperature, and a tendency to the Type II singlet state, and diamagnetism.[78]

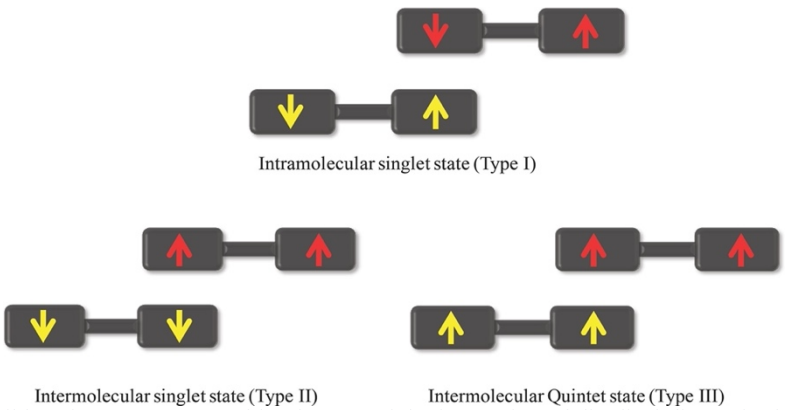

Figure 2.4.1: Possible spin states generated by the 'very tight' interaction of diradical dimers in the solid-state. The dark boxes, containing the arrows, correspond to the triazinyl moiety. Reproduced with permission from Ref. 75 and John Wiley and Sons.

Diradical **63**, also has broad absorbance in the UV-vis NIR region, making it ideal for use as an organic photodetector. When coupled with a butyric acid methyl ester polymer to account for the UV region, the photodetector developed from the material showed responsiveness between 300-1200 nm (Figure 2.4.2). The detectivity, a measure of performance of a photodetector, was particularly good in this region due to the low dark current seen for thin films of the material, reducing the need for the introduction of electron/hole blocking layers, as is the case for traditional organic photodetectors.[78]

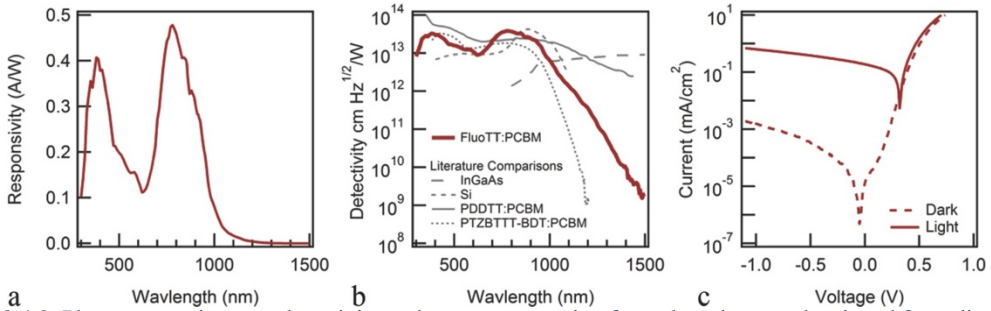

Figure 2.4.2: Photo responsiveness, detectivity and current generation for a photodetector developed from diradical **63** and a butyric acid methyl ester polymer. Reproduced with permission from Ref. 75 and John Wiley and Sons.

Blatter radicals have also been coupled with themselves in so-called Chichibabin's (**64**) and Müller's (**65**) type hydrocarbons (Scheme 2.4.2).[79] This work builds upon that carried out by Chichibabin and Müller with regards to triphenylmethyl-type diradicals.[80, 81] Interest in these materials stems from their small singlet-triplet state energy gaps ($\Delta E_{S\text{-}T}$) which allows for applications in optics, organic electronics and spintronics.[79] Blatter radical-type diradicals of this nature have been shown to give $\Delta E_{S\text{-}T}$ values ranging from 1.05 to -1.27 kcal mol^{-1} which is smaller than those of the original Chichibabin's and Müller's hydrocarbons.[80, 81] As seen in Scheme 2.4.2, synthesis of these species occurs via the combination of a para-amino phenyl species and a (*Z*)-1-[chloro(phenyl)-methylene]-2-phenyl-hydrazine, followed by aerial oxidation. It should be noted that the yields of these species were particularly low with 6 % for n=0 and 14 % for n=1, hindering large scale application.[79] With regards to applications of such diradical species, the authors fail to discuss photochemical and magnetic properties in any detail. As such further work is required to explore these materials.

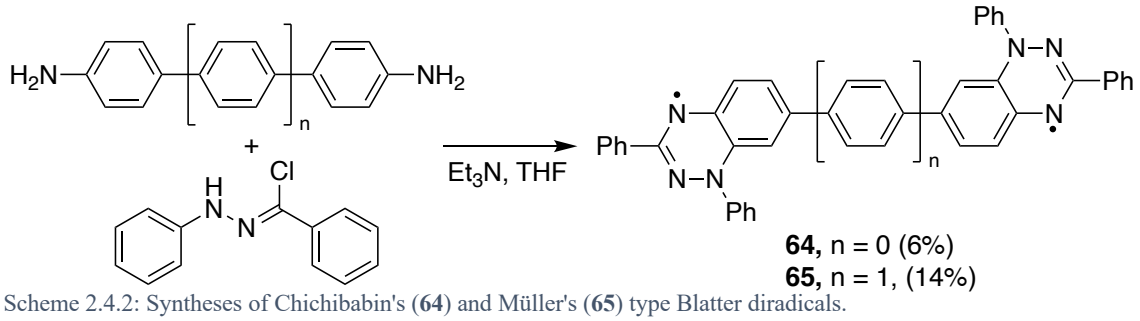

Scheme 2.4.2: Syntheses of Chichibabin's (**64**) and Müller's (**65**) type Blatter diradicals.

Blatter radicals have not just been coupled with themselves when it comes to diradicals, but also coupled with other persistent radicals. For example, coupling has been achieved through the N-Ph group to a nitroxide radical (**67**), as well as through the *C*(7)-position (**66**) as seen in Scheme 2.4.3.[53, 54, 82] These species take advantage of the spin delocalisation about the Blatter radical in particular on the fused phenyl ring as well as the N-Ph ring. Synthesis of these diradicals utilises the inherent stability of Blatter radicals, allowing for effective post synthetic modification without the destruction of radical character.[82, 83]

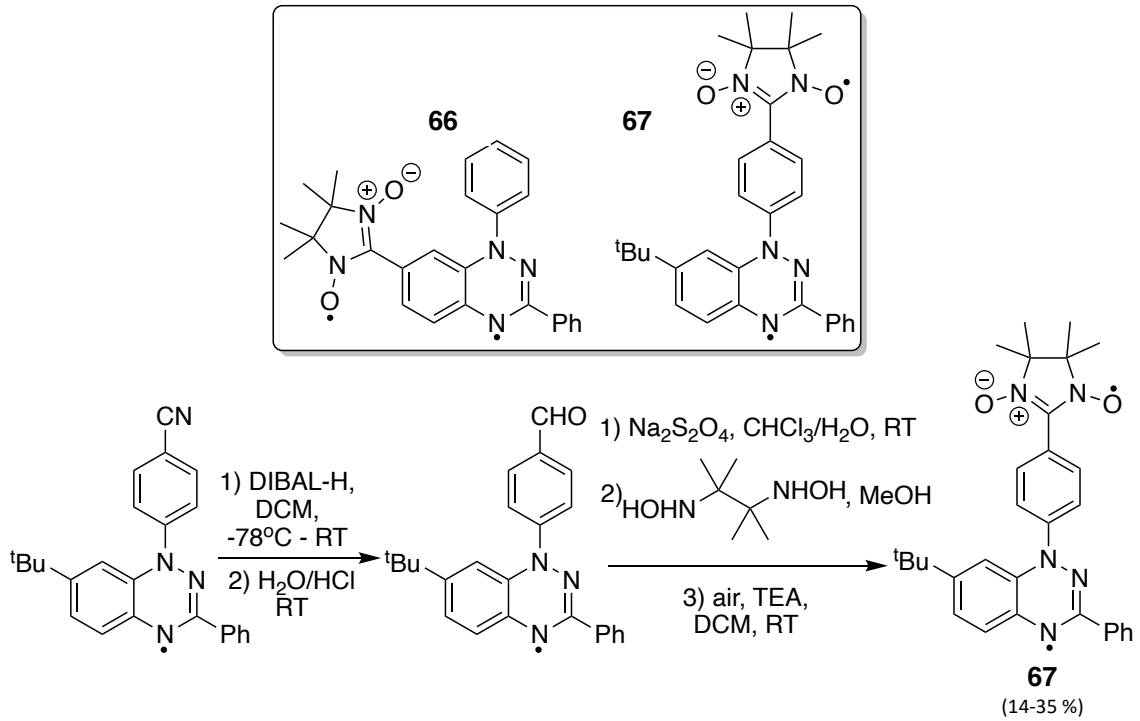

Scheme 2.4.3: Synthesis of Blatter-nitroxide coupled diradical (**67**). Diradical **66** is synthesised in a similar manner, but the initial nitrile is on the C(7)-position, replacing the ^{t}Bu group

The first of these two diradicals synthesised was **67**, which was found to be stable with respect to sublimation at 140 °C and 6 x 10^{-6} mbar. However, at room temperature, it could not truly be described as high spin due to some population of the singlet state ($\Delta E_{S\text{-}T} \sim 0.5$ kcal mol^{-1} compared to thermal energy at RT ~ 0.6 kcal mol^{-1}).[82, 83] The singlet

state leads to a loss of magnetism as spin pairing quenches bulk properties and therefore is undesirable. It was postulated that, if ΔE_{S-T} could be slightly raised, without decreasing bulk stability, magnetic properties could be improved. Computationally, diradical **66** had a slightly greater ΔE_{S-T} and hence was explored as a second generation diradical of **67**. ΔE_{S-T} was found to be ~1.7 kcal mol^{-1} and hence according to the Boltzmann distribution can be estimated to have ≥ 95 % occupancy of the ground-state triplet at RT. Hence, it can be predicted that the magnetic properties of this species were much more advantageous.[82, 83] Weiss constants for diradicals **67** and **66** were found to be approximately -6 and -14 K implying significant antiferromagnetic interactions between the triplet diradicals. Radical **66** was more extensively studied and found to exist of nearly isotropic 1-D antiferromagnetic Heisenberg chains at low temperature. These curious properties allow for future developments in purely organic magnetic and electronic materials.[82]

A final, more recent example, based on the work highlighted in Scheme 2.4.3, couples two Blatter radicals but via a C(3)-C(7) coupling (**68**) (Scheme 2.4.4). The potential advantages of this approach are that the SOMO character is strongly localised on these two positions, allowing the potential for strong coupling between these spins. The advantages of this radical is the excellent thermal robustness provided by the Blatter radical. For example, diradicals **66**/**67** decompose at 160-175 °C whereas this more recent example can withstand temperatures above 264 °C. The synthesis of this radical installs the radical character at the end of the synthetic strategy which avoids the need to consider REDOX decomposition at this position during synthesis. Taking advantage of the cross reactivity of the highlighted aryl iodide, sequential copper couplings, amide couplings and imine formations give the Blatter diradical in moderate yields.[84]

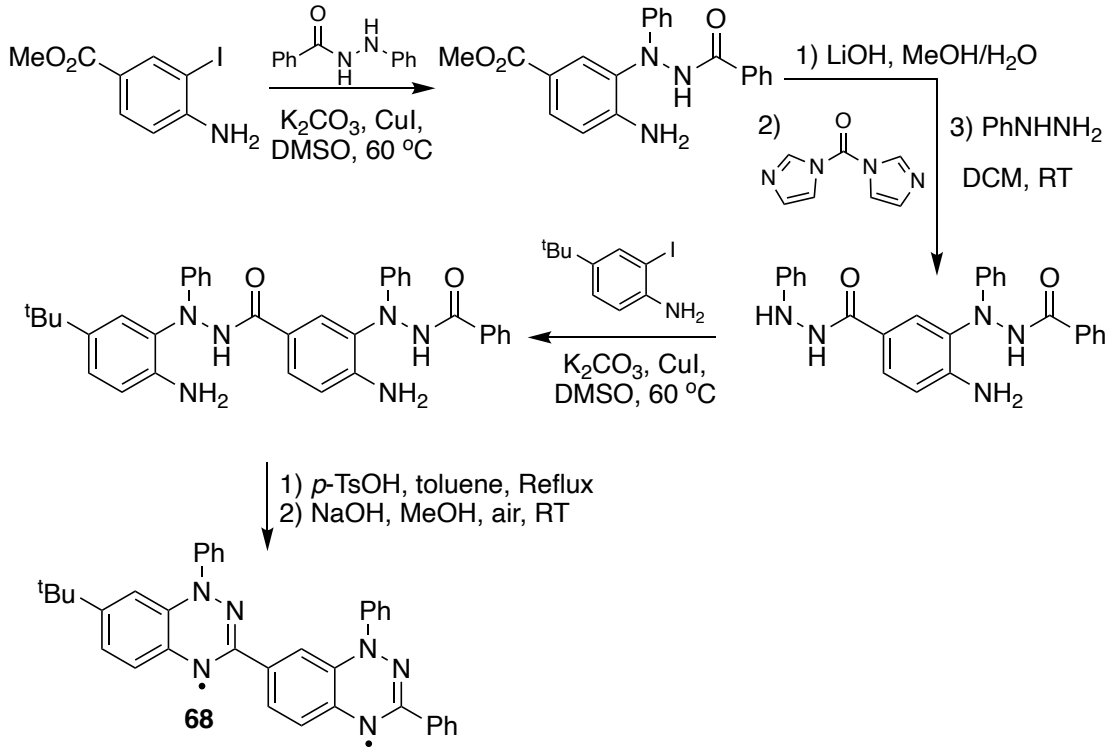

Scheme 2.4.4. Synthesis of C(3)-C(7) coupled Blatter diradicals (**68**), which have significantly enhanced thermal stability in comparison to previous examples.

2.4.3. The Synthesis of Blatter Di-Radicals

Direct Tethering of Amino Blatter Radicals

The simplest approach to the synthesis of Blatter diradicals would be to take two amino-Blatter radicals (**25**) and couple them via the amine groups to a central linker. Previous work in our group attempted this with oxalyl chloride but instead saw a cyclisation occur (**69**) (Scheme 2.4.5). The short chain length and flexibility in this case would be envisaged to favour a self-cyclisation to the stable 5-membered ring. It was proposed that increasing the rigidity of the crosslinking reagent, or increasing the length, to eliminate the risk of cyclisation could yield di-radicals.

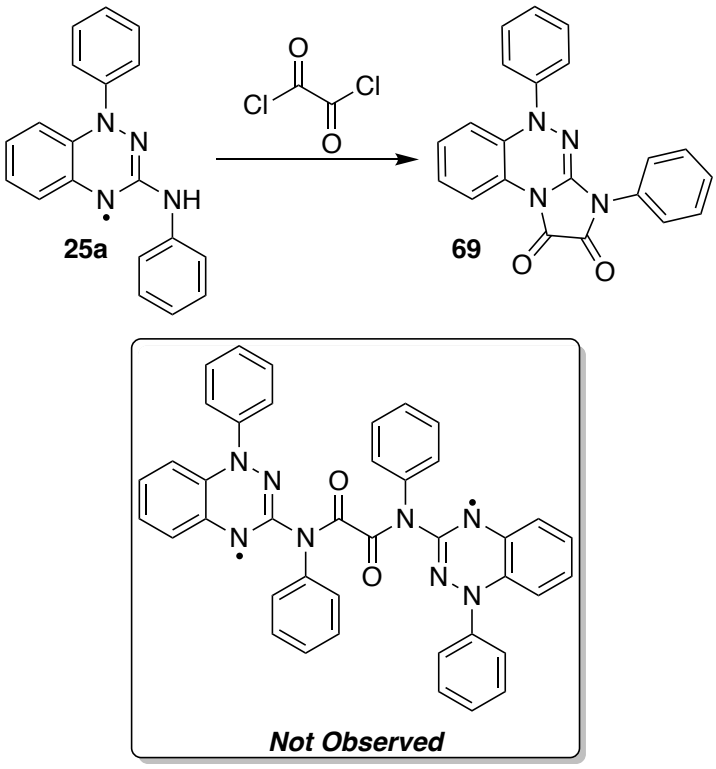

Scheme 2.4.5 . Attempted isolation of Blatter diradicals via an oxalyl chloride linker instead lead to formation of the cyclised compound (**69**).

As an initial test reaction, benzoyl chloride was reacted with amino-Blatter radical (**25**) (Scheme 2.4.6). Over the course of 3 days a characteristic colour change from green to red was observed suggesting the addition of an acyl group to the Blatter radical scaffold (**70**). Monitoring by LC-MS also showed clean conversion to the desired product and after work up, NMR analysis suggested that the radical character remained. Considering that there are two free nitrogen atoms which could feasibly react, it was promising to see retainment of radical character. However, reviewing the data it was more likely that there was cross reactivity to a product mixture (**70**/**71**). These structural isomers are very similar and subsequent isolation was not possible by any explored method. In this case, no disubstitution of benzoyl chloride to a single amino-Blatter radical was observed, likely due to the steric clash of having so many phenyl rings in close proximity.

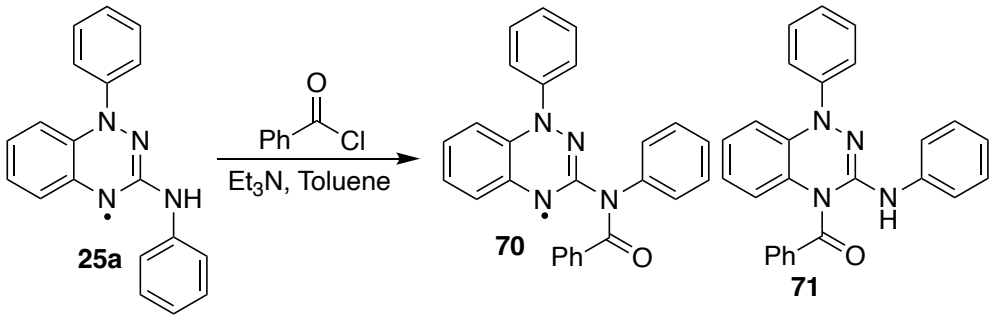

Scheme 2.4.6. Reaction of amino-Blatter radicals (**24a**) with benzoyl chloride led to a product mixture which was not possible to separate by the purification methods explored.

An alternative approach to the synthesis of diradicals coupled via the exocyclic aniline would be via a benzyl-type linker. There are two potential routes to access this: substitution chemistry or reductive amination. Initially reductive amination was explored as it was hoped that the exocyclic amine nucleophilicity would be higher than the ring-nitrogen. However, it was envisaged that the exocyclic amine would be unreactive with an aldehyde considering the cumbersome steric and electronic factors. Nevertheless, a reductive amination was explored using sodium triacetoxyborohydride (STAB) as the reductant (Scheme 2.4.7). STAB was chosen as a particularly mild reductant as this should not reduce the aromatic aldehyde or the radical centre. As the reaction was likely to be particularly slow owing to the hindered amine group, a mild reductant was appropriate as others such as sodium borohydride would see competing aldehyde or radical reduction. Unfortunately, reactions with aldehydes did not proceed, likely due to the reduced electrophilicity at nitrogen. Introduction of a Lewis acid to increase the reactivity of the aldehyde and drive the reaction were also unsuccessful.

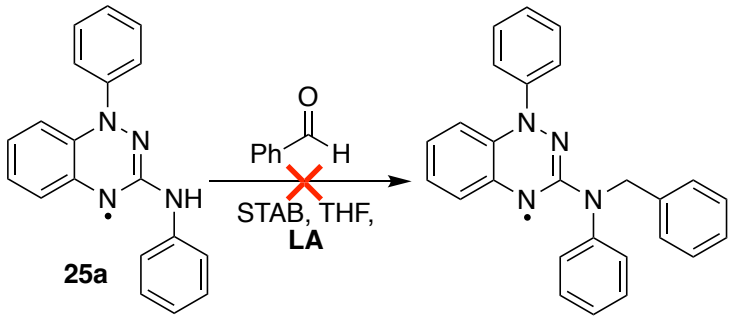

Scheme 2.4.7. Attempted reductive amination using benzaldehyde and sodium triacetoxyborohydride (STAB) showed no reaction likely due to the enhanced steric strain and reduced nucleophilicity of the exocyclic amino group.

Initial scoping of the substitution route first focussed on attempted benzylation of the amino Blatter radical (**25a**) with benzyl bromide, with sodium hydride in DMF (Scheme 2.4.8). This reaction was particularly messy, forming a mix of both structural isomers with both the radical centre and exocyclic amino group appearing to react. Such a complicated reaction outcome led to the decision to abandon this approach. Instead, attempts to isolate Blatter diradicals by first coupling two Nitron (**6**) molecules around a central linker were explored.

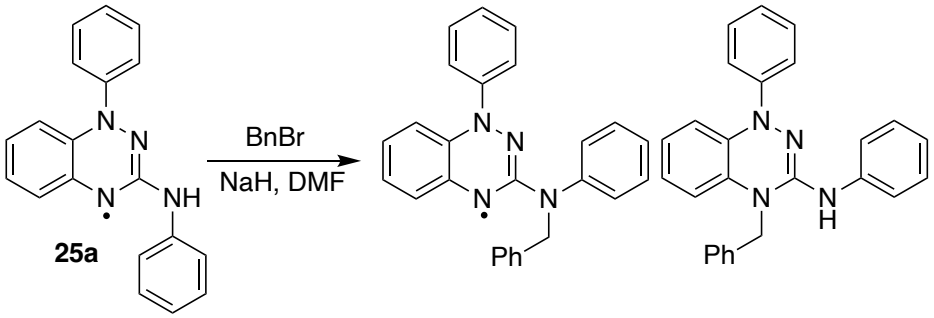

Scheme 2.4.8. Exploration of benzylation of the amino Blatter radical again formed a mixture of products which could not be resolved.

Blatter Diradicals from Di-Nitron Precursors

Coupling of Blatter radicals to form di-radicals is complicated by both the lack of reactivity of the exocyclic amino group and the need to maintain radical character. This is the case for many of the Blatter di-radicals reported in the introduction as evidenced by the poor yields in the majority of syntheses. The benefit of the Nitron (**6**) to Blatter radical (**25**) transformation is that the key steps, such as triazabutadiene formation, occur *in situ* and do not require complex isolations and purifications. This provides a significant advantage as the more sensitive radical centre is installed at the end. Two possible approaches to the synthesis of the precursor di-Nitron derivatives were suggested: reaction of amidrazones either with orthoesters or with disubstituted aldehydes (Scheme 2.4.9).

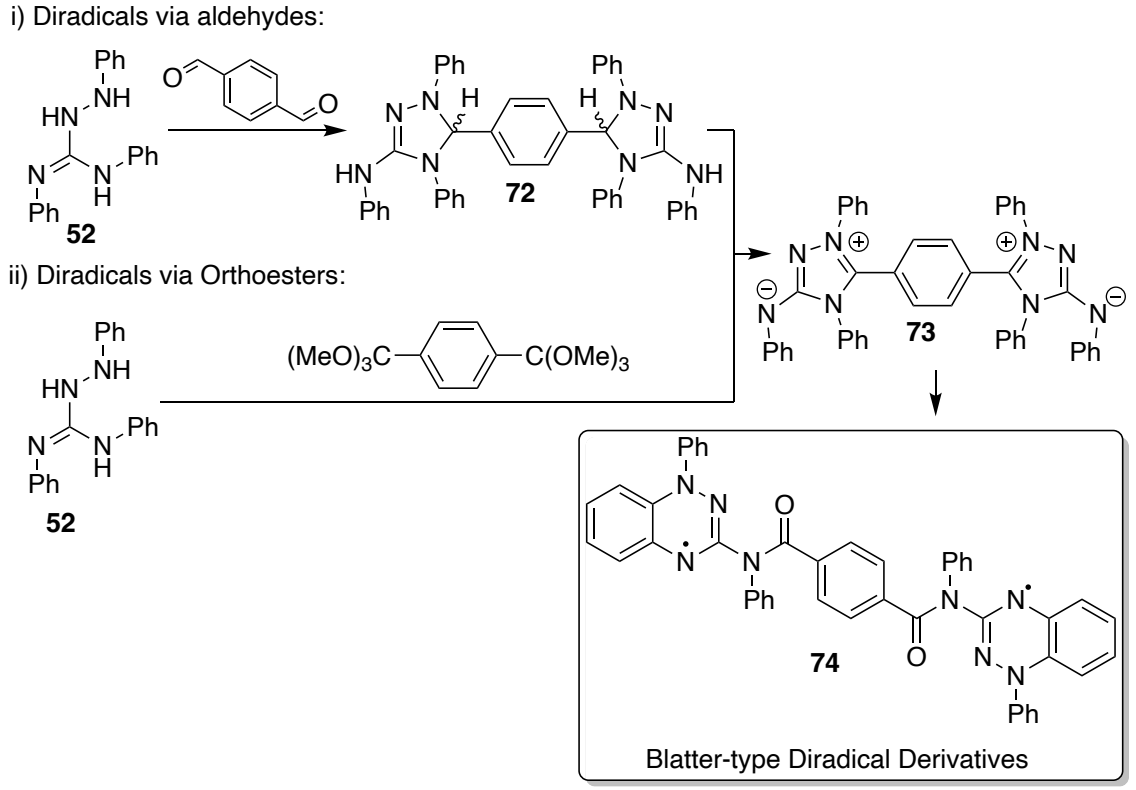

Scheme 2.4.9. Proposed synthetic strategies to Blatter diradicals via initial synthesis of di-Nitron derivatives. Both methods required initial synthetic exploration to this new 1,2,4-triazolium class.

Nitron tethering using aldehydes

As an initial scope, terephthalaldehyde was refluxed with amidrazone (**52**) in IPA, following the procedure outlined in the initial Nitron synthesis paper.[58] Unfortunately, this proved unsuccessful, likely due to the reduced electrophilicity of the aromatic aldehyde and lower nucleophilicity of the amidrazone in comparison to typical imine formations.

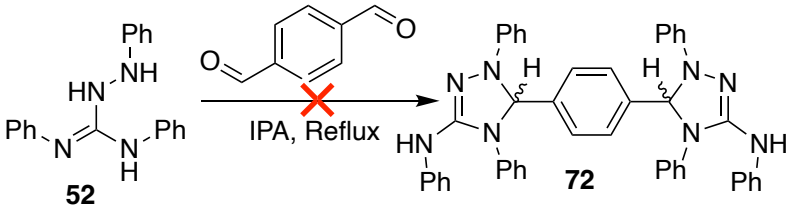

Scheme 2.4.10. Initial reaction following the procedure of Kriven'ko and Morozova to attempt to isolate a di-triazole about a central phenyl linker. Reaction did not proceed and so alternative methods were explored.

To explore more appropriate conditions for condensation and cyclisation, 4-trifluoromethylbenzaldehyde was used as a model substrate for terephthalaldehyde. This was chosen as upon condensation it forms a single product, as opposed to the di-aldehyde which has mono- and di-addition products. The trifluoromethyl group has a σ_p-Hammett value of 0.54 and Field induction parameter of 0.38 in comparison to an aldehyde group of $\sigma_p = 0.42$ and $F = 0.33$.[70] The proximity in magnitude of these constants allow the trifluoromethyl- moiety to be considered as a non-reactive aldehyde in this instance.

A synthetic strategy was explored using pyrrolidine as an organocatalyst, in DCM with molecular sieves to sequester water.[85] At room temperature this reaction showed some conversion but still very limited. Exploring this synthetic procedure further, pyrrolidine was initially removed, and the reaction heated to 80 ºC for 2 hrs with microwave heating. This showed significant conversion to the desired triazole however appeared to stall at 50 %. Further increases in temperature showed no further conversion to the desired triazole. Returning to 80 ºC, the inclusion of 10 mol % pyrrolidine was found to give 100 % conversion within 1.5 hours of reaction. The product (**73**) was subsequently isolated by concentration of the reaction medium *in vacuo* and recrystallisation from hot methanol in good yields (Scheme 2.4.11).

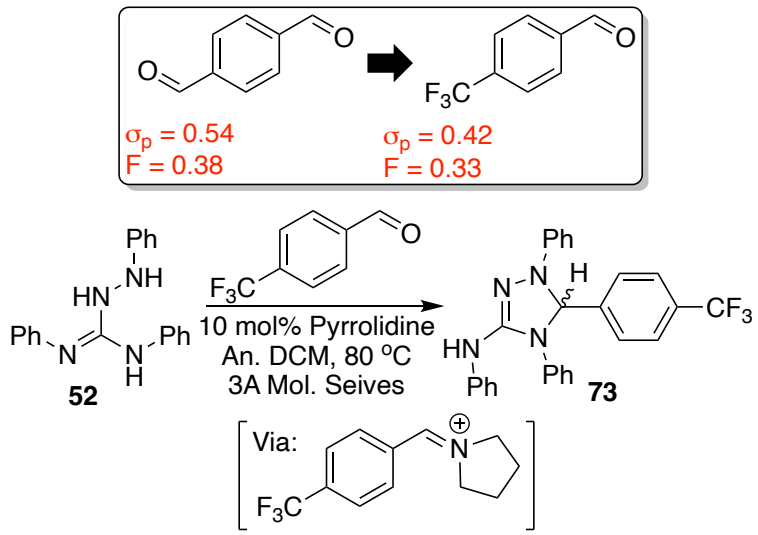

Scheme 2.4.11. Moving to 4-trifluoromethylbenzaldehyde as a non-reactive model for terephthalaldehyde allowed for development of a straightforward synthetic procedure to isolate the triazole. Catalytic pyrrolidine was found to be essential for reaction presumably due to Schiff-base catalysis.

Analysis of triazole **73** implied that it was not oxidatively stable in solution, readily converting to the desired triazolium (**74**) evidenced by decay of the C(3)-H peak of the triazole and a characteristic loss of H_2 by mass spectrometry. To reach full conversion a selection of methods were attempted including palladium on carbon in air and bubbling air through a solution of the triazolium and manganese (II) oxide. None of these procedures were particularly successful. Two final procedures explored were the use of 2,3-dichloro-5,6-dicyano-1,4-benzoquinone (DDQ), a common oxidant for installing an aromatic system and the sodium nitrite/acetic acid oxidation system established for the Nitron derivatives above (**6**) (Scheme 2.4.12). Pleasingly, both procedures proceeded to complete conversion. The key issue with the DDQ oxidation was the isolation of the final di-triazolium. The reduced DDQ and triazolium could not be separated by all techniques attempted whereas, using the acetic acid/sodium nitrite route isolation was possible by precipitation into ammonium hydroxide solution.

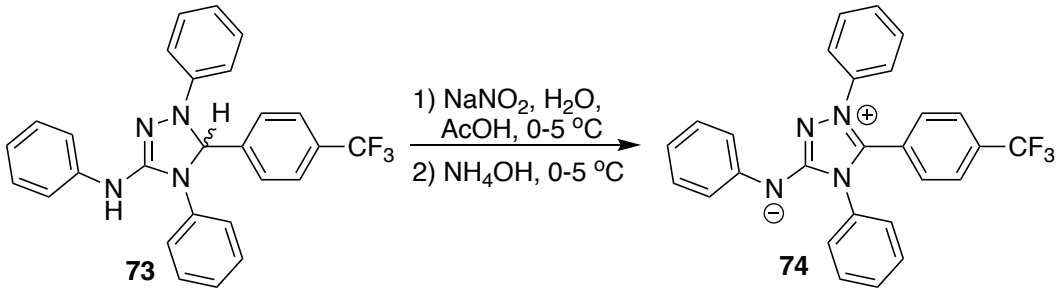

Scheme 2.4.12. Final oxidation conditions to isolate C(3)-functionalised Nitron derivatives, as developed for the synthetic strategy to a broader range of Nitron derivatives as discussed in Chapter 2.2.

With a synthetic strategy developed it was applied to the synthesis of two different di-triazoliums using terephthalaldehyde and isophthalaldehyde (Scheme 2.4.13). Initial

cyclisation with the amidrazone (**52**) proceeded nicely and careful control of the stoichiometry allowed for almost full conversion to the disubstituted products (**72** & **75**). In the case of isophthalaldehyde, a greater amount of the mono-substituted compound was seen by LC-MS attributed to the increased steric demand about the aldehyde linker unit. The di-triazoles (**72** & **75**) were subsequently precipitated from the concentrated reaction media with MeOH and isolated as white solids which slowly discoloured in air. Pleasingly, this isolation method was successful in separating both the mono- and di-substitution products. Oxidation of the triazoles (**72** & **75**) to the triazoliums was slightly more complicated. The *para*-substituted triazolium (**76**) was readily accessed in moderate yields from the precursor triazole (**72**). In the case of the *meta*-substituted compound, the compound decomposed quickly when attempting to isolate from aqueous solution. It is thought that in this case, the Nitron moieties are forced into too closer contact, and this steric strain is readily relieved by hydrolysis of the compound back to triazabutadiene (**54**).

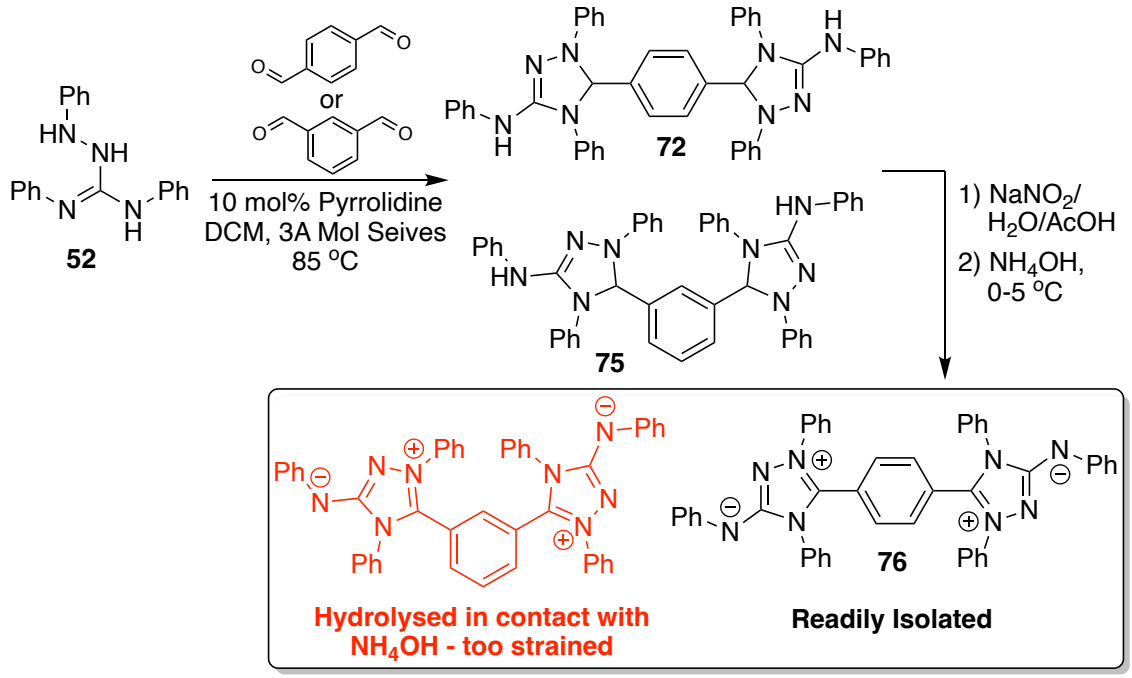

Scheme 2.4.13. Final isolation of tethered Nitron (**76**) using the developed synthetic strategy from amidrazones (**52**) and aldehydes. Unfortunately, isolation of the *meta*-substituted compound was not possible due to hydrolysis upon aqueous work up.

Characterisation of compound **76** was challenging owing to its poor solubility in the majority of organic solvents. Analysis by mass spectroscopy did show the expected mass for both a mono-cationic species and dicationic (m/z value of mass/2). N-protonation was found to improve the solubility of this compound allowing NMR spectra to be obtained. Moreover, suitable crystals for XRD analysis were formed by slow evaporation

of acetone from a HCl/acetone mix containing the solute. The crystal structure obtained from this analysis is shown in Figure 2.4.3.

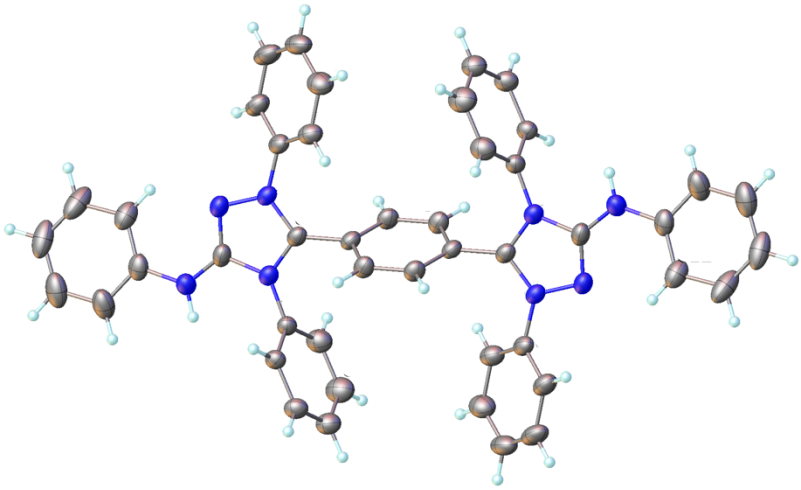

Figure 2.4.3. Determined crystal structure for di-Nitron (**76**). Crystals were isolated by slow evaporation of acetone from an acetone/HCl mix.

Nitron tethering using orthoesters

As shown in Scheme 2.4.9, an alternative route to the di-Nitron derivatives would be via the use of orthoester chemistry. As an initial scope, amidrazone (**52**) was refluxed in trimethyl orthobenzoate with ammonium tetrafluoroborate overnight. During this time the desired product (**77**) precipitated from the reaction as a white solid. Subsequent recrystallisation from methanol yielded the desired product as a white crystalline solid as the tetrafluoroborate salt. The characteristic yellow zwitterionic form could again be readily isolated by a saturated bicarbonate wash (Scheme 2.4.14). Considering the XRD crystal structure isolated (Figure 2.4.4), the key differences in comparison to Nitron-BF_4 (**6a**) is that the counterion coordinates to the exocyclic amino group as opposed to the C(3)-H which is no longer present. In considering the twist of the N(2) and N(4) phenyl groups, Table 2.4.1 compares both Nitron (**6a**) and the C(3)-Ph Nitron (**77**). As seen, the N(2) twists out of the plane to a much greater extent for the C(3)-Ph Nitron (**77**) as opposed to C(3)-H. A planar geometry would be more favoured due to greater π-orbital overlap however in the case of the C(3)-Ph, steric clashes prevent this.

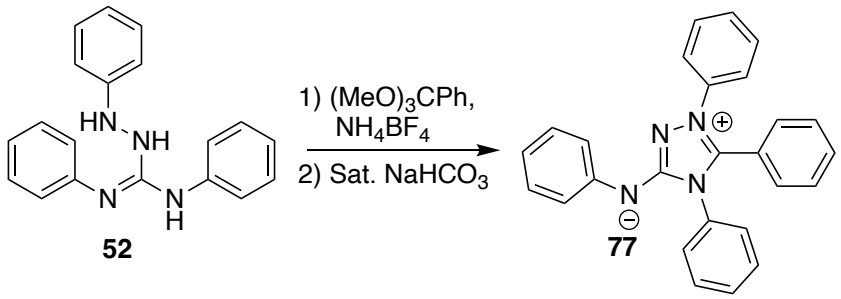

Scheme 2.4.14. Synthesis of a C(3)-Ph substituted Nitron (**77**) using trimethyl orthobenzoate.

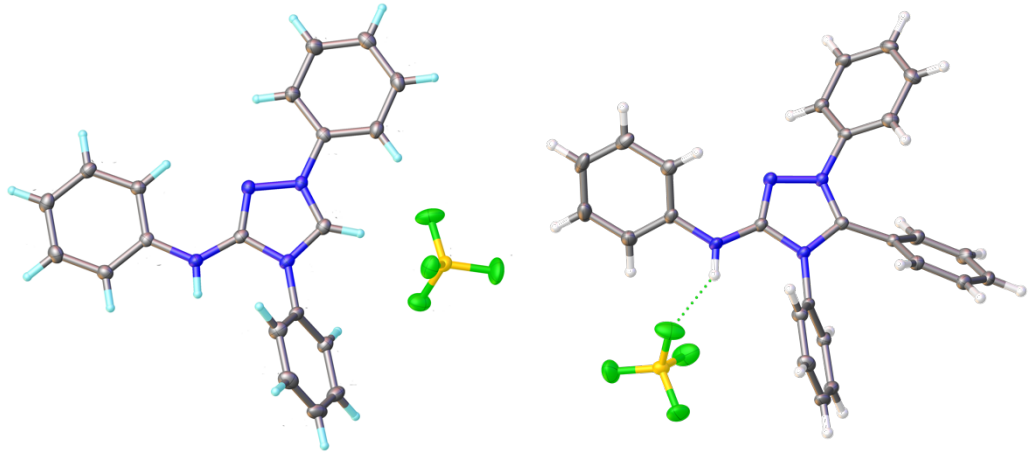

Figure 2.4.4. Isolated crystal structures for Nitron (**6a**) (left) and C(3)-Ph Nitron (**77**) (right) showing the slight alterations in structure upon introduction of a bulky group at the C(3) position.

Table 2.4.1. Summary of the key N-Ph dihedral angles with respect to the central 1,2,4-triazolium core showing a significant increase in N(4)-twist upon inclusion of a C(3)-phenyl group.

Molecule	N(2)-Ph twist / °	N(4)-Ph twist / °
6a	5.168	59.196
77	39.202	65.173

In order to access tethered Nitron derivatives using orthoester chemistry, a synthetic strategy to an aromatic containing two orthoester functionalities is required. Initially, the reaction of bromobenzene to form the Grignard reagent and subsequent reaction with tetramethyl orthocarbonate was explored (Scheme 2.4.15). This reaction failed to proceed at room temperature and increasing the temperature at the orthocarbonate addition did not help. The orthocarbonate was thought to not be a reactive enough substrate for the Grignard reagent. An alternative approach is reaction of substate (**78**) with methanol and sodium methoxide; however, exploration of this route also failed to yield the desired orthoesters. Due to the adjacent aromatic ring adding to the steric bulk, the substitution would be expected to proceed via a S_N1-type process. However, the electron withdrawing chlorine atoms would disfavour formation of carbocation. If considering a S_N2-type process it could also be argued that formation of the partial

positive charge at carbon would be disfavoured. The significant success that occurred with the aldehyde coupling route led to the orthoester approach being abandoned.

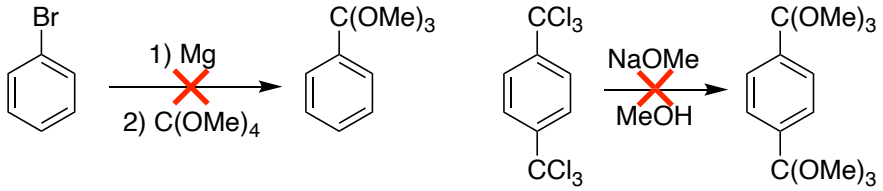

78

Scheme 2.4.15. Failed syntheses of orthoesters. Left: via traditional Grignard chemistry. Right: via substitution chemistry.

2.4.4. Di-Nitrons to Blatter-type Diradicals

The *para*-di-Nitron derivative (**76**) isolated via coupling of the aldehydes was subsequently explored in the typical Nitron to Blatter radical rearrangement conditions. Under the usual conditions of 99:1 acetonitrile:water, the compound was not fully soluble but, as the reaction proceeded it was hoped solubility would improve. Monitoring by LC-MS, masses corresponding to mono- and di-radicals **79** and **74** appeared; however, the reaction was particularly slow and other decomposition reactions also appeared to occur. Considering the fundamental knowledge gained from the synthesis of Blatter radicals (**24**) as highlighted in Chapter 2.3, it is not surprising that radical conversion might be slow. Considering ring opening appears to occur much more quickly on the carbenic tautomer, and inserting a C(3)-aryl group eliminates the propensity for carbene formation. This slow ring opening was also observed for compound **77**.

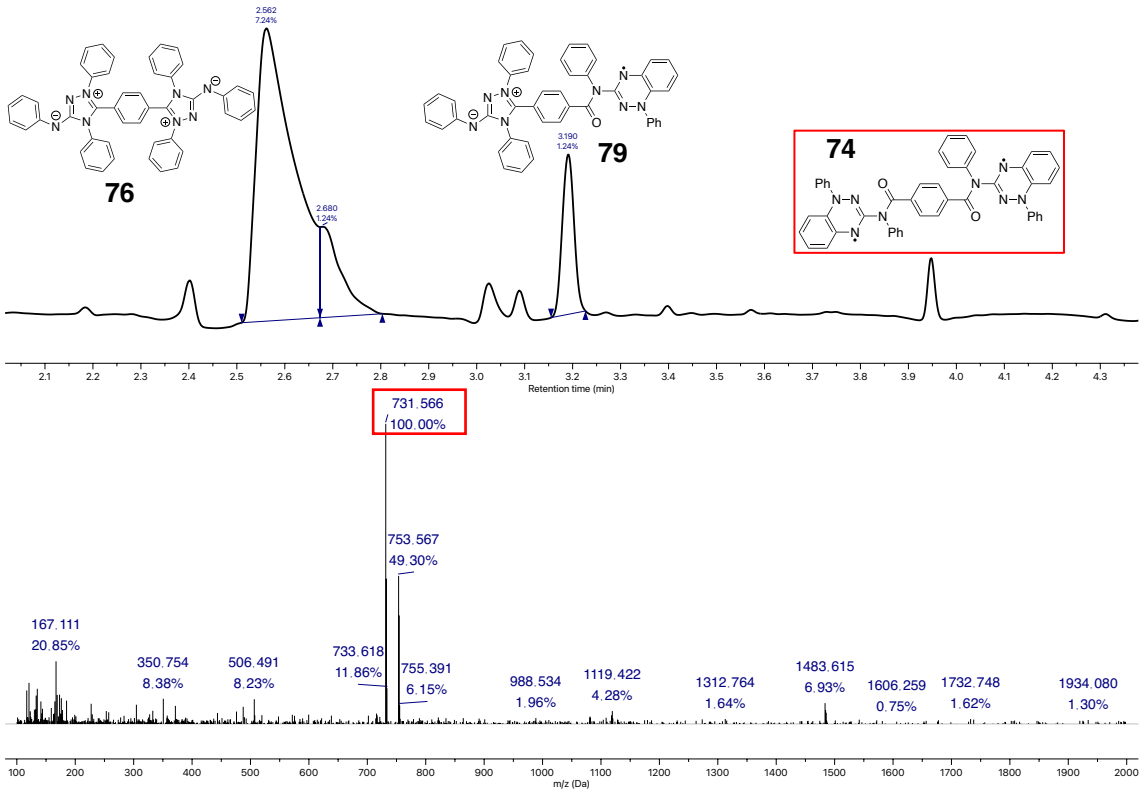

Figure 2.4.5. LC-MS trace showing the potential formation of the Blatter diradical. The peak at Rt = 2.56 min is the starting di-triazolium, a peak at Rt = 3.19 min could be the mono-radical and the peak at Rt = 3.95 min is attributed to the proposed diradical. The mass spectrum for the compound eluted at Rt = 3.95 min is also displayed.

Despite shutting down the carbene tautomerisation by insertion of aryl groups at the C(3) position, it may still be possible to isolate radicals via this method. Previously our group have shown a small selection of Nitron to Blatter radical formations using C(3)-subsituted Nitrons including C(3)-propyl and C(3)-cyclopentyl derivatives (Scheme 2.3.1). Both of these required the addition of mild base and oxidant to aid the transformation. However, it should be noted that this vastly complicates the conversion due to other degradation reactions. Nevertheless, a selection of conditions were explored to try and speed up ring opening and electrocyclization to the desired Blatter di-radicals including a range of bases, oxidants and temperatures.

Of the explored methods, some did appear to speed up the proposed radical formation by LC-MS; however, reactions were messy and subsequent isolation of the desired Blatter diradicals was not possible by the explored routes. It appears that the limitations of this approach are a lower solubility in acetonitrile, which so far is the only solvent found to facilitate radical formation. Alongside the lack of C(3)-H, disallowing formation of a carbene at this position and so slowing down hydrolytic ring opening significantly.

2.4.5. Conclusions

This section highlights the attempted syntheses of Blatter di-radicals via a variety of methods. Initial approaches of coupling amino Blatter radicals (**25**) using various chemistries failed due to the reduced nucleophilicity of this nitrogen and competing reaction with the ring nitrogen. To avoid the need to isolate Blatter radicals before coupling to form diradicals, an alternative approach is to couple two Nitrons about a central linker (**76**). This required development of a synthetic strategy and this was found to be possible via condensation chemistry with aldehydes. Unfortunately, exploration of radical formation via the previously explored conditions of acetonitrile/water (99:1) did not result in isolation of the desired radical; however, circumstantial evidence for radical formation (**74**) was observed by LC-MS amongst other degradation products. It is hoped that future work could develop a cleaner approach to diradical formation, perhaps using solvents which better solubilise the starting di-Nitron (**76**).

2.5. Conclusions

These studies have modernised the synthetic route to Nitron (**6a**), reducing the need for more hazardous reagents and improving the yield. By exploring the scope of this synthetic strategy, a much larger library of derivatives is now available. Importantly this synthetic route is generally very tolerant of functional groups but, does require some alternative strategies in the case of very electron withdrawing N-aryl substituents. Increasing the library of available Nitron derivatives allowed the scope of the Nitron (**6**) to Blatter radical (**24**) rearrangement to be tested and a selection of seven new radicals were isolated and characterised. Importantly, synthetic observations led to our consideration of the role of tautomerism in Blatter radical formations. We predicted that hydrolytic ring opening of Nitron occurred at the carbene not the zwitterion and estimations of pK^{T} values (through determination of C(3)-H and NH acidities) supported our synthetic observations.

The isolation and application of di-radicals is currently receiving significant attention owing to intriguing electronic properties. Direct coupling of amino Blatter radicals (**25**) was challenging due to competing reaction of both the ring and exocyclic nitrogen atoms. To circumvent this, a fused-Nitron (**76**) around a central aromatic linker was designed and synthetic strategies to this developed. Once isolated, a range of conditions to isolate the di-Blatter radical were explored and some circumstantial evidence through mass spectrometry for its formation was determined. Considering the understanding developed on the role of Nitron tautomerisation in Blatter radical formation, it was not surprising that radical formation was very slow for this di-Nitron (**76**). Hopefully future work can explore synthetic procedures to these di-radicals in greater detail.

2.6. References

11. I. Ratera and J. Veciana, *Chem. Soc. Rev.*, 2012, **41**, 303-349.
12. B. D. Koivisto and R. G. Hicks, *Coord. Chem. Rev.*, 2005, **249**, 2612-2630.
19. L. Benhamou, E. Chardon, G. Lavigne, S. Bellemin-Laponnaz and V. Cesar, *Chem. Rev.*, 2011, **111**, 2705-2733.
21. J. A. Grant, Z. Lu, D. E. Tucker, B. M. Hockin, D. S. Yufit, M. A. Fox, R. Kataky, V. Chechik and A. C. O'Donoghue, *Nat. Commun.*, 2017, **8**, 15088.
23. H. M. Blatter and H. Lukaszewski, *Tetrahedron Lett.*, 1968, **9**, 2701-2705.
24. A. Bodzioch, M. Zheng, P. Kaszynski and G. Utecht, *J. Org. Chem.*, 2014, **79**, 7294-7310.
25. A. A. Berezin, C. P. Constantinides, S. I. Mirallai, M. Manoli, L. L. Cao, J. M. Rawson and P. A. Koutentis, *Org. Biomol. Chem.*, 2013, **11**, 6780-6795.
26. A. A. Berezin, G. Zissimou, C. P. Constantinides, Y. Beldjoudi, J. M. Rawson and P. A. Koutentis, *J. Org. Chem.*, 2014, **79**, 314-327.
27. C. P. Constantinides, E. Obijalska and P. Kaszynski, *Org. Lett.*, 2016, **18**, 916-919.
28. A. C. Savva, S. I. Mirallai, G. A. Zissimou, A. A. Berezin, M. Demetriades, A. Kourtellaris, C. P. Constantinides, C. Nicolaides, T. Trypiniotis and P. A. Koutentis, *J. Org. Chem.*, 2017, **82**, 7564-7575.
29. G. Karecla, P. Papagiorgis, N. Panagi, G. A. Zissimou, C. P. Constantinides, P. A. Koutentis, G. Itskos and S. C. Hayes, *New J. Chem.*, 2017, **41**, 8604-8613.
30. P. Bartos, B. Anand, A. Pietrzak and P. Kaszynski, *Org. Lett.*, 2020, **22**, 180-184.
31. A. T. Gubaidullin, B. I. Buzykin, I. A. Litvinov and N. G. Gazetdinova, *Russ. J. Gen. Chem.*, 2004, **74**, 939-943.
32. I. U. F. A. Neugebauer, *Chem. Ber.*, 1981, **114**, 2423-2430.
33. D. G. Neilson, R. Roger, J. W. M. Heatlie and L. R. Newlands, *Chem. Rev.*, 1970, **70**, 151-170.
34. H. S. R. Huisgen, I. Brüning, *Chem. Ber.*, 1969, **102**, 1102-1116.
35. D. Pomiklo, A. Bodzioch, A. Pietrzak and P. Kaszynski, *Org. Lett.*, 2019, **21**, 6995-6999.
36. A. Bodzioch, D. Pomiklo, M. Celeda, A. Pietrzak and P. Kaszynski, *J. Org. Chem.*, 2019, **84**, 6377-6394.
37. M. Sheng, D. Frurip and D. Gorman, *J. Loss. Prev. Process. Ind.*, 2015, **38**, 114-118.
38. S. H. M. A. Almeer, I. A. Zogby and S. S. M. Hassan, *Talanta*, 2014, **129**, 191-197.
39. H.-H. Yang, L.-T. Hsieh and S.-K. Cheng, *Chemosphere*, 2005, **60**, 1447-1453.
40. Y. Takahashi, Y. Miura and N. Yoshioka, *Chem. Lett.*, 2014, **43**, 1236-1238.
41. C. P. Constantinides, P. A. Koutentis, H. Krassos, J. M. Rawson and A. J. Tasiopoulos, *J. Org. Chem.*, 2011, **76**, 2798-2806.
42. D. H. R. Barton, J. W. Ducker, W. A. Lord and P. D. Magnus, *J. Chem. Soc., Perkin trans. 1*, 1976, 38-42.
43. A. A. Berezin and P. A. Koutentis, *Org. Biomol. Chem.*, 2014, **12**, 1641-1648.
44. J. Velik, V. Baliharova, J. Fink-Gremmels, S. Bull, J. Lamka and L. Skalova, *Res. Vet. Sci.*, 2004, **76**, 95-108.
45. Salahuddin, M. Shaharyar and A. Mazumder, *Arab. J. Chem.*, 2017, **10**, S157-S173.

46. P. Kaszynski, C. P. Constantinides and V. G. Young, Jr., *Angew. Chem. Int. Ed.*, 2016, **55**, 11149-11152.
47. A. Parikh, H. Parikh and K. Parikh, in *Named Reactions in Organic Synthesis*, 2006, ch. 94, pp. 348-350.
48. M. A. Fox, E. Gaillard and C. C. Chen, *J. Am. Chem. Soc.*, 1987, **109**, 7088-7094.
49. D. Matuschek, S. Eusterwiemann, L. Stegemann, C. Doerenkamp, B. Wibbeling, C. G. Daniliuc, N. L. Doltsinis, C. A. Strassert, H. Eckert and A. Studer, *Chem. Sci.*, 2015, **6**, 4712-4716.
50. Y. Hattori, T. Kusamoto and H. Nishihara, *Angew. Chem. Int. Ed.*, 2014, **53**, 11845-11848.
51. P. Coppo, M. Duati, V. N. Kozhevnikov, J. W. Hofstraat and L. De Cola, *Angew. Chem. Int. Ed.*, 2005, **44**, 1806-1810.
52. Y. Yang, M. Lowry, C. M. Schowalter, S. O. Fakayode, J. O. Escobedo, X. Xu, H. Zhang, T. J. Jensen, F. R. Fronczek, I. M. Warner and R. M. Strongin, *J. Am. Chem. Soc.*, 2006, **128**, 14081-14092.
53. A. Bajaj and M. E. Ali, *J. Phys. Chem. C*, 2019, **123**, 15186-15194.
54. K. Mukai, K. Inoue, N. Achiwa, J. B. Jamali, C. Krieger and F. A. Neugebauer, *Chem. Phys. Lett.*, 1994, 569-575.
55. L. J. Keane, S. I. Mirallai, M. Sweeney, M. P. Carty, G. A. Zissimou, A. A. Berezin, P. A. Koutentis and F. Aldabbagh, *Molecules*, 2018, **23**.
56. D. Mustacich and G. Powis, *Biochem.*, 2000, **346**, 1-8.
57. E. M. Zeman, J. M. Brown, M. J. Lemmon, V. K. Hirst and W. W. Lee, *Int. J. Radiat. Oncol. Biol. Phys.*, 1986, **12**, 1239-1242.
58. A. P. Kriven'ko and N. A. Morozova, *Russ. J. App. Chem.*, 2006, **79**, 506-507.
59. W. E. Motzer, *Environ. Forensics*, 2001, **2**, 301-311.
60. C. S. Marvel and V. d. Vigneaud, *J. Am. Chem. Soc.*, 1924, **46**, 2661-2663.
61. P. J. Quinlivan, A. Loo, D. G. Shlian, J. Martinez and G. Parkin, *Organometallics*, 2021, **40**, 166-183.
62. D. Enders and T. Balensiefer, *Acc. Chem. Res.*, 2004, **37**, 534-541.
63. D. Enders, K. Breuer, U. Kallfass and T. Balensiefer, *Synthesis*, 2003, **2003**, 1292-1295.
64. M. S. Kerr, J. Read de Alaniz and T. Rovis, *J. Org. Chem.*, 2005, **70**, 5725-5728.
65. C. Duangkamol, M. Pattarawarapan and W. Phakhodee, *Monatsh. Chem.*, 2016, **147**, 1945-1949.
66. A. R. Ali, H. Ghosh and B. K. Patel, *Tetrahedron Lett.*, 2010, **51**, 1019-1021.
67. H. G. Khorana, *Chem. Rev.*, 1953, **53**, 145-166.
68. R. Wessel, *Ber. Dtsch. Chem. Ges.*, 1888, **21**, 2272-2278.
69. H. Wu, Y.-F. Sun, C. Zhang, C.-B. Miao and H.-T. Yang, *Tetrahedron Lett.*, 2018, **59**, 739-742.
70. C. Hansch, A. Leo and R. W. Taft, *Chem. Rev.*, 1991, **91**, 165-195.
71. J. Zhu, I. Moreno, P. Quinn, D. S. Yufit, L. Song, C. M. Young, Z. Duan, A. R. Tyler, P. G. Waddell, M. J. Hall, M. R. Probert, A. D. Smith and A. C. O'Donoghue, *J. Org. Chem.*, 2022, **87**, 4241-4253.
72. F. J. M. Rogers, P. L. Norcott and M. L. Coote, *Org. Biomol. Chem.*, 2020, **18**, 8255-8277.
73. Y. Ji, L. Long and Y. Zheng, *Mater. Chem. Front.*, 2020, **4**, 3433-3443.
74. F. Saenz, M. Tamski, J. Milani, C. Roussel, H. Frauenrath and J.-P. Ansermet, *Chem. Comm.*, 2022, **58**, 689-692.

75. M. D. Liptak, K. C. Gross, P. G. Seybold, S. Feldgus and G. C. Shields, *J. Am. Chem. Soc.*, 2002, **124**, 6421-6427.
76. R. S. Massey, C. J. Collett, A. G. Lindsay, A. D. Smith and A. C. O'Donoghue, *J. Am. Chem. Soc.*, 2012, **134**, 20421-20432.
77. X. Hu, H. Chen, L. Zhao, M.-s. Miao, X. Zheng and Y. Zheng, *J. Mat. Chem. C*, 2019, **7**, 10460-10464.
78. Y. Zheng, M. S. Miao, G. Dantelle, N. D. Eisenmenger, G. Wu, I. Yavuz, M. L. Chabinyc, K. N. Houk and F. Wudl, *Adv. Mater.*, 2015, **27**, 1718-1723.
79. X. Hu, H. Chen, L. Zhao, M. Miao, J. Han, J. Wang, J. Guo, Y. Hu and Y. Zheng, *Chem. Commun.*, 2019, **55**, 7812-7815.
80. A. E. Tschitschibabin, *Ber. Dtsch. Chem. Ges.*, 1907, **40**, 3056-3058.
81. E. Müller and H. Pfanz, *Ber. Dtsch. Chem. Ges.*, 1941, **74**, 1051-1074.
82. N. Gallagher, H. Zhang, T. Junghoefer, E. Giangrisostomi, R. Ovsyannikov, M. Pink, S. Rajca, M. B. Casu and A. Rajca, *J. Am. Chem. Soc.*, 2019, **141**, 4764-4774.
83. N. M. Gallagher, J. J. Bauer, M. Pink, S. Rajca and A. Rajca, *J. Am. Chem. Soc.*, 2016, **138**, 9377-9380.
84. S. Zhang, M. Pink, T. Junghoefer, W. Zhao, S.-N. Hsu, S. Rajca, A. Calzolari, B. W. Boudouris, M. B. Casu and A. Rajca, *J. Am. Chem. Soc.*, 2022, **144**, 6059-6070.
85. S. Morales, F. G. Guijarro, J. L. García Ruano and M. B. Cid, *J. Am. Chem. Soc.*, 2014, **136**, 1082-1089.

3. The Design, Synthesis and Evaluation of Non-Native Cofactors for Biocatalysis

3.0. Foreword

Since the first discovery of enzymes in 1833 and subsequently of enzyme cofactors in 1905, two distinct fields of biocatalysis and organocatalysis have independently developed. These two vast areas of research have very similar characteristics and aims of catalysing organic transformations, in more sustainable conditions, with limited need for toxic reagents or solvents. However, there has been very little work to develop collaborative approaches to catalysis which encompass both fields. This chapter outlines initial studies into developments of synergistic developments within the fields of NHC-organocatalysis and thiamine pyrophosphate-dependent enzymes. Thiamine pyrophosphate is itself classed as an NHC and inspired the field of organocatalysis; however, until now there has been no attempt to introduce the subsequent chemical developments in NHC-organocatalysis into the field of TPP-dependent biocatalysis.

Chapter 3.1 outlines the key enzyme cofactors which have seen application within organocatalysis, alongside applications in biocatalysis and examples of synergistic approaches to develop non-native mimics (chemomimetic biocatalysis). Chapter 3.2 discusses the synthesis of a more catalytically active 1,2,4-triazolium mimic of thiamine pyrophosphate, based on previous synthetic and mechanistic studies on NHC-organocatalysis. Within the synthetic studies it was found that the hydrolysis of the pyrophosphate bonds of thiamine pyrophosphate and the novel cofactor mimic was occurring during purification and storage. Chapter 3.3 explores the aqueous stability of thiamine pyrophosphate across the p*H* spectrum to inform handling, purification and storage. Finally, Chapters 3.4 and 3.5 discuss the evaluation of the novel cofactor mimic, exploring the carbon acidity in comparison to thiamine, relevant to the propensity for carbene formation. Alongside this catalytic evaluation in both organocatalytic and biocatalytic transformations is explored.

3.1. Cofactor Catalysis: The Synergistic Relationship of Bio- and Organo-Catalysis

3.1.1. Introduction

Often described as the perfect catalysts, enzymes have provided inspiration to much of organic chemistry, notably the field of organocatalysis. Despite traditionally being recognised as two distinct fields, biocatalysis and organocatalysis originated as, and are merging towards, a single entity once more. Enzymes offer huge advantages to chemical processes, operating under mild reaction conditions, in aqueous solvents to deliver complex molecular architectures with excellent stereoselectivities.[86, 87] With the imperative drive to 'greener' chemical processes, the use of enzymes in catalysis is seen as key to developing a sustainable future. In terms of traditional limitations of development in this area, wild-type enzymes do not usually possess the desired substrate scope or tolerance to a range of conditions to tackle the broad requirements of process chemistry. Furthermore, the natural repertoire of enzyme-catalysed transformations does not extend to many reactions important to modern day synthetic chemistry. Major developments in protein engineering in recent decades, such as directed evolution, have enabled access to enzymes with activities and specificities tailored to the desired chemical process (Figure 3.1.1).[88-93]

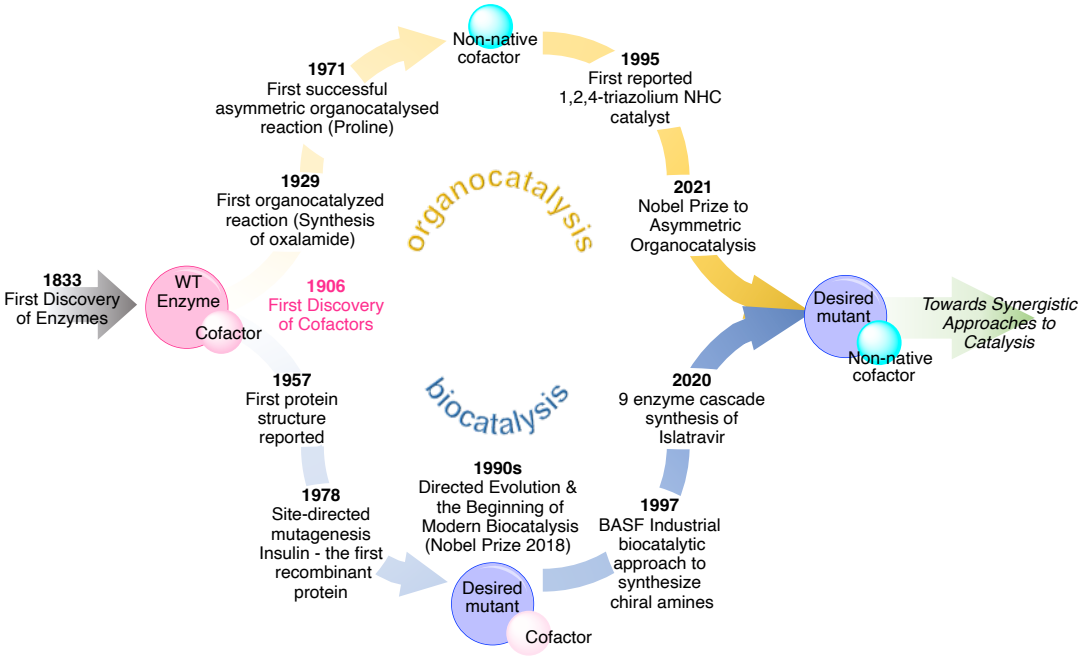

Figure 3.1.1. Overview timeline of independent developments in biocatalysis and organocatalysis. Scheme developed with Prof. David Hodgson.

One significant opportunity for biocatalysis is cofactor engineering. Enzymes work in tandem with cofactors, which have catalytic properties of their own.[94] Cofactor catalysis provided inspiration in the large field of organocatalysis, with many of the common organocatalysts in modern synthetic chemistry using basic cofactor scaffolds derived from biology. Within the bioinformatics database of 27 cofactors, we have identified a selection of seven which have been used as organocatalyst scaffolds.[95] Chemical intuition has helped modify these cofactors for catalytic benefit leading to enhanced reactivities, stereoselectivities and reaction scope of the catalyst. Recent explorations in biocatalysis have seen the application of native cofactors with wild-type or mutant enzymes to extend substrate scope, reaction chemoselectivity and, in limited cases, enable the catalysis of non-native transformations. To date, however, there has been limited exploration of the application of chemically modified (non-native) cofactors in enzymatic biocatalysis. In particular, the many recent advances in organocatalysis have resulted in optimised organocatalysts with significant structural differences from their cofactor biomimetic origins, but with enhanced substrate scopes and significantly broader reaction scopes.[96-104] The combination of chemically modified cofactors with cofactor dependent enzyme could provide opportunities for biocatalysis of new-to-nature chemistry with stereo-control provided by the enzyme. Furthermore, a significant recent shift of emphasis in organocatalysis over the past 5 years has been the use of more sustainable solvent media rather than traditional organic solvents. Organocatalysts that function in more polar, aqueous environments are potentially excellent candidates as non-native cofactors for enzymatic biocatalysis.

3.1.2. Review Outline

Within this review, the key cofactors which have been used in organocatalytic settings and modifications which have enhanced their reactivities are highlighted. Where available, the application of chemically modified cofactors within biocatalytic environments and the effects on reaction outcome are discussed. Both organo- and biocatalysis have their advantages and disadvantages. Biocatalysis requires more costly enzymes and substrate scope can be limited; however, it allows organic reactions to be carried out under more sustainable conditions, such as low temperatures and aqueous environments, with inherent stereoselectivity. Organocatalysis requires the timely and potentially challenging synthesis of chiral catalysts, but its enhanced substrate scope and

greater accessibility to the typical organic chemist are significant benefits. Synergistic approaches, combining the fundamental knowledge developed in both bio- and organo-catalysis could unveil new areas of chemistry, particularly through the introduction of non-native cofactors to biocatalytic transformations to enhance reactivity and scope.

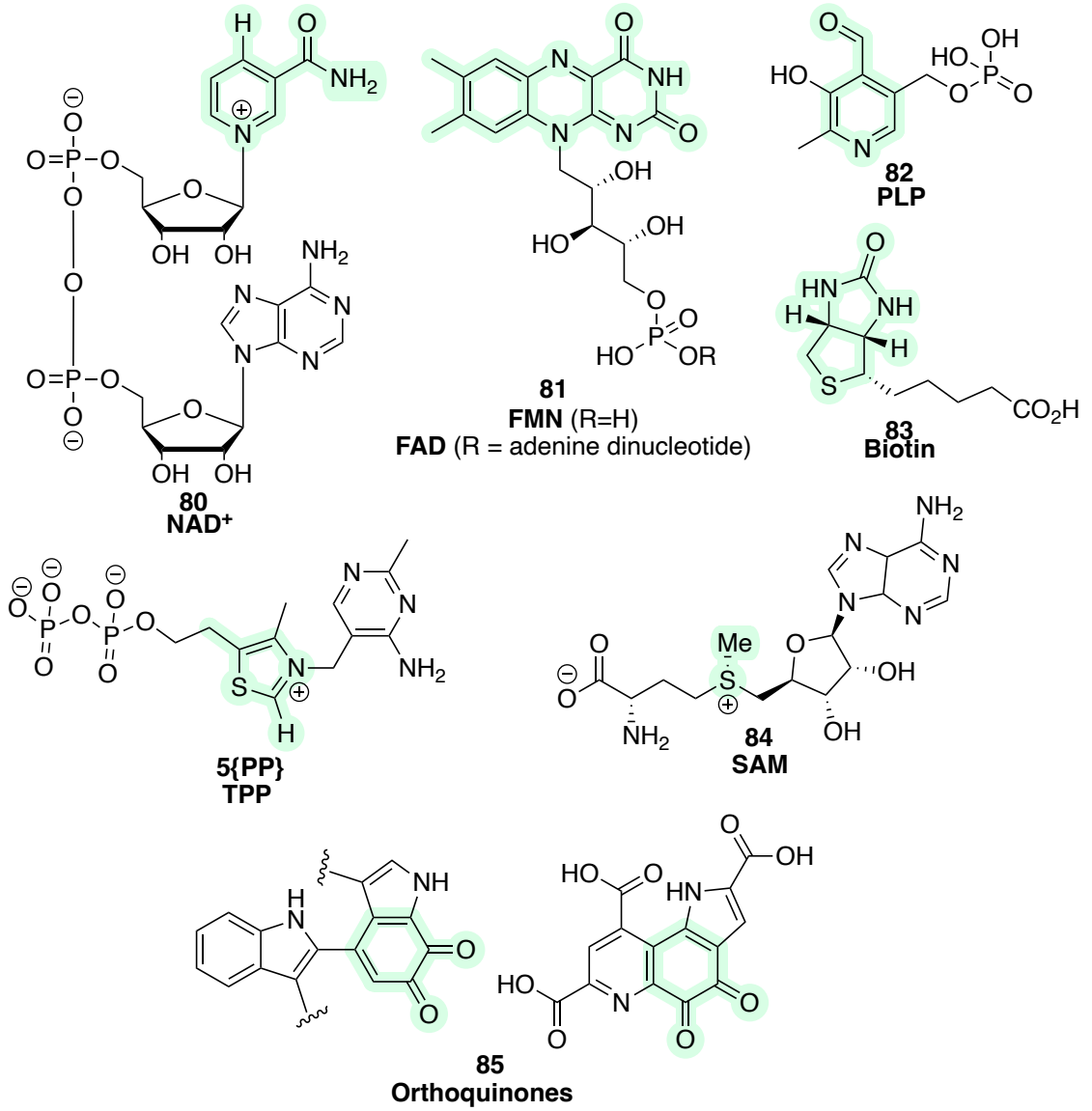

Figure 3.1.2. The key cofactors which have been used in organocatalysis and are subject of this review, with the key catalytic moieties highlighted in green.

3.1.3. Nicotinamide Cofactors (80)

Nicotinamide cofactors, NAD^+/NADH (**80/80{H}**) and $NADP^+$/NADPH, are responsible primarily for the transfer of hydride within biological systems. Often they work in tandem with flavin mononucleotide (**81**) and an enzymatic partner. They consist of 2 key structural moieties: an electrochemically active nicotinamide and an adenosyl dinucleotide which differentiates the anabolic ($NADP^+$/NADPH) and catabolic

(NAD^+/NADH) pathways.[105] These differences are essential from a cellular perspective, but are less relevant from the perspective of biomimetic catalysis.[106] Within biological systems NADH couples to a wide range of enzymes however, key to biocatalysis are ene-reductases and oxidoreductases. During these reactions NAD^+/NADH is used stoichiometrically to transfer hydride to C=X systems (typically, ketones, aldehydes, imines, alkenes) and therefore must be reformed by other oxidation or reduction processes within the cell.[107] Typically this regeneration involves flavin-type cofactors which will be discussed below (Chapter 3.1.4).

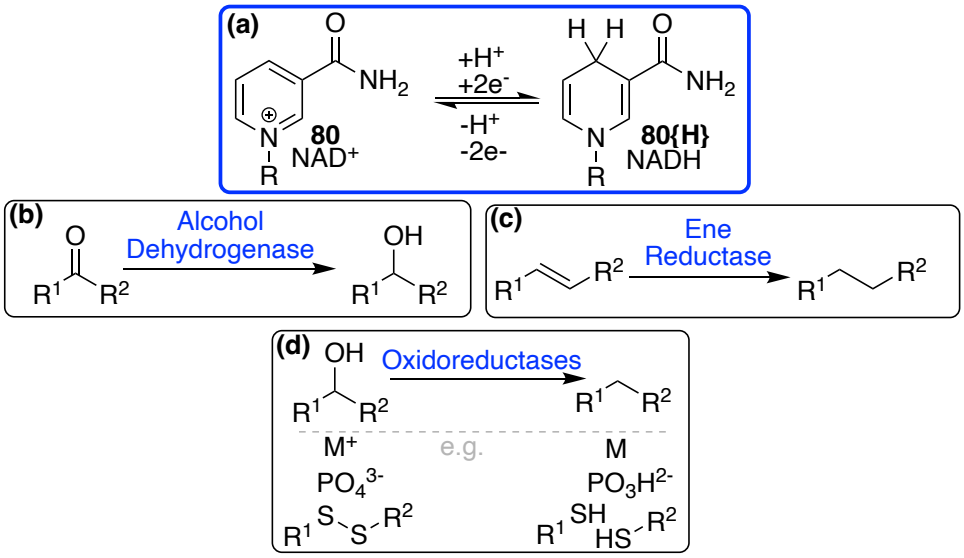

Figure 3.1.3. (a) The key reaction of NAD(H) (**80{H}**), a two-electron oxidation/reduction; (b)-(d) native NAD(H) dependent enzymes include alcohol dehydrogenases, ene reductases and oxidoreductases.

Biocatalytic systems encompassing NADH-dependent enzymes have been explored for a variety of applications. More recently a deuterated-NADH (**80{D}**) cofactor has been used for the stereoselective deuteration of a range of alkene and carbonyl systems (Scheme 3.1.1). This stereoselective deuteration technique is advantageous in the synthesis of deuterated drug molecules. Deuterated drug molecules are useful in determining mechanisms of action and metabolic profiles, taking advantage of the isotopic label as a tracer and kinetic isotope effects. Biocatalytic deuteration has the advantage of excellent enantioselectivity, with no metal catalyst and a relatively inexpensive source of deuterium (D_2O) with hydrogen gas as the sacrificial reductant for recycling NAD(**D**) (**80{D}**). The catalytic system used is a heterogeneous system of two enzymes adsorbed to a solid particle. These include a hydrogenase with a nickel-iron active site and an NAD^+ reductase with a flavin mononucleotide (**81**) active site. A range of pharmaceutically relevant substrates were explored (**86-87**) and excellent yields, stereoselectivities and deuterium incorporation were observed.[108] The requirement for a

second hydrogenase enzyme highlights a key challenge for NADH-biocatalysis: the need for inexpensive and simple techniques for cofactor recycling.

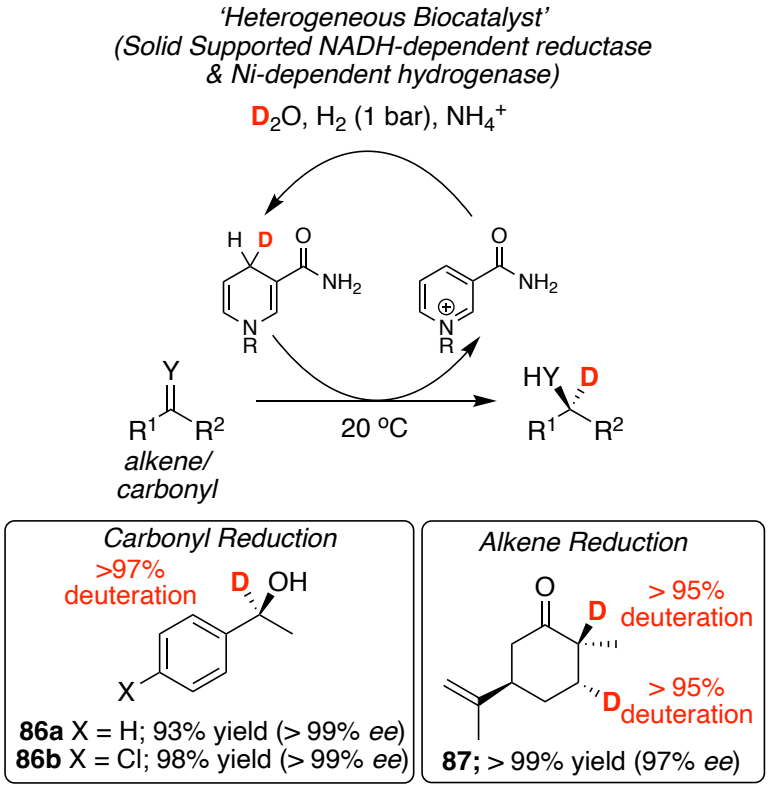

Scheme 3.1.1. Applications of NAD(H) (**80{H}**) dependent enzymes in biocatalysis for the deuteration of a range of substrates. The heterogeneous biocatalyst refers to two enzymes on a solid support (a hydrogenase enzyme, with Ni-cofactors, and an NAD(H)-dependent reductase).

As with many cofactors, NADH (**80{H}**) has activity of its own that has been harnessed by synthetic chemists accordingly. Typically, selective reductions utilise homogeneous metal catalysts or classic reductants ($NaBH_4$/$LiAlH_4$) with stereoselective ligands; however, the metal-free processes within nature have provided the inspiration to drive to more sustainable, organocatalytic methodologies. Initial studies of Westheimer and Mauzerall were the first to show that dihydropyridine analogues of NADH, Hantzsch esters (**88**/**89**), could successful mediate hydride transfer (Figure 3.1.4).[109] This work opened a field of organocatalysis focussed on asymmetric hydrogenations, important in the development of stereocentres.[110] Organocatalytic systems combining both iminium ion catalysis (**90**) and Hantzsch esters (**88**) have been developed to give high yielding, enantioselective reductions without the need for metal catalysts.[111]

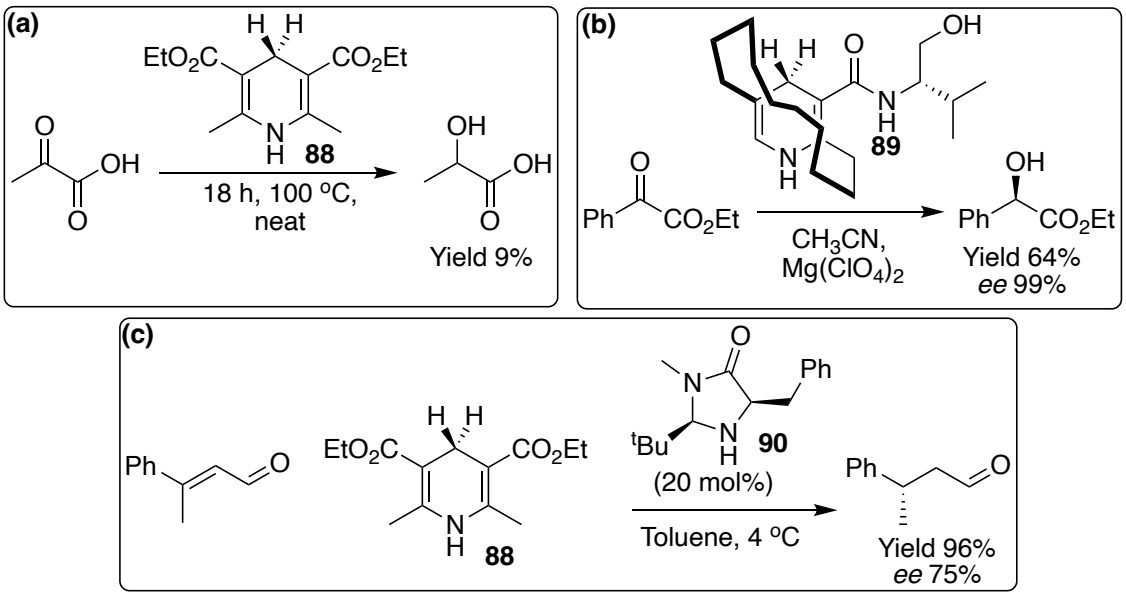

Figure 3.1.4. (a) Hantzsch esters (**88**) hydride transfer for the reduction of pyruvic acid; (b) use of a chiral Hantzsch ester (**89**) for the selective reduction of a ketone; (c) Hantzsch ester (**88**) reduction coupled with pyrrolidine-type enamine catalyst (**90**) for selective reduction of a Michael acceptor.

More recently, a selection of mimics of NADH (**80{H}a-c**) have been designed and used in tandem with an ene-reductase, alongside flavin mononucleotide (**81**) to reduce activated alkenes (Figure 3.1.5). In addition, a selection of biocatalytic, stereoselective epoxidations and hydroxylations have also been reported.[112, 113] The use of chemical intuition has allowed improvements in performance beyond that of the natural cofactor in some cases (faster rates of reduction, $k_{red,}$ despite poorer binding affinities, K_D). Other examples have also developed mimics that seek to enhance activity in native reactions, such as that of cytochrome c reduction. Interestingly, wild-type enzyme showed no reaction with the mimics but, a double mutant (W1064S/R966d) gave significant enhancement in NADH mimic activity to the same order of magnitude as the native cofactor.[113] This example highlights the need for synergistic approaches combining the key developments in organo- and bio-catalysis.

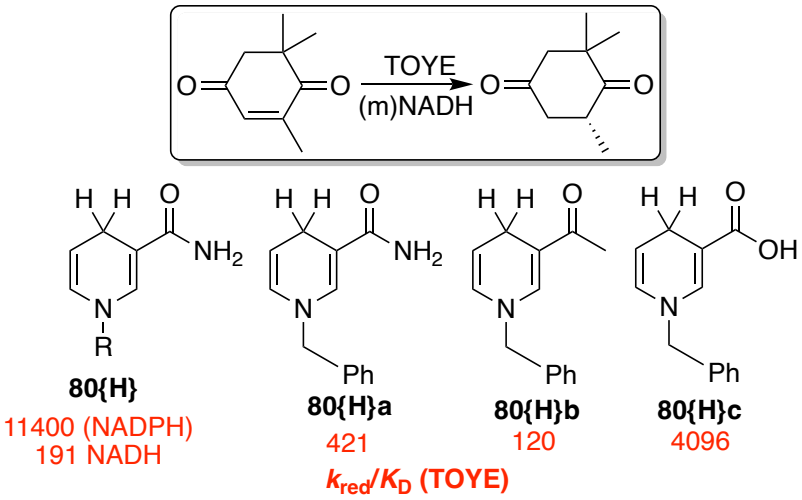

Figure 3.1.5. Application of non-native NADH mimics in a biocatalytic reduction using the Old Yellow Enzyme.

One remaining disadvantage of NADH (**80{H}**) biocatalysis is that wasteful, stoichiometric amounts of the hydride donor are required in most cases. It was shown that a catalytic amount of a rhodium complex could be installed to recycle the hydride donors, and is itself recycled with the use of formate.[105] This promising development reduces the amounts of the hydride donor required to catalytic levels and paves the way for the use of alternative catalysts, potentially less expensive, less toxic and more earth abundant, in the same recycling role. Other approaches to cofactor recycling have been explored, particularly in continuous flow with enzymes immobilised on a solid carbon nanotube support.[114, 115] Recycling methods include using other enzyme systems and sacrificial substrates but, these result in large amounts of carbon waste. Under continuous flow conditions, NADH (**80{H}**) recycling was possible through use of hydrogen gas, significantly reducing waste and the need for costly, stoichiometric amounts of NADH. A variety of reductions of classic imine and carbonyl systems were attempted giving high conversions, turnover numbers and very high enantiomeric excesses (Figure 3.1.6).[114, 115]

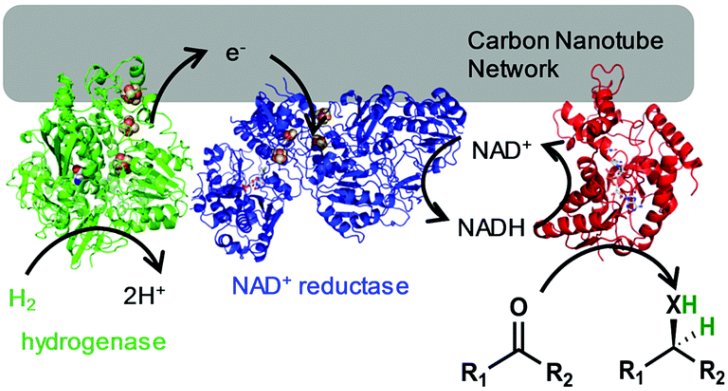

Figure 3.1.6. Solid supported NADH catalysts and Ni-dependent hydrogenase for NAD^+ recycling under continuous flow conditions. Reproduced with permission from Ref. 111 and the Royal Society of Chemistry.

3.1.4. Flavin Cofactors (81)

Despite often being used in tandem with NADH in biological systems, Flavin cofactors are not limited to hydride/hydrogen transfers. They have also been found to also facilitate halogenations, C-C bond formations and reductions of alkene and nitro groups.[116] Within biological systems, Flavin typically has either a mononucleotide (FMN) or adenine dinucleotide (FAD) prosthetic group; however, it is the central flavin moiety which is responsible for its electron transfer properties. Biological applications of flavoenzymes include two-electron oxidations in major metabolic systems, halogenations of major natural products, photorepair of DNA damage and in blue-light sensing cryptochromes.[117] The key mechanistic step in the majority of flavin-dependent oxidations is formation of reactive flavin hydroperoxide, which is able to transfer an oxygen atom to a substrate.[118] As with NADH, Flavin cofactors require regeneration during REDOX processes, typically via another enzymatic cycle, coupled with the nicotinamide cofactor. In developing biocatalytic and organocatalytic processes this must be considered.[119]

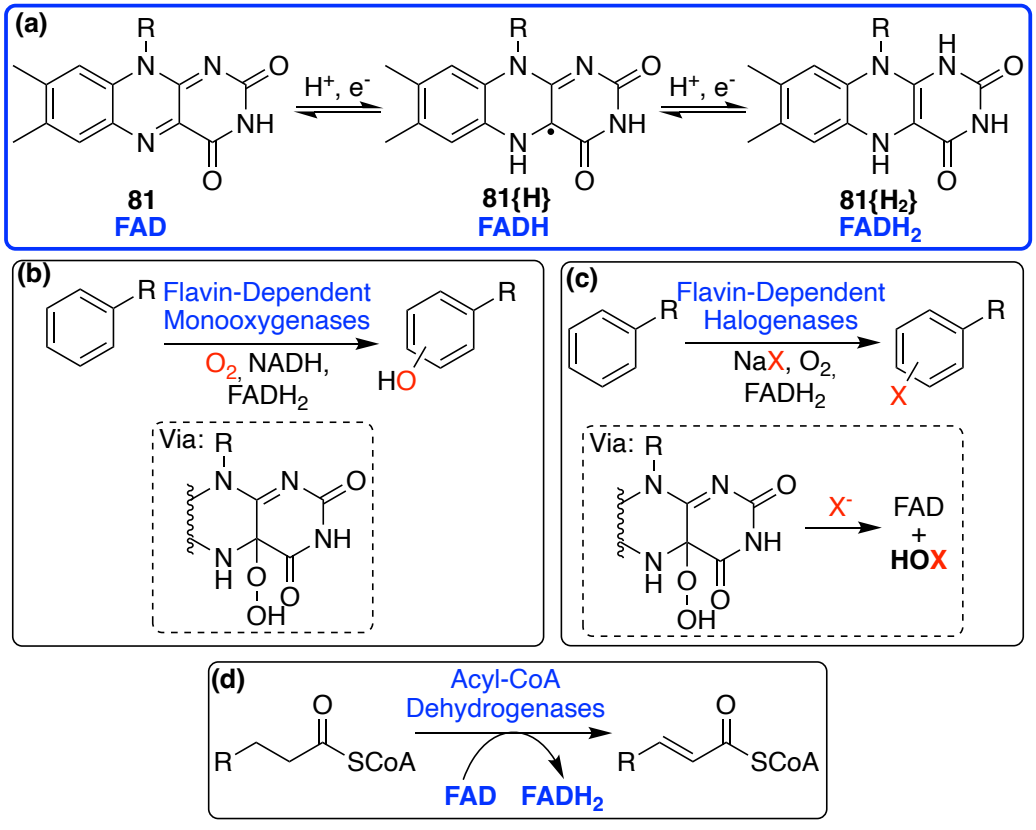

Figure 3.1.7. (a) The key reactions of FAD (**81**), two one-electron oxidation/reductions; (b)-(d) native FAD dependent enzymes include monooxygenases, halogenases and dehydrogenases.

Flavin cofactors (**81**), in tandem with a dependent enzyme, have been broadly used in biocatalysis. Notably, they have been used for regioselective halogenations of aromatic compounds with inorganic halides, via tryptophan halogenases. These provide the key

advantage of being selective whilst avoiding the need for typically hazardous chemical halogenating reagents (Figure 3.1.8). Moreover, structure guided mutagenesis has allowed the development of enzymes with different regioselectivities and broader substrate scopes with potential for industrial applications.[120] More recently, expanding the scope of flavin-dependent halogenations, a selection of enantioselective halocyclisations showcased non-native transformations (Figure 3.1.8). Typically, these transformations have been carried out with vanadium haloperoxidases; however, mutated flavin-dependent halogenases, typically used in arene halogenations, have now been developed to perform this enantioselective transformation in good-excellent yields. A variety of enzyme mutants were explored and whilst it was found that mutants developed for typical arene halogenations could catalyse halocyclisations, the majority of native enzymes could not.[121]

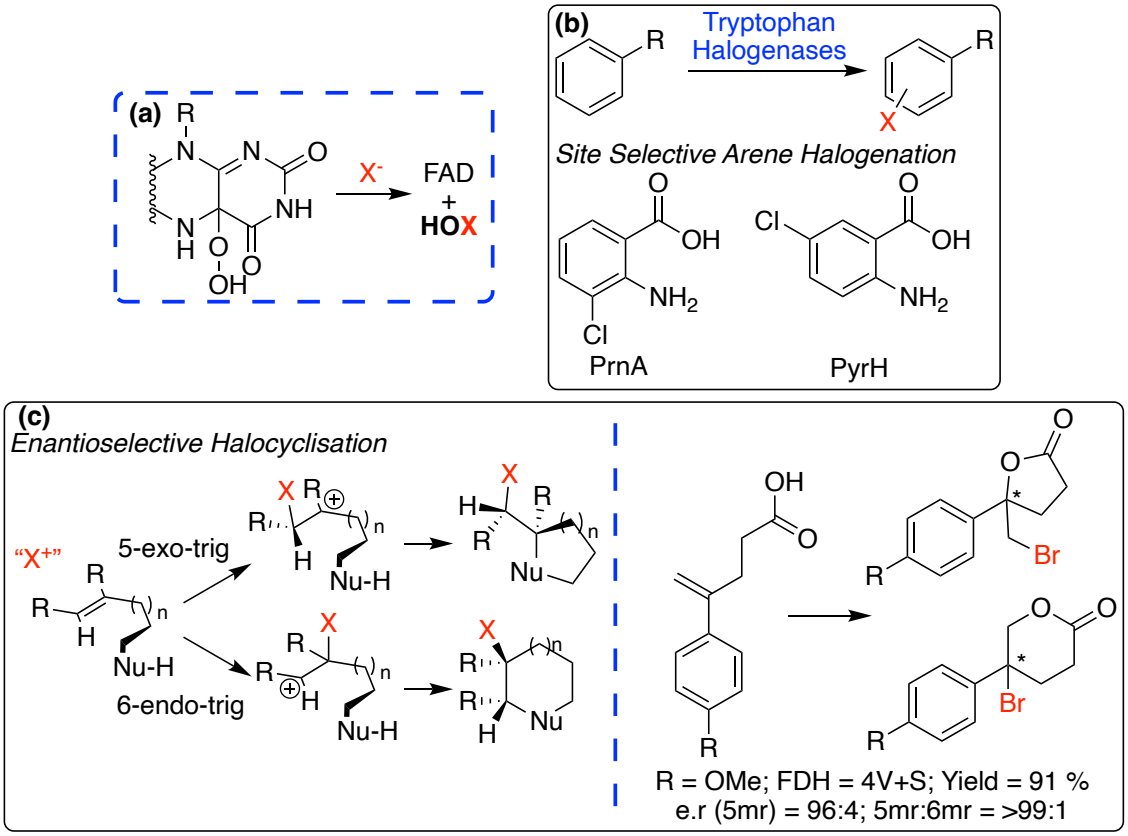

Figure 3.1.8. (a) The key flavin-dependent step – generation of HOX *in situ* as the active halogenating reagent; (b) Previous applications of tryptophan halogenases in the site selective halogenation of aromatics; (c) the enantionselective halocyclization can form 5- or 6- membered rings, tryptophan halogenases were developed to favour the 5 membered ring (5mr) in high e.r.s.

Other biocatalytic applications show oxidised flavin used for the synthesis of imines from amines by monoamine oxidases,[122] the synthesis of enantioenriched amino acids and polymer building blocks using ene reductases[123] and oxidations using Bayer-Villiger monooxygenases. All of these examples have been subject to previous reviews.[119, 123]

As organocatalysts, flavin cofactors and derivatives have been used for a range of transformations. Flavin hydroperoxide is unstable and requires stabilisation within the enzyme active site with specific protein interactions; however, organocatalytic generation of this unstable compound has been possible through chemical modifications to flavin. Backbone alkylation of flavin (**81a**) permits formation of stable hydroperoxides which can be used for organocatalytic oxidations with inexpensive oxidants. Moreover, catalytic loadings of alkyl-flavins were possible by introducing hydrazine as the reducing agent to regenerate flavin, before continued reaction with molecular oxygen to generate the active oxidant (Figure 3.1.9(a)).[118] Alongside this, the alkylated phosphine N(5)-adducts (**81b**) have been used to catalyse aerobic Mitsunobu reactions. The benefit of this method is that the active Mitsunobu reagent is regenerated by molecular oxygen as opposed to toxic and explosive azodicarboxylates (Figure 3.1.9 (b)).[124]

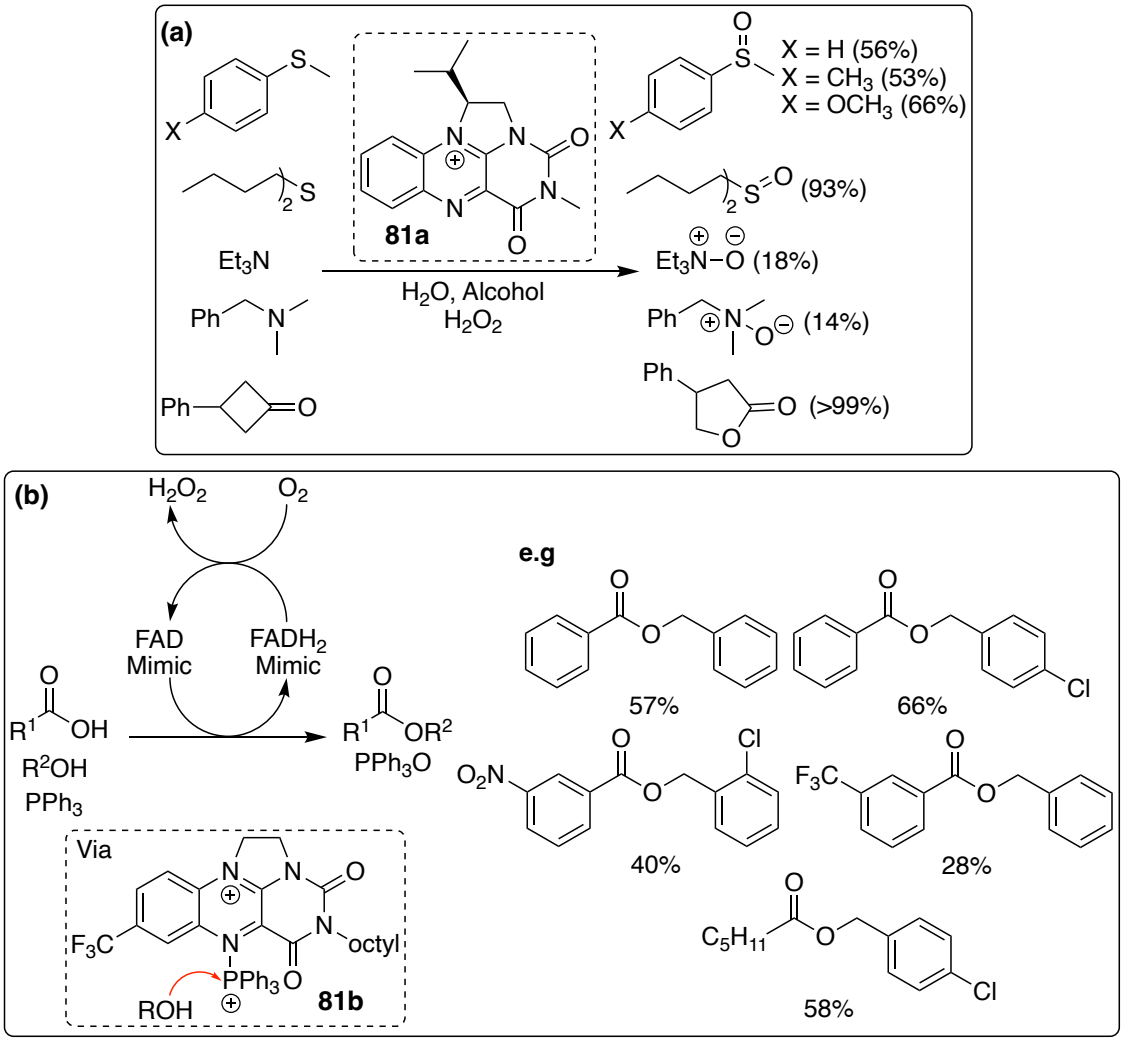

Figure 3.1.9. Organocatalytic applications of flavin mimics (**81a/b**): (a) A range of oxidations via the hydroperoxyl-flavin adduct (**81a{OOH}**); (b) A flavin-catalysed Mitsunobu esterification which proceeds via a flavin-triphenylphosphine adduct (**81b**).

Alongside oxidation reactions, flavin cofactors (**81**) have been employed in the challenging reductions of carbon-carbon double bonds through the catalytic generation of a strong reductant, diimide, from hydrazine. Despite significant interest in flavin-based organocatalysis, examples of enantioselective syntheses are limited. Chiral groups have been employed as N-alkyl/aryl substiutents, however, *ee*s have not exceeded 65 %. Chiral aromatic groups have typically been designed to direct the stereo-outcome through π–π stacking.[125] Alternative approaches to choreograph stereochemistry have used artificial receptors such as cyclodextrins and non-enzymatic proteins bound to flavin cofactors (**81c**). These have allowed access to *ee*s of up to 86 % which, compared to flavin alone, are excellent, however, do not match those of biocatalytic transformations.[118, 126, 127]

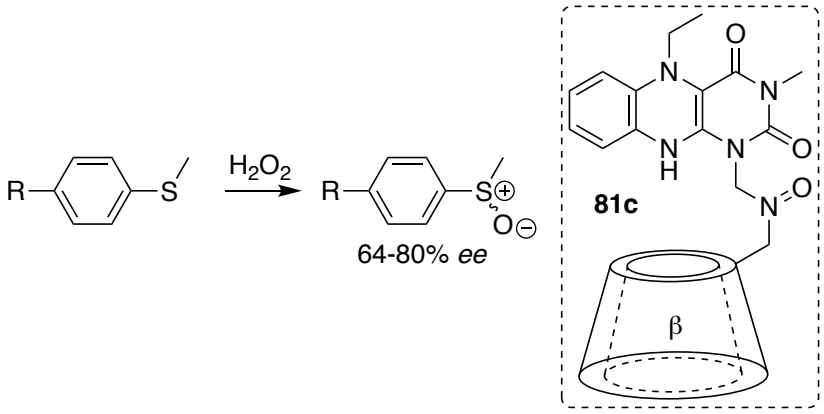

Scheme 3.1.2. Enantioselective flavin organocatalysis using a β-cyclodextrin.

Most biomimetic analogues of flavin have been developed to stabilise the flavin hydroperoxide intermediate outside of a biological setting. As such, reintroduction of these analogues to enzymes has not been explored. Nevertheless, examples such as the bridged N-alkyl derivative (**81b**) used to catalyse the Mitsunobu reaction could be explored in a biocatalytic environment to develop new transformations.

3.1.5. Pyridoxal Phosphate (PLP) (82)

PLP (**82**) is a cofactor for a broad range of enzyme-catalysed reactions of amino acids, reducing the activation barrier for formation of α-carbanions.[128] Mechanistically, it is proposed that a lysine residue within the enzyme active site forms a Schiff-base with PLP (**82{E}**).[128] Upon substrate binding this enzyme-cofactor iminium ion is cleaved to form a PLP-substrate iminium ion (**82{S}**), activating the substrate towards a variety of transformations including decarboxylation, racemisation and transamination (Figure 3.1.10).[128] In a small molecule model study to quantitatively evaluate enzyme-PLP

catalysis of amino acid racemization, it has been shown that upon formation of an iminium ion of acetone, the C(α)-H pK_a is reduced by 7 units from 21 to 14.[129, 130]

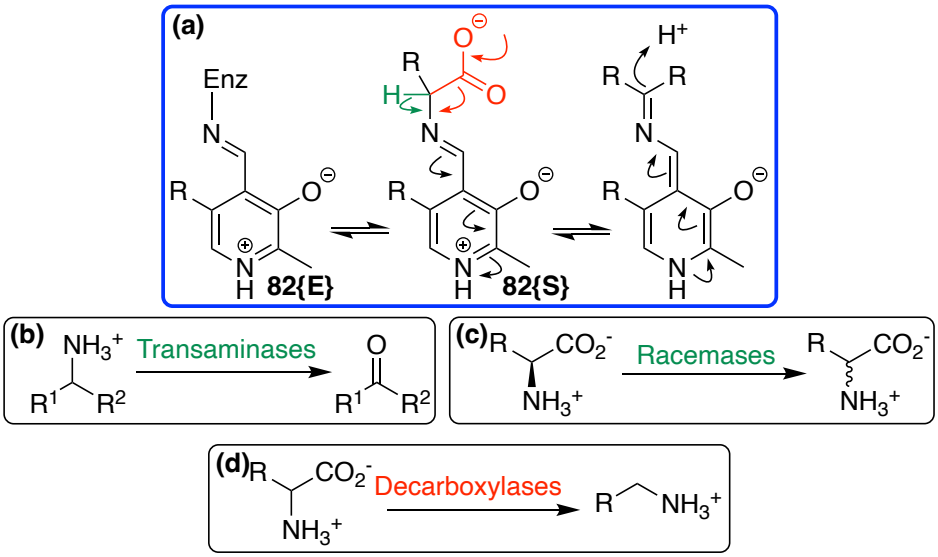

Figure 3.1.10. (a) The key reactions of PLP are decarboxylation, or deprotonation of a bound amino acid; (b)-(d) native PLP dependent enzymes include transaminases, racemases and decarboxylases.

Biological PLP-dependent transformations have inspired two fields of organocatalysis: reactions at carbonyl groups catalysed by amines and reactions of amines catalysed by aldehydes. The latter is most similar to PLP-catalysis and various analogues have been explored however both areas are broadly classed within enamine and iminium ion catalysis. Development of PLP-biomimetics is challenging owing to the need to meet three criteria: (1) the carbonyl component of the cofactor mimic must have significant electron-withdrawing character to activate the α-position of the amine towards deprotonation; (2) the catalyst-substrate iminium ion must be less reactive than the reacting electrophile at the α-amino position; (3) the carbonyl catalyst must direct the approaching electrophile for asymmetric reactions.[131, 132] Recently, a biomimetic PLP derivative (**82a**) has been developed to catalyse an asymmetric Mannich reaction between glycinate and N-diphenylphosphinyl imines. Reactions were high yielding with excellent enantiomeric selectivities and substrate scope (Figure 3.1.11).[131] These products can readily be deprotected to yield chiral diamines in high yields, *dr*s and *ee*s. A pyridoxamine catalyst (**91**) has also been developed for biomimetic, asymmetric transaminations. This catalyst, again, has inbuilt chirality allowing it to control the diastereo-outcomes and provides a novel approach to the synthesis of complex peptides (Figure 3.1.11).[133] Alongside this, there has been significant exploration of aldehyde catalysis for a range of transformations including hydroaminations, hydrations and

hydrolyses. Generally, the aldehyde catalysts are not directly based on the structure of PLP, instead linking chiral groups to an aldehyde; however, their modes of action are similar: activating the α-amino position to perform challenging transformations.[134]

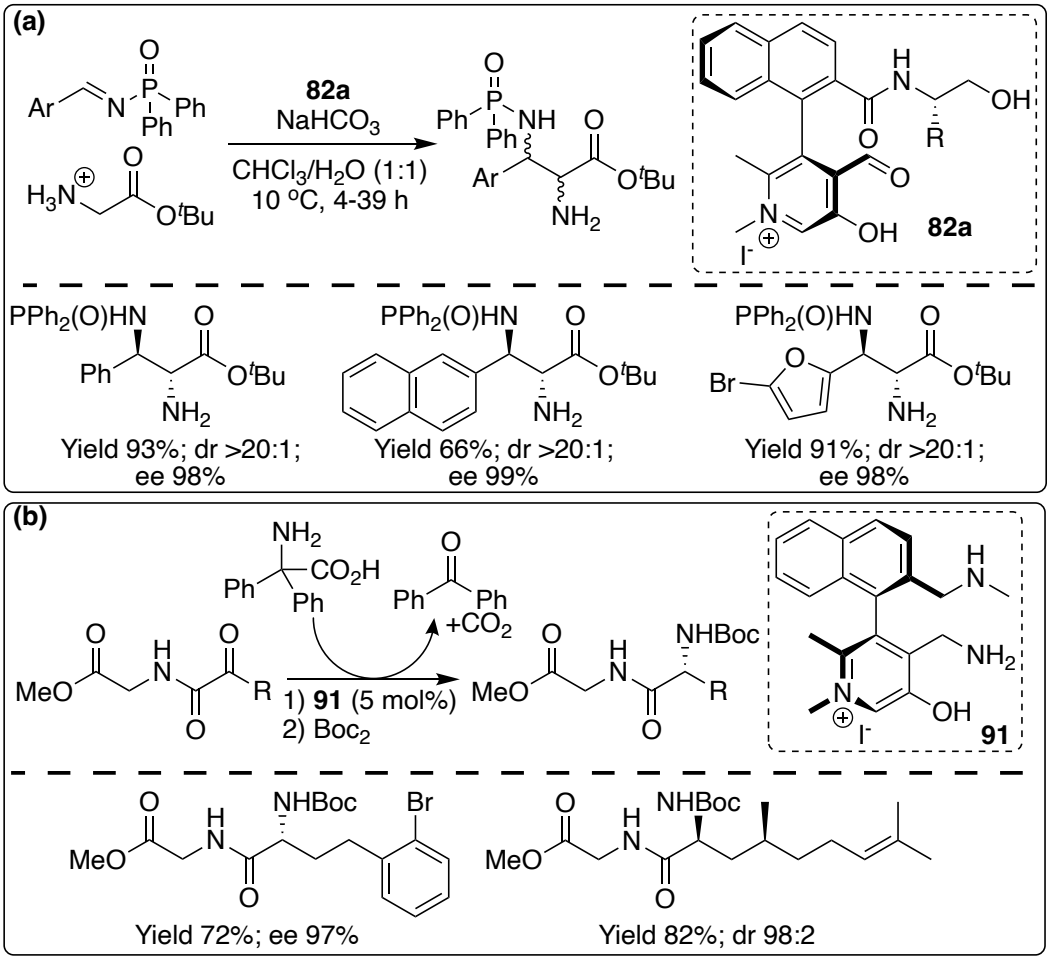

Figure 3.1.11. Asymmetric organocatalytic transformations catalysed by mimics of PLP: (a) asymmetric Mannich reaction between glycinate and N-diphenylphosphinyl imines, catalysed by **82a**; (b) asymmetric transaminations catalysed by catalyst **91**.

In a biocatalysis context, PLP-dependent enzymes using native cofactor have been used to catalyse the formation of a range of pipecolate structures which are typically challenging to synthesise, yet are important within the pharmaceutical industry.[135] Transaminases are particularly useful biocatalysts for accessing synthetically challenging and expensive chiral amine building blocks.[136] A selection, specifically ω–transaminases, have good substrate scope and can accept aliphatic amines and ketones alongside amino and keto acids.[137] In nature, transaminases are generally (*S*)-selective; however, engineering techniques have allowed access to some (*R*)-selective systems with increased substrate scopes.[138-140] A notable example of their application is the large scale production of an anti-diabetic drug, Sitagliptin.[141] A selection of other PLP-dependent enzymes have also been used broadly for important chemical transformations. These

include lysine decarboxylase for the synthesis of cadaverine (**92**), a useful compound for the polymer industry; threonine aldolase for the synthesis of β-hydroxy-α-amino acids (**93**), core building blocks in many antibiotics and immunosuppressants; and, finally, cystathionine (**94**) β–lyase for the synthesis of volatile sulphur containing compounds for the food and fragrance industry (Figure 3.1.12).[136]

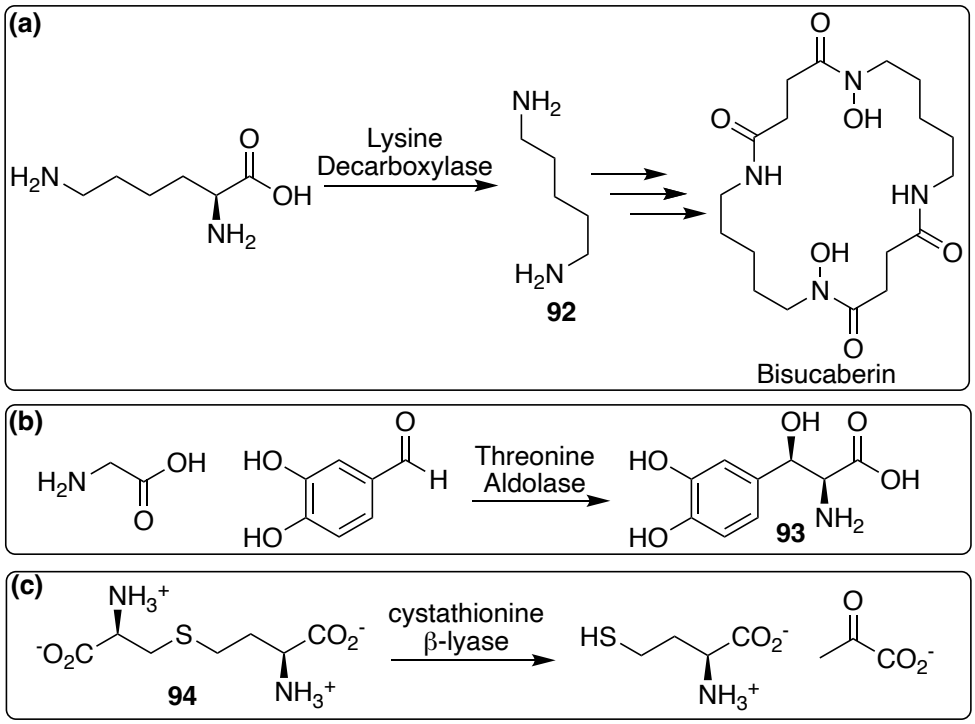

Figure 3.1.12. Industrial biocatalytic applications of PLP-dependent biocatalysts: (a) Lysine carboxylase in the synthesis of cadaverine (**92**) and subsequently the chelate, Bisucaberin; (b) Threonine aldolase in the synthesis of synthesis of β-hydroxy-α-amino acids (**93**) for pharmaceuticals; (c) cystathionine (**94**) β–lyase for the synthesis of volatile sulphur containing compounds for the food and fragrance industry.

Despite the broad exploration of PLP-dependent biocatalysis, there has been limited exploration of non-native reactions and cofactors, such as the utilisation of the modified cofactor analogues successful in organocatalysis, in enzymatic biocatalysis with PLP-dependent enzymes. Perhaps the broadness of reactivity and scope of PLP-dependent enzymes limits the need for such exploration; however, the ability to carry out challenging transformations on industrial scales in a sustainable manner warrants an exploration of PLP-dependent enzymes in non-native environments with non-native cofactors.

3.1.6. Biotin (83)

Biotin (**83**) is most synonymous with the formation of very tight binding streptavidin-biotin host guest complexes, which have been utilised widely for affinity capture purposes. As an enzyme cofactor, it is covalently bound, via its valerate side chain,

through amide bond to carboxylase enzymes. It transfers carbon dioxide via two half-reactions (Figure 3.1.13) across three classes of biotin-dependent enzymes: carboxylases (Class I), decarboxylases (Class II) and transcarboxylases (Class III). Eukaryotic biotin-dependent enzymes are all Class I and include pyruvate carboxylase (gluconeogenesis), propionyl-CoA carboxylase (odd-chain fatty acid synthesis) and acetyl-CoA carboxylase (fatty acid synthesis).[142] Mechanistically, it is proposed that the covalent adduct of biotin and carbon dioxide (**83{CO_2}**) cleaves, resulting in an enolate-type intermediate at the urea moiety of biotin. Subsequently enolization of a substrate such as pyruvate, by the biotin-intermediate, results in a nucleophile capable of reacting with the released carbon dioxide (Figure 3.1.13).[142, 143]

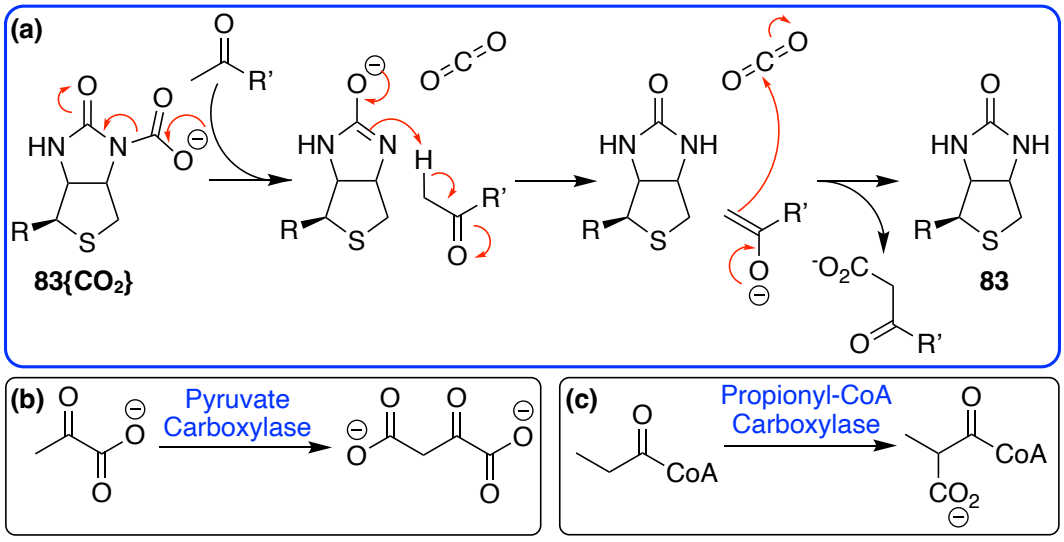

Figure 3.1.13. (a) The key reaction of biotin (**83**) in biotin-dependent enzymes; (b)-(c) native biotin dependent enzymes include pyruvate and propionyl carboxylases.

Despite the transfer of carbon dioxide being a useful transformation within synthetic chemistry, to our knowledge there are no organocatalytic or biocatalytic carboxylation applications of biotin (**83**) or biotin mimics. Instead, organocatalysis has taken advantage of the very tight binding within biotin-streptavidin complexes to introduce enzyme-like control on the outcomes of organocatalytic reactions. Unlike the covalently linked biotin-carboxylase enzymes, the biotin-streptavidin complex expresses a high affinity for the ureido-moiety. This leaves the valerate sidechain available for further chemical modifications to insert various organocatalysts (Figure 3.1.14). A range of transformations have been explored including iminium ion catalysis in the reaction of cinnamaldehyde with nitromethane,[144] enamine-catalysed aldol reactions,[145] anion-π catalysis[146] and organocatalytic transfer hydrogenations.[147] In providing a supramolecular streptavidin host, with inherent asymmetry, transformations were carried

out with good diastereo- and enantio-selectivity; however, the selectivities do not match those observed within truly biocatalytic reactions with enzyme-cofactor complexes. This is likely due to there being no true 'active-site' in these complexes, with the catalytic centres extended on the valerate tether, slightly removed from the supramolecular binding centre.

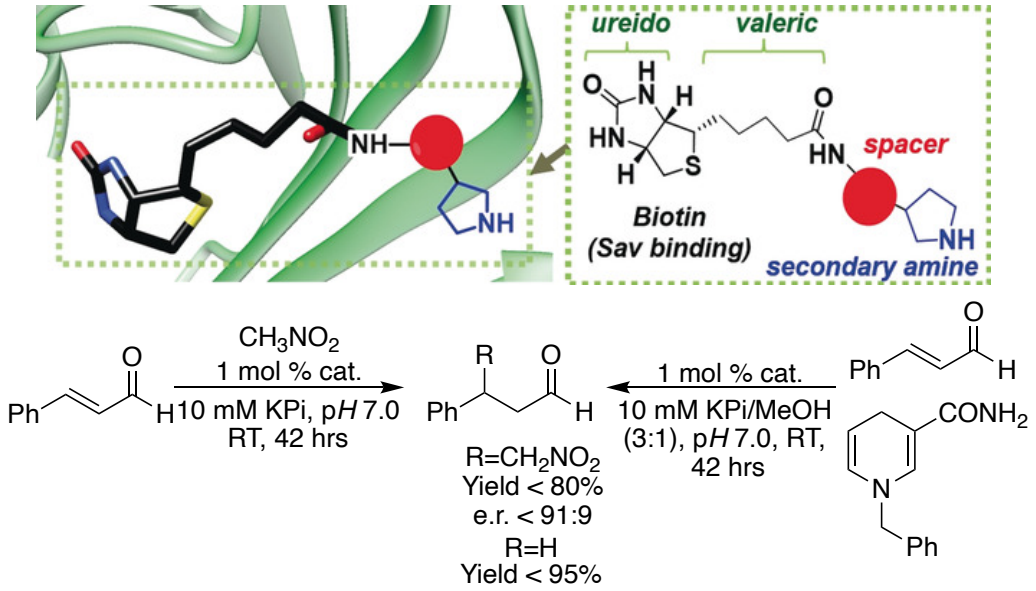

Figure 3.1.14. Biotin-streptavidin host-guest complexes with terminal secondary amine functionalisation for the 'enzyme-like' catalysis or Michael-type reactions. Reproduced from Ref. 142.

3.1.7. S-Adenosyl Methionine (SAM) (84)

SAM (**84**) is a common cofactor in all living organisms, involved in many key metabolic processes (Figure 3.1.15). Key to its function is a trivalent sulphur atom, enhancing the electrophilicity of an adjacent methyl group. Primarily, it couples with a methyl transferase enzyme to act as a methyl-donor to C, N, O and S to modify small molecule metabolites and other complex biomolecule such as lipids, proteins and nucleic acids. Mechanistically, this is thought to be via a S_N2-displacement. In the case of non-nucleophilic substrates, SAM-dependent enzymes can also catalyse radical type reactions including methylations, decarboxylations, hydroxylations and a range of cyclisations. Radical reactions require [4Fe-4S] cluster metalloenzyme systems which are beyond the scope of this review into organocatalysis.[148-150]

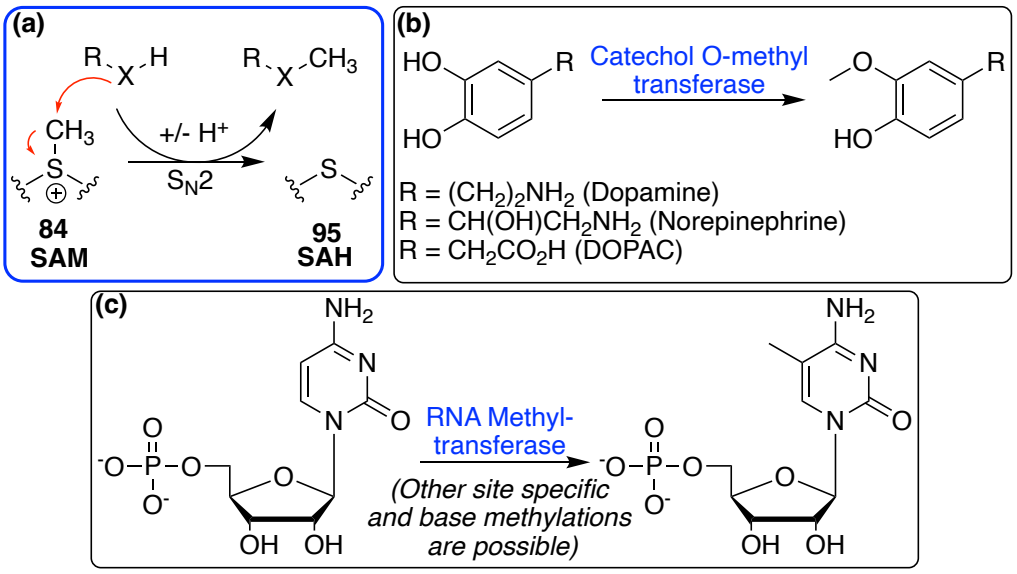

Figure 3.1.15. (a) The key reaction of SAM (**84**) in SAM-dependent enzymes; (b)-(c) native SAM-dependent enzymes include catechol O-methyl transferases and RNA-methyl transferase.

To our knowledge, there has been no exploration of SAM (**84**), or derivatives, as standalone cofactor catalysts for methyl transfer but, there has been significant exploration into biocatalytic applications. Methylation is a useful, late-stage modification used by chemists to alter the biological properties of a compound. Although, typically, methylation of heteroatoms in organic chemistry is straightforward, SAM-dependent enzymes provide the ability to readily control the stereochemistry of the methylated product, with reaction under mild conditions. A key downfall of the use of SAM (**84**) is that, as with NADH (**80{H}**), stoichiometric amounts of the cofactor are required; moreover, the chemical synthesis of SAM is complicated by the final methylation step producing a mixture of diastereomers.[151, 152] Chemoenzymatic syntheses have allowed the isolation of diasteromerically refined SAM (**84**), but it is still a complex, unstable and expensive compound. A range of recycling methods have been explored, reducing the amount of the expensive SAM (**84**) cofactor to catalytic amounts. Often these recycling methods use another enzymatic system and methyl halide as a source of methyl group. For example, a SAM-dependent methyl transferase has been used with only catalytic amounts SAM (**84**) cofactor, and has been recycled with a coupled halide methyltransferase and methyl iodide (Figure 3.1.16).[151] Despite this advantage with regards to cofactor recycling, it requires the use of methyl iodide. This counteracts a key benefit of biocatalysis in that it typically avoids the need for hazardous reagents.

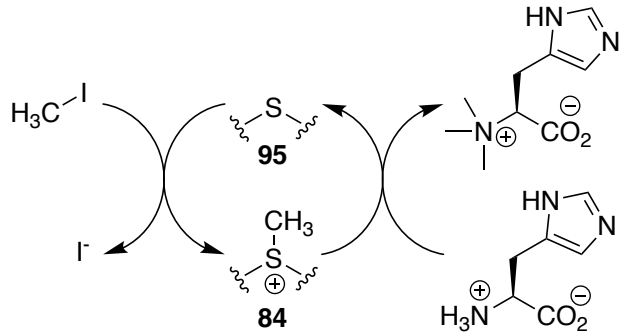

Figure 3.1.16. Biocatalytic methylation of histidine using a SAM-dependent methyl transferase with methyl iodide as the sacrificial source of methyl.

Despite a lack of SAM (**84**) biomimetic development for organocatalysis, cofactor modifications have been explored to isolate alternative products in biocatalytic transformations. In particular, SAM-modifications have focussed on the aim of isolating halo-methylated compounds, in particular fluoromethylation. Fluoromethylation, as a late-stage modification, alters biological properties to a significantly greater extent than methylation, often enhancing bioavailability. Moreover, sources of fluorine can be used as NMR/MRI probes (^{19}F) and as radiotracers (^{18}F). F-SAM (**84{F}**) can be accessed through the use of halide methyltransferases and fluoromethyl iodide. It was found that this could then add a fluoromethyl group to a range of substrates such as histidine, dimethyl glycine, 2-ketoarginine and others (Figure 3.1.17).[153]

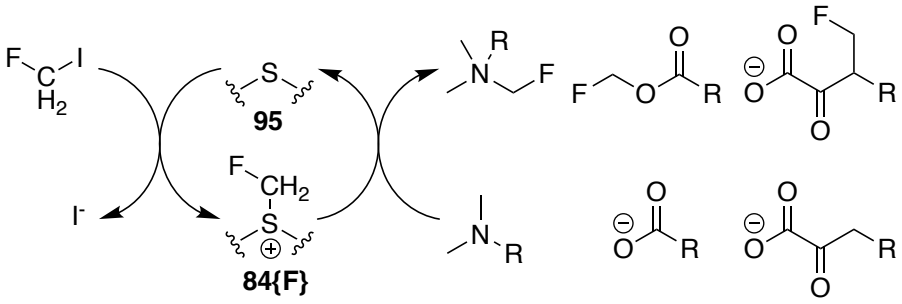

Figure 3.1.17. SAM-modifications through the use of fluoromethyl iodide as the 'methyl' source for applications in the fluoromethylation of a range of substrates.

3.1.8. Thiamine Pyrophosphate (5{PP})

Perhaps one of the most quintessential cofactors amongst chemists is thiamine pyrophosphate (**5{PP}**) owing to its pivotal role in the development of NHC organocatalysis. It is a cofactor to many carbon-carbon bond making and breaking enzymes including pyruvate decarboxylase, pyruvate oxidase, benzaldehyde lyase and benzoyl formate decarboxylase (Figure 3.1.18).[154] Although discovered in the early 1900s, the catalytic mechanism was elucidated around 50 years later, when Breslow noted

the enhanced *C*(2)-H acidity and proposed the formation of the enaminol, or Breslow, intermediate (**96**).[155, 156]

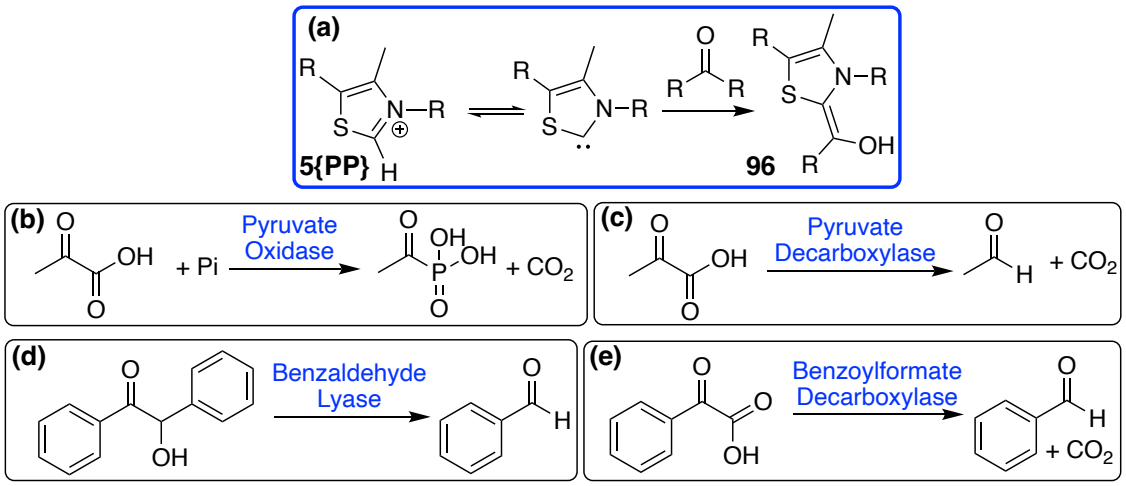

Figure 3.1.18. (a) The key reaction of thiamine pyrophosphate in TPP-dependent enzymes; (b)-(e) native TPP-dependent enzymes include pyruvate oxidase, pyruvate decarboxylase, benzaldehyde lyase and benzoylformate decarboxylase.

Subsequent screening of a vast array of similar catalysts, primarily in benzoin and Stetter model reactions, found that of the N-heterocycles explored, 1,2,4-triazoliums were the most active and selective (Figure 3.1.19).[4, 6, 8, 9, 64, 157-165] The higher reactivity was attributed to the enhanced C(3)-H acidity of both the pre-catalyst and the subsequent adduct. The added propensity for functionalisation just one atom removed from the reactive centre is also attractive as it allows for greater asymmetric control. Finally, the higher activity provides effective catalysis of more complex chemistry such as the hydroacylation of unactivated alkenes. Importantly, this chemistry is significantly more challenging via thiazolium catalysed routes.

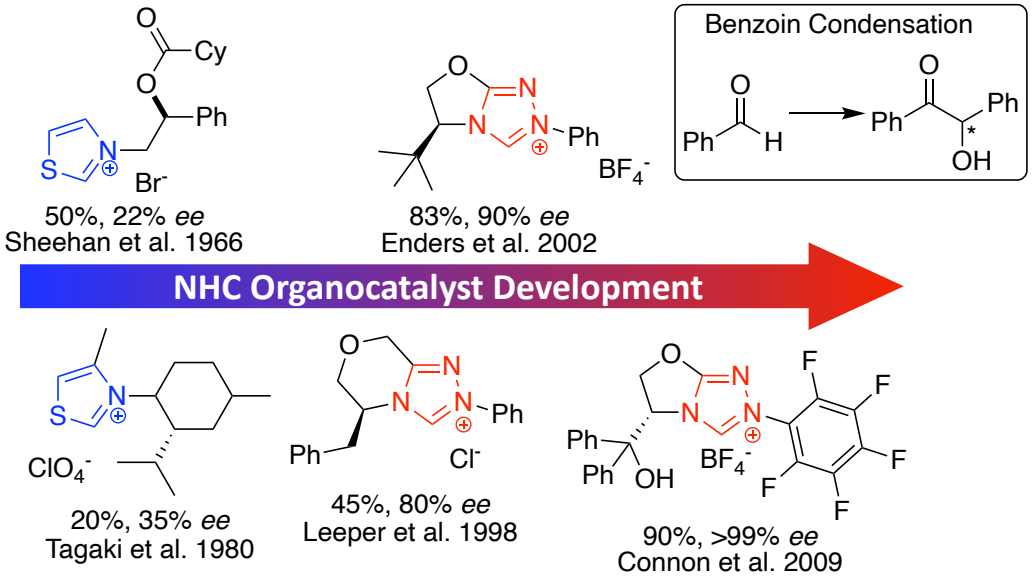

Figure 3.1.19. Development of NHC-organocatalysts, starting from thiazoliums and moving towards the more catalytically active 1,2,4-triazoliums. Yields and *ee*s refer to catalysis of the benzoin condensation (inset).

Interestingly, enzymatic model benzoin and Stetter reactions have also been explored, using thiamine pyrophosphate (**5{PP}**) as the carbenic catalyst (Figure 3.1.20). Impressively, although expected for enzymatic reactions, very high enantiomeric excesses and product selectivities could be achieved in absence of stereo-directing groups within the thiazolium cofactor/organocatalyst. This is due to the intrinsic selectivity of the enzyme active site, where intermediates and transition states can only fit in certain orientations, directing the final stereo-outcome. In comparison, a stereo and chemoselective cross-benzoin has been challenging via traditional organocatalytic routes. Typically, these have involved using bulky chiral groups to the azolium scaffold (e.g. **7**), often with a detrimental effect on solubility. These enzymatic reactions were carried out in aqueous environments using minimal amounts of a sustainable solvent to aid solubilisation of greasy substrates. This provides the scope for classical organic reactions to be carried out in aqueous environments; however, there is a limit to substrate solubility, resulting in the need for surfactants or co-solvents for enhanced phase mixing. Although yields for the enzyme-catalysed benzoin condensations were very impressive, yields of the Stetter reactions were poor. This perhaps highlights the limits of the thiazolium core, which typically struggles to catalyse such reactions. Within organocatalysis, 1,2,4-triazoliums more successfully catalyse such reactions and it remains to be seen whether such advances can be applied to biocatalytic transformations.

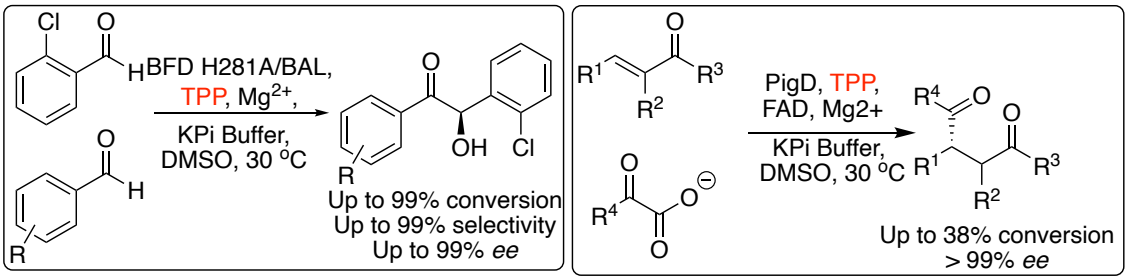

Figure 3.1.20. Biocatalytic applications of TPP-dependent enzymes: (a) The highly selective crossed benzoin condensation catalysed by benzoyl formate decarboxylase and benzaldehyde lyase; (b) The biocatalytic Stetter reaction catalysed by PigD shows high selectivity but poor yields.

3.1.9. Quinone-Like Cofactors (85)

There are several quinone-based cofactors including menaquinone, orthoquinones, topaquinone, pyrroloquinoline quinone (PQQ), and ubiquinone. So far, it is PQQ and orthoquinones which have received the most attention. Their native reactions involve the transfer of electrons, similar to nicotinamide (**80**) and flavin (**81**) cofactors and so far they have mainly been identified in bacteria. PQQ is a highly multifunctional cofactor, bound to an enzyme by electrostatics, and has been found to show excellent REDOX cycling.

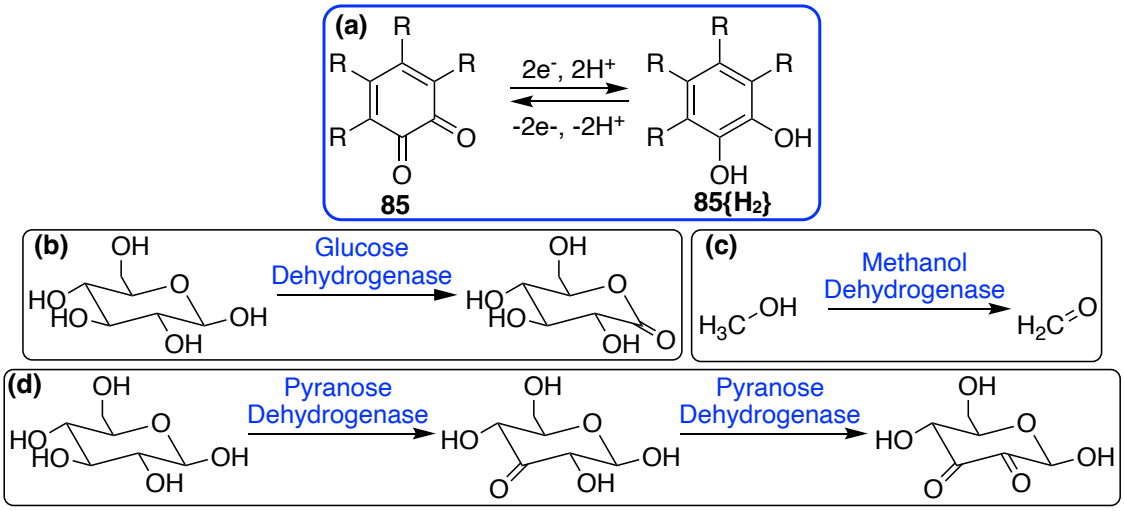

Figure 3.1.21. (a) The key reaction of quinones in quinone-dependent enzymes; (b)-(d) native PQQ-dependent enzymes include glucose, methanol and pyranose dehydrogenases.

In organocatalysis, a range of more basic quinone-based catalysts (**84a-c**) have been explored in transformations such as the aerobic C-H oxidation of amines to isolate imines (Figure 3.1.22). Here, the quinone organocatalyst activates a proton adjacent to the amine. Proposed mechanisms are either via a covalent or non-covalent direct hydrogen abstraction process. Interestingly, through the design of this new catalyst, a more complex range of branched imines was accessible in comparison to nature.[166] This highlights the benefits of organocatalysis in organic synthesis and the potential benefits of a synergistic approach to biocatalysis.

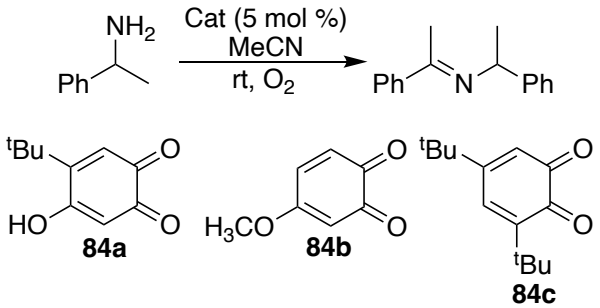

Figure 3.1.22. Quinone-organocatalysed aerobic C-H oxidations of amines to isolate imines.

To the best of our knowledge, there has been no exploration of quinone-dependent enzymes in biocatalytic transformations or of the above developed organocatalysts as non-native cofactors. This is likely due to more focus being paid to the quintessential REDOX enzymes of NADH/FADH dependent processes. However, this area is ripe for future exploitation to harness and tailor biological processes towards the needs of chemical processes. Previous reviews of PQQ-dependent enzymes have highlighted their potential applications in biocatalysis.[167]

3.1.10. Critical Analysis

This review highlights some of the excellent advances in the areas of organocatalysis and biocatalysis, and the benefits of a synergistic approach to these areas. The potentials of combining these fields to explore biocatalytic approaches to new-to-nature chemistry for more sustainable chemical processes are vast, but there are significant challenges. Traditionally, biocatalysis is limited by substrate scope, which can be poor beyond minor variations to the native substrate; however, directed evolution has allowed rapid screening and selection of desired mutations to be tackled. Enzymes work in aqueous environments, which from a sustainability viewpoint is ideal to reduce toxic solvent waste. Practically, most chemical feedstocks and subsequent products are not water soluble and so either surfactants or mixed solvent systems may be required. Managing the mixed waste streams from these processes can be more complex than managing organic solvent waste. Mixed aqueous waste streams cannot be released into the environment as they will poison watercourses and vastly reduce water-based biodiversity. Moreover, separating mixed aqueous waste-streams, for example DMSO-water mixes, is not straightforward. This provides challenges for use of aqueous solvent systems. It should also be highlighted that the stability of transition states in aqueous environments can disfavour intermolecular reactions in competition with solvation; however, the ability of enzymes to provide a cavity that is free from water, which lowers activation energies, could facilitate these reactions.

In developing non-native cofactors, novel and potentially difficult synthetic strategies are required. In comparison to utilising the native, biologically derived cofactors this is significantly more complex; however, the potential to access a broader range of biologically catalysed chemistry warrants exploration. Traditional syntheses of chiral organocatalysts are complicated and requires careful purification to isolate the enantio-resolved catalysts. In contrast, developing non-native cofactors can utilise typically more straightforward achiral synthetic strategies as the inherent chirality in enzyme active sites can provide enantioselectivity.

Despite these potential drawbacks, the significant advantages possible from exploring the areas of non-native cofactor biocatalysis warrant investigation. The potential to catalyse

complex organic chemistry under mild conditions could both reduce reliance on harmful organic solvents and reduce energy requirements in these processes.

3.1.11. Conclusions

Biocatalysis has emerged as a key solution in the drive to develop more sustainable processes within the chemical industry. Moreover, organocatalysis with inspiration from enzymes has grown from strength to strength in recent years with a more recent focus on catalysis in sustainable solvent media. This review has highlighted the entwinned developments within biocatalysis and organocatalysis. For a sustainable (bio)chemical future there is no 'one size fits all' answer and we need diverse catalytic solutions. Building on the extensive knowledge gained in organocatalysis and protein engineering over the last few decades, opportunities are presented for novel catalysis combining knowledge from both areas.

3.2. Synthesis and Phosphorylation of 1,2,4-Triazolium Mimics of Thiamine Pyrophosphate

3.2.1. Foreword

This section discusses the synthesis of a 1,2,4-triazolium mimic (**26{PP}**) of thiamine pyrophosphate (**5{PP}**). Previous work by Kevin Maduka developed a synthetic strategy to the non-pyrophosphorylated mimic. Here, improvements to the synthesis and extension to phosphorylation are reported. Phosphate chemistry is challenging owing to the water sensitive nature of phosphorylating reagents, the challenging purification of the highly charged compounds produced and challenges with solubility in organic solvents. Pyrophosphate groups attached to the ethylene linker of thiamine (**5**) and the planned 1,2,4-triazolium mimic (**26**) are thought to be essential to binding within enzyme active sites. Previous studies on thiamine mimics as co-factor inhibitors have shown that binding only occurs when a pyrophosphate is present, and that pyrophosphate equivalents such as methylene diphosphonate do not bind to TPP-dependent enzymes.[168] Therefore, for the development of a co-factor mimic for catalytic benefit, pyrophosphorylation is essential. This chapter highlights the challenges of inserting a pyrophosphate group and techniques for purification of the target compounds.

3.2.2. Introduction

The Discovery of Thiamine (5)

NHC organocatalysis has its origins in biology, in particular thiamine (**5**) and TPP (**5{PP}**)-dependent enzymes. The discovery of thiamine can be traced to the late 19th and early 20th centuries, where scientists were attempting to tackle and discover the source of a disease known as 'beriberi' in East Asia. Key symptoms included polyneuritis and oedema with the condition eventually weakening the heart and leading to death. In particular, the condition affected men, pregnant women and their infants, rarely affecting higher income populations or the poorest of society.[169] Observations on diet showed that those eating washed rice would likely succumb to this disease however those eating unwashed rice would not. It was therefore proposed that the disease was caused by a deficiency, later attributed to a lack of vitamin B1 (or thiamine (**5**)).[169]

The structure of thiamine (**5**) took longer to determine but, in 1926, crystals were finally obtained and by 1933 the empirical formula of a salt had been assigned as $C_{12}H_{16}N_4OS.2(HCl)$. All that remained was to determine the structure and credit for this goes to Robert R. Williams (1886-1965). Williams used sodium sulphite to split thiamine into two, easily identifiable parts – a thiazolium and a pyrimidine, with a methylene bridge between the *C*(3) of the pyrimidine and *N*(3) of the thiazolium (Figure 3.2.1).[170] Moreover, after collaboration with Merck, in 1936 he was able to publish a synthesis of thiamine, eventually leading to the development of a supplement for treatment of 'beriberi'.[169]

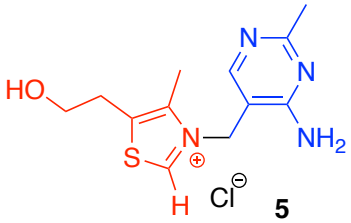

Figure 3.2.1: The elucidated structure of thiamine (**5**) (aka vitamin B1) with the thiazolium ring (red) connected to a pyrimidine (blue) via a methylene bridge.

The Chemical Synthesis of Thiamine (5)

A synthetic route to thiamine (**5**) starting from ethyl 3-ethoxypropionate (**97**), an inexpensive, commercially available ester is highlighted in Scheme 3.2.1. Reaction with ethyl formate, acetamidine, $POCl_3$ and ammonia generate the pyrimidine ring, via intermediates **98**-**102**. Following this, reaction with 4-methyl-5-*β*-hydroxyethyl thiazole (**103**) yielded the target thiamine (**5**) as the bromide salt, which was readily converted to the chloride salt.[171] Interestingly, proof of synthesis also included the fact that it was "*identical with the natural in composition… and antineuritic potency'*.[6]

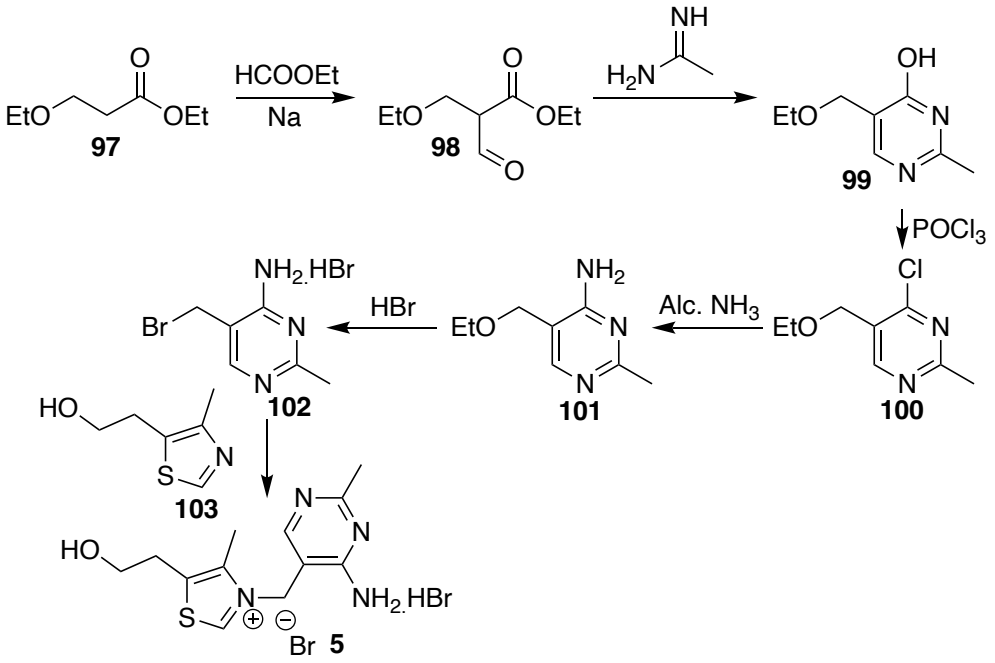

Scheme 3.2.1. The first chemical synthesis of thiamine (**5**).

The Biosynthesis of Thiamine (5)

Although humans must obtain thiamine from their diets, many single molecular organisms have developed biosynthetic pathways. The biosynthetic pathway in *Bacillus subtilis* (Scheme 3.2.2) is well characterised and representative of the majority of pathways and will be discussed herein.[96]

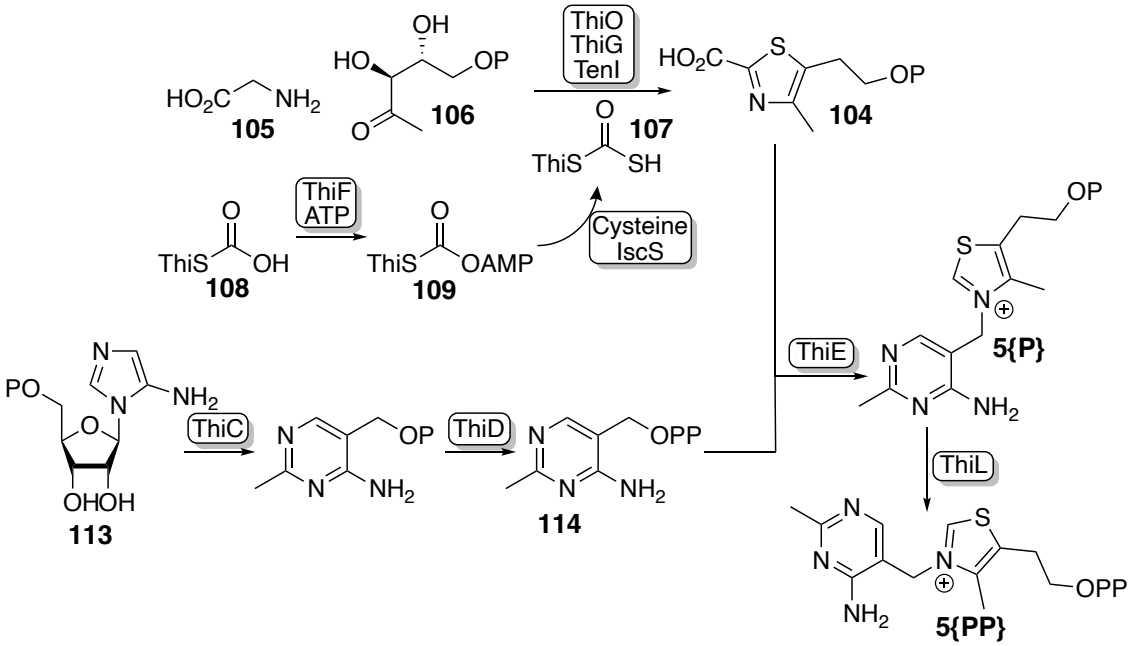

Scheme 3.2.2: The biosynthesis of thiamine pyrophosphate in *B. subtilis*.

With regards to formation of the thiazole (**104**), oxidative condensation of glycine (**105**), deoxy-D-xylulose-5-phosphate (**106**) and a sulphide carrier protein with a thiocarboxylate

at its *C*-terminus (**107**) is used. Compound **107** is formed by adenylation of the terminal carboxylate (**108** to **109**) catalysed by ThiF. The thiocarboxylate is installed by reaction of the adenylated-terminal acyl (**109**) with IscS persulphide forming a mixed disulphide, which is reduced to **107**. The current mechanistic hypothesis for this conversion is shown in Scheme 3.2.3, with initial imine formation with lysine 96 of ThiG (**110**), followed by tautomerisation to **111**. Addition of ThiSCOSH (**107**) and an O/S acyl shift follow this before loss of water to afford **112**. Addition of the gloxyl-imine (**105**) and resultant cyclisation yields the target thiazole (**104**).[96]

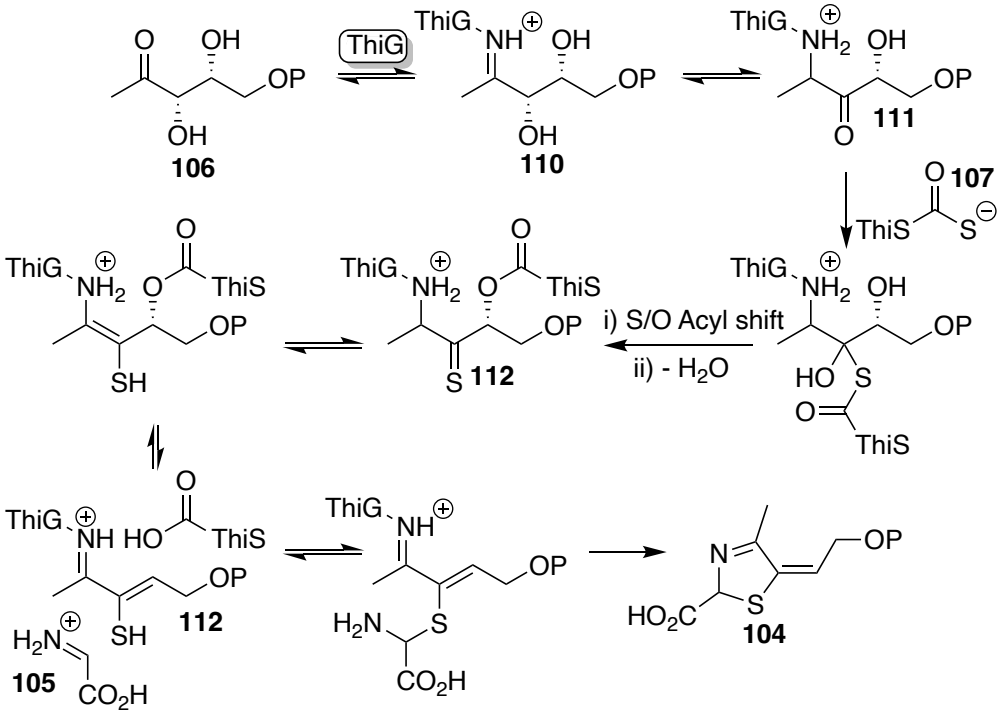

Scheme 3.2.3: Proposed mechanism for thiazole (**104**) formation in *B. subtilis*.

Formation of the pyrimidine moiety of thiamine involves the unusual rearrangement of aminoimidazole ribotide (**113**) or AIR. This curious conversion has only been observed in the biosynthesis of thiamine and so far remains mechanistically unresolved.[172] The final combination of a pyrimidine (**114**) and thiazole (**104**) is one which is, from a synthetic chemist's standpoint, particularly challenging. As with many biosynthetic pathways, this obstacle is overcome by the utilisation of enzymatic processes, in this case thiamine phosphate synthase. As seen in Scheme 3.2.4, the reaction proceeds via a dissociative mechanism, forming the pyrimidinium carbocation, which is stabilised by the *ortho*-aniline substituent. Mechanistically, this conclusion was reinforced by a positional isotope effect and a large decrease in rate upon substitution of the methyl group for carbocation destabilising groups.[173] Interestingly, within the enzyme active site it has been reported that an intermediate structure in which the carbocation is trapped between

the pyrophosphate leaving group and incumbent thiazole has been reported.[174] This structure appears more like a S_N2 mechanism; however, enzyme dynamics are more complex than this and the isolation of a true carbocation would instead signify a dissociative mechanism in which leaving group and nucleophile are in close proximity to the reactive centre.

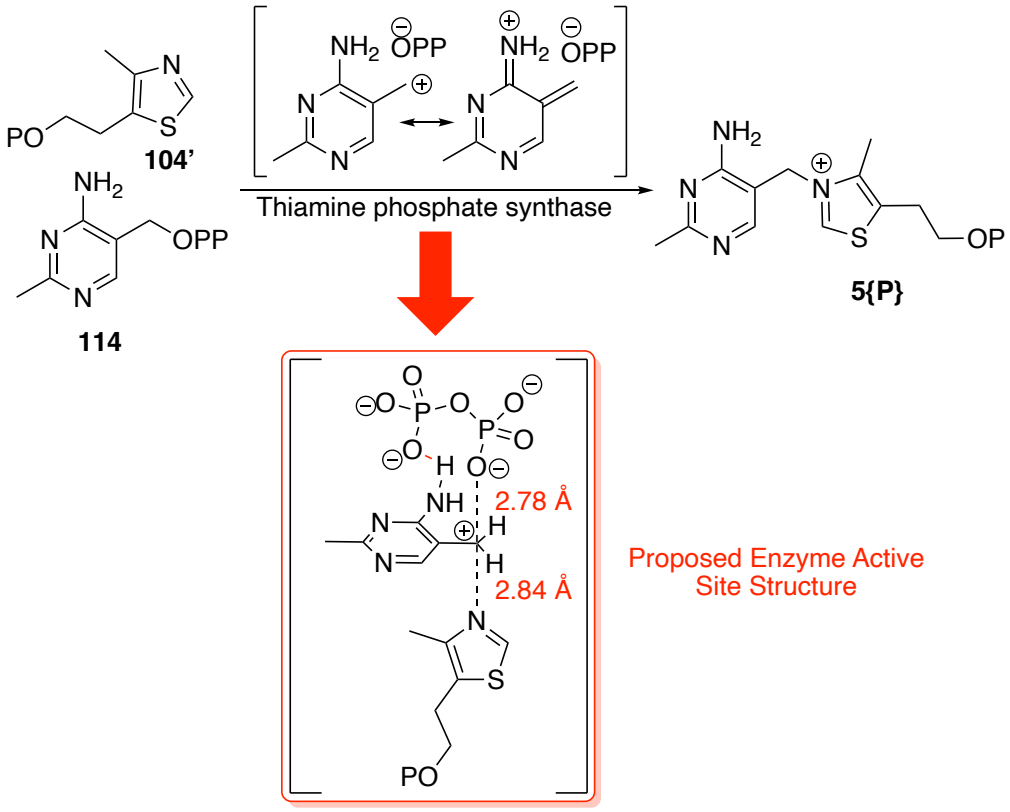

Scheme 3.2.4: Final biosynthetic pathway combining the thiazole with the pyrimidine, via an S_N1-type process. Also shown is the proposed transition-state structure.

TPP-Dependent Enzymes and Non-Native Cofactors

There has been limited exploration of the synthesis of TPP mimics and their enzymatic binding. In particular, there has been no investigation into the design and application of TPP mimics for catalytic benefit. The first reported mimics were explored as mechanistic probes in the thiamine synthase enzyme to show a dissociative-type process for reaction of the precursor pyrimidine and thiazole.[173] Other TPP mimics have explored alterations to both the pyrimidine ring and the thiazolium centre (Figure 3.2.2). It was shown that alterations on the pyrimidine ring could vastly alter enzyme binding and that the N(1) position was involved in active site binding. This hydrogen bonding interaction is thought to increase the basicity of the pyrimidine-amino group enabling it to act as a better proton acceptor for the C(2)-H thiazolium position. The proton acceptor role of this amino group

was further evidenced by the loss of catalytic activity upon replacement with a thiol, hydroxyl or dimethylamino group.[168]

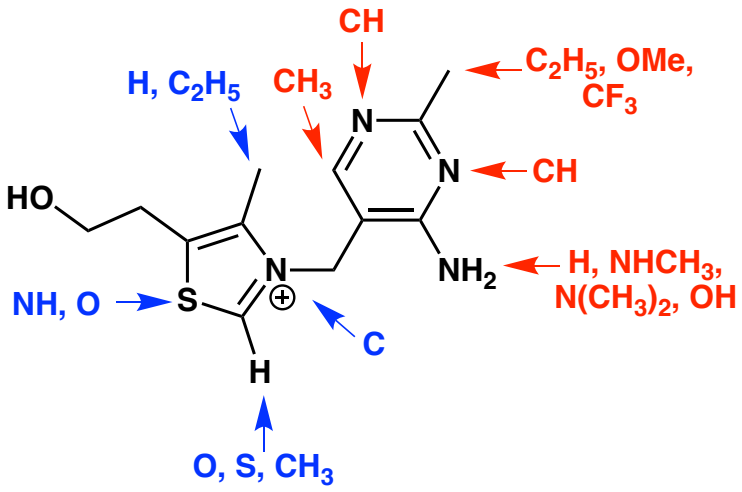

Figure 3.2.2. A summary of some of the modifications explored of thiamine for investigations into both mechanisms of and binding to TPP-dependent enzymes.

Thiazolium-site modifications have also been explored, typically resulting in tight-binding TPP-dependent enzyme inhibitors. For example, 3-deazathiamine diphosphate (**115**) was found to be an essentially irreversible inhibitor of pyruvate decarboxylase from *Zymomonas mobilis*, binding ~25000 times more tightly that native TPP (**5{PP}**). This neutral cofactor is almost a like-for-like TPP (**5{PP}**) replica; however, the lack of a cationic nitrogen vastly decreases the C(2)-H acidity to that of a typical C-H bond (pK_a ~ 40) and so eliminates the catalytic activity. It was typically found that all neutral analogues of thiamine, including 1,2,3-triazole-type mimics (**116**), were very strong binding inhibitors.[168, 175, 176] This can perhaps be linked to tighter phosphate binding to the magnesium ion due to loss of cation-cation electrostatic repulsion.

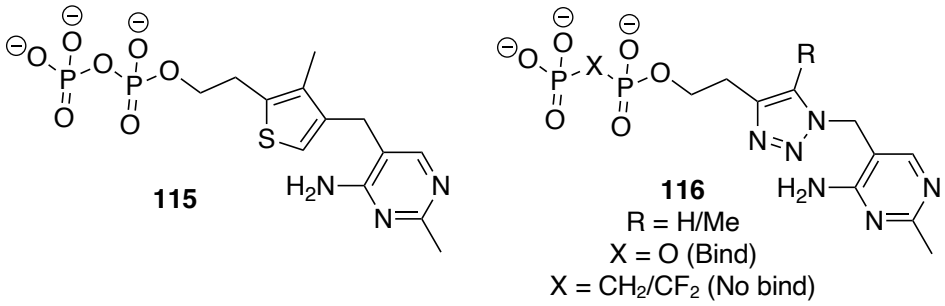

Figure 3.2.3. Thiamine mimics developed as cofactor inhibitors for TPP-dependent enzymes. Phosphates were found to be essential for binding and changing X to CF_2 and CH_2 prevented binding.

Phosphorylation Techniques

Phosphorylation is an important technology in many areas of biological chemistry, in particular the insertion of pyro- or polyphosphates. Phosphate groups are highly prevalent in biological systems including metabolic processes (ATP, TPP), genetic storage (DNA, RNA) and cell compartmentalisation (phospholipids).[177] In biology, phosphorylation is achieved via phosphorylase enzymes such as polynucleotide phosphorylase, which can degrade RNA using inorganic phosphate or synthesise RNA from nucleoside diphosphates.[178] Chemical phosphorylation methods are significantly more challenging and remain an under developed area of chemistry. Most of the techniques have been developed for nucleotide chemistry, but are transferrable to other areas, including this project. For the proposed thiamine mimic (**26**) to bind to an enzyme active site pyrophosphorylation is thought to be essential. Thiamine pyrophosphate (**5{PP}**) binds to enzymes via an electrostatic interaction between the pyrophosphate and a bound magnesium ion (Figure 3.2.4).

Figure 3.2.4. Snapshot of the crystal structure of benzaldehyde lyase from *Pseudomonas fluorescens* highlighting the bound thiamine (**5{PP}**) via electrostatic interactions to a magnesium ion highlighted in red. Structure manipulated from the protein databank, structure number 2AG1.[179]

Chemical pyrophosphorylation is typically achieved in one of two ways: direct installation of a pyrophosphate via a nucleophilic displacement of a terminal alcohol or modular addition of phosphate groups to a terminal alcohol. Pyrophosphate groups can be installed by reaction of tris(tetra-N-butylammonium) hydrogen pyrophosphate (**117**) with tosylated terminal alcohol groups. Here the pyrophosphate group acts as a nucleophile and substitutes the tosylated alcohol (Scheme 3.2.5), whilst the hydrophobic tetraalkylammonium groups aid solubility of the pyrophosphate in organic solvents.[180, 181] This methodology was used to synthesise a range of TPP-dependent enzyme inhibitors

with similar structures to thiamine (Figure 3.2.2; Figure 3.2.3).[168, 175, 176] Typically the yields of these reactions are very low owing to decomposition of the starting reagent and also poor nucleophilicity. The key challenges of this strategy are the water sensitive nature of the chemistry alongside the inherent hygroscopicity of alkylammonium salt. These reagents are synthesised by passing a solution of disodium dihydrogen pyrophosphate through a cation exchange resin (in its protonated form) followed by titration of the acidic eluent with tetra-*n*-butylammonium hydroxide. It is important to maintain a 3:1 ratio of ammonium to pyrophosphate as this retains the nucleophilicity of the trianion.[180, 182]

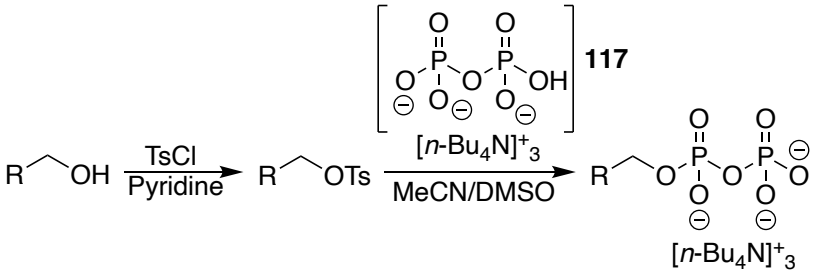

Scheme 3.2.5. Synthesis of pyrophosphates by activating terminal alcohols towards substitution reactions by tosylation, followed by reaction with hydrophobic ammonium pyrophosphate salts (**117**).[180, 182]

Another approach to the synthesis of pyrophosphates is a sequential addition of phosphate. In this case, the terminal alcohol behaves as a nucleophile, first attacking a monophosphate with a good leaving group. Subsequent reaction with another phosphate source can install pyrophosphate bonds and be further used to synthesise triphosphates. Initial phosphate sources include species such as phosphorus oxychloride (**118**) and subsequent reaction could use phosphorus(III) species such as a phosphoramidite (**119**) in a phosphitylation reaction (Scheme 3.2.6).[181, 183] In this reaction, the fluorenylmethyl-protected phosphoramidite (**119**) undergoes a nucleophilic displacement with the monophosphate oxygen, with the aid of a tetrazole (**120**) reagent. Subsequent oxidation yields the protected diphosphate followed by deprotection to the desired pyrophosphate species.[183] This approach is explored in more detail later in this chapter.

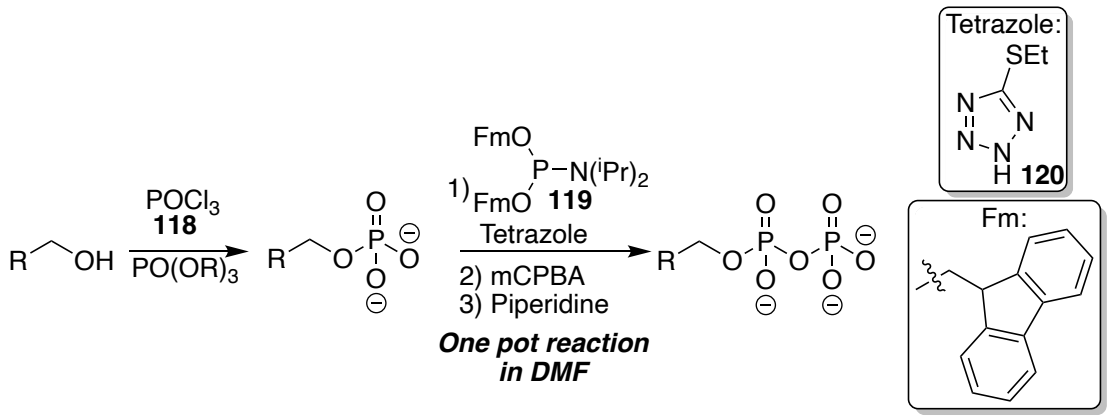

Scheme 3.2.6. Iterative synthesis of a pyrophosphate by initial reaction with a phosphate source such as phosphorus oxychloride and subsequent phosphitylation and oxidation to add a second phosphoryl group.[181, 183]

3.2.3. Further developments in the synthesis of thiamine mimics (pre-phosphorylation)

Previous work by Kevin Maduka developed a new, modular synthetic strategy to 1,2,4-triazoliums and isolated the first catalytically relevant mimic of thiamine (Scheme 3.2.7). Typically, 1,2,4-triazoliums are synthesised from corresponding amides via activation of the carbonyl towards nucleophilic substitution and isolation of an amidrazone (**21**), as highlighted in Chapter 1 (Scheme 1.3.2). Subsequent ring closure yields the desired 1,2,4-triazolium. Owing to the complexity of the 1,2,4-triazolium substitution pattern in this case, this approach was not possible. Instead, starting from commercially available methyl 3-hydroxypropanoate (**121**), derived from a 4-membered lactone, the hydrazide (**122**) is formed. Inserting the pyrimidine ring is particularly challenging and efforts to synthesise this via a range of methods were not successful. Instead, making use of the inherently weak methylene linker, sacrificial thiamine (**5**) and catalytic sodium sulphite were used. Interestingly, the initial structure determination of thiamine used equimolar sodium sulphite to cleave this bond, leaving a thiazole (**104'**) and pyrimidine (**114'**) which were structurally resolved using elemental analysis (Scheme 3.2.8).[169, 184, 185] After insertion of the pyrimidine moiety, treatment with methyl isothiocyanate and ring closure in mild base gave the precursor thione (**123**). Finally, oxidation with hydrogen peroxide under acidic conditions gave the desired 1,2,4-triazolium (**26**) in high purity but in low yields.

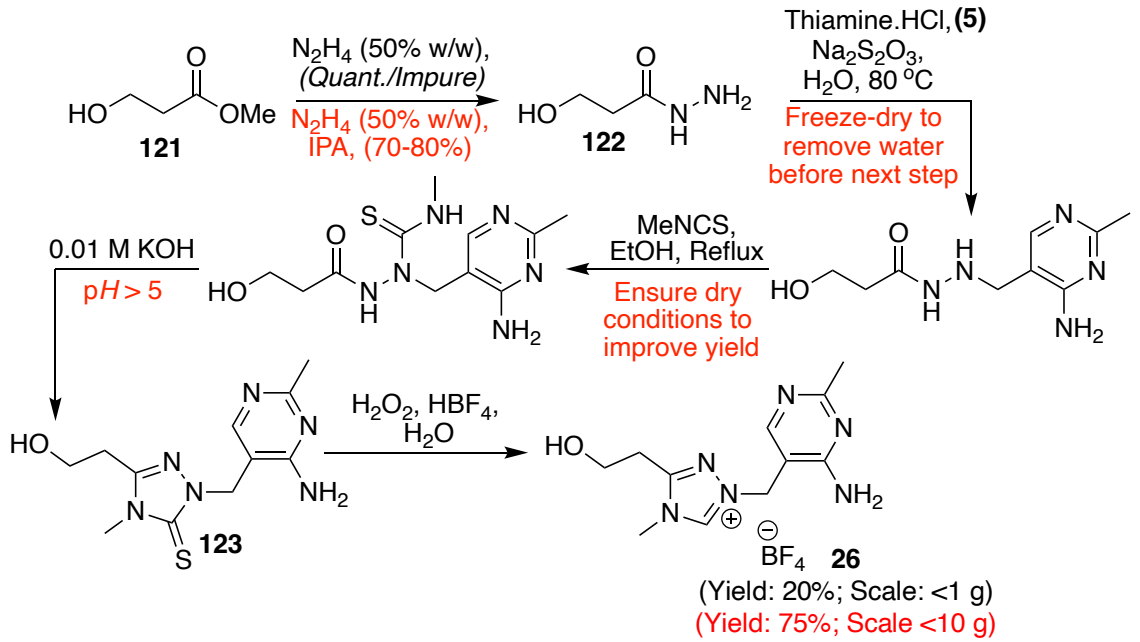

Scheme 3.2.7. Synthetic route to a 1,2,4-triazolium mimic of thiamine. Shown in red are the more recent developments to improve throughput and scalability of the synthetic procedure.

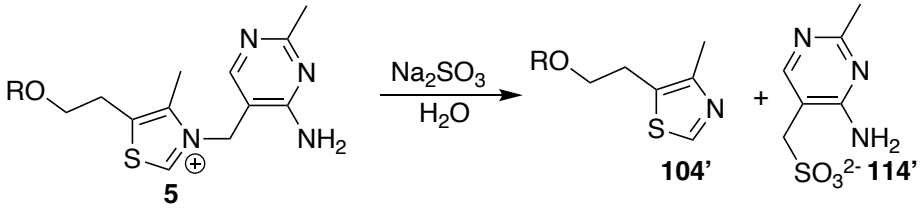

Scheme 3.2.8. Initial structural elucidation of thiamine (**5**) made use of the weak methylene linker and stoichiometric sodium sulphite to isolate two more readily characterizable fragments. Our synthetic strategy also uses this approach but with catalytic sodium sulphite to activate the methylene linker towards substitution chemistry.

In exploring subsequent phosphorylation reactions of the 1,2,4-triazolium mimic, it became obvious that throughput of the reaction needed significant enhancement. Previous attempts at increasing the scale of the reaction had led to reduction in isolated yield (~20%). To tackle the low throughput, the synthesis was revisited, particularly focussing on the exothermic hydrazide (**122**) formation. At higher scale it had been found that a double addition of the ester (**121**) to hydrazine was occurring, reducing yields and purity of the target compound. To improve the yield and control of this reaction, isopropanol was used as solvent and the reaction kept at 0-5 °C during hydrazine addition. The formed hydrazide (**122**) was insoluble in the reaction solvent and precipitated as a white solid. No residual hydrazine was trapped in the solid as was the case with the previous syntheses and this increased the yield at the next step, where trace hydrazine had proven troublesome. The thione (**123**) forming step had always appeared very low yielding. After precipitation and filtration of the thione (**123**) product, the filtrate was analysed by LC-MS and appeared to still contain significant amounts of the thione (**123**).

The p*H* of this solution was found to be less than 5, despite the reaction being carried out in 0.01 M KOH. Upon treatment with further potassium hydroxide, the thione (**123**) precipitated from the reaction in very high yields. The pyrimidine-NH_2 has an estimated conjugate-acid pK_a value of ~5 and so the solution p*H* must be above this for isolation.[186] These modifications allowed overall 1,2,4-triazolium (**26**) yields to be dramatically improved to up to 75% on scales up to 10 g.

It is anticipated that the minimum requirement for cofactor binding to an enzyme is the pyrophosphate group; however, the remaining substitution about the central triazolium could be altered. Particularly, the pyrimidine could be switched for an N-aryl group (Figure 3.2.5). In doing so, previous fundamental knowledge developed in the field of organocatalysis, such as the effect of the N-aryl group on the C(3)-H acidity and subsequent role in catalysis could be exploited. In exploring an N-phenyl mimic (**27**), the broader applicability of this new modular synthetic strategy to 1,2,4-triazoliums is also highlighted.

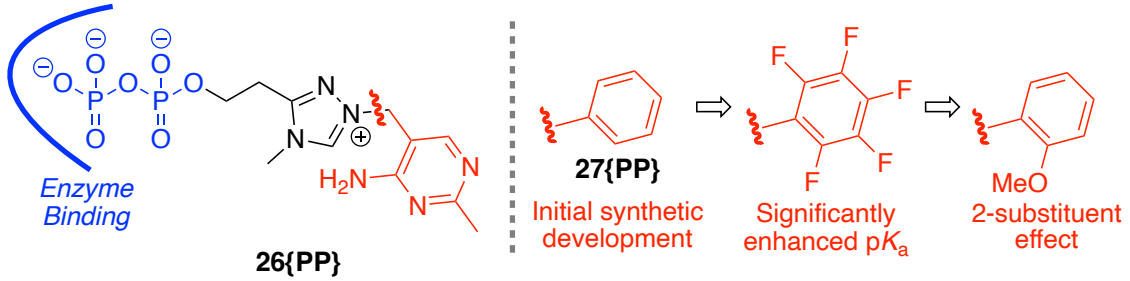

Figure 3.2.5. Potential catalyst evolution assuming that the key to enzyme binding is the pyrophosphate group. This would allow exploration of N-aryl groups to enhance reactivity.[6, 9, 157, 160]

Synthesis of N-phenyl mimics (**27**) of thiamine relied on first synthesising the respective hydrazides (**124**). Following the synthetic strategies in Scheme 3.2.7 did not prove successful due to the reduced nucleophilicity of phenyl hydrazine in comparison to hydrazine and so a range of other approaches were explored (Scheme 3.2.9). To prevent cross reactivity of the terminal alcohol, benzyl-protection was explored and it was found that the most successful technique was to use silver oxide as a Lewis acid to catalyse the benzylation reaction.[187] The use of an amide coupling reagent (HATU) and also formation of the acyl chloride were explored to activate the ester group (first hydrolysed to the carboxylic acid) towards reaction with the less reactive phenylhydrazine. Both reactions were complicated by formation of the di-substituted hydrazide (**125**), which could be avoided through a lengthy protecting procedure for the aniline-nitrogen of the

hydrazine; however, it was found that reaction in neat triethylamine yielded the desired hydrazide (**124**) in low yields and this was the approach taken forward.

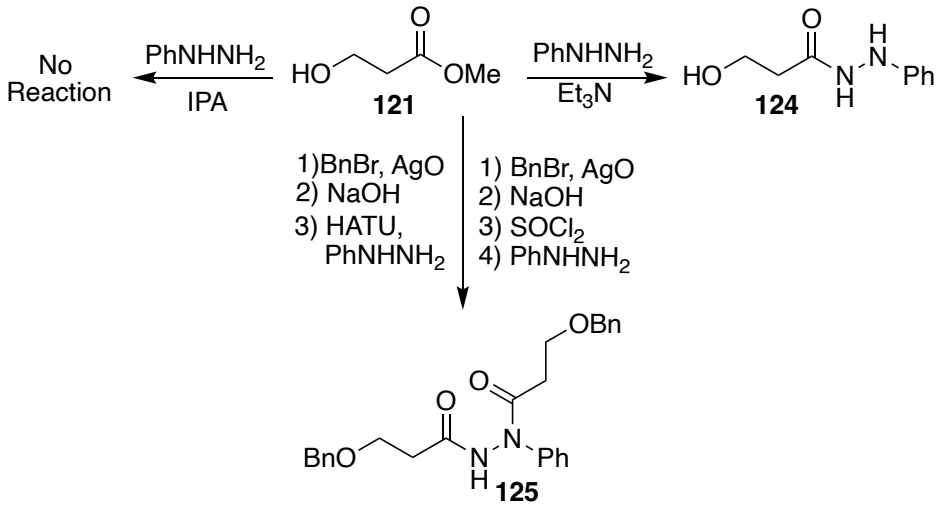

Scheme 3.2.9. Synthetic strategies explored to isolate the desired N-phenyl hydrazide for the synthesis of N-aryl thiamine mimics. Multiple approaches were explored but eventually refluxing in triethylamine was most successful.

Isolation of the corresponding thiones (**127**) was significantly more straightforward as the intermediates formed from reaction of the hydrazide with methyl isothiocyanate remained in solution and cyclised *in situ*. Purification and isolation were very straightforward via column chromatography to yield pure thiones which could be readily desulphurised to the triazolium tetrafluoroborate salts in good yields. The success of these syntheses highlights the broader applicability of this new, modular approach to the synthesis of 1,2,4-triazolium ions with pendent hydroxy-alkyl linkers.

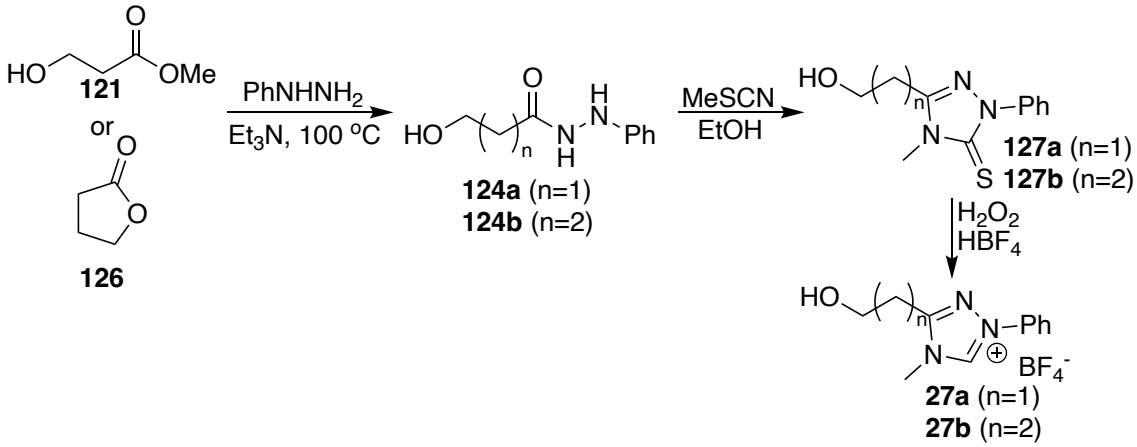

Scheme 3.2.10. Developed synthetic strategy for the synthesis of N-aryl thiamine mimics (**27**), highlighting the broader applicability of the newly developed modular 1,2,4-triazolium synthesis.

3.2.4. Phosphorylation Reactions

Direct Synthesis of the Mimic Pyrophosphate

Initial work by Kevin Maduka had attempted to pyrophosphorylate the terminal alcohol of the 1,2,4-triazolium mimic (**26**) by treatment with tosyl chloride followed by reaction with tetrabutylammonium pyrophosphate salts (**116**) as discussed above (Scheme 3.2.11). However, reaction of the 1,2,4-triazolium ion (**26**) with tosyl chloride did not proceed due to poor solubility of the 1,2,4-triazolium salt in organic solvents. Moreover, the hygroscopic nature of the 1,2,4-triazolium tetrafluoroborate salt (**26**), coupled with the hygroscopicity of the ammonium phosphate salts (**116**) would have later caused significant complications for this reaction. As such, alternative methods were explored.

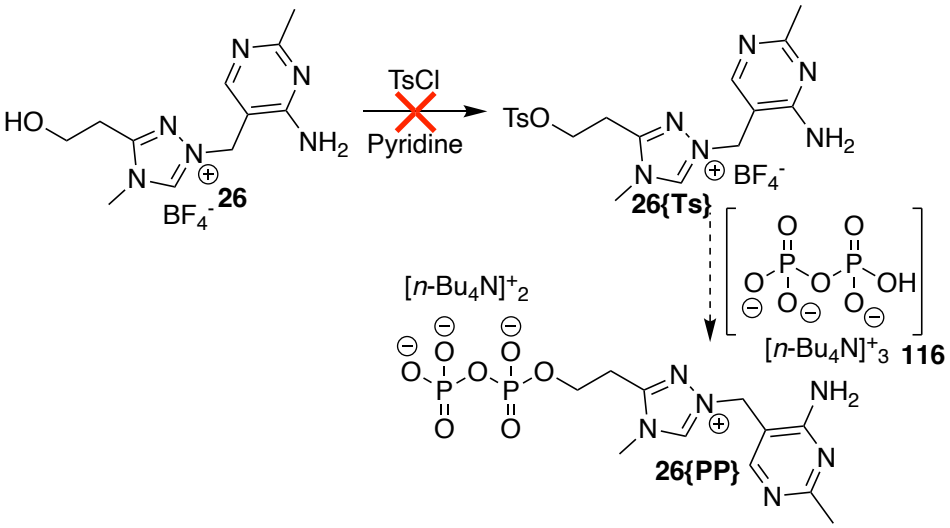

Scheme 3.2.11. Initial synthesis towards pyrophosphate **26{PP}** attempted to use a displacement approach with tetrabutylammonium pyrophosphate salts (**116**) but, it was abandoned due to difficulty with tosylation.

Following a patented procedure (WO 2016/079576 A1)[188] for the synthesis of thiamine pyrophosphate (**5{PP}**), both thiamine (**5**) and the 1,2,4-triazolium mimic (**26**) were treated with polyphosphoric acid (PPA) as highlighted in Scheme 3.2.12. Synthetically, this approach is very straightforward and takes minimal time and effort; however, polyphosphoric acid is a mixture of complex phosphates and this leads to a mixture of products. Products included the desired pyrophosphate alongside monophosphate, and polyphosphate of **26** but, also significant amounts of inorganic phosphates and polyphosphates.

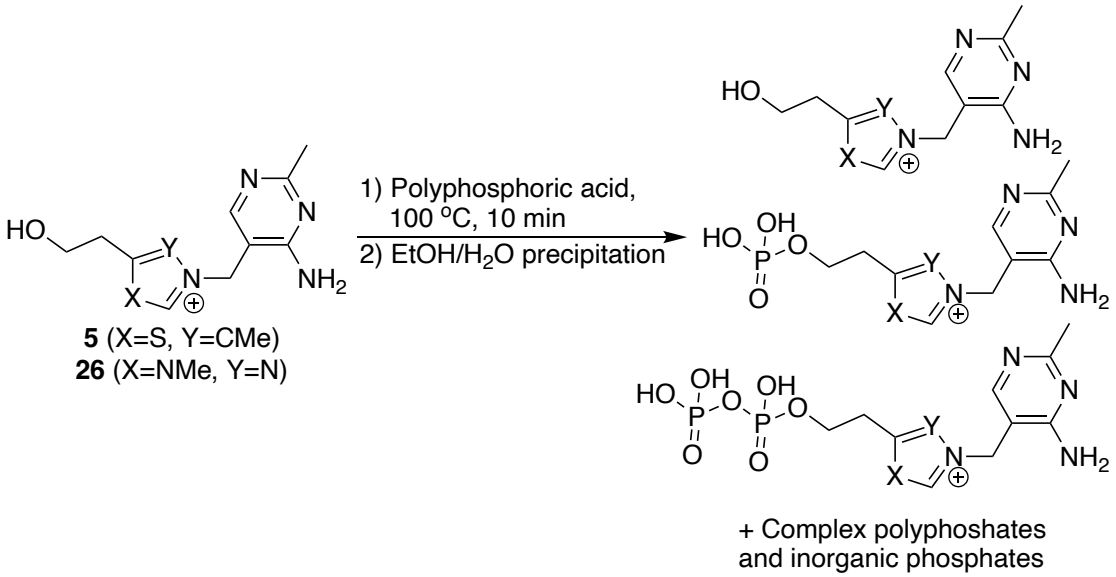

Scheme 3.2.12. Reaction of the 1,2,4-triazolium mimic (**26**) and thiamine (**5**) with polyphosphoric acid gave a complex mixture which did include the desired pyrophosphate. Unfortunately, this was in a complex mixture and was not the major product which made isolation very challenging.

Using reference samples of thiamine (**5**), thiamine monophosphate (**5{P}**) and thiamine pyrophosphate (**5{PP}**), a purification technique was developed using strong anion exchange chromatography on a CaptoQ resin with triethylammonium bicarbonate (TEAB) buffer (0-2 M gradient, p*H* 8) by Carlotta Pagli. This was successful in resolving the desired pyrophosphate (**5{PP}**) in low yields from the crude reaction material. Although scale up of the reaction was attempted, high throughput of this approach was challenging due to two key factors. The desired pyrophosphate (**5{PP}**) is not the major product and so minimal amounts are isolated; moreover, CaptoQ resin is designed for the purification of large, bulky protein molecules with anionic residues. As such, the loading capacity of this media for small anionic compounds is poor. Coupled with the very low flow rates required for the CaptoQ resin, this made the purification method exceptionally slow and poor yielding. This highlighted two key areas for improvement: a cleaner synthetic strategy was essential for isolating reasonable yields of the triazolium pyrophosphate and a purification technique with higher throughput was also needed to reduce lead time.

Sequential Phosphate Addition to the 1,2,4-Triazolium ion (26)

Monophosphates can be accessed by reaction of substrates with phosphorus(V) oxychloride ($POCl_3$) (**118**) in a solid-state, mechanochemical reaction. Starting with thiamine (**5**) as a model substrate, this reaction was slow and so achieving full conversion was very challenging owing to competing $POCl_3$ hydrolysis. Alternatively, the reaction

could be achieved under inert conditions in neat $POCl_3$ with vigorous stirring. This heterogeneous reaction proceeded over a week to high (>80 %) conversion (Scheme 3.2.13). Reaction monitoring was very straightforward owing to the formation of a well-resolved apparent quartet in the ^1H NMR spectrum in D_2O due to J-coupling to both the adjacent alkyl CH_2 and phosphorus centre (this should be a doublet of triplets or triplet of doublets but both are 3-bond coupling constants with similar magnitudes).

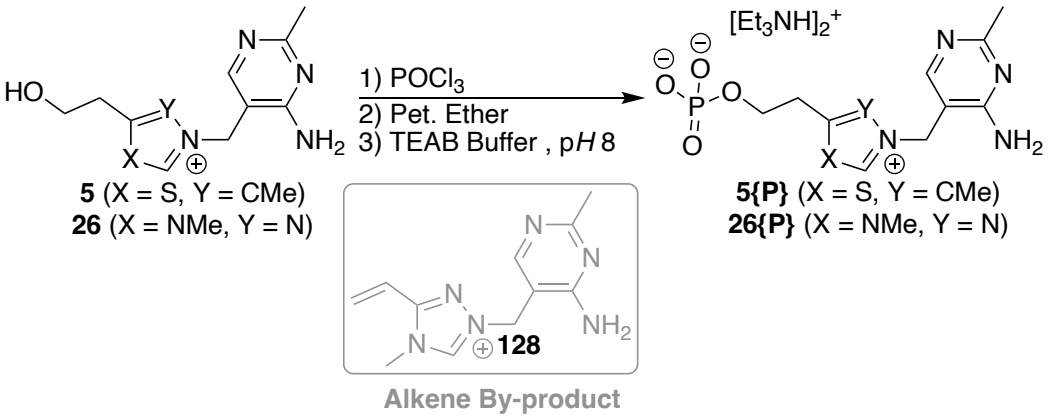

Scheme 3.2.13. Reactions of the thiamine (**5**) and 1,2,4-triazolium ion mimic (**26**) with $POCl_3$ followed by work up led to formation of the desired monophosphate alongside an alkene by-product (**128**). Purification was challenging due to lack of retention by anion exchange chromatography and significant residual inorganic phosphate being present.

Isolation of crude material was possible by treating with petroleum ether and filtering to remove the majority of the excess $POCl_3$ before quenching to p*H* 8 with TEAB buffer. Attempts with the 1,2,4-triazolium ion mimic (**26**) of thiamine were more challenging owing to the formation of an oil upon treatment with petroleum ether. This oil trapped significant residual $POCl_3$ and so upon quenching with TEAB buffer a significant exotherm occurred which led to formation of an alkene product (**128**) by phosphate elimination.

Owing to access to updated purification instruments, purification was attempted using a Teledyne Puriflash system on a weak anion exchange, amine column with the same 2 M TEAB system as previously used. Although thiamine monophosphate (**5{P}**) showed some retention via the method, allowing a certain level of purification, access to the 1,2,4-triazolium mimic monophosphate (**26{P}**) was difficult due to a lack of retention. The cationic azoliums of both thiamine (**5{P}**) and the mimic (**26{P}**) distort the overall anionic nature of the compounds, reducing retention by anion exchange chromatography. The fact that thiamine monophosphate (**5{P}**) appears to show better retention than the mimic monophosphate (**26{P}**) at the same p*H* TEAB buffer highlights a slight change in

phosphate pK_a, and therefore ionisation, with the mimic monophosphate (**26{P}**) being slightly less acidic.

Regardless of the difficulty in purification, the crude mimic monophosphate (**26{P}**) was continued into the subsequent step. Homoligation of a terminal phosphate is possible via phosphitylation. This involves initial coupling to a fluorenyl-protected phosphorus(III) reagent (**119**) to give **129** before oxidation to the phosphorus(V) centre (**130**) and deprotection to yield the pyrophosphate (**26{PP}**) (Scheme 3.2.14). Although the reaction appeared successful, significant levels of inorganic phosphate greatly outcompeted reaction with the desired mimic monophosphate.

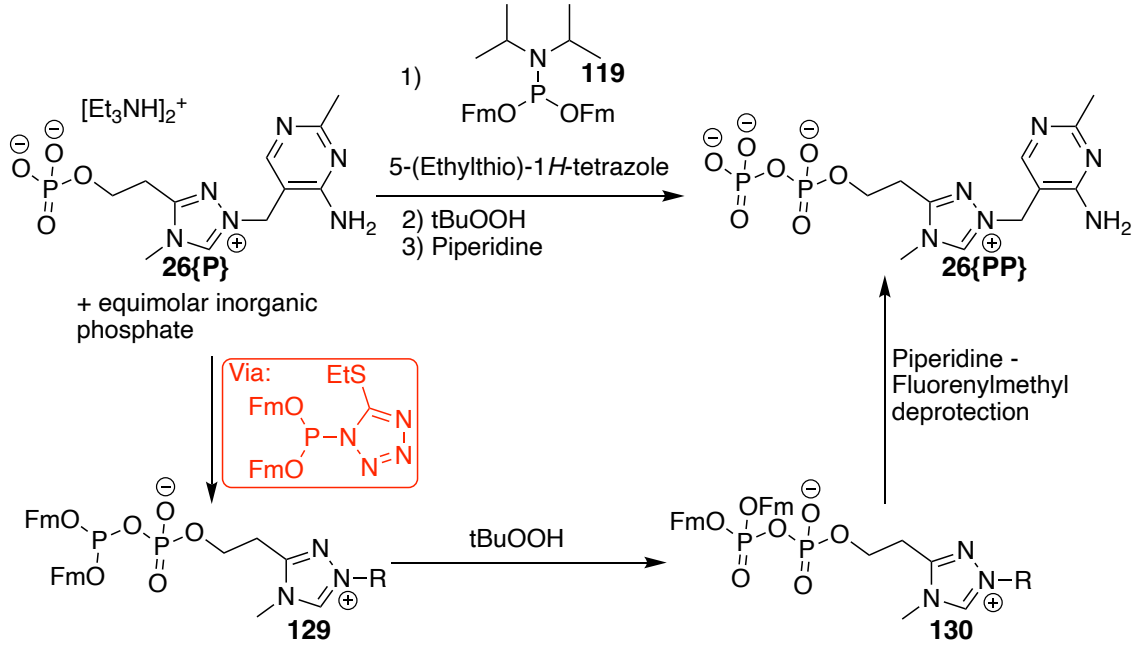

Scheme 3.2.14. Pyrophosphate synthesis by addition of a phosphoramidite reagent (**119**) to a monophosphate (**26{P}**), followed by oxidation (**130**) and deprotection (**26{PP}**). In the case of the 1,2,4-triazolium this reaction was complicated by significant levels of inorganic phosphate formation and poor solubility in the reaction solvents of DMF or DMSO.

Proceeding to the desired 1,2,4-triazolium mimic (**26{PP}**) via this approach was extensively studied; however, significant hurdles were present which were difficult to overcome. The cationic nature of the starting substrates not only hinders solubility in organic solvents, but also reduces the retention by anion exchange chromatography making purification very challenging. An alternative approach was to consider phosphorylation of the neutral precursor thione (**123**) before oxidising to the final triazolium (**26{PP}**).

Sequential Phosphate Addition to the precursor thione (123)

Following on from the synthesis of the 1,2,4-triazolium mimic monophosphate (**26{P}**), the same synthesis was attempted with the thione (**123**). The first attempt proceeded very cleanly and gave high conversion to the desired monophosphate (**123{P}**), again evidenced by formation of an apparent quartet for the C*H*$_2$O-P group. In an attempt to increase the yield of the monophosphate (**123{P}**) and decrease the reaction times, the starting material and reaction vessel were dried thoroughly before reaction. Unexpectedly, this resulted in no reaction occurring even over several days and with heating. Finally, an equivalent of water was added to one of these reactions which led to rapid reaction to form the monophosphate (**123{P}**). This highlights a key mechanistic ambiguity within this well-known reaction. To further explore this reaction, fewer equivalents of $POCl_3$ (**118**) were employed (5 rather than a significant excess) and acetonitrile was added as the solvent. Although initially insoluble as the starting thione (**123**), as phosphorylation occurred the white precipitate dissolved into solution and proceeded to > 90% conversion (Scheme 3.2.15). Importantly, it was found that in the absence of water the reaction would not proceed at all, implying that $POCl_3$ (**118**) is not the active phosphorylating reagent (Table 3.2.1).

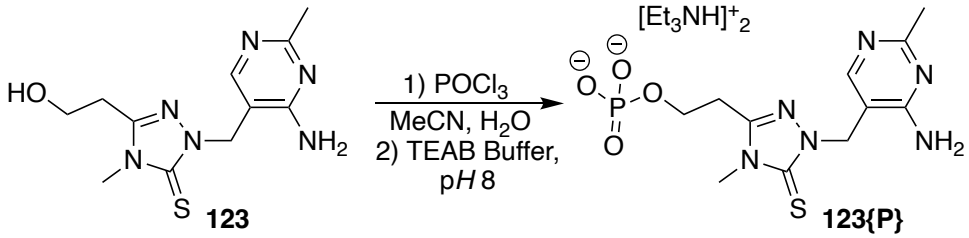

Scheme 3.2.15. Synthetic strategy to isolate a thione monophosphate (**123{P}**) using $POCl_3$. Water was found to be vital for reaction to occur.

Table 3.2.1. Iterations of the reaction of $POCl_3$ with thione showing the evolution to the conditions shown in Scheme 3.2.15.

Entry	Equivalents of $POCl_3$ (118)	Equivalents of Water	Solvent	Temperature	Outcome[a]
1	Neat	'Not dried'	$POCl_3$	RT	>90% conversion, 1 week
2	Neat	0	$POCl_3$	RT	No conversion
3	Neat	0	$POCl_3$	80 °C	No conversion
4	Neat	1	$POCl_3$	RT	>90% conversion, < 24 h
5	5	1	MeCN	RT	>90% conversion, 24 h
6	5	0.5	MeCN	RT	>90% conversion, 24 h
7	5	0.1	MeCN	RT	~30% conversion, 24 h
8	10	1	MeCN	RT	>90% conversion, 24 h
9	10	0.5	MeCN	RT	>90% conversion, 24 h
10	10	0.1	MeCN	RT	~30% conversion, 24 h
11	2	1	MeCN	RT	~30% conversion, 24 h
12	2	0.5	MeCN	RT	~30% conversion, 24 h
13	2	0.1	MeCN	RT	~30% conversion, 24 h

[a]Conversion was determined by ^{1}H NMR spectroscopy through monitoring of the CH_2O-R (R=H/PO_3) peaks.

Previous work has shown that initial hydrolysis of phosphorus(V) oxychloride (**118**) to phosphorus(V) dichloridate (**131**) is rapid ($t_{1/2}$ = 0.01 s) but that further hydrolysis to phosphorus(V) monochloridate (**132**) is much slower ($t_{1/2}$ = 250 s) (Figure 3.2.6).[189, 190] Conditions for these kinetic experiments were significantly different to the synthetic procedure: for kinetic monitoring, low concentrations of phosphorus(V) oxychloride (**118**) were used; the solvent used was water (a solvolysis) as opposed to acetonitrile used synthetically; importantly, water was in excess for these kinetic studies, resulting in an essentially first-order process, as opposed to the one equivalent used in the synthetic procedure, resulting in a bimolecular process. Nevertheless, these rates of hydrolysis give an indication as to a potential explanation for the synthetic observations. One possibility is that phosphorus(V) dichloridate (**131**) is the more active phosphorylating agent; however, the additional oxygen, which can push electron density into the phosphorus(V) centre by resonance is more likely to reduce the overall electrophilicity. An alternative

suggestion is that the longer-lived dichloridate can react with another molecule of $POCl_3$ (**118**) forming a phospho-anhydride activated species (**133**) (Figure 3.2.6). Some evidence for this comes from ^{1}H-^{31}P HMBC NMR spectra which show a small amount of a proposed anhydride (-10 – -12 ppm). This could form by sequential phosphorylations in the reaction or by competition of both the phosphate and chloride leaving group abilities in the diphosphoryl chloride species. (Figure 3.2.7). To further probe the potential mechanism of the reaction a NMR scale reaction was monitored continually by ^{31}P NMR spectroscopy over 24 h. Unfortunately, this provided no greater insight into the mechanism owing to inhomogeneity within the sample which greatly complicated both the peak shimming and the overall kinetics (considering both kinetics of reaction and solubilisation).

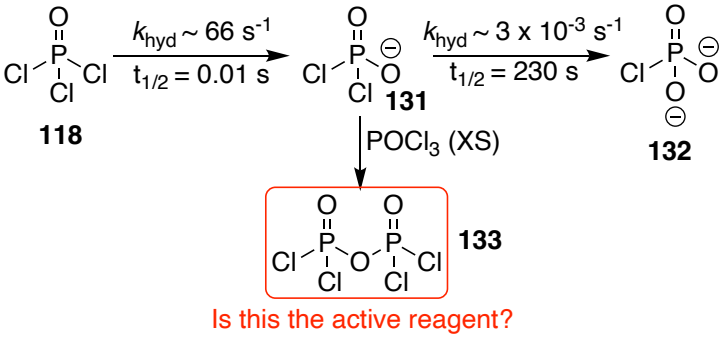

Figure 3.2.6. Hydrolysis of $POCl_3$ (**118**) to the dichloridate anion (**131**) has been determined to be rapid in the presence of excess water but, this species is longer lived and more slowly hydrolyses to the monochloridate anion (**132**). Reaction of the longer-lived dichloridate anion (**131**) with excess $POCl_3$ (**118**) could form an activated phosphoanhydride (**133**) as the active reagent in the monophosphorylation reaction.

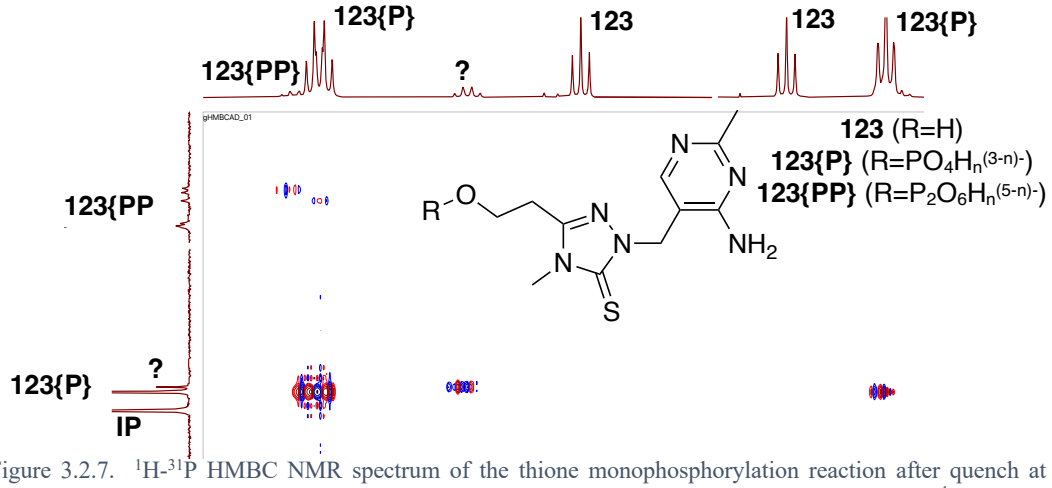

Figure 3.2.7. ^{1}H-^{31}P HMBC NMR spectrum of the thione monophosphorylation reaction after quench at ~70 % conversion. As seen significant monophosphate (**123{P}**) is formed evidenced by a quartet in the ^{1}H NMR spectrum coupling to a triplet in the $^{31}P[^{1}H]$ spectrum. Significant inorganic phosphate (**IP**) is present along with starting material (**123**). Interestingly there appears to be some formation of a pyrophosphate (**123{PP}**) species, based on appearance of second quartet in the ^{1}H NMR spectrum and a two doublets at ~ -10 ppm in the ^{31}P spectrum, which is circumstantial evidence for formation of an activated anhydride (Figure 3.2.6).

With regards to work-up and purification, reaction with the thione (**123**) provides significant advantages in comparison to the 1,2,4-triazolium mimic monophosphate (**12{P}**). Firstly, in reducing the number of equivalents of $POCl_3$ and using acetonitrile as solvent, the residual inorganic phosphate can be significantly reduced by first evaporating solvent and excess $POCl_3$ *in vacuo*. Moreover, upon quenching with TEAB buffer to p*H* 8 the residual starting thione (**123**) precipitates out of solution providing straightforward purification. Finally, owing to the lack of a cationic centre, the thione (**123**) shows significantly better retention on both weak and strong anion exchange columns. It was noted during the work up that NMR spectral features, characteristic of a terminal alkene, formed that were not present during the reaction. It is proposed that base-promoted elimination occurs upon quenching the reaction with TEAB buffer (Scheme 3.2.16). Efforts to cool the reaction to limit this did not appear to reduce the levels of alkene formed and so removal of this, along with residual inorganic phosphate, relied on further purification steps.

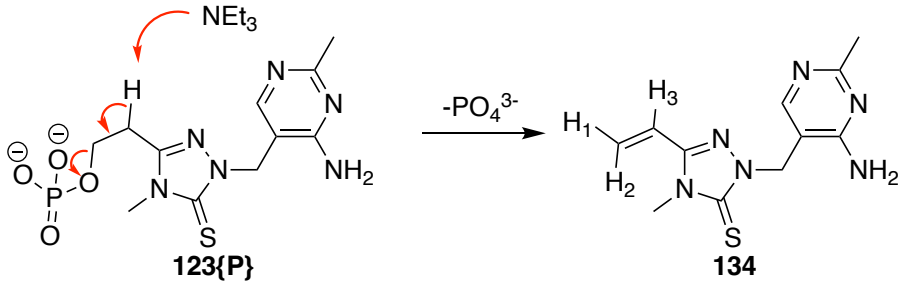

Scheme 3.2.16. TEAB buffer-promoted phosphate elimination to form the terminal alkene product (**134**) as evidenced in Figure 3.2.8.

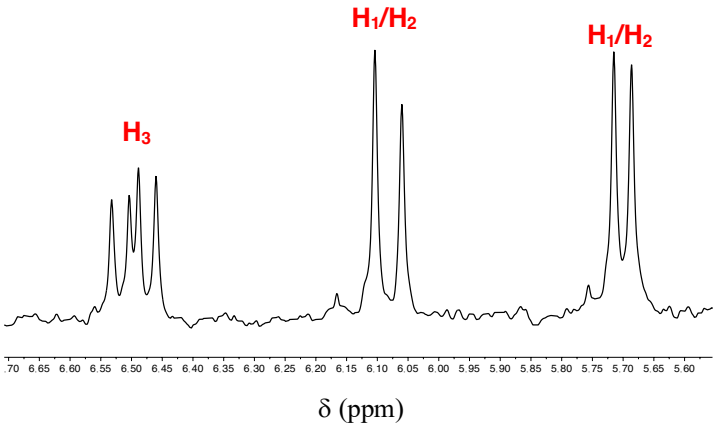

Figure 3.2.8. NMR evidence of the terminal alkene elimination product (**123**) formed upon work-up of the thione monophosphorylation (**123{P}**) reaction.

Further purification of the thione monophosphate (**123{P}**), to remove both inorganic phosphate and the elimination product (**134**) involved multiple iterations. Teledyne weak

anion exchange columns are stable at p*H* 8 allowing TEAB buffer to be used. Targeting a buffer of this p*H* should result in near-full ionisation of the monophosphate group, maximising retention by anion exchange chromatography. Moreover, this p*H* is below the point at which it was found the methylene linker rapidly cleaved (see Chapter 3.3 on stability studies). Purification with this column media was successful in retaining the monophosphate (**123{P}**) to isolate very pure thione monophosphate as the triethylammonium salt. Unfortunately, subsequent repeats highlighted a lack of reproducibility in this method suggesting that either the columns were not as stable as suggested at p*H* 8 or the buffer eluent was not a constant composition.

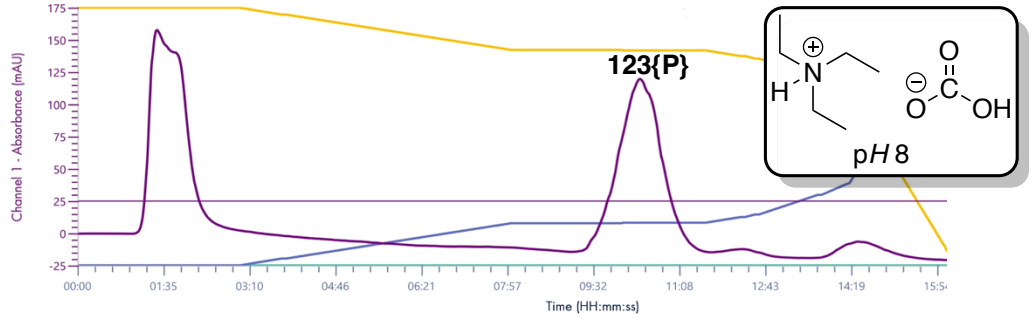

Figure 3.2.9. Elution trace (thick purple) for the weak anion exchange column (Teledyne-ISCO Redisep Rf Gold® Amine Columns) with TEAB buffer (blue line). Initially non-retained material passes through (1 m 30 s) before the retained monophosphate (**123{P}**) is eluted (9 m 30 s) at 16.4 % 1M (0.164 M) TEAB buffer. The yellow line shows the % amount of water and the thin purple line at 25 mAU is the threshold set for fraction collection. Inset shows the TEAB buffer used in this purification at p*H* 8.

To explore other available stationary phases, strong anion exchange columns from Interchim were also explored. These use a quaternary ammonium group bonded to the silica surface, which has considerably lower stability above p*H* 7. Although initially explored using p*H* 8 TEAB buffer, the reproducibility and longevity of the columns was very poor. Switching to a triethylammonium acetate (TEAA) buffer at p*H* 5 provided significant improvements in both column durability and retention (Figure 3.2.10). The major drawback of using TEAA buffer as opposed to TEAB buffer is that the acetic acid is significantly less volatile and so difficult to remove. Removal is possible by repeated freeze-drying and dissolution in water over 4-5 iterations.

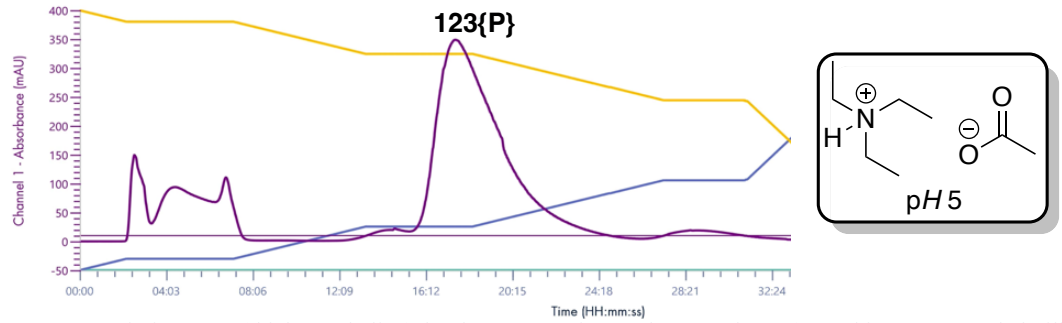

Figure 3.2.10. Elution trace (thick purple line) for the strong anion exchange column (Interchim SAX Bonded Silica Columns) with TEAA buffer (blue line). Initially non-retained material passes through (0-8 m 00 s) before the retained monophosphate (**123{P}**) is eluted (16 m 10 s) at 16.8 % (0.168 M) 1M TEAA buffer. The yellow line shows the % amount of water and the thin purple line at 10 mAU is the threshold set for fraction collection. Inset shows the TEAA buffer used at pH 5 in this purification.

Table 3.2.2. Summary of key characteristics of the two different anion exchange columns used within this project.

Property	Teledyne-ISCO Redisep Rf Gold® Amine Columns (30g)	Interchim SAX Bonded Silica Columns (25 g)
Silica Particle Size (mm)	20-40	50
pH Stability	<9	1.5-7
End Capping	Secondary amine, functionalised silica	Quaternary ammonium, bonded silica
Loading	Up to 600 mg	Up to 250 mg
Elution Profile	TEAB Buffer (0 → 2 M, p*H* 8) TEAA Buffer (0 → 2 M, p*H* 5)	TEAB Buffer (0 → 2 M, p*H* 8) TEAA Buffer (0 → 2 M, p*H* 5)
Durability	~20 runs (TEAB) >30 runs (TEAA)	<2 runs (TEAB) ~20 runs (TEAA)

The Interchim strong anion exchange columns also showed good retention, and reproducible results with the TEAA buffer system; however, it was still found that durability was an issue. This is likely due to the bonded silica system hydrolysing over time as the p*H* is close to the maximum specified p*H* for this system. Returning to the Teledyne weak anion exchange columns, retention and reproducibility were maintained and the durability was vastly improved. Pleasingly, under the conditions of 0 → 2 M TEAA buffer at p*H* 5 the Teledyne column could be used for >30 runs, where ~300 mg of purified material could be isolated per run.

Following isolation of the purified thione monophosphate (**123{P}**), with minimal inorganic phosphate remaining, addition of the final phosphate group was explored via the previously discussed phosphitylation method of Jessen and co-workers (Scheme 3.2.17). Starting with the TEAA-purified material, which had no residual inorganic phosphate remaining, reaction with phosphoramidite (**119**) and the tetrazole (**120**)

activating reagent proceeded cleanly as seen by ^{31}P NMR spectroscopy (Figure 3.2.11 (2)). Upon oxidation of the phosphorus(III) to a phosphorus(V) with t-butyl hydroperoxide the formation of the P(V)-P(V) anhydride is observed (Figure 3.2.11 (3)). Finally, fluorenylmethyl deprotection with piperidine gave the characteristic two doublets by $^{31}P\{^{1}H\}$ NMR spectroscopy (Figure 3.2.11 (4)). Unfortunately, at this point hydrolysis of the pyrophosphate group also appeared to occur, resulting in ~20% return of the monophosphate. Isolation of crude material was possible through precipitation with diethyl ether. Further purification was carried out initially with a sodium iodide/acetone precipitation to give a mix of the thione pyro- and monophosphate.

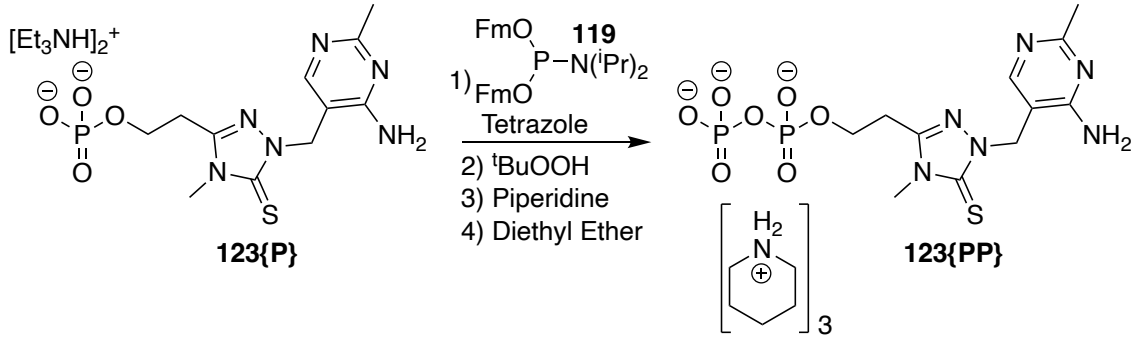

Scheme 3.2.17. Pyrophosphorylation of the thione using the Jessen method of phosphitylation, Scheme 3.2.6 highlights the intermediates formed and Figure 3.2.11 shows the ^{31}P NMR spectroscopy tracking of these intermediates.

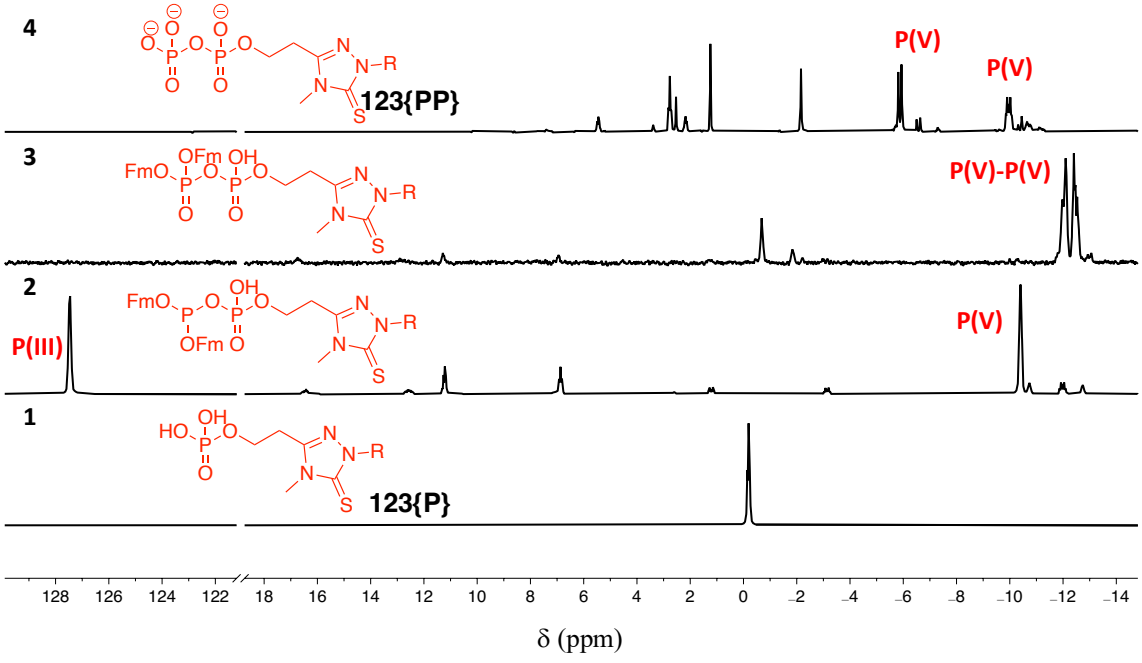

Figure 3.2.11. ^{31}P NMR spectra tracking the iterative stages of the phosphitylation reaction (Scheme 3.2.17) starting from the initial thione (**123{P}**), forming the P(III)-P(V) anhydride, oxidation to the fluorenylmethyl-protected P(V)-P(V) anhydride and deprotection. Other peaks correspond to by-products of this complex reaction.

At this point, there were two approaches to isolate the final 1,2,4-triazolium pyrophosphate (**26{PP}**): purification of the thione (**123{PP}**) and then desulphurisation to the 1,2,4-triazolium; or, oxidation to the 1,2,4-triazolium followed by purification to

remove the residual monophosphate. Initially, to explore the final desulphurisation of the thione pyrophosphate (**123{PP}**), a synthetic strategy was established using minimal hydrogen peroxide in an overnight reaction to isolate the triazolium (**26{PP}**). The reaction could be readily monitored by observing a characteristic downfield shift of both the N-Me and the methylene linker as a cationic centre is formed. Importantly, this conversion was very clean, with no cross reactivity occurring at the more sensitive pyrophosphate bond. Isolation of the crude 1,2,4-triazolium (**26{PP}**) was achieved by precipitation with sodium iodide and acetone; however, first it was important to quench residual hydrogen peroxide with either sodium iodide or thiosulfate due to the possibility of forming explosive triacetoxyhydroperoxide in dilute mixtures of hydrogen peroxide and acetone.[191]

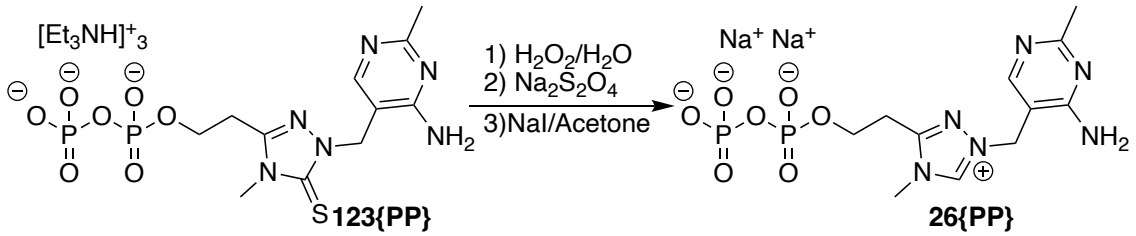

Scheme 3.2.18. Final desulphurisation of the thione pyrophosphate to the 1,2,4-triazolium pyrophosphate with hydrogen peroxide, followed by quench with sodium thiosulphate and isolation with sodium iodide/acetone precipitation.

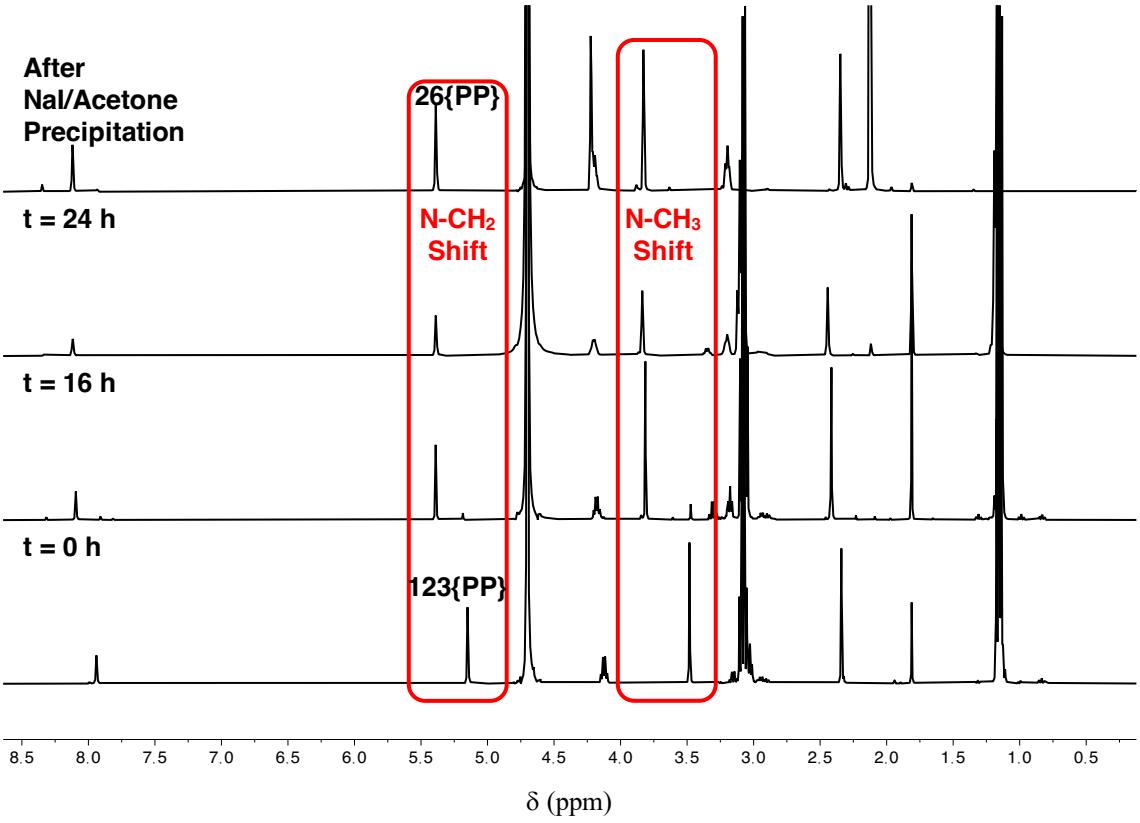

Figure 3.2.12. ^{1}H NMR spectra tracking the desulphurisation on the thione pyrophosphate to the 1,2,4-triazolium pyrophosphate mimic.

The thione pyrophosphate (**123{PP}**) was expected to be the easier substrate to purify by anion exchange chromatography owing to the lack of cationic centre. Considering that the desulphurisation reaction occurred so cleanly, it was decided to purify at the thione stage. Initially, purification was carried out as for the thione monophosphate (**123{PP}**) with the Teledyne weak anion exchange stationary phase and a 2 M p*H* 7 TEAA buffer eluent. Under these conditions, it was found that the pyrophosphate (**123{PP}**) was too strongly bound to the stationary phase and that 100% 2 M buffer was required to elute the material. To reduce the retention, a p*H* 5 TEAA buffer system (0 → 2 M) was explored. This was expected to reduce the ionisation of the pyrophosphate (**123{PP}**) as it was estimated to be below the final phosphate pK_a (~ 6.0-6.5). As expected, this greatly reduced the retention of the thione pyrophosphate and allowed isolation of purified material. Importantly, the ^{31}P NMR spectrum highlighted that the only phosphorus species present was the pyrophosphate.

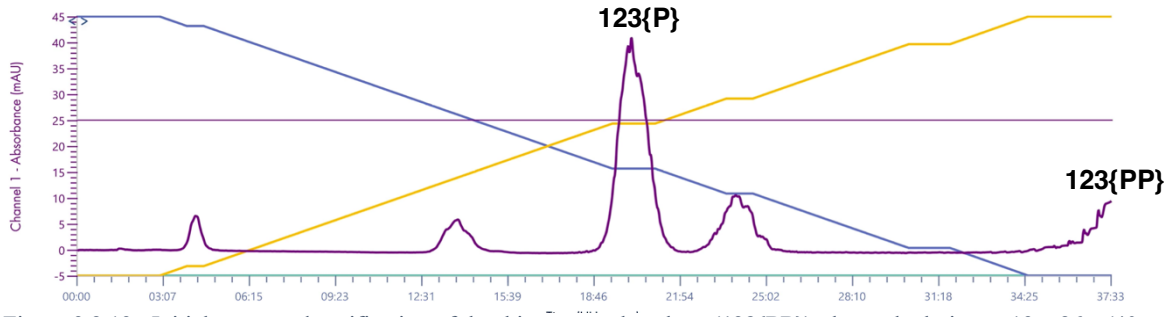

Figure 3.2.13. Initial attempted purification of the thione pyrophosphate (**123{PP}**), the peak eluting at 19m 26 s (40 % 2 M TEAA buffer at p*H* 7) was found to be the monophosphate (**123{P}**) in this case. At the end, the increase in absorbance highlights the thione pyrophosphate (**123{PP}**) beginning to elute. The yellow line highlights the proportion of TEAA buffer, the blue line highlights the proportion of water and the dark purple shows the UV-trace. The thin purple line shows the threshold for fraction collection.

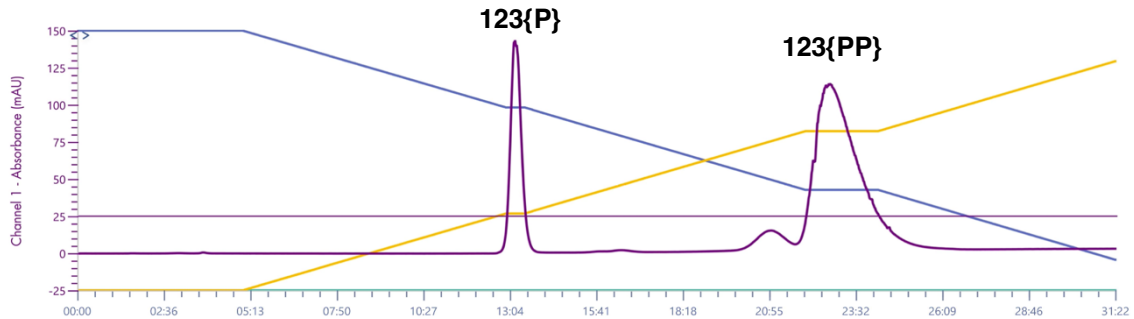

Figure 3.2.14. Thione pyrophosphate (**123{PP}**) purification carried out with 2 M TEAA buffer at p*H* 5 showing lower retention of the thione pyrophosphate (**123{PP}**), eluting at 22m 07s (1.2 M TEAA buffer). The peak at 13m 00s shows elution of the thione monophosphate (**123{PP}**) (0.6 M TEAA buffer). The yellow line highlights the proportion of TEAA buffer, the blue line highlights the proportion of water and the dark purple shows the UV-trace. The thin purple line shows the threshold for fraction collection.

Finally, using the synthetic strategy developed for desulphurisation (Scheme 3.2.18), the 1,2,4-triazolium pyrophosphate (**26{PP}**) could be isolated. In the first instance, sodium thiosulphate was used to quench excess hydrogen peroxide before sodium iodide/acetone

precipitation. Unfortunately, this led to a cross reactivity with acetone, forming a by-product that was not removed during the precipitation. Subsequent hydrogen peroxide quenching was performed with sodium iodide and the by-product was avoided.

3.2.5. Conclusions

This chapter highlights the synthesis of a 1,2,4-triazolium mimic (**26{PP}**) of thiamine pyrophosphate (**5{PP}**), and exploration of the broader applicability of this synthetic strategy. The synthesis of the 1,2,4-triazolium mimic pyrophosphate (**26{PP}**) proved to be particularly challenging owing to the need to develop complex aqueous purification techniques and new synthetic strategies. Importantly, it was found that phosphorylations on the thione precursor (**123**) proceeded more readily, with significantly easier purification owing to the lack of a neutralising cationic charge (in comparison to the 1,2,4-triazolium ion) of this compound. A clean, reproducible synthetic strategy to the desired pyrophosphate has been developed using phosphorus oxychloride (**118**), and crucially water, to insert the first phosphate group. Subsequent reaction with a phosphoramidite reagent (**119**), followed by oxidation, gave the thione pyrophosphate (**123{PP}**). Finally, desulphurisation of this purified thione pyrophosphate cleanly afforded the 1,2,4-triazolium mimic pyrophosphate (**26{PP}**) (yields < 20%, up to 400 mg scale). Careful control of p*H* throughout this complex synthetic procedure was found to be crucial to the success. From isolation of the thione (**123**), which is soluble in aqueous solution above p*H* 5, to carefully balancing p*H* during anion exchange chromatography, p*H* control was essential. A key aspect of the chemistry, which was exploited, was the knowledge that sodium iodide is soluble in acetone, but phosphate salts of sodium are not. This allowed for straightforward isolation of the key products and intermediates from aqueous solutions.

The isolated 1,2,4-triazolium pyrophosphate (**26{PP}**) is the first 1,2,4-triazolium mimic of thiamine with the carbenic centre intact. Section 3.4 and 3.5 will explore the initial evaluation of this novel cofactor as both a standalone catalyst and as a cofactor to TPP-dependent enzymes.

3.3. Pyrophosphate Hydrolysis Studies

3.3.1. Foreword

Despite broad applications of thiamine pyrophosphate (TPP) (**5{PP}**) throughout biological chemistry, there has not been a systematic screening of its stability across the p*H* range. This section discusses the development of a p*H*-hydrolysis profile across the available p*H* range. Such information is important for understanding shelf-life and appropriate conditions for handling TPP (**5{PP}**) and similar cofactor mimics. In particular this study was devised to direct the development of purification techniques for the synthesis of a pyrophosphate of the 1,2,4-triazolium mimic (**26{PP}**) of thiamine. As thiamine pyrophosphate (**5{PP}**) is commercially available in greater quantities, this substrate was chosen for study. Knowledge of the p*H* stability of thiamine pyrophosphate was then extrapolated to other 1,2,4-triazolium cofactor mimics.

3.3.2. Introduction

Phosphorus is highly abundant within chemical biology, with over 99% of its chemistry occurring in the phosphorus(V) oxidation state. The high abundance led to a famous quotation from Alexander Lord Todd: *'I would guess that if life exists anywhere else in the universe it will do so only on a planet on which phosphorus is readily available.'*[192] Adult humans contain around 0.8 kg of phosphorus, in phosphate form, of which 85% is sequestered in teeth and bones and the remaining in soft tissue. Biological applications of phosphates include genetic storage, where DNA (**138**) requires very stable phosphodiester bonds; lipid membranes (**135**), where phosphate head groups and lipid tail groups allow for self-assembling compartments; energy conversion, which relies on the energetics of phosphorus anhydrides (**137**); signalling and information flow, a set of low molecular weight secondary messengers such as cyclic adenosine monophosphate (cAMP) (**136**) and protein post-translational phosphorylation. Relevant to the present project, many enzyme cofactors contain phosphate groups to improve binding, often to a metal counterion, within an active site Figure 3.3.1.[193]

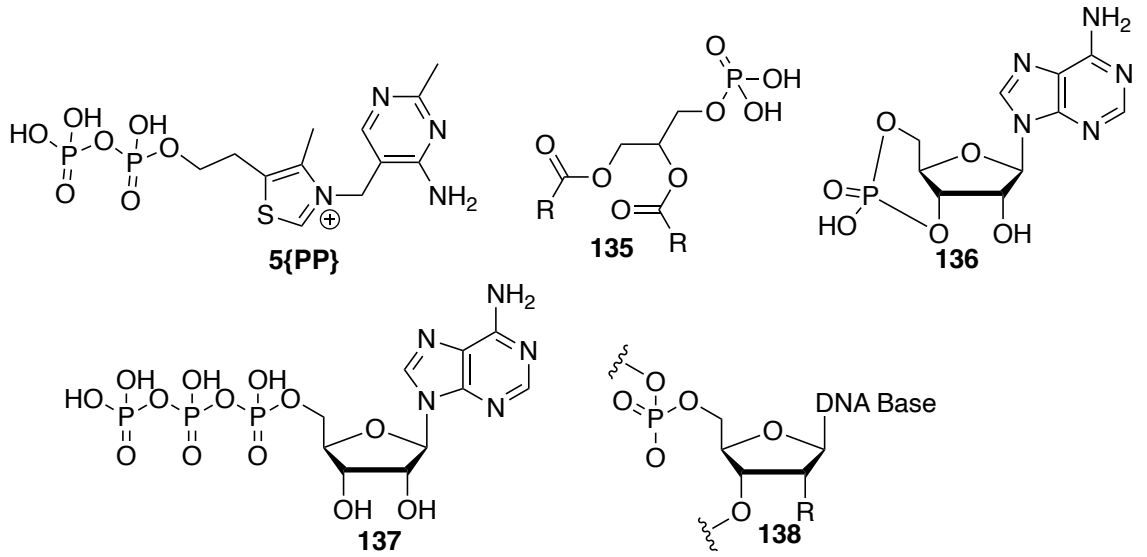

Figure 3.3.1. A selection of common phosphorylated biomolecules including thiamine pyrophosphate (**5{PP}**), phospholipids (**135**), cAMP (**136**), ATP (**137**) and the DNA backbone (**138**).

Phosphorus anhydride bonds are found within thiamine pyrophosphate (**5{PP}**) alongside adenine triphosphate (**137{PPP}**) and diphosphate (**137{PP}**) which have roles within energy regulation in cells. Pyrophosphate bonds contain a significantly larger amount of energy (in ATP (**137{PPP}**), POP = -30 kJ mol^{-1} compared to the COP = -15 kJ mol^{-1}). Hydrolytic enzymes can readily release this energy for use in metabolic processes.[177] It has been found that under non-enzymatic conditions, the hydrolysis of pyrophosphate systems is very slow. Speciation is an important factor and, although there is no exact literature data for the pK_a values aligned with the three protonation states of the phosphates on thiamine (**5{PP}**), values for free pyrophosphoric acid (**139**) are ~0.8, ~2.0, ~6.3 and ~9.1 for pK_a[1-4] (Figure 3.3.2).[181] Inorganic pyrophosphate was found to hydrolyse with a rate constant of 6×10^{-4} s^{-1} ($t_{1/2}$ ~ 20 mins) for the di-anion (p*H* 5-8) and 7×10^{-5} s^{-1} ($t_{1/2}$ ~ 2.8 hrs) for the tri-anion (p*H* 8-10) at elevated temperatures of 70 ºC. Hydrolysis in 0.1 M sodium hydroxide, with pyrophosphate fully ionised, found no reaction even after 40 days.[194] This can be rationalised by a build-up in negative charge at the phosphate centre reducing propensity for attack of the nucleophile (water).

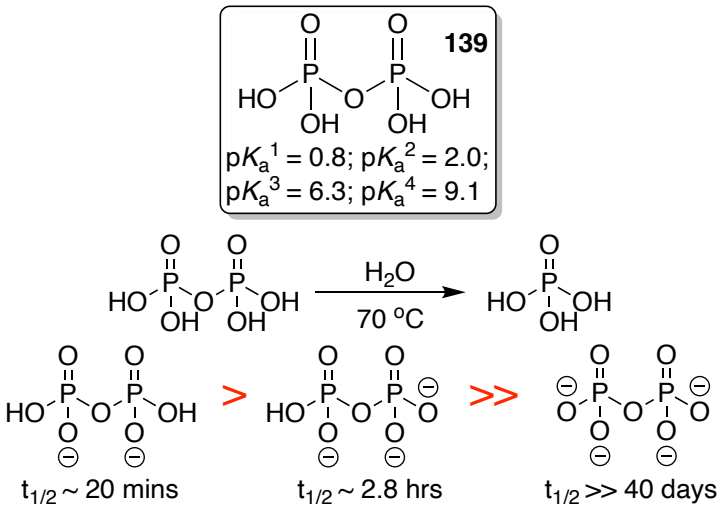

Figure 3.3.2. Hydrolysis of inorganic pyrophosphate is typically slow, with increased p*H* dramatically decreasing the rate as each acid dissociation occurs.

These studies were carried out using radioactive-labelled phosphorus with a complicated work-up method. This likely leads to discrepancies in the partitioning and quantification of radioactivity and greater error in experimental results. A more modern approach to monitoring kinetic processes is to use NMR spectroscopy. Although there has been no direct study on the hydrolysis of ATP(**137{PPP}**)/ADP(**137{PP}**) with NMR spectroscopy, methanolysis of ADP ((**137{PP}**)) has been explored (Scheme 3.3.1). In this case, samples were incubated in buffers (0.1 M, p*H* 4.8-9.0) at 50 and 110 ºC, before evacuating to dryness and taking up in D_2O for analysis. A more direct approach, which reduces lag-time between sampling and measurement time would be the direct monitoring of an NMR tube scale reaction. Nevertheless, rate constants for methanolysis were determined for ADP (**137{PP}**), in the p*H*-independent region, as $k = 6.8 \times 10^{-10}$ s^{-1} (2 M methanol) and compared to a hydrolysis rate of 5.3×10^{-9} s^{-1}. These relate to half-lives of 32 years and 4.1 years at 25 ºC, respectively, highlighting the inherent stability of the pyrophosphate bond in the absence of hydrolytic enzymes.[195]

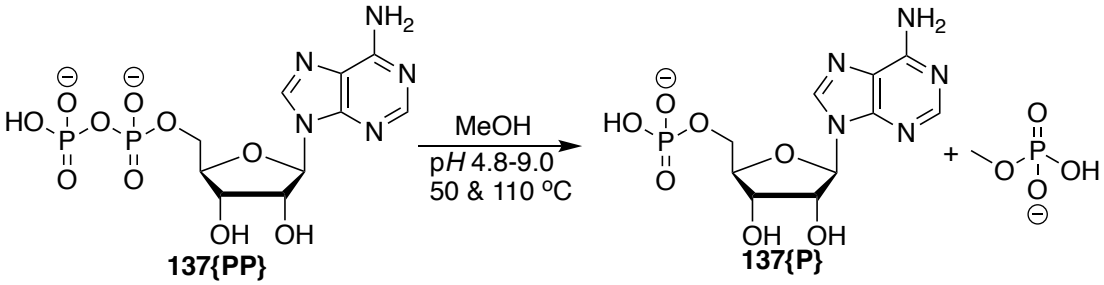

Scheme 3.3.1. The methanolysis of ADP to AMP from p*H* 4.8-9.0 monitored by NMR spectroscopy.

NMR spectroscopy is a powerful tool for monitoring kinetics as the signals are typically quantitative and correspond to the number of nuclei. For reliable quantitation it is

important to consider the signal acquisition parameters, of which T_1 is often overlooked. T_1 refers to spin-lattice decay and its magnitude places limits on the acquisition rates of consecutive scans. Generally, the time between scans must be at least 5 x T_1, allowing for ≥ 99.3 % relaxation. In a kinetic experiment, it is important to consider the T_1 of the various nuclei in a sample and ensure that the time between scans (t_R) is at least 5 x T_1 for all components. Failure to do so results in unevenly relaxed samples which can suppress certain signals and give incorrect integrals. For example, Figure 3.3.3 highlights the ^{31}P NMR spectra for triphenylphosphine and its oxide using different t_R values. Only when t_R is greater than 5 × T_1 for the relevant signals of triphenylphosphine can these two peaks be compared quantitatively.

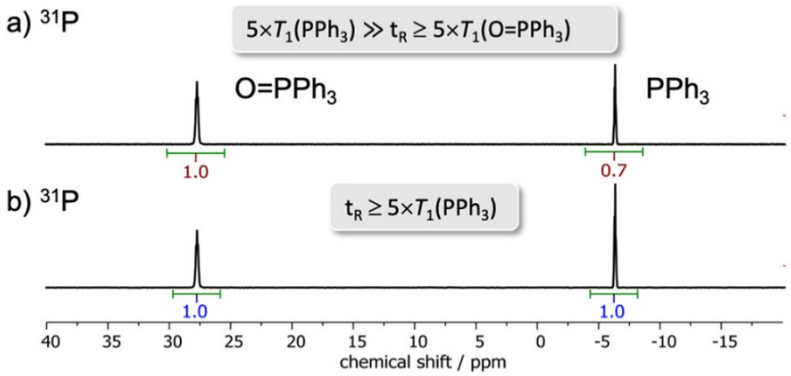

Figure 3.3.3. ^{31}P NMR spectra for a 1:1 mix of triphenylphosphine oxide and triphenylphosphine, showing the importance of t_R > 5 × T_1 for effective quantitation: a) highlights the integral differences when T_1>> t_R with triphenylphosphine integrating <1; b) highlights 1:1 integrals when $t_R \geq 5T_1$.

T_1 is typically influenced by the nucleus itself as well as the surrounding nuclei which can enhance relaxation by providing alternative pathways. It is therefore important to measure T_1 values for nuclei intended for kinetic experiments to ensure accurate quantitation of signals. There are multiple ways to measure T_1 summarised in Figure 3.3.4. Inversion recovery is the most common method of determination, often installed as a pre-set program on NMR spectrometers.[196] It starts with a 180° pulse, followed by a 90° pulse after a delay period, τ, before monitoring the decay. A Fourier transformation gives a partially relaxed spectrum and a plot of this with respect to τ gives T_1, Figure 3.3.4(a).[197] Saturation recovery has been used in the determination of T_1 values for radical species in solution. This requires separation of the free-induction-decay and saturation-recovery signal to extract the latter.[198] The signal is fully saturated by equally spaced 90° pulses before altering τ to determine T_1. Progressive recovery monitors the signal peak height as a function of the applied radiofrequency. This requires a known value for T_2 to extract the desired T_1 value, which must be determined by alternative methods.[199] The

benefits of this method is the avoidance of the need for monitoring a delay period, reducing experiment time. Finally, FLIPS is a more modern technique which provides a rougher estimate of T_1 but with reduced experiment time. Rather than a stepwise analysis of relaxation recovery, it requires a scan following each pulse so that all data can be collected in a single experiment.[196]

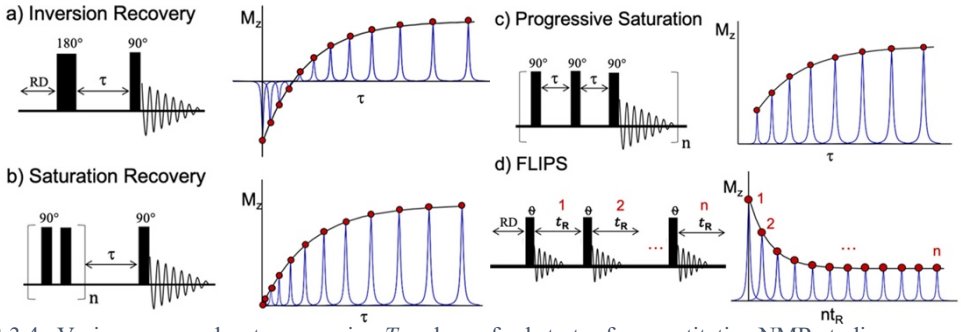

Figure 3.3.4. Various approaches to measuring T_1 values of substrates for quantitative NMR studies.

Accurate quantitation by NMR spectroscopy allows for reliable kinetic tracking of reactions, such as in the case of the present study on the hydrolysis of thiamine pyrophosphate (**5{PP}**). When considering the p*H*-hydrolysis profile of TPP (**5{PP}**), it is important to consider the different mechanisms of reaction at phosphorus. There are 3 key mechanisms to consider for reaction of a nucleophile at phosphorus: (1) Dissociative $S_N1(P)$, where first a group leaves forming a 4-coordinate, planar phosphorus cation which is attacked by a nucleophile; (2) Associative $S_N1(P)$ (addition-elimination), where a nucleophile attacks forming a 'stable' phosphorane intermediate, followed by loss of a leaving group; (3) $S_N2(P)$, via formation of a trigonal bipyramidal phosphorane transition state, with stereochemical inversion (Figure 3.3.5).[200] These mechanisms can be considered when monitoring the hydrolysis of thiamine pyrophosphate. It can be expected that hydrolysis reactions of thiamine pyrophosphate will proceed via $S_N2(P)$ or addition-elimination mechanisms, or a mixture of the two. $S_N1(P)$-type mechanisms are much less common owing to the need to form the unstable phosphorane intermediate.

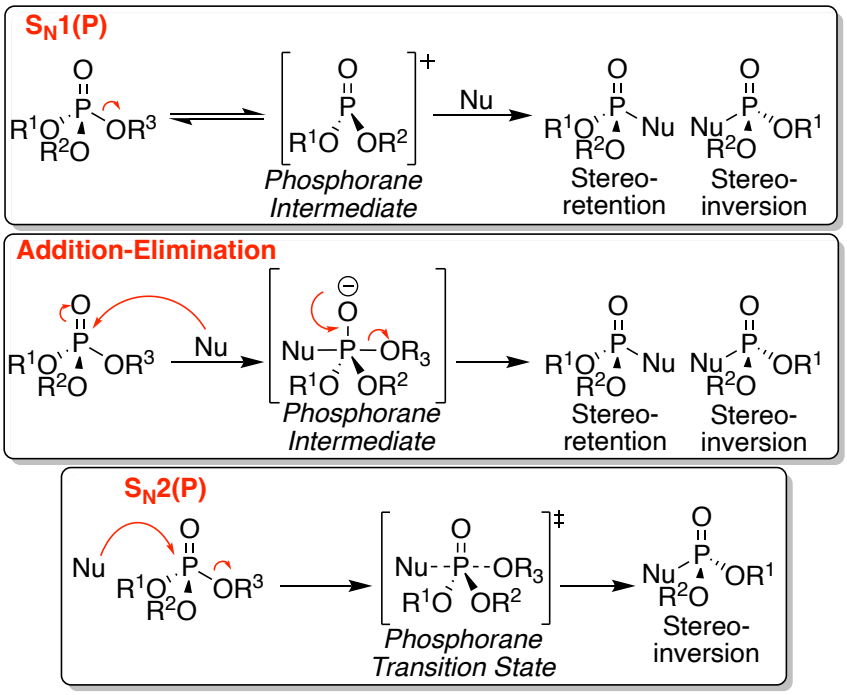

Figure 3.3.5. Potential mechanisms for substitution reactions at phosphorus(V) systems. Typically, $S_N1(P)$-type mechanisms are rare, with the majority proceeding via a mix of $S_N2(P)$ or Addition-Elimination.

3.3.3. Results and Discussion

The aim of this set of experiments was to explore the hydrolytic stability of thiamine pyrophosphate (**5{PP}**), in particular the pyrophosphate bond, in order to guide the purification of the 1,2,4-triazolium mimic (**26{PP}**). It had been noted in preliminary studies that the pyrophosphate group might be cleaving to give the monophosphate when undergoing freeze-drying under non-p*H* controlled conditions. Within the literature, there is no reported study on the stability of thiamine pyrophosphate (**5{PP}**) across the p*H* region. When carrying out studies with TPP-dependent enzymes, cofactor stability is important to consider.

To guide the development of an NMR spectroscopic method for tracking the hydrolysis of thiamine pyrophosphate (**5{PP}**), it was useful to determine the T_1 values of the three components: thiamine pyrophosphate (**5{PP}**), thiamine monophosphate (**5{P}**) and methylene diphosphonate (**140**). Methylene diphosphonate was the internal standard of choice in this experiment as it gave a well-resolved singlet by $^{31}P\{^1H\}$ NMR spectroscopy; was well removed from the phosphate region, so could be cleanly integrated; finally, it was stable in aqueous solution throughout the timeframe of these experiments (several months). T_1 values were determined using the pre-programmed

inversion recovery method within the NMR spectrometer, as described in the introduction. Values are summarised in Table 3.3.1 and show that under the standard ^{31}P NMR spectroscopy conditions, there is no concern about the effect of T_1, which is small and comparable in all cases. The relaxation time used for the present NMR spectroscopy studies was 2.07 s, which is on a similar timescale to the T_1 values of the substrates. This is not 5 × T_1 and hence full relaxation will not have occurred in all cases; however, a compromise must be made between acquisition time and relaxation. Moreover, as hydrolysis is predicted to be a unimolecular process (fitting to first-order kinetics), absolute integrals are not required, instead the change in integral over time can be monitored as a fraction of substrate remaining, F(S).

Table 3.3.1. Summary of the T_1 values determined for the substrates of interest in this hydrolysis study. Values were determined using the pre-programmed inversion recovery approach in a 500 MHz NMR spectrometer at 25 °C.

Phosphorus Compound	T_1(P) / s	T_1(H) / s
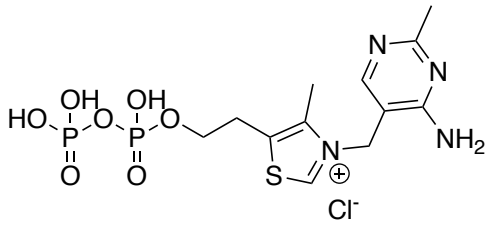 **5{PP}**	1.4 ± 0.2 1.6 ± 0.1 1.2 ± 0.1 1.2 ± 0.2	1.09 ± 0.01[a]
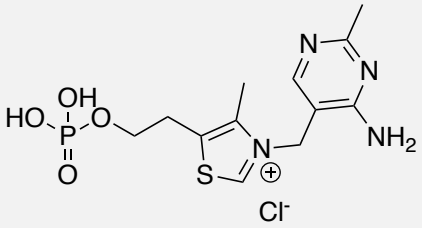 **5{P}**	2.5 ± 0.1	1.06 ± 0.01[a]
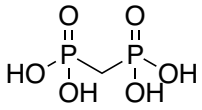 **140**	4.0 ± 0.4	1.06 ± 0.02[a]

[a] T_1(H) values refer to the CH_2 methylene bridge in all compounds.

Hydrolysis of thiamine pyrophosphate (**5{PP}**) was monitored by NMR spectroscopy over 24 hours to 6 months at a range of p*D* values from 0-14 at buffer concentration of 0.2 M and ionic strength, I = 1.0 M (KCl) (Scheme 3.3.2). Table 3.3.2 summarises the buffers used in these studies and measured p*D* values, determined by adding a correction of 0.4 to the measured output of the p*H* probe. Reactions were carried out in NMR tubes, incubated at 25 °C in a thermostated water bath or, in the case of faster reaction times, within the NMR spectrometer probe. In comparison to studies of the stability of the pyrophosphates of ADP (**137{PP}**) and ATP (**137{PPP}**), this choice of temperature is

significantly lower but, this is more realistic from a storage and handling perspective of TPP (**5{PP}**).

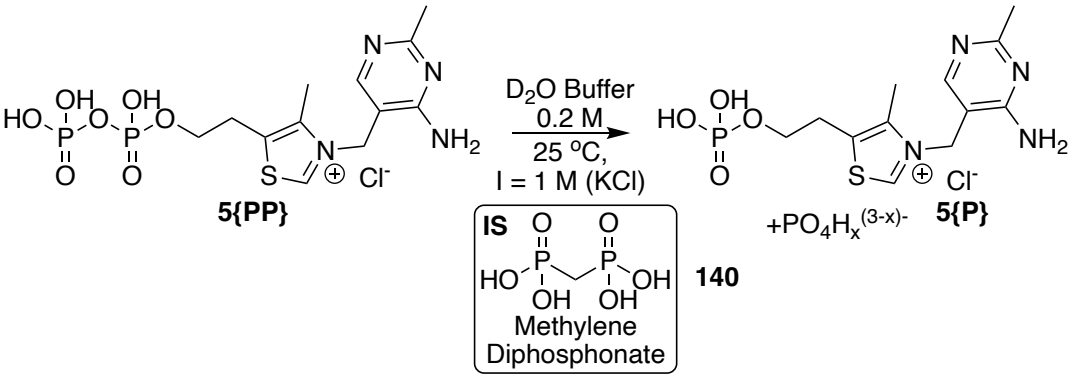

Scheme 3.3.2. Hydrolysis studies on thiamine pyrophosphate (**5{PP}**) monitoring by $^{31}P\{^{1}H\}$ NMR spectroscopy with methylene diphosphonate (**140**) internal standard. 0.2 M buffers were used and a constant ionic strength of 1 M was maintained with potassium chloride.

Table 3.3.2. Summary of the buffers used in the hydrolysis studies, the measure p*H* values and the corrected p*D* values.

Buffer	Concentration	Free Base / %	p*H* Measured	p*D* correction[a]
DCl	0.5	N/A	-0.06	0.36
	0.25		0.40	0.80
	0.1		0.66	1.06
	0.05		0.98	1.38
Potassium Formate	0.2	50	2.88	3.28
		90	3.57	3.97
Potassium Acetate	0.2	10	4.03	4.43
		50	4.50	4.90
		90	5.11	5.51
Triethanolamine Hydrochloride	0.2	50	6.50	6.90
		90	8.19	8.59
Triethylamine Hydrochloride	0.2	10	9.10	9.50
		50	11.08	11.48
		90	11.81	12.21
KOD	0.1	N/A	12.60	13.00

[a]The p*D* correction is determined as the value measured on the p*H* probe with a factor of 0.4 added.[201]

NMR spectra were collated and overlayed, with baseline and phase corrections. Figure 3.3.6 highlights relevant $^{31}P\{^{1}H\}$ NMR spectra for the sample run at p*D* 1.06 at t=752 s, t=969029 s (11 days) and t=1979531 s (23 days). The thiamine pyrophosphate (**5{PP}**) peaks decrease over time and the thiamine monophosphate (**5{P}**) and inorganic phosphate (P_i) peaks increase with time as hydrolysis occurs. The fraction of TPP (**5{PP}**), F(TPP) and of TMP (**5{P}**), F(TMP), were determined by comparison to relevant integrals (A_{TPP}) to the integral of the internal standard (A_{IS}) (Equation 3.3.1/Equation 3.3.2). A plot of F(S) against time showed an excellent fit ($R^2 = 0.998$) to a first-order decay of TPP (Equation 3.3.3, Figure 3.3.7), validating the shorter relaxation delay used

in the acquisition of the spectra. As a first order process, plotting the natural logarithm of F(TPP) with respect to time gave a linear plot with gradient equal to the rate constant for hydrolysis, $-k_{hyd}$, (Equation 3.3.4, Figure 3.3.8). As the rates were typically slow, fitting to an exponential decay was challenging, and plotting to the integrated rate law gave more reliable estimates of $k_{hyd.}$ Typically NMR spectroscopy is a reliable method for kinetic monitoring of a reaction, nevertheless measurement errors should be acknowledged. The key error in this case results from the well-established lower sensitivity of ^{31}P NMR spectroscopy in comparison to ^{1}H NMR spectroscopy. This lower sensitivity reduces the signal to noise ratio, resulting in larger errors in the measured integrals, particularly when monitoring such small changes in these slow reactions. These integral errors are more evident in the slower hydrolysis reactions such as p*D* 5.50 where a lower R^2 value is obtained for the linear fit of ln{F(TPP)} against time (See Appendix 7.2).

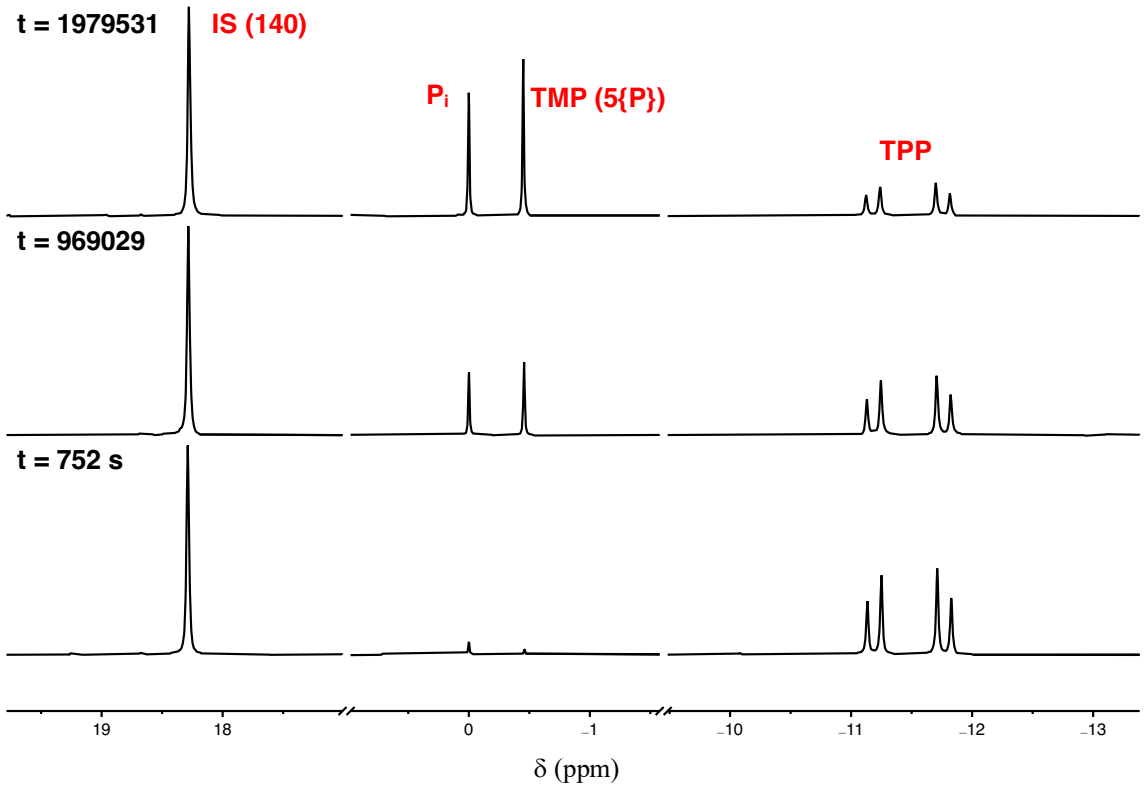

Figure 3.3.6. Representative spectra for the hydrolysis of TPP (**5{PP}**) at p*D* 1.06 showing decrease in the TPP peaks over time and corresponding growth in the TMP and P_i peaks, with the internal standard peak remaining constant.

$$F(TPP) = \frac{(A_{TPP}/A_{IS})_t}{(A_{TPP}/A_{IS})_0} \qquad \textbf{Equation 3.3.1}$$

$$F(TMP) = \frac{(A_{TMP}/A_{IS})_t}{(A_{TPP}/A_{IS})_0} \qquad \textbf{Equation 3.3.2}$$

$$F(S) = Exp(-k_{hyd}t) \qquad \textbf{Equation 3.3.3}$$

$$Ln\{F(S)\} = -k_{hyd}t + C \qquad \textbf{Equation 3.3.4}$$

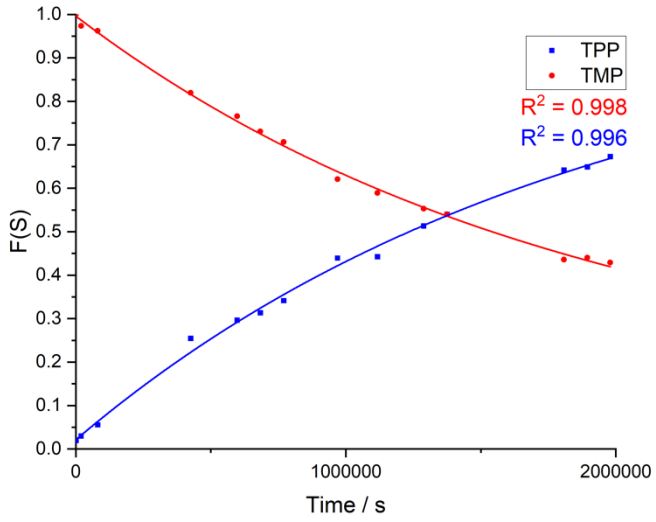

Figure 3.3.7. Plot of F(S) (S=TPP or TMP) over time for the hydrolysis of TPP (**5{PP}**) at p*D* 1.06, monitored by ^{31}P NMR spectroscopy. Solid lines show a first order fit (Equation 3.3.2) with excellent R^2 values.

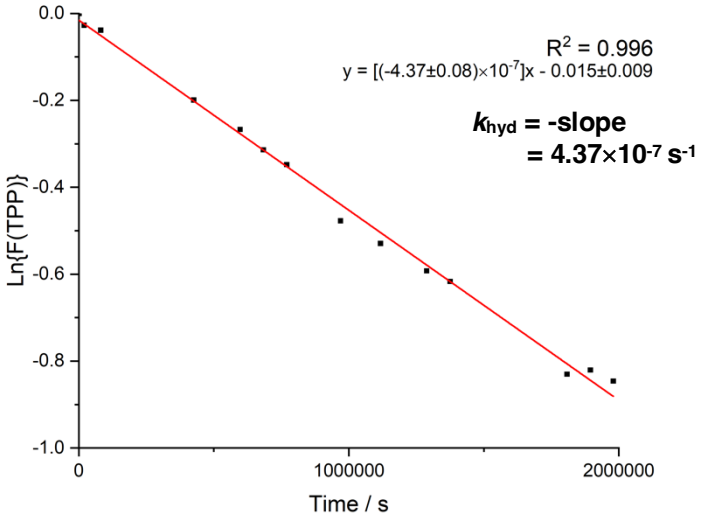

Figure 3.3.8. Plot of ln{F(TPP)} against time shows linear behaviour with gradient equal to -k_{hyd} as per Equation 3.3.3, as shown here for hydrolysis at p*D* 1.06.

This analysis was carried out across the p*H*-range from 0-13, monitoring decay of the TPP (**5{PP}**) peaks. Spectral overlay and plots of F(S) with respect to time can be found in Appendix 7.2. Table 3.3.3 summarised the values obtained for k_{hyd} from p*D* values 0.36-6.90. At higher p*D* values (> 7) hydrolysis was too slow to measure and instead cleavage of the methylene linker became competitive. The magnitudes of these values

are similar, if not slightly higher, than values for ADP (**137{PP}**) and ATP (**137{PPP}**) hydrolysis and methanolysis at 25 °C implying a slightly more labile pyrophosphate group in this case. Nevertheless, k_{hyd} values are still significantly small under typical biological conditions (p*H* 6-7.5) that the rate of hydrolysis can be considered negligible. It does however highlight that control of p*H* is important as, at lower values, hydrolysis becomes more significant. Thiamine pyrophosphate (**5{PP}**) is sold as its fully protonated hydrochloride salt and upon dissolution in water gives an acidic solution (p*H* < 3). Hydrolysis at this p*H* is significantly faster and so it is important that it is dissolved into buffered solutions to achieve the desired p*H* value.

Table 3.3.3. Summary of the values for k_{hyd} determined from plots of ln(F{TPP}) vs time at the p*D* values of this study. Also highlighted are the half-lives for hydrolysis, demonstrating the significant stability of these POP bonds.

p*D*	k_{hyd} / x10^{-8} s^{-1}	$t_{1/2}$ / days
0.36	417 ± 11	1.9
0.80	88.4 ± 4.9	9.1
1.06	43.7 ± 0.8	18.4
1.38	12.2 ± 0.4	69.7
1.90	5.77 ± 0.5	158
3.28	2.93 ± 0.21	274
3.97	2.42 ± 0.18	332
4.43	2.70 ± 0.11	297
4.90	2.11 ± 0.09	380
5.51	2.36 ± 0.13	340
6.90	1.62 ± 0.21	495
8.59	-[a]	>500

[a]Although integrals for the pyrophosphate (**5{PP}**) decreased slowly over the course of the experiment, no corresponding monophosphate peaks appeared, instead it was found that the methylene linker cleaved at this p*D* and above.

The data in Table 3.3.3 can be manipulated to construct a p*D*-rate profile through plotting p*D* against log(k_{hyd}). Typically, the observed rate constant, k_{obs}, can be broken down further into acid-dependent, base-dependent and p*H*-independent regions with second order rate constants assigned k_H, k_{H2O} and k_{HO} respectively (Equation 3.3.5). Plotting log(k_{obs}) against p*H* gives mechanistic insights into the influences on rates of reaction across the p*H* range.

$$k_{obs} = k_H[H^+] + k_{H2O} + k_{HO}[HO] \qquad \textbf{Equation 3.3.5}$$

Figure 3.3.9 highlights the key features typically observed in p*H*-rate profiles. Figure 3.3.9(a) shows a slope of -1 and 0 coupled together, representative of acid catalysed and p*H*-independent components. Typically, the rate constant for a p*H*-independent region

below other regions of the profile can be attributed to a solvent-mediated uncatalysed process. Figure 3.3.9(b) also shows a p*H*-independent component alongside a slope of +1 representing a base-catalysed region. Figure 3.3.9(c)/(d) show acid and base catalysed regions, respectively but, the levelling off to saturation is observed indicative of an ionisation process. Figure 3.3.9(e) highlights a slope of 0 showing that the process is completely uncatalysed by acid/base; finally, Figure 3.3.9(f) shows acid and base catalysis with no p*H*-independent component. All of these components can be described by Equation 3.3.4 or variations of this, and typical plots can be a compilation of all of these features.[202]

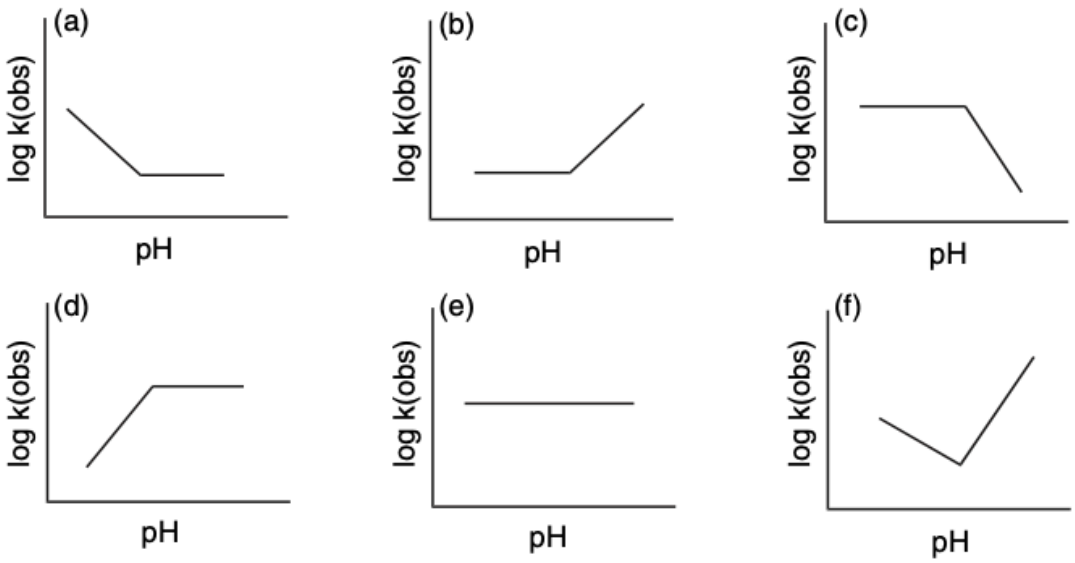

Figure 3.3.9. Typical behaviour observed in p*H*-rate profiles: (a) Acid-catalysis at low p*H* with a p*H*-independent region at higher p*H*; (b) base-catalysis at high p*H* with a p*H*-independent region at lower p*H*; (c) acid-catalysed process reaching saturation kinetics; (d) base-catalysed process reaching saturation kinetics; (e) no p*H*-independence; (f) acid and base catalysis with no p*H*-independent component. Reproduced with permission from Ref. 204.[203]

The appearance of the p*D*-hydrolysis plot of TPP (**5{PP}**) most resembles the profile in Figure 3.3.9(a), with a region of ~-1(-1.17) slope below p*D* 3 and of ~0 (-0.07) above p*D* 3 (Figure 3.3.10). Importantly there is no slope of +1 highlighting no observed base-catalysed hydrolysis. This is unsurprising considering that under basic conditions, the pyrophosphate group is likely fully ionised and so attack of negatively charged hydroxide ions will be strongly disfavoured. Before further interpretation of the p*D*-hydrolysis profile for TPP, it is important to consider the speciation across the p*D* range.

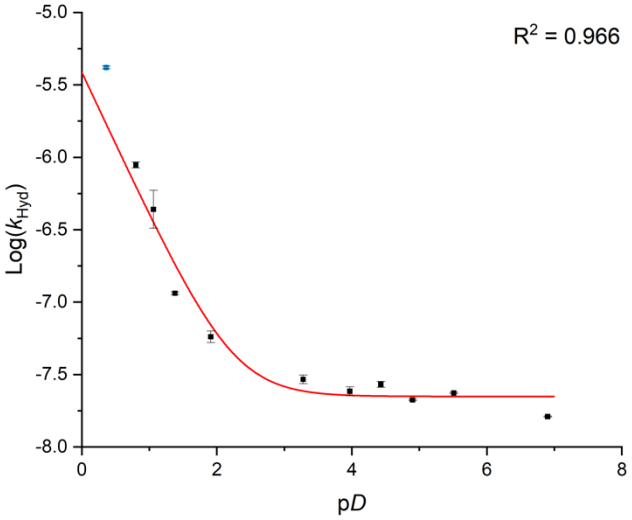

Figure 3.3.10. p*D*-Rate profile for the hydrolysis of thiamine pyrophosphate (**5{PP}**) shows a region of slope = -1 below p*D* = 3 and a slope of 0 from 3-7. Above p*D* 7, pyrophosphate hydrolysis was very slow and was outcompeted by cleavage at the methylene bridge thus rate constants could not be accessed. The red line shows the fit to Equations 3.3.6 and 3.3.8 as discussed in the text.

Inorganic pyrophosphate has pK_a values of ~0.8, ~2.0, ~6.3 and ~9.1; however, in the case of TPP, there are only the latter 3 oxygen pK_as to consider. The cationic thiazolium moiety will shift these pK_a values lower through providing local stabilisation for build-up of electron density. An extreme example of this is the Nitron derivatives (**6**) in Chapter 2.3, which had exocyclic pK_a values for formation of N^- of 8-10 is aided by the nearby cationic nitrogen and tautomerisation (Table 2.3.7). If considering analogous formation of the N^- on aniline, values would be > 30. It can therefore be expected that the cationic thiazolium will decrease all the pK_a values in comparison to inorganic pyrophosphate, with pK_a^1 being most shifted. Values of < 0, < 2, and < 8 can be roughly predicted. The pyrimidinyl-N pK_a should also be considered, for non-phosphorylated thiamine (**5**), this has been predicted as ~5.5.[204] As it is far removed from the pyrophosphate group, it is unlikely to have a significant effect on the rate of hydrolysis (Scheme 3.3.3).

Considering the above discussion of TPP (**5{PP}**) speciation across the p*D* range of this study, it is likely that the initial speciation pK_a^1 (**I**/**II**) is far below the first value explored. It should however be noted that the value for k_{hyd} at p*D* 0.36 deviates significantly from a line of slope -1. This could be linked to a speciation effect. There is a slight reduction in rate at p*D* ~7 and this could be linked to both pK_a^2 and pK_a^3 as both would reduce the rate of hydrolysis. The more marked effect is likely the formation of the pyrophosphate dianion (**IV**); for example, a similar shift from dianion to trianion of inorganic

pyrophosphate led to a decrease in rate by one order of magnitude. Most notably, hydrolysis rates above p*D* 8.5 could not be determined as pyrophosphate hydrolysis was particularly slow (no observed monophosphate formation across 3-4 months) and competing hydrolysis of the methylene linker occurred. This vast reduction in rate of hydrolysis likely signifies the formation of the pyrophosphate trianion (**V**), pK_a[4], which would greatly disfavour hydrolysis due to the high local concentration of electron density repelling nucleophilic water or hydroxide. The same trend is observed for inorganic pyrophosphate (**139**), with the final speciation event to the tetra-anion coinciding with a dramatic reduction in rate of hydrolysis.

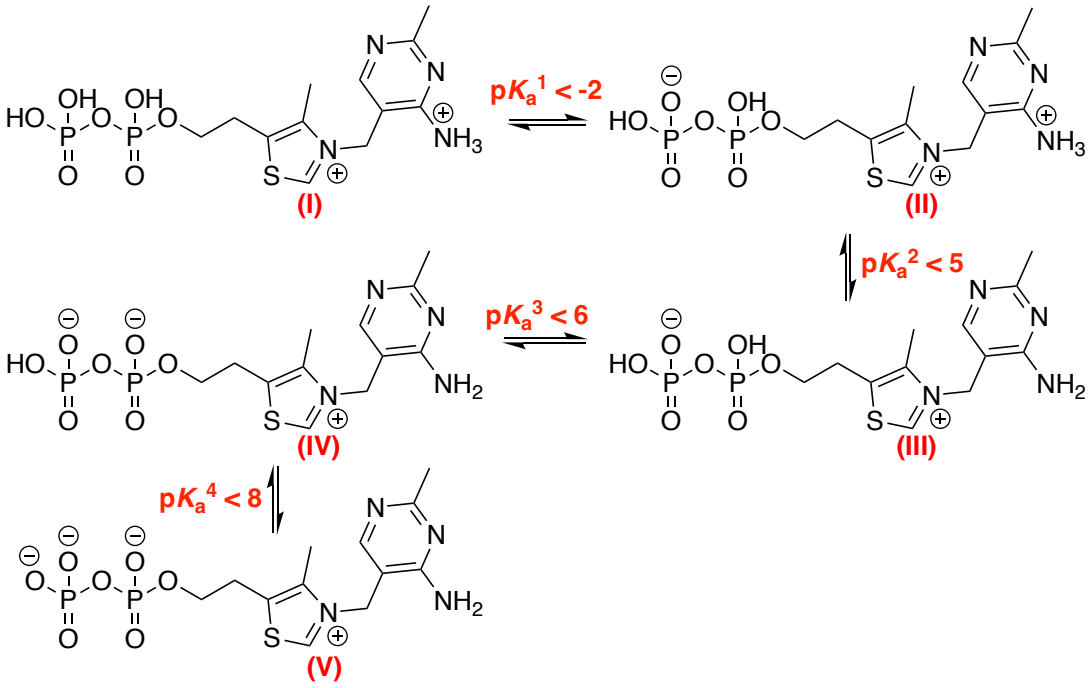

Scheme 3.3.3. Proposed speciation events for thiamine pyrophosphate (**5{PP}**) and estimated pK_a values. These values must be considered in relation to the p*D*-rate profile for hydrolysis of the pyrophosphate of **5{PP}** (Figure 3.3.10).

Two different approaches to fitting the p*D*-hydrolysis profile to obtain mechanistic insights have been explored: (1) A classical fit to a change in mechanism from uncatalysed (k_{D2O}) to acid-catalysed region (k_D) (Equation 3.3.6), which does not take into account speciation changes; (2) A fit which considers no change in mechanism (all uncatalysed) but instead a change in speciation (F^{SH}/F^{S-} with rate constants $k_{D2O}{}^{SH}/k_{D2O}{}^{S-}$) about an undetermined acid dissociation constant (K_a) (Equation 3.3.7 & Equation 3.3.8). Both fits gave identical appearances and R^2 values (Figure 3.3.10) and kinetic constants are summarised in Table 3.3.3. In both cases, the point at p*D* 0.36 was removed from the fitting as it deviated significantly from the slope of -1 and reduced the overall fit quality.

$$Log(k_{Obs}) = Log(k_D 10^{-pD} + k_{D2O}) \qquad \textbf{Equation 3.3.6}$$

$$Log(k_{Obs}) = Log(k_{D2O} F^{SH} + k_{D2O} F^{S-}) \qquad \textbf{Equation 3.3.7}$$

$$Log(k_{Obs}) = Log\left(\frac{k_{D2O} 10^{-pD}}{10^{-pD} + K_a} + \frac{k_{D2O} K_a}{10^{-pD} + K_a}\right) \qquad \textbf{Equation 3.3.8}$$

Table 3.3.4. Summary of the kinetic parameters determined from fitting the hydrolysis profile in Figure 3.3.10 to Equations 3.3.6 and 3.3.8.

Fitting Function	Constant	Determined Values	R^2
(1) Equation 3.3.6	k_D	$(3.84 \pm 0.6) \times 10^{-6}$ M^{-1} s^{-1}	0.966
	k_{D2O}	$(2.23 \pm 0.3) \times 10^{-8}$ s^{-1}	
(2) Equation 3.3.8	k_{D2O}^{SH}	1.3×10^{-3} s^{-1}	0.966
	k_{D2O}^{S-}	2.2×10^{-8} s^{-1}	
	K_a (pK_a)	190 (-2.5)	

Fitting the data to Equation 3.3.6 gives a useful insight into what could be described as the p*D*-dependent and -independent regions. Both k_D and k_{D2O} are small, highlighting the inherent stability of the pyrophosphate bond, with k_{D2O} having a 2-order of magnitude lower value highlighting the enhanced stability under physiological conditions. Fitting the hydrolysis profile to Equation 3.3.8 is more challenging as there are 3 unknown parameters (k_{H2O}^{SH}, k_{H2O}^{S-} & K_a). This should increase the overall quality of the fit as R^2 is increased; however, adding an extra term also increases the error in the fitting parameters as there are multiple results which converge to similar fits. Nevertheless, a fit of this data gives a high R^2 and the outputted parameters summarised in Table 3.3.4. Values for uncertainty in these values were large and unreliable and so were excluded in this case. This value of K_a reflects a pK_a of -2.5 which is not an unreasonable prediction considering Scheme 3.3.3.

Kinetically tracking the cleavage of the methylene bridge was more challenging owing to it occurring rapidly and overlapping NMR spectral peaks for starting TPP and cleaved products. Although only qualitative investigation was possible, it appeared that the rate rapidly increased as p*D* increased from 8-13, suggesting a base-catalysed process. This suggests a p*D*-rate profile for this process would likely have an appearance like Figure 3.3.9(b), where the p*H*-independent reaction is very slow (no visible methylene bridge

cleavage from p*D* 0-7). Mechanistically, the hydrolysis at the methylene linker is most likely a S_N1-type process, considering the intermediate carbocation can be stabilised by the adjacent aromatic pyrimidine (Scheme 3.3.4).

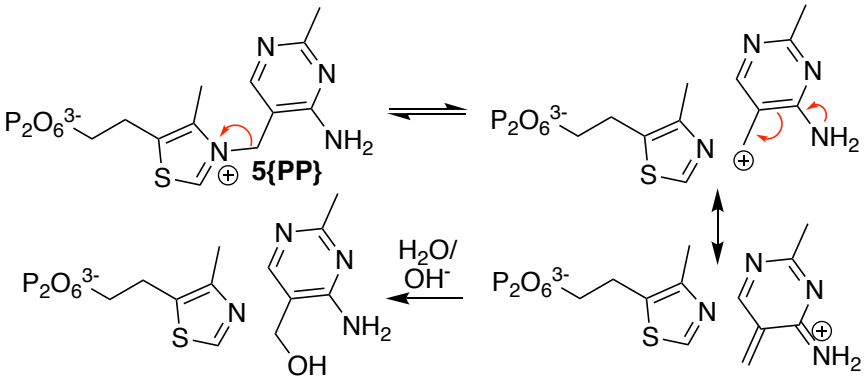

Scheme 3.3.4. Proposed mechanism for methylene linker cleavage of **5{PP}** at p*D* > 8: an S_N1 process is most likely due to the cation-stabilising propensity of the aromatic pyrimidinyl moiety.

3.3.4. Conclusion

This chapter has highlighted the investigations into the stability of thiamine pyrophosphate (**5{PP}**) in order to direct the purification of cofactor mimics outlined in Chapter 3.2. Phosphorus NMR spectroscopy was used as a powerful tool for kinetic tracking. Although T_1 values for substrates were determined, the unimolecular nature of hydrolysis meant that a shorter relaxation delay could be used to obtain meaningful kinetic analysis. It was found that under acidic conditions (p*D* < 3) the rate of hydrolysis increased however above 3-8 the hydrolysis was slow and constant. This is most likely a shift between an acid catalysed and uncatalysed process, as fitted in Figure 3.3.10. Above p*D* 8, the pyrophosphate group appeared very stable and so no base-catalysed region of +1 slope was observed; however, the cleavage of the central methylene linker became significant. These results also highlight that aqueous stock solutions of TPP (**5{PP}**) are best stored at p*H* 3-7 to minimise hydrolytic decomposition.

3.4. Evaluation of Proton Transfer at Azolium Ions

3.4.1. Foreword

This chapter discusses evaluation of the C(3)-H acidity of thiamine pyrophosphate (**5{PP}**) novel cofactors developed in Chapter 3.2. Initially, the background theory relevant to determination of the carbon acid pK_a values is presented. Subsequently, experimental determination of carbon acid pK_as for relevant compounds are discussed. This chapter lays the ground work for the catalytic evaluation of the novel cofactor mimic (**26{PP}**) as discussed in Chapter 3.5.

3.4.2. Introduction

As outlined in Chapter 1 and Chapter 3.1, common to all NHC-catalysed reactions is formation of a carbene via deprotonation of the parent azolium ion (Scheme 3.4.1). Knowledge of relative acidities of azolium ions is therefore essential for understanding their reactivities and catalytic potential. For deprotonation by water, the equilibrium may be described as an acid dissociation, with constant K_a (Equation 3.4.1), or more commonly expressed as pK_a (Equation 3.4.2).

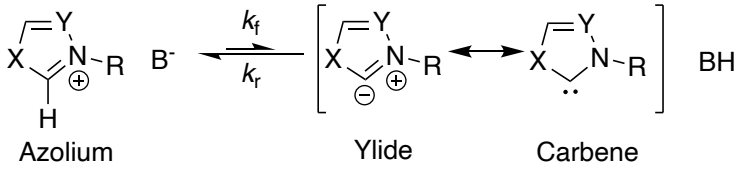

Scheme 3.4.1. Acid dissociation of azolium ions (X=S/N, Y=N/C-R) in the presence of base, when this base is water an acid dissociation constant, K_a, defines this equilibrium.

$$K_a = \frac{[Carbene][H_3O^+]}{[Azolium]} \qquad \textbf{Equation 3.4.1}$$

$$pK_a = -log_{10}K_a \qquad \textbf{Equation 3.4.2}$$

Approaches to determining carbon acid pK_a values for strong carbon acids attempt to observe equilibrium concentrations of acid and base in aqueous solution via spectrophotometric or potentiometric techniques.[205] Azolium ions are weak carbon acids and this equilibrium is therefore shifted heavily towards the acid with minimal conjugate base present, below detectable limits. An alternative approach is to use a kinetic approach instead of the thermodynamic approach described above. All equilibrium constants,

including the acid dissociation, K_a, can be expressed in terms of rate constants of forward (k_f, M s^{-1}) and reverse (k_r, s^{-1}) reactions (Equation 3.4.3).

$$K_a = \frac{k_f}{k_r} \qquad \textbf{Equation 3.4.3}$$

Typically for these weak carbon acids, the rate of the forward reaction is relatively slow and can be accessed by NMR spectroscopy. The value for k_f can be estimated as k_{ex}, the rate constant of exchange (Scheme 3.4.2).[206] Deprotonation of the carbon acid is considered as a pre-equilibrium, with equilibrium constant (K_1) and rate constants (k_1/k_{-1}), followed by solvent reorganisation, k_{reorg}. Both of which contribute to the rate of exchange (Scheme 3.4.2). The protonation of carbenes in aqueous solutions has previously been determined to be rapid and non-rate limiting.[207] Therefore, according to the principle of microscopic reversibility the overall rate constant for deuteration of carbene can be estimated as the rate constant for solvent reorganisation (~10^{11} s^{-1}).[207]

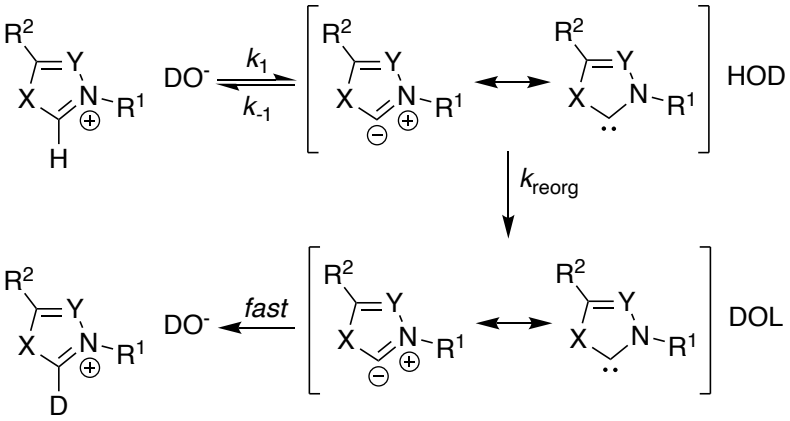

Scheme 3.4.2. Deuteroxide dependent H/D exchange of azolium ions (X=N/S, Y=N/C-R) shows a pre-equilibrium to form a carbene-HOD complex, followed by solvent reorganisation (k_{reorg}) and rapid re-protonation by DOL (L=H/D).

Assessing k_{ex} across a range of buffer p*D* values permits access to the second order rate constant for deuteroxide-catalysed exchange, k_{DO}, according to Equation 3.4.4. The solution phase basicity of deuteroxide is greater than that of hydroxide and therefore a correction much be applied to obtain k_{HO}. This is done by applying the secondary isotope relationship of k_{DO}/k_{HO} = 2.4. Finally, values of pK_a may be estimated according to Equation 3.4.5, where k_{HOH} is the rate of re-protonation by water, estimated as k_{reorg} (10^{11} s^{-1}) and K_W is the ionic product of water, $10^{-14.87}$ M^2 at 25 °C (pK_w = 14.87).

$$k_{ex} = k_{DO}[DO^-] \qquad \textbf{Equation 3.4.4}$$

$$pK_a = pK_W + log_{10}\left(\frac{k_{HOH}}{k_{HO}}\right) \qquad \textbf{Equation 3.4.5}$$

The first reported study of the kinetic acidity of heterocyclic azolium ions compared oxazolium (**141**), thiazolium (**142**) and imidazolium (**143**) ions at 38 °C (Figure 3.4.1).[208] It was found that oxazoliums were most acidic, followed by thiazoliums and then imidazoliums (larger values of k_{DO} imply greater acidity). Deprotonation is a thermodynamically unfavourable process and therefore the transition state is more carbene-like than conjugate acid, in keeping with Hammond's Postulate. The higher rate constant of H/D exchange of the oxazolium can be explained by destabilisation of the acid by the electron withdrawing oxygen atom. The differences between the thiazolium (**142**) and imidazolium (**143**) are not explained by the inductive effect, as the reduced electronegativity at sulphur would predict a smaller rate constant of H/D-exchange. Several studies have attempted to rationalise the observed trend, considering polarizability of the sulphur and also access to the sulphur 3d-orbital.[209] However, kinetic studies by Amyes *et al.* concluded that the imidazole-2-ylidene was actually more stable in aqueous solution than the corresponding thiazole-2-ylidene. Considering a thermodynamic cycle to model a 1,2-hydrogen shift at the carbene, the effect of changing X (X = S (**142**); X = NMe (**143**)) is the sum of the hydrogen shift from the neutral azole to the carbene and the protonation of the azole to the azolium (Figure 3.4.2). The differences in pK_as at carbon of 3.9 and at nitrogen of 4.7 give a difference in K_{azole}, the equilibrium constant between carbene and neutral azole, of -0.8. It is therefore concluded that the 3.9 pKa unit difference observed between thiazoliums (**142**) and imidazoliums (**143**) is due to the relative stabilities of the azolium ions in comparison to their neutral azoles, not the carbenes (Figure 3.4.2).[210]

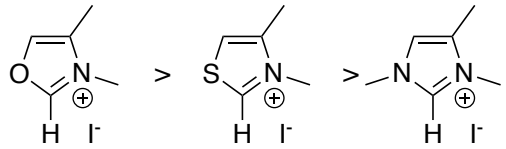

	141	**142**	**143**
k_{DO} (M^{-1} s^{-1})	3.8×10^7	3.7×10^5	1.3×10^2

Figure 3.4.1. Relative second order rate constants for deuteroxide dependent H/D exchange of three azolium ions.

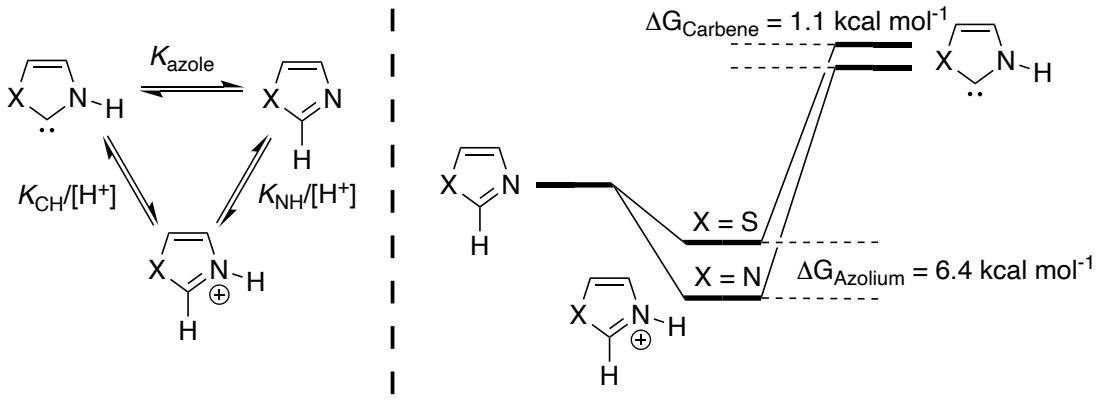

Figure 3.4.2. Left: Thermodynamic cycle used to determine K_{azole}, the equilibrium constant between neutral azoles and their carbenic tautomers, through knowledge of both the CH and NH pK_a values. Right: Relative energies of the azoles, azoliums and carbenes for thiazoliums (**142** (X=S)) and imidazoliums (**143** (X=NMe)) showing that it is the relative energies of the azoles and azoliums which determine the observed trend in k_{DO} in Figure 3.4.1.

Various studies have explored the carbon acid p*K*a of thiamine (**5**) and values of 12-19 have been reported. Of these, a value of ~18 reported by Washabaugh and Jencks, based on the kinetic approach briefly described above, is most reasonable.[204] H/D-exchange was monitored at 30 °C and constant ionic strength (I = 2 M, NaCl) in DCl, sodium acetate and sodium phosphate buffers. A plot of log(k_{obs}) against p*D* shows the expected first order dependence on deuteroxide above p*D* 0, with plateauing due to dependence on D_2O below 0, according to Equation 3.4.6 (Figure 3.4.3). The slight deviation from linearity for thiamine at p*D* ~ 5.5 is attributed to deprotonation of the pyrimidinyl N(1) position (pK_a ~ 5.5), reducing the rate of exchange due to a reduced inductive effect on the C(2)-H position.[204]

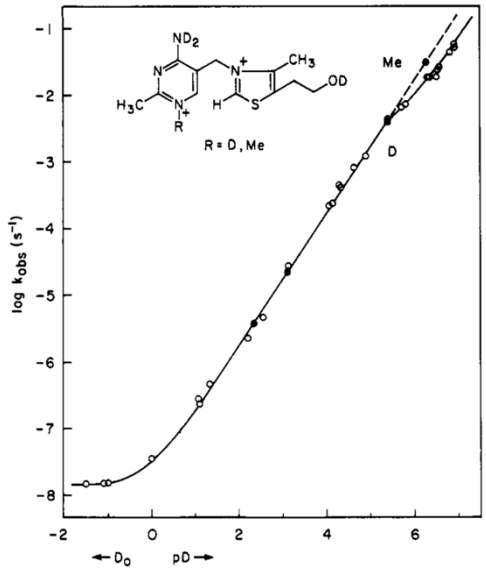

Figure 3.4.3. Logk_{Obs} vs p*D* plot for thiamine (**5**) from p*D* -2-6 shows typical first order dependence on deuteroxide above pD -1, with a levelling off due to D_2O dependent exchange at very low p*D* according to Equation 3.3.6. Above p*D* 5.5, the plot shifts from first order dependence due to deprotonation at the pyrimidine ring, this can be included in k_{Obs} as per Equation 3.3.7.

$$k_{obs} = k_{DO}[DO^-] + k_{H2O}$$ **Equation 3.4.6**

A range of thiazolium ion derivatives were also explored considering either deuteroxide or D_2O catalysed processes (slope of 1 or 0 respectively on a log(k_{obs})vs p*D* plot) showing excellent agreement between the two values of pK_a (Table 3.4.1).[204]

Table 3.4.1. Reported pK_a values for a selection of thiazolium ions including thiamine, by Jencks' and co-workers determined based on both the deuteroxide and D_2O dependent regions, showing excellent agreement.

Substrate	R^1	R^2	pK_a (D_2O)	pK_a (DO^-)
	Me	H	18.7	18.9
	CH_2Ph	H	-	18.2
	CH_2CN	H	16.9	16.9
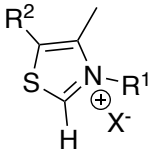	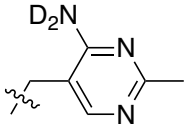	CH_2CH_2OD	-[a]	18.0
	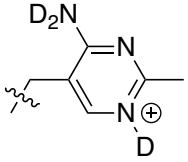	CH_2CH_2OD	17.7	17.6

[a]Determination of D_2O dependent H/D exchange requires values of pD < 0, at these values the pyrimidine ring is fully protonated (pKa ~ 5.5).

More recently, Massey *et al.* reported pK_a values for twenty 1,2,4-triazolium ions (**61**) using a similar approach as described above. Values for k_{ex} were measured at a range of p*D* values in deuterated buffers at a constant ionic strength (I = 1 M, KCl) at 25 °C. Determination of the second order rate constants for deuteroxide-catalysed exchange, k_{DO}, allowed for estimation of values of pK_a (Table 3.4.2).[76] Values for 1,2,4-triazolium ions are typically 1-2 units lower than those of thiazolium ions. This is typically explained by inclusion of another electron withdrawing nitrogen atom into the azolium structure. In considering the case of the oxazolium (**141**) versus the thiazolium (**142**) above, this destabilises the 1,2,4-triazolium to a greater extent, in comparison to the 1,2,4-triazolyl-3-ylidene. This work also clearly highlights the effect of changing the N-aryl substituent, with more electron withdrawing substituents further exacerbating the azolium instability in comparison to the deprotonated carbene.

Table 3.4.2. Summary of pK_a values for a series of 1,2,4-triazolium salts showing that an increase in the N-Ar electron withdrawing effect, signified by a larger Hammett-σ constant, leads to a higher acidity.[76]

Substrate	Ar	Hammett σ[a]	k_{DO} / $\times 10^7$ M^{-1} s^{-1}	pK_a
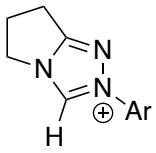 **61**	Ph	0	6.82	17.5
	4-$MeOC_6H_4$	-0.27	4.20	17.8
	Mesityl	-	5.29	17.6
	4-FC_6H_4	0.06	8.66	17.4
	4-CNC_6H_4	0.66	31.8	16.9
	C_6F_5	~1.50[b]	68.2	16.5

[a] Hammett-σ values obtained from Hansch and co-worksers.[70] [b]A Hammett-σ value for the pentafluorophenyl group is difficult to determine due to ortho-substituent effects. Values have been estimated from various spectroscopic data, including this value determined from observing changes in the carbonyl stretching frequency for a selection of esters.[211]

3.4.3. Previous Work

Previous work by Kevin Maduka led to the isolation of non-pyrophosphorylated 1,2,4-triazolium mimic (**26**) of thiamine (**5**) and explored H/D exchange at the C(3)-H position in a series of D_2O buffered solutions at 25 °C and I = 1 M (KCl). ^{1}H NMR spectroscopy was used to monitor the loss of the C(2/3)-H peak at ~9.9-9.5 ppm and this was used to determine pseudo first- and second-order rate constants. Manipulation of these rate constants allowed for estimation of the C(2/3)-H pK_a values according to Equation 3.4.5 (Table 3.4.3).

Table 3.4.3. Summary of C-H pK_a values determined for thiamine, 1,2,4-triazolium thiamine mimics and a reference tri-methyl triazolium from H/D exchange experiments by Kevin Maduka.

Substrate	R^1	R^2	X	k_{DO} / $\times 10^7$ M^{-1} s^{-1}	pK_a
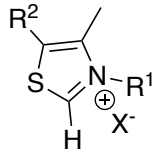	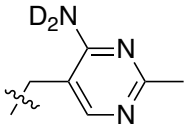	CH_2CH_2OD	Cl	3.01	18.9
		CH_2CH_2OD	NO_3^-	3.03	18.9
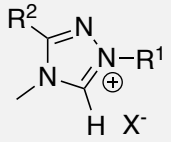	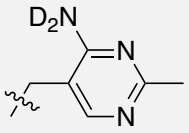 Me	CH_2CH_2OD	BF_4^-	85.8	17.4
		Me	BF_4^-	10.3	17.4
		$CH_2CH_2CH_2OD$	BF_4^-	77.7	17.5
		$CH_2CH(OD)CH_3$	BF_4^-	77.1	17.5
		Me	I^-	7.36	18.5

Values for C-H acidity of the 1,2,4-triazolium derivatives (thiamine mimics (**26**); trimethyl triazolium (**144**)) in comparison, thiamine (**5**) was ~ 1.5 units lower, highlighting the inherently greater acidity of the 1,2,4-triazolium scaffold. As discussed previously, this can be attributed to the much greater electron withdrawing effect of three

ring nitrogen atoms in comparison to the N/S of the thiazolium ring. The pK_a determined for thiamine (**5**) in this study was 18.9, in comparison to the value of 18.0 determined by Jencks; however, these studies were at different ionic strengths and temperatures with Jencks using 30 °C and I = 2 M (NaCl).

Interestingly the trimethyl triazolium (R^1=R^2=Me) (**144**) showed a 10-fold slower reactivity towards deuteroxide, reflected in a pK_a of 18.5. This suggests that the overall effect of the pyrimidinyl group is electron withdrawing, enhancing reactivity at the carbenic position. In fact, the 1,2,4-triazolium mimic has a similar C(3)-H pK_a to the N-phenyl triazolium in Table 3.4.2. This suggests that despite the CH_2 alkyl linker, it has the electron withdrawing characteristics of an N-aryl group owing to the dominating influence of the pyrimidinyl nitrogens.

3.4.4. Results and Discussion

Effect of Phosphorylation on C-H Acidity

All studies to date have explored the C-H acidity of thiamine (**5**) but there has been little exploration of the acidity of thiamine pyrophosphate (**5{PP}**). As the pyrophosphate group is essential for enzyme binding, it is important to explore the effect of this group on the overall acidity. It can be predicted that the anionic nature of the phosphate will increase electron density near the thiazolium, disfavouring deprotonation and increasing the carbon acid pK_a.

To evaluate the C(2)-H acidity of thiamine pyrophosphate (**5{PP}**), H/D exchange in a series of deuterated buffers (Table 3.4.4) was monitored at 25 °C and ionic strength, I = 1 M (KCl) by ^{1}H NMR spectroscopy (500 MHz) (Scheme 3.4.3). A tetramethyl-ammonium chloride (TMACl) internal standard was used in these cases in order to calculate fraction of substrate (F(S)). A representative set of NMR spectra are shown in Figure 3.4.4 at time intervals 1581 s, 36909 s and 85293 s for pD 3.80 showing decay of the C(2)-H peak at 9.65 ppm.

Table 3.4.4. Summary of the buffers used, the measured p*H* values and the corrected p*D* values for H/D exchange of thiamine pyrophosphate **5{PP}**.

Buffer	Concentration	Free Base / %	p*H* Measured	p*D* correction[a]
DCl	0.5	N/A	-0.04	0.36
	0.25		0.40	0.80
	0.1		0.66	1.06
	0.05		0.98	1.38
Potassium Formate	0.2	50	2.88	3.28
		90	3.57	3.97
Potassium Acetate	0.2	10	4.03	4.43
		50	4.50	4.90
		90	5.11	5.51

[a]The p*D* correction is determined as the value measured on the p*H* probe with a factor of 0.4 added.[201]

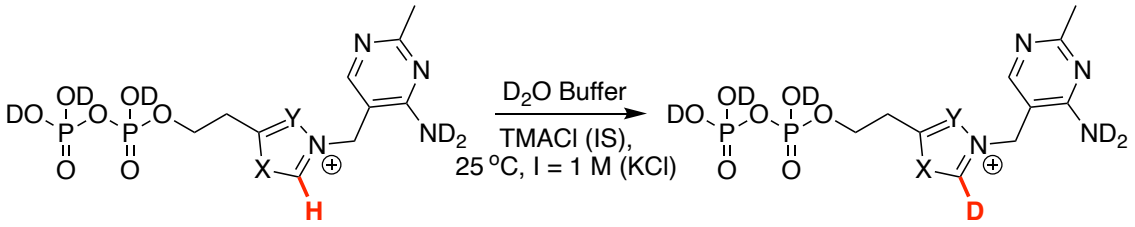

Scheme 3.4.3. H/D exchange reactions of thiamine pyrophosphate (**5{PP}**) and the triazolium mimic pyrophosphate (**26{PP}**) using D_2O buffers summarised in Table 3.4.4, monitored by ^{1}H NMR spectroscopy as shown in Figure 3.4.4 (TPP, **5{PP}**) and Figure 3.4.7 (**26{PP}**).

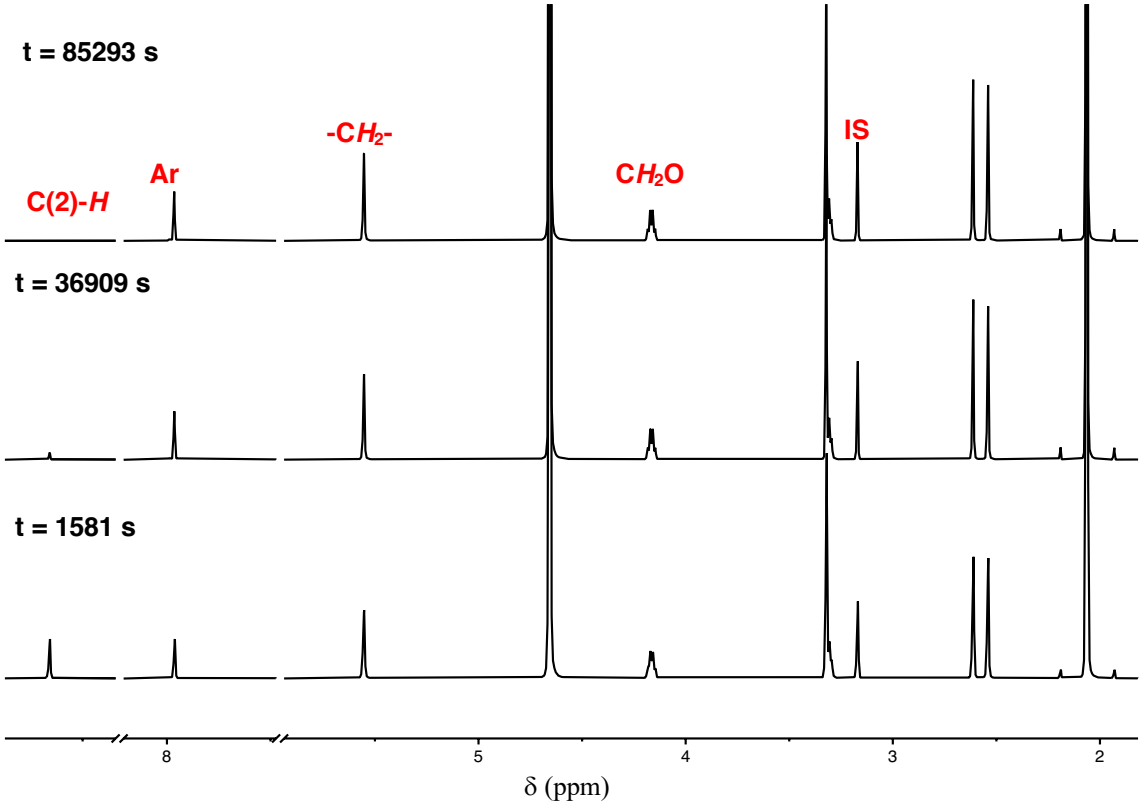

Figure 3.4.4. Representative ^{1}H NMR spectra for the H/D-exchange of the C(2)-H of TPP (**5{PP}**) in potassium acetate buffer (p*D* 3.81, I = 1 M (KCl)) at 25 °C.

Across the p*D* range of this experiment, the rate of decay of the C(2)-H integral (A_{CH}) was monitored in comparison to the tetramethylammonium chloride internal standard peak (A_{IS}) to determine a fraction of substrate (F(S)) (Equation 3.4.7). A plot of F(S) against time (Figure 3.4.5 for pD 3.80, see Appendix 7.3.1 for remaining plots) showed first order dependence (Equation 3.4.8) and thus a plot of ln{F(S)} against time yielded a straight line with gradient equal to k_{ex}, the rate of exchange (Equation 3.4.9, Figure 3.4.6). Values for k_{ex} at all p*D* values are summarised in Table 3.4.5.

$$F(S) = \frac{(A_{CH}/A_{IS})_t}{(A_{CH}/A_{IS})_0} \qquad \textbf{Equation 3.4.7}$$

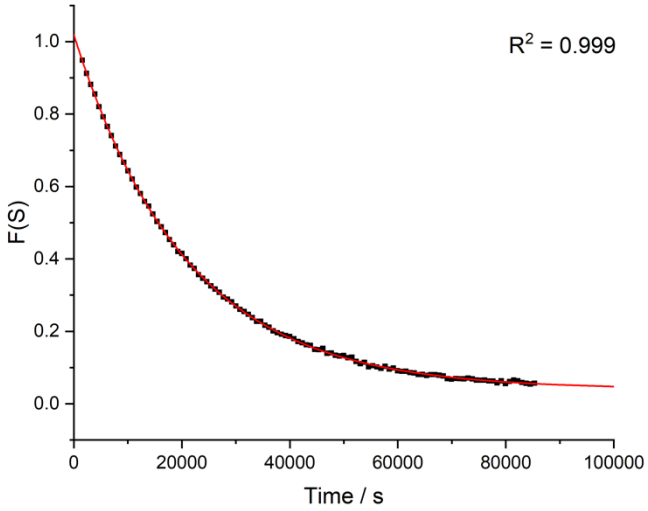

Figure 3.4.5. A representative plot of F(S) against time for the C(2)-H/D exchange for TPP (**5{PP}**) in potassium acetate buffer (p*D* 3.81, I = 1 M (KCl)) at 25 °C.

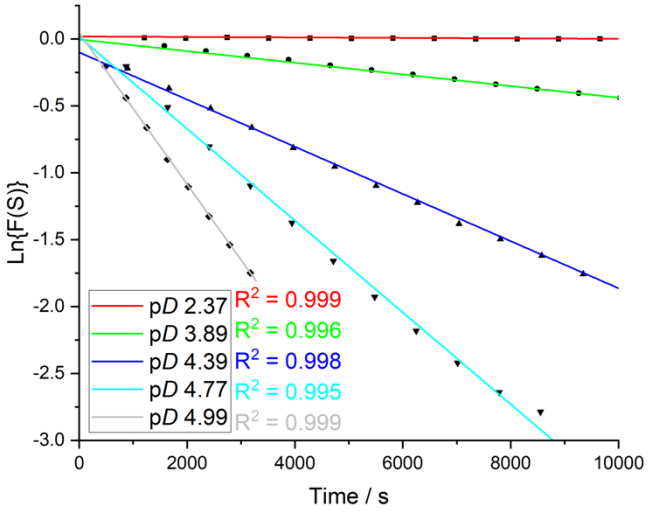

Figure 3.4.6. A representative selection of semilogarithmic plots of fraction of substrate against time for H/D-exchange of TPP (**5{PP}**) at a range of p*D* values using buffers summarised in Table 3.4.4.

$$F(S) = Exp(-k_{ex}t) \qquad \textbf{Equation 3.4.8}$$

$$Ln\{F(S)\} = -k_{ex}t + C \qquad \textbf{Equation 3.4.9}$$

Table 3.4.5. Summary of the rate constants for exchange, k_{ex}, determined as the gradient of plots of ln{F(S)} against time (Figure 3.4.6). Values for $t_{1/2}$ were determined according to Equation 3.4.10 as the half-life for a first-order process.

p*D*	k_{ex} /×10^{-6} s^{-1}	$t_{1/2}$ / h
2.37	1.68 ± 0.01	114
2.90	6.09 ± 0.01	31.6
3.73	35.2 ± 0.1	5.47
3.81	42.4 ± 0.1	4.55
3.89	61.7 ± 0.6	3.12
4.06	67.7 ± 0.5	2.84
4.39	180 ± 2	1.07
4.74	276 ± 5	0.700
4.77	355 ± 6	0.543
4.89	439 ± 10	0.438
4.99	559 ± 6	0.345

$$t_{\frac{1}{2}} = \frac{\ln(2)}{k_{ex}} \qquad \textbf{Equation 3.4.9}$$

Owing to the complexity in synthesis of the 1,2,4-triazolium pyrophosphate mimic (**26{PP}**) of thiamine pyrophosphate (**5{PP}**) and the resulting limited availability of material, H/D-exchange at only a handful of p*D* values was explored. A representative

set of NMR-spectra for this exchange are shown in Figure 3.4.7, in which the C(3)-H peak can be seen to decrease in size. In this case, the material used was not pure and a mixture of monophosphate (**26{P}**) and pyrophosphate (**26{PP}**) are present; however, peaks for the pyrophosphate were resolvable and estimates of H/D exchange could be determined.

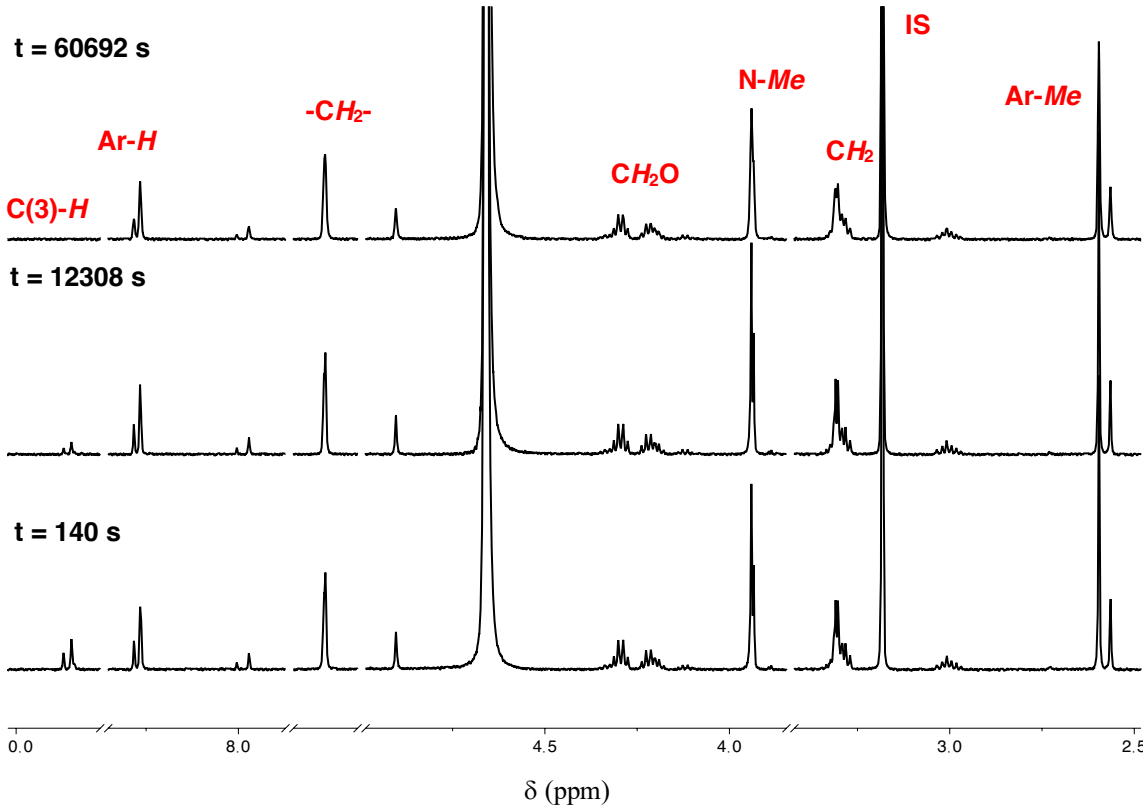

Figure 3.4.7. Representative ^{1}H NMR spectra for the H/D-exchange of the C(3)-H of **26{PP}** in potassium acetate buffer (p*D* 3.70, I = 1 M (KCl)) at 25 °C. Decay over time of the peak at 9.85 ppm was monitored and a plot of this decay is shown in Figure 3.4.5.

As with TPP (**5{PP}**) a plot of C(3)-H decay for **26{PP}** as a fraction of substrate (F(S)) against time displays first-order exponential decay and a plot of the natural logarithm (ln{F(S)}) against time gives a straight line with gradient equal to the rate of exchange, k_{ex} (Figure 3.4.8; Figure 3.4.9). Table 3.4.6 summarises the values determined for k_{ex} at the p*D* values explored alongside $t_{1/2}$ values.

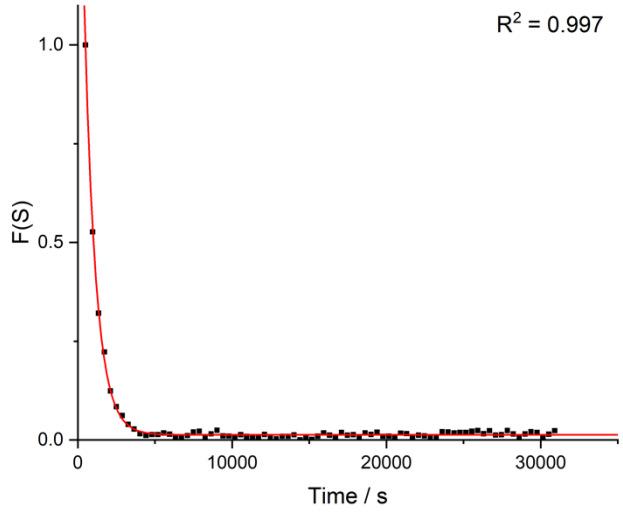

Figure 3.4.8. A representative plot of F(S) against time for the C(3)-H/D exchange for (**26{PP}**) in potassium acetate buffer (p*D* 3.81, I = 1 M (KCl)) at 25 °C.

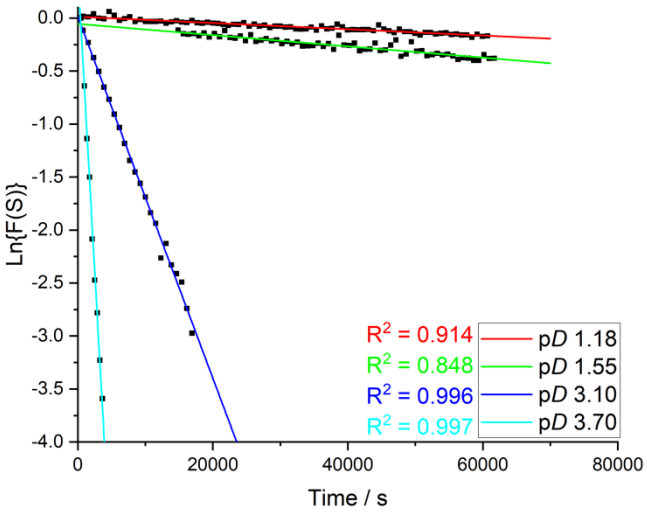

Figure 3.4.9. A selection of plots of the natural logarithm of fraction of substrate (ln{F(S)}) against time for H/D-exchange of **26{PP}** at a range of p*D* values shown using buffers summarised in Table 3.4.6.

Table 3.4.6. Summary of the rate constants for exchange, k_{ex}, determined as the gradient of plots of ln{F(S)} against time for **26{PP}** (Figure 3.4.6). Values for $t_{1/2}$ were determined according to Equation 3.4.10 as the half-life for a first-order process.

p*D*	k_{ex} /×10^{-6} s^{-1}	$t_{1/2}$ / h
1.18	2.96 ± 0.1	65
1.55	5.31 ± 0.3	36.3
3.10	17.0 ± 0.02	11.3
3.70	112 ± 3	1.72

As in Chapter 3.3, p*D*-rate profiles can be constructed by plotting p*D* against log(k_{ex}) to infer mechanistic characteristics of H/D exchange at **5{PP}** and **26{PP}**. In the case of

the previously discussed pyrophosphate hydrolysis, a slope of -1 and 0 were fit to acid catalysed and uncatalyzed processes (Figure 3.4.10). In this case, only slopes of +1 (0.97/1.01) are observed, characteristic of a deuteroxide catalysed exchange process (Equation 3.4.4). As a base-catalysed process, second-order rate constants for deuteroxide catalysed exchange can be determined according to Equation 3.4.4 (Figure 3.4.11). Values for k_{DO} can be estimated as the slope of these plots and manipulated to determine a value for k_{HO} through the isotopic relationship $k_{DO}/k_{HO} = 2.4$. Using Equation 3.4.5 and an estimate of $k_{HOH} = k_{reorg} \sim 10^{11}$ s^{-1} as previously discussed allows estimates for pK_a to be determined (Table 3.4.7).

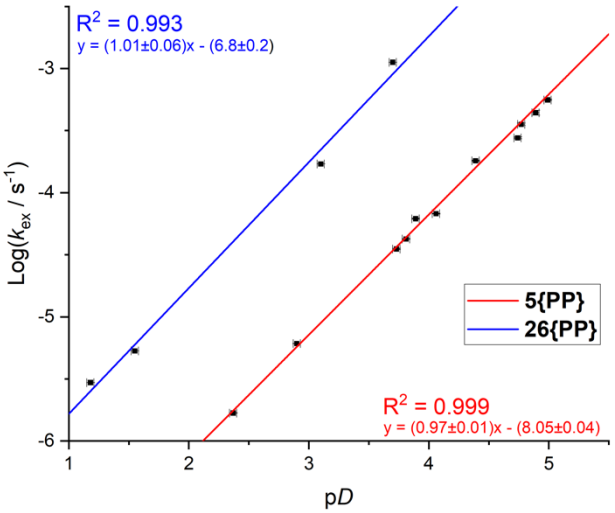

Figure 3.4.10. p*D*-Rate profiles for the H/D-exchange at the C(2/3)-H positions of TPP(**5{PP}**), red, and **26{PP}**, blue, showing the expected gradient for a process with first-order dependence on deuteroxide (+1). There is an increase in log(k_{ex}) of ~ 1 for **26{PP}** at a given p*D* highlighting an ~10-fold increase in k_{ex}.

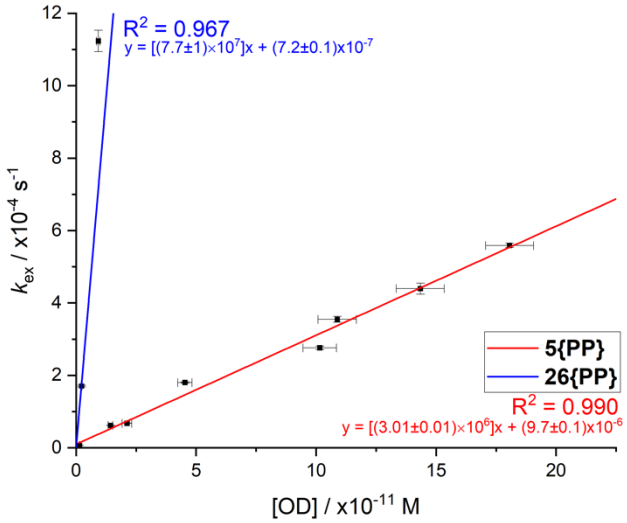

Figure 3.4.11. Determination of the pseudo-second order rate constant for deuteroxide catalysed exchange through plotting k_{ex} vs [DO^-] across the p*D* range for TPP (**5{PP}**), red, and **26{PP}**, blue.

Table 3.4.7. Summary of pK_a values for TPP (**5{PP}**) and the mimic pyrophosphate (**26{PP}**) highlighting an increase of ~1 pK_a unit when a pyrophosphate group is introduced.

Compound	k_{DO} / ×10^6 M^{-1} s^{-1}	k_{HO} / ×10^6 M^{-1} s^{-1}	pK_a
5{PP}	3.01 ± 0.01	1.25 ± 0.04	19.8
26{PP}	77 ± 10	32 ± 4	18.4 ± 0.1
5	*30.1*	-	*18.9*
26	*858*	-	*17.4*

A pK_a of 19.8 for TPP (**5{PP}**) reflects an ~ 10-fold drop in C(2)-H acidity compared to non-pyrophosphorylated thiamine (**5**). This can be attributed to the increased electron density provided by the pyrophosphate group, which is likely in its mono-anionic form at the p*D* values explored. Moreover, at the p*D* values explored in this study, it is likely that the pyrimidinyl group is protonated (pK_a ~ 5.5)[204]. Previous studies on thiamine (**5**) showed ~0.4 pK_a unit increase in acidity when the pyrimidine ring is protonated. Therefore, under physiological conditions (p*H* ~ 7) it is likely that the pK_a value for thiamine shifts to slightly over 20. The pK_a value determined for **26{PP}** of 18.4 also reflects a similar drop in magnitude.

Previous studies on the C(2)-H acidity of thiamine pyrophosphate (**5{PP}**) are limited however the lability has been assessed through H/D-exchange at both 38 °C and 28 °C. In these studies, no assessment of the second order rate constants for deuteroxide catalysed exchange, or pK_a estimations are determined; however, half-lives for exchange at various buffer p*D*s are determined. Crevat *et al*. reported a half-life of 23 mins at p*D*

4.44, corresponding to a rate of exchange of ~5×10^{-4} s^{-1}.[212] This is of a similar order of magnitude to our reported value for k_{ex} = 1.8×10^{-4} s^{-1} ($t_{1/2}$ ~ 1 h) under slightly different experimental conditions (25 °C and I = 1 M for our studies; 28 °C and 38 °C with no specified ionic strength for previous studies).[212] Moreover, this work also notes ~10-fold decrease in half-life from TPP (**5{PP}**) to thiamine (**5**), as observed in this evaluation of the C(2)-H pK_a value.

Importantly this work reflects the successful synthesis of a more acidic mimic of TPP in development of **26{PP}**. It is hoped this increased acidity will be reflected in studies as a catalyst and as a cofactor in classic NHC-catalysed and TPP-dependent transformations.

N-Aryl Thiamine Mimics

Alongside thiamine pyrophosphate (**5{PP}**) and the mimic pyrophosphate (**26{PP}**) exploration of an N-phenyl thiamine mimic (**27b**) was also explored (Scheme 3.4.4). The C(5)-propyl linked compound, isolated from the starting 5-membered lactone, was most readily accessible and studied in greater detail. Hydrogen-deuterium exchange was explored as per the conditions discussed above, albeit at fewer values of p*D*. A representative set of spectra at t= 455 s, 3143 s and 17351 s for H/D exchange at p*D* 3.26 are shown in Figure 3.4.12, with the C(3)-H peak highlighted at 10.1 ppm.

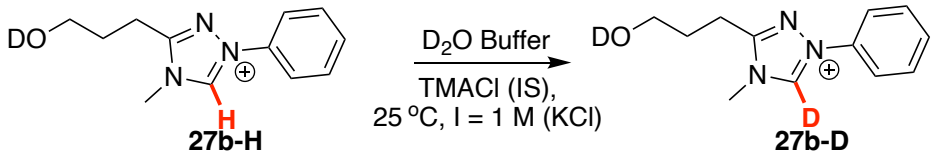

Scheme 3.4.4. H/D exchange reactions of N-Ph thiamine mimic (**27b**) using D_2O buffers summarised in Table 3.4.4, monitored by ^1H NMR spectroscopy as shown in Figure 3.4.12.

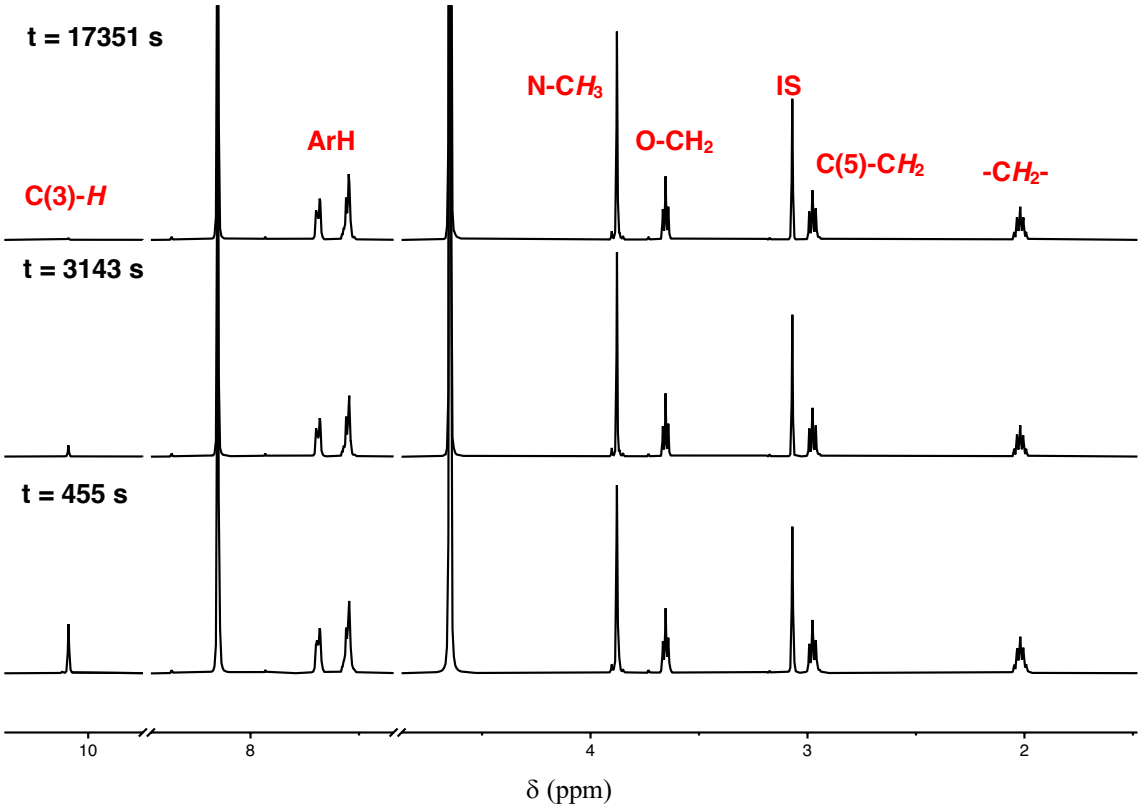

Figure 3.4.12. Representative ^{1}H NMR spectra for the H/D-exchange of the C(3)-H of **27b** in potassium acetate buffer (p*D* 4.05, I = 1 M (KCl)) at 25 °C.

Fraction of substrate was determined as per previous studies (Equation 3.4.7). C(3)-H/D-Exchange again displayed first-order kinetic characteristics (Figure 3.4.13) and plotting the natural logarithm of fraction of substrate against time gave a linear plot with gradient equal to -k_{ex} (Figure 3.4.14). Table 3.4.8 summarises values for k_{ex} and half-lives for H/D exchange determined using Equation 3.4.9.

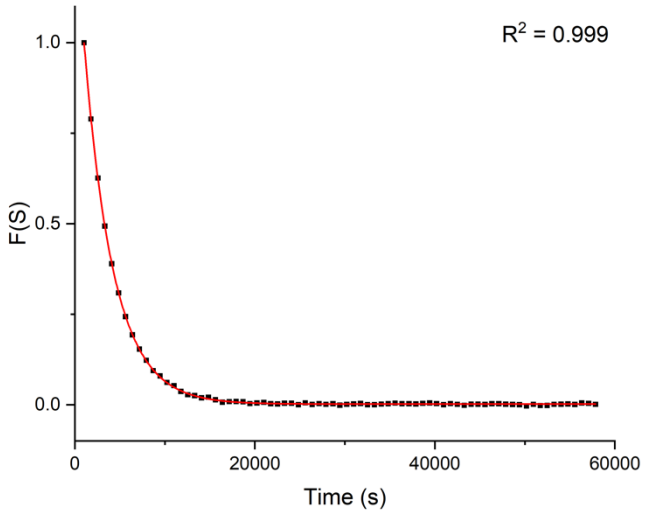

Figure 3.4.13. A representative plot of F(S) against time for the C(3)-H/D exchange for (**27b**) in potassium acetate buffer (p*D* 3.81, I = 1 M (KCl)) at 25 °C.

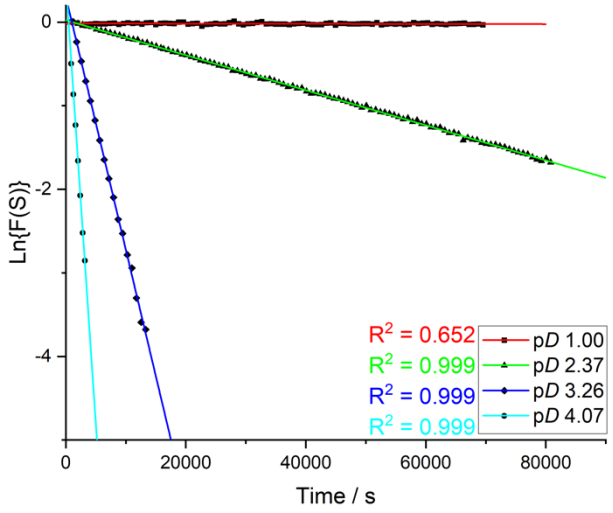

Figure 3.4.14. Plots of the natural logarithm of fraction of substrate (ln{F(S)}) against time for H/D-exchange of **27b** at a range of p*D* values shown using buffers summarised in Table 3.4.8.

Table 3.4.8. Summary of the rate constants for exchange, k_{ex}, determined as the gradient of plots of ln{F(S)} against time for **27b** (Figure 3.4.6). Values for $t_{1/2}$ were determined according to Equation 3.4.10 as the half-life for a first-order process.

p*D*	k_{ex} / $\times 10^{-6}$ s^{-1}	$t_{1/2}$ / h
1.00	1.08 ± 0.06	178
2.30	21.0 ± 0.1	9.18
3.26	303 ± 2	0.64
4.05	1040 ± 10	0.19
4.07	1060 ± 10	0.18

A p*D*-rate plot shows a slope of +1 (+1.3±0.2) highlighting first-order dependence on deuteroxide. A second-order rate constant for deuteroxide catalysed reaction can be determined as k_{DO} = 4.74 $\times 10^{7}$ M^{-1} s^{-1} highlighting an order of magnitude increase in comparison to thiamine pyrophosphate (**5{PP}**). Further manipulation of this value to obtain k_{HO} and estimation of k_{HOH} as k_{reorg} allows prediction of the pK_a = 18.6 ± 0.1.

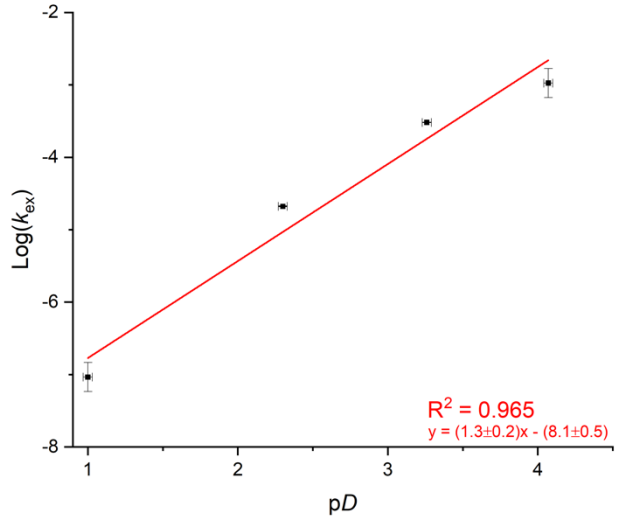

Figure 3.4.15. p*D*-Rate profile for the H/D-exchange at the C(/3)-H position of **27b** showing the expected gradient for a process with first-order dependence on deuteroxide (+1).

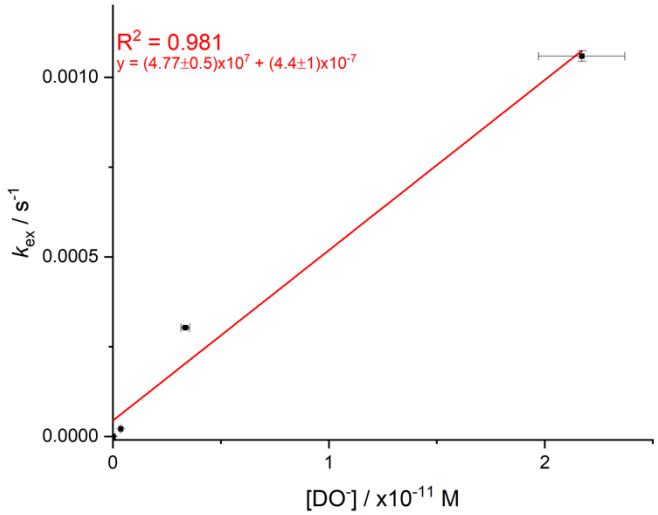

Figure 3.4.16. Determination of the pseudo-second order rate constant for deuteroxide catalysed exchange through plotting k_{ex} vs [DO$^-$] across the p*D* range for **27b**.

The pK_a value estimation of 18.6 is higher than anticipated for a non-pyrophosphorylated 1,2,4-triazolium mimic. It should be noted that to accurately predict the pK_a values a significant number of points on these plots are still needed. Although more acidic than thiamine pyrophosphate (**5{PP}**), as would be predicted considering the reduction in electron density, it is only marginally more acidic than thiamine (**5**). In comparison to the 1,2,4-triazolium mimic (**26{PP}**), the N-Ph triazolium is ~1 unit higher in pK_a. This change highlights the electron withdrawing nature of the pyrimidine ring, which appears to behave more like an electron withdrawing aromatic than a benzyl group. In considering other N-phenyl substituted 1,2,4-triazoliums, it would be anticipated that the C(3)-H pK_a

would be ~ 17.5. Work in our group has highlighted the importance of ring strain on the C(3)-H acidity of a range of 1,2,4-triazoliums. As the fused ring size is increased, the C(3)-H acidity decreases for a given N-aryl substituent (Figure 3.4.7). This has been attributed to small increases in the N-C-N bond angle with increasing ring size for both the acid and subsequent carbene. With regards to the carbene the drop in acidity can therefore be attributed to increased p-orbital character (or decreased s-orbital character) when considering a hybridisation model of bonding.[71] Negative charges experience greater stabilisation from orbitals of s-character which penetrate more closely to the positively charged nucleus. In the case of the N-aryl mimic (**27b**) pK_a value, there is a significantly greater increase in acidity in comparison to the small shifts observed in Figure 3.4.17 but, this trend goes some way to explaining the pK_a determined.

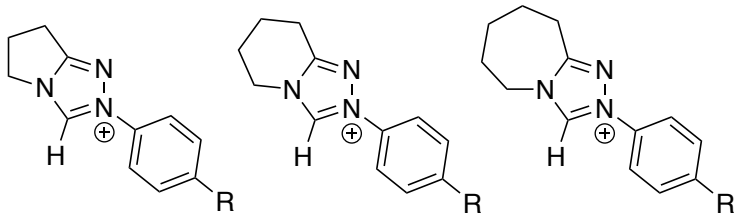

Figure 3.4.17. Effect of fused ring size on the C(3)-H of fused ring 1,2,4-triazolium ions: increasing ring size decreases the acidity.

It should be noted that the purpose of the N-aryl mimic (**27**) synthetic development is to allow application of previously developed fundamental knowledge of 1,2,4-triazolium catalysis to this new field. So, although the N-Ph catalyst is of interest, more interesting catalysts will include pentafluorophenyl or 2-substituted aromatics, which have been found to vastly improve the acidity and catalytic activity of NHC organocatalysts.

3.4.5. Conclusions

The C-H acidity of thiamine pyrophosphate (**5{PP}**) has been determined, complementing the previous studies on both non-phosphorylated thiamine (**5**) and the novel 1,2,4-triazolium mimic (**26**). As would be anticipated, the increase in electron density provided by the anionic pyrophosphate groups, increases the observed pK_a by ~1.5 units. The novel 1,2,4-triazolium mimic (**26{PP}**) was also explored at a smaller range of pD values and a more rough estimate for pK_a of 18.4 shows a similar trend. It should be noted these values are for aqueous conditions and enzyme active sites exclude water. As such the true pK_a values at the active site will differ by several orders of

magnitude. Nevertheless, the observed trends are expected to be maintained in different phases.

Interestingly, the N-Ph triazolium mimic (**27b**) explored in this case had a significantly higher pK_a value than anticipated. This ideally requires further study but, could be attributed to the effect of fused-rings compared to this N-Me compound. Importantly, it highlights the intriguing effect of the pyrimidinyl group in thiamine. Which, despite being connected via a CH_2 linker, results in a higher acidity than the N-phenyl mimic. This can be attributed to the highly electron withdrawing nature of the pyrimidinyl nitrogens.

3.4. Catalytic Evaluation of Cofactor Mimics

3.4.1. Foreword

This chapter describes the evaluation of the developed 1,2,4-triazolium cofactor mimic (**26{PP}**) in a series of organocatalytic and biocatalytic experiments, compared to thiamine (**5{PP}**). Initial experiments explored classic NHC-organocatalysed benzoin condensations without enzyme. The synthetic challenges of isolating sufficient quantities of the pyrophosphorylated 1,2,4-triazolium mimic (**26{PP}**) limited enzyme studies. Once significant quantities were isolated, evaluation of cofactor compatibility with commercially available TPP-dependent enzymes (pyruvate decarboxylase and pyruvate oxidase) was explored. Native enzymatic reactions were initially explored using spectrophotometric analysis with coupled assays. Subsequent exploration of a non-native biocatalytic transformation was explored, monitoring by NMR spectroscopy. It should be noted that this chapter highlights only the initial studies of the novel cofactor and significant further work will be required to truly evaluate this cofactor.

3.4.2. Introduction

Mechanistic Analysis of NHC Catalysed Transformations

The evaluation of new NHC-organocatalysts typically explores their efficacy in model carbon-carbon bond forming benzoin (**148**) reactions (Scheme 3.4.1). This reaction has been extensively studied back to the work of Wohler and Leibig, reporting the cyanide ion catalysed reaction.[213] Subsequent work by Ukai and coworkers reported the thiazolium catalysed reaction; however, it was the work of Ronald Breslow, a renowned physical organic chemist, which determined the mechanism. Pre-catalyst deprotonation to the active NHC followed by addition to an aldehyde forms the initial hydroxyaryl adduct (**145**). Subsequent deprotonation forms an enaminol intermediate (**146**), also referred to as the Breslow intermediate, which can react with another molecule of aldehyde forming a second adduct (**147**).[156, 214] Finally, benzoin (**148**) is released, reforming the NHC catalyst. It is thought that the majority of NHC-catalysed reactions proceed through these intermediates and this has been extrapolated to the role of thiamine in TPP-dependent enzymes.

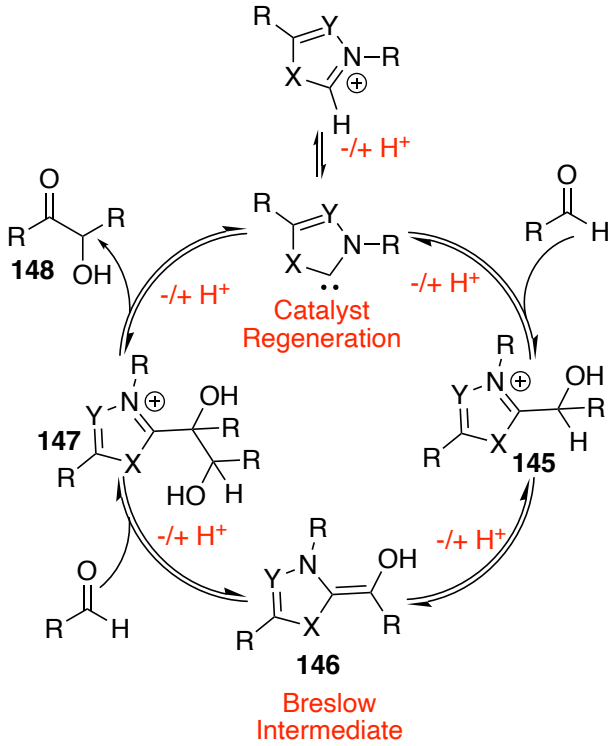

Scheme 3.4.1. The catalytic cycle for the benzoin condensation: initial pre-catalyst deprotonation gives the carbene, which reacts with an aldehyde forming the hydroxyaryl adduct (**145**); deprotonation of this adduct (**145**) yields an enaminol intermediate often referred to as the Breslow intermediate (**146**) which attacks another molecule of aldehyde to form the second adduct (**146**) and finally releases benzoin (**148**).

Since the proposal of this mechanism, work has been undertaken to find evidence for the Breslow intermediate (**146**) through isolation or other kinetic studies. Computational studies by Houk and other parties have provided *ab initio* evidence for the Breslow intermediate and also predicted the experimentally observed product outcomes.[164, 215-217] Mechanistic studies have focussed on isolation of Breslow intermediates with Rovis and Mayr respectively reporting the isolation of O/N-methylated analogues (**149**/**146{OMe}**) from 1,2,4-triazolium ions (Figure 3.4.1).[218, 219] Berkessel independently reported the isolation and characterisation of Breslow intermediates from imidazolyl, imidazolinyl and thiazolyl-derived (**146a**) NHCs; however, to date, there has been no reported isolation of unmodified 1,2,4-triazolium derived Breslow intermediates.[220-223]

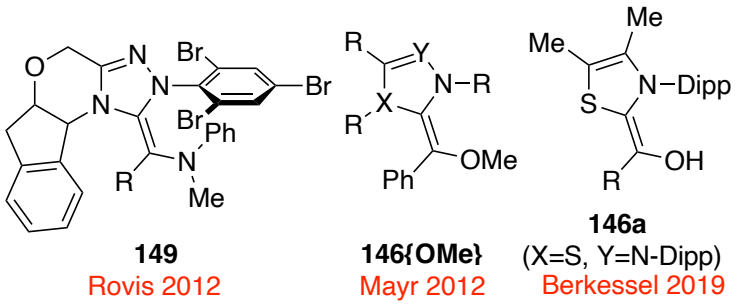

Figure 3.4.1. Isolated Breslow-type intermediates of 1,2,4-triazoliums and thiazoliums. To date there has been no reported isolation of unmodified 1,2,4-triazolium derived Breslow intermediates.

NHCs do not just catalyse the benzoin condensation and have been explored in a variety of more complex transformations. These include Stetter reactions between an aldehyde and Michael acceptor, the hydroacylation of unactivated alkenes and aldehyde C-H arylation (Scheme 3.4.2). Importantly, it has been found that the scope of transformations available to 1,2,4-triazolium NHCs in comparison to their thiazolium counterparts is vastly improved. This highlights a key motivator for this project in attempting to introduce new-to-nature chemistry to biocatalytic transformations.

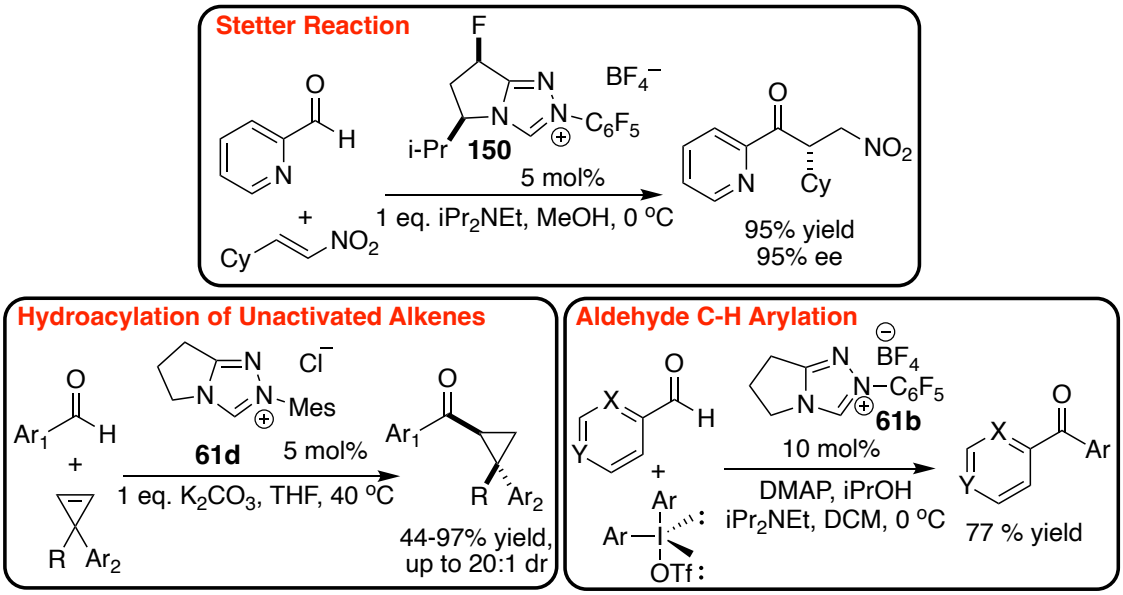

Scheme 3.4.2. Beyond the benzoin condensation: key NHC catalysed processes. All proceed to greater yields and selectivities when catalysed by 1,2,4-triazolium ions.

Work in our group has focussed particularly on the kinetic evaluation of 1,2,4-triazolium ions in model benzoin and Stetter reactions.[6, 9] A series of 1,2,4-triazolium-aldehyde adducts (**145{OMe}a** (X=N-R, Y=N)) were isolated and shown to form reversibly. Kinetic evaluation of the C(α)-H acidity through H/D-exchange gave information on the structural effects of catalysts and aldehydes on Breslow intermediate formation (Scheme 3.4.3). Moreover, the stoichiometric analysis of adduct formation allowed for determination of rate constants for adduct formation and for decay back to the pre-catalyst.[6, 9]

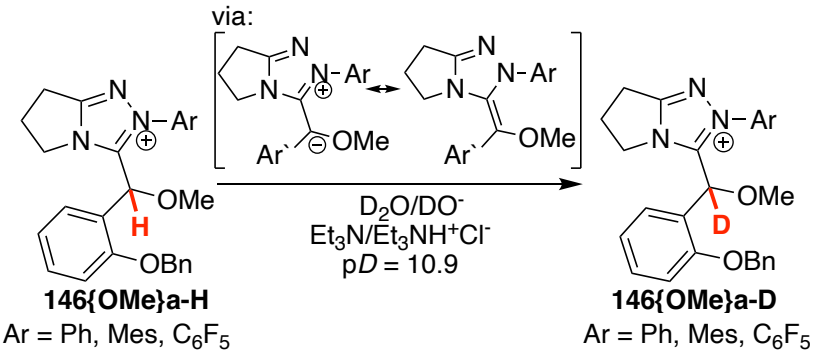

Scheme 3.4.3. H/D-exchange reactions on hydroxyaryl adducts (**146{OMe}**), highlighting the enhanced C(α) acidity and providing evidence for Breslow intermediates.

Detailed mechanistic analysis of the overall benzoin and Stetter reactions is challenging owing to changes in reaction order dependent on the concentration of benzaldehyde, catalyst decomposition over time and the changes in concentration of base over time due to side reaction to form benzoic acid. Similar problems often occur with enzymatic reactions and an initial rate method can be employed to circumvent these issues. Leeper and co-workers were first to demonstrate this with a thiazolium ion (**151**) catalysed benzoin condensation, determining a first order dependence on [PhCHO] and a pseudo-first order rate constant, $k_{cat} = 6 \times 10^{-6}$ s^{-1} (Figure 3.4.2).[224]

Our group recently repeated this analysis for a selection of 1,2,4-triazolium ion catalysts (**61**), showing initial first-order dependence on [PhCHO] moving to zeroth-order at higher [PhCHO] (Figure 3.4.2). This data could be fit to a steady-state rate equation to infer rate constants for product formation (k_p) and Breslow intermediate formation (k_{BI}) (Equation 3.5.1). Moreover, changes in v_{max} could be plotted against N-aryl substituent Hammett σ-values, showing an excellent fit ($R^2 = 0.998$) and a ρ-value of 1.66. This value sits firmly between reference values of 1.44 for the acid dissociation of benzoic acids in methanol and 3.32 for the acid dissociation of protonated anilines. This provides evidence for a significant increase in electron density on N(2) of the triazolium after adduct deprotonation and is further evidence for the Breslow intermediate.[160]

$$v = \frac{k_P v_{max}[PhCHO]}{k_{-BI} + k_P[PhCHO]} = \frac{k_P k_{BI}[Cat.][PhCHO]}{k_{-BI} + k_P[PhCHO]} \quad \textbf{Equation 3.5.1}$$

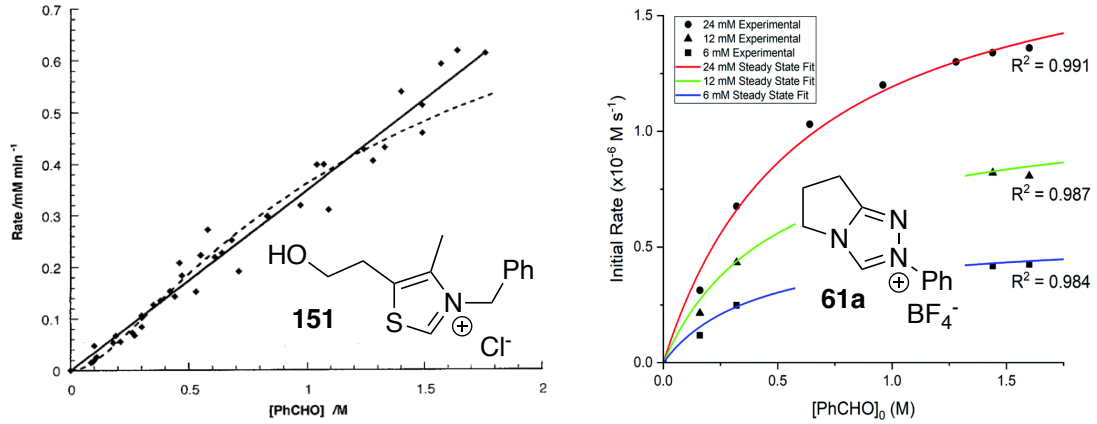

Figure 3.4.2. Left: Initial rates plots of the thiazolium (**151**) catalysed benzoin condensation shows linear dependence across the full range. Graph reproduced with permission from Ref. 224; Right: Initial rates plots of the 1,2,4-triazolium (**61**) catalysed benzoin condensation shows a change in reaction order (plateau) over the 0-1.5 M benzaldehyde range.

Kinetic Analysis of Enzymatic Transformations

Enzymatic transformations are thought to proceed through 4 key processes: enzyme-substrate binding, defined by a dissociation constant, K_d; substrate activation due to conformational change of the protein; reaction to product, typically involving a cofactor such as TPP (**5{PP}**) or NADH (**80{H}**); and enzyme-product separation, with a separate $K_d^{(P)}$ (Figure 3.4.3). Enzyme kinetics are typically studied under an initial rates regime, where only the first 10% of reaction conversion is monitored at various substrate concentrations. This has various benefits in that catalyst degradation, changes in conditions (such as p*H*) and, importantly, product inhibition on substrate consumption are suppressed (Figure 3.4.3). Moreover, as all enzymatic reactions are reversible, monitoring to 10% reaction allows these reverse reactions to be ignored as product concentrations are so low. Key to the kinetic analysis of enzymatic reactions is the Michaelis-Menten Equation (Equation 3.5.2).[225] This treats the formation of an enzyme-substrate complex as an equilibrium process and allows for the steady-state assumptions to be applied as for Equation 3.5.1 above.

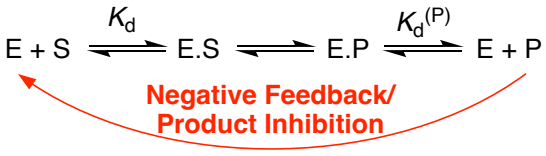

Figure 3.4.3. Typical enzyme catalysed reactions, for which Michaelis-Menten kinetics are based, considers enzyme-substrate binding, reaction and then enzyme-product dissociation. Initial rates studies are used to monitor reactions to minimise the effects of product inhibition.

Application of steady-state analysis through the Michaelis-Menten equation (Equation 3.5.2) allows for extrapolation of two kinetic parameters: ν_{max}, the maximum rate for a given enzyme concentration; K_M, the Michaelis-Menten constant, formally defined as the

substrate concentration at half of v_{max}. K_M can be more readily related to the key steps in enzymatic transformations (Figure 3.4.3) according to Equation 3.5.3, where k_a and k_d are the rate constants for substrate association and dissociation (with dissociation constant K_D (Equation 3.5.4)), respectively, and k_{cat} is the rate of product formation. These parameters are used to describe enzymatic processes and extrapolate mechanistic features.

$$v = \frac{v_{max}[S]}{K_M + [S]} \qquad \textbf{Equation 3.5.2}$$

$$K_M = \frac{k_a + k_{cat}}{k_d} \qquad \textbf{Equation 3.5.3}$$

$$K_d = \frac{k_a}{k_d} \qquad \textbf{Equation 3.5.4}$$

Significant work has been undertaken to determine the mechanistic role of thiamine pyrophosphate (**5{PP}**) in TPP-dependent enzymes. TPP (**5{PP}**) is a 'true' catalyst, in the sense that many cofactors behave as co-reactants instead (e.g. NADH (**80{H}**) is consumed and must be reformed). As a heterocyclic azolium ion, thiamine (**5{PP}**) has enhanced C(2)-H acidity (estimates from our work give a pK_a of 19.8, see Chapter 3.4) and therefore can be deprotonated to form a carbene and subsequently form an acyl anion intermediate similar to the Breslow intermediate. From here, various enzymatic reactions can yield protonation (as is the case for pyruvate decarboxylase), oxidation (as is the case for pyruvate oxidase), carboligation (as is the case for benzaldehyde lyases) and other reactions. Although TPP alone could carry out these transformations, reactions would be significantly slower with no inherent selectivity for specific products, diastereomers or enantiomers. Moreover, the vast majority of these conversions would require non-physiological conditions such as strongly acidic or basic conditions for appreciable turnover without the presence of an enzyme.[226]

TPP-Dependent Enzymes in Biocatalysis

Chapter 3.1 highlights briefly some applications of TPP-dependent enzymes in biocatalysis. Benzoin and Stetter reactions have been explored in significant detail as the key reactions used to evaluate NHC organocatalysts. As such, direct comparisons between biocatalytic and organocatalytic transformations can be made. A range of other carbon-carbon bond forming biocatalytic transformations have been explored with TPP-

dependent enzymes. Significant contributions from Martina Pohl and co-workers not only developed the enzymatically catalysed benzoin and Stetter reactions but have further explored alternative carboligation reactions. Pyruvate decarboxylases have not been extensively explored as biocatalysts largely owing to a high specificity for substrate, pyruvate. Recently, pyruvate decarboxylase from *Acetobacter pasteurianus* (*Ap*PDC) has been shown to catalyse the formation of (*S*)-phenylacetylcarbinol (**152**) ((*S*)-PAC), a valuable intermediate in the pharmaceutical industry (Scheme 3.4.4).[227] The key benefits of this approach are that acetaldehyde is generated *in situ* as an enaminol-type intermediate, after decarboxylation of pyruvate. This avoids the need to handle highly reactive, and toxic acetaldehyde. Moreover, through a process of mutagenesis, the *Ap*PDC could be modified to enhance stereoselectivity to obtain the high *ee*s required for the pharmaceutical industry.

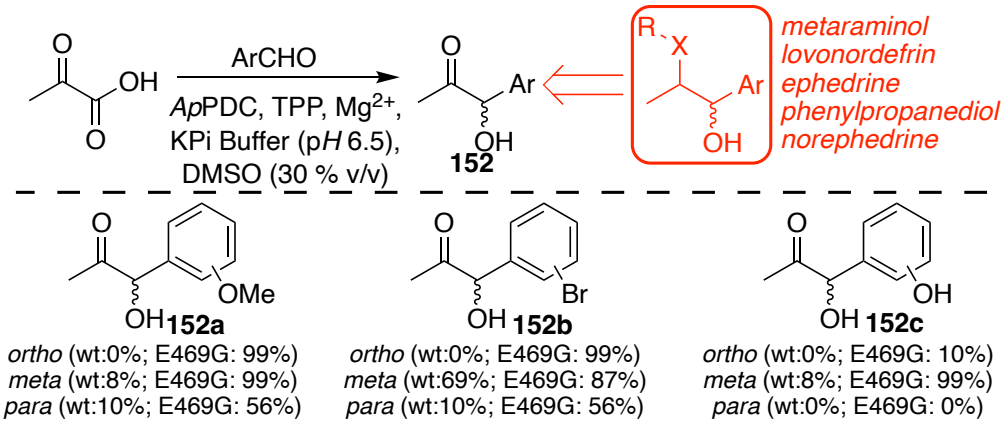

Scheme 3.4.4. *Ap*PDC catalysed carboligations to form a range of phenylacetylcarbinols (**152**) (PACs), which are key intermediates in the synthesis of a range of pharmaceuticals. (wt = wild-type enzyme; E469G = mutated enzyme variant)

So far, biocatalytic transformations using TPP-dependent enzymes have focussed on enzymatic mutagenesis to tailor the activity to a desired application. There has been no exploration of cofactor modification to attempt to improve catalytic scope of existing reactions and for catalysis of non-native transformations.

3.4.3. Previous Work

Previous work by Kevin Maduka evaluated the catalytic proficiency of the non-pyrophosphorylated 1,2,4-triazolium mimic (**26{PP}**) in a series of benzoin and Stetter reactions, in comparison to non-phosphorylated thiamine. NMR spectroscopy was used to track formation of the initial adduct (**146a**) with 2-methoxybenzaldehyde at equimolar concentrations of aldehyde and catalyst in deuterated methanol and triethylammonium chloride buffer (2:1 Et_3N:Et_3NHCl). 2-Methoxybenzaldehyde was chosen as this benzoin reaction stalls at the initial adduct, allowing for accurate determination of the rates of formation and decay. Table 3.4.1 summarises rate and equilibrium constants for this transformation (Scheme 3.4.5).

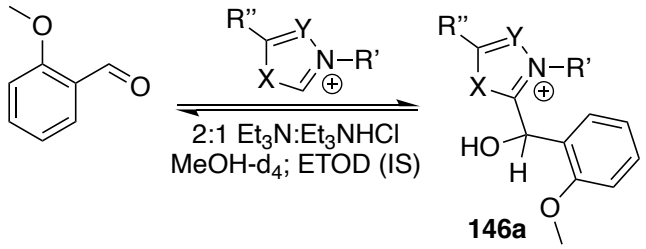

Scheme 3.4.5. Formation of the 2-methoxy hydroxyaryl adduct (**146a**) with thiamine (**5**, X=S, Y=CCH_3, R' = pyrimidinyl, R'' = CH_2CH_2OH), the 1,2,4-triazolium mimic (**26**, X=Y=N, R' = pyrimidinyl, R'' = CH_2CH_2OH), and a trimethyl 1,2,4-triazolium (**144**, X=NMe, Y=N, R'=R''=Me).

Table 3.4.1. Summary of the kinetic constants for rate of formation and decay of adduct (**146a**) and equilibrium constant for the catalysts studied in previous work by Kevin Maduka.

Catalyst	k_1 / $\times 10^{-4}$ M^{-1} s^{-1}	k_{-1} / $\times 10^{-5}$ s^{-1}	K / M^{-1}
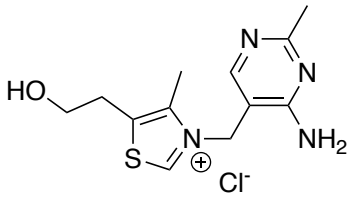 **5**	5.02	2.88	17.4
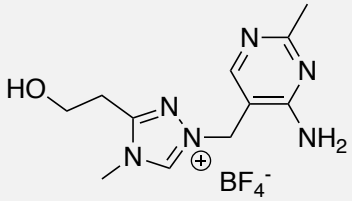 **26**	23.1	4.66	49.5
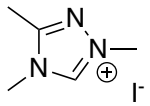 **144**	13.9	2.05	67.7

The significantly larger value for *K* for the 1,2,4-triazolium mimic (**26**) in comparison to thiamine (**5**) reflects a significantly larger concentration of the adduct present at equilibrium. Adduct formation consists of two steps (Scheme 3.4.1): (1) Deprotonation of the pre-catalyst to form the active carbene catalyst; (2) Addition of the carbene into the aldehyde to form the hydroxyaryl adduct. As previously discussed, the C-H acidity of the 1,2,4-triazolium mimic (**26**) is an order of magnitude higher than thiamine (**5**) and hence more carbene is present at equilibrium. However, assuming that nucleophilicity follows the same trend as basicity, addition of a less basic NHC to the carbonyl would be expected to be slower for the 1,2,4-triazolium ion (**26**). The rate of adduct formation is faster for the 1,2,4-triazolium ions (**26**) than the thiazolium ion (**5**) in Table 3.4.1, highlighting that acidity of the pre-catalyst has a greater effect on rate of hydroxyaryl adduct (**146a**) formation. Rates of decay of hydroxyaryl adduct (**146a**) back to aldehyde are of similar magnitude, with the 1,2,4-triazolium mimic (**26**) being slightly faster, presumably due to it being a more active catalyst. Finally, equilibrium constants reflect greater concentrations of hydroxyaryl adduct (**146a**) for both 1,2,4-triazolium ions (**26**/**144**) than for the thiazolium ion (**5**), reflecting the enhanced reactivity of the 1,2,4-triazolium ions. The trimethyl 1,2,4-triazolium ion (**144**) has a slightly higher equilibrium constant than the 1,2,4-triazolium mimic (**26**) and this could reflect a steric effect. The mimic (**26**) is much bulkier than the trimethyl 1,2,4-triazolium (**144**) and will likely clash more with the aryl-aldehyde upon hydroxyaryl adduct (**146a**) formation.

Alongside evaluating the catalytic potential of the new 1,2,4-triazolium mimic (**26**) in model benzoin and Stetter reactions in the absence of enzyme, computational docking studies were explored. The GOLD software, part of the Cambridge crystallographic suite of programs, was used to evaluate binding of TPP (**5{PP}**) and the mimic pyrophosphate (**26{PP}**). Hermes® software was used to prepare the ligands and enzymes before the docking studies were explored. To run GOLD docking experiments, a genetic algorithm, based on the Darwinian concept of natural selection is employed. This allows the protein-ligand interactions to be defined and an output measure of fit defined as a scoring function. There are a range of scoring functions which can be generated, and this work chose ChemPLP (Piecewise Linear Potential) as the most appropriate. ChemPLP scores are interpreted as more negative values representing better fit of the ligand.

A selection of TPP-dependent enzymes were explored, but of most relevance to the work discussed in this chapter are results for pyruvate decarboxylase. A range of crystal structures for pyruvate decarboxylase from different sources were obtained from the protein database and fitness tests explored (Table 3.4.2). All PDC enzymes were similar in overall structure, consisting of 4 identical subunits with similar molecular weights. Interestingly a broad spread of 'fitness scores' were determined, with *Zymomonas Mobilis* giving the overall best result. This broad spread highlights an important consideration when exploring biocatalytic reactions in this chapter: the same enzyme from different sources may give contrasting results.

Table 3.4.2. Summary of the results of computational docking studies for the new cofactor mimic (**26{PP}**) in pyruvate decarboxylase from a variety of microorganisms. RMSD refers to the root mean squared deviation and PLP a measure of fitness in which more negative values imply a better fit.

Enzyme Structure Code[a]	Source	RMSD	PLP Score
2NXW	*Azospirillum brasilense*	3.9	28.3
2VJY	*Kluyveromyces lactis*	9.0	22.7
2V4K	unspecified	7.7	29.0
2WVA	*Zymomonas mobilis*	3.8	22.6
2WVG	*Zymomonas mobilis*	9.4	30.1
4COK	*Gluconacetobacter diazotrophicus*	8.9	24.4
4MZX	*Pseudomonas putida*	8.7	39.5
4ZP1	***Zymomonas mobilis***	**36.1**	**-293.5**
5NPU	Artificial gene sequencing	5.0	71.9
5TMA	*Zymomonas mobilis*	9.1	37.9
6EFG	*Kluyveromyces lactis*	14.6	28.3
6EFH	*Kluyveromyces lactis*	8.9	36.0

[a]Structure codes refer to catalogue numbers within the protein databank.

The docking pose which generated the lowest fitness score of -293.5 for the triazolium mimic pyrophosphate (**26{PP}**) shows a very similar structure to that of TPP (**5{PP}**) (Figure 3.4.4). Importantly, the C(2)-H and C(3)-H peaks for TPP and the mimic, respectively, are oriented in the same direction. For catalytic activity within the enzyme

active site, it is important that the reactive, carbenic position is directed into the active site, where reaction with a carbonyl can be accommodated. The key structural difference between TPP and mimic appears to be the orientation of the pyrimidinyl group. The effect on activity on this is unknown; however, the amino-group is thought to deprotonate the C(2)-H position in an intramolecular process in the active site of the enzyme. This basicity of the amino group has been shown to be enhanced upon binding to the active site due to protein backbone interactions.[168] The alternative conformation adopted for the mimic appears to reduce the propensity for intramolecular deprotonation and this may reduce the catalytic potential of this mimic.

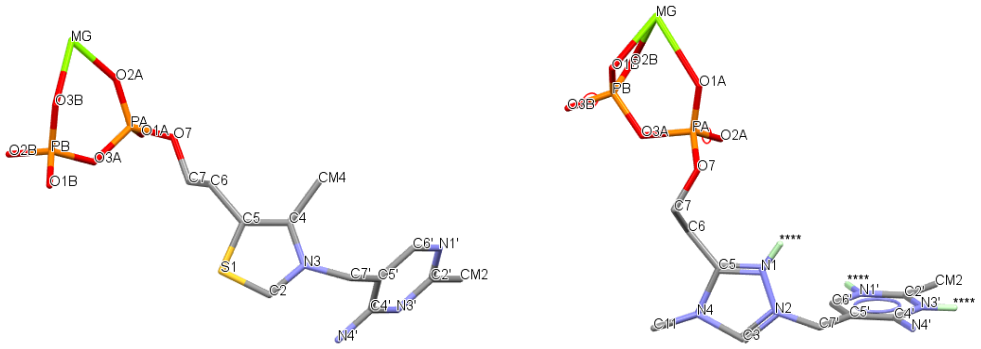

Figure 3.4.4. Binding conformations of TPP (**5{PP}**), left, and the cofactor mimic (**26{PP}**), right, in *Zymomonas mobilis*.

Computational docking studies can give a useful insight into potential binding conformations, which can be related to catalytic activity. Importantly, they are predictive simulations and do not necessarily reflect true experimental results. The following section discusses 'real-world' experimental evaluation of the novel cofactor in a selection of TPP-dependent enzymes.

3.4.4. Results and Discussion

Effect of Phosphorylation on Non-Enzymatic Reactions

Section 3.4 explored the effect on C-H acidity of bringing a negatively charged pyrophosphate group into close proximity of the carbenic centre. An increase in pK_a of 1-2 units was observed for both thiamine pyrophosphate (**5{PP}**) and the 1,2,4-triazolium mimic (**26{PP}**). As highlighted above, work by Kevin Maduka has shown that the mimic (**26**) and thiamine (**5**) are catalytically active in benzoin condensations; however, these studies do not consider the pyrophosphate group. In can be expected that rates of reaction will be diminished owing to the decreased acidity (pK_a ~ 1.5 units higher). In fact, the only aldehyde which was possible to study was 2-methoxybenzaldehyde, owing to the

previously reported rate enhancement of a 2-substituent (Scheme 3.4.6).[9] As previously mentioned, the other benefit of using 2-methoxybenzaldehyde is that it stalls at initial adduct (**146b**) formation, and rate constants for this step can be readily extrapolated. Figure 3.4.5 shows a ^{1}H NMR spectral overlay for the formation of adduct catalysed by thiamine pyrophosphate (**5{PP}**), with key peaks highlighted.

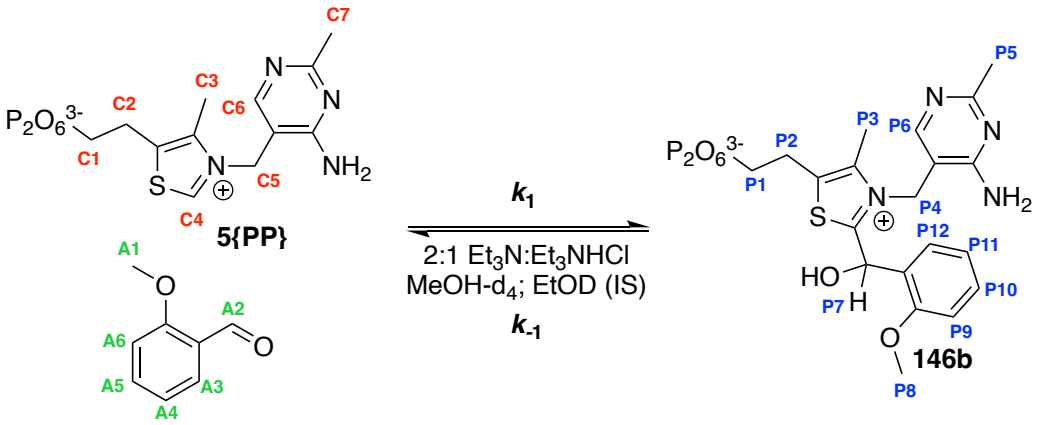

Scheme 3.4.6. Adduct (**146b**) formation with thiamine pyrophosphate (**5{PP}**), monitored kinetically with ^{1}H NMR spectroscopy. Key peaks in the NMR spectra (Figure 3.4.5) are assigned with coloured labels shown.

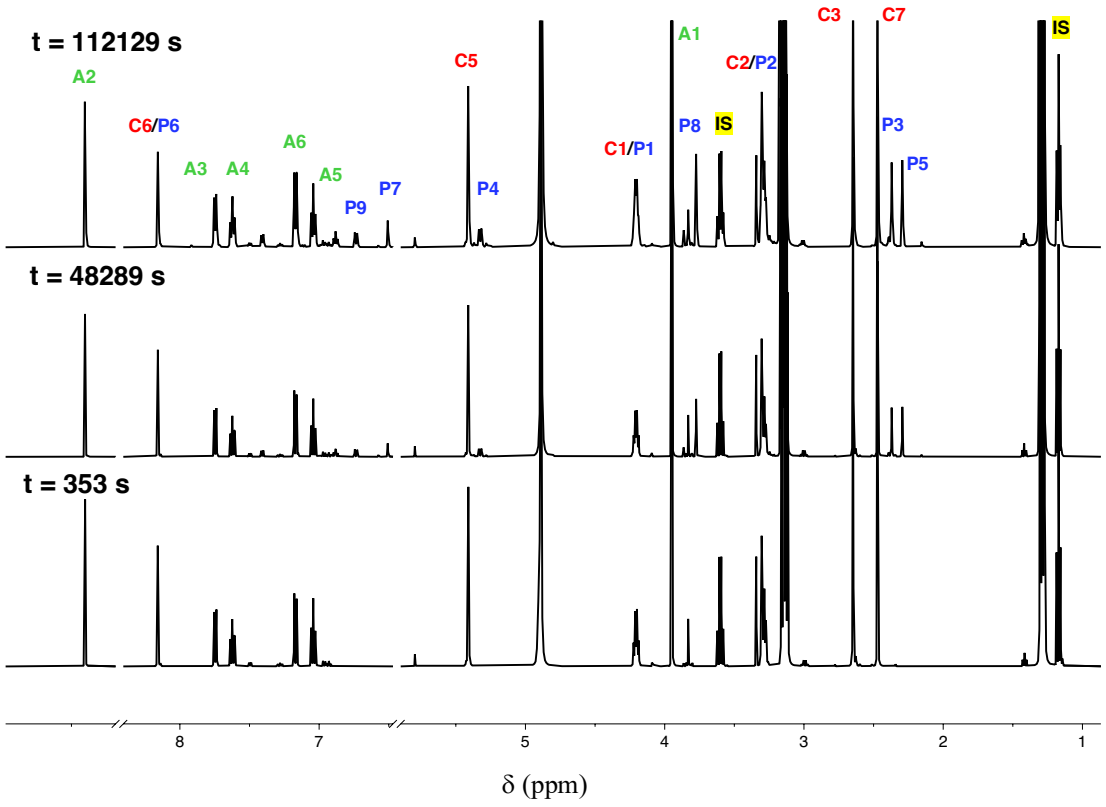

Figure 3.4.5. Representative ^{1}H NMR spectra for the formation of adduct **146b** as shown in Scheme 3.4.6 at Time = 353 s, 48289 s and 112129 s.

Plotting formation of the hydroxyaryl adduct (**146b**), alongside decay of aldehyde and catalyst, with respect to time by integrating with respect to the internal standard allows for estimation of k_1, k_{-1} and K_1. In this case the **C5**, **A1** and **P4** NMR signals were monitored to evaluate catalyst (**5{PP}**), aldehyde and adduct (**146b**) concentrations

respectively. As equilibrium had not been reached, a global fitting using Berkeley-Madonna software was used to give estimates of rate and equilibrium constants (Figure 3.4.6), summarised in Table 3.4.3. Values show approximately an order of magnitude drop in rate constant of adduct formation for thiamine pyrophosphate (**5{PP}**) in comparison to thiamine (**5**). This correlates to the approximately one order of magnitude drop in C(2)-H acidity observed in Section 3.4. The equilibrium is shifted in favour of the adduct to a greater extent in the case of thiamine pyrophosphate compared to thiamine. This shift could reflect a stabilising effect of the pyrophosphate group of the aryl-group through inductive effects.

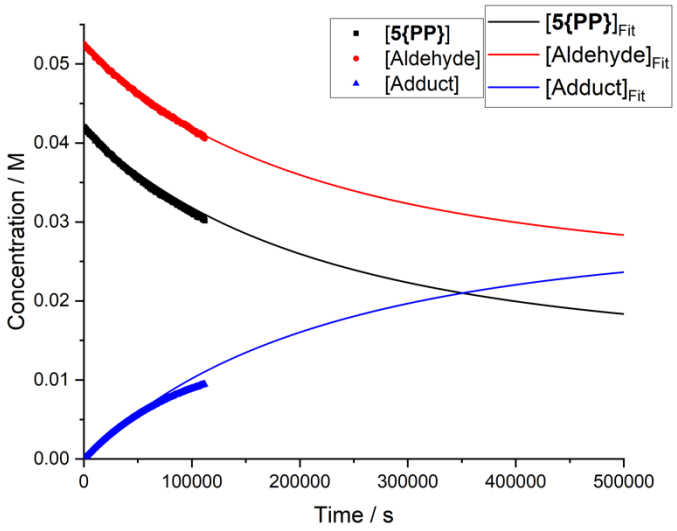

Figure 3.4.6. Plots of aldehyde, catalyst (**5{PP}**) and adduct concentrations over time for the adduct formation reaction (Scheme 3.4.6) (data points) and global fitting from Berkeley-Madonna software (lines) to determine rate and equilibrium constants for adduct formation.

Table 3.4.3. Summary of the kinetic data determined through global fitting of aldehyde, catalyst (**5{PP}**) and adduct formation with Berkeley-Madonna fitting software. Also shown are the previous results for thiamine (**5**), discussed above.

	k_1 / M^{-1} s^{-1}	k_{-1} / s^{-1}	K_1 / M^{-1}
5{PP}	6.27×10^{-5}	8.24×10^{-7}	76.1
***5*[a]**	*5.02×10^{-4}*	*2.88×10^{-5}*	*17.4*

[a]Values previously determined by Kevin Maduka.

Biocatalytic Evaluation – Spectrophotometric Analysis

Initial biocatalytic evaluation of the novel cofactor started with native reactions of readily available TPP-dependent enzymes pyruvate decarboxylase from *Saccharomyces cerevisiae* (*Sc*PDC) and pyruvate oxidase from *Aerococcus sp.* (*A*sPOx) . Initially, both enzymes were explored with native TPP (**5{PP}**) in order to explore their native ν_{max} and

K_M values. Monitoring enzymatic reactions with UV-vis spectroscopy requires a component of the assay to absorb between 200-800 nm. In the case of pyruvate decarboxylase, the native reaction, which converts sodium pyruvate to acetaldehyde, is coupled with a horse liver alcohol dehydrogenase reaction (Scheme 3.4.7). Acetaldehyde is reduced to ethanol by the dehydrogenase and cofactor NADH (**80{H}**) is oxidised to NAD^+(**80**). Monitoring absorbance at 365 nm allows linear plots of NADH consumption to be generated, the slope of which gives the initial rate (Table 3.4.4, Figure 3.4.7). Plotting the initial rate as a function of concentration of sodium pyruvate allows Michaelis-Menten plots to be generated and values for K_M and ν_{max} to be generated (Table 3.4.5, Figure 3.4.8). A specific enzyme plot can also be constructed by plotting the concentration of pyruvate against the rate/[Enzyme], with the plateau giving a value for k_{cat}. Enzyme concentration for the pyruvate decarboxylase assay was determined to be 0.333 nM, which correlates to 1.33 nM of active sites (tetrameric enzyme). This gives a value of k_{cat} = 358 s^{-1} which is in excellent agreement with the previously reported value of 320 s^{-1}.[228]

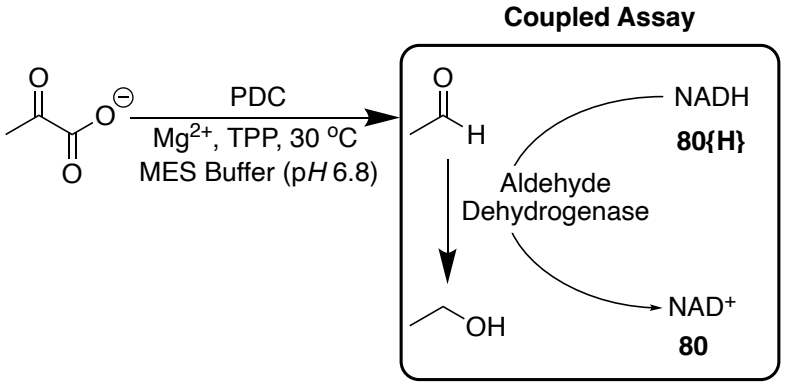

Scheme 3.4.7. Coupled assay for pyruvate decarboxylase in which pyruvate is decarboxylated to acetaldehyde and a subsequently reduced to ethanol. The reaction is monitored via spectrophotometric determination of NADH (**80{H}**) consumption for the second process by UV-Vis spectroscopy at 365 nm.

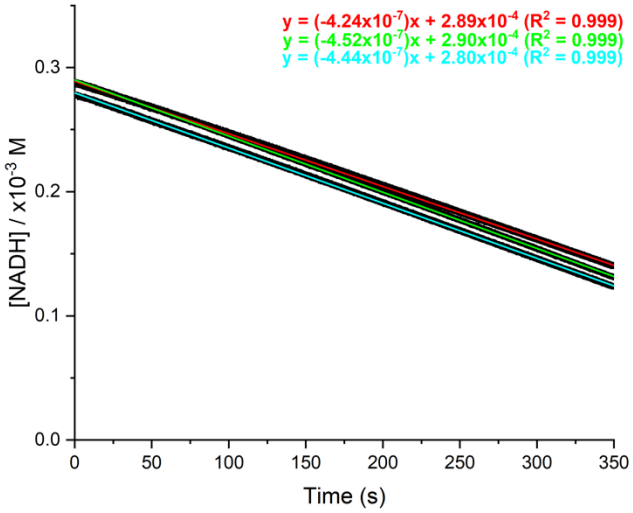

Figure 3.4.7. Representative plots of NADH (**80{H}**) consumption in the coupled assay shown in Scheme 3.4.7. Concentration of pyruvate in this case was 30 mM and the three lines represent three repeats highlighting the reproducibility. Concentration of NADH ([NADH]) was calculated as A/ε at 365 nm.

Table 3.4.4. Summary of the kinetic data for the coupled *Sc*PDC assay shown in Scheme 3.4.7 used to plot the Michaelis Menten and specific enzyme plots in Figure 3.4.8.

[Pyruvate] / $\times 10^{-3}$ M	Rate $\times 10^{-8}$ / M s^{-1}	Average Rate $\times 10^{-8}$ / M s^{-1}	Rate / [*Sc*PDC][a] / s^{-1}
5	8.16 8.26 8.25	8.22	61.7
10	18.8 17.1 17.0	17.6	133
20	26.5 27.1 26.3	26.7	201
50	37.0 36.0 36.1	36.4	272
100	41.2 39.8 38.9	40.0	300
150	44.3 42.1 40.2	42.2	316
300	44.6 45.4 42.6	44.1	331

[a][Enzyme] was defined as the [Protein] added to the 1 ml cuvette, multiplied by 4 as pyruvate decarboxylase is a tetrameric enzyme with four active sites.

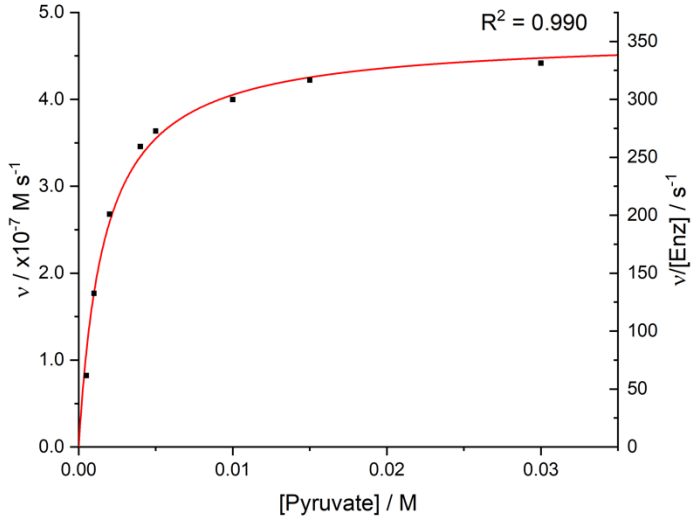

Figure 3.4.8. Michaelis-Menten plot (left-side axis) and specific enzyme plot (right-side axis) for *Sc*PDC in this study. Kinetic constants determined from these analyses are summarised in Table 3.4.5.

Table 3.4.5. Summary of key kinetic constants determined from the initial assay set up of *Sc*PDC.

Constant	Value
v_{max}	$(4.72 \pm 0.2) \times 10^{-7}$ M s^{-1}
K_M	$(1.7 \pm 0.2) \times 10^{-3}$ M
k_{cat}	354 ± 8 s^{-1}

Following the above study of pyruvate decarboxylase with native TPP (**5{PP}**) cofactor, a range of conditions were explored to assess the 1,2,4-triazolium pyrophosphate mimic (**26{PP}**). These first relied on isolation of the *apo*-enzyme of pyruvate decarboxylase (without cofactor). This could be readily isolated by dialysis using Slide-a-Lyzer dialysis cassettes with a 2000 molecular weight cut off, in a p*H* 8.5 HEPES (50 mM) buffer. Dialysis was performed over 3-5 days, replacing buffer daily, in a cold room at 0-8 °C.

Conversion to *apo*-enzyme was evaluated by initially repeating the above coupled assay without addition of thiamine pyrophosphate (**5{PP}**). If no activity was observed with no added cofactor, but addition of TPP (**5{PP}**) led to a return of activity, *apo*-enzyme had been isolated. In some cases, a small amount of residual activity was observed for pyruvate decarboxylase due to residual bound cofactor. When isolating *apo*-enzyme there is always a compromise to be made with time spent dialysing the enzyme against enzyme denaturation. Typically, *apo*-enzyme is substantially less stable than cofactor bound enzyme and denatures more readily. As such, in these cases, experiments were

still carried out and differences between no-cofactor and added cofactor mimic (**26{PP}**) were carefully considered. Figure 3.4.9 (Table 3.4.6) summarises the reactions explored with native TPP (**5{PP}**), cofactor mimic (**26{PP}**) and *apo*-enzyme. Interestingly, it was useful for residual bound TPP to be present in the *apo*-enzyme in this case as it allowed comparison to the mimic, which further decreased the rate of NADH (**80{H}**) consumption. This suggests that the mimic is binding competitively with the enzyme as only at higher concentrations of the mimic is activity completely switched off. Moreover, after mimic (**26{PP}**) addition, 5 mM (**5{PP}**) TPP was added and a slow return to activity was observed.

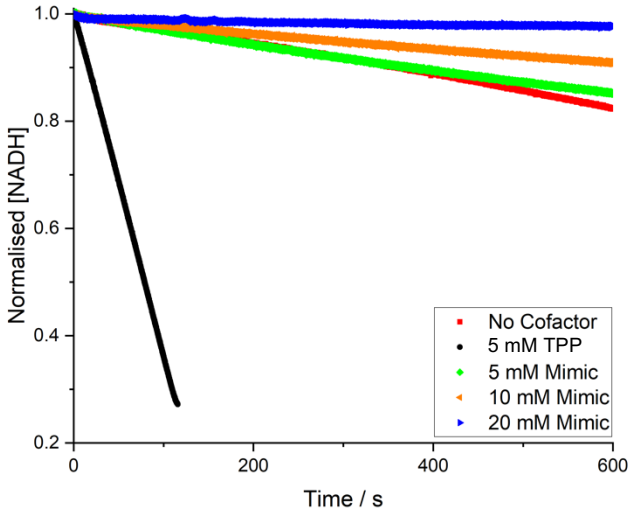

Figure 3.4.9. Initial studies of *apo*-PDC showing a small amount of residual activity with no cofactor addition (due to residual TPP), high activity with TPP (**5{PP}**) addition and loss of activity with increasing mimic (**26{PP}**).

Table 3.4.6. Summary of the kinetic studies of *apo*-PDC showing a significant drop in rate for the mimic (**26{PP}**). The small amount of activity is likely due to a small amount of residual TPP (**5{PP}**).

Entry	[Enzyme] / units ml^{-1}	[Cofactor] / mM	ν / M s^{-1}
1	5	None	2.86×10^{-4}[a]
2	5	5 (TPP)	6.44×10^{-3}
3	5	5 (Mimic)	2.44×10^{-4}
4	5	10 (Mimic)	1.44×10^{-4}
5	5	20 (Mimic)	2.62×10^{-5}

[a]Although no cofactor was added in this case, activity was still observed due to residual bound cofactor from the *apo*-enzyme preparation.

The value for K_D for TPP (**5{PP}**) in *Sc*PDC is 23 μM and it is likely that K_D is much higher for the 1,2,4-triazolium mimic (**26{PP}**) as a non-native substrate. As such the mimic concentration was explored at higher concentrations of 10 mM and 20 mM. At

each increase in concentration of **26{PP}** no increase in activity was observed and instead a drop in activity in comparison to the background.

The above experiments were repeated using pyruvate oxidase from *Aerococcus sp.* (*A*sPOx), coupled with horseradish peroxidase which converts formed hydrogen peroxide to water and a quinonimine dye (Scheme 3.4.8). In this case, the formation of the purple quinonimine dye is monitored by UV-vis spectroscopy at 550 nm, giving linear initial rate plots (Figure 3.4.10). Gradients of these plots give initial rates of conversion (Table 3.4.7) and these data were used to construct Michaelis-Menten and specific enzyme plots (Figure 3.4.11). Pyruvate oxidase has two substrates, pyruvate and phosphate, and both of the concentrations of these could be changed to determine Michaelis-Menten plots; however, when reducing phosphate concentration, buffering capacity of the solution is reduced and results vary more significantly. As pyruvate consumption is more consistent, this was the substrate of choice for reaction monitoring. A value for k_{cat} of 281 s^{-1} (Table 3.4.8) was obtained in this case, which is similar in values for other pyruvate oxidases from similar species (k_{cat} = 87 s^{-1} for POx from E.*coli*). A value for *Aerococcus Viridians* would be more comparable as the pyruvate oxidase used in our study is from *Aerococcus sp.,* but this could not be located within the literature.

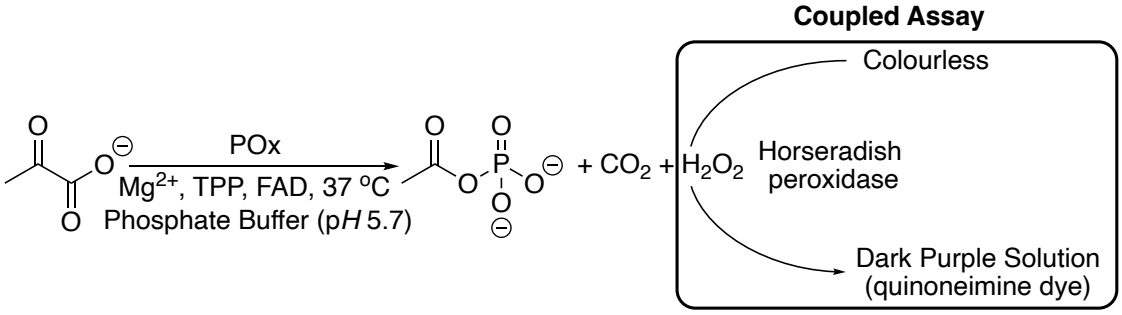

Scheme 3.4.8. Coupled assay for pyruvate oxidase in which pyruvate is decarboxylated and reacted with inorganic phosphate. The coupled assay converts formed hydrogen peroxide to water and a quinoneimine dye, which is spectrophotometrically monitored at 550 nm.

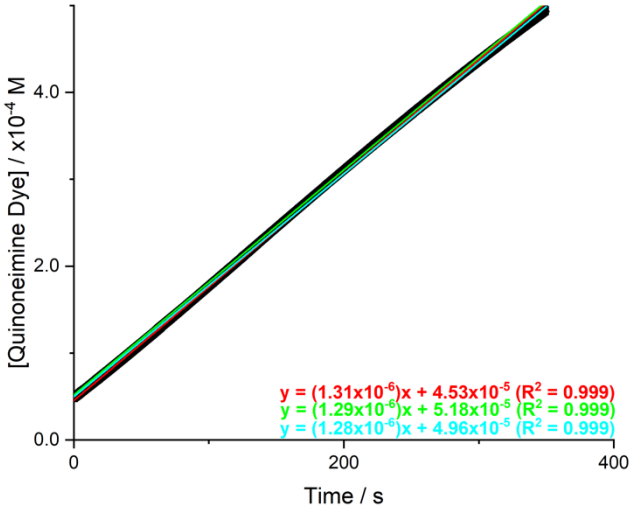

Figure 3.4.10. Representative plot of quinoneimine formation in the coupled assay shown in Scheme 3.4.8. Concentration of pyruvate in this case was 20 mM and the three lines represent three repeats highlighting the reproducibility. Concentration of quinoneimine dye was calculated as A/ε at 550 nm.

Table 3.4.7. Summary of the kinetic data for the coupled *As*POx assay shown in Scheme 3.4.8 used to plot the Michaelis Menten plot and Specific enzyme plots (Figure 3.4.11).

[Pyruvate] / $\times 10^{-3}$ M	**Rate / $\times 10^{-7}$ M s^{-1}**	**Average Rate / $\times 10^{-7}$ M s^{-1}**	**Rate / [*As*POx][a] / s^{-1}**
0.1	2.94 3.02 3.02	2.98	65.6
0.25	5.15 5.13 5.15	5.14	113
0.5	8.44 8.07 8.17	8.25	181
1.0	10.3 9.78 9.73	10.1	221
2.5	10.8 10.9 11.2	11.0	241
5.0	12.4 11.5 10.8	11.6	254
10.0	12.8 12.9 13.1	12.9	284
20.0	12.8 12.6 12.1	12.5	275

[a][Enzyme] was defined as the [Protein] added to the 1 ml cuvette, multiplied by 4 as pyruvate decarboxylase is a tetrameric enzyme with four active sites.

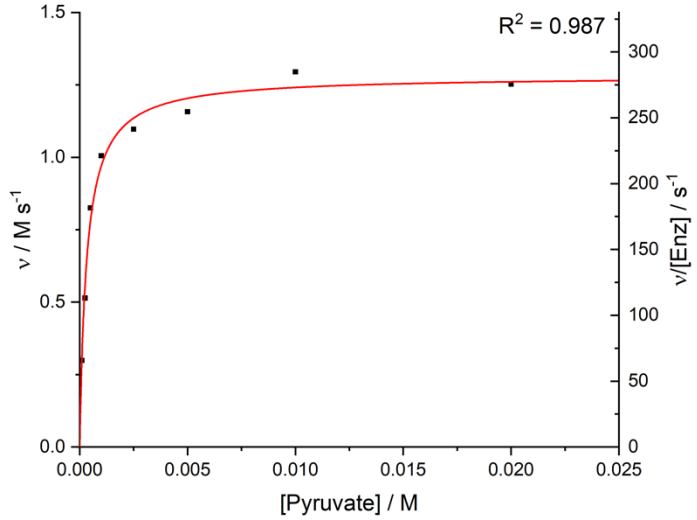

Figure 3.4.11. Michaelis-Menten plot (left-side axis) and specific enzyme plot (right-side axis) for *As*POx in this study. Kinetic constants determined from these analyses are summarised in Table 3.4.8.

Table 3.4.8. Summary of key kinetic constants determined from the initial assay set up of *As*POx.

Constant	Value
ν_{max}	$(1.28 \pm 0.03) \times 10^{-6}$ M s^{-1}
K_M	$(3.2 \pm 0.4) \times 10^{-5}$ M
k_{cat}	281 ± 6 s^{-1}

Apo-Pyruvate oxidase was prepared following the same procedure as for pyruvate decarboxylase. A small amount of activity was observed at high enzyme concentrations in the assay, likely due to residual bound cofactor (**5{PP}**); however, this was minimal and significant comparisons could be made when varying the TPP (**5{PP}**) and cofactor mimic (**26{PP}**) concentrations (Figure 3.4.12). As with pyruvate decarboxylase, the addition of TPP (**5{PP}**) gave significant return of activity; however, addition of mimic pyrophosphate (**26{PP}**) did not show activity above that of the background. Moreover, adding significantly higher levels of mimic (> 10 mM) at higher enzyme concentrations showed activity drop below that of the background. The fact that this coupled assay forms a visible purple dye allowed the reaction to be monitored for a longer period. Figure 3.4.13 shows a comparison of two assays of pyruvate oxidase after 24 hrs. The left-hand cuvette contains native TPP (**5{PP}**) cofactor and rapidly formed a dark purple solution with very little-no light transmission. The right-hand cuvette contains the mimic pyrophosphate (**26{PP}**) and shows insignificant purple colour formed suggesting longer reaction times do not improve the conversion.

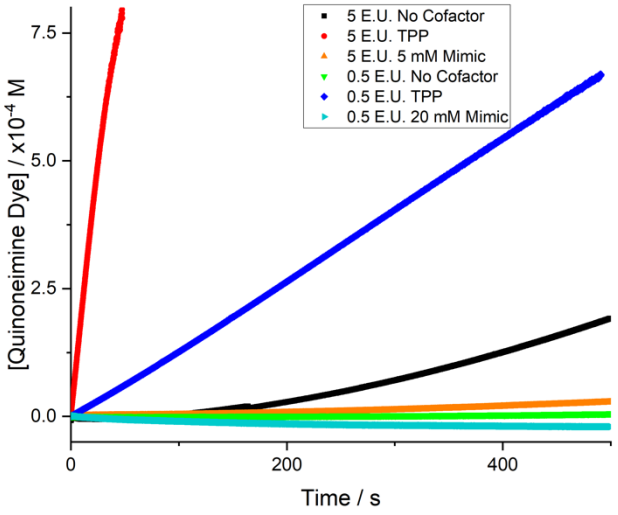

Figure 3.4.12. Studies of *apo*-POx showing a small amount of residual activity with no cofactor addition (due to residual TPP), high activity with TPP (**5{PP}**) addition and loss of activity with increasing mimic (**26{PP}**). E.U. refers to enzyme units, 1 E.U. is defined as the amount of the enzyme that catalyses the conversion of one micromole of substrate per minute under the specified conditions of the assay method.

Table 3.4.9. Summary of the kinetic studies of *apo*-POx and showing a significant drop in rate for the mimic (**26{PP}**). The small amount of activity is likely due to a small amount of residual TPP.

Entry	[Enzyme] / units ml^{-1}	[Cofactor] / mM	ν / M s^{-1}
1	5	None	4.03×10^{-7}[a]
2	5	5 (TPP)	1.70×10^{-5}
3	5	5 (Mimic)	5.37×10^{-8}
4	0.5	None	1.01×10^{-8}
5	0.5	5 (TPP)	1.38×10^{-6}
6	0.5	20 (Mimic)	0[b]

[a]Although no cofactor was added in this case, activity was still observed due to residual bound cofactor from the *apo*-enzyme preparation. [b]This entry gave a negative gradient due to slight drift caused by mixing artifacts in the cuvette. Overall, a rate of 0 is observed as there is no increase in absorbance due to quininoneimine dye formation.

Figure 3.4.13. UV-Vis spectroscopy cuvettes of *apo*-Pox with TPP (left) and mimic (**26{PP}**) (right) after 24 hours showing a dark-purple quinoneimine dye formed for TPP and insignificant purple-dye formation for the mimic.

The above studies both show that introducing the non-native cofactor mimic (**26{PP}**) as a replacement for TPP (**5{PP}**) leads to a loss of enzymatic activity, beyond that of the

background. It therefore appears that the cofactor can bind to the enzyme, in the correct place; however, it is inhibiting these native reactions, as opposed to enhancing, as it is not promoting the catalysis of pyruvate decarboxylation in both cases. To give further insight into these results, a selection of more quantitative NMR studies were undertaken.

Biocatalytic Evaluation – Quantitative NMR Analysis

Spectrophotometric assessment of enzyme activity provides useful information with regards to changes in activity when introducing a non-native cofactor; however, as with all spectrophotometric kinetic studies, they do not give conclusive evidence of product formation or enzyme activity. NMR spectroscopy is a powerful tool for kinetic analysis as spectral peaks for product formation and reagent consumption can be readily monitored. To further explore the effect of replacing the TPP (**5{PP}**) cofactor with the synthesised non-native 1,2,4-triazolium mimic (**26{PP}**), an NMR spectroscopy-based assay was developed.

As highlighted within the introductory section (Chapter 3.5.1), pyruvate decarboxylase from *Acetobacter pasteurianus* (and mutants of) has been shown to catalyse the non-native reaction of pyruvate with a range of aldehydes to form arylacetylcarbinols (**152**) (Scheme 3.4.4).[227] Pyruvate decarboxylase from yeast, a readily commercially available and inexpensive enzyme, has not been reported to catalyse these reactions. Tracking of enzymatic reactions using NMR spectroscopy is typically challenging for a number of reasons: enzyme concentrations are typically high and the protein backbone signals can mask the signals of interest for reaction monitoring. Proteins must be dialysed in D_2O to reduce the size of the water peak, this requires large quantities of expensive deuterated solvent. Increases in viscosity due to high enzyme concentrations can increase T_2 relaxation and broaden signals. Finally, buffer signals can greatly complicate and further mask the key signals for reaction monitoring. Specific pulse sequences in the NMR spectrometer can be used to suppress both protein and water signals which would allow effective reaction monitoring. Alternatively, using heteronuclear NMR spectroscopy (e.g. ^{13}C or ^{19}F) would avoid many of the above practical issues. ^{13}C NMR spectroscopy is a useful technique as the natural abundance of ^{13}C is only 1.1 % and so at relatively low concentrations, the majority of peaks do not appear above the baseline. In using a ^{13}C enriched pyruvate source (**153**), starting material, product and by-product peaks can

be readily assigned. In these studies, 4-fluorobenzaldehyde was chosen as the aldehyde of choice as previous work using HPLC for reaction monitoring has shown up to 99% conversion to the desired carbinol (**152d**); moreover, it provides another handle for ^{19}F NMR spectroscopic monitoring of these reactions.

The reaction was initially carried out as per the previous synthetic studies: 300 mM of methyl-labelled ^{13}C pyruvate (**153**), 100 mM 4-fluorobenzaldehyde, 0.25 mM thiamine pyrophosphate (**5{PP}**), and 1.5 mg ml^{-1} pyruvate decarboxylase were mixed in 50 mM phosphate buffer (p*H* 6.7) and 30% v/v DMSO-d_6 to aid solubilisation (Scheme 3.4.9). Pleasingly, the peak assigned to the starting material decreased in magnitude and new peaks formed at 27.6 ppm. Under the experimental conditions outlined in previous studies, a large excess of pyruvate is used. It was found that after consumption of the aldehyde, decarboxylation of pyruvate continued, forming highly reactive acetaldehyde, complicating the NMR spectra. To avoid this, the reaction conditions were altered to reduce the concentration of pyruvate (**153**) to 60 mM, with excess aldehyde (100 mM). Pleasingly, it was found that this limited visible by-product formation in the ^{13}C NMR spectra (Figure 3.4.14); moreover, analysis of the final ^{19}F NMR spectrum highlighted complete conversion of pyruvate to carbinol at t ~ 78923 s (22 h) as the integrals showed a 40:60 ratio of aldehyde to carbinol (Figure 3.4.15).

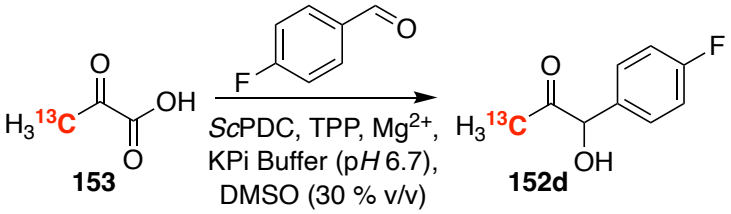

Scheme 3.4.9. Biocatalytic synthesis of carbinol (**152d**) with ^{13}C-labelled pyruvic acid and 4-fluorobenzaldehyde, allowing for NMR spectroscopic tracking of the conversion. *Sc*PDC was the enzyme of choice for these studies.

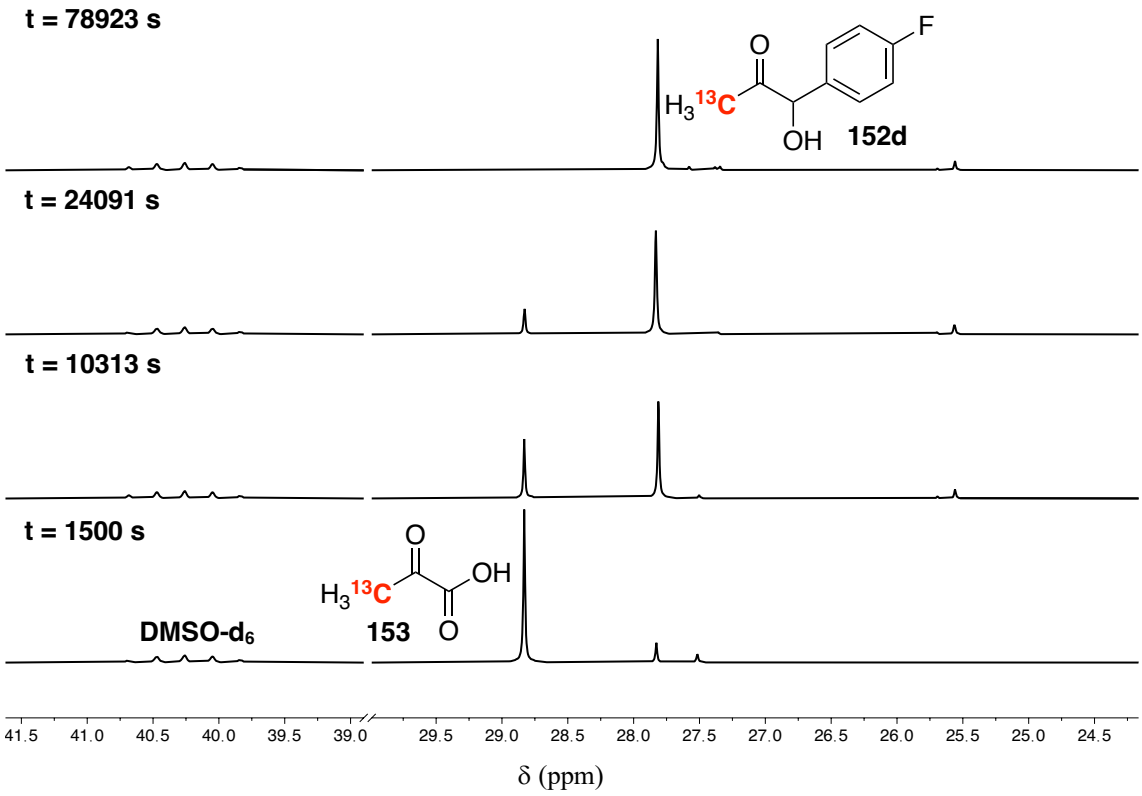

Figure 3.4.14. Representative ^{13}C NMR spectra for the formation of carbinol **152d** as shown in Scheme 3.4.9.

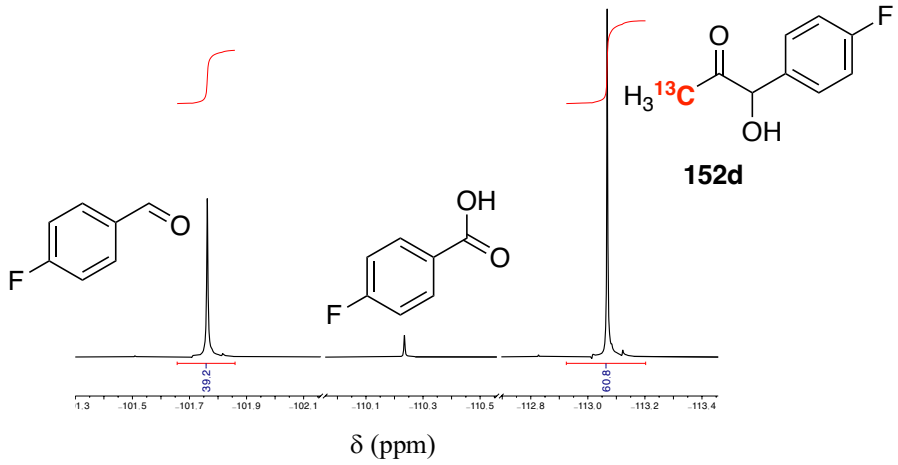

Figure 3.4.15. Final ^{19}F NMR spectrum for the reaction shown in Scheme 3.4.9, where 4-fluorobenzaldehyde was added at 100 mM and ^{13}C-pyruvic acid at 60 mM. Complete conversion to the carbinol(**152d**) is evidenced by integral ratios of 4:6 for aldehyde:carbinol.

As with the spectrophotometric assays, *apo*-PDC was prepared and used in this NMR spectroscopy study with native TPP (**5{PP}**), no added cofactor and with the mimic cofactor (**26{PP}**). It was found that the background (no cofactor) activity was slightly higher than anticipated due to residual bound cofactor (TPP). This again allowed for direct comparisons to the mimic (**26{PP}**). It was found that there was a slight increase in activity for 0.2 mM addition of cofactor mimic (**26{PP}**) in comparison to the

background but, a significant drop in activity for 10 mM mimic. (Figure 3.4.16; Table 3.4.10). The increased activity for 0.2 mM **26{PP}** could be due to either true cofactor activity or experimental error and repeats would be required to truly explore this result. A decease in activity at 10 mM **26{PP}** can be attributed to either binding in the active site in a non-active conformation or allosteric binding at such high concentrations.

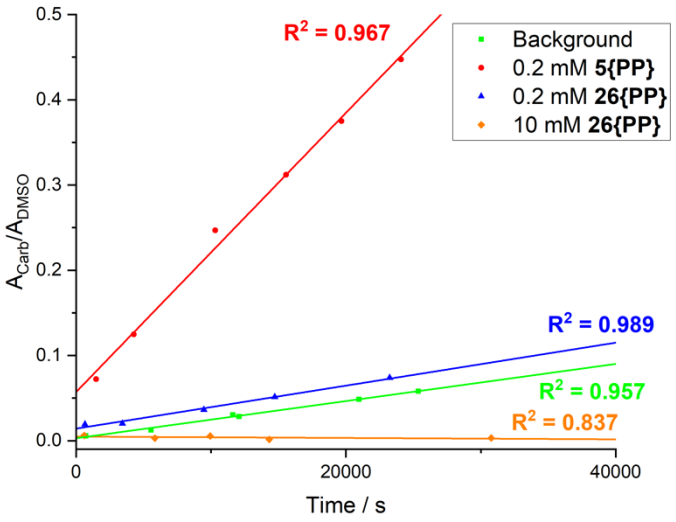

Figure 3.4.16. Plots of carbinol (**152d**) integral divided by the integral for d_6-DMSO for a selection of the biocatalytic carbinol syntheses (Scheme 3.4.9). Straight lines were fitted to the 'initial rate' regime, before plateauing, and compared to the gradient of the background reaction (no cofactor) (Table 3.4.10).

Table 3.4.10. Summary of relative initial rates of formation of carbinol (**152d**) and consumption of pyruvate (**153**) determined as the gradient of plots of carbinol/pyruvate integrals, relative to the integral for DMSO-d_6, before plateauing.

Cofactor	Concentration	Relative Initial Carbinol (152d) Formation Rates[a]	Relative Initial Pyruvate (153) Consumption Rates[b, c]
None	N/A	1.0	1.0
5{PP}	0.2 mM	7.7	3.5
26{PP}	0.2 mM	1.2	1.8
	10 mM	0.00012	0.73

[a]Relative initial carbinol (**152d**) formation is determined as the gradient of a plot of A_{carb}/A_{DMSO} before plateauing, divided by the same plot for the background reaction (no cofactor). [b]Relative initial pyruvate (**153**) consumption is determined as the gradient of a plot of A_{Pyr}/A_{DMSO} before plateauing, divided by the same plot for the background reaction (no cofactor). [c]A plot of pyruvate consumption (S. Figure 7.5.13) gave poorer fits to straight lines and this was assumed to be due to it being a very large integral to start with and small changes in [Pyr] not being measurable above the uncertainty.

There are a selection of potential explanations for the observed loss in activity when introducing the cofactor mimic (**26{PP}**). One is that the N-Me group (which is moved in the mimic in comparison to TPP) shifts the position of the active C(3)-H so that it no longer points into the active site of the enzyme, preventing reaction. Binding studies by Kevin Maduka predicted that the C(3)-H would still point into the active site; however,

these computational studies are only a rough prediction. Another explanation could be that the pyrimidinyl group shifts in orientation (as predicted from the computational binding studies). This could lead to a lack of hydrogen bonding interactions with the protein backbone, which have been found to increase the pK_a of the amino group in TPP (**5{PP}**). A drop in the basicity of this group could reduce the propensity for the proposed intramolecular deprotonation (Figure 3.4.17).

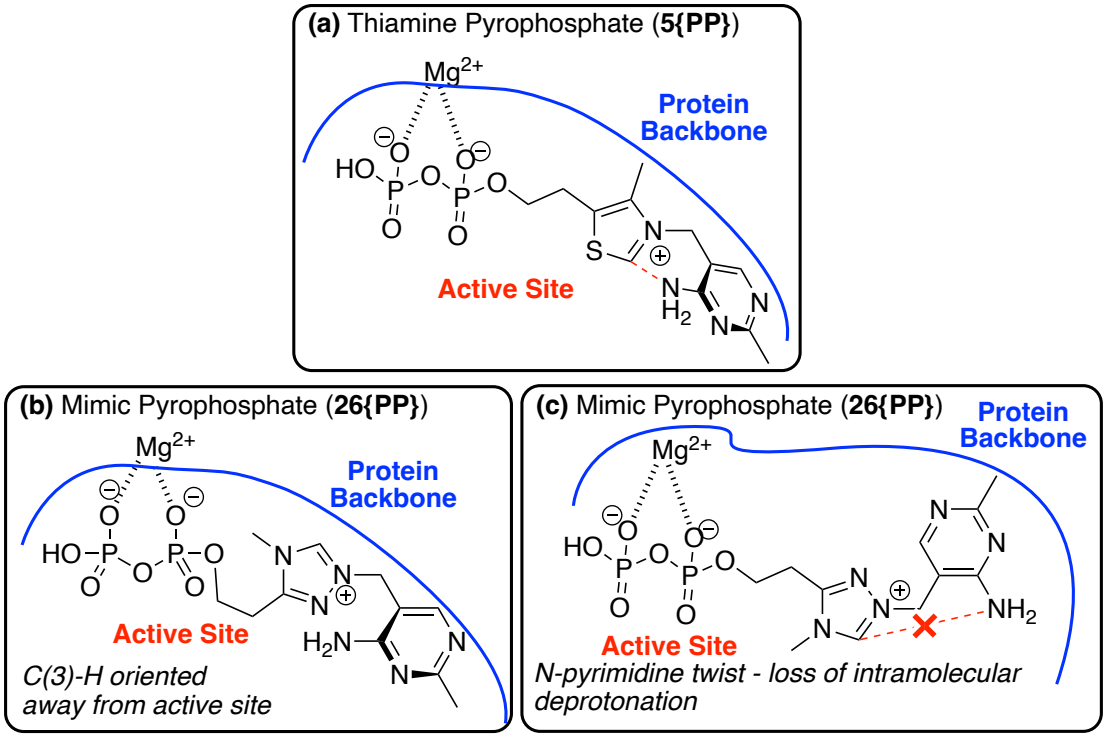

Figure 3.4.17. (a) Schematic representation of thiamine pyrophosphate (**5{PP}**) binding in the active site of TPP-dependent enzymes via electrostatic interactions to magnesium. The pyrimidinyl group is thought to be oriented to allow for intramolecular deprotonation of the C(2)-H positon. (b) a proposed binding conformation for 1,2,4-triazolium mimic (**26{PP}**) in which the N-Me causes a twist in the 1,2,4-triazolium core, resulting in the C(3)-H pointing away from the active site. This proposal is not supported by computational docking studies (Figure 3.4.4) (c) An alternative binding proposal in which the C(3)-H points into the active site but the N-pyrimidinyl group is oriented so that intramolecular deprotonation is not possible. This proposal is supported by computational docking studies (Figure 3.4.4).

*Sc*PDC is not an enzyme which has seen extensive study in biocatalytic transformations and this could be attributed to a level of rigidity in its active site. This rigidity could lead to the rejection of non-native substrates and cofactors. Therefore, future work should focus on a range of other enzymes to fully explore this novel mimic.

3.4.5. Conclusions

Owing to the complexity and time-consuming nature of the synthetic development of the mimic pyrophosphate (**26{PP}**), studies of the mimic in enzymatic reactions have not been as broad as originally planned. Nevertheless, this chapter highlights initial assay

establishment and studies of cofactor mimic in comparison to native TPP (**5{PP}**) through both spectrophotometric and NMR spectroscopy analyses. In all cases, it was found that the cofactor mimic (**26{PP}**) was less active than TPP in enzymatic reactions. Explanations for this include a complete lack of binding or binding occurring but the cofactor mimic is in a structurally less active conformation. The latter explanation is the current working hypothesis.

Taken at face value, these findings could be viewed as a negative result; however, the fact that the mimic (**26{PP}**) binds to the active site is promising. There is a vast selection of TPP-dependent enzymes, with dramatically different active site conformations to be explored; moreover, the development of enzyme mutagenesis and directed evolution can further modify the enzyme active site to favour mimic binding and catalytic activity.

Additionally, the NMR spectroscopy method we employed to monitor biocatalysis using both ^{13}C and ^{19}F NMR techniques is novel in this context to assess benzoin-type product formation. This will form the basis of future enzymatic reaction monitoring.

3.5. Conclusions

This chapter has outlined the initial investigations into what is an emerging field within organic chemistry: the synthetic development of enzyme cofactor mimics to target more diverse biocatalytic transformations. Chapter 3.1 reviews relevant developments in the areas of biocatalysis and organocatalysis (based on cofactor scaffolds) alongside synergistic approaches to developing new biocatalytic processes. Importantly this review highlights the burgeoning potential of this field and the key cofactors which have not received interest with regards to chemomimetic biocatalysis.

Thiamine pyrophosphate (**5{PP}**) inspired the vast field of NHC-organocatalysis but, until now there had been no reported exploration of TPP chemomimetics within biocatalysis. Chapter 3.2 discusses the synthetic development of the first catalytically relevant mimic of TPP (**26{PP}**) to attempt to enhance native TPP-dependent enzymatic transformation and increase the scope of non-native reactions. Chapter 3.4 highlights the evaluations of the carbon acid pK_a values for both TPP (**5{PP}**) and the 1,2,4-triazolium mimic (**26{PP}**), highlighting a ~1.5 unit decrease in pK_a upon changing from a thiazolium to triazolium central NHC ring. This increase in acidity is reflected in the enhanced rates of non-enzymatic benzoin catalysis in Chapter 3.5. Initially enzyme studies have focussed on commercially available and inexpensive enzymes pyruvate decarboxylase from *Saccharomyces cerevisiae* and pyruvate oxidase from *Aerococcus sp.* in both spectrophotometric and NMR spectroscopic assays. Initial studies on these limited systems suggest that the novel mimic (**26{PP}**) binds to the active site; however, the loss of activity implies that the conformation of binding is less catalytically active. Nevertheless, this work is promising and moving forwards to explore a variety of other TPP-dependent enzymes and mutants, which may be more tolerant to changes in cofactor.

Finally, Chapter 3.3 highlighted a study into the stability of TPP (**5{PP}**) in aqueous solutions across the full p*H*-range. In deuterated buffers, rates of pyrophosphate hydrolysis were measurable from p*D* 1-7 showing typically slow hydrolysis. Above values of p*D* 8, pyrophosphate hydrolysis was too slow to measure but, cleavage of the methylene link became competitive. These results are useful when considering the handling, storage and purification of TPP and mimics during synthesis and catalytic evaluation.

3.6. References

4. D. M. Flanigan, F. Romanov-Michailidis, N. A. White and T. Rovis, *Chem. Rev.*, 2015, **115**, 9307-9387.
6. C. J. Collett, R. S. Massey, O. R. Maguire, A. S. Batsanov, A. C. O'Donoghue and A. D. Smith, *Chem. Sci.*, 2013, **4**.
8. R. S. Massey, C. J. Collett, A. G. Lindsay, A. D. Smith and A. C. O'Donoghue, *J. Am. Chem. Soc.*, 2012, **134**, 20421-20432.
9. C. J. Collett, R. S. Massey, J. E. Taylor, O. R. Maguire, A. C. O'Donoghue and A. D. Smith, *Angew. Chem. Int. Ed.*, 2015, **54**, 6887-6892.
64. M. S. Kerr, J. Read de Alaniz and T. Rovis, *J. Org. Chem.*, 2005, **70**, 5725-5728.
70. C. Hansch, A. Leo and R. W. Taft, *Chem. Rev.*, 1991, **91**, 165-195.
71. J. Zhu, I. Moreno, P. Quinn, D. S. Yufit, L. Song, C. M. Young, Z. Duan, A. R. Tyler, P. G. Waddell, M. J. Hall, M. R. Probert, A. D. Smith and A. C. O'Donoghue, *J. Org. Chem.*, 2022, **87**, 4241-4253.
76. R. S. Massey, C. J. Collett, A. G. Lindsay, A. D. Smith and A. C. O'Donoghue, *J. Am. Chem. Soc.*, 2012, **134**, 20421-20432.
86. R. A. Sheldon, D. Brady and M. L. Bode, *Chem. Sci.*, 2020, **11**, 2587-2605.
87. M. D. Truppo, *ACS Med. Chem. Lett.*, 2017, **8**, 476-480.
88. C. K. Prier and F. H. Arnold, *J. Am. Chem. Soc.*, 2015, **137**, 13992-14006.
89. F. H. Arnold, *Angew. Chem. Int. Ed.*, 2018, **57**, 4143-4148.
90. C. K. Prier, R. K. Zhang, A. R. Buller, S. Brinkmann-Chen and F. H. Arnold, *Nat. Chem.*, 2017, **9**, 629-634.
91. R. B. Leveson-Gower, C. Mayer and G. Roelfes, *Nat. Rev. Chem.*, 2019, **3**, 687-705.
92. J. W. Schafer, I. Zoi, D. Antoniou and S. D. Schwartz, *J. Am. Chem. Soc.*, 2019, **141**, 10431-10439.
93. E. Watkins-Dulaney, S. Straathof and F. Arnold, *ChemBioChem*, 2021, **22**, 5-16.
94. M. K. Akhtar and P. R. Jones, *Front. Bioeng. Biotechnol.*, 2014, **2**.
95. J. D. Fischer, G. L. Holliday and J. M. Thornton, *Bioinfom.*, 2010, **26**, 2496-2497.
96. T. P. Begley and S. E. Ealick, in *Comprehensive Natural Products II*, eds. H.-W. Liu and L. Mander, Elsevier, Oxford, 2010, DOI: https://doi.org/10.1016/B978-008045382-8.00148-9, pp. 547-559.
97. N. Melnyk, I. Iribarren, E. Mates-Torres and C. Trujillo, *Chem. Eur. J.*, 2022, **28**.
98. S. Mukherjee, J. W. Yang, S. Hoffmann and B. List, *Chem. Rev.*, 2007, **107**, 5471-5569.
99. R. P. Wurz, *Chem. Rev.*, 2007, **107**, 5570-5595.
100. A. Erkkilä, I. Majander and P. M. Pihko, *Chem. Rev.*, 2007, **107**, 5416-5470.
101. B. List, *Chem. Rev.*, 2007, **107**, 5413-5415.
102. D. Enders, O. Niemeier and A. Henseler, *Chem. Rev.*, 2007, **107**, 5606-5655.
103. M. J. Gaunt and C. C. C. Johansson, *Chem. Rev.*, 2007, **107**, 5596-5605.
104. A. G. Doyle and E. N. Jacobsen, *Chem. Rev.*, 2007, **107**, 5713-5743.
105. T. Knaus, C. E. Paul, C. W. Levy, S. de Vries, F. G. Mutti, F. Hollmann and N. S. Scrutton, *J. Am. Chem. Soc.*, 2016, **138**, 1033-1039.
106. J. K. B. Cahn, C. A. Werlang, A. Baumschlager, S. Brinkmann-Chen, S. L. Mayo and F. H. Arnold, *ACS Synth. Biol.*, 2017, **6**, 326-333.

107. L. Sellés Vidal, C. L. Kelly, P. M. Mordaka and J. T. Heap, *Biochim. Biophys. Acta - Gen. Sub.*, 2018, **1866**, 327-347.
108. J. S. Rowbotham, M. A. Ramirez, O. Lenz, H. A. Reeve and K. A. Vincent, *Nat. Commun.*, 2020, **11**, 1454.
109. D. Mauzerall and F. H. Westheimer, *J. Am. Chem. Soc.*, 1955, **77**, 2261-2264.
110. S. J. Connon, *Org. Biomol. Chem.*, 2007, **5**, 3407-3417.
111. S. G. Ouellet, A. M. Walji and D. W. C. Macmillan, *Acc. Chem. Res.*, 2007, **40**, 1327-1339.
112. C. E. Paul, D. Tischler, A. Riedel, T. Heine, N. Itoh and F. Hollmann, *ACS Catal.*, 2015, **5**, 2961-2965.
113. J. D. Ryan, R. H. Fish and D. S. Clark, *ChemBioChem*, 2008, **9**, 2579-2582.
114. C. Zor, H. A. Reeve, J. Quinson, L. A. Thompson, T. H. Lonsdale, F. Dillon, N. Grobert and K. A. Vincent, *Chem. Comm.*, 2017, **53**, 9839-9841.
115. L. A. Thompson, J. S. Rowbotham, J. H. Nicholson, M. A. Ramirez, C. Zor, H. A. Reeve, N. Grobert and K. A. Vincent, *ChemCatChem*, 2020, **12**, 3913-3918.
116. M. Desage-El Murr, *ChemCatChem*, 2020, **12**, 53-62.
117. S. O. Mansoorabadi, C. J. Thibodeaux and H.-w. Liu, *J. Org. Chem.*, 2007, **72**, 6329-6342.
118. G. de Gonzalo and M. W. Fraaije, *ChemCatChem*, 2013, **5**, 403-415.
119. S. A. Baker Dockrey and A. R. H. Narayan, *Tetrahedron*, 2019, **75**, 1115-1121.
120. S. A. Shepherd, C. Karthikeyan, J. Latham, A.-W. Struck, M. L. Thompson, B. R. K. Menon, M. Q. Styles, C. Levy, D. Leys and J. Micklefield, *Chem. Sci.*, 2015, **6**, 3454-3460.
121. D. Mondal, B. F. Fisher, Y. Jiang and J. C. Lewis, *Nat. Commun.*, 2021, **12**, 3268.
122. N. S. Scrutton, *Nat. Prod. Rep.*, 2004, **21**, 722-730.
123. H. S. Toogood, J. M. Gardiner and N. S. Scrutton, *ChemCatChem*, 2010, **2**, 892-914.
124. M. März, M. Babor and R. Cibulka, *Eur. J. Org. Chem.*, 2019, **2019**, 3264-3268.
125. R. Cibulka, *Eur. J. Org. Chem.*, 2015, **2015**, 915-932.
126. V. Mojr, V. Herzig, M. Buděšínský, R. Cibulka and T. Kraus, *Chem. Comm.*, 2010, **46**, 7599-7601.
127. G. de Gonzalo, C. Smit, J. Jin, A. J. Minnaard and M. W. Fraaije, *Chem. Comm.*, 2011, **47**, 11050-11052.
128. J. Liang, Q. Han, Y. Tan, H. Ding and J. Li, *Front. Mol. Biosci.*, 2019, **6**.
129. J. P. Richard, T. L. Amyes, J. Crugeiras and A. Rios, *Curr. Opin. Chem. Biol.*, 2009, **13**, 475-483.
130. J. P. Richard, T. L. Amyes, J. Crugeiras and A. Rios, *Biochim. Biophys. Acta - Gen. Sub.*, 2011, **1814**, 1419-1425.
131. J. Chen, X. Gong, J. Li, Y. Li, J. Ma, C. Hou, G. Zhao, W. Yuan and B. Zhao, *Science*, 2018, **360**, 1438-1442.
132. S. Li, X.-Y. Chen and D. Enders, *Chem.*, 2018, **4**, 2026-2028.
133. W. Cai, X. Qiao, H. Zhang, B. Li, J. Guo, L. Zhang, W.-W. Chen and B. Zhao, *Nat. Commun.*, 2021, **12**, 5174.
134. B.-J. Li, C. Ei-Nachef and A. M. Beauchemin, *Chem. Comm.*, 2017, **53**, 13192-13204.
135. M. Chen, C.-T. Liu and Y. Tang, *J. Am. Chem. Soc.*, 2020, **142**, 10506-10515.
136. J. F. Rocha, A. F. Pina, S. F. Sousa and N. M. F. S. A. Cerqueira, *Catal. Sci. Technol.*, 2019, **9**, 4864-4876.

137. S. A. Kelly, S. Pohle, S. Wharry, S. Mix, C. C. R. Allen, T. S. Moody and B. F. Gilmore, *Chem. Rev.*, 2018, **118**, 349-367.
138. I. V. Pavlidis, M. S. Weiß, M. Genz, P. Spurr, S. P. Hanlon, B. Wirz, H. Iding and U. T. Bornscheuer, *Nat. Chem.*, 2016, **8**, 1076-1082.
139. M. S. Weiß, I. V. Pavlidis, P. Spurr, S. P. Hanlon, B. Wirz, H. Iding and U. T. Bornscheuer, *Org. Biomol. Chem.*, 2016, **14**, 10249-10254.
140. M. S. Weiß, I. V. Pavlidis, P. Spurr, S. P. Hanlon, B. Wirz, H. Iding and U. T. Bornscheuer, *ChemBioChem*, 2017, **18**, 1022-1026.
141. C. K. Savile, J. M. Janey, E. C. Mundorff, J. C. Moore, S. Tam, W. R. Jarvis, J. C. Colbeck, A. Krebber, F. J. Fleitz, J. Brands, P. N. Devine, G. W. Huisman and G. J. Hughes, *Science*, 2010, **329**, 305-309.
142. G. L. Waldrop, H. M. Holden and M. St Maurice, *Protein. Sci.*, 2012, **21**, 1597-1619.
143. A. D. Lietzan and M. St. Maurice, *Arch. Biochem. Biophys.*, 2014, **544**, 75-86.
144. A. R. Nödling, K. Świderek, R. Castillo, J. W. Hall, A. Angelastro, L. C. Morrill, Y. Jin, Y.-H. Tsai, V. Moliner and L. Y. P. Luk, *Angew. Chem. Int. Ed.*, 2018, **57**, 12478-12482.
145. N. Santi, L. C. Morrill and L. Y. P. Luk, *Molecules (Basel, Switzerland)*, 2020, **25**, 2457.
146. Y. Cotelle, V. Lebrun, N. Sakai, T. R. Ward and S. Matile, *ACS Cent. Sci.*, 2016, **2**, 388-393.
147. N. Santi, L. C. Morrill, K. Świderek, V. Moliner and L. Y. P. Luk, *Chem. Comm.*, 2021, **57**, 1919-1922.
148. Q. Zhang, W. A. van der Donk and W. Liu, *Acc. Chem. Res.*, 2012, **45**, 555-564.
149. Q. Sun, M. Huang and Y. Wei, *Acta Pharm. Sin. B*, 2021, **11**, 632-650.
150. M. Schapira, *ACS Chem. Bio.*, 2016, **11**, 575-582.
151. C. Liao and F. P. Seebeck, *Nat. Catal.*, 2019, **2**, 696-701.
152. S. Mordhorst, J. Siegrist, M. Müller, M. Richter and J. N. Andexer, *Angew. Chem. Int. Ed.*, 2017, **56**, 4037-4041.
153. J. Peng, C. Liao, C. Bauer and F. P. Seebeck, *Angew. Chem. Int. Ed.*, 2021, **60**, 27178-27183.
154. A. Tylicki, Z. Łotowski, M. Siemieniuk and A. Ratkiewicz, *Biosci. Rep.*, 2018, **38**.
155. R. Breslow, *Tetrahedron Lett.*, 1959, **1**, 22-26.
156. R. Breslow, *J. Am. Chem. Soc.*, 1958, **80**, 3719-3726.
157. C. J. Collett, C. M. Young, R. S. Massey, A. C. O'Donoghue and A. D. Smith, *Eur. J. Org. Chem.*, 2021, **2021**, 3670-3675.
158. J. C. Sheehan and T. Hara, *J. Org. Chem.*, 1974, **39**, 1196-1199.
159. T. Waichiro, T. Yoshiharu and Y. Yumihiko, *Bull. Chem. Soc. Jpn.*, 1980, **53**, 478-480.
160. R. S. Massey, J. Murray, C. J. Collett, J. Zhu, A. D. Smith and A. C. O'Donoghue, *Org. Biomol. Chem.*, 2021, **19**, 387-393.
161. R. L. Knight and F. J. Leeper, *J. Chem. Soc., Perkin trans. 1*, 1998, DOI: 10.1039/A803635G, 1891-1894.
162. D. Enders and U. Kallfass, *Angew. Chem. Int. Ed.*, 2002, **41**, 1743-1745.
163. L. Baragwanath, C. A. Rose, K. Zeitler and S. J. Connon, *J. Org. Chem.*, 2009, **74**, 9214-9217.
164. D. A. DiRocco, E. L. Noey, K. N. Houk and T. Rovis, *Angew. Chem. Int. Ed.*, 2012, **51**, 2391-2394.

165. Y. Niu, N. Wang, A. Munoz, J. Xu, H. Zeng, T. Rovis and J. K. Lee, *J. Am. Chem. Soc.*, 2017, **139**, 14917-14930.
166. Y. Qin, L. Zhang, J. Lv, S. Luo and J.-P. Cheng, *Org. Lett.*, 2015, **17**, 1469-1472.
167. K. Takeda, K. Umezawa, A. Várnai, V. G. H. Eijsink, K. Igarashi, M. Yoshida and N. Nakamura, *Curr. Opin. Chem. Biol.*, 2019, **49**, 113-121.
168. K. Agyei-Owusu and F. J. Leeper, *FEBS J*, 2009, **276**, 2905-2916.
169. K. J. Carpenter, *Ann. Nutr. Metab.*, 2012, **61**, 259-264.
170. A. Tylicki, Z. Lotowski, M. Siemieniuk and A. Ratkiewicz, *Biosci. Rep.*, 2018, **38**.
171. R. R. Williams and J. K. Cline, *J. Am. Chem. Soc.*, 1936, **58**, 1504-1505.
172. A. Chatterjee, Y. Li, Y. Zhang, T. L. Grove, M. Lee, C. Krebs, S. J. Booker, T. P. Begley and S. E. Ealick, *Nat. Chem. Biol.*, 2008, **4**, 758-765.
173. J. J. Reddick, R. Nicewonger and T. P. Begley, *Biochemistry*, 2001, **40**, 10095-10102.
174. D. H. Peapus, H.-J. Chiu, N. Campobasso, J. J. Reddick, T. P. Begley and S. E. Ealick, *Biochemistry*, 2001, **40**, 10103-10114.
175. K. M. Erixon, C. L. Dabalos and F. J. Leeper, *Chem. Comm.*, 2007, DOI: 10.1039/B615861G, 960-962.
176. S. Mann, C. Perez Melero, D. Hawksley and F. J. Leeper, *Org. Biomol. Chem.*, 2004, **2**, 1732-1741.
177. W. E. G. Müller, H. C. Schröder and X. Wang, *The Biochemist*, 2019, **41**, 22-27.
178. B. K. Mohanty and S. R. Kushner, *PNAS*, 2000, **97**, 11966-11971.
179. T. G. Mosbacher, M. Mueller and G. E. Schulz, *FEBS*, 2005, **272**, 6067-6076.
180. V. M. Dixit, F. M. Laskovics, W. I. Noall and C. D. Poulter, *J. Org. Chem.*, 1981, **46**, 1967-1969.
181. D. R. W. Hodgson, in *Advances in Physical Organic Chemistry*, eds. I. H. Williams and N. H. Williams, Academic Press, 2017, vol. 51, pp. 187-219.
182. H. J. Korhonen, H. L. Bolt, L. Vicente-Gines, D. C. Perks and D. R. W. Hodgson, *Phosphorus Sulfur Silicon Relat. Elem.*, 2015, **190**, 758-762.
183. G. S. Cremosnik, A. Hofer and H. J. Jessen, *Angew. Chem. Int. Ed.*, 2014, **53**, 286-289.
184. R. R. Williams, R. E. Waterman, J. C. Keresztesy and E. R. Buchman, *J. Am. Chem. Soc.*, 1935, **57**, 536-537.
185. K. J. Carpenter, *J. Nutr.*, 2003, **133**, 975-984.
186. K. A. Edwards, N. Tu-Maung, K. Cheng, B. Wang, A. J. Baeumner and C. E. Kraft, *ChemistryOpen*, 2017, **6**, 178-191.
187. A. Bouzide and G. Sauvé, *Tetrahedron Lett.*, 1997, **38**, 5945-5948.
188. M. Ingale, K. Patel, J. Mangrolia, M. Patel and M. Nyati, *WO. Pat.*, WO2016/079576A1, 2016.
189. M. M. Achmatowicz, O. R. Thiel, J. T. Colyer, J. Hu, M. V. S. Elipe, J. Tomaskevitch, J. S. Tedrow and R. D. Larsen, *Org. Process Res. Dev.*, 2010, **14**, 1490-1500.
190. R. J. Delley, A. C. O'Donoghue and D. R. W. Hodgson, *J. Org. Chem.*, 2012, **77**, 5829-5831.
191. J. C. Oxley, J. Brady, S. A. Wilson and J. L. Smith, *J. Chem. Health Saf.*, 2012, **19**, 27-33.
192. M. W. Bowler, M. J. Cliff, J. P. Waltho and G. M. Blackburn, *New J. Chem.*, 2010, **34**, 784-794.

193. C. T. Walsh, in *The Chemical Biology of Phosphorus*, The Royal Society of Chemistry, 2021, DOI: 10.1039/9781839162312-00003, pp. 3-26.
194. D. O. Campbell and M. L. Kilpatrick, *J. Am. Chem. Soc.*, 1954, **76**, 893-901.
195. R. B. Stockbridge and R. Wolfenden, *J. Biol. Chem.*, 2009, **284**, 22747-22757.
196. R. Wei, C. L. Dickson, D. Uhrín and G. C. Lloyd-Jones, *J. Org. Chem.*, 2021, **86**, 9023-9029.
197. R. L. Vold, J. S. Waugh, M. P. Klein and D. E. Phelps, *J. Chem. Phys.*, 1968, **48**, 3831-3832.
198. M. Huisjen and J. S. Hyde, *J. Chem. Phys.*, 1974, **60**, 1682-1683.
199. R. Freeman and H. D. W. Hill, *J. Chem. Phys.*, 1971, **54**, 3367-3377.
200. O. I. Kolodiazhnyi and A. Kolodiazhna, *Tetrahedron: Asymmetry*, 2017, **28**, 1651-1674.
201. K. A. Rubinson, *Anal. Methods*, 2017, **9**, 2744-2750.
202. G. M. Loudon, *J. Chem. Ed.*, 1991, **68**, 973.
203. F. A. Carey and R. J. Sundberg, in *Advanced Organic Chemistry: Part A: Structure and Mechanisms*, eds. F. A. Carey and R. J. Sundberg, Springer US, Boston, MA, 2007, DOI: 10.1007/978-0-387-44899-2_3, pp. 253-388.
204. M. W. Washabaugh and W. P. Jencks, *Biochemistry*, 1988, **27**, 5044-5053.
205. J. Reijenga, A. van Hoof, A. van Loon and B. Teunissen, *Anal. Chem. Insights*, 2013, **8**, 53-71.
206. F. G. Bordwell, W. S. Matthews and N. R. Vanier, *J. Am. Chem. Soc.*, 1975, **97**, 442-443.
207. J. Peon, D. Polshakov and B. Kohler, *J. Am. Chem. Soc.*, 2002, **124**, 6428-6438.
208. P. Haake, L. P. Bausher and W. B. Miller, *J. Am. Chem. Soc.*, 1969, **91**, 1113-1119.
209. M. M. E. Scheffers-Sap and H. M. Buck, *J. Am. Chem. Soc.*, 1979, **101**, 4807-4811.
210. T. L. Amyes, S. T. Diver, J. P. Richard, F. M. Rivas and K. Toth, *J. Am. Chem. Soc.*, 2004, **126**, 4366-4374.
211. T. Korenaga, K. Kadowaki, T. Ema and T. Sakai, *J. Org. Chem.*, 2004, **69**, 7340-7343.
212. A. M. Chauvet-Monges, C. Rogeret, C. Briand and A. Crevat, *Biochim. Biophys. Acta - Gen. Sub.*, 1973, **304**, 748-752.
213. Wöhler and Liebig, *Annalen der Pharmacie*, 1832, **3**, 249-282.
214. R. Breslow and R. Kim, *Tetrahedron Lett.*, 1994, **35**, 699-702.
215. T. Dudding and K. N. Houk, *PNAS*, 2004, **101**, 5770-5775.
216. S. M. Langdon, C. Y. Legault and M. Gravel, *J. Org. Chem.*, 2015, **80**, 3597-3610.
217. Y. He and Y. Xue, *J. Phys. Chem. A*, 2011, **115**, 1408-1417.
218. D. A. DiRocco, K. M. Oberg and T. Rovis, *J. Am. Chem. Soc.*, 2012, **134**, 6143-6145.
219. B. Maji and H. Mayr, *Angew. Chem. Int. Ed.*, 2012, **51**, 10408-10412.
220. A. Berkessel, S. Elfert, K. Etzenbach-Effers and J. H. Teles, *Angew. Chem. Int. Ed.*, 2010, **49**, 7120-7124.
221. M. Paul, J.-M. Neudörfl and A. Berkessel, *Angew. Chem. Int. Ed.*, 2019, **58**, 10596-10600.
222. M. Paul, P. Sudkaow, A. Wessels, N. E. Schlorer, J. M. Neudorfl and A. Berkessel, *Angew. Chem. Int. Ed.*, 2018, **57**, 8310-8315.
223. A. Berkessel, S. Elfert, V. R. Yatham, J. M. Neudorfl, N. E. Schlorer and J. H. Teles, *Angew. Chem. Int. Ed.*, 2012, **51**, 12370-12374.

224. M. J. White and F. J. Leeper, *J. Org. Chem.*, 2001, **66**, 5124-5131.
225. A. Cornish-Bowden, *Perspect. Sci.*, 2015, **4**, 3-9.
226. R. Kluger and K. Tittmann, *Chem. Rev.*, 2008, **108**, 1797-1833.
227. T. Sehl, S. Bock, L. Marx, Z. Maugeri, L. Walter, R. Westphal, C. Vogel, U. Menyes, M. Erhardt, M. Müller, M. Pohl and D. Rother, *Green Chem.*, 2017, **19**, 380-384.
228. S. Sun, R. G. Duggleby and R. L. Schowen, *J. Am. Chem. Soc.*, 1995, **117**, 7317-7322.

4. New 1,2,4-Triazolium Scaffolds for Organocatalysis: Initial Studies

4.0. Foreword

This thesis has focussed on N-heterocyclic carbenes with applications in the unusual formation of Blatter radicals and within biocatalysis. Organocatalysis is the most prominent application of NHCs and the scaffolds explored in this thesis have not previously been evaluated as organocatalysts. This chapter provides initial evaluation of the catalytic potential of these scaffolds, in particular Nitron derivatives (**6**). Organocatalysis still relies heavily on non-sustainable solvents such as DCM and THF. Initial studies into applications of NHC organocatalysis in more sustainable aqueous environments are also discussed. Initial work in each of the areas discussed below was carried out by a 4th year project student, Tom Richardson, under my supervision. Further investigation in each area was carried out as my own work.

4.1. Introduction

4.1.1. Sustainable Chemical Processes

Green chemistry is a concept established in the early 1990s and is defined as the 'design of chemical products and processes to reduce or eliminate the use and generation of hazardous substances'.[229, 230] Since this time, the field has grown dramatically, with a big drive for improvements in the sustainability of the chemical industry. When considering green chemistry, a set of twelve design principles are considered (Table 4.1.1). Importantly, each of these twelve factors should be applied when designing chemical processes.[229]

NHC-organocatalysis can be considered a relatively sustainable field: atom economy is high (disregarding catalyst use), chemical syntheses are typically non-hazardous, energy efficiency is good (typically reactions are carried out at room temperature) and reagents are considered safer (organocatalysts are much less toxic than inorganic counterparts). However, considering the field as a whole, there are still significant areas for improvement, particularly with regard to solvent use.

Table 4.1.1. The 12 Principles of Green Chemistry.[229]

Principle	Definition
Prevention	It is better to prevent waste than to treat or clean up waste after it has been created.
Atom Economy	Synthetic methods should be designed to maximize incorporation of all materials used in the process into the final product.
Less Hazardous Chemical Synthesis	Wherever practicable, synthetic methods should be designed to use and generate substances that possess little or no toxicity to human health and the environment.
Designing Safer Chemicals	Chemical products should be designed to preserve efficacy of function while reducing toxicity.
Safer Solvents and Auxiliaries	The use of auxiliary substances (e.g., solvents, separation agents, etc.) should be made unnecessary wherever possible and, innocuous when used.
Design for Energy Efficiency	Energy requirements should be recognized for their environmental and economic impacts and should be minimized. Synthetic methods should be conducted at ambient temperature and pressure.
Use of Renewable Feedstocks	A raw material or feedstock should be renewable rather than depleting whenever technically and economically practicable.
Reduce Derivatives	Unnecessary derivatization (use of blocking groups, protection/deprotection, temporary modification of physical/chemical processes) should be minimized or avoided if possible, because such steps require additional reagents and can generate waste.
Catalysis	Catalytic reagents (as selective as possible) are superior to stoichiometric reagents.
Design for Degradation	Chemical products should be designed so that at the end of their function they break down into innocuous degradation products and do not persist in the environment.
Real-time Analysis for Pollution Prevention	Analytical methodologies need to be further developed to allow for real-time, in-process monitoring and control prior to the formation of hazardous substances.
Inherently Safer Chemistry for Accident Prevention	Substances and the form of a substance used in a chemical process should be chosen to minimize the potential for chemical accidents, including releases, explosions, and fires.

4.1.2. Evaluation of Classic Solvents in Organic Synthesis

Many traditional organic solvents are considered non-sustainable and environmentally hazardous. One of the key approaches to evaluation of the 'green' credentials of a solvent is a life cycle assessment (LCA). LCAs evaluate processes, taking consideration of environmental impact, emissions, use of resources, environmental impact and effect of human health.[231]

Work by Fischer *et al*. evaluated a range of common laboratory solvents in a LCA, by measuring their cumulative energy demand.[231] This method is a good overall indicator of solvent 'greenness' due to the high correlation with other complex factors such as eco-indicators. Importantly this work demonstrated that solvents such as THF, isopropanol and cyclohexanone are not viable as green solvents owing to their petrochemical origins and environmental impacts during production and subsequent disposal. This method of considering organic solvents gives a useful reference for what can be described as sustainable solvents but, does not always coincide with environmental health and safety descriptors (Figure 4.1.1). For example, hexane and heptane score highly when considering the CED (cumulative energy demand) method but poorly with regards to EHS (environmental health and safety). This illustrates the complex nature of solvent classification and the inherent challenges when considering sustainable solvents.

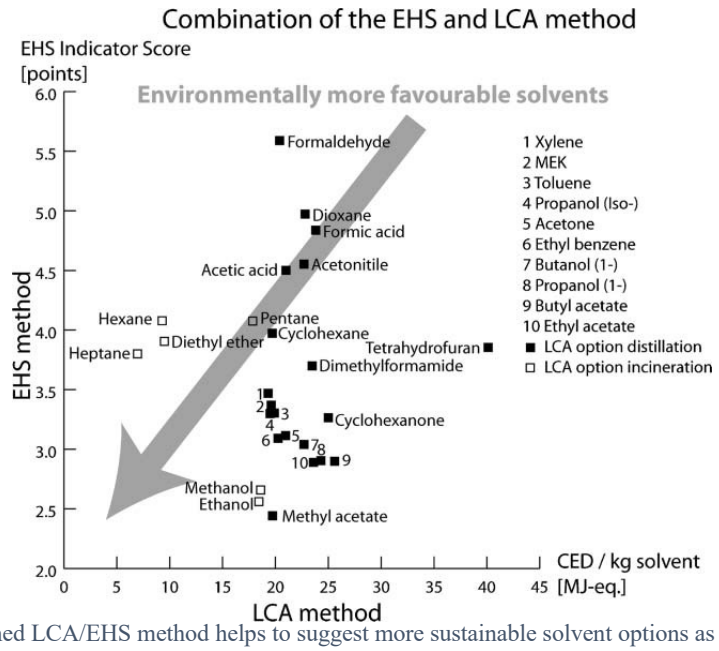

Figure 4.1.1. A combined LCA/EHS method helps to suggest more sustainable solvent options as those in the bottom left of the plot. Reproduced with permission from Ref. 228 and the Royal Society of Chemistry.

The analysis discussed above does not consider halogenated solvents, which are typically considered to be highly detrimental to the environment and human health. DCM is a key solvent used in many synthetic procedures however it is both a suspected carcinogen and has also been found to be ozone depleting within the atmosphere.[232] Although there is currently no legislative drive to move away from DCM, as was the case for carbon tetrachloride, it is likely that greater attention will be paid to its applications in future.

There is no doubt that the chemical industry will receive greater scrutiny in future as the push to more sustainable processes becomes more urgent. Alternative, more sustainable,

solvent solutions will be required to replace the commonly used but environmentally detrimental solvents currently in use.

4.1.3. Alternative Solvents

There are a variety of alternative solvents currently under investigation as replacements for less sustainable examples. One key approach is to use bio-derived alternatives such as bioethanol. Bioethanol is typically isolated from yeast fermentation of lignocellulosic biomass (corn, sugarcane) for the biofuel market. Applications would also be possible for organic synthesis. Another example is the use of 2-methyltetrahydrofuran (2-MeTHF) (**154**) as a bio-derived alternative to THF (Scheme 4.1.1). 2-MeTHF can be generated by the hydrogenation of furfural (**155**), which is obtained from the feedstock intermediates such as levulinic acid (**156**). Levulinic acid can be isolated from the acid hydrolysis of cellulosic material. 2-MeTHF is a significantly more sustainable solvent than THF and also has much lower toxicity.[233] The key disadvantage of using bio-derived solvents is that most are derived from lignocellulosic biomass. This results in crop producing land being diverted from food to solvent production. Considering the global issue of food security, particularly in third world and developing countries, this raises significant ethical dilemmas. Moreover, it should be noted that the process of synthesising 2-MeTHF still requires the input of fossil fuels in the form of hydrogen from natural gas. Renewable approaches to generate hydrogen are available including the electrolysis of water.[234]

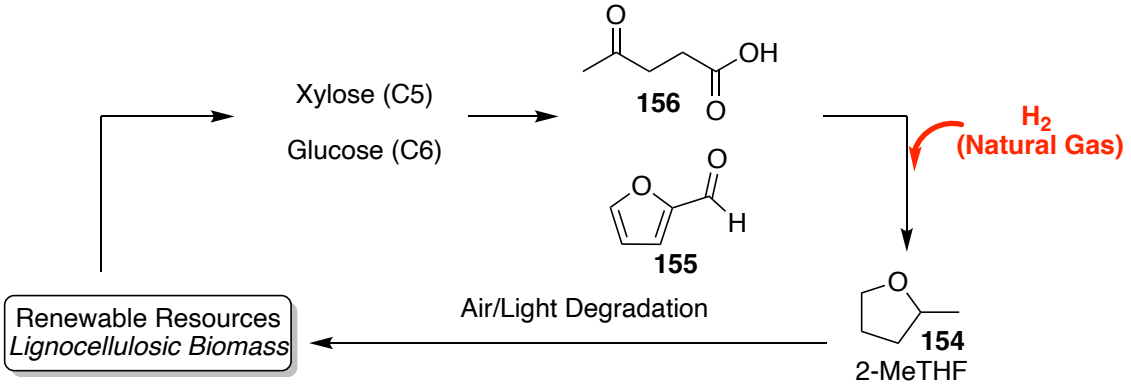

Scheme 4.1.1. The synthesis and breakdown of 2-MeTHF of which hydrogenation is still a key part of the process.

Other examples of solvents explored as more sustainable solutions include ionic liquids (ILs), molten organic salts with low volatility (Figure 4.1.2); deep eutectic solvents (DESs), mixtures of Brønsted/Lewis acids and bases (Figure 4.1.2); and supercritical CO_2 ($scCO_2$), which refers to CO_2 in a liquid state at T_c = 31 °C and p_c = 72.8 atm. ILs are seen as advantageous due to their high solvation ability and low volatility; however,

typical synthetic procedures to generate ILs still require the use of organic solvents. Moreover, waste treatment is important as many are environmentally hazardous. DESs can be generated from entirely biorenewable sources such as ammonium salts, sugars and organic acids and can be compatible with bio-transformations. Despite being synthesised from non-toxic precursors, it has been found that that the toxicity is increased upon DES formation and this should be a consideration in their application. Finally, $scCO_2$ is particularly useful as an extractive solvent as well as for synthetic reactions involving gases. However, for reactions involving solids, organic cosolvents are typically required to aid solubility.[233]

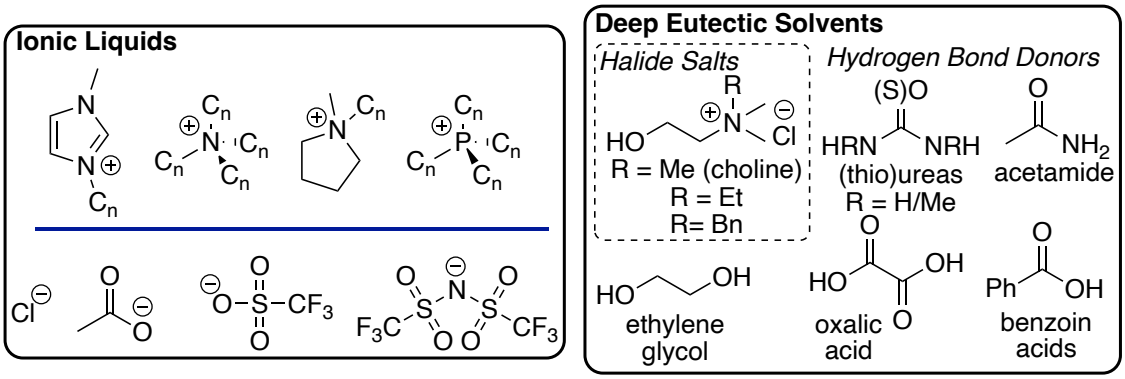

Figure 4.1.2. Examples of components of ionic liquids (left) where C_n = alkyl chain, typically n>4, and deep eutectic solvents (right).

As a solvent, water is often overlooked as an alternative in organic synthesis. Water is often considered detrimental to organic reactions and is excluded by drying processes and the use of hydrophobic organic solvents; however, if some of the challenges presented by using water as a solvent are overcome it could provide a very sustainable solution. The most obvious obstacle to using water as solvent to organic reactions is the solubility of reagents. Recent studies have shown that this is not necessarily an issue: solubility is not key to reaction efficiency, and it can aid catalyst and product separation at work-up stage.[235] Other approaches to aid solubility include the use of surfactants to generate hydrophobic cavities (Figure 4.1.3(b)), co-solvents to improve miscibility or for biphasic reactions, the use of enzymes (Chapter 3) or the development of water-soluble catalysts.[236] Many organic reagents also suffer from hydrolytic instability, for example acyl chlorides or metal-lithium reagents. Whilst in general this is a key limiting factor, it has been shown that rapid mixing allows reaction to occur 'on water' (Figure 4.1.3(a)).[237] In these cases, reagents do not come into contact with water as such, but instead sit on the surface. Despite a lack of understanding of this process it has been shown that even organolithium reagents can react in this fashion and not undergo hydrolysis.[235, 238]

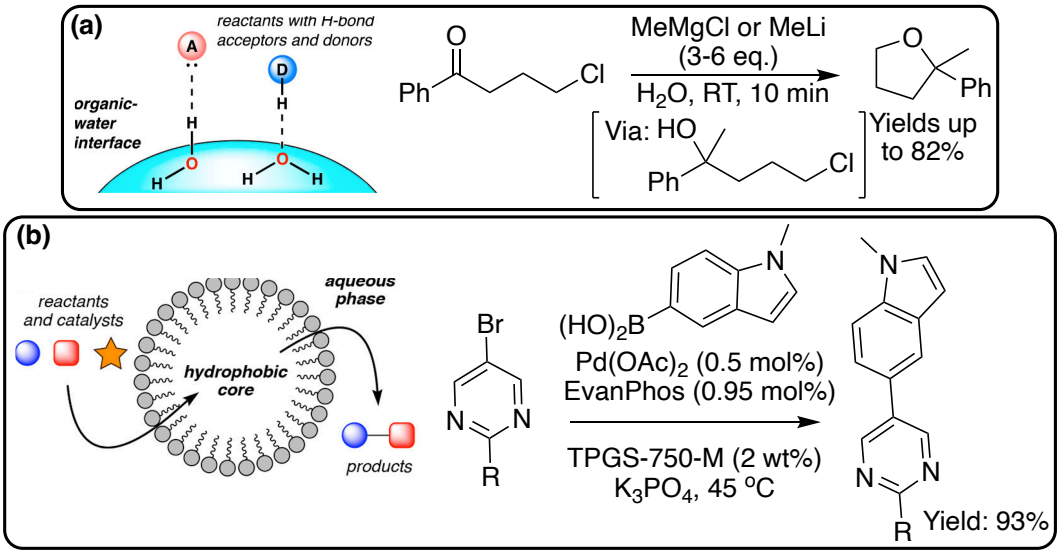

Figure 4.1.3. (a) Organometallic reactions on water have been shown to be possible even for highly reactive organolithium reagents; (b) A key approach to improving reactivity in water is to use surfactants (e.g. TPGS-750-M) to aid solubility and stabilise transition states. Adapted with permission from D. K. Romney, F. H. Arnold, B. H. Lipshutz and C.-J. Li, *J. Org. Chem.*, 2018, **83**, 7319-7322. Copyright 2022 American Chemical Society.

Finally, the hydrogen bonding capacity of water can disrupt hydrogen bond formation in reaction, destabilising key intermediates and transition states. This can alter product selectivity and disfavour reactions. There have been advances in synthetic chemistry to avoid this, particularly in providing hydrophobic binding cavities. Cyclodextrins, cyclic polymers and enzymes have been used to aid transition state stabilisation.[238]

There is no single ideal solution to replacing non-sustainable organic solvents within chemical synthesis. Recent advances do provide options which may be viable future alternatives to some of the most environmentally detrimental solvents.

4.1.4. NHC Organocatalysis in Sustainable Solvents

To date, there has been limited exploration of NHC organocatalysis in more sustainable solvents. Past reviews highlight the prevalence of both THF and DCM in typical reactions such as the benzoin condensation and Stetter reaction.[4, 102] The reliance of this field on these solvents highlights the importance of exploring alternatives should future legislation place limits on use.

An asymmetric benzoin condensation has been demonstrated under aqueous conditions, with high yields and *ee*s for benzoin (**148**), using NHC-catalyst (**157**) (Scheme 4.1.2).[239] Reaction times were typically shorter than for those in organic solvents and the authors propose a rate enhancement provided by water acting as a proton-shuttle. The catalyst

used in this case is not well-designed for applications in water, as such a hydrophobic scaffold will limit solubility. This could help explain why yields are lower than those typically observed for 1,2,4-triazolium catalysts with N-pentafluorophenyl substituents. Nevertheless, this highlights the potential for NHC-organocatalysis in water, with perhaps greater future focus on catalyst design.

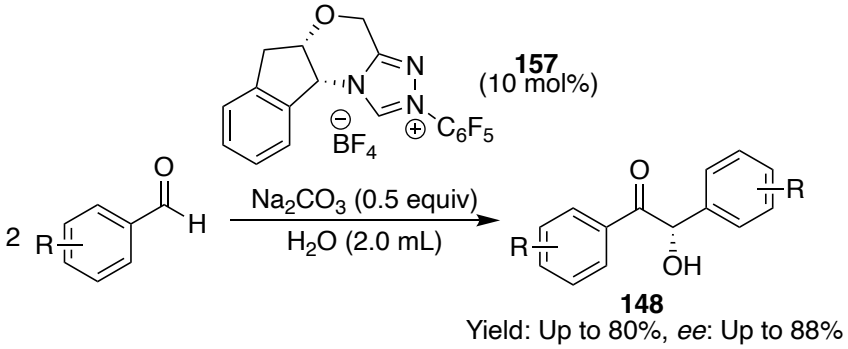

Scheme 4.1.2. A benzoin condensation carried out in aqueous conditions using catalyst **157**. To our knowledge, this is the only example to date of a fully aqueous 1,2,4-triazolium catalysed benzoin condensation.

NHC-organocatalysis using an imidazolium pre-catalyst (**158**) was employed for the synthesis of a range of spirocycles in aqueous media (Scheme 4.1.3).[240, 241] Rate enhancements were noted when reactions were carried out in brine, attributed to a hydrophobic hydration effect. Hydrophobic hydration is defined as 'the process of cavity formation in liquid water, the insertion of an apolar solute particle, the onset of solute-solvent interactions, and the concomitant reordering of the water molecules in close proximity to the solute'.[242] The hydrophobic, surfactant like NHCs are thought to form micelle-like structures where non-polar substrates can accumulate and react.

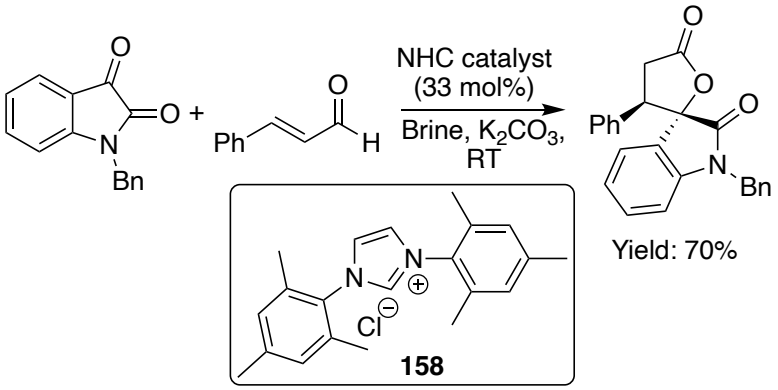

Scheme 4.1.3. Organocatalytic spirocycle synthesis in good yields under aqueous conditions. Brine was found to enhance reaction rate and yield, attributed to the hydrophobic effect.

There have been limited studies of NHC-organocatalysis in ionic liquids, deep eutectic solvents or $scCO_2$. With regards to $scCO_2$ this is not surprising, considering NHCs typically react with carbonyl systems. In fact, NHC systems have been utilised for the fixation of CO_2 and the synthesis of carbonates.[243] Many ionic liquids are composed of

imidazolium salts, which are examples of NHC pre-catalysts. Imidazolium-based ionic liquids were therefore explored in the NHC-catalysed synthesis of a lactone in comparison to standard THF. It was found that reaction in ILs was particularly slow and this was attributed to unfavourable carbene-cation interactions and proton-exchange alongside the poor catalytic activity of the formed carbene within an ionic liquid.[244]

4.2. Evaluation of New Catalyst Scaffolds

4.2.1. Nitron Derivatives as Organocatalysts

Despite previous studies highlighting the carbenic nature of Nitron (**6**), there has been no reported survey of its catalytic potential.[22] Exploration of this area may have been limited by the instability of Nitron (**6a**), which we have found to ring open in a range of polar solvents and spontaneously form radicals in acetonitrile. Chapter 2 highlighted studies into developing a broader synthetic strategy to Nitron derivatives, alongside propensity for Blatter radical formation. Two key conclusions were drawn: electron withdrawing substituents on the exocyclic N-aryl group and N-methylation stabilise Nitron with respect to hydrolytic ring opening at C(3). This was attributed to shifting (or eliminating) the tautomerisation to the carbene. This knowledge can subsequently be used to design more stable Nitron derivatives, which can be screened for catalytic potential.

Carbon acidity of NHC pre-catalysts is typically an excellent measure of catalytic proficiency due indications of the level of active carbenic catalyst at equilibrium. Moreover, increased pre-catalyst acidity correlates to enhanced rates of deprotonation in NHC-catalysed processes, in particular formation of the Breslow intermediate from the precursor hydroxyaryl adduct. Rates of H/D-exchange at a given p*D* value can typically be used as a measure of acidity, with higher rates implying greater acidity. Table 4.2.1 summarises the exchange rate constants, k_{ex}, in 0.1 M DCl at 25 °C for Nitron derivatives (**6**) synthesised in Chapter 2. These were comparable to a selection of 5-membered fused ring 1,2,4-triazoliums (**61**) more typically used in organocatalysis, under the same conditions.

Table 4.2.1. Summary of rate constants for H/D exchange (k_{ex}) in 0.1 M DCl, I = 1 M, at 25 °C for Nitron derivatives (**6**) and 5-membered ring catalysts (**61**). Hammett constants shown and values for k_{ex} were used to construct the Hammett plots in Figure 4.2.1.

Compound	Ar^1	Ar^2	Hammett-σ[a]	k_{ex} (30% v/v MeCN) / $\times 10^{-6}$ s^{-1}	k_{ex} (50% v/v MeCN) / $\times 10^{-6}$ s^{-1}
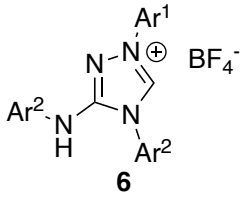 **6**	Ph	Ph	0	6.39±0.01	5.38 ± 0.05
	Ph	4-$F_3CC_6H_4$	0.54	33.7 ± 1.5	49.5 ± 0.3
	Ph	4-$EtOC_6H_4$	-0.24	3.01 ± 0.02	2.12 ± 0.03
	4-$F_3CC_6H_4$	4-$F_3CC_6H_4$	1.08[b]	-	204 ± 6.5
	4-$MeOC_6H_4$	4-$F_3CC_6H_4$	0.19[b]	-	22.2 ± 0.2
	4-FC_6H_4	Ph	0.06	7.27 ± 0.01	-
	4-NCC_6H_4	Ph	0.66	61.3 ± 0.2	-
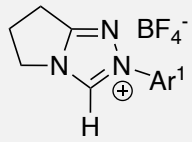 **61**	Ph	-	0	9.46[c]	-
	4-FC_6H_4	-	0.06	16.4[c]	-
	4-NCC_6H_4	-	0.66	64.5[c]	-
	4-$MeOC_6H_4$	-	-0.27	8.80[c]	-

[a]Hammett-σ values obtained from Hansch and co-worksers.[70] [b]Hammett constants were determined as the sum of the Hammett constant for substituents on both Ar^1 and Ar^2.[c]k_{ex} values taken from Massey *et al.* (2012).[76]

Hammett plots for Nitron derivatives (**6**) (in 30% and 50% MeCN) and the 5 membered ring catalyst (**61**) (in 30% MeCN) highlight that similar magnitudes of k_{ex} and relatively similar trends with respect to N-aryl substituent effects are observed (Figure 4.2.1). Hammett-ρ values are determined as the slope of a plot of k_{ex} against Hammett-σ substituent constants. Rate or equilibrium constants can be used in Hammett plots, with rate constants giving information on transition state formation and equilibrium constants providing insights into overall product formation. The sign (+/-) gives information on whether charge is built up or lost in a process, with a positive value reflecting an increase in electron density. Hammett-σ constants are determined from the reference reaction of the acid dissociation of substituted benzoic acids. Magnitudes of ρ therefore reflect a relative sensitivity to substituent change, with $\rho > 1$ suggesting greater sensitivity and $\rho < 1$ suggesting lower sensitivity in comparison to the reference.

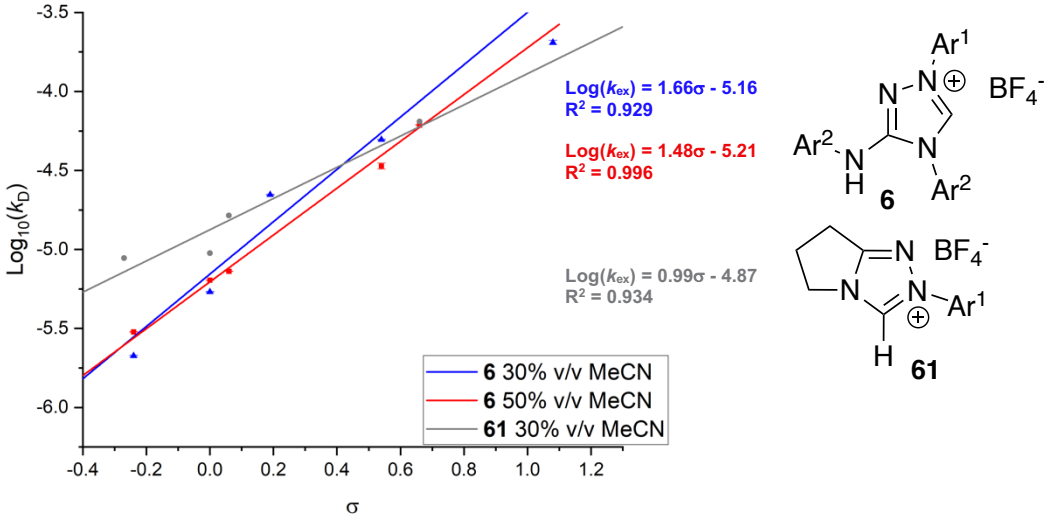

Figure 4.2.1. Hammett plots for Nitron derivatives (**6**) in 30% acetonitrile and 50% acetonitrile in comparison to 5-membered ring catalysts (**61**) in 30% acetonitrile.

Observed experimental values for ρ are all positive, as would be predicted for a deprotonation process, where an increase in electron density is observed. Values for ρ in the case of Nitron derivatives in different proportions of acetonitrile are roughly similar (ρ = 1.66 for 30% MeCN; ρ = 1.48 in 50% MeCN) and suggest a significantly greater sensitivity to substituent change than the reference benzoic acid dissociation. The 5-membered ring catalysts (**61**) (ρ = 0.99) gave a similar sensitivity to substituent change compared to the reference reaction. The greater sensitivity to substituent change of Nitron derivatives could be explained by a greater increase in electron density in the vicinity of Ar^1 and Ar^2. This could imply a greater carbenic contribution in comparison to an ylide for Nitrons (**6**) in comparison to the 5-membered ring catalyst (**61**) (Scheme 4.2.1).

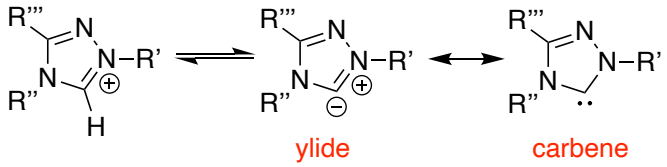

Scheme 4.2.1. Deprotonation of 1,2,4-triazoliums leads to formation of a negative charge at the C(3)-position (ylide) which can also be expressed as a carbene upon shifting the electron density to the more electronegative nitrogen atom.

Importantly, Figure 4.2.1 highlights that values for k_{ex} for Nitron derivatives (**6**) are similar to those of the 5-membered ring catalyst (**61**) suggesting C(3)-H acidity should be similar. The Nitron derivatives chosen for catalytic studies were compound **6j** (Ar^1=Ar^2=4-$F_3CC_6H_4$), as the most acidic of the Nitron derivatives prepared, with Nitron **6i** (Ar^1 = 4-NCC_6H_4, Ar^2 = Ph) also particularly acidic. Finally, parent Nitron (**6a**) was utilised as it is both commercially available and a reference example. Initial catalyst

evaluation focussed on synthetic applications of catalysts in the benzoin condensation, following the method of Connon *et al*. (Scheme 4.2.2).[163] Using NMR spectroscopy and LC-MS to monitor reactions and, where possible, % yield determination, catalysts could be compared. Results were compared to the highly acidic catalyst **61f**, of similar structure to that of Connon *et al*. (**7**), without stereodirecting groups.

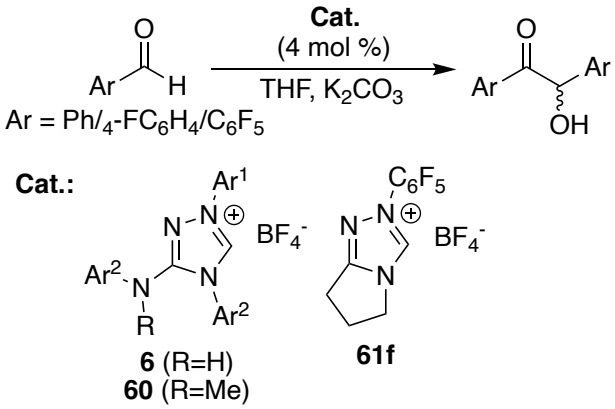

Scheme 4.2.2. The synthetic benzoin condensation used to evaluate the Nitron derivatives as potential catalysts. Conditions used were the same as those described by Connon for the very high yielding and enantioselective benzoin condensation.[163]

Table 4.2.2. Summary of the benzoin condensations explored with the Nitron catalysts developed in Chapter 2 and some N-methylated derivatives in comparison to the highly active catalyst **61f**.

Catalyst	Aldehyde	Hydroxyaryl Adduct Evidence	Benzoin Evidence	Yield / %
61f	PhCHO	Y	Y	74 (90)[b]
6a	PhCHO	N	N[a]	-
6i		N	N[a]	-
6j	PhCHO	N	N	-
	C_6F_5CHO	Y	N	-
	4-FC_6H_4CHO	N	N	-
60a	PhCHO	N	N	-
	C_6F_5CHO	Y	N	-
	4-FC_6H_4CHO	N	N	-
60i	PhCHO	N	N	-

[a]Catalysts were found to decompose (ring open) during the course of the reaction so were abandoned.[b] 90% yield was the best reported by Connon *et al.* for a similar catalyst structure.[163]

Initial studies showed no propensity for benzoin formation for any of the Nitron derivatives explored and this was attributed in part to ring opening under the basic conditions of the reactions. Although **6j** was found to not ring open to form Blatter radicals under previously explored conditions (Chapter 2), **6a** and **6i** were both found to be susceptible to ring opening. Moreover, under the basic conditions required for the benzoin condensation, it was unknown whether ring opening of **6j** could also occur.

Exocyclic nitrogen methylation was found to stabilise Nitron (**6a**) with respect to ring opening; furthermore, studies of H/D exchange of methylated Nitron (**60a**) gave a value of $k_{ex} = 5.13 \times 10^{-6}$ s^{-1} (Nitron (**6a**), $k_{ex} = 6.39 \times 10^{-6}$ s^{-1}) highlighting only a small change in the acidity upon methylation. As such, methylation of the three catalysts was also explored to target a series of 6 catalysts for study. Methylation of compound **6i** was found to be very straightforward, following the same procedure as parent Nitron (**6a**) methylation (Scheme 4.2.3). However, compound **6j** was very difficult to methylate due to the significantly reduced nucleophilicity of the exocyclic nitrogen. A range of methods for methylation was explored. Use of trimethyloxonium tetrafluoroborate or acidic methanol as methylating agents was not successful. Attempted methylation with methyl iodide at 45 °C did proceed to the desired product but, an increase in temperature to 100 °C, in high pressure apparatus, yielded the desired compound. Unfortunately, methylation in this case occurred at both the exocyclic nitrogen and the C(3) position giving a mix of products which could not be isolated by purification.

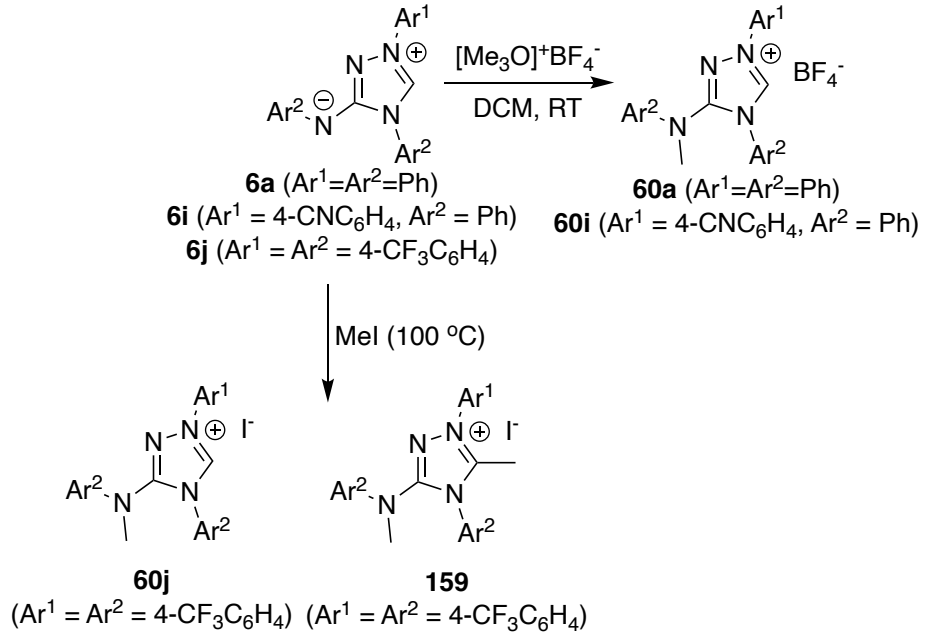

6a (Ar^1=Ar^2=Ph)
6i (Ar^1 = 4-CNC_6H_4, Ar^2 = Ph)
6j (Ar^1 = Ar^2 = 4-$CF_3C_6H_4$)

60a (Ar^1=Ar^2=Ph)
60i (Ar^1 = 4-CNC_6H_4, Ar^2 = Ph)

60j (Ar^1 = Ar^2 = 4-$CF_3C_6H_4$)

159 (Ar^1 = Ar^2 = 4-$CF_3C_6H_4$)

Scheme 4.2.3. Synthesis of N-Me Nitron derivatives using trimethyloxonium tetrafluoroborate. This route did not work for Nitron **6j** and therefore methyl iodide was employed instead which led to a di-methylated compound (**159**).

Initial results are highlighted in Table 4.2.2 for benzaldehyde, 4-fluorobenzaldehyde and pentafluorophenylaldehyde for all catalysts studied. These reactions did not appear to be providing evidence of benzoin formation over the period of 3 days. The most reactive aldehyde, pentafluorophenyl benzaldehyde, did appear to show formation of the initial hydroxyaryl adduct (**146**), but stalled at this point. Further investigation used a more quantitative, mechanistic approach as previously discussed in Chapter 3.5.

A selection of experiments were explored using our groups typical reaction conditions for kinetic evaluation of the benzoin condensation with 2-methoxybenzaldehyde (Scheme 4.2.4). A representative set of spectra is shown in Figure 4.2.2 for catalyst **60i**. Unfortunately, all experiments proceeded in this fashion, with no assignable formation of adduct (**146c**) or benzoin (**148**) over the course of 48 hours.

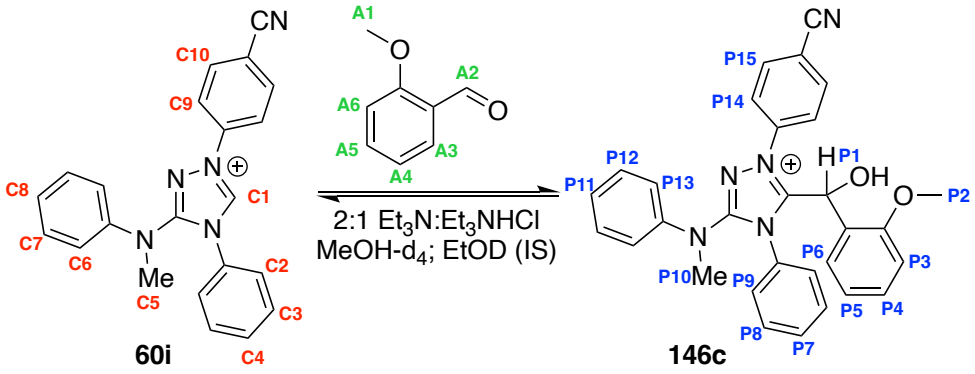

Scheme 4.2.4. Attempted adduct (**146c**) formation with Nitron catalyst **60i**, monitored kinetically with ^{1}H NMR spectroscopy. Key peaks in the NMR spectra (Figure 4.2.2) are assigned with coloured labels shown.

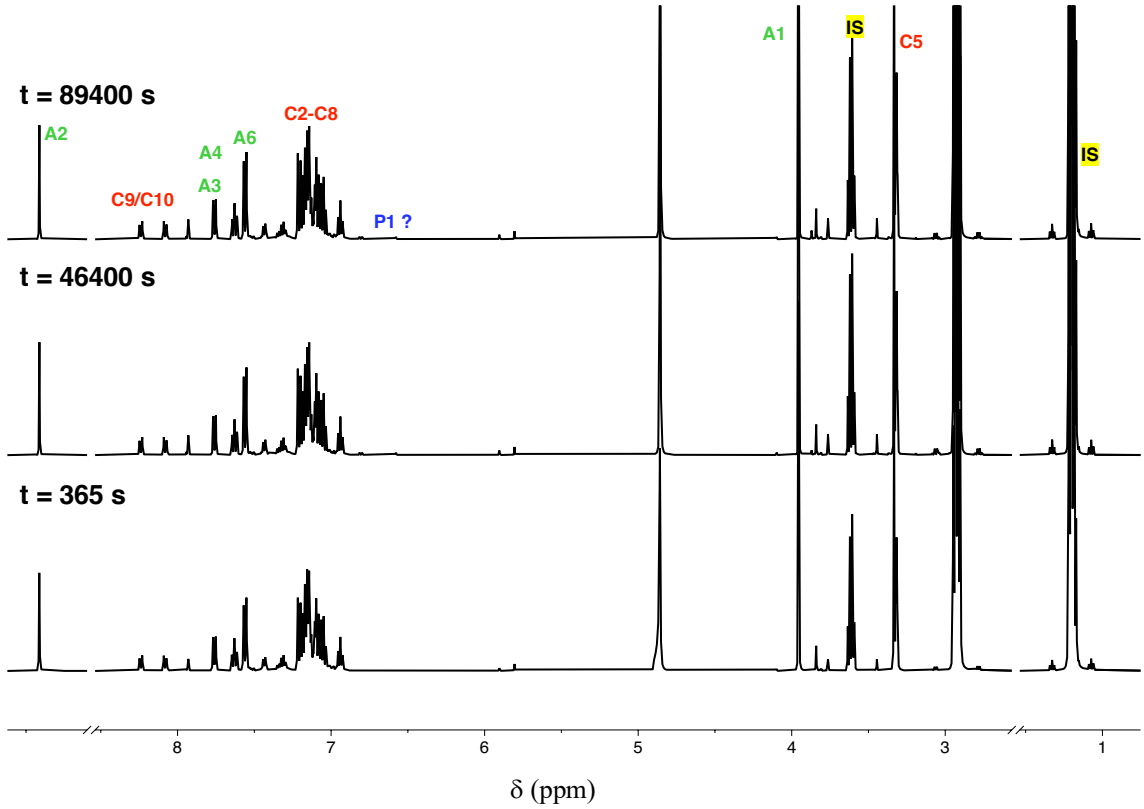

Figure 4.2.2. Representative ^{1}H NMR spectra for the attempted formation of adduct **146c** as shown in Scheme 3.4.6 at Time = 365 s, 46400 s and 89400 s.

These results are unexpected: Nitron derivatives have measurable carbenic character and very similar kinetic acidities to 5-membered ring catalysts, which have been shown to have catalytic behaviour. Structurally, there are very few of the commonly employed 1,2,4-triazolium catalysts with N(2) and N(4) aryl substituents. Typical catalysts possess

an N(2)-aryl substituent and N(4)-alkyl substituent. Another similar structured 1,2,4-triazolium is compound **160** which is often referred to as Enders' Carbene (when deprotonated).[63, 102, 245] There has been limited catalytic application of **160** and typically it has been used with very reactive aldehydes such as formaldehyde (Scheme 4.2.5). This could suggest that the addition of two N-phenyl groups near the C(3)-position, despite not affecting the acidity, reduces the nucleophilicity of the carbene.

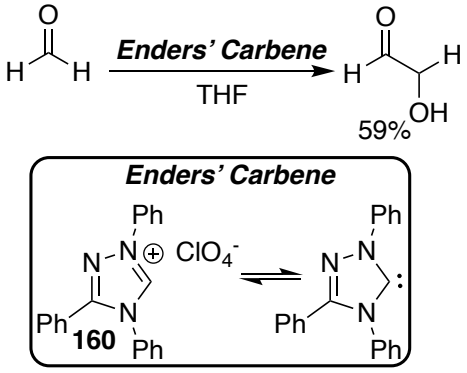

Scheme 4.2.5. The formoin condensation catalysed by Enders' carbene.

Overall, there is no full explanation for the observed lack of catalytic performance, given the determined k_{ex} values. Carbenes formed from Nitron derivatives (**6**) do appear to have significantly different chemical behaviour to those of other 1,2,4-triazoliums. This has been further evidenced by role of the carbenic tautomer of Nitron within the Nitron to Blatter radical rearrangement (Chapter 2).

4.2.2. N-Aryl Thiamine Mimics as Organocatalysts

The N-aryl thiamine mimics (**27a** & **27b**) developed in Chapter 3 are a new 1,2,4-triazolium scaffold and studies on the H/D exchange highlighted a relatively acidic C(3)-H proton for compound **27b**. The acidity was however much lower than for a range of other 1,2,4-triazolium pre-catalysts. Therefore, this project targeted changes to the N-aryl group to increase acidity. An N-C_6F_5 substituted compound (**27c**) was attempted (Scheme 4.2.6) but, synthetically this was particularly challenging. Initial formation of the hydrazide (**124c**) took longer as would be expected considering the reduced nitrogen electrophilicity brought about by the electron withdrawing pentafluorophenyl substituent. Moreover, under the relatively harsh conditions of this reaction (100 °C, triethylamine), it was found that the pentafluorophenyl ring undergoes hydrodefluorination at the *para*-position (**124d**). This results in the formation of two products, in similar amounts, with

similar properties, which were not possible to resolve. Therefore, these were continued into the subsequent step as a mixture.

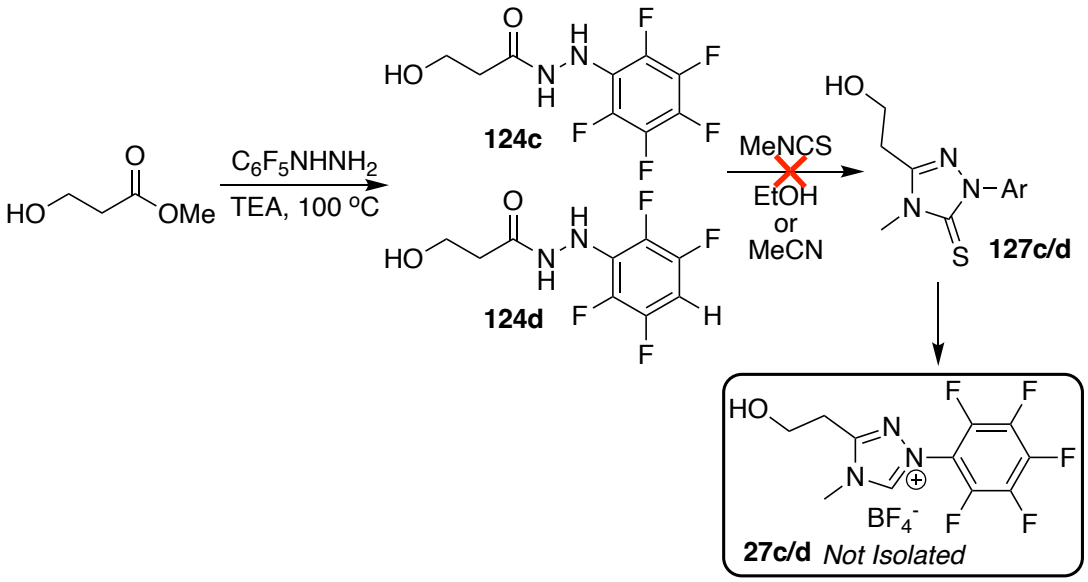

Scheme 4.2.6. Attempted synthesis of the N-C_6F_5 thiamine mimic **27c/d** was initially complicated by hydrodefluorination of the pentafluorophenyl ring. Subsequent ring closure with methyl isothiocyanate did not proceed, likely due to the vastly decreased nucleophilicity at nitrogen.

Reaction with methyl isothiocyanate was expected to be straightforward to yield the target thiones (**127c/d**). Unfortunately, under the reaction conditions (ethanol, reflux) no reaction occurred, and solvent outcompeted the formation of the thione. To favour reaction of the hydrazide with methyl isothiocyanate, a non-competitive solvent (MeCN) was also explored but with no success. It appears that inclusion of a pentafluorophenyl group into the scaffold, via the already developed synthetic strategy, is not possible due to the vastly reduced nucleophilicity of the nitrogen atoms of this hydrazine.

An alternative to the highly electron withdrawing pentafluorophenyl group is to use a 4-cyanophenyl group instead (**27e**). This was also explored however the hydrazide (**124e**) was not formed in this case. The poor solubility of this hydrazine, which was instead used as the hydrochloride salt, appeared to prevent reactivity, even at elevated temperatures. These findings highlight that although the new synthetic strategy to thiamine mimics is relatively broad, certain steps require more attention to improve isolated yields and reactivity.

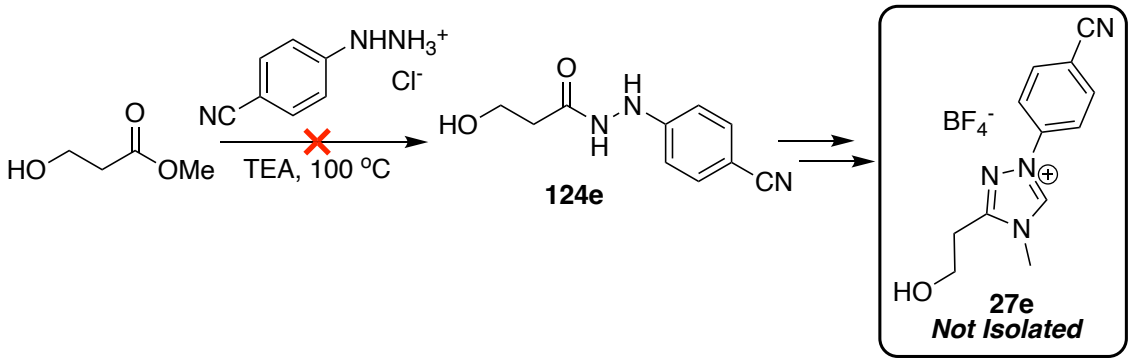

Scheme 4.2.7. Attempted synthesis of the N-C_6H_4CN thiamine mimic **27e** was not possible as reaction of the N-arylhydrazine and starting ester did not proceed.

As a baseline catalyst, compound **27a**, with an N-phenyl substituent was explored in benzoin condensations. Although a C(3)-H pK_a for this compound has not been determined, a value for of 18.6 for **27b** was previously estimated (Chapter 3.4) which is similar to **27a**. Previous studies on this 1,2,4-triazolium scaffold had found that changes in alkyl chain length did not significantly influence the C(3)-H acidity, as would be expected. Initial studies focussed on our standard experimental conditions for kinetic tracking of benzoin condensations, with 2-methoxybenzaldehyde (Scheme 4.2.8). Although reaction with the aldehyde was found to occur, an equilibrium was reached quickly, with a significant shift towards starting reagents. It was found that the rate constant for decay of the hydroxyaryl adduct (**146d**) (k_{-1}) was of a similar order of magnitude to previously explored heterocyclic azolium ions in Chapter 3.5 but, that for hydroxyaryl adduct (**146d**) formation (k_1) was significantly smaller in this case (10-100 fold lower). The values for rate and equilibrium constants are lower than what might be anticipated for a 1,2,4-triazolium; for example, the 5-membered ring catalyst (**61a**) with an N-phenyl substituent shows more than 1000-fold rate enhancement for the formation of adduct (**146e**). Catalyst **61a** has an estimated pK_a value of 17.5 and hence is significantly more acidic than catalyst **27a**. Values are most similar to thiamine pyrophosphate (**5{PP}**), which has a pK_a of 19.8, but the equilibrium is still shifted significantly in favour of catalyst suggesting a destabilised adduct in this case.

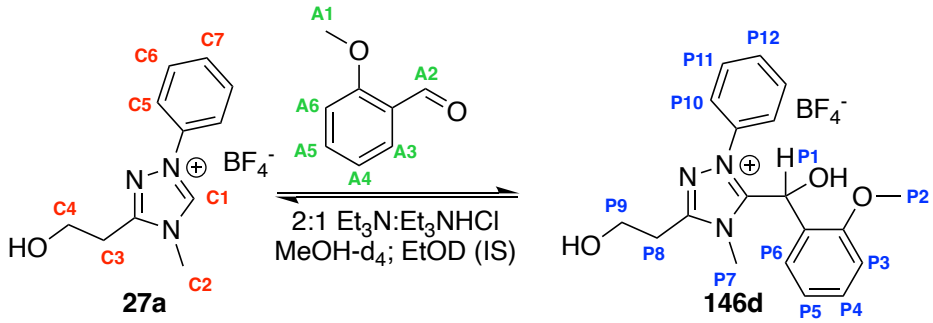

Scheme 4.2.8. Kinetic tracking of adduct (**146d**) formation with N-Ph thiamine mimic catalyst **27a**, monitored by ^{1}H NMR spectroscopy. Key peaks in the ^{1}H NMR spectra (Figure 4.2.3) are assigned with coloured labels shown.

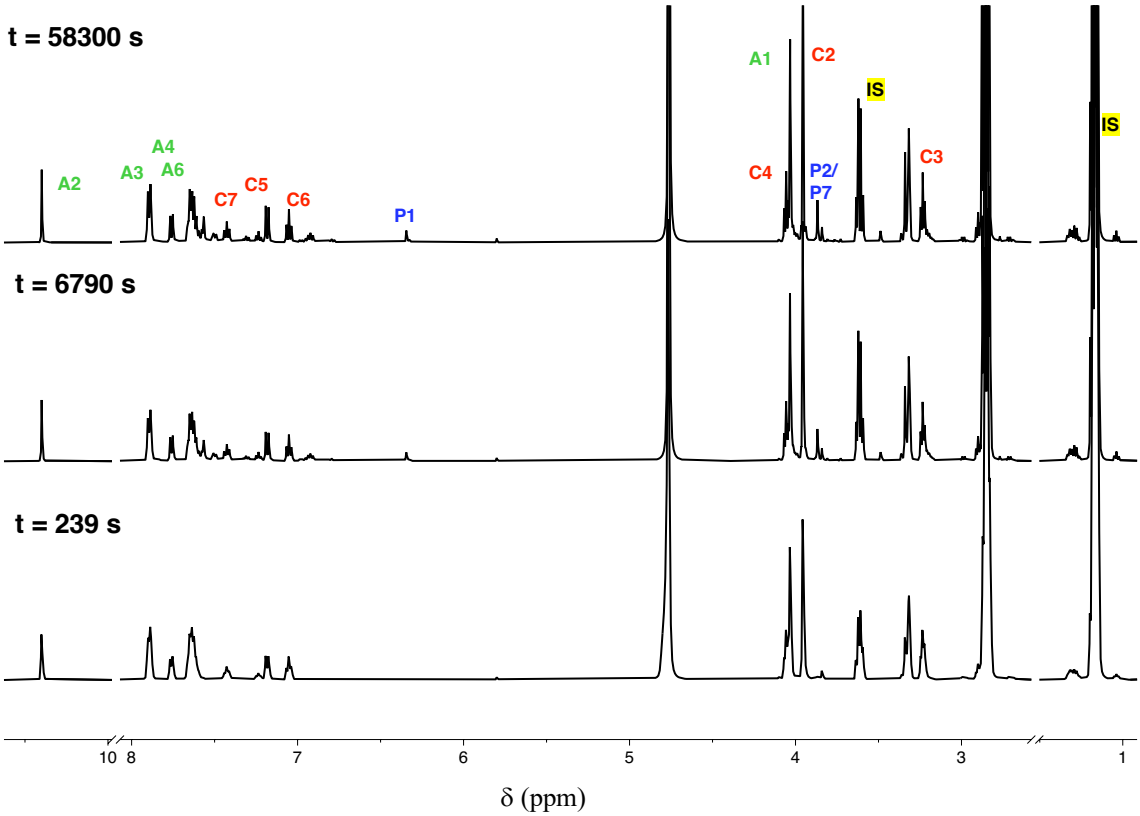

Figure 4.2.3. Representative ^{1}H NMR spectra for the attempted formation of adduct **146d** as shown in Scheme 4.2.8 at Time = 239 s, 6790 s and 58300 s.

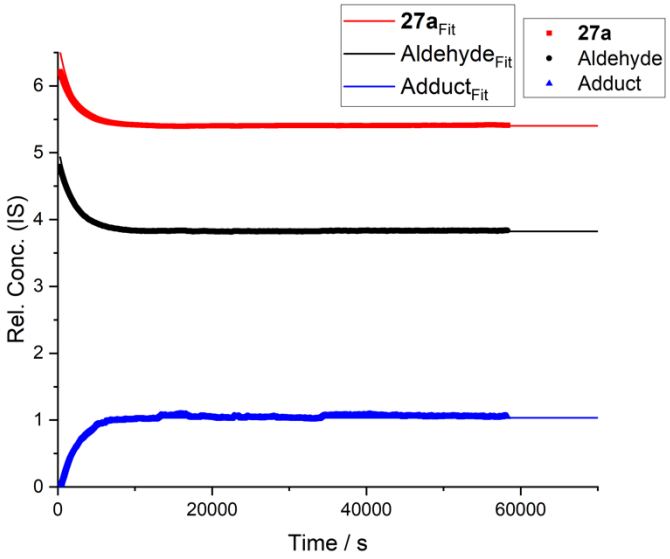

Figure 4.2.4. Plot of integrals with respect to the internal standard integral against time for catalyst, aldehyde and adduct peaks for the reaction in Scheme 4.2.8. Lines denoted **27a**$_{Fit}$, aldehyde$_{fit}$ and adduct$_{Fit}$ refer to fitted curves using Berkely-Madonna software to extract values for k_1, k_{-1} and K_1.

Table 4.2.3. Summary of rate and equilibrium constants for formation/decay of adducts (**146**) for the reaction shown in Scheme 4.2.8 and comparative values from Chapter 3.5.

	pK_a^{CH}	k_1 / ×10^{-5} M^{-1} s^{-1}	k_{-1} / ×10^{-5} s^{-1}	K_1 / M^{-1}
27a	18.6	1.76	3.51	0.0426
26[a]	18.9	*231*	*4.66*	*49.5*
5[a]	*17.4*	*50.2*	*2.88*	*17.4*
5{PP}[a]	*18.4*	*6.27*	*0.0824*	*76.1*
61a[b]	*17.5*	*3440*	*29.2*	*118*

[a]Values reported previously in Chapter 3.5. [b]Values reported by C. Collet *et al.* (2015).[9]

Although these results suggest that the N-Ph triazolium mimic (**27a**) is not a particularly good organocatalyst, they do show that this new scaffold will catalyse a benzoin condensation. An N-Ph substituted catalyst was never likely to show the highest activity and further N-aryl substituents could be explored once the synthetic strategy is further improved. Unlike most other 1,2,4-triazoliums, these N-phenyl mimics have a terminal alcohol which could undergo further functionalisation. For example, reaction with phosphorus oxychloride to form a monophosphate. Although this will reduce the C(3)-H pK_a further (1-2 unit increase, Chapter 3.4), the water solubility will be vastly improved. In considering the future of organocatalysis, it is important to consider more water-soluble catalyst scaffolds as there is a drive to move away from organic solvents.

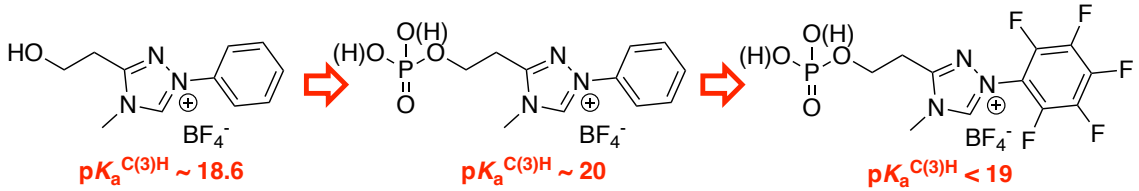

Scheme 4.2.9. Future catalyst evolution to target NHC organocatalysis under aqueous conditions.

4.3. Catalyst Evaluation in Sustainable Media

Alongside exploration of the new 1,2,4-triazolium scaffolds, more traditional triazolium salts were evaluated for performance in sustainable solvent systems. Benzoin condensations are typically carried out in either THF or DCM which, as highlighted above, are particularly deleterious to the environment. Initially, 2-methyltetrahydrofuran (2-MeTHF) (**154**) was explored as a replacement solvent and reaction results compared with THF. 2-MeTHF is derived from plant-based origins (Scheme 4.1.1) and is therefore much more sustainable; moreover, it can be broken down within the environment back to non-harmful chemicals.

Use of water as a reaction solvent is significantly more sustainable than organic solvents. As previously mentioned, this causes various issues including changes in transition state stabilisation and reagent solubilisation. To improve solubility, approaches include use of surfactants or use of a small amount of a co-solvent. Typically, DMSO is used as a co-solvent as it is fully water miscible and very good at solubilising an array of organic compounds. The issue with using DMSO is that it is non-volatile and fully water miscible: a mixed aqueous waste stream cannot be released back into the environment and costly water treatment is therefore required. As mentioned, 2-MeTHF is a bio-derived solvent, with some water miscibility (although much lower than DMSO). Alongside exploring 5% DMSO-water solvent mixtures, 5% 2-MeTHF was also explored in the benzoin condensation, with particularly acidic catalyst **61f (**Scheme 4.3.1**)**. Pleasingly, the reactions proceeded rapidly and benzoin precipitated from the reaction mixture within an hour. This rate enhancement could be attributed to an 'on-water' reaction which have been shown to have faster reaction times. The reactions were held overnight to allow complete reaction to occur, before filtering the product. Very high yields of pure benzoin were isolated, with no need for organic solvent extraction or column chromatography (Table 4.3.1). If desired, purification via recrystallisation is possible using ethanol/water mixtures (ethanol can be derived from bio-based sources) to further improve the purity.

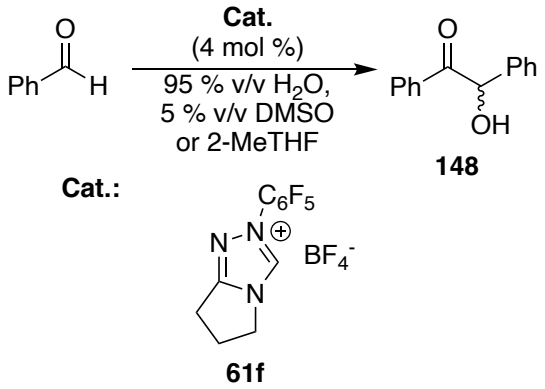

Scheme 4.3.1. Exploration of NHC organocatalysis in aqueous conditions with 5% cosolvent, as a more sustainable approach to the benzoin condensation.

Table 4.3.1. Summary of yields (after recrystallisation) of benzoin from the benzoin condensation shown in Scheme 4.3.1.

Catalyst	Solvent System[a]	Time / h	Yield / %
61f	2-MeTHF/H_2O	< 3	74
	DMSO/H_2O	< 3	87

[a]Reaction conditions: 1 mol. eq. benzaldehyde, 1 mol. eq. K_2CO_3, 5% v/v DMSO/2-MeTHF, 95% H_2O/D_2O.

These results are not the first reported example of the benzoin condensation under aqueous conditions. A previous example used catalyst **157** to perform asymmetric benzoin condensations in water with relatively high enantiomeric ratios (Scheme 4.1.2). It should be noted that the experimental procedure in this case did not recognise that benzoin product precipitated from the reaction mixture within an hour. Instead this work had isolated benzoin by concentration *in vacuo* after 8-24 h. Moreover, purification was performed by column chromatography using petroleum ether and ethyl acetate. Use of organic solvents at the purification stage (particularly petroleum ether) negates the use of more sustainable conditions at the synthesis stage as column chromatography typically requires large quantities of solvent. The more holistic approach described in this work has taken into account both synthesis and purification, alongside consideration of the organic solvents used, to develop a more sustainable process in total.

There is a lot more work which could be explored as part of this project: aldehyde scope needs expanding, evaluation using asymmetric catalysts and future exploration of other NHC-catalysed processes. This short discussion hopefully highlights a potential new direction for NHC-organocatalysis.

4.4. Conclusions

This chapter briefly discusses exploration into previously unexplored NHC-scaffolds in model benzoin condensations. Intriguingly, despite possessing significant carbene character and C(3)-H acidity, Nitron derivatives (**6a**, **6i**, **6j**, **60a**, **60i**) showed no propensity for catalysis. This unexpected result is difficult to explain but, could be attributed to the unusual nature of the carbene formed from Nitron. N-Ph triazolium mimic (**27a**) was also explored as a baseline catalyst for future exploration. Although hydroxyaryl adduct formation occurred, the N-Ph substituted catalyst showed relatively poor reactivity in these studies. Further study of these catalysts, in particular isolation of derivatives with more electron withdrawing N-aryl substituents, is required to evaluate their full potential.

A brief exploration of NHC-organocatalysis of a benzoin condensation in more sustainable, aqueous environments showed promise. Benzoin was found to rapidly precipitate from the reaction media in high yields and purity, without the need for solvent-thirsty column chromatography. This initial investigation could provide a promising starting point for future investigations into more sustainable organocatalysed processes.

4.5. References

4. D. M. Flanigan, F. Romanov-Michailidis, N. A. White and T. Rovis, *Chem. Rev.*, 2015, **115**, 9307-9387.
9. C. J. Collett, R. S. Massey, J. E. Taylor, O. R. Maguire, A. C. O'Donoghue and A. D. Smith, *Angew. Chem. Int. Ed.*, 2015, **54**, 6887-6892.
22. C. Färber, M. Leibold, C. Bruhn, M. Maurer and U. Siemeling, *Chem. Comm.*, 2012, **48**, 227-229.
63. D. Enders, K. Breuer, U. Kallfass and T. Balensiefer, *Synthesis*, 2003, **2003**, 1292-1295.
70. C. Hansch, A. Leo and R. W. Taft, *Chem. Rev.*, 1991, **91**, 165-195.
76. R. S. Massey, C. J. Collett, A. G. Lindsay, A. D. Smith and A. C. O'Donoghue, *J. Am. Chem. Soc.*, 2012, **134**, 20421-20432.
102. D. Enders, O. Niemeier and A. Henseler, *Chem. Rev.*, 2007, **107**, 5606-5655.
163. L. Baragwanath, C. A. Rose, K. Zeitler and S. J. Connon, *J. Org. Chem.*, 2009, **74**, 9214-9217.
229. P. Anastas and N. Eghbali, *Chem. Soc. Rev.*, 2010, **39**, 301-312.
230. P. T. Anastas, *Chem. Rev.*, 2007, **107**, 2167-2168.
231. C. Capello, U. Fischer and K. Hungerbühler, *Green Chem.*, 2007, **9**, 927-934.
232. F. P. Byrne, S. Jin, G. Paggiola, T. H. M. Petchey, J. H. Clark, T. J. Farmer, A. J. Hunt, C. Robert McElroy and J. Sherwood, *Sustain. Chem. Process.*, 2016, **4**, 7.
233. C. J. Clarke, W.-C. Tu, O. Levers, A. Bröhl and J. P. Hallett, *Chem. Rev.*, 2018, **118**, 747-800.
234. E. Amores, M. Sánchez, N. Rojas and M. Sánchez-Molina, in *Sustainable Fuel Technologies Handbook*, eds. S. Dutta and C. Mustansar Hussain, Academic Press, 2021, DOI: https://doi.org/10.1016/B978-0-12-822989-7.00010-X, pp. 271-313.
235. D. K. Romney, F. H. Arnold, B. H. Lipshutz and C.-J. Li, *J. Org. Chem.*, 2018, **83**, 7319-7322.
236. B. H. Lipshutz, S. Ghorai and M. Cortes-Clerget, *Chem. Eur. J.*, 2018, **24**, 6672-6695.
237. L. Cicco, S. Sblendorio, R. Mansueto, F. M. Perna, A. Salomone, S. Florio and V. Capriati, *Chem. Sci.*, 2016, **7**, 1192-1199.
238. M. P. van der Helm, B. Klemm and R. Eelkema, *Nat. Rev. Chem.*, 2019, **3**, 491-508.
239. J. Yan, R. Sun, K. Shi, K. Li, L. Yang and G. Zhong, *J. Org. Chem.*, 2018, **83**, 7547-7552.
240. P. Suresh, S. Thamotharan and S. Selva Ganesan, *ChemistrySelect*, 2021, **6**, 2036-2040.
241. P. Suresh, S. Thamotharan and S. S. Ganesan, *Cat. Comm.*, 2018, **111**, 47-51.
242. W. Blokzijl and J. B. F. N. Engberts, *Angew. Chem. Int. Ed.*, 1993, **32**, 1545-1579.
243. Y. Kayaki, M. Yamamoto and T. Ikariya, *Angew. Chem. Int. Ed.*, 2009, **48**, 4194-4197.
244. M. H. Dunn, M. L. Cole and J. B. Harper, *RSC Adv.*, 2012, **2**, 10160-10162.
245. D. Enders, K. Breuer, G. Raabe, J. Runsink, J. H. Teles, J.-P. Melder, K. Ebel and S. Brode, *Angew. Chem. Int. Ed.*, 1995, **34**, 1021-1023.

5. Conclusions & Future Work

5.0. Conclusions

The intriguing nature of carbenes as divalent carbon compounds has led to broad applications, most notably the fields of organocatalysis and metal-carbene complexes. This thesis has focussed particularly on carbenes formed from 1,2,4-triazolium ions with broad ranging applications.

Chapter 2 discussed an in-depth study of the Nitron (**6**) to Blatter-type radical (**24**) rearrangement, first reported in our group in 2017.[21] Nitron (**6**) is a 1,2,4-triazolium with an exocyclic C(5)-anilino substituent. Blatter radicals (**15/24/25**) are a class of persistent radical which have received increased attention in the past decade owing to improved synthetic access. They have been shown to be bench-stable for months, attributed to stabilisation of the SOMO (single occupied molecular orbital) across three ring nitrogen atoms and the fused aryl ring. Recent applications include within organic batteries and as paramagnetic signal enhancement reagents in NMR spectroscopy.[74] To isolate novel Blatter-type radicals via the Nitron to Blatter radical rearrangement, a greater number of Nitron derivatives were targeted. This initially required revisiting the historic synthesis of Nitron (**6a**) and introducing more modern synthetic innovations.[58] These included the use of iodine and triethylamine for the initial thiourea desulphurisation and the use of trimethyl orthoformate for ring closing of the amidrazones. Detailed evaluation of by-product formation enabled manipulation of conditions towards the desired Nitron derivative product. Importantly these innovations gave improved yields and a broader scope of Nitron derivatives (**6a-m**), with less toxic and environmentally hazardous reagents.

The new Nitron derivatives (**6**) were evaluated in the Nitron to Blatter radical (**24**) rearrangement by stirring in acetonitrile (2% water). Interestingly, the propensity for ring opening and subsequent Blatter radical formation followed the opposite trend to that predicted. Nitron derivatives with electron withdrawing N-aryl substituents were observed to ring open very slowly, despite enhanced electrophilicity at the C(3)-H position in the zwitterionic form. Nitron exists in a tautomeric equilibrium with a carbenic form. Experimental observations were attributed to the underpinning implications of this tautomerism with regards to Blatter radical syntheses. Subsequent analysis of both the exocyclic nitrogen and carbon pK_a values through both

spectrophotometric and NMR spectroscopic analysis allowed estimation of the positions of tautomeric equilibria for different substitution patterns. Importantly the trend showed that electron donating groups typically shifted the equilibrium in favour of the carbenic form, which was thought to be the more hydrolytically labile tautomer.

Organic diradicals, coupled via small organic tethers, have received particular interest recently owing to the intriguing magnetic properties which arise from having two unpaired electrons in close proximity. Typical synthetic strategies to Blatter diradicals initially isolate the mono-radicals before attempting coupling procedures. This presents multiple challenges including cross reactivity at the radical nitrogen position and harsh reaction conditions quenching the radical state. An alternative approach, viable due to the reported Nitron to Blatter radical rearrangement, is to couple two Nitron molecules about a central linker and attempt to isolate radicals by the discussed rearrangement in acetonitrile. Pleasingly, synthesis of the precursor di-Nitron (**73**) was possible through a pyrrolidine-catalysed imine cyclisation, followed by subsequent oxidation. Compound isolation was verified specifically through mass spectrometry and X-ray crystallography. Within this work, conditions to isolate the Blatter diradical (**74**) were not determined; however, promising evidence for radical formation was observed.

Throughout the studies on Nitron (**6**) and Blatter radicals (**24**), the underpinning role of the N-heterocyclic carbene is key. Importantly, the requirement for significant levels of carbenic character of the Nitron are thought to be essential for hydrolytic ring opening. Nevertheless, in cases where the carbenic character is eliminated, such as the C(3)-linked di-Nitron (**73**), it is hoped that conditions can be developed to enhance rates of hydrolytic ring opening and subsequent electrocyclization.

Chapter 3 presented the synthesis and evaluation of the first 1,2,4-triazolium cofactor mimic (**26{PP}**) of thiamine pyrophosphate (**5{PP}**). There has been no exploration of the introduction of non-native cofactor mimics into TPP-dependent enzymatic systems to attempt to enhance the rate, scope and yield and alter product selectivities of biocatalytic transformations. Development of a synthetic strategy to a 1,2,4-triazolium mimic of thiamine pyrophosphate was challenging, particularly the development of sequential phosphorylation reactions and aqueous purification techniques to isolate the pyrophosphate. A pyrophosphate group is thought to be essential for binding via

electrostatic interactions with a bound magnesium ion within the enzyme active site. Nevertheless, through in-depth exploration of various synthetic routes, the cofactor mimic could be isolated in sufficient yield, which permitted subsequent cofactor evaluation.

Cofactor evaluation included determination of the C(3)-H acidity, through analysis of the rate of deuterium exchange in a series of deuterated buffers. It was found that the pK_a values of 17.4 (non-pyrophosphorylated (**26**)) and 18.4 (pyrophosphorylated (**26{PP}**)) reflected a ~1.5 unit decrease in comparison to thiamine (**5**). In NHC organocatalysis, C-H acidity is typically used as a measure of pre-catalyst ability as it reflects a greater concentration of the active carbene catalyst at equilibrium. Moreover, increased acidity of the pre-catalyst can also be extrapolated to greater propensity for deprotonation at key steps in NHC-catalysed processes, for example, Breslow intermediate formation from the precursor hydroxyaryl adduct. The enhanced acidity of the 1,2,4-triazolium mimic (**26**) was reflected in model benzoin condensation studies in which the formation of the initial hydroxyaryl adduct was monitored. An order of magnitude rate enhancement was observed in the case of the 1,2,4-triazolium mimic (**26**) (non-pyrophosphorylated) in comparison to thiamine (**5**).

Proof of principle investigations compared the commercially available and inexpensive TPP-dependent enzymes, pyruvate decarboxylase (from *Saccharomyces cerevisiae*) and pyruvate oxidase (from *Aerococcus sp.*) with native cofactor (TPP, **5{PP}**) and the cofactor mimic (**26{PP}**). A range of spectrophotometric coupled assays and NMR spectroscopic studies were used and typically showed that decreasing activity was observed with increasing concentrations of the cofactor mimic (**26{PP}**). Despite not showing the desired enhanced reactivity, these results are promising as they suggest that the cofactor mimic is binding to the enzyme active site, albeit possibly in a conformation that does not favour reaction. *Sc*PDC and *As*POx have not been previously studied in biocatalysis, which could be due to rigid active sites with poor tolerance to non-native substrates. The potential directions of this project including broader exploration of more tolerant enzyme hosts will be presented in the Future Work Section 5.1. Chapter 3 clearly demonstrates the importance of p*H* control within organic chemistry: consideration of speciation for product isolation, purification, hydrolytic stability and enzyme binding were all essential to this work.

Finally, Chapter 4 sought to link the two key projects discussed within this thesis by highlighting the initial studies into future directions for NHC organocatalysis. Nitron derivatives (**6**) have not previously been reported as scaffolds in NHC organocatalysis, despite having carbene character. These studies found Nitron derivatives (**6**/**60**) had 5-10 fold higher rates of H/D-exchange in 0.1 M DCl to the most commonly employed NHC organocatalyst scaffolds (**61**). This suggested that Nitron derivatives had similar acidities to typical NHC organocatalysts; however, no catalytic activity in synthetic or mechanistic studies was found for all Nitron derivatives explored. These results were surprising, given that C(3)-H acidity is typically an excellent measure of catalyst activity. This likely highlights a difference in chemical nature in the carbenes formed from Nitron compared to those of other 1,2,4-triazoliums. This has already been observed considering the key attack of water at Nitron (**6**) in the formation of Blatter radicals (**24**). In contrast, typical 1,2,4-triazolioums employed in organocatalysis are stable to hydrolytic ring opening except at high p*H*s.

The synthesis of thiamine mimics highlighted in Chapter 3.2 developed a new modular synthesis to a scaffold with a terminal alcohol. 1,2,4-triazolium catalysts (**27**) with this substitution pattern have not been previously reported. Importantly this alcohol group gives the propensity for future functionalisation particularly in the development of catalysts for aqueous environments. With increased focus on the environmental impact of the chemical industry, futureproofing of chemical processes must consider more sustainable solvent systems. Chapter 4 also discusses an 'on water' benzoin condensation using a particularly acidic NHC organocatalyst. Although the use of this catalyst in the benzoin condensation has previously been reported, this reaction was found to occur particularly rapidly (< 1 h) and precipitated benzoin straight from the reaction media. These rate enhancements and benefits with regards to isolation have not been previously reported.

Throughout this thesis the development of novel synthetic strategies, coupled with kinetic and mechanistic analysis has led to improved understanding and innovation in three key applications of 1,2,4-triazoliums: biocatalysis, organocatalysis and in the synthesis of Blatter-type radicals. Potential future areas of study are highlighted below.

5.1. Future Work

The improved mechanistic understanding of the Nitron (**6**) to Blatter radical (**24**) rearrangement developed within this thesis now permits thorough investigation into the applications of this new Blatter radical scaffold. In particular, exploration of Blatter radicals within biological chemistry has been limited. Previous work highlighted that Blatter radicals (**15j/k**) showed a promising level of cytotoxicity towards both breast and prostate cancer cell lines.[55] Furthermore, Blatter-type radical intermediates have been implicated in the mechanism of Tirapazamine (**47**), a stage-III clinical trial anti-cancer compound (Figure 5.1.1).[57] Work in our group is currently exploring the cytotoxicity of radicals reported in this thesis in a range of cell lines through *in vitro* assays.

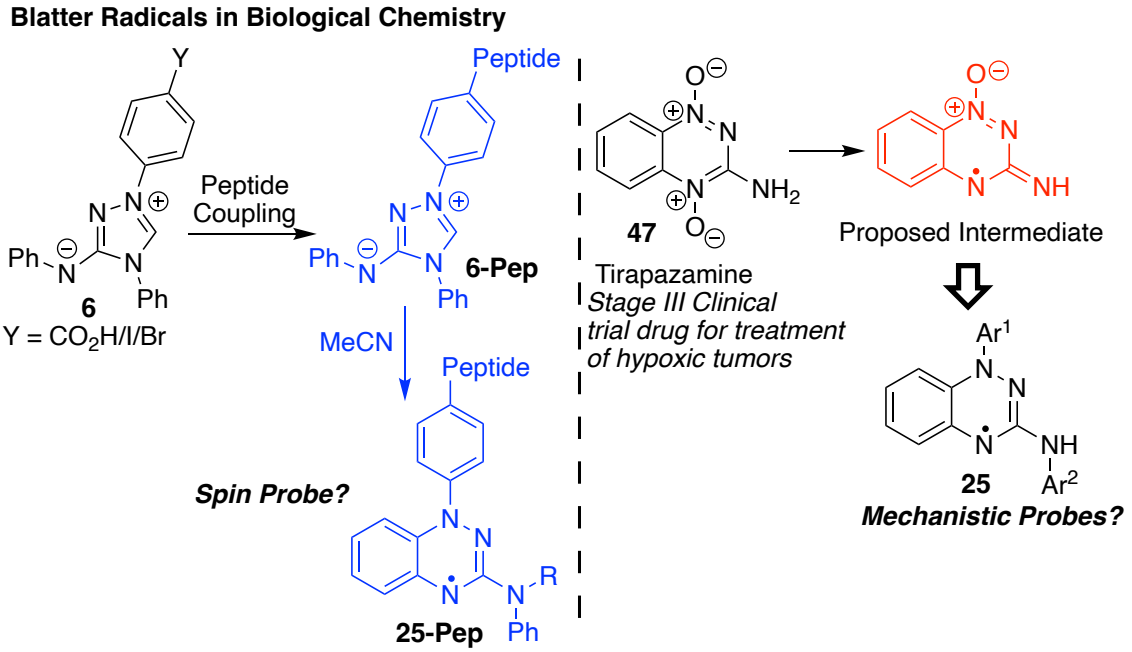

Figure 5.1.1. Potential areas of exploration of Blatter radicals in biological chemistry. Left: Coupling of Nitrons (**6**) through amide bonds or C-C cross couplings to peptides (**6-Pep**) for spin probe applications; Right: Application of Blatter-type radicals (**25**) as mechanistic probes for the mode of action of Tirapazamine (**47**) in the treatment of hypoxic tumours. Compounds in blue highlight key future compounds to explore.

The persistent organic radical TEMPO (**12**) can be used within biological chemistry as a spin-probe.[246] This involves bonding TEMPO radicals to biological scaffolds, typically proteins, and using EPR spectroscopy to determine radical-radical distances. This technique can complement other technologies such as Förster resonance energy transfer (FRET). Blatter radicals have not been explored as spin probes and this is likely due to complications with loss of radical character under synthetic conditions. However, mechanistic understanding of the Nitron (**6**) to Blatter radical (**24**) rearrangement suggests that radical formation is tolerant to functional group change at Ar^1 (Figure 5.1.1).

Therefore, coupling to proteins or other biomolecules could be achieved through this group through amide couplings, or cross-couplings to precursor Nitron derivatives (**6-Pep**) before subjecting the peptide-Nitron conjugate to the radical (**25-Pep**) forming rearrangement.

The synthesis of Blatter-type diradicals is particularly interesting owing to the intriguing properties of coupling two paramagnetic species in close proximity. Chapter 2.4 highlighted the synthesis of a coupled di-Nitron (**73**) and exploration into the isolation of the desired di-radical (**74**). Under a variety of conditions explored in this thesis, the di-radical (**74**) could not be isolated; however, circumstantial evidence through LC-MS suggested its formation. Future work could focus on screening an array of conditions including a range of p*H* values and oxidants to isolate the desired radical in higher yields (Figure 5.1.2).

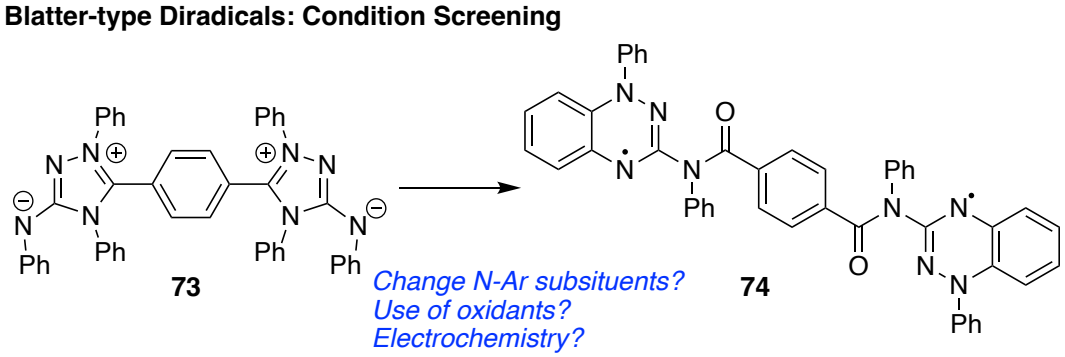

Figure 5.1.2. Future exploration of Blatter-type diradicals should screen conditions for diradical (**74**) formation and substituent change which could favour ring opening and electrocyclization.

Finally, the N-Ph substituted radicals first reported in our group have recently been shown to have beneficial properties in the process of overhauser dynamic nuclear polarisation (o-DNP). Here the paramagnetic nature of stable organic radicals is used to enhance the relaxation times of compounds in solution, to increase the signal intensity. Blatter radicals (**24a/25a**) were found to perform better than the usual compound of use, TEMPOL (**12b**), due to a smaller peak-peak ΔE^{REDOX}. The *p*-cyano-substituted radicals (**24i/25i**) isolated in this work had a significantly smaller ΔE^{REDOX} and could be explored as an o-DNP reagent (Figure 5.1.3).

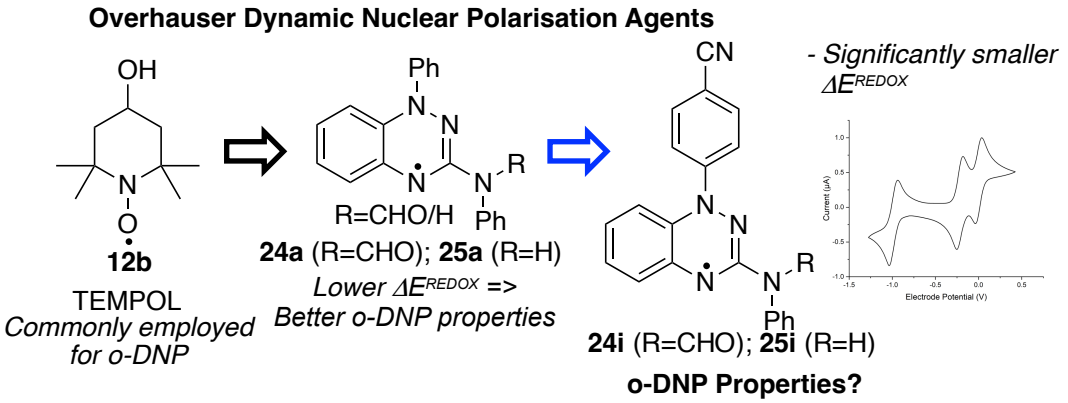

Figure 5.1.3. Potential future applications of Blatter radicals (**24**/**25**) as o-DNP agents for signal enhancement within NMR spectroscopy. Work has shown that N-Ph substituted amino- (**24a**) and amido-Blatter radicals (**25a**) have better signal enhancement properties than TEMPOL (**12b**), a commonly employed o-DNP agent, due to a smaller ΔE^{REDOX}. Work is this thesis has isolated Blatter radicals with much smaller ΔE^{REDOX} values.

Chapter 3 lays the groundwork for considerable future study into the exploration of the 1,2,4-triazolium cofactor mimic (**26{PP}**) within TPP-dependent enzymes. The synthetic strategy to isolate the pyrophosphorylated 1,2,4-triazolium mimic is reproducible but still presents some challenges. In particular scalability is a challenge and this is mostly due to the large excess of phosphorus oxychloride used which must be quenched. To further develop this synthetic strategy, a study into improved scale would aid the isolated of greater quantities of the cofactor mimic for further study. Moreover, the role of water in the monophosphorylation could be further investigated through kinetic and mechanistic evaluation to determine the active phosphorylating species for this reaction. The proposed reactive intermediate, diphosphoryl chloride (**133**), is commercially available and studies could initially focus on its use as a mechanistic probe (Figure 5.1.4).

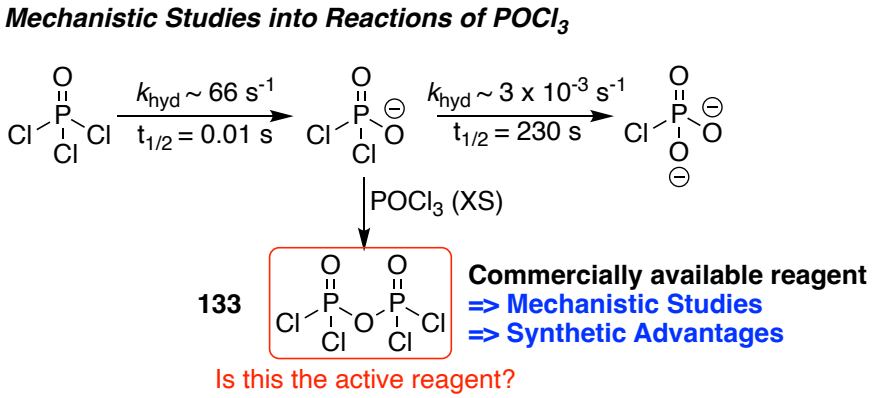

Figure 5.1.4. Future mechanistic studies on the reaction of $POCl_3$ in phosphorylation reactions could use diphosphoryl chloride (**133**), a commercially available reagent, as a mechanistic probe.

The role of the pyrimidinyl group in enzyme binding and cofactor activity is still unclear. There are proposals that it is involved in an intramolecular deprotonation within the active site but, this has not been evidenced. Despite the N-Ph 1,2,4-triazolium mimic (**27a/b**)

having a higher carbon acid pK_a than predicted, future iterations could make use of previous work on NHC-organocatalysis. In particular, the inclusion of a pentafluorophenyl group vastly enhances the acidity and 2-substituents on the N-aryl group also enhance the rate of NHC-catalysed reactions (Figure 5.1.5); these substituents could be assessed as part of a triazolium cofactor mimic.

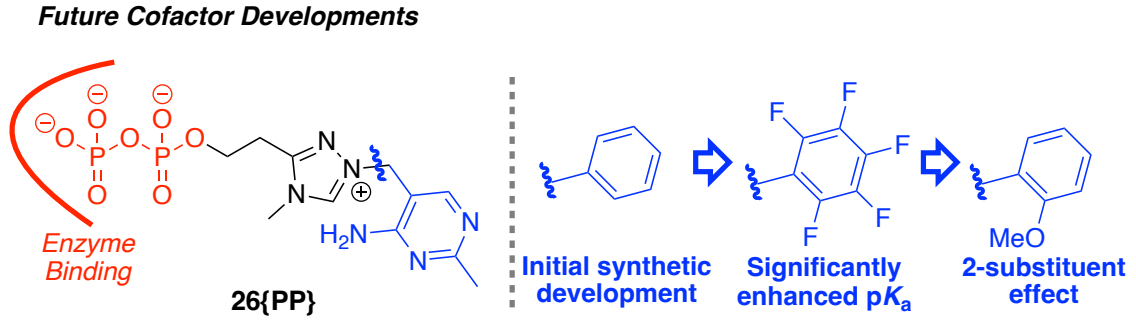

Figure 5.1.5. Future potential cofactor mimic developments. The pyrophosphate group is thought to be essential to binding via a bound magnesium ion. The role of the pyrmidinyl group is unclear and other N-substituents, such as a pentafluorophenyl group could give significantly enhanced C(3)-H acidity.

Although the initial enzyme studies within this thesis highlighted no rate enhancement when the 1,2,4-triazolium mimic (**26{PP}**) was introduced, cofactor mimic binding was still evidenced. This binding suggests that the loss of activity is due to a conformational discrepancy, not a lack of activity. Thanks to the development of enzyme mutagenesis and directed evolution, active site conformations can be manipulated and refined. This could allow for active site binding of the cofactor mimic in a form in which it is active. Alongside exploration of enzyme mutagenesis, there is a still a vast range of native TPP-dependent enzymes to explore. The biggest challenge is selecting the most appropriate of these enzymes. Through use of both docking studies and exploration of previous work on TPP-dependent enzyme biocatalysis, a selection of enzymes with more tolerant active site conformations could be collated.

Chapter 4 highlighted the initial studies into the use of new 1,2,4-triazolium scaffolds in NHC organocatalysis and exploration of the use of sustainable aqueous solvent conditions. The most surprising result was the lack of catalytic activity of Nitron (**6**/**60**) derivatives, which is still unexplained. Future work could explore the nature of carbenes formed from Nitron (**6**) in greater detail. The different chemical nature possessed by these carbenes could provide further insights into the overall field of NHC organocatalysis.

The N-Ph triazolium mimic (**27a**) showed promising results in a model benzoin study, in which rate constants for formation and decay of the hydroxyaryl adduct were measured.

Although values were lower than for the most commonly employed 5-membered ring catalysts (**61**), future catalyst iterations could significantly improve upon this. In particular, an N-pentafluorophenyl substituted catalyst is seen as a key target in future work. Synthetic approaches to catalyst **27d** in this work proved unsuccessful, this was attributed to the reduced nucleophilicity of the hydrazine nitrogens. One approach to counteract this could be to use a more activated isothiocyanate, such as pentafluorophenyl isothiocyanate. This would significantly alter the scaffold of the catalyst, with no N-Me group present; however it is expected to significantly enhance the acidity of the catalyst (**161**) (Figure 5.1.6). As discussed, it may be that two N-aryl groups adjacent to the C(3)-position (such as Nitron) disfavour reaction. This hypothesis has not been proven and should not prevent exploration of this catalyst structure.

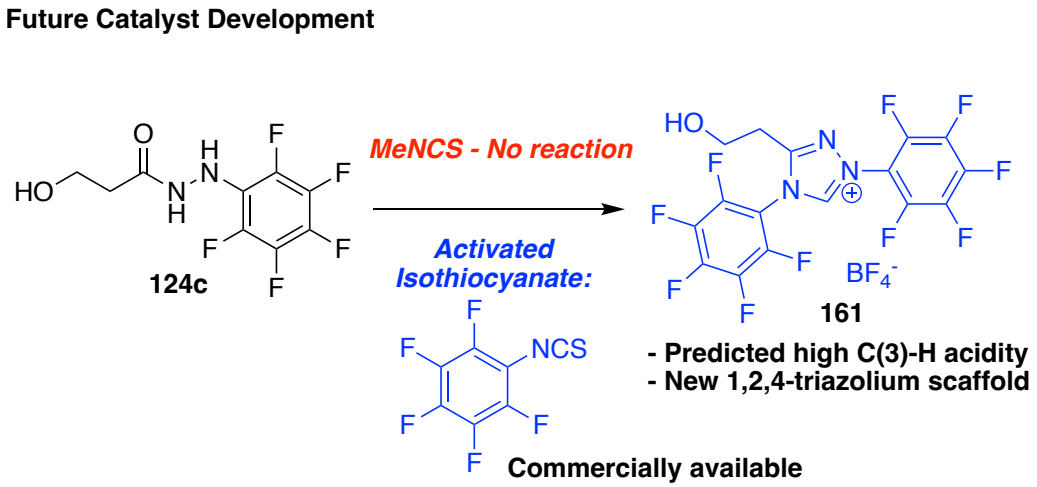

Figure 5.1.6. Future catalyst development could use a more reactive isothiocyanate, such as pentafluorophenyl isothiocyanate, to drive reaction with the less nucleophilic N-aryl nitrogen on hydrazide (**124c**). This will give catalyst **161** which is another new catalyst for screening.

Finally, initial investigations into the NHC organocatalysis of a benzoin condensation in aqueous conditions was discussed. Rates were enhanced in comparison to reactions in THF, attributed to an 'on-water' rate enhancement. Significant work is still required in this area to fully explore this benzoin condensation. There is also significant scope for catalyst development in this area. In particular, the 1,2,4-triazolium mimic catalysts (**27**) have a terminal alcohol which could be functionalised with a monophosphate group to aid water solubility. Moreover, if a longer alkyl chain was used, with a compound such as that proposed above (**161**), the structure would have a surfactant-like structure. This could allow these compounds to behave as both catalyst and surfactant to solubilise hydrophobic reagents via micelle formation (Figure 5.1.7).

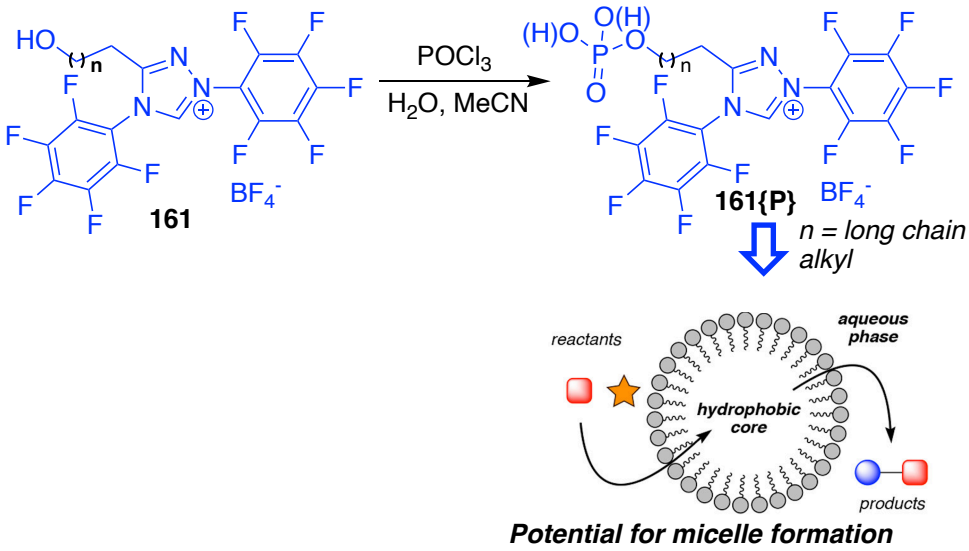

Figure 5.1.7. Monophosphorylation of catalyst **161,** with longer N-alkyl chains, could allow formation of a surfactant-like NHC organocatalyst which has the potential to form micelle-like structures in aqueous media. This could be a avenue for NHC-organocatalysis in aqueous media. The micelle schematic is adapted with permission from D. K. Romney, F. H. Arnold, B. H. Lipshutz and C.-J. Li, *J. Org. Chem.*, 2018, **83**, 7319-7322. Copyright 2022 American Chemical Society.

The three key areas of research described in this thesis are all ripe for future exploration. Chapters 3 and 4 highlight areas of bio- and organocatalysis which future work can significantly build upon. Chapter 2 presents a more complete study on the synthesis of Blatter radicals and key mechanistic understanding. It is hoped that this will allow for future exploitation of key properties of both Nitron derivatives and Blatter radicals.

5.2. References

21. J. A. Grant, Z. Lu, D. E. Tucker, B. M. Hockin, D. S. Yufit, M. A. Fox, R. Kataky, V. Chechik and A. C. O'Donoghue, *Nat. Commun.*, 2017, **8**, 15088.
55. L. J. Keane, S. I. Mirallai, M. Sweeney, M. P. Carty, G. A. Zissimou, A. A. Berezin, P. A. Koutentis and F. Aldabbagh, *Molecules*, 2018, **23**.
57. E. M. Zeman, J. M. Brown, M. J. Lemmon, V. K. Hirst and W. W. Lee, *Int. J. Radiat. Oncol. Biol. Phys.*, 1986, **12**, 1239-1242.
58. A. P. Kriven'ko and N. A. Morozova, *Russ. J. App. Chem.*, 2006, **79**, 506-507.
74. F. Saenz, M. Tamski, J. Milani, C. Roussel, H. Frauenrath and J.-P. Ansermet, *Chem. Comm.*, 2022, **58**, 689-692.
246. A. J. Fielding, M. G. Concilio, G. Heaven and M. A. Hollas, *Molecules*, 2014, **19**, 16998-17025.

6. Experimental

6.0. General

6.0.1. Materials

Materials were obtained from Sigma Aldrich, Alfa Aesar, Tokyo Chemicals Industry and Fluorochem and used with no further purification or characterisation. Deuterated solvents were used from Cambridge isotope laboratories.

6.0.2. Instrumentation

NMR Spectroscopy: ^{1}H, ^{13}C and ^{19}F NMR spectra were obtained on various instruments summarised in Table 6.0.1.

Table 6.0.1. Summary of the NMR operating frequencies and nuclei.

Spectrometer	Operating Frequencies and Nuclei
Bruker Avance III-HD-400 (*A4*)	399.95 MHz, ^{1}H; 100.57 MHz, ^{13}C; 376.50 MHz, ^{19}F; 161.91 MHz, ^{31}P
Bruker Avance III-HD-400 (*B4*)	400.07 MHz, ^{1}H; 100.60 MHz, ^{13}C; 161.95 MHz, ^{31}P
Bruker Neo- 400 (*N4*)	400.20 MHz, ^{1}H; 100.63 MHz, ^{13}C
Varian VNMRS-600 (*P6*)	599.42 MHz, ^{1}H; 150.72, ^{13}C
Varian VNMRS-500 (C5)	499.49 MHz; ^{1}H; 202.20 MHz, ^{31}P

Spectral assignments were reported in order: chemical shift (ppm), integration, multiplicity, coupling constants (Hz) and assignment. Reference solvents were $CDCl_3$ and DMSO with reference peaks set to 7.26 and 2.50 ppm respectively.[247]

LC-MS(ESI): LC-MS was carried out using the electrospray ionisation technique with both a TQD (triple quadrupole) and SQD (single quadrupole) mass spectrometer and an Acquity UPLC (ultra-performance liquid chromatography) (Waters Ltd., UK). Positive and negative ions are produced and detected between a mass range of 100-2000 amu. A UV absorption plot between 210-400 nm is obtained by an internal photodiode array.

GC-MS(EI): GC-MS was carried out using the electron impact technique on a Shimadzu QP2010-Utra at 70 eV for a mass range 35-650 amu.

ASAP-MS: ASAP-MS was obtained using a Xevo QToF tandem MS (Waters Ltd., UK) with ASAP ion source.

HRMS: High resolution MS was obtained was obtained using a Synapt G2s UPLC ES MS/MS (Waters Ltd., UK), with both ES and ASAP ion sources.

Elemental Analysis: Solid analyte was used for elemental analysis on an Exeter CE-440 Elemental Analyser.

IR Spectroscopy: Infrared spectra were run using neat liquid or solid samples on a Perkin Elmer FT-IR Frontier spectrometer.

UV-Visible Spectroscopy: Ultraviolent to visible spectra were recorded using samples dissolved in an appropriate solvent in a quartz cuvette on a Varian Cary 100 Bio Spectrophotometers maintained at 25°C, unless otherwise stated.

p*H*/p*D* Measurements: All solution used in the exchange studies were maintained at 25 °C measured with a Radiometer Analytical RadioLab® p*H* 210 standard p*H* meter fitted with a radiometer electrode filled with saturated KCl solution. Calibration of the setup is at intervals of 1.6 – 4.0, 4.0 – 7.0 (phosphate), and 7.0 – 10.0 (borate) and 10.0 – 12.45 (saturated calcium chloride). The reading for the p*D* value was determined by adding 0.4 to the instrument reading. Previous work in our group found the activity of coefficient for hydroxide ion (γ_{HO}) for the model of electrode in use to be 0.73.

6.1. Experimental – From Nitron to Stable Blatter-type Radicals

6.1.1. Synthesis of Nitron Derivatives

General Procedure 1: The Synthesis of Thioureas (49)

To a solution of aryl isothiocyanate (1 mol. eq.) in acetonitrile, aniline (1 mol. eq.) was added and the reaction stirred at room temperature for 30 mins. During this time, the desired product precipitated as a colourless solid and was obtained via filtration. If required, recrystallisation from methanol can be undertaken.[248]

1,3-Bis(4-ethoxyphenyl)thiourea (49d)

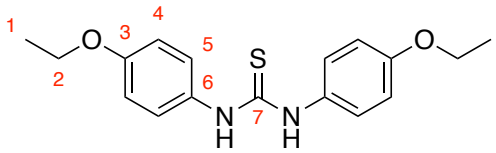

Following General Procedure 1, the title compound could be obtained in a quantitative yield. **^{1}H NMR** (600 MHz, DMSO-d_6) δ 9.40 (1H, s, N*H*), 7.29 (2H, d, J = 9.0, *H*-5), 6.88 (2H, d, J = 9.0, *H*-4), 4.00 (2H, q, J = 7.0, *H*-2), 1.32 (3H, t, J = 7.0, *H*-1); **^{13}C NMR** (150 MHz, DMSO-d_6) δ 180.6 (*C*-7), 156.2 (*C*-6), 132.6, (*C*-3), 126.5 (*C*-5), 114.6 (*C*-4), 63.6 (*C*-2), 15.2 (*C*-1); **MS** (ESI, *m/z*, %): 317.9 ([M+H]$^{+}$, 100 %).

1-(4-Ethoxyphenyl)-3-(4-(trifluoromethyl)phenyl)thiourea (49e)

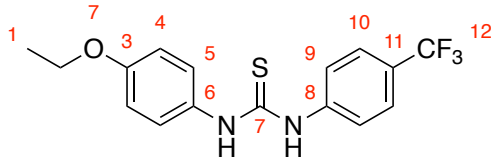

Following General Procedure 1, the title compound could be obtained in a quantitative yield. **^{1}H NMR** (600 MHz, $CDCl_3$) δ 9.94 (1H, s, N*H*), 9.86 (1H, s, N*H*), 7.74 (2H, d, J = 8.5, *H*-9), 7.66 (2H, d, J = 8.5, *H*-10), 7.32 (2H, d, J = 9.0, *H*-5), 6.90 (2H, d, J = 9.0, *H*-4), 4.01 (2H, q, J = 7.1, *H*-2), 1.32 (3H, t, J = 7.1, *H*-1); **^{13}C NMR** (150 MHz, $CDCl_3$) δ 180.1 (*C*-7), 156.5 (*C*-3), 144.0 (*C*-8), 132.2 (*C*-6), 126.4 (*C*-5), 125.9 (q, $^{3}J_{CF}$ = 3.8, *C*-10), 125.0 (q, $^{1}J_{CF}$ = 230, *C*-12), 124.0 (q, $^{2}J_{CF}$ = 12.0, *C*-11), 123.2 (*C*-9), 114.7 (*C*-4), 63.6 (*C*-2), 15.1 (*C*-1); **MS** (ESI, *m/z*, %): 341.8 ([M+H]$^{+}$, 100 %).

General Procedure 2: The Synthesis of Carbodiimides (50)

To a solution of thiourea (1 mol. eq.) and triethylamine (2 mol. eq.) in EtOAc cooled over ice, iodine (2.2 mol. eq.) was added portion wise over 15 mins before stirring at room temperature for 2 h. The reaction mixture was filtered under vacuum, and the filtrate washed with 10 % aqueous sodium thiosulfate, dried ($MgSO_4$) and concentrated *in vacuo*. The resultant brown oil was taken up in hexane and filtered through celite, removing a pale-yellow precipitate. Upon concentration, products were carried forwards to the next step with no further purification.[66]

_N,N'_-bis(phenyl)methanediimine (50a)

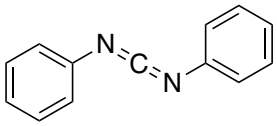

MS (EI, *m/z*, %): 194.4 ($[M]^+$, 100 %); **HRMS** (ESI): Calcd. For $C_{13}H_{11}N_2$: 195.022; Found 195.0928.

_N,N'_-bis(4-methylphenyl)methanediimine (50b)

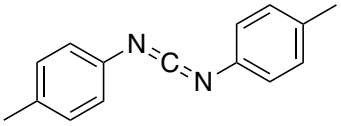

MS (ESI, *m/z*, %): 223.25 ($[M+H]^+$, 97.2 %); **HRMS** (ESI): Calcd. For $C_{15}H_{15}N_2$: 223.1235; Found 223.1220.

_N,N'_-bis[4-(trifluoromethyl)phenyl]methanediimine (50c)

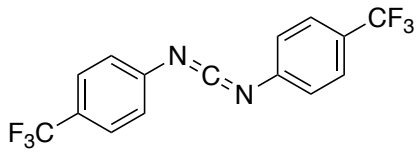

^{19}F NMR (376 MHz, d_6-DMSO) δ -60.7; **MS** (ASAP, *m/z*, %): 331.066 ($[M+H]^+$, 57.0 %), 332.071 ($[M+2H]^+$, 10.3); **HRMS** (ASAP): Calcd. For $C_{15}H_8N_2F_6$: 330.0592; Found 330.0597.

***N,N'*-bis[(4-ethoxy]phenyl]methanediimine (50d)**

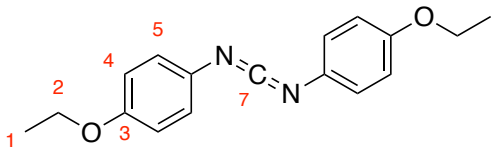

^{1}H NMR (600 MHz, $CDCl_3$) δ 7.09 (4H, dt, J = 9.0, 2.3 H, *H*-5), 6.84 (4H, dt, J = 9.0 , 2.3, *H*-4), 4.01 (4H, q, J = 6.9, *H*-2), 1.41 (6H, t, J = 6.9, *H*-1); **^{13}C NMR** (150 MHz, $CDCl_3$) δ 156.7 (*C*-3), 136.5 (*C*-7), 131.1 (*C*-6), 125.0 (*C*-5), 115.4 (*C*-4), 37.4 (*C*-2), 14.8 (*C*-1); **MS** (ESI, *m/z*, %): 283.33 ($[M+H]^+$, 100 %), 284.36 ($[M+2H]^+$, 15.0); **HRMS** (ESI): Calcd. For $C_{17}H_{19}N_2O_2$: 283.1447; Found 283.1451.

***N*-[4-(trifluoromethyl)phenyl]-*N'*-[4-(ethoxy)phenyl]methanediimine (50e)**

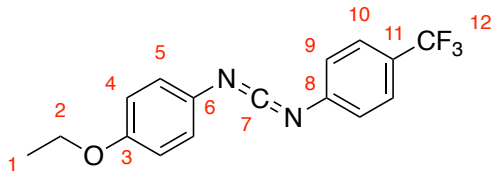

^{1}H NMR (600 MHz, $CDCl_3$) δ 7.57 (2H, d, J = 8.3, *H*-10), 7.25 (2H, d, J = 8.3, *H*-9), 7.11 (2H, d, J = 8.9, *H*-5), 6.86 (2H, d, J = 8.9, *H*-4), 4.02 (2H, q, J = 7.0, *H*-2), 1.42 (3H, t, 7.0, *H*-1); **^{13}C NMR** (150 MHz, $CDCl_3$) δ 157.3 (*C*-3), 143.0 (*C*-8), 134.5 (*C*-7), 129.3 (*C*-6), 127.6-126.9 (q, $^{2}J_{CF}$ = 32.7, *C*-11), 126.7-121.3 (br. q, $^{1}J_{CF}$ = 271, C-12), 126.6 (q, $^{3}J_{CF}$ = 4.2, *C*-10), 125.5 (*C*-5), 124.2 (*C*-9), 115.4 (*C*-4), 63.8 (*C*-2), 14.7 (*C*-1).

General Procedure 3: The Synthesis of Amidrazones (51)

Crude carbodiimide (**50**) (1 mol. eq.) was added to anhydrous, degassed toluene under an argon atmosphere. Arylhydrazine (1 mol. eq.) was added and the reaction stirred overnight at room temperature. Where appropriate, the resulting precipitate was isolated by filtration yielding the desired amidrazone as a white solid, unstable with respect to oxidation. Recrystallisation was possible for more stable derivatives (typically containing electron withdrawing substituents) from either isopropanol or ethanol.

***N,N′′*-bis(phenyl)-*N′*-(phenylamino)guanidine (51a)**

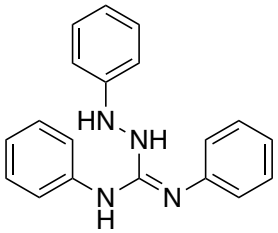

Following General Procedure 3, the title compound could be obtained as a white solid (6.1 g, 93%). **MS** (ESI, *m/z*, %): 302.91 ([M]$^+$, 70.4 %), 304.56 ([M+2H]$^+$, 100). 305.31 ([M+3H]$^+$, 34); **HRMS** (ESI): Calcd. For $C_{19}H_{19}N_4$: 303.1610; Found 303.1605.

***N,N′′*-bis(4-methylphenyl)-*N′*-(phenylamino)guanidine (51b)**

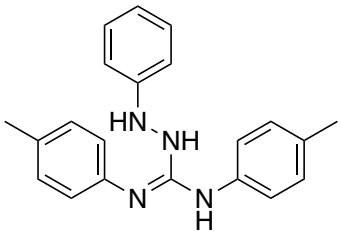

Following General Procedure 3, the title compound could be obtained as a pale pink solid (1.9 g, 45%); **MS** (ESI, *m/z*, %): 331.27 ([M+H]$^+$, 99.4 %), 332.23 ([M+2H]$^+$, 100.00), 333.30 ([M+3H]$^+$, 28.1); **HRMS** (ESI): Calcd. For $C_{21}H_{23}N_4$: 331.1923; Found: 331.1930.

***N,N′′*-bis[4-(trifluoromethyl)phenyl]-*N′*-(phenylamino)guanidine (51c)**

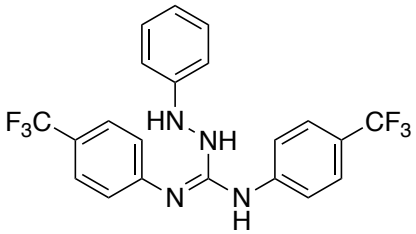

Following General Procedure 3, the title compound could be obtained as a white solid (1.9 g, 45%); **^{19}F NMR** (376 MHz, $CDCl_3$) δ -61.8; **MS** (ESI, *m/z*, %): 439.37 ([M+H]$^+$, 100 %), 440.36 ([M+2H]$^+$, 73.4), 441.35 ([M+3H]$^+$, 18.5); **HRMS** (ESI): Calcd. For $C_{21}H_{17}N_4F_6$: 339.1357; Found: 331.1362.

***N,N′′*-bis[4-ethoxyphenyl]-*N′*-(phenylamino)guanidine (51d)**

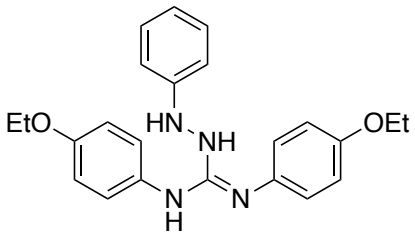

Following General Procedure 3, the title compound could be obtained as a white solid (0.51 g, 41%). **MS** (ESI, *m/z*, %): 391.42 ([M+H]$^+$, 100 %), 392.48 ([M+2H]$^+$, 62.1), 393.48 ([M+3H]$^+$, 16.5); **HRMS** (ESI): Calcd. For $C_{23}H_{27}N_4O_2$: 391.2134; Found: 391.2133.

***N*-[4-ethoxyphenyl]-*N′′*-[4-(trifluoromethyl)phenyl]-*N′*-(phenylamino)guanidine (51e)**

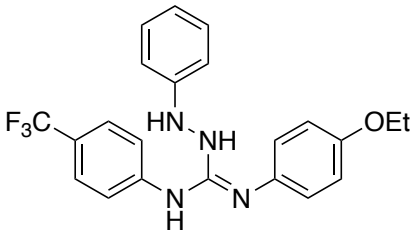

Following General Procedure 3, the title compound could be obtained as a a red oil which was continued to the next step with no further purification. **MS** (ESI, *m/z*, %): 415.40 ([M+H]$^+$, 100 %), 416.46 ([M+2H]$^+$, 64.9), 417.45 ([M+3H]$^+$, 13.0), 418.48 ([M+4H]$^+$, 1.1 %).

***N,N′′*-bis(phenyl)-*N′*-(4-methoxyphenylamino)guanidine (51f)**

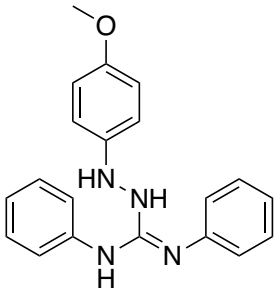

Following General Procedure 3, altered for use of 4-methoxyphenylhydrazine hydrochloride salt by addition of 1.1 mol. eq. of triethylamine to the reaction, the title compound was filtered from toluene. Subsequently this was dissolved in DCM and washed with sat. bicarbonate solution, dried ($MgSO_4$) and concentrated *in vacuo* to yield a pale pink solid (3.96 g, 54%). **MS** (ESI, *m/z*, %): 333.35 ([M+H]$^+$, 100 %), 334.40

([M+2H]$^+$, 48.9), 335.40 ([M+3H]$^+$, 9.3); **HRMS** (ESI): Calcd. For $C_{20}H_{21}N_4O$: 333.1715; Found: 333.1720.

***N,N′′*-bis(phenyl)-*N′*-(4-fluorophenylamino)guanidine (51h)**

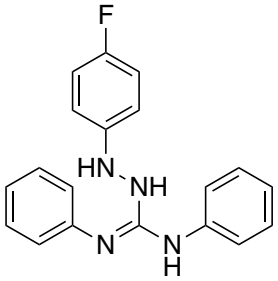

Following General Procedure 3, altered for use of the 4-fluorophenylhydrazine hydrochloride salt by addition of 1.1 mol. eq. of triethylamine to the reaction, the title compound was filtered from toluene. Subsequently this was dissolved in DCM and washed with sat. bicarbonate solution, dried ($MgSO_4$) and concentrated *in vacuo* to yield a pale pink solid (5.4 g, 78%). **MS** (ESI, *m/z*, %): 321.34 ([M+H]$^+$, 100 %), 322.04 ([M+2H]$^+$, 64.1); **HRMS** (ESI): Calcd. For $C_{19}H_{18}FN_4$: 321.1516; Found: 321.1530.

***N,N′′*-bis(phenyl)-*N′*-(4-cyanophenylamino)guanidine (51i)**

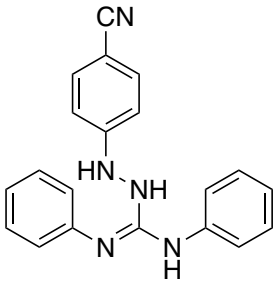

Following General Procedure 3, altered for use of the 4-cyanophenylhydrazine hydrochloride salt by addition of 1.1 mol. eq. of triethylamine to the reaction, the title compound was filtered from toluene. Subsequently this was dissolved in DCM and washed with sat. bicarbonate solution, dried ($MgSO_4$) and concentrated *in vacuo* to yield a pale pink solid which was recrystallised from IPA to give a white solid (2.7 g, 38%). **MS** (ESI, *m/z*, %): 328.45 ([M+H]$^+$, 100 %), 329.47 ([M+2H]$^+$, 20.6); **HRMS** (ESI): Calcd. For $C_{20}H_{18}N_5$: 328.1562; Found: 328.1544.

_N,N''_-bis[4-(trifluoromethyl)phenyl]-_N'_-[(4-(trifluoromethyl)phenyl)amino] guanidine (51j)

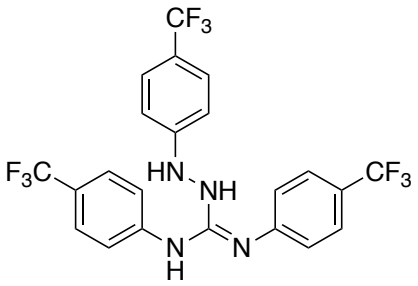

Following General Procedure 3, crude amidrazone was isolated after concentration *in* vacuo to give an orange oil which was continued to the next step with no further purification. **MS** (ESI, *m/z*, %): 507.38 ([M+H]$^+$, 100 %), 508.44 ([M+2H]$^+$, 61.4), 509.45 ([M+3H]$^+$, 12.6); **HRMS** (ESI): Calcd. For $C_{22}H_{16}F_9N_4$: 507.1231; Found: 507.1228.

_N,N''_-bis[4-(trifluoromethyl)phenyl]-_N'_-[(4-methoxyphenyl)amino] guanidine (51m)

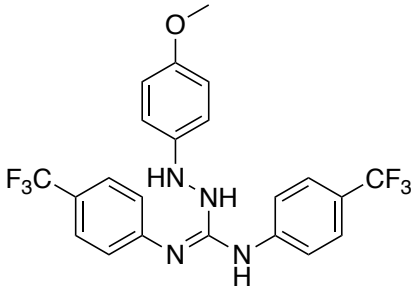

Following General Procedure 3, crude amidrazone was isolated after concentration *in* vacuo to give an orange oil which was continued to the next step with no further purification. **MS** (ESI, *m/z*, %): 469.91 (100%, [M+H]$^+$); **HRMS** (ESI): Calcd. For $C_{22}H_{18}N_4F_6O$: 469.1463; Found: 169.1450.

General Procedure 4: The Synthesis of Triazoles

Amidrazone (**3**) was dissolved in isopropyl alcohol (0.8 mmol ml^{-1}) and formaldehyde (0.4 mmol ml^{-1} (40 % aqueous solution)) was added before heating to reflux. Within an hour, a pale precipitate formed and the reaction was cooled and filtered. Recrystallisation from methanol yielded the title triazoles.

1-(4-methoxyphenyl)-*N*,4-bis[4-(trifluoromethyl)phenyl]-4,5-dihydro-1H-1,2,4-triazol-3-amine (52)

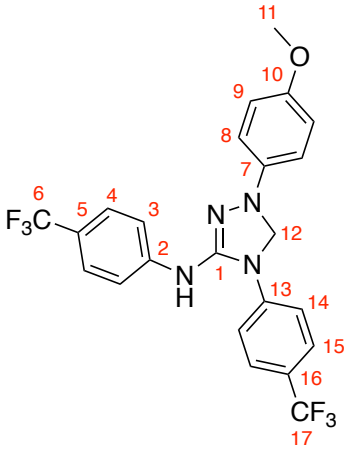

Following General Procedure 4, the title compound could be obtained as a white solid (0.47 g, 86%); **^{1}H NMR** (600 MHz, d_6-DMSO) δ 9.41 (1H, s, N*H*), 7.70 (2H, d, J = 8.6, *H*-15), 7.67 (2H, d, J = 8.8, *H*-3), 7.62 (2H, d, J = 8.8, *H*-4), 7.33 (2H, d, J = 8.6, *H*-14), 6.96 (2H, dt, J = 9.2, 2.1, *H*-8), 6.86 (2H, dt, J = 9.2, 2.1, *H*-9), 5.23 (2H, s, *H*-12), 3.68 (3H, s, *H*-11); **^{13}C NMR** (150 MHz, d_6-DMSO) δ 153.6 (*C*-10), 145.3 (*C*-1), 144.8 (*C*-13), 144.8 (*C*-2), 141.9 (*C*-7), 127.8-122.4 (q, J = 270, *C*-4), 124.9 (q, J =270, *C*-17), 127.6-122.2 (q, J = 3.6, *C*-15), 126.6 (q, J = 3.8, *C*-4), 123.3 (q, J = 32, *C*-16), 121.2 (q, J = 32, *C*-6), 120.4 (*C*-14), 117.5 (*C*-3), 115.5 (*C*-8), 114.9 (*C*-9), 73.0 (*C*-12), 55.8 (*C*-11); **^{19}F NMR** (376 MHz, d_6-DMSO) δ -61.8, -62.2; **MS** (ESI, *m/z*, %): 481.334 ($[M+H]^+$, 100 %), 482.40 ($[M+2H]^+$, 66), 483.39 ($[M+3H]^+$, 16); **HRMS** (ESI): $[M+H]^+$ $C_{23}H_{19}F_6N_4O$: 481.1463; Found: 481.1455.

1 - [3 - (trifluoromethyl)phenyl] - *N*,3 - bis[4 - (trifluoromethyl)phenyl] - 2,3 - dihydro - 1H - imidazol - 4 - amine (52)

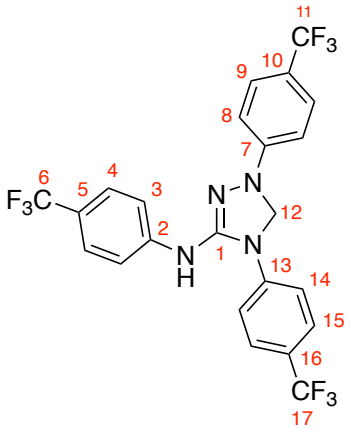

Following General Procedure 3, the title compound could be obtained as a white solid (1.29 g, 30%); **^{1}H NMR** (600 MHz, d_6-DMSO) δ 9.50 (1H, s, *NH*), 7.74 (2H, d, J = 8.6,

H-9), 7.69 (2H, d, J = 8.7, *H*-3), 7.64 (2H, d, J = 8.7, *H*-4), 7.55 (2H, d, J = 8.7, *H*-15), 7.40 (2H, d, J = 8.6, *H*-8), 7.02 (2H, d, J = 8.7, *H*-14), 5.47 (2H, s, *H*-12); **^{13}C NMR** (150 MHz, d_6-DMSO) δ 148.1 (*C*-13), 146.12 (*C*-1), 144.4 (*C*-2), 144.1 (*C*-7), 128.2-122.9 (q, J = 270, *C*-11), 127.8-122.4 (q, J = 271, *C*-6), 127.5-122.1 (q, J = 272, *C*-17) 126.9, (q, J = 3.0, *C*-9), 126.7 (q, J = 3.6, *C*-15), 126.6 (q, J = 3.7, *C*-4), 123.9 (q, J = 12.8, *C*-10), 121.6 (q, J = 32.5, *C*-5), 121.0 (*C*-8), 118.2 (q, J = 32.5, *C*-16), 117.8 (*C*-3), 112.4 (*C*-14), 70.5 (*C*-12); **MS** (ESI, *m/z*, %): 519.38 ([M+H]$^+$, 100 %), 520.40 ([M+2H]$^+$, 40);); **HRMS** (ESI): Calcd. For $C_{23}H_{15}F_9N_4$: 517.1075; Found: 517.1084.

General Procedure 5: Synthesis of Nitron Derivatives from Amidrazones

Amidrazone (**3**) (1 mol. eq.) and ammonium tetrafluoroborate (1 mol eq.) were placed under an argon atmosphere and heated to reflux in trimethyl orthoformate (Excess) overnight. Purification for each derivative is discussed separately.

General Procedure 6: Synthesis of Nitron Derivatives from Triazoles

Triazoles **52** were dissolved in minimal acetic acid and stirred at room temperature. Sodium nitrite (1.7 mol. eq.) was dissolved in water (1 ml) and then added dropwise to the reaction. After a rapid colour change to dark red-purple, the solution slowly turned a pale yellow colour. After 30 mins the reaction was added dropwise to 5 N ammonium hydroxide solution, over ice, forming a yellow precipitate which was isolated by filtration then dried on the high vacuum line overnight.

1,4-phenyl-3-(phenyl)amino-1,2,4-triazolium Tetrafluoroborate (6a)

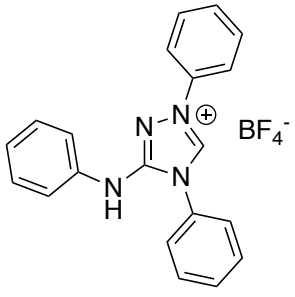

Following General Procedure 5, the title compound could be isolated as a white solid of the BF_4 salt upon cooling. Recrystallisation from MeOH yielded the desired product as a white crystalline solid (1.36 g, 69%). **^{1}H NMR** (400 MHz, d_6-DMSO) δ 10.87 (1H, s, C*H*), 9.73 (1H, br. s, N*H*), 8.03-7.10 (15H, Ar-*H*); **^{13}C NMR** (150 MHz, d_6-DMSO) δ 151.0, 135.5, 131.8, 131.1, 130.8, 130.7, 129.6, 127.3, 123.9, 120.5, 119.6; **MS** (ESI, *m/z*,

%): 313.31 ([M]$^+$, 100%), 314.34 ([M+H]$^+$, 38.3); **HRMS** (ESI): Calcd. For $C_{20}H_{17}N_4$: 313.1453; Found: 313.1438.

1-phenyl-4-(4-methylphenyl)-3-(4-methylphenyl)amino-1,2,4-triazolium inner salt (6b)

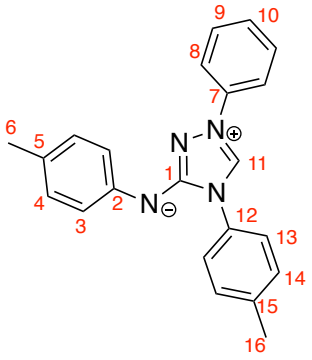

Following General Procedure 5 and concentration *in vacuo* the resultant grey-brown oil was taken up in DCM (20 ml) and washed with sat. $KHCO_3$ (10 ml) then water (10 ml) before drying ($MgSO_4$) giving a yellow solution. DCM was removed *in vacuo* to give crude product as a brown oil, which was triturated and recrystallised from IPA to yield the pure product as a yellow solid (0.067 g, 16%). **^{1}H NMR** (600 MHz, d_6-DMSO) δ 10.20 (1H, s, *H*-11), 7.97 (2H, d, J = 7.9, *H*-8), 7.84 (2H, d, J = 7.4, *H*-13), 7.63 (2H, dd, J = 7.6, *H*-9), 7.48 (1H, t, J = 7.6, *H*-10), 7.38 (2H, d, 7.9, *H*-14), 7.26 (2H, d, J = 7.9, *H*-3), 6.91 (2H, d, J = 7.9, *H*-4), 2.40 (3H, s, *H*-16), 2.19 (3H, s, *H*-6); **^{13}C NMR** (150 MHz, d_6-DMSO) δ 153.8 (*C*-1), 137.6 (*C*-15), 136.2 (*C*-7), 133.4 (*C*-11), 131.7 (*C*-12), 129.6 (*C*-9), 129.3 (*C*-14), 128.5 (*C*-4), 128.4 (*C*-10), 125.5 (*C*-5), 124.8 (*C*-13), 121.9 (*C*-3), 119.1 (*C*-8), 20.7 (*C*-16), 20.5 (*C*-6); **MS** (ESI, *m/z*, %): 341.25 ([M+H]$^+$, 100 %); **HRMS** (ESI): [M+H]$^+$ $C_{22}H_{21}N_4$: 341.1766; Found: 341.1768.

1-phenyl-4-(4-(trifluoromethyl)phenyl)-3-(4-(trifluoromethyl)phenyl)amino-1,2,4-triazolium inner salt (6c)

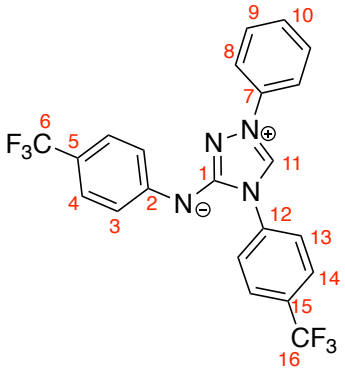

Following General Procedure 5 and concentration *in vacuo*, the resultant red oil was taken up in DCM giving a red solution and white precipitate. This white precipitate was isolated as the tetrafluoroborate salt of the desired product. Washing with sat. bicarbonate solution and extracting into DCM, before recrystallising from MeOH/H_2O yield the desired product as a yellow solid (1.41 g, 88%). Elemental analysis: Calcd. for $C_{22}H_{14}F_6N_4$: C, 58.93; H, 3.15; N, 12.50; Found: C, 58.46; H, 3.10; N, 12.39; **^{1}H NMR** (600 MHz, $CDCl_3$) δ 10.44 (1H, s, *H*-11), 8.28 (2H, d, J = 8.3, *H*-13), 8.02 (4H, d, *H*-14, -8), 7.67 (2H, t, J = 8.3, *H*-9), 7.54 (2H, t, *H*-10), 7.51 (2H, d, J = 8.5, *H*-3), 7.42 (2H, d, J = 8.5, *H*-4); **^{13}C NMR** (150 MHz, d_6-DMSO) δ 154.7 (*C*-1), 154.4 (*C*-2), 137.7 (*C*-12), 136.4 (*C*-7), 134.8 (*C*-11), 130.2 (*C*-9), 129.4 (*C*-10), 126.6 (q, $^3J_{CF}$ = 3.3, *C*-14), 126.2 (*C*-13), 125.6 (q, $^3J_{CF}$ = 3.7, *C*-4), 125.2 (q, $^2J_{CF}$ = 35.6, *C*-15), 122.1 (*C*-3), 120.0 (*C*-8), 117.1 (q, $^2J_{CF}$ = 30.9, *C*-5); **^{19}F NMR** (376 MHz, d_6-DMSO) δ -58.6, -60.9; **MS** (ESI, *m/z*, %): 449.37 ($[M+H]^+$, 100 %), 450.39 ($[M+2H]^+$, 61.1); **HRMS** (ESI): $[M+H]^+$ $C_{22}H_{15}F_6N_4$: 449.1201; Found: 449.1202.

1-phenyl-4-(4-ethoxyphenyl)-3-(4-ethoxyphenyl)amino-1,2,4-triazolium inner salt (6d)

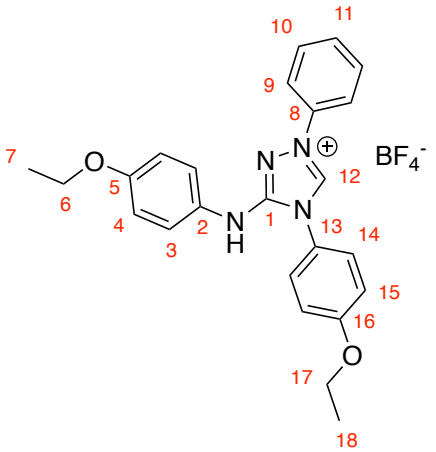

Following General Procedure 5**,** a white solid precipitated from the reaction mixture and was isolated by vacuum filtration (1.29 g, 76%). **^{1}H NMR** (600 MHz, DMSO-d_6) δ 10.70 (1H, s, *H*-12), 9.35 (1H, s, N*H*), 7.92 (2H, m, *H*-9), 7.71 (2H, dt, J = 9.1, 2.1, *H*-14), 7.67 (2H, m, *H*-10), 7.57 (1H, tt, *H*-11), 7.50 (2H, dt, J = 9.0, 2.2, *H*-3), 7.22 (2H, dt, J = 9.1, 2.1, *H*-15), 6.92 (2H, dt, J = 9.0, 2.2, *H*-4), 4.13 (2H, q, J = 6.8, *H*-17), 3.98 (2H, q, J = 7.0, *H*-6), 1.36 (3H, t, J = 6.8, *H*-18), 1.29 (3H, t, J = 7.0, *H*-7); **^{13}C NMR** (150 MHz, d_6-DMSO) δ 160.9 (*C*-16), 155.3 (*C*-5), 151.8 (*C*-1), 139.6 (*C*-12), 135.5 (*C*-8), 131.6 (*C*-13), 130.6 (*C*-10), 130.4 (*C*-11), 129.0 (*C*-14), 123.2 (*C*-2), 121.7 (*C*-3), 120.33 (*C*-9), 116.1 (*C*-15), 115.2 (*C*-4), 64.2 (*C*-17), 63.6 (*C*-6), 15.1 (*C*-18), 15.0 (*C*-7); **MS** (ESI, *m/z*, %): 401.44 ($[M+H]^+$, 100 %), 402.45 ($[M+2H]^+$, 63.1), 403.46 ($[M+3H]^+$, 6.0); **HRMS** (ESI): Calcd. For $C_{24}H_{25}N_4O_2$: 401.1978; Found: 401.1990.

1-(4-methoxyphenyl)-4-phenyl-3-(phenyl)amino-1,2,4-triazolium inner salt (6f)

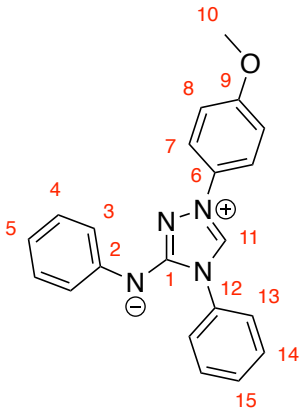

Following General Procedure 5 the BF_4 salt could be isolated by filtration from the cooled reaction mixture (2.9 g, 57%). The inner salt could be isolated by taking up in DCM and washing with sat. bicarbonate solution giving a bright yellow solution. This was dried ($MgSO_4$) and concentrated *in vacuo* giving a yellow-orange solid. Recrystallisation from MeOH/H_2O yielded the title compound as a yellow solid. **^{1}H NMR** (600 MHz, DMSO-d_6) δ 10.11 (1H, s, *H*-11), 7.98 (2H, dd, J = 8.5, 1.3, *H*-13), 7.91 (2H, d, J = 9.0, *H*-7), 7.59 (2H, m, J = 8.5, 7.2, *H*-14), 7.48 (1H, tt, J = 7.2, 1.3, *H*-15), 7.36 (2H, dd, J = 8.5, 1.2, *H*-3), 7.18 (2H, d, J = 9.0, *H*-8), 7.10 (2H, m, J = 8.5, 7.1, *H*-4), 6.61 (1H, tt, J = 7.1, 1.2, *H*-5), 3.84 (3H, s, *H*-10); **^{13}C NMR** (150 MHz, d_6-DMSO) δ 159.7 (*C*-9), 154.5 (*C*-1), 151.0 (*C*-2), 134.7 (*C*-12), 133.1 (*C*-11), 130.0 (*C*-6), 129.3 (*C*-14), 128.4 (*C*-15, -4), 125.4 (*C*-13), 122.5 (*C*-3), 121.3 (*C*-7), 117.6 (*C*-5), 115.2 (*C*-8), 56.1 (*C*-10); **MS** (ESI, *m/z*, %): 343.31 ([M+H]$^+$, 100 %), 344.37 ([M+2H]$^+$, 66.8), 345.40 ([M+3H]$^+$, 15.1); **HRMS** (ESI): Calcd. For $C_{21}H_{19}N_4O$: 343.1559; Found: 343.1581.

1-(4-fluorophenyl)-4-phenyl-3-(phenyl)amino-1,2,4-triazolium inner salt (6g)

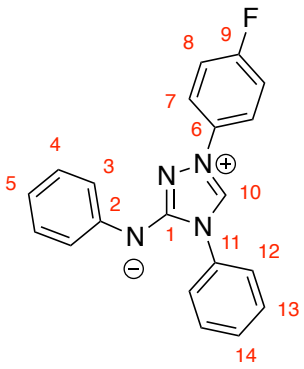

Following General Procedure 5, the white, tetrafluoroborate salt was isolated as a precipitate from the reaction media (2.8 g, 65%). The zwitterion can be isolated by suspending in DCM (100 ml), washing with 0.5 M NaOH solution (2 x 20 ml) and water

(1 x 20 ml) before drying ($MgSO_4$) and concentrating *in vacuo*. **^{1}H NMR** (600 MHz, d_6-DMSO) δ 10.22 (1H, s, *H*-10), 8.03 (2H, m, *H*-7), 7.97 (2H, d, J = 7.6, *H*-12), 7.60 (2H, t, J = 7.6, *H*-13), 7.53-7.47 (3H, m, *H*-8, *H*-14), 7.37 (2H, d, *H*-3), 7.11 (2H, t, *H*-4), 6.63 (1H, t, *H*-5); **^{13}C NMR** (150 MHz, d_6-DMSO) δ 161.9 (d, $^1J_{CF}$ = 246.2, *C*-9), 154.3 (*C*-1), 150.8 (*C*-2), 134.6 (*C*-11), 134.2 (*C*-10), 133.1 (d, $^3J_{CF}$ = 2.6, *C*-6), 129.4 (*C*-13), 128.6 (*C*-14), 128.4 (*C*-4), 125.5 (*C*-12), 122.5 (*C*-3), 122.0 (d, $^3J_{CF}$ = 8.8, *C*-7), 117.8 (*C*-5), 117.1 (d, $^2J_{CF}$ = 23.4, *C*-8); **^{19}F{^{1}H} NMR** (376 MHz, d_6-DMSO) δ -113.09; **MS** (ESI, *m/z*, %): 331.33 ($[M+H]^+$, 100 %), 332.36 ($[M+2H]^+$, 65.1), 333.34 ($[M+3H]^+$, 9.3); **HRMS** (ESI): Calcd. For $C_{20}H_{16}FN_4$: 331.1359; Found: 331.1376.

1-(4-cyanophenyl)-4-phenyl-3-(phenyl)amino-1,2,4-triazolium Tetrafluoroborate (6i)

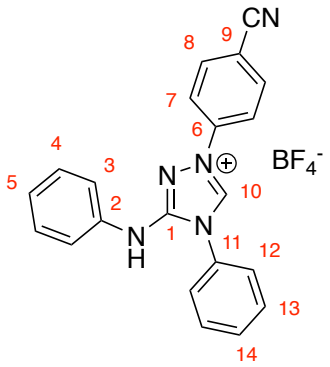

Following General Procedure 5, the white tetrafluoroborate salt was isolated as a precipitate from the reaction media (1.9 g, 55%). **^{1}H NMR** (600 MHz, d_6-DMSO) δ 11.01 (1H, s, *H*-10), 9.79 (1H, s, N*H*), 8.22 (2H, dt, J = 9.3, 2.0, *H*-8), 8.12 (2H, dt. J = 9.3, 2.0, *H*-7), 7.83-7.80 (2H, m, *H*-12), 7.78-7.73 (3H, m, *H*-13, -14), 7.64 (2H, dd, *H*-3), 7.40 (2H, m, *H*-4), 7.11 (1H, tt, *H*-5); **^{13}C NMR** (150 MHZ, d_6-DMSO) δ 151.1 (C-1), 141.2 (*C*-10), 138.4 (*C*-2), 138.4 (*C*-9), 135.0 (*C*-8), 132.0 (*C*-14), 131.0 (*C*-11), 130.8 (*C*-13), 129.6 (*C*-4), 127.2 (*C*-12), 124.1 (*C*-5), 121.0 (*C*-7), 119.7 (*C*-3), 118.3 (*C*N), 112.9 (*C*-6); **MS** (ESI, *m/z*, %): 338.44 ($[M+H]^+$, 100 %), 339.43 ($[M+2H]^+$, 22.7); **HRMS** (ESI): Calcd. For $C_{21}H_{16}N_5$: 338.1406; Found: 338.1382.

1,4-bis(4-(trifluoromethyl)phenyl)-3-((4-(trifluoromethyl)phenyl)amino)-1,2,4-triazolium Inner Salt (6j)

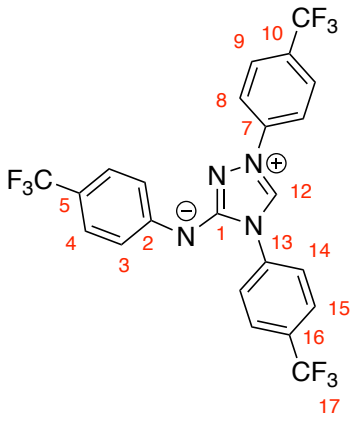

Following General Procedure 6, a yellow-orange solid of the title compound was obtained in a quantitative yield. Elemental analysis: Calcd. for $C_{23}H_{13}F_9N_4$: C, 53.50; H, 2.54; N, 10.85; Found: C, 53.36; H, 2.56; N, 10.85; **^{1}H NMR** (600 MHz, DMSO-d_6) δ 10.6 (1H, s, *H*-12), 8.27 (2H, d, J = 8.1, *H*-8), 8.23 (2H, d, J = 8.7, *H*-14), 8.09 (2H, d, J = 8.7, *H*-15), 8.04 (2H, d, J = 8.1, *H*-9), 7.52 (2H, d, J = 8.7, *H*-3), 7.43 (2H, d, J = 8.7, *H*-4); **^{13}C NMR** (150 MHz, $CDCl_3$) δ 154.5 (*C*-1), 154.2 (*C*-2), 139.2 (*C*-13), 137.6 (*C*-7), 136.4 (*C*-12), 129.2 (q, $^2J_{CF}$ = 35.3, *C*-16), 129.1 (q, $^2J_{CF}$ = 33.3, *C*-10), 127.6 (q, $^3J_{CF}$ = 4.7, *C*-15), 126.6 (q, $^3J_{CF}$ = 4.7, *C*-9), 126.3 (*C*-8), 125.6 (q, $^3J_{CF}$ = 4.8, *C*-4), 122.2 (*C*-3), 120.4 (*C*-14); **MS** (ESI, *m/z*, %): 517.32 ([M+H]$^+$, 100%), 518.35 ([M+2H]$^+$, 63.8). 519.34 ([M+2H]$^+$, 12.5);); **HRMS** (ESI): Calcd. for $C_{23}H_{14}F_9N_4$: 517.1075; Found: 517.1083.

1-(4-methoxyphenyl)-4-(4-(trifluoromethyl)phenyl)-3-((4-(trifluoromethyl)phenyl) amino)-1,2,4-triazolium Inner Salt (6m)

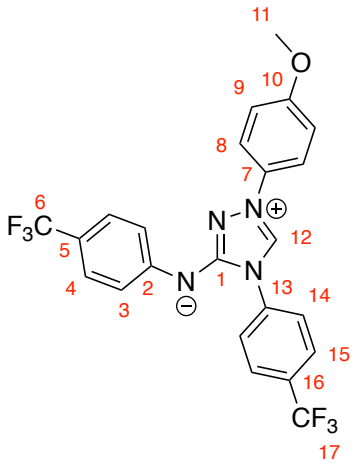

Following General Procedure 6, a yellow-orange solid of the title compound was obtained in a quantitative yield. **^{1}H NMR** (600 MHz, $CDCl_3$) δ 8.63 (1H, s, *H*-12), 7.99 (2H, d, J = 8.6, *H*-14), 7.73 (2H, d, J = 8.6, *H*-15), 7.65 (2H, dt, J = 9.0, 2.1, *H*-8), 7.54 (2H, d, J =

8.3, *H*-3), 7.44 (2H, d, J = 8.3, *H*-4), 7.04 (2H, dt, J = 9.0, 2.1, *H*-9), 3.91 (3H, s, *H*-11); **^{13}C NMR** (150 MHz, $CDCl_3$) δ 160.6 (*C*-10), 154.6 (*C*-1), 152.3 (*C*-2), 136.3 (*C*-13), 130.6 (q, $^2J_{CF}$ = 33.3, *C*-16), 128.9 (*C*-7), 128.2 (*C*-12), 126.5 (q, $^3J_{CF}$ = 3.7, *C*-15), 125.6 (q, $^3J_{CF}$ = 4.0, *C*-4), 124.7 (*C*-14), 121.8 (*C*-3), 121.3 (*C*-8), 120.2 (q, $^2J_{CF}$ = 32.4, *C*-5), 114.9 (*C*-9), 55.7 (*C*-11); **^{19}F{^{1}H} NMR** (376 MHz, d_6-DMSO) -60.89, -62.71; ; **MS** (ESI, *m/z*, %): 479.32 ([M+H]$^+$, 100%), 480.38 ([M+2H]$^+$, 66.9). 481.41 ([M+2H]$^+$, 21.5);); **HRMS** (ESI): Calcd. for $C_{23}H_{17}F_6N_4O$: 479.1307; Found: 479.1317.

6.1.2. N^5-Adducts

General Procedure 7: The Synthesis of N^5-Adducts

To anhydrous, toluene (150 ml) which had been purged with argon, crude carbodiimide (**50**) (1 mol. eq.) was charged and cooled over ice under an argon atmosphere. Arylhydrazine (0.5 mol. eq.) was added dropwise over 15 mins and the reaction stirred over ice for 30 mins and at RT overnight during which time a precipitate formed. Title compounds could be isolated by filtration and subsequently recrystallised from IPA.

***N*,1,4-triphenyl-5-(phenylimino)-4,5-dihydro-1H-1,2,4-triazol-3-amine (55a)**

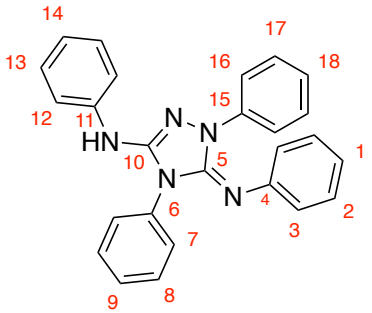

Following General Procedure 7, the title compound was isolated as a white solid (0.94 g, 57%). **^{1}H NMR** (600 MHz, d_6-DMSO) δ 7.97 (1H, s, N*H*), 7.89 (2H, d, *H*-3), 7.52 (2H, d, *H*-12), 7.34-7.22 (9H, m, *H*-2, -13, -9, -8, -7), 7.07 (2H, t, *H*-1), 6.91 (2H, t, *H*-14), 6.74 (2H, t, *H*-17), 6.49-6.43 (3H, m, *H*-16, -18); **^{13}C NMR** (150 MHz, d_6-DMSO) δ 147.7, 145.4, 142.0, 140.5, 139.6, 133.1, 129.5, 129.4, 129.1, 129.1, 128.8, 128.1, 124.2, 122.1, 121.9, 120.1, 118.6; **MS** (ASAP, *m/z*, %): 404.17 ([M+H]$^+$, 100%), 406.20 ([M+2H]$^+$, 70); **HRMS** (ESI): Calcd. For $C_{26}H_{22}N_5$: 404.1875; Found: 404.1870.

4-bis(4-methylphenyl)-5-[(4-methylphenyl)imino]-1-phenyl-4,5-dihydro-1H-1,2,4-triazol-3-amine (55b)

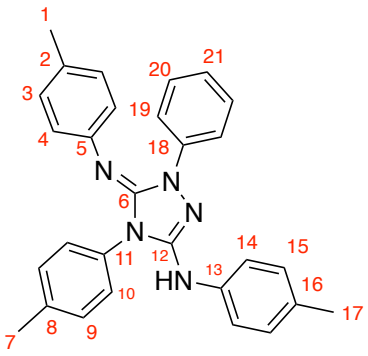

Following General Procedure 7, the title compound was isolated as a white solid (1.53 g, 34%). **^{1}H NMR** (600 MHz, d_6-DMSO) δ 7.86 (1H, Br. S, N*H*), 7.82 (2H, d, J = 7.7, *H*-19), 7.43 (2H, d, *H*-4), 7.31 (2H, dd, J = 6.7, 1.8, *H*-20), 7.18 (2H, d, *H*-14), 7.07 (5H, m, *H*-3, *H*-15, *H*-21), 6.57 (2H, d, J = 7.4, *H*-9), 6.35 (2H, d, J = 7.4, *H*-10), 2.27 (3H, s, *H*-1), 2.22 (3H, s, *H*-17), 2.04 (3H, s, *H*-7); **^{13}C NMR** (150 MHz, d_6-DMSO) δ 138.0 (*C*-2), 137.2 (*C*-5), 130.2 (*C*-16), 129.4 (*C*-3), 128.9 (*C*-15), 128.7 (*C*-14), 128.2 (*C*-20), 128.0 (*C*-9), 121.4 (*C*-10), 119.6 (*C*-19), 118.2 (*C*-4), 20.6 (*C*-1), 20.1 (*C*-17), 20.1 (*C*-7); **MS** (ESI, *m/z*, %): 448.32 ($[M+3H]^+$, 100 %); **HRMS** (ESI): Calcd. For $C_{29}H_{28}N_5$: 446.2345; Found: 446.2348.

4 - diphenyl - 5 - (phenylimino) - 1 - [4 - (trifluoromethyl)phenyl] - 4,5 - dihydro - 1H - 1,2,4 - triazol - 3 - amine (55c)

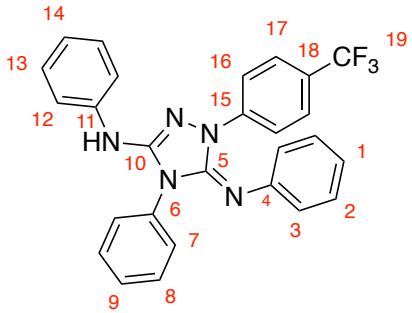

Following General Procedure 7, the title compound was isolated as a white solid (1.55 g, 41%). **^{1}H NMR** (600 MHz, d_6-DMSO) δ 8.31 (2H, d, J = 8.9 Hz, *H*-16), 7.99 (1H, s, N*H*), 7.75 (2H, d, J = 8.9 Hz, *H*-17), 7.57 (2H, d, *H*-12), 7.30-7.26 (4H, m, *H*-13, *H*-7), 7.23-7.17 (3H, m, *H*-8, *H*-9), 6.96 (1H, t, *H*-14), 6.78 (2H, t, *H*-2), 6.53 (1H, t, *H*-1), 6.50 (2H, d, *H*-3); **^{13}C NMR** (150 MHz, d_6-DMSO) δ 146.8 (*C*-4), 146.1 (*C*-5), 142.6 (*C*-15), 141.1 (*C*-10), 140.2 (*C*-6), 132.7 (*C*-11), 129.7 (*C*-7), 129.4 (*C*-8), 129.2 (*C*-9), 129.1 (*C*-13), 128.1 (*C*-2), 127.6-122.2 (q, $^{1}J_{CF}$ = 272, *C*-19), 126.2 (q, $^{3}J_{CF}$ = 4.0, *C*-17), 123.3 (q, $^{2}J_{CF}$ = 33, *C*-18), 122.3 (*C*-3), 122.2 (*C*-14), 120.6 (*C*-1), 118.9 (*C*-12), 118.6 (*C*-16).

4 - diphenyl - 5 - (phenylimino) - 1 - [4 - cyanophenyl] - 4,5 - dihydro - 1H - 1,2,4 - triazol - 3 - amine (55d)

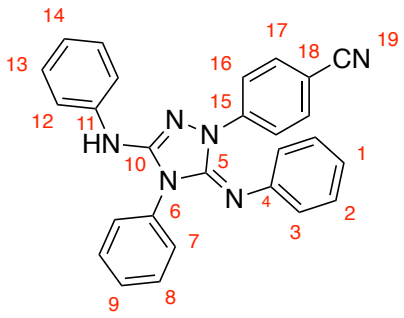

Following General Procedure 7, the title compound was isolated as a white solid (1.61 g, 37%). **^{1}H NMR** (600 MHz, d_6-DMSO) δ 8.31 (2H, dt, *H*-16), 7.97 (1H, s, N*H*), 7.83 (2H, dt, *H*-17), 7.55 (2H, d, *H*-12), 7.29-7.23 (4H, m, *H*-13, -2), 7.19-7.12 (3H, m, *H*-1, -3), 6.95 (1H, tt, *H*-14), 6.75 (2H, tt, *H*-8), 6.51 (1H, tt, *H*-9), 6.47 (2H, d, *H*-7); **^{13}C NMR** (150 MHz, d_6-DMSO) δ 146.6, 146.3, 143.0, 140.9, 140.0, 133.5, 132.6, 129.8, 129.4, 129.3, 129.1, 128.1, 122.4, 122.2, 120.8, 119.8, 119.1, 118.3, 104.7; **MS** (ESI, *m/z*, %): 429.75 ([M+H]$^{+}$, 100%); **HRMS** (ESI): Calcd. For $C_{27}H_{21}N_6$: 429.1828; Found: 429.1809.

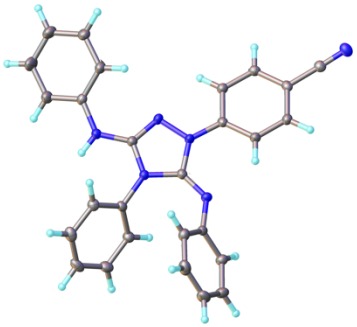

1-phenyl-*N*,4-bis(4-ethoxyphenyl)-5-((4-ethoxyphenyl)imino)l-4,5-dihydro-1*H*-1,2,4-triazol-3-amine (55e)

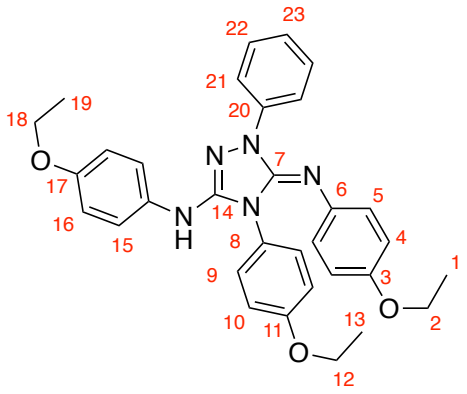

Following General Procedure 7, the title compound was isolated as a white solid (0.75 g, 66%). **^{1}H NMR** (600 MHz, d_6-DMSO) δ 7.88 (2H, d, *H*-21), 7.42 (2H, d, *H*-5), 7.29 (2H, t, *H*-22), 7.09 (2H, d, *H*-15), 7.02 (1H, t, *H*-23), 6.80 (2H, d, *H*-4), 6.72 (1H, br. s, N*H*), 6.70 (2H, d, *H*-16), 6.31 (4H, s, *H*-9, -10), 3.92 (4H, m, *H*-2, -18), 3.74 (2H, q, *H*-12), 1.25 (6H, m, *H*-1,-19), 1.17 (3H, t, *H*-13); **^{13}C NMR** (150 MHz, d_6-DMSO) δ 158.8, 153.9, 152.4, 146.1, 142.1, 139.8, 130.9, 130.1, 128.7, 125.5, 123.6, 122.9, 120.5, 120.4, 119.5, 115.1, 114.8, 114.5, 63.7, 63.6, 15.1, 15.0, 14.9; **MS** (ESI, *m/z*, %): 537.14 ($[M+H]^+$, 100%).

1-phenyl-*N*,4-bis(4-(trifluoromethyl)phenyl)-5-((4-(trifluoromethyl)phenyl)imino)-4,5-dihydro-1*H*-1,2,4-triazol-3-amine (55f)

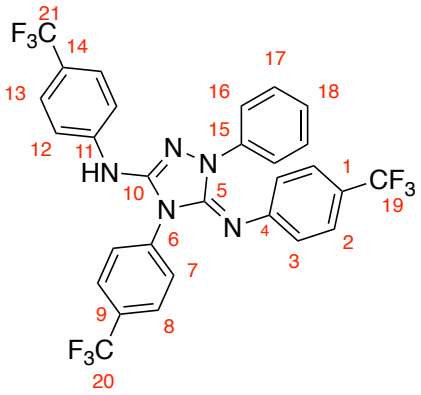

Following General Procedure 7, the title compound was isolated as a white solid (0.8 g, 63%). **^{1}H NMR** (600 MHz, d_6-DMSO) δ 8.74 (1H, s, N*H*), 7.93 (2H, d, *H*-16), 7.71 (2H, d, *H*-12), 7.61 (2H, d, *H*-13), 7.58 (4H, s, *H*-2, -3), 7.37 (2H, t, *H*-17), 7.15 (1H, t, *H*-18), 7.00 (2H, d, *H*-7), 6.59 (2H, d, *H*-8); **^{13}C NMR** (150 MHz, d_6-DMSO) δ 151.5, 144.2, 141.9, 139.1, 136.2, 130.6, 129.8, 129.6, 129.3, 129.0, 128.6, 126.5, 125.9, 125.7, 125.1,

124.9, 122.4, 120.3, 118.1; **MS** (ASAP, *m/z*, %): 608.10 ($[M+H]^+$, 100%), 609.2 ($[M+2H]^+$, 68); **HRMS** (ESI): Calcd. For $C_{29}H_{19}N_5F_9$: 608.1497; Found: 608.1508.

6.1.3. Amido-Blatter radicals

General Procedure 8: The Synthesis of Amido Blatter radicals[21]

Nitron (**6**) was dissolved in acetonitrile (99 ml) along with 1% water (1 ml) and stirred with exposure to air for 72 h. The solution was then dried in vacuo to give crude black crystals. This was re-crystallised from minimal hot ethanol to yield radical **24.**

N-phenyl-N-(1-phenyl-1,4-dihydrobenzo[e][1,2,4]triazin-3-yl)formamide Radical (24a)[21]

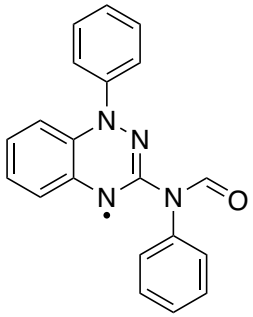

Following General Procedure 8, the title compound was isolated as a dark red solid (0.85 g, 82%). Elemental analysis: Calcd. for $C_{20}H_{15}N_4O$: C, 73.38; H, 4.62; N, 17.11; Found: C, 72.95; H, 4.60; N, 17.12; **MS** (ESI, *m/z*, %): 327.19 (M^+, 100 %), 328.18 ($[M+H]^+$, 33.9), 329.13 ($[M+2H]^+$, 5.8), **HRMS** (ESI): Calcd. For $C_{20}H_{15}N_4O$: 327.1246; Found: 327.1252; ν_{max} / cm^{-1} 3065 (CH), 1680 (C=O).

N-(7-ethoxy-1-phenyl-1,4-dihydrobenzo[e][1,2,4]triazin-3-yl)-N-(4-ethoxyphenyl) formamide Radical (24d)

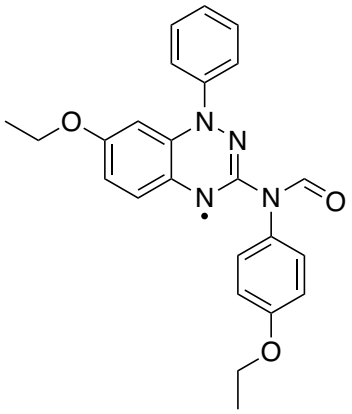

Following General Procedure 8, modified for use of the tetrafluoroborate salt of Nitron **6d** through addition of 3 mol. eq. of triethylamine, a dark red solid was isolated (0.35 g, 41%). Elemental analysis: Calcd. for $C_{24}H_{13}N_4O_3$: C, 69.38; H, 5.58; N, 13.49; Found: C, 68.99; H, 5.46; N, 13.48; **MS** (ESI, *m/z*, %): 415.62 (M^+, 100%); **HRMS** (ESI): Calcd. For $C_{24}H_{13}N_4O_3$: 415.1770; Found: 415.1783; **IR**: ν_{max} / cm^{-1} 2928 (CH), 1692 (C=O).

N-(1-(4-methoxyphenyl)-1,4-dihydrobenzo[e][1,2,4]triazin-3-yl)-N-phenyl formamide Radical (24f)

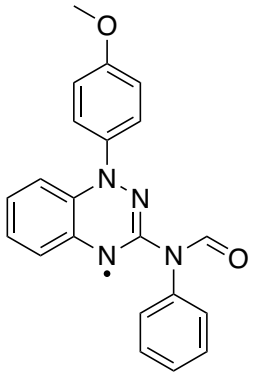

Following General Procedure 8, modified for use of the tetrafluoroborate salt of Nitron **6f** through addition of 3 mol. eq. of triethylamine, a dark red solid was isolated (0.37 g, 45%). Elemental analysis: Calcd. for $C_{21}H_{17}N_4O_2$: C, 70.58; H, 4.79; N, 15.68; Found: C, 70.21; H, 4.68; N, 15.65. **MS** (ESI, *m/z*, %): 357.28 (M^+, 100 %), 358.31 ($[M+H]^+$, 61.9); **HRMS** (ESI): Calcd. For $C_{21}H_{17}N_4O_2$: 357.1352; Found: 357.1345; **IR**: ν_{max} / cm^{-1} 2962 (CH), 1674 (C=O).

N-(1-(4-fluorophenyl)-1,4-dihydrobenzo[e][1,2,4]triazin-3-yl)-N-phenylformamide Radical (24g)

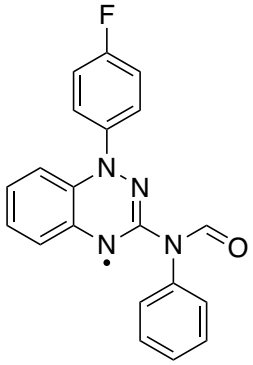

Following General Procedure 8, the title compound was isolated as a dark red solid (0.78 g, 75%). Elemental analysis: Calcd. for $C_{20}H_{14}N_4OF$: C, 69.56; H, 4.09; N, 16.22; Found: C, 69.33, H, 4.14; N, 16.71; **MS** (ESI, *m/z*, %): 345.36 (M^+, 100 %), 346.35 ($[M+H]^+$, 33.7); **HRMS** (ESI): Calcd. For $C_{20}H_{14}N_4OF$: 345.1152; Found: 345.1148; **IR**: ν_{max} / cm^{-1} 3070 (CH), 1686 (C=O).

N-(1-(4-cyanophenyl)-1,4-dihydrobenzo[e][1,2,4]triazin-3-yl)-N-phenylformamide Radical (24i)

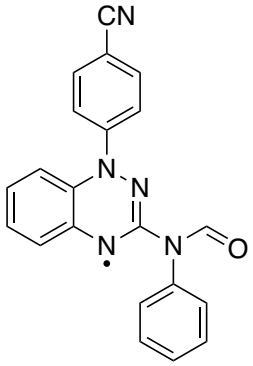

Following General Procedure 8, modified for use of the tetrafluoroborate salt of Nitron **6i** through addition of 3 mol. eq. of triethylamine, a dark red solid was isolated (0.50 g, 60%). **MS** (ESI, *m/z*, %): 352.46 (M^+, 100%), 353.41 ($[M+H]^+$, 29.6); **HRMS** (ESI): Calcd. For $C_{21}H_{14}N_5O$: 352.1198; Found: 352.1194; **IR**: ν_{max} / cm^{-1} 3244 (CH), 2223 (C≡N), 1693 (C=O).

6.1.4. Amino-Blatter radicals

General Procedure 9: The Synthesis of Amino Blatter Radicals

Amido-Blatter radical (**24**) was stirred at RT in 5 M HCl (60 ml) in MeOH/H_2O (1:1) (60 ml) for 24 h before concentrating *in vacuo*. The resulting oil was taken up in DCM, washed with sat. $KHCO_3$ solution (3 x 20 ml), dried and re-concentrated. The resultant green precipitate was recrystallised from EtOH/H_2O to yield the desired radical.

N,1-diphenyl-1,4-dihydrobenzo[e][1,2,4]triazin-3-amine Radical (25a)[21]

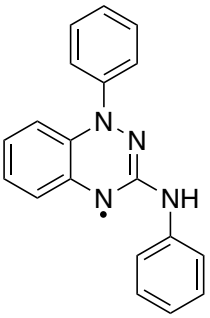

Following General Procedure 9, the title compound was isolated as a dark green solid (0.4 g, 87%). **MS** (ESI, *m/z*, %): 299.23 (M^+, 55.6), 300.21 ($[M+H]^+$, 59.8), 301.26 ($[M+2H]^+$, 63.7), 302.21 ($[M+3H]^+$, 100). **HRMS** (ESI): Calcd. For $C_{19}H_{15}N_4$: 299.1297; Found: 299.1294.

1-(4-methoxyphenyl)-N-phenyl-1,4-dihydrobenzo[e][1,2,4]triazin-3-amine Radical (25f)

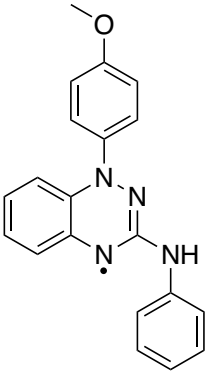

Following General Procedure 9, the title compound was isolated as a dark green solid (0.21 g, 76%); **MS** (ESI, *m/z*, %): 328.35 (M^+, 79.6 %), 330.34 ($[M+H]^+$, 60.4), 331.33 (($[M+2H]^+$, 100); **HRMS** (ESI): Calcd. For $C_{20}H_{17}N_4O$: 329.1402; Found: 329.1411; **IR**: ν_{max} / cm^{-1} 3320br (NH), 2959 (CH).

1-(4-fluorophenyl)-N-phenyl-1,4-dihydrobenzo[e][1,2,4]triazin-3-amine Radical (25g)

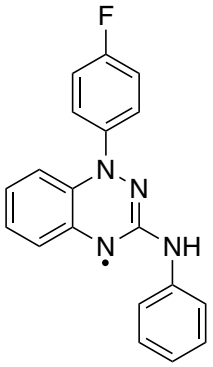

Following General Procedure 9, the title compound was isolated as a dark green solid (0.81 g, 88%); **MS** (ESI, *m/z*, %): 317.17 (M^+, 59.5 %), 319.51 ($[M+H]^+$, 100) **HRMS** (ESI): Calcd. For $C_{19}H_{14}N_4F$: 317.1202; Found: 317.1203; **IR**: ν_{max} / cm^{-1} 3297br (NH), 3053 (CH).

1-(4-cyanophenyl)-N-phenyl-1,4-dihydrobenzo[e][1,2,4]triazin-3-amine Radical (25i)

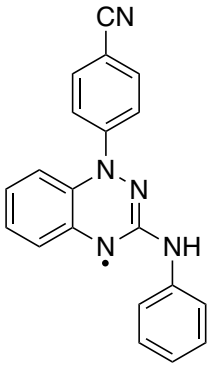

Following General Procedure 9, the title compound was isolated as a dark green solid (0.22 g, 80%); **MS** (ESI, *m/z*, %): 324.40 (M^+, 86.8 %), 326.29 ($[M+2H]^+$, 100), 327.32 (($[M+3H]^+$, 37.4); **HRMS** (ESI): Calcd. For $C_{20}H_{14}N_5$: 324.1249; Found: 324.1265; **IR**: ν_{max} / cm^{-1} 3338br (NH).

6.1.5. Parent Blatter Radical (15)

N'-phenyl-N-(phenylamino)benzenecarboximidamide (21a)[63]

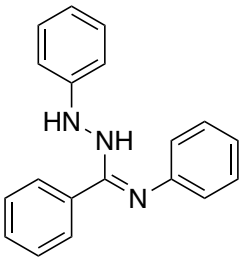

Benzanilide (5 g, 25.4 mmol), thionyl chloride (5.5 ml, 76 mmol) and toluene (25 ml) were charged to a dry flask under an argon atmosphere and heated to 90 °C for 7 hrs before concentrating *in vacuo*. Upon leaving to stand overnight a yellow oil crystallised into an orange solid which was subsequently dissolved in anhydrous THF (25 ml) and triethylamine (5.3 ml, 38.1 mmol). Phenylhydrazine (2.5 ml, 25.4 mmol) was added and a moderate exotherm controlled with an ice bath, before stirring overnight at RT. Upon completion, the reaction material was concentrated *in vacuo* and then refluxed in 2 % acetic acid (70 ml) for 30 mins, forming a white precipitate. This was isolated by filtration and washed with water (30 ml) and MeOH (30 ml) to yield the desired amidrazone as a fine, white solid (3.9 g, 53%). **^{1}H NMR** (600 MHz, DMSO-d_6) δ 6.59 (2H, d, Ar-*H*), 6.67-6.73 (2H, m, Ar-*H*), 7.05-7.34 (9H, m, Ar-*H*), 7.58 (2H, d, Ar-*H*), 8.01 (1H, s, N*H*), 9.14 (1H, s, N*H*); **^{13}C NMR** (150 MHz, d_6-DMSO) δ 146.2, 143.5, 137.6, 135.6, 129.4, 129.2, 128.6, 128.5, 127.6, 119.6, 119.0, 116.9, 113.1; **MS** (ESI, *m/z*, %): 288.28 ($[M+H]^+$, 100 %), 289.33 ($[M+2H]^+$, 51.9), 290.34 ($[M+3H]^+$, 6.6); **HRMS** (ESI): Calcd. For $C_{19}H_{18}N_3$: 288.1501; Found: 288.1498.

1,3-diphenyl-1,4-dihydro-1,2,4-benzotriazinyl (Blatter) radical (15a)[24]

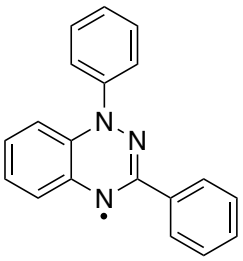

Amidrazone (**21a**) (3.90 g, 13.6 mmol) was dissolved in DCM (30 ml) and then DBU (0.2 ml, 1.36 mmol) and Pd/C (23 mg, 0.22 mmol) were added and stirred at RT overnight. A further addition of Pd/C (23 mg, 0.22 mmol) saw complete conversion to radical by LC-MS. Reaction was filtered through a silica plug with further DCM (100 ml) and then concentrated *in vacuo*. Subsequent recrystallisation from isopropyl alcohol

yielded the desired radical as a black solid (2.0 g, 52%). Elemental analysis: Calcd for $C_{19}H_{14}N_3$: C, 80.26; H, 4.96; N, 14.78; Found: C, 79.96; H, 5.00; N, 14.60; **MS** (ESI, *m/z*, %): 284.30 ($[M+H]^+$, 100 %), 285.31 ($[M+2H]^+$, 34.7), 286.30 ($[M+3H]^+$, 4.1).

6.1.6. Methylated Nitrons

General Procedure 10: The methylation of Nitrons

Nitron (**6**, 1 mol. eq.) and trimethyloxonium tetrafluoroborate (1.1 mol. eq.) were added to a dry flask under argon. Anhydrous DCM was added and the solution was left to stir overnight at room temperature. After this, the reaction mixture was quenched with water (50 ml) and the resulting aqueous layer was washed with DCM (2 x 50 ml). The combined organic layers were dried ($MgSO_4$) and concentrated *in vacuo*. Purification was possible by recrystallisation in IPA or by column chromatography using 98:2 DCM:MeOH.

3-(Methyl(phenyl)amino)-1,4-diphenyl-4H-1,2,4-triazol-1-ium Tetrafluoroborate (60a)

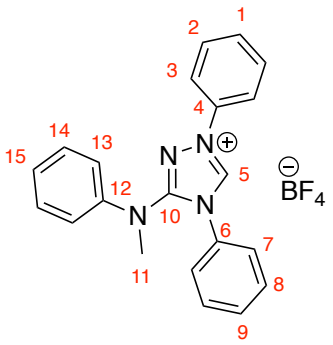

Following General Procedure 10, the title compound was isolated as a white solid (1.13 g, 43%); **^{1}H NMR** (400 MHz, $CDCl_3$) δ 9.69 (1H, s, *H*-5), 7.97 (2H, dd, ^3J = 8.2 Hz, 1.6 Hz, *H*-3), 7.56–7.47 (3H, m, *H*-1, -2), 7.35–7.31 (2H, m, *H*-7) 7.22–7.12 (3H, m, *H*-8, -9), 7.08–7.03 (2H, m, *H*-13), 6.98–6.91(3H, m, *H*-14, -15), 3.52 (3H, s, *H*-11); **^{13}C NMR** (151 MHz, $CDCl_3$) δ 154.7 (*C*-10), 142.6 (*C*-4), 138.7 (*C*-5), 135.0 (*C*-6), 131.2 (*C*-12), 130.8 (*C*-1), 130.6 (*C*-8), 130.2 (*C*-2), 129.8 (*C*-13), 129.6 (*C*-9), 127.0 (*C*-14), 125.9 (*C*-7), 124.7 (*C*-15), 121.0 (*C*-3), 42.9 (*C*-11); **MS** (ESI, *m/z*, %): 327.31 ($[M]^+$, 100 %), 328.37 ($[M + H]^+$, 70.4), 329.36 ($[M + 2H]^+$, 13.1); **HRMS** (ESI): Calcd. For $C_{21}H_{19}N_4$ 327.1610; Found 327.1613.

6.1.7. Diradicals

N,1,4 - triphenyl - 5 - [4 - (trifluoromethyl)phenyl] - 4,5 - dihydro - 1H - 1,2,4 - triazol - 3 - amine (73)

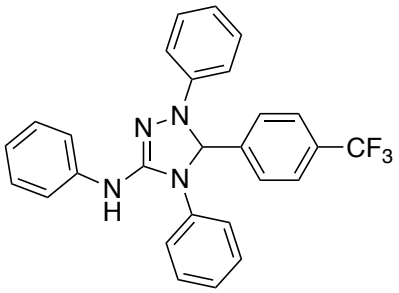

Amidrazone (**52**) (0.5 g, 1.65 mmol) and 3 Å molecular sieves (~5) were placed in a microwave vial under argon. DCM (5 ml) and 4-trifluoromethylbenzaldehyde (0.23 ml, 1.65 mmol) were charged before addition of pyrrolidine (0.014 ml, 0.165 mmol). The reaction was then heated to 80 ºC by microwave for 2 h, noting conversion of a colourless slurry to a red solution, before concentrating *in vacuo*. Subsequent recrystallisation in MeOH yielded the title compound as a pale yellow solid (0.4 g, 53%). **^{1}H NMR** (400 MHz, $CDCl_3$) 7.67 (4H, s, Ar-*H*), 7.50 (2H, d, Ar-*H*), 7.42-7.22 (9H, m, Ar-*H*), 7.08-6.98 (4H, m, Ar-*H*), 6.88 (1H, t, Ar-*H*); **^{19}F NMR** (376 MHz, $CDCl_3$) δ -62.53; **MS** (ESI, *m/z*, %): 457.40 ($[M]^+$, 100 %), 459.40 ($[M+H]^+$, 89 %); **HRMS** (ESI): Calcd. For $C_{27}H_{22}N_4F_3$: 459.1797; Found: 459.1814.

5 - {4 - [1,4 - diphenyl - 3 - (phenylamino) - 4,5 - dihydro - 1H-1,2,4 - triazol - 5 - yl]phenyl} - N,1,4 - triphenyl - 4,5 - dihydro - 1H - 1,2,4 - triazol - 3 - amine (72)

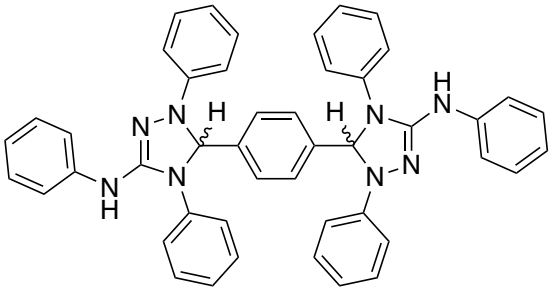

Amidrazone (**52**) (1.0 g, 3.31 mmol), terephthalaldehyde (0.22 g, 1.65 mmol) and 3 Å molecular sieves (~5) were placed in a microwave vial under argon. DCM (10 ml) and pyrrolidine (0.026 ml, 0.33 mmol) were added and the reaction was heated to 80 ºC by microwave for 2 h. Upon completion, DCM was reduced to half the volume *in vacuo* then MeOH added forming a white solid which was filtered to obtain the title compound

(0.8 g, 68%). **^{1}H NMR** (400 MHz, $CDCl_3$) δ 7.56-7.50 (8H, m, Ar-*H*), 7.40-7.19 (14H, m, Ar-*H*), 7.07-6.95 (10H, m, Ar-*H*), 6.86 (2H, t, Ar-*H*), 5.97 (2H, s, NC*H*(Ar)N), 5.57 (1H, br. s, N*H*), 5.54 (1H, br. s, N*H*); **^{13}C NMR** (151 MHz, $CDCl_3$) δ 148.1, 148.1, 146.0, 145.9, 141.3, 141.3, 139.4, 139.3, 138.2, 138.0, 130.0, 130.0, 129.0, 128.8, 128.8, 128.4, 128.4, 127.7, 127.7, 127.4, 127.2, 121.8, 119.3, 119.3, 117.4, 117.4, 113.8, 113.7, 86.7, 86.7; **MS** (ESI, *m/z*, %): 701.59 ($[M]^+$, 54%), 351.97 ($[M+2H]^{2+}$, 100 %); **HRMS** (ESI): Calcd. For $C_{46}H_{37}N_8$: 701.3141; Found: 701.3153.

5 - {3 - [1,4 - diphenyl - 3 - (phenylamino) - 4,5 - dihydro - 1H - 1,2,4 - triazol - 5 - yl]phenyl} - N,1,4 - triphenyl - 4,5 - dihydro - 1H - 1,2,4 - triazol - 3 - amine (75)

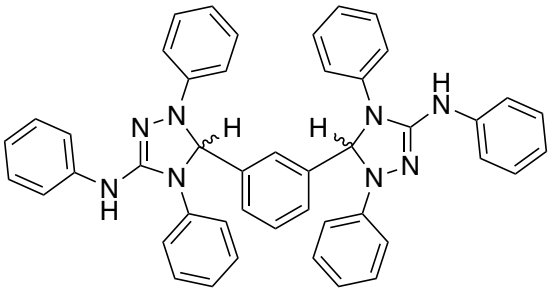

Amidrazone (**52**) (1.0 g, 3.31 mmol), isophthalaldehyde (0.22 g, 1.65 mmol) and 3 Å molecular sieves (~5) were placed in a microwave vial under argon. DCM (10 ml) and pyrrolidine (0.026 ml, 0.33 mmol) were added and the reaction was then heated to 80 ºC by microwave for 2 h. Upon completion, DCM was reduced to half the volume *in vacuo* then MeOH added forming a white solid which was filtered to obtain the title compound (0.44 g, 38%). **^{1}H NMR** (400 MHz, $CDCl_3$) δ 7.53-6.80 (34H, m, Ar-*H*), 5.96 (2H, s, NC*H*(Ar)N), 5.52 (1H, br. s, N*H*), 5.46 (1H, br. s, N*H*); **MS** (ESI, *m/z*, %): 701.55 ($[M]^+$, 56 %), 351.82 ($[M+2H]^{2+}$, 100); **HRMS** (ESI): Calcd. For $C_{46}H_{37}N_8$: 701.3141; Found: 701.3133.

1,4,5 - triphenyl - 3 - (phenylamino) - 4H - 1,2,4 - triazolium inner salt (77)

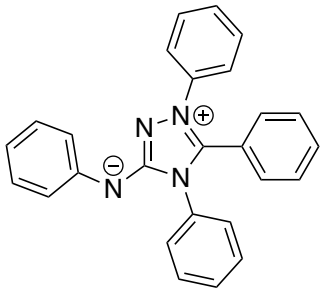

Amidrazone (**52**) (1.0 g, 3.31 mmol) and ammonium tetrafluoroborate (0.34 g, 3.31 mmol) were placed in a flask under argon. Trimethyl orthobenzoate (5 ml) was added and the reaction heated to 100 ºC overnight forming a white precipitate. The white precipitate of the tetrafluoroborate salt of the title compound was filtered (1.06 g, 63%). **^{1}H NMR** (400 MHz, $CDCl_3$) δ (1H, s, N*H*), 7.74-7.33 (19H, m, Ar-*H*), 7.10 (1H, t, Ar-*H*); Subsequent dissolution in DCM (20 ml), washing with sat. bicarbonate solution (3 x 10 ml) and water (1 x 10 ml), drying ($MgSO_4$) and concentration *in vacuo* gave a characteristic yellow solid of the title compound (0.7 g, 54 %). **^{1}H NMR** (400 MHz, $CDCl_3$) δ7.74-7.33 (19H, m, Ar-*H*), 7.10 (1H, t, Ar-*H*); **^{13}C NMR** (151 MHz, d_6-DMSO) δ 151.8, 148.3, 137.9, 135.5, 132.6, 131.8, 130.7, 130.4, 129.9, 129.5, 128.9, 128.8, 128.3, 125.5, 123.9, 119.9, 119.8; **MS** (ESI, *m/z*, %): 389.87 (100%, $[M+H]^+$); **HRMS** (ESI): Calcd. For $C_{26}H_{21}N_4$: 389.1766; Found: 389.1771.

1,4 - diphenyl - 3 - (phenylamino) - 5 - [4 - (trifluoromethyl)phenyl] - 4H - 1,2,4-triazolium inner salt (74)

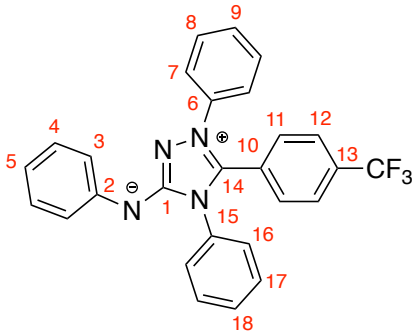

Triazole (**73**) (0.4 g, 0.87 mmol) was dissolved in acetic acid (3 ml) and cooled over ice. $NaNO_2$ (0.10 g, 1.48 mmol) in water (1 ml) was added dropwise forming a dark purple solution which slowly turns yellow. After stirring for an hour at RT, the reaction mixture was added dropwise to ammonium hydroxide solution (8 M), over ice forming an orange precipitate which was collected by filtration. This gave the desired product as an orange-yellow solid in a quantitative yield. **^{1}H NMR** (600 MHz, d_6-DMSO) δ 7.70 (2H, d, *H*-

11), 7.62 (2H, d, *H*-12), 7.52-7.34 (10H, m, *H*-16-18, *H*-7, -9), 7.24 (2H, d, *H*-3), 7.01 (2H, t, *H*-4), 6.54 (1H, t, *H*-5); **^{13}C NMR** (151 MHz, d_6-DMSO) δ 155.7, 143.0, 136.9, 134.0, 132.1, 131.4 (q), 130.0, 129.8, 129.4, 129.3, 129.2, 128.3, 127.4, 126.2, 126.0 (q), 124.8, 123.0, 122.5, 117.3; **HRMS** (ESI): Calcd. For $C_{27}H_{20}F_3N_4$: 457.1640; Found: 457.1644.

5 - {4 - [1,4 - diphenyl - 3 - (phenylamino) - 4H - 1,2,4 - triazol - 1 - ylium - 5 - yl]phenyl} - 1,4 - diphenyl - 3 - (phenylamino) - 4H - 1,2,4 - triazol - 1 - ylium (73)

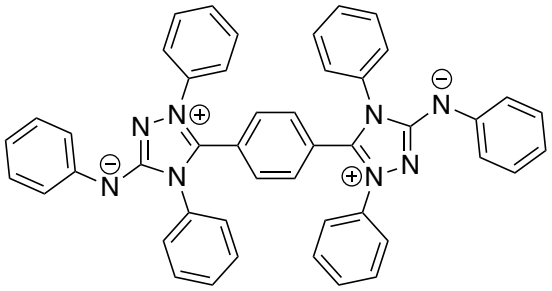

Di-triazole (**75**) (0.5 g, 0.71 mmol) was dissolved in minimal acetic acid before sodium nitrite (0.17 g, 2.42 mmol) in water (1 ml) was added dropwise at 0-5 °C. Upon complete addition, the reaction was stirred for 30 mins before added it dropwise to ice cold ammonium hydroxide solution (5 M, 200 ml) forming a bright red precipitate which was isolated by filtration to give an orange-red powder in a quantitative yield. **^{1}H NMR** (400 MHz, d_6-DMSO) δ 7.67-6.96 (34H, m, Ar-*H*); **^{13}C NMR** (151 MHz, d_4-MeOD) δ 151.8, 146.5, 138.5, 137.7, 134.9, 131.9, 131.3, 131.0, 130.5, 129.6, 129.4, 128.8, 128.1, 125.3, 124.4, 124.1, 119.9; **HRMS** (ESI): Calcd. For $C_{46}H_{35}N_8$: 699.2985; Found: 699.2984.

1,4-diphenyl-5-(4-(phenyl(1-phenyl-1,4-dihydrobenzo[e][1,2,4]triazin-3-yl) carbamoyl)phenyl)-3-(phenylamino)-4H-1,2,4-triazol-1-ium Radical (79)

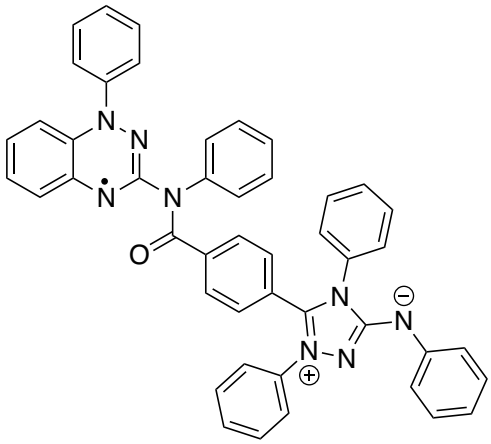

Di-Nitron **73** (0.1 g, 0.14 mmol) was dissolved in acetonitrile water, following General procedure 8, monitoring by LC-MS. No products were isolated however LC-MS evidence for this compound was observed. **HRMS** (ESI): Calcd. For $C_{46}H_{35}N_8O$: 715.2934; Found: 715.2929.

6.1.8. Ring-Opening: Nitron vs NitronMe

~ 6 mg (~20 mM) of substrate were dissolved in a solution of d-MeCN/D_2O (99:1) and a MeOD internal standard (20 mM) (1 ml). The reaction mixture was transferred to an NMR tube and monitored regularly over a 6-day period for radical formation through observing line broadening in ^{1}H NMR spectroscopy.

6.1.9. Exocyclic NH pK_a Determination

Nitron derivatives were dissolved in acetonitrile (10 mM) and added to a series of buffers (33 % v/v MeCN) from p*H* 0-13 (Table 6.1.1) to reach a concentration of 1 mM. UV-Vis spectra were recorded at each p*H* value, monitoring for changes in absorbance at various wavelengths. UV-Vis measurements were taken using a Cary 100 UV-Vis spectrophotometer, thermostated at 25 ^{o}C with matched 3 ml quartz cuvettes. Data manipulation as discussed in Chapter 2.3 allowed for estimation of exocyclic pK_a values.

Table 6.1.1. Summary of buffers used and p*H* ranges obtainable with a series of buffers used in the spectrophotometric determination of NH pK_a values for Nitron derivatives (**6**).

Buffer System	Concentration / M	p*K*a	Approximate p*H*-Range
HCl	0.01-0.5	N/A	0.3-2.0
Potassium Formate	0.1	3.75	2.8-4.8
Potassium Acetate	0.1	4.25	3.3-5.3
Triethanolamine Hydrochloride	0.1	7.76	6.8-8.8
Potassium Phosphate (monobasic/dibasic)	0.1	7.2	6.2-8.2
Potassium Carbonate	0.1	10.25	9.3-11.3
Triethylammonium Hydrochloride	0.1	10.75	9.8-11.8
Potassium Hydroxide	0.01-0.5	N/A	12-14

6.1.10. C(3)-H/D Exchange Experiments

~2 mg (~10 mM) of Nitron derivatives were dissolved in 0.33 ml of acetonitrile before H/D exchange was initiated by addition of 0.66 ml of 0.1 M DCl (Ionic strength = 0.3 M) with tetramethylammonium chloride internal standard. Mixing time was recorded and the sample placed in an NMR tube and spectra were taken regularly with the NMR tube thermostated at 25 °C over 24-48 h. NMR parameters are summarised in Table 6.1.2.

Table 6.1.2. NMR Spectrometer parameters used in the monitoring of H/D-exchange of Nitron derivatives (**6**).

Parameter	Value
Scans[a]	32 or 16
Relaxation Delay	20.000 s
Acquisition Time	4.000 s
Pulse Width	11.4000
Receiver Gain	40
Frequency	499.50 MHz
τ[b]	24 s

[a]For p*D* values at which H/D exchange was significantly faster, the number of scans was reduced to 16 to ensure that a maximum number of spectra were obtained during the first half-life of exchange. [b]The value for τ is the sum of the relaxation delay and the acquisition time.

6.1.11. Cyclic Voltammetry

A potentiostat (PalmSens EmStat3) interfaced with a computer was used for the electrochemical measurements. A three-electrode cell containing a Pt wire pseudo-reference electrode, a Pt counter electrode and a Pt working electrode were used.

Cyclic voltammetry measurements were carried out on amido and amino Blatter radicals as 1 mM quantities in Bu_4NPF_6 solutions (0.1 M) in degassed, dried acetonitrile. The electrolyte, Bu_4NPF_6, was dried before use and inert conditions were maintained during measurements. Decamethylferrocene (Cp^*_2Fe) and ferrocene (Cp_2Fe) were used as internal references for amido and amino radicals respectively. A scan rate of 50 mV s^{-1} was used for measurements. All potentials are quoted relative to the ferrocenium/ferrocene (Cp_2Fe^+/Cp_2Fe) couple. The decamethylferrocenium/ decamethylferrocene ($Cp^*_2Fe^+/Cp^*_2Fe$) couple has a half-cell potential of -0.50 V relative to the Cp_2Fe^+/Cp_2Fe couple in this setup.

6.1.12. EPR Measurements

EPR spectra were recorded on a Bruker EMX Micro spectrometer operating at X-band (9.5 GHz frequency), power 5 mW, modulation frequency 100 kHz, modulation amplitude 1 G. The spectra were recorded at room temperature using 0.1 mM solutions of radicals in degassed toluene.

6.2. Experimental – The Design, Synthesis and Evaluation of Non-Native Cofactors for Biocatalysis

6.2.1. Synthesis of Thiamine Mimics

3-Hydroxypropanehydrazide (122)

Iteration 1 Synthesis

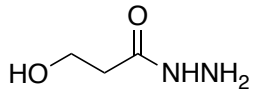

Hydrazine hydrate (2.0 ml, 4.0 mmol) was added dropwise to methyl 3-hydroxypropanoate (1.0 ml, 1.0 mmol) at RT and stirred for 2 h. The reaction material was concentrated *in vacuo* and the resultant gelatinous material triturated with hexane, filtered and dried thoroughly overnight yielding a white, crystalline solid in a quantitative yield (crude).

Iteration 2 Synthesis

Methyl 3-hydroxypropanoate (10 ml, 10 mmol) was dissolved in IPA and cooled over ice. Hydrazine hydrate (8 ml, 50% w/w aqueous solution) was added dropwise over 30 mins and the reaction stirred over ice for 1 h and at RT overnight. A white precipitate formed overnight and the flask was placed in a freezer (-18 °C) for 1 hour, before filtering under vacuum to yield the title compound (0.78 g, 75%). **^{1}H NMR** (400 MHz, D_2O) δ 3.71 (2H, t, J = 6.1 Hz, C*H*$_2$OH), 2.31 (2H, t, J = 6.1 Hz, C*H*$_2$CO).

1-[(4-amino-2-methylpyrimidin-5-yl)methyl]-3-(2-hydroxyethyl)-4-methyl-4,5-dihydro-1H-1,2,4-triazole-5-thione (123)

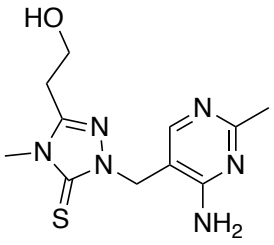

To degassed water (100 ml), hydrazide (**122)** (2.00 g, 19.2 mmol), thiamine hydrochloride (2.00 g, 6.0 mmol) and sodium sulphite (0.076 g, 0.6 mmol) were charged and heated to 50 ºC with stirring overnight, under argon. Upon completion reaction was lyophilised to give a white solid which was taken up in absolute ethanol (135 ml). Methyl isothiocyanate (2.60 g, 36 mmol) was added and the reaction was refluxed for 1 day. with

The initial precipitate dissolved forming a clear solution before the product precipitated as a white solid. Upon cooling, this compound was isolated as a white precipitate by filtration and continued to the next step with no further purification.

The isolated white solid (1.63 g, 5.46 mmol), was dissolved in 0.01 M KOH (120 ml) and refluxed overnight. Upon cooling, further treatment of the solution of p*H* ~ 8 led to precipitation of a fluffy white solid of the thione (1.53 g, 91%). **^{1}H NMR** (600 MHz, DMSO-d_6) δ 7.93 (1H, s, Ar-*H*), 6.83 (2H, br. s, NH_2), 5.11(2H, s, -CH_2-), 4.91 (1H, t, J = 5.6 Hz, O*H*), 3.68 (2H, dt, J = 5.6, 6.3, CH_2OH), 3.50 (3H, s, N_4-CH_3), 2.85 (2H, t, J = 6.3, C_5-CH_2), 2.30 (3H, s, Ar-CH_3); **^{13}C NMR** (150 MHz, DMSO-d_6) δ 167.0 (CH_3-C_{Ar}), 166.1 (*C*S), 161.8 (*C*-NH_2), 156.2 (C_{Ar}-H), 151.5 (C_5), 108.4 (C_{Ar}-CH_2), 58.6 (*C*H_2-OH), 46.3 (-*C*H_2-), 31.9 (N_4-*C*H_3), 29.0 (C_5-*C*H_2), 25.6 (Ar-*C*H_3); **MS** (ESI, *m/z*, %): 281.32 ([M+H]$^+$, 100 %); **HRMS** (ESI): Calcd. For $C_{11}H_{17}N_6OS$: 281.1185; Found: 281.1194.

1-[(4-amino-2-methylpyrimidin-5-yl)methyl]-3-(2-hydroxyethyl)-4-methyl-4H-1,2,4-triazol-1-ium tetrafluoroborate (26)

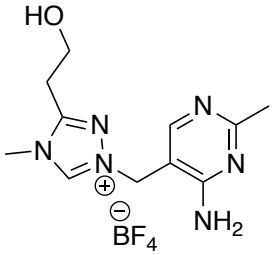

To thione (**123**) (0.725g, 2.59 mmol), in water (22 ml), 50 % w/w tetrafluoroboric acid (0.36 ml, 2.9 mmol) was added slowly at 0 ºC and the slurry dissolved. Hydrogen peroxide solution (3.7 ml, 36 mmol) was added dropwise and the reaction stirred at 0 ºC for 2 h. The reaction mixture was then lyophilized overnight to yield the desired triazolium as a hygroscopic, white precipitate in a quantitative yield. **^{1}H NMR** (600 MHz, D_2O) δ 8.16 (1H, s, Ar-*H*), 5.45 (1H, s, -CH_2-), 3.87 (2H, t, J = 6.1, CH_2OH), 3.78 (3H, s, N_4-CH_3), 3.03 (2H, t, J = 6.1 Hz, C_5-CH_2), 2.45 (3H, s, Ar-CH_3); **^{13}C NMR** (150 MHz, D_2O) δ 164.0 (CH_3*C*), 163.2 (*C*NH_2), 155.8 (C_5), 147.3 (C_{Ar}-H), 143.6, 143.4, 143.1 (C_3), 106.8 (C_{Ar}-CH_2), 57.7 (*C*H_2OH), 48.1 (-*C*H_2-), 33.0 (N_4-*C*H_3) 26.8 (C_5-*C*H_2), 21.4 (Ar-*C*H_3); **MS** (ESI, *m/z*, %): 249.38 ([M]$^+$, 100 %). **HRMS** (ESI): Calcd. For $C_{11}H_{17}N_6O$: 249.1469, Found: 249.1464.

6.2.2. N-Phenyl Mimics

General Procedure 11: The Synthesis of Aryl Hydrazides

Ester (1 mol. eq.) and aryl hydrazine (1 mol. eq.) were added to a sealed microwave vial under inert atmosphere and refluxed at 100 °C in anhydrous triethylamine (2.5 mmol ml^{-1}) for 1-3 days. The solution was concentrated *in vacuo* giving a red-orange solid. Recrystallisation in DCM or chloroform yielded the desired hydrazides as colourless, crystalline solids.

3-Hydroxypropanephenylhydrazide (124a)

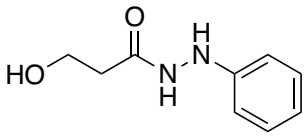

Following General Procedure 11, methyl 3-hydroxypropanoate (2 ml, 20.9 mmol) and phenyl hydrazine (2.5 ml, 20.9 mmol) were reacted giving a crystalline solid (1.25 g, 33%). **^{1}H NMR** (600 MHz, $CDCl_3$) δ 7.17 (2H, dd, J = 7.4, 8.5, *H*-3), 6.82 (2H, dd, J = 8.5, 1.0, *H*-2), 6.79 (1H, tt, J = 7.4, 1.0 Hz, *H*-4); **^{13}C NMR** (150 MHz, $CDCl_3$) δ 172.7 (*C*O), 148.4 (*C*-1), 128.5 (*C*-3), 119.6 (*C*-2), 112.7 (*C*-4), 57.7 (CH_2OH), 36.9 (CH_2CO); **MS** (ESI, *m/z*, %): 181.15 ($[M+H]^+$, 100 %), 182.19 ($[M+2H]^+$, 14.5); **HRMS** (ESI): Calcd. For $C_9H_{13}N_2O_2$: 181.0977; Found: 181.0987.

4-Hydroxybutanephenylhydrazide (124b)

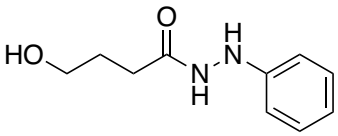

Following General Procedure 11, γ-butyrolactone (2 ml, 26.0 mmol) and phenyl hydrazine (2.6 ml, 26.0 mmol) were reacted giving a crystalline solid (1.96 g, 40 %). **^{1}H NMR** (600 MHz, DMSO-d_6) δ 9.58 (1H, d, J = 2.9 Hz, CON*H*), 7.64 (1H, d, J = 2.8 Hz, N*H*-Ar), 7.12 (2H, dd, *H*-3), 6.68 (3H, m, *H*-2, *H*-4), 4.49 (1H, t, O*H*), 3.41 (2H, m, CH_2OH), 2.20 (2H, t, CH_2CO), 1.69 (2H, m, CH_2), **^{13}C NMR** (150 MHz, $CDCl_3$) δ 172.5 (*C*O), 149.9 (*C*-1), 129.1 (*C*-3), 118.9 (*C*-4), 112.5 (*C*-2), 60.6 (CH_2OH), 30.6 (CH_2CO), 29.0 (CH_2); **MS** (ESI, *m/z*, %): 194.31 ($[M+H]^+$, 100 %), 196.30 ($[M+2H]^+$, 10.8); **HRMS** (ESI): Calcd. For $C_{10}H_{15}N_2O_2$: 195.1134; Found: 195.1142.

General Procedure 12: The synthesis of N-aryl Thiones

Aryl hydrazide (1 mol eq.) and methyl isothiocyanate (6 mol eq.) were refluxed in ethanol for 5 days. Upon completion the reaction was concentrated *in vacuo* giving a yellow oil. Subsequent purification by column chromatography in DCM/MeOH (97:3) yielded the desired thiones as white solids.

1-Phenyl-3-(2-hydroxyethyl)-4-methyl-4,5-dihydro-1H-1,2,4-triazole-5-thione (127a)

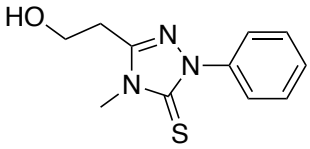

Following General Procedure 12, the title compound could be isolated as a clear oil which slowly precipitated to a white solid (65%); **^{1}H NMR** (600 MHz, $CDCl_3$) δ 7.96 (2H, d, J = 7.4 Hz, *Ar*-2), 7.46 (2H, t, J = 7.4 Hz, *Ar*-3), 7.37 (1H, tt, J = 7.4 Hz, *Ar*-4), 4.06 (2H, t, J = 5.8 Hz, CH_2O), 3.60 (3H, s, CH_3), 2.92, (2H, t, J = 5.8 Hz, C_5CH_2); **^{13}C NMR** (150 MHz, $CDCl_3$) δ 166.8 (*CS*), 150.2 (C_5), 138.2 (*Ar*-1), 128.9 (*Ar*-3), 128.2 (*Ar*-4), 124.1 (*Ar*-2), 59.0 (*C*H_2O), 31.5 (*C*H_3), 28.9 (C_5CH_2); **MS** (ESI, *m/z*, %): 236.36 ($[M+H]^+$, 100 %), 237.27 ($[M+2H]^+$, 15.7); **HRMS** (ESI): Calcd. For $C_{11}H_{14}N_3OS$: 236.0858; Found: 236.0868.

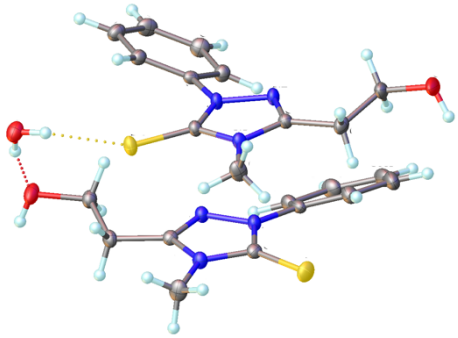

1-Phenyl-3-(3-hydroxypropyl)-4-methyl-4,5-dihydro-1H-1,2,4-triazole-5-thione (127b)

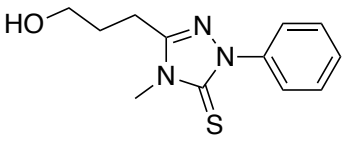

Following General Procedure 11, the title compound could be isolated as a white solid (1.82 g, 72%); **^{1}H NMR** (600 MHz, $CDCl_3$) δ 7.96 (2H, d, J = 7.7 Hz, *Ar*-2), 7.46 (2H, t, J = 7.7 Hz, *Ar*-3), 7.35 (1H, tt, J = 7.5 Hz, *Ar*-4), 3.77 (2H, t, J = 5.8 Hz, CH_2OH), 3.61

(3H, s, C*H*$_3$), 2.84 (2H, d, J = 7.4 Hz, C$_5$C*H*$_2$), 2.04 (2H, tt, J = 5.8, 7.4 Hz, C*H*$_2$); **^{13}C NMR** (150 MHz, CDCl$_3$) δ 166.7 (*C*S), 151.4 (*C*$_5$), 138.2 (*Ar*-1), 128.7 (*Ar*-3), 128.0 (*Ar*-4), 124.0 (*Ar*-2), 61.2 (*C*H$_2$OH), 28.4 (*C*H$_2$), 22.1 (C$_5$*C*H$_2$); **MS** (ESI, *m/z*, %): 250.27 ([M+H]$^+$, 100 %), 272.31 ([M+Na]$^+$, 28.4); **HRMS** (ESI): Calcd. For $C_{12}H_{15}N_3OS$: 250.1014; Found: 250.1026.

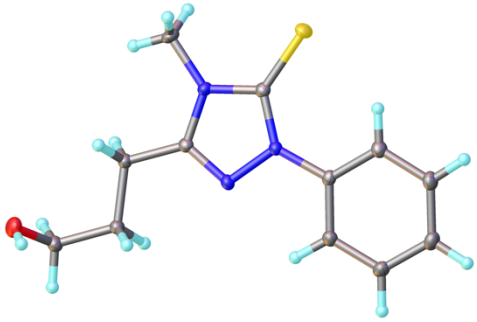

General procedure for the oxidation of thiones to 1,2,4-triazoliums

Thione (1 mol. eq.) was added to water (10 ml mmol^{-1}) and tetrafluoroboric acid added dropwise until complete dissolution. Following this, 30 wt % hydrogen peroxide (5 mol. eq.) was added dropwise over ice and the reaction stirred for 4 h. The reaction was neutralised and lyophilised giving a white solid of the desired product in a quantitative yield, with residual sodium tetrafluoroborate present.

3-(2-hydroxyethyl)-4-methyl-1-phenyl-4H-1,2,4-triazol-1-ium Tetrafluoroborate (27a)

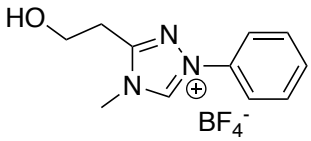

Following General Procedure 11, the title compound could be isolated as a white solid in a quantitative yield. **^{1}H NMR** (400 MHz, MeOH-d$_4$) δ 7.94-7.86 (2H, m, Ar-*H*), 7.70-7.59 (3H, m, Ar-*H*), 4.07 (2H, t, J = 6.2 Hz, C*H*$_2$O), 4.04 (3H, s, NC*H*$_3$), 3.24 (2H t, J = 6.2 Hz, C$_5$C*H*$_2$); **^{13}C NMR** (150 MHz, D$_2$O) δ 155.6, 134.7, 130.9 130.2, 121.1, 57.8, 33.1, 26.8; **MS** (ESI, *m/z*, %): 204.24 ([M]$^+$, 100 %), 205.27 ([M+H]$^+$, 33.5); **HRMS** (ESI): Calcd. For $C_{11}H_{14}N_3O$: 204.1137; Found: 204.1150.

3-(3-hydroxypropyl)-4-methyl-1-phenyl-4H-1,2,4-triazol-1-ium Tetrafluoroborate (27b)

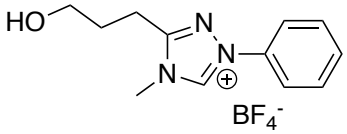

Following General Procedure 11, the title compound could be isolated as a white solid in a quantitative yield. **^{1}H NMR** (600 MHz, DMSO-d_6) δ 10.70 (1H, s, C_3-*H*), 7.85 (2H, d, Ar_2-*H*), 7.68 (2H, t, Ar_3-*H*), 7.60 (1H, t, Ar_4-*H*); 4.67 (1H, t, O*H*), 3.89 (3H, s, CH_3), 3.54 (2H, q, CH_2O), 3.00 (2H, t, C_5CH_2), 1.93 (2H, quint., -CH_2-); **^{13}C NMR** (150 MHz, $CDCl_3$) δ 157.8 (*C*$_5$), 142.6 (*C*$_3$), 130.8 (Ar_4-*C*), 130.7 (Ar_3-*C*), 120.8 (Ar_2-*C*), 59.8 (*C*H$_3$), 33.5 (*C*H$_2$O), 29.0 (C_5*C*H$_2$), 20.8 (-*C*H$_2$-); **MS** (ESI, *m/z*, %): 218.34 ([M]$^+$, 100%); **HRMS** (ESI): Calcd. For $C_{12}H_{16}N_3O$: 218.1293; Found: 218.1307.

6.2.3. Phosphorylation Reactions

Method A (Polyphosphoric acid)

1-[(4-amino-2-methylpyrimidin-5-yl)methyl]-3-(2-hydroxyethyl)-4-methyl-4H-1,2,4-triazol-1-ium pyrophosphate (26{PP})

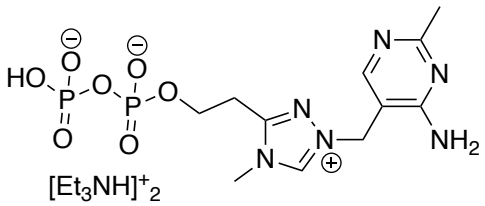

Substate (1 mol eq.) and polyphosphoric acid (100 mol. eq.) were heated at 100 ºC for 10-15 mins until the gum turned from a white to yellow colour. The mixture was cooled and triturated with ethanol before filtering. The solid was taken up in an ethanol-water mix (5:1) and stored at -18 ºC overnight before filtering to obtain a grey, sticky solid. Purification was carried out by ion exchange chromatography with a stepwise gradient with triethylammonium carbonate buffers (1mM to 0.5 M, p*H* 8). The title compound was isolated in poor yields (<20 mg, <10%) **^{1}H NMR** (600 MHz, D_2O) δ (1H, s, Ar-*H*), 5.44 (2H, s, -CH_2-), 4.16 (2H, app. q, CH_2O), 3.81 (3H, s, N_4CH_3), 3.16 (2H, t, C_5CH_2), 2.45 (3H, s, Ar-CH_3); **^{31}P NMR** (162 MHz, D_2O) δ-10.86 (d), -11.57 (d).

Method B-1 (Sequential Phosphate Addition to azolium ions)

Thiamine Monophosphate (5{P})

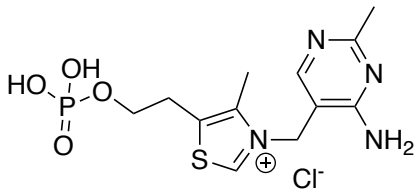

Thiamine chloride (**5**) (0.1 g, 0.26 mmol) was stirred in phosphorus(V) oxychloride (1 ml, 10.7 mmol) for 6 h at room temperature. Upon completion, dry ether was added and the reaction filtered and further washed with dry ether. The isolated solid was quenched with 1 M triethylamine carbonate buffer (pH ~ 7.5) before lyophilising. Crude material was purified by weak anion exchange chromatography with TEAB buffer (0-2 M, p*H* 8). **^{1}H NMR** (400 MHz, D_2O (p*D* < 1)) δ 9.38 (1H, s, C_2-*H*), 7.67 (1H, s, Ar-*H*), 5.24 (2H, s, -CH_2-), 3.90 (2H, q, O-CH_2), 3.03 (2H, t, C_4-CH_2), 2.29 (3H, s, C_5-CH_3), 2.22 (3H, s, Ar-CH_3); **^{31}P NMR** (162 MHz, D_2O) δ - 0.96.

Thiamine Pyrophosphate (5{PP})

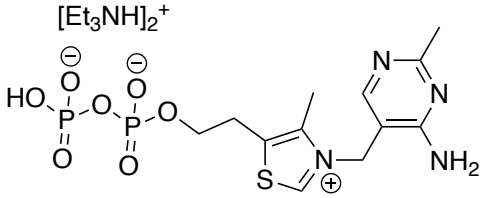

Thiamine monophosphate triethylammonium (0.1 g, 0.183 mmol) was added to DMSO (5 ml) and phosphoramidite (0.11 g, 0.220 mmol) and stirred at room temperature. 5-(Ethylthio)-1*H*- tetrazole (0.029 g, 0.220 mmol) was added and the reaction was stirred at RT for 10 mins, monitoring by ^{31}P NMR spectroscopy. Upon complete consumption of the phosphoramidite, tert-butyl hydroperoxide (0.17 ml, 0.915 mmol) was added carefully, dropwise and then stirred for 5 mins before the addition of 5 % v/v piperidine. Upon complete deprotection of the fluorenyl groups, DCM (0.5 ml) was added followed by diethyl ether (15 ml) and the reaction placed in the fridge overnight. The organic phase was subsequently decanted leaving the crude product as an orange oil. **^{1}H NMR** (400 MHz, D_2O) δ9.40 (1H, s, Ar-*H*), 5.44 (2H, s, -CH_2-), 4.16 (2H, app. q, CH_2O), 3.81 (3H, s, N_4CH_3), 3.16 (2H, t, C_5CH_2), 2.45 (3H, s, Ar-CH_3); **^{31}P NMR** (162 MHz, D_2O) δ - 10.86 (d), -11.57 (d).

Mimic Monophosphate (26{P})

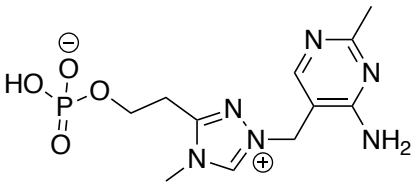

1,2,4-triazolium mimic (**26**) (0.4 g, 1.2 mmol) was stirred in phosphorus(V) oxychloride (5 ml, 53.5 mmol) for 6 h at room temperature. Upon completion, dry ether was added and the reaction filtered and further washed with dry ether. The isolated solid was quenched with 1 M triethylamine carbonate buffer (pH ~ 7.5) before lyophilising. Crude material was purified by weak anion exchange chromatography with TEAB buffer (0-2 M, p*H* 8). **^{1}H NMR** (400 MHz, D_2O) δ 8.28 (1H, s, Ar-*H*), 5.57 (2H, s, -CH_2-), 4.15 (2H, q, O-CH_2), 3.97 (3H, s, N-CH_3), 3.29 (2H, t, C_5-CH_2), 2.52 (3H, s, Ar-CH_3); **^{31}P NMR** (162 MHz, D_2O) δ 3.31.

Method B-2 (Sequential Phosphate Addition to Thione

2-(1-((4-amino-2-methylpyrimidin-5-yl)methyl)-4-methyl-5-thioxo-4,5-dihydro-1H-1,2,4-triazol-3-yl)ethyl phosphate triethylammonium salt (123({P})

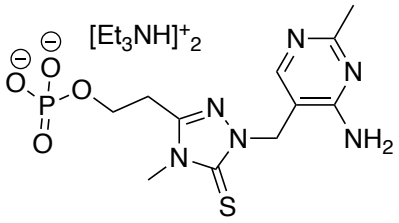

1-[(4-amino-2-methylpyrimidin-5-yl)methyl]-3-(2-hydroxyethyl)-4-methyl-4,5-dihydro-1H-1,2,4-triazole-5-thione (**123**) (1.0 g, 3.6 mmol) was stirred in acetonitrile (25 ml) and water (64 µl, 3.57 mmol) over ice. Phosphorus oxychloride (1.7 ml, 17.9 mmol) was added dropwise over 5 mins and the reaction stirred overnight before concentrating *in vacuo*. Triethylammonium bicarbonate buffer (2 M, p*H* 8) was added dropwise over ice until neutralised and then the solution lyophilised and redissolved in water (50 ml). Sodium iodide (1M) was added dropwise until a white precipitate formed and the sample placed over ice for 2 h and centrifuged to isolate. The white solid was dissolved in water and purified by weak anion exchange chromatography using a gradient from 0-100 % 2 M triethylammonium acetate buffer at p*H* 7, before lyophilising the eluent 3-4 times to remove residual acetic acid and giving the product as a white solid (0.2 g, 10%). **^{1}H NMR** (600 MHz, D_2O) δ 7.95 (1H, s, Ar-*H*), 5.14 (2H, s, -CH_2-), 3.99 (2H, q, O-CH_2), 3.45 (3H, s, N-CH_3), 2.96 (2H, t, C_5-CH_2), 2.35 (3H, s, Ar-CH_3); **^{13}C NMR** (150 MHz,

D_2O) δ 165.1 (CS), 164.4 (C_{Ar}-CH_3), 162.6 (C_{Ar}-NH_2), 151.9 (C_5-CH_2), 148.5 (C_{Ar}-H), 109.0 (C_{Ar}-CH_2), 61.5 (O-CH_2), 45.9 (-CH_2-), 31.7 (N-CH_3), 26.5 (C_5-CH_2), 22.0 (C_{Ar}-CH_3); **^{31}P NMR** (276 MHz, D_2O) δ 0.84 (t); **MS** (ESI, *m/z*, %): 361.27 ([M+H]$^+$, 100 %), 362.30 ([M+2H]$^+$, 14.1); **HRMS** (ESI): Calcd. For $C_{11}H_{18}N_6O_4PS$: 361.0848; Found: 361.0854.

2-(1-((4-amino-2-methylpyrimidin-5-yl)methyl)-4-methyl-5-thioxo-4,5-dihydro-1H-1,2,4-triazol-3-yl)ethyl diphosphate (123{PP})

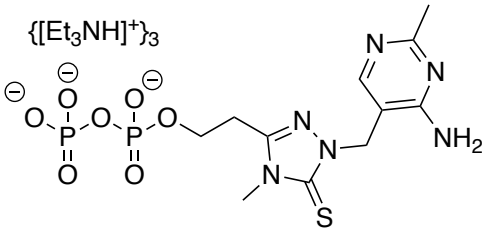

2-(1-((4-amino-2-methylpyrimidin-5-yl)methyl)-4-methyl-5-thioxo-4,5-dihydro-1H-1,2,4-triazol-3-yl)ethyl phosphate triethylammonium salt (**123{P}**) (0.219 g, 0.389 mmol), was stirred in DMF (25 ml) with bis((9H-fluoren-9-yl)methyl) diisopropyl-phosphoramidite (0.384 g, 0.778 mmol) and 5-(ethylthio)-1H-tetrazole (0.101 g, 0.778 mmol) for 30 mins. Upon complete consumption of the monophosphate peak by ^{31}P NMR spectroscopy t-butyl hydroperoxide (1.4 ml, 7.78 mmol) was added dropwise and the reaction stirred for 5 mins before added piperidine (1.25 ml) and stirring for a further 20 mins. Finally, diethyl ether was added until a sticky white solid formed and the liquid phase was pipetted off. Subsequent purification was carried out by weak anion exchange chromatography with a 0-100 % gradient of triethylammonium acetate buffer (2 M, p*H* 5) yielding a white solid (0.35 g, 95%). **^{1}H NMR** (600 MHz, D_2O) δ 7.97 (1H, s, Ar-H), 5.10 (2H, s, Ar-CH_2), 4.09 (2H, q, O-CH_2), 3.46 (N-CH_3), 3.00 (2H, t, CH_2-C_5), 2.27 (3H, s, Ar-CH_3); **^{13}C NMR** (150 MHz, D_2O) δ 167.1 (C_{Ar}-CH_3), 164.2 (C=S), 161.9 (C_{Ar}-NH_2), 154.6 (C_{Ar}-H), 151.0 (C_5) 108.41 (CH_2-C_{Ar}), 46.5 (Ar-CH_2), 61.8 (O-CH_2), 31.7 (N-CH_3), 26.3 (CH_2-C_5), 23.0 (Ar-CH_3); **^{31}P NMR** (162 MHz, D_2O) δ -7.74 (d), -11.14 (dt); **HRMS** (ESI): Calcd. For $C_{11}H_{19}N_6O_7P_2S$: 441.0511; Found: 441.0512.

1-((4-amino-2-methylpyrimidin-5-yl)methyl)-3-(2-((hydroxy(phosphonooxy) phosphoryl)oxy)ethyl)-4-methyl-4H-1,2,4-triazol-1-ium (26{PP})

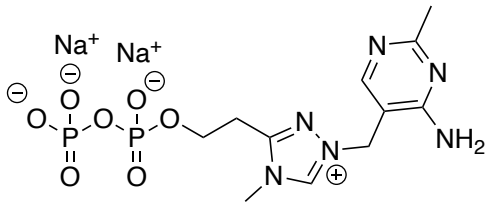

2-(1-((4-amino-2-methylpyrimidin-5-yl)methyl)-4-methyl-5-thioxo-4,5-dihydro-1H-1,2,4-triazol-3-yl)ethyl diphosphate (**123{PP}**) (0.3 g,0.4 mmol) was dissolved in water (5 ml), 30 wt. % hydrogen peroxide added (37 µl, 2.0 mmol) and stirred overnight at RT. Upon complete conversion, sodium thiosulphate (0.24 g) was added to ensure a complete quench of hydrogen peroxide. Once fully quenched, sodium iodide in acetone (1 M) was added until a white precipitate formed. The white solid was isolated by centrifugation in a quantitative yield. **^{1}H NMR** (600 MHz, D_2O) δ 8.10 (1H, s, Ar-*H*), 5.36 (2H, s, Ar-CH_2), 4.18 (2H, q, O-CH_2), 3.81 (3H, s, N-CH_3), 3.18 (2H, t, CH_2CH_2), 2.33 (Ar-CH_3); **^{13}C NMR** (150 MHz, D_2O) δ 168.8 (C_{Ar}-CH_3), 162.1 (C_{Ar}-NH_2), 157.2 (C_{Ar}-CH), 155.6 (C_5), 142.2 (C_3), 105.6 (CH_2-C_{Ar}), 62.0 (O-CH_2), 49.5 (-CH_2-Ar), 33.3 (N-CH_3), 25.4 (C_5-CH_2), 24.0 (Ar-CH_3); **^{31}P NMR** (276 MHz, D_2O) δ -6.05 (d), -10.84 (dt). **MS** (ESI, *m/z*, %): 409.48 (32%, M^+), 431.41 (100, $[M+Na]^+$); **HRMS** (ESI): Calcd. For $C_{11}H_{19}N_6O_7P_2$: 409. 0790; Found: 409.0787.

6.2.4. TPP Hydrolysis Studies

~ 6 mg (13 mM) of thiamine pyrophosphate (**5{PP}**) were dissolved in 1 ml of 0.2 M buffered D_2O with methylene diphosphonate internal standard (7.5 mM). The time of mixing was recorded and the solution transferred to an NMR tube and monitored regularly for up to 2 months by ^{31}P NMR spectroscopy. Spectrometer parameters are summarised in Table 6.2.1.

Table 6.2.1. Spectrometer parameters used for ^{31}P NMR spectroscopic monitoring of the hydrolysis of thiamine pyrophosphate (**5{PP}**).

Parameter	Value
Scans	128
Relaxation Delay	2 s
Acquisition Time	0.6685 s
Pulse Width	13.000
Receiver Gain	207.8
Frequency	161.95 MHz
τ^a	2.6685 s

[a]The value for τ is the sum of the relaxation delay and the acquisition time.

6.2.5. H/D Exchange Experiments

~ 6 mg (7.5 mM) of substrate were dissolved in a 0.1 M D_2O buffer (2 ml) (10-90 % formate/acetate) with 2 mM TMACl as internal standard, recording the mixing time and final p*H* of the solution. The solutions were transferred to NMR tubes and placed in a pre-shimmed NMR instrument and monitored regularly for 12-48 h with the parameters described in Table 6.2.2.

Table 6.2.2. Spectrometer parameters used for ^{1}H NMR spectroscopic monitoring of the H/D exchange of substrates in Chapter 3.4.

Parameter	Value
Scans[a]	32 or 16
Relaxation Delay	20.000 s
Acquisition Time	4.000 s
Pulse Width	11.4000
Receiver Gain	40
Frequency	499.50 MHz
τ[b]	24 s

[a]For p*D* values at which H/D exchange was significantly faster, the number of scans was reduced to 16 to ensure that a maximum number of spectra were obtained during the first half-life of exchange. [b]The value for τ is the sum of the relaxation delay and the acquisition time.

6.2.6. Model Benzoin Reactions

To a buffered methanol-d_4 solution (0.107 M : 0.053 M, Et_3N : Et_3NHCl), with 40 mM ethanol- OD as internal standard, catalyst (~40 mM was dissolved). Reaction was initiated by addition to aldehyde (~40 mM), recording the time of mixing, before transferring to an NMR tube and monitoring for 24-48 h with the parameters described in Table 6.2.3.

Table 6.2.3. Spectrometer parameters used for ^{1}H NMR spectroscopic monitoring of hydroxyaryl adduct formation reactions as model Benzoin condensations.

Parameter	Value
Scans	32
Relaxation Delay	5.000 s
Acquisition Time	2.000 s
Pulse Width	5.7000
Receiver Gain	30
Frequency	499.49 MHz
τ[a]	7 s

[a]The value for τ is the sum of the relaxation delay and the acquisition time.

6.2.7. Enzyme Assays – Coupled Assays via UV-Vis Spectroscopy

Pyruvate Decarboxylase

Following the procedure of Showen et al.[228] pyruvate decarboxylation activity was monitored by the coupled alcohol dehydrogenase catalysed, acetaldehyde reduction by NADH. Reduction of NADH was monitored by UV-vis spectroscopy with a Cary 100 spectrophotometer at 360 nm (ε = 3670 M^{-1} cm^{-1}; this wavelength reduced the contribution to the absorbance of sodium pyruvate compared to 240 nm). Reaction was initiated by addition of sodium pyruvate (0.25 mM-30 mM) to a solution of cofactor (TPP or cofactor mimic; 5 mM), NADH (0.25 mM), $MgCl_2$ (5 mM), alcohol dehydrogenase (10 units/ml) and pyruvate decarboxylase (0.5 units/ml) in MES buffer (50 mM, pH 6.5) all thermostated to 30 °C.

Pyruvate Oxidase[249]

Pyruvate oxidase activity was measured following the procedure of Cornacchione and Hu, by the coupled formation of a quinoneimine dye catalysed by horseradish peroxidase.[249] Quninoneimine dye formation was monitored by UV-vis spectroscopy with a Cary 100 Spectrophotometer at 550 nm. Reaction was initiated by the addition of sodium pyruvate (0.1-20 mM) to a solution of $MgCl_2$ (10 mM), FAD (0.01 mM), TPP (0.2 mM), N-ethyl-N-(2-hydroxy-3-sulfopro- pyl)-*m*-toluidine (0.6 mM), 4-aminoantipyrine (0.5 mM), horseradish peroxidase (5 u ml^{-1}), and pyruvate oxidase (0.5 u ml^{-1}) in phosphate buffer (50 mM, p*H* 6.5). Reactions were carried out in 1 ml or 100 µl cuvettes, thermostated at 37 °C before initiation.

6.2.8. Enzyme Assays – Reaction monitoring with NMR Spectroscopy

A solution of ^{13}C-labelled pyruvate (60 mM), 4-fluorobenzaldehyde (100 mM), magnesium chloride (2.5 mM) and cofactor (**5{PP}**/**26{PP}**) (0.2-10 mM) in D_2O-potassium phosphate buffer (50 mM, p*D* 6.5) with 30% v/v deuterated DMSO was prepared. At a time recorded as t_{mix}, 5 units ml^{-1} of enzyme (0.8 mg of enzyme for *Sc*PDC purchased from Sigma Aldrich) was added and the solution transferred to an NMR tube. The reaction was monitored by ^{13}C NMR spectroscopy using a spectrometer with a

cryoprobe to increase the sensitivity with respect to ^{13}C NMR and increase the speed of data collection. NMR spectra were obtained ~every hour for 8-12 h and a final spectrum at ~24 h after t_{mix}. NMR spectrometer parameters are summarised in Table 6.2.4.

Table 6.2.4. Spectrometer parameters used for ^{13}C NMR spectroscopic monitoring of reaction of ^{13}C-labelled pyruvate with 4-fluorobenzaldehyde to form a phenylacetyl carbinol.

Parameter	Value
Scans	128
Relaxation Delay	2.0 s
Acquisition Time	1.376 s
Pulse Width	10.000
Receiver Gain	5.2
Frequency	100.62 MHz
τ^a	3.376 s

[a]The value for τ is the sum of the relaxation delay and the acquisition time.

6.3. Experimental – New 1,2,4-Triazolium Scaffolds for Organocatalysis: Initial Studies

6.3.1. Catalyst Syntheses

1-(4-cyanophenyl)-3-(methyl(phenyl)amino)-4-phenyl-4H-1,2,4-triazol-1-ium Tetrafluoroborate (60i)

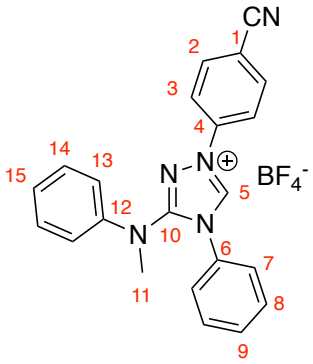

Following General Procedure 10, the title compound could be isolated as a white solid (0.13 g, 13%). **^{1}H NMR** (600 MHz, DMSO-d_6) δ 11.04 (1H, s, *H*-5), 8.24 (2H, dt, *H*-3), 8.20 (2H, dt, *H*-2), 7.45-7.42 (2H, m, *H*-8), 7.35-7.33 (3H, m, *H*-9, -7), 7.11-7.06 (4H, m, *H*-13, -14), 6.97-6.92 (1H, m, *H*-15), 3.50 (3H, s, *H*-11); **^{13}C NMR** (150 MHz, D_2O) δ 154.1, 143.0, 142.9, 138.4, 135.1, 132.0, 131.0, 129.8, 129.6, 126.0, 125.8, 123.5, 121.0, 118.2, 113.1, 42.3; **MS** (ESI, *m/z*, %): 352.78 (100%, M^+); **HRMS** (ESI): Calcd. For $C_{22}H_{18}N_5$: 352.1562; Found: 352.1517.

3-hydroxy-*N*'-(pentafluorophenyl)propanehydrazide (124c/124d)

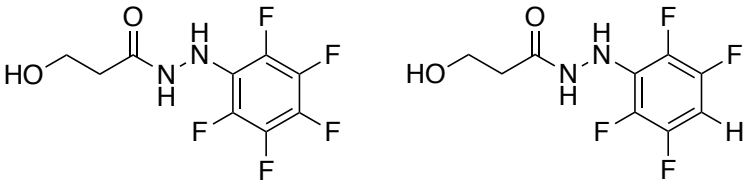

Following the General Procedure 11, methyl 3-hydroxypropanoate (2 ml, 20.9 mmol) and pentafluorophenylhydrazine (4.1 g, 20.9 mmol) were reacted to give a crude white solid (0.82 g) which was an inseparable mixture of **124c** and **124d**.

124c: ^{1}H NMR (400 MHz, DMSO) δ 10.01 (1H, d, ^{3}J = 3.5 Hz, N*H*), 8.06 (1H, s, NH), 3.62–3.56 (2H, m, CH_2-O), 2.25 (2H, q, CH_2-CO); **^{19}F NMR** (376 MHz, DMSO) δ -157.4 – -157.5 (m), -165.1 – -165.3 (m), -170.4 (tt); **MS** (ESI, *m/z*, %): 271.20 ($[M + H]^+$, 100 %), 272.23 ($[M + 2H]^+$, 9.67), 293.21 ($[M + Na]^+$, 50.8); **HRMS** (ESI): Calcd. For $C_9H_8F_5N_2O_2$ 271.0506; Found 271.0495.

124d: **^{1}H NMR** (400 MHz, DMSO) δ 10.01 (1H, d, ^{3}J = 3.5 Hz, N*H*), 7.93 (1H, s, N*H*), 7.16 (tt, Ar-*H*), 3.62–3.56 (2H, m, CH_2-O), 2.25 (2H, q, CH_2-CO); **^{19}F NMR** (376 MHz, DMSO) δ -141.6 – -141.8 (m), -157.9 – -158.1 (m); **MS** (ESI, *m/z*, %): 253.23 ([M + H]$^+$, 100 %), 254.22 ([M + 2H]$^+$, 8.98), 275.20 ([M + Na]$^+$, 39.5); **HRMS** (ESI): Calcd. For $C_9H_9F_4N_2O_2$ 253.0600; Found 253.0611.

6.3.2. Synthetic Benzoin Condensation Reactions

Benzoin Reactions in THF[163]

Following the procedure of Connon and coworkers, 1,2,4-triazolium catalyst (**38** or **62**, 1 mol eq.) and potassium carbonate (1 mol eq.) were added to a round bottom flask, which was then evacuated and filled with argon. To this, THF and benzaldehyde (25 mol eq.) were added and the reaction was left to stir at room temperature for 20 h. After this, the reaction mixture concentrated *in vacuo* to isolate an off-white solid which was purified by column chromatography (hexane : EtOAc, 65:35). Benzoin was isolated as a white solid.

Benzoin Reactions in Aqueous Conditions

1,2,4-Triazolium catalyst (1 mol eq.) and potassium carbonate (1 mol eq.) were added to a round bottom flask, which was then evacuated and filled with argon. To this, a solvent mixture of either 2-MeTHF/D_2O or d-DMSO/D_2O (5 %/ 95 % v/v) was added with benzaldehyde (25 mol eq.) and rapid formation of a white precipitate was observed. The reaction was left to stir at room temperature for 20 h. After this, the reaction mixture was filtered under vacuum, removing an off-white solid which was purified by column chromatography (hexane : EtOAc, 65:35) – isolating benzoin as a white solid.

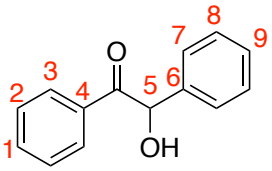

^{1}H NMR (400 MHz, $CDCl_3$) δ 7.93–7.90 (2H, m, *H*-3), 7.52 (1H, tt, *H*-1), 7.42–7.27 (7H, m, *H*-2, -7, -8, -9), 5.96 (1H, d, *H*-5), 4.56 (1H, d, O*H*); **^{13}C NMR** (101 MHz, $CDCl_3$) δ 199.1 (*C*O), 139.2 (*C*-4), 134.1 (*C*-6), 133.6 (*C*-1), 129.3 (*C*-7), 129.3 (*C*-8), 128.8 (*C*-3), 128.7 (*C*-2), 127.9 (*C*-9), 76.4 (*C*-5); **MS** (ESI, *m/z*, %) 195.195 ([M – OH]$^+$, 100 %),

235.214 ([M + Na]$^+$, 92.8), 236.240 ([M + Na + H]$^+$, 24.2), 237.228 ([M + Na + 2H]$^+$, 2.89).

6.3.3. Model Benzoin Reactions (Kinetic Monitoring)

Reactions were carried out as described in Section 6.3.6, with the same experimental conditions and NMR spectrometer parameters.

6.4. References

21. J. A. Grant, Z. Lu, D. E. Tucker, B. M. Hockin, D. S. Yufit, M. A. Fox, R. Kataky, V. Chechik and A. C. O'Donoghue, *Nat. Commun.*, 2017, **8**, 15088.
24. A. Bodzioch, M. Zheng, P. Kaszynski and G. Utecht, *J. Org. Chem.*, 2014, **79**, 7294-7310.
63. D. Enders, K. Breuer, U. Kallfass and T. Balensiefer, *Synthesis*, 2003, **2003**, 1292-1295.
66. A. R. Ali, H. Ghosh and B. K. Patel, *Tetrahedron Lett.*, 2010, **51**, 1019-1021.
163. L. Baragwanath, C. A. Rose, K. Zeitler and S. J. Connon, *J. Org. Chem.*, 2009, **74**, 9214-9217.
228. S. Sun, R. G. Duggleby and R. L. Schowen, *J. Am. Chem. Soc.*, 1995, **117**, 7317-7322.
247. H. E. Gottlieb, V. Kotlyar and A. Nudelman, *J. Org. Chem.*, 1997, **62**, 7512-7515.
248. K. Inamoto, C. Hasegawa, K. Hiroya and T. Doi, *Org. Lett.*, 2008, **10**, 5147-5150.
249. L. P. Cornacchione and L. T. Hu, *BMC Microbiology*, 2020, **20**, 128.

7. Appendix

7.0. Characterisation of Blatter Radicals

7.0.1. EPR Spectra

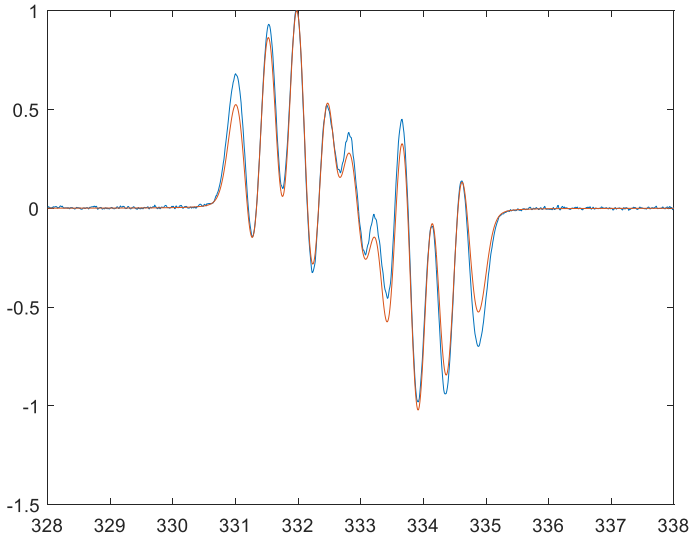

S. Figure 7.0.1. Experimental EPR spectrum for amido Blatter radical (**24a**) (blue) and simulated spectrum (orange).

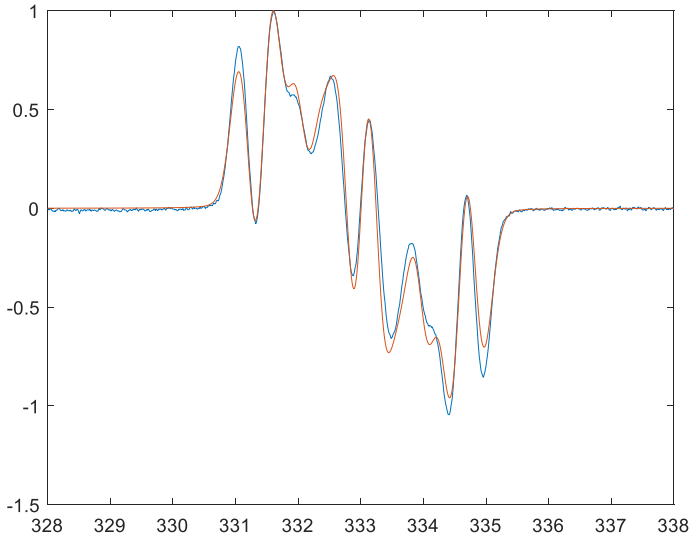

S. Figure 7.0.2. Experimental EPR spectrum for amido Blatter radical (**25a**) (blue) and simulated spectrum (orange).

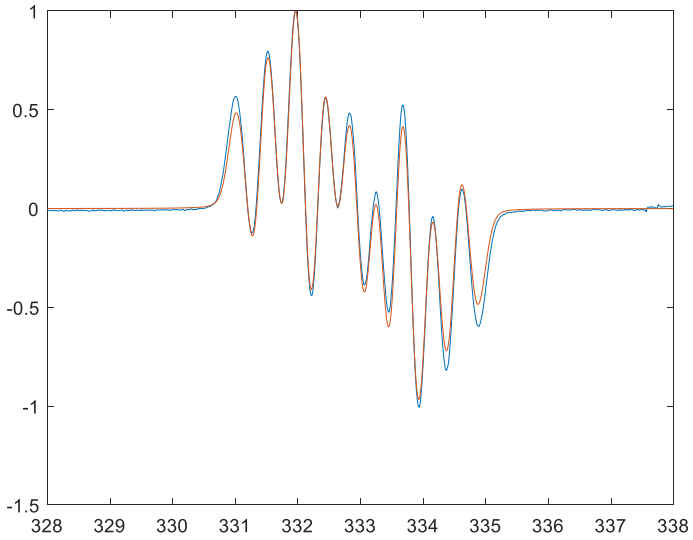

S. Figure 7.0.3. Experimental EPR spectrum for amido Blatter radical (**24f**) (blue) and simulated spectrum (orange).

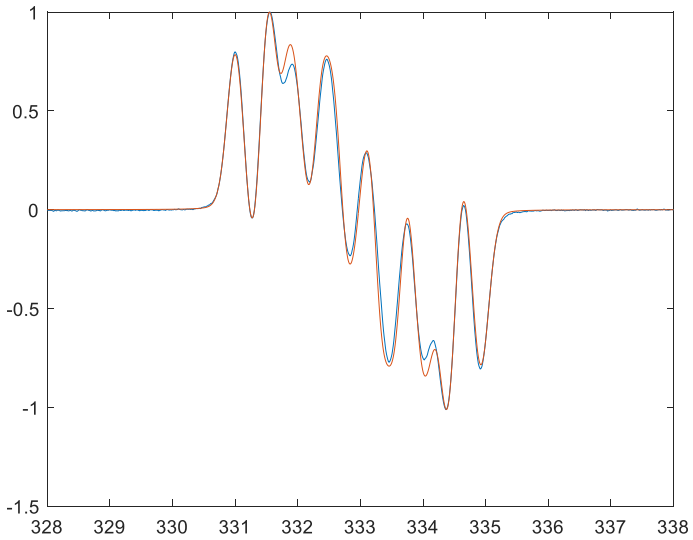

S. Figure 7.0.4. Experimental EPR spectrum for amido Blatter radical (**25f**) (blue) and simulated spectrum (orange).

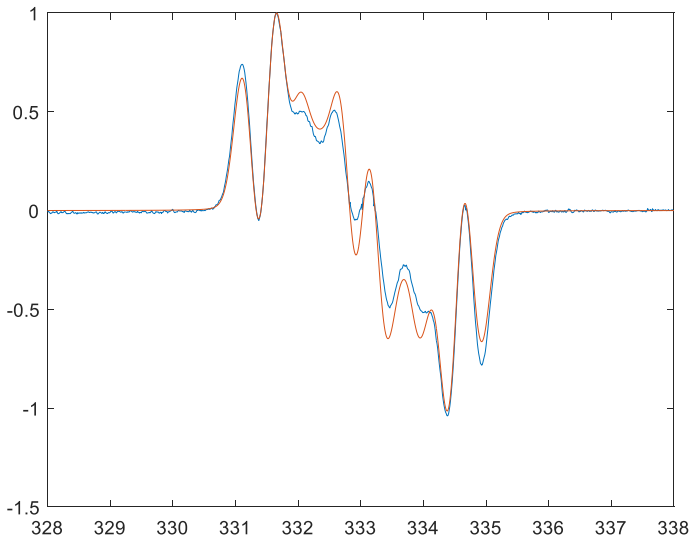

S. Figure 7.0.5. Experimental EPR spectrum for amido Blatter radical (**24g**) (blue) and simulated spectrum (orange).

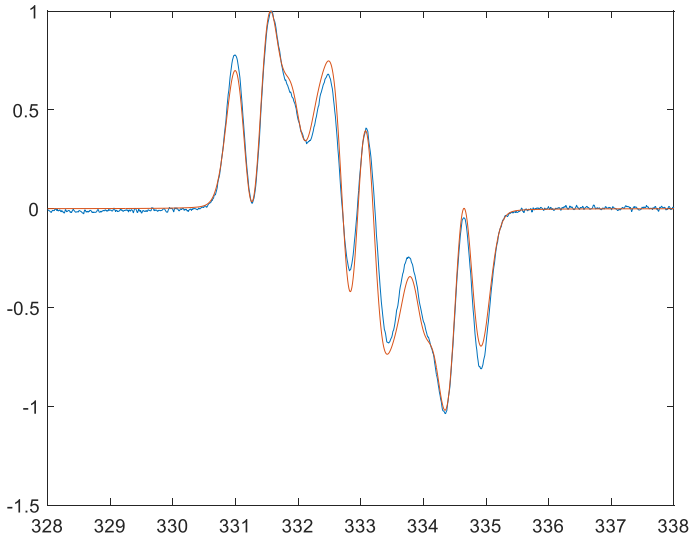

S. Figure 7.0.6. Experimental EPR spectrum for amido Blatter radical (**25g**) (blue) and simulated spectrum (orange).

7.1. Exploring the Tautomerisation of Nitron

7.1.1. Exocyclic Nitrogen pK_a Determination

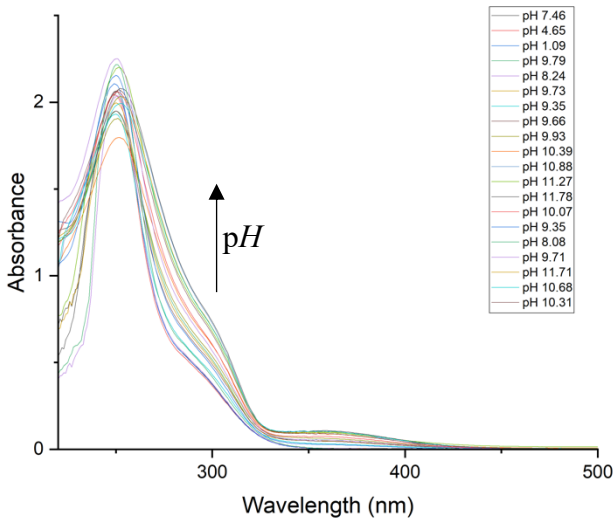

S. Figure 7.1.1. UV-Vis absorbance spectra collected for Nitron derivative (**6a**) across the p*H* range 1-13, change of absorbance at 360 nm was used to estimate the exocyclic nitrogen pK_a using Equations 2.3.2-2.3.7.

S. Table 7.1.1. Summary of absorbance at 360 nm for Nitron (**6a**) determined by UV-Vis spectrophotometry.

p*H*	Absorbance	Uncertainty
1.09	0.00379622	4.7922E-06
4.65	0.00362099	4.571E-06
7.46	0.00425142	5.3668E-06
8.08	0.00321094	4.0533E-06
8.24	0.00521914	6.5884E-06
9.35	0.0311097	3.9271E-05
9.35	0.02698972	3.4071E-05
9.66	0.04526347	5.7139E-05
9.71	0.05271611	6.6546E-05
9.73	0.04691035	5.9218E-05
9.79	0.05300119	6.6906E-05
9.93	0.06201928	7.829E-05
10.07	0.07266593	9.173E-05
10.31	0.08816452	0.00011129
10.39	0.08636326	0.00010902
10.68	0.1004042	0.00012675
10.88	0.10296886	0.00012998
11.27	0.09640743	0.0001217
11.71	0.09699047	0.00012244
11.78	0.10664563	0.00013462

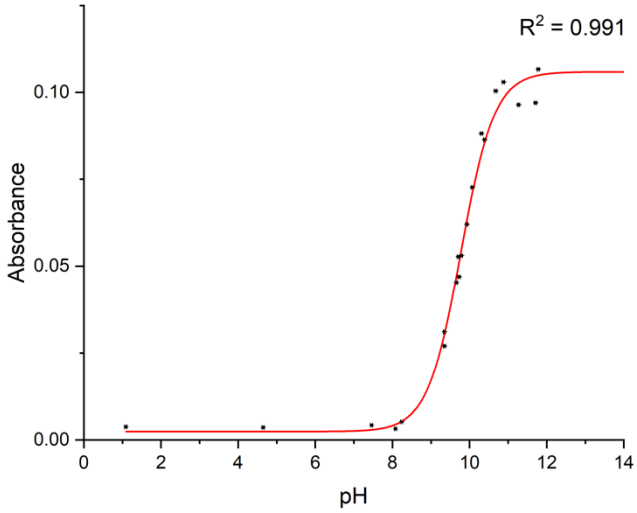

S. Figure 7.1.2. Plot of p*H* vs Absorbance at 360 nm for derivative **6a**, and fitted curve to Equation 2.3.2, to determine a value for *K*a and therefore pK_a, according to Equation 2.3.8.

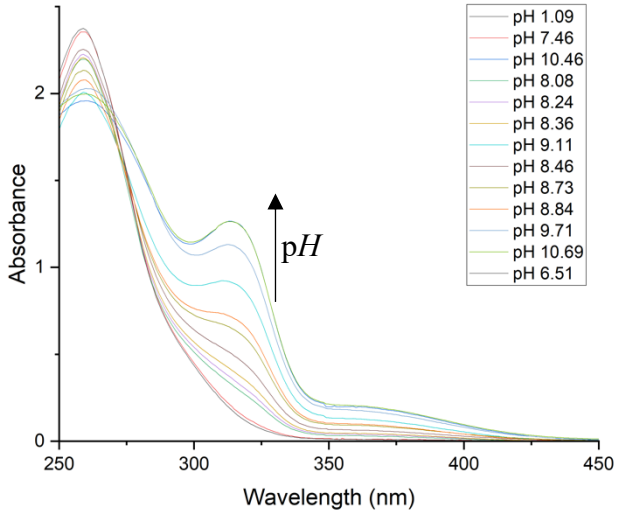

S. Figure 7.1.3. UV-Vis absorbance spectra collected for Nitron derivative (**6c**) across the p*H* range 1-13, change of absorbance at 320 nm was used to estimate the exocyclic nitrogen pK_a using Equations 2.3.2-2.3.7.

S. Table 7.1.2. Summary of absorbance at 320 nm for Nitron (**6c**) determined by UV-Vis spectrophotometry

p*H*	Absorbance	Uncertainty
1.09	0.13092102	0.00016527
6.51	0.16580354	0.0002093
7.46	0.18494885	0.00023347
8.08	0.31251608	0.00039451
8.24	0.3503491	0.00044227
8.36	0.39880681	0.00050344
8.46	0.49049258	0.00061918
8.73	0.64117536	0.00080939
8.84	0.70561019	0.00089073

9.11	0.90753104	0.00114563
9.71	1.12343525	0.00141817
9.99	1.17842984	0.0014876
10.46	1.2612857	0.00159219
10.69	1.25954712	0.00159

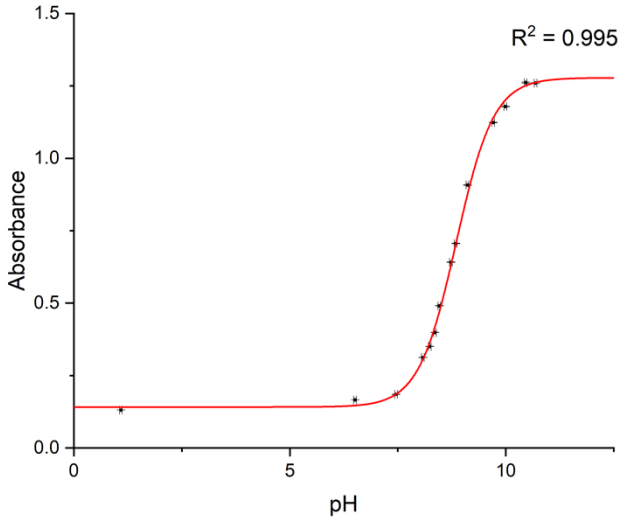

S. Figure 7.1.4. Plot of p*H* vs Absorbance at 320 nm for derivative **6a**, and fitted curve to Equation 2.3.2, to determine a value for *K*a and therefore pK_a, according to Equation 2.3.8.

S. Table 7.1.3. Summary of absorbance at 360 nm for Nitron (**6d**) determined by UV-Vis spectrophotometry.

p*H*	**Absorbance**	**Uncertainty**
1.09	0.00761858	9.6173E-06
4.65	0.00789177	9.9622E-06
7.46	0.00831565	1.0497E-05
9.35	0.01523689	1.9234E-05
9.71	0.02241699	2.8298E-05
10.07	0.03689248	4.6571E-05
10.32	0.04712192	5.9485E-05
10.98	0.07679501	9.6943E-05
12.06	0.09562601	0.00012071
12.35	0.09772408	0.00012336
12.8	0.09836049	0.00012417
13.1	0.10263103	0.00012956

7.1.2. C(3)-H Deuterium Exchange

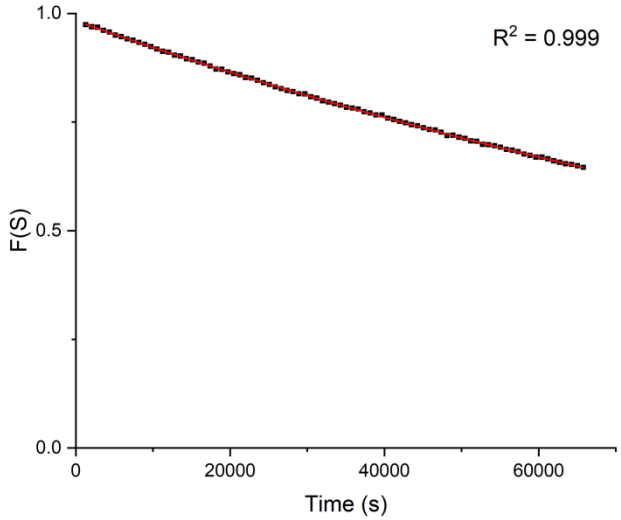

S. Figure 7.1.5. Plot of F(S) against time for the decay of the C(3)-H peak of Nitron derivative **6a** in 0.1 M DCl at 25 °C (30% v/v MeCN) displaying an excellent fit (R^2 = 0.999) to a first-order decay.

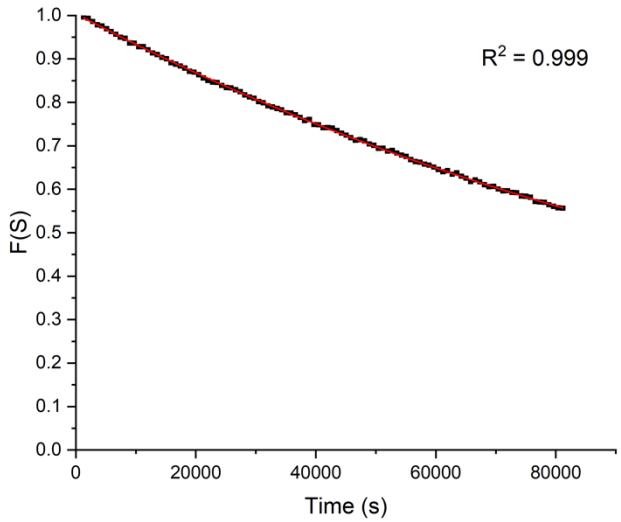

S. Figure 7.1.6. Plot of F(S) against time for the decay of the C(3)-H peak of Nitron derivative **6g** in 0.1 M DCl at 25 °C (30% v/v MeCN) displaying an excellent fit (R^2 = 0.999) to a first-order decay.

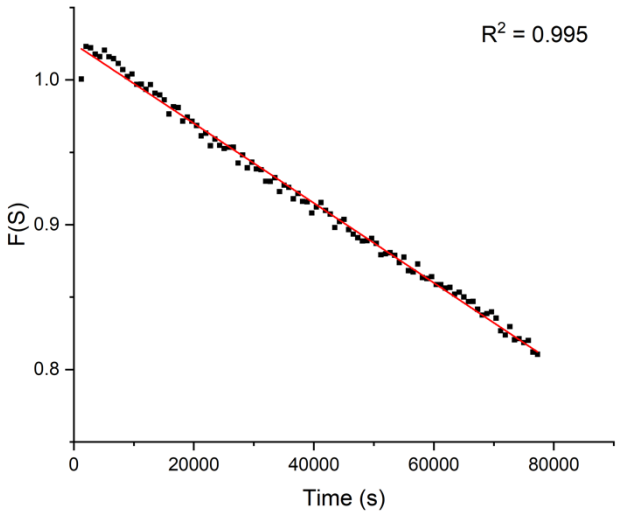

S. Figure 7.1.7. Plot of F(S) against time for the decay of the C(3)-H peak of Nitron derivative **6d** in 0.1 M DCl at 25 °C (30% v/v MeCN) displaying an excellent fit (R^2 = 0.995) to a first-order decay.

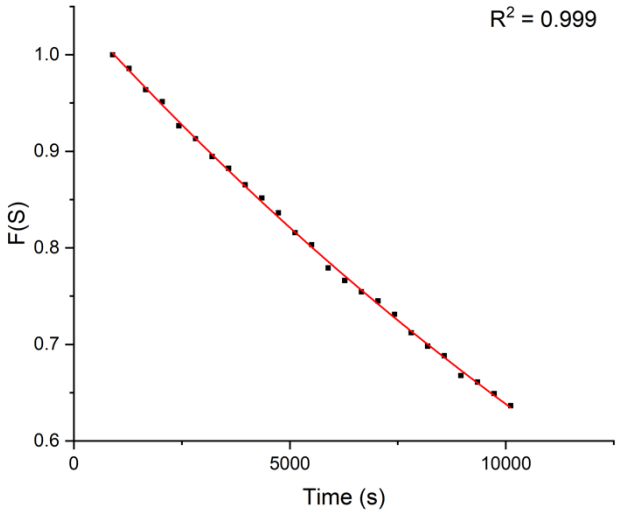

S. Figure 7.1.8. Plot of F(S) against time for the decay of the C(3)-H peak of Nitron derivative **6c** in 0.1 M DCl at 25 °C (50% v/v MeCN) displaying an excellent fit (R^2 = 0.997) to a first-order decay.

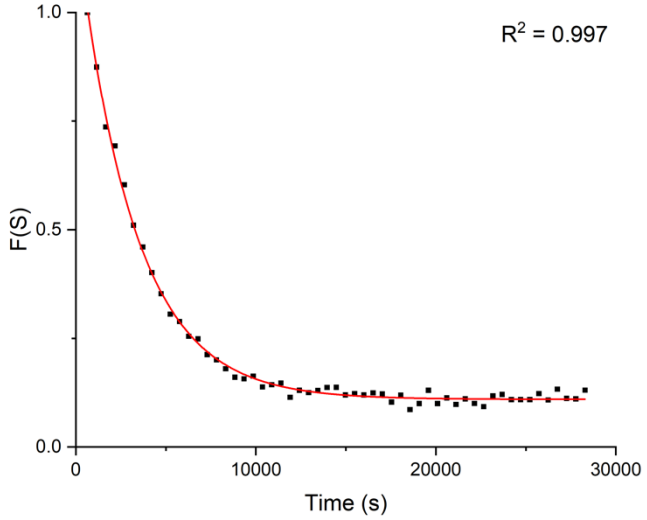

S. Figure 7.1.9. Plot of F(S) against time for the decay of the C(3)-H peak of Nitron derivative **6j** in 0.1 M DCl at 25 °C (50% v/v MeCN) displaying an excellent fit (R^2 = 0.997) to a first-order decay.

7.2. Pyrophosphate Hydrolysis Studies

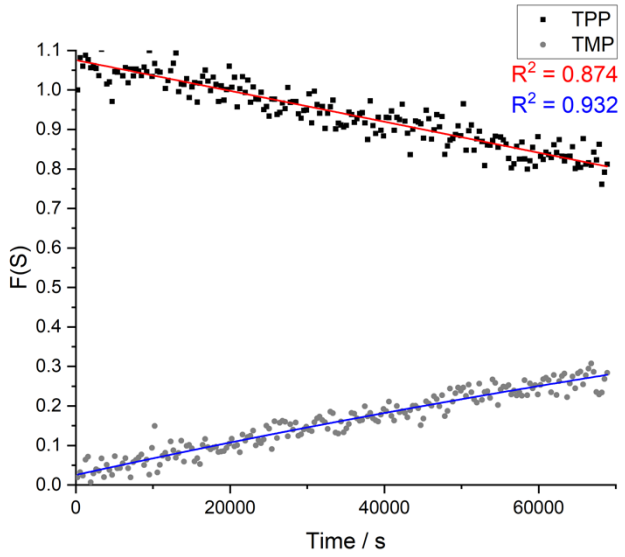

S. Figure 7.2.1. Plot of F(S) (S=TPP or TMP) over time for the hydrolysis of TPP (**5{PP}**) at p*D* 0.36, monitored by ^{31}P NMR spectroscopy. Solid lines show a first order fit (Equation 3.3.2) with excellent R^2 values.

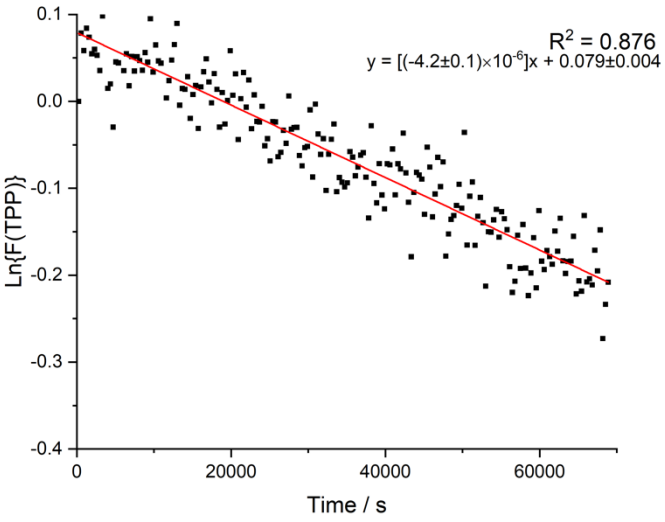

S. Figure 7.2.2. Plot of ln{F(TPP)} against time shows linear behaviour with gradient equal to $-k_{hyd}$ as per Equation 3.3.3, as shown here for hydrolysis at p*D* 0.36.

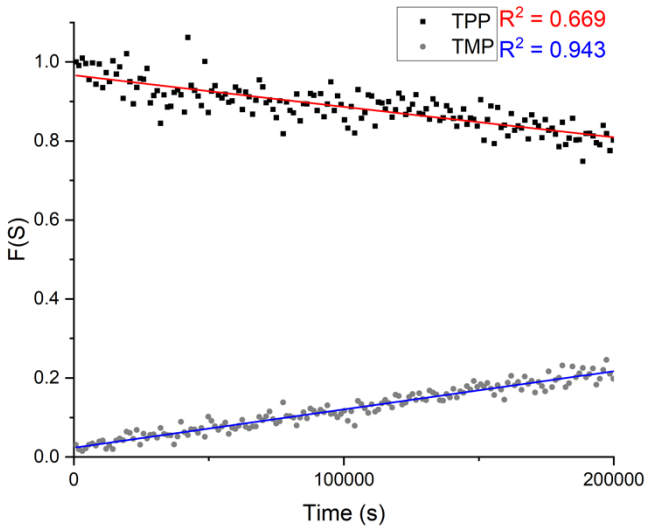

S. Figure 7.2.3. Plot of F(S) (S=TPP or TMP) over time for the hydrolysis of TPP (**5{PP}**) at p*D* 0.80, monitored by ^{31}P NMR spectroscopy. Solid lines show a first order fit (Equation 3.3.2) with excellent R^2 values.

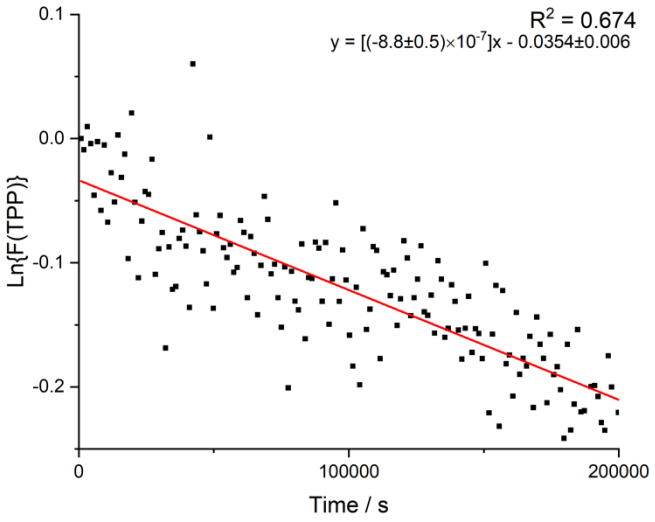

S. Figure 7.2.4. Plot of ln{F(TPP)} against time shows linear behaviour with gradient equal to $-k_{hyd}$ as per Equation 3.3.3, as shown here for hydrolysis at p*D* 0.80.

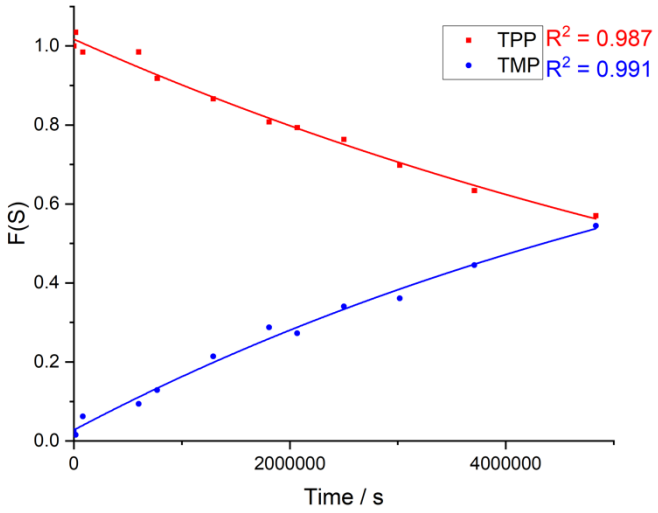

S. Figure 7.2.5. Plot of F(S) (S=TPP or TMP) over time for the hydrolysis of TPP (**5{PP}**) at p*D* 1.38, monitored by ^{31}P NMR spectroscopy. Solid lines show a first order fit (Equation 3.3.2) with excellent R^2 values.

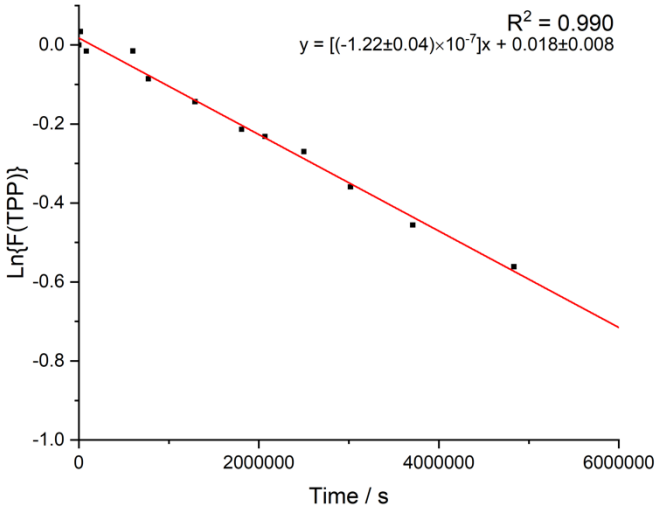

S. Figure 7.2.6. Plot of ln{F(TPP)} against time shows linear behaviour with gradient equal to $-k_{hyd}$ as per Equation 3.3.3, as shown here for hydrolysis at p*D* 1.38.

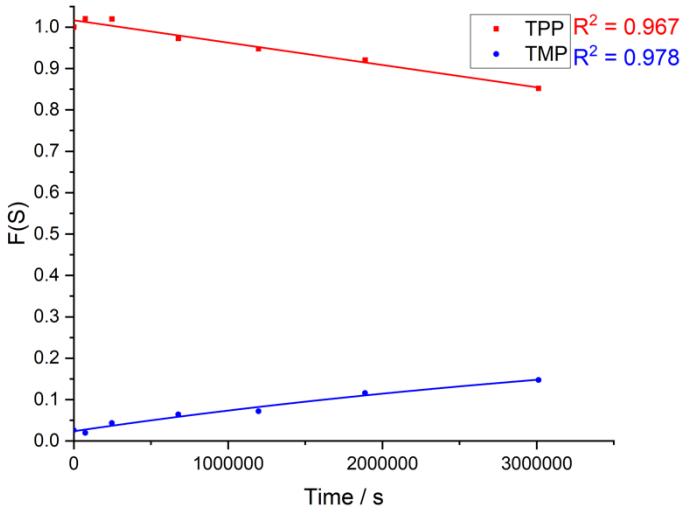

S. Figure 7.2.7. Plot of F(S) (S=TPP or TMP) over time for the hydrolysis of TPP (**5{PP}**) at p*D* 1.90, monitored by ^{31}P NMR spectroscopy. Solid lines show a first order fit (Equation 3.3.2) with excellent R^2 values.

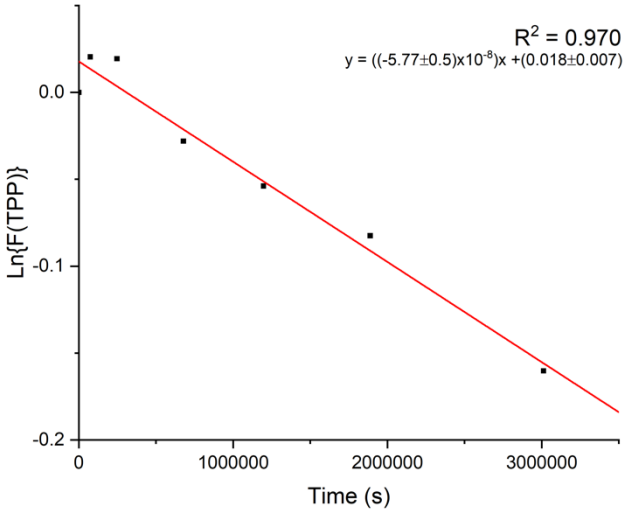

S. Figure 7.2.8. Plot of ln{F(TPP)} against time shows linear behaviour with gradient equal to $-k_{hyd}$ as per Equation 3.3.3, as shown here for hydrolysis at p*D* 1.90.

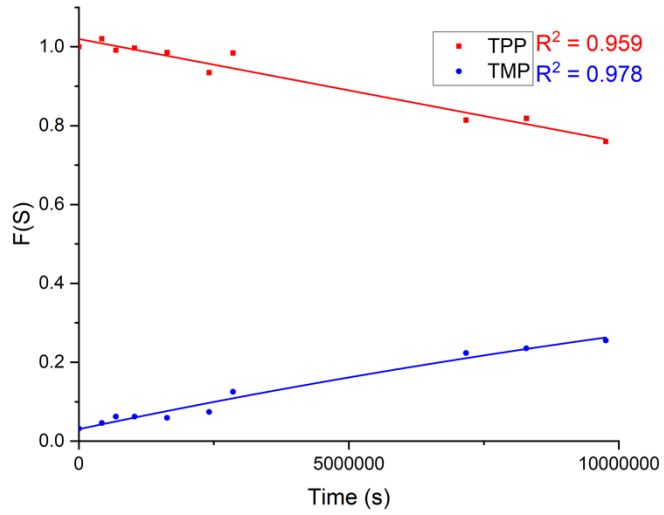

S. Figure 7.2.9. Plot of F(S) (S=TPP or TMP) over time for the hydrolysis of TPP (**5{PP}**) at p*D* 3.28, monitored by ^{31}P NMR spectroscopy. Solid lines show a first order fit (Equation 3.3.2) with excellent R^2 values.

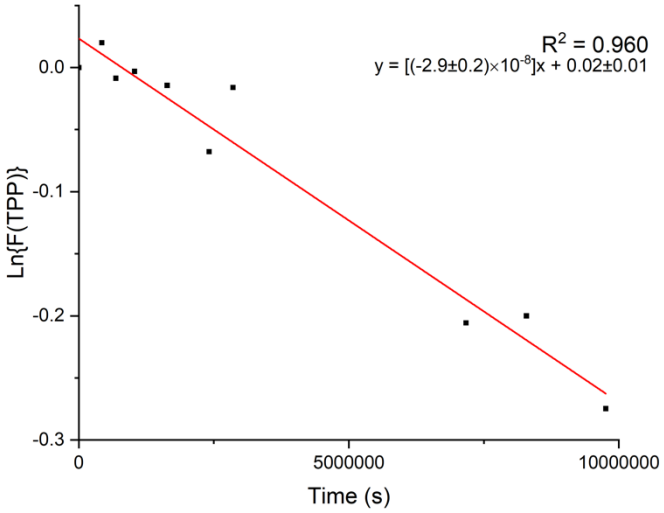

S. Figure 7.2.10. Plot of ln{F(TPP)} against time shows linear behaviour with gradient equal to $-k_{hyd}$ as per Equation 3.3.3, as shown here for hydrolysis at p*D* 3.28.

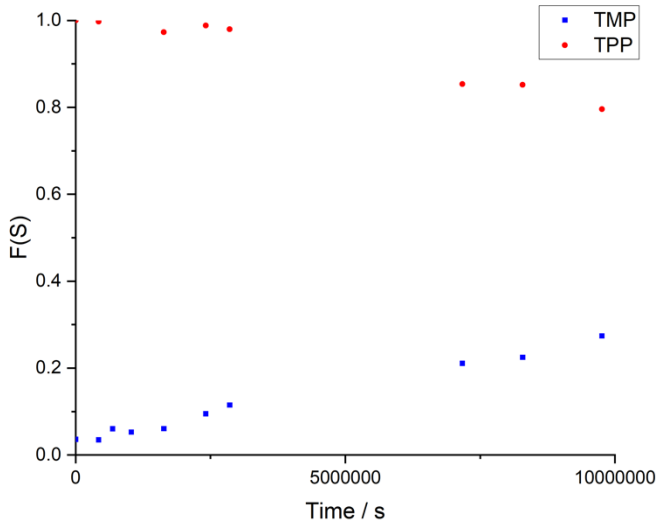

S. Figure 7.2.11. Plot of F(S) (S=TPP or TMP) over time for the hydrolysis of TPP (**5{PP}**) at p*D* 3.97, monitored by ^{31}P NMR spectroscopy.

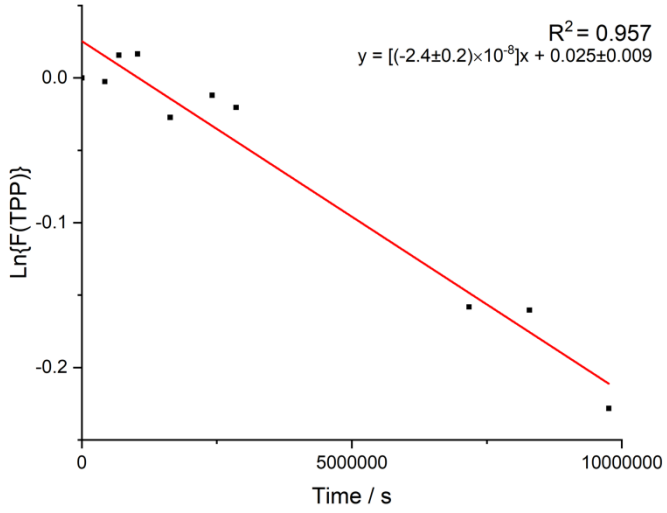

S. Figure 7.2.12. Plot of ln{F(TPP)} against time shows linear behaviour with gradient equal to $-k_{hyd}$ as per Equation 3.3.3, as shown here for hydrolysis at p*D* 3.97.

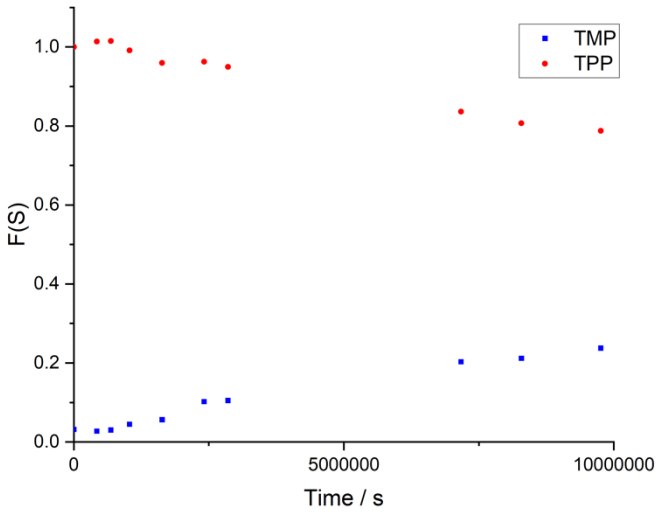

S. Figure 7.2.13. Plot of F(S) (S=TPP or TMP) over time for the hydrolysis of TPP (**5{PP}**) at p*D* 4.43, monitored by ^{31}P NMR spectroscopy.

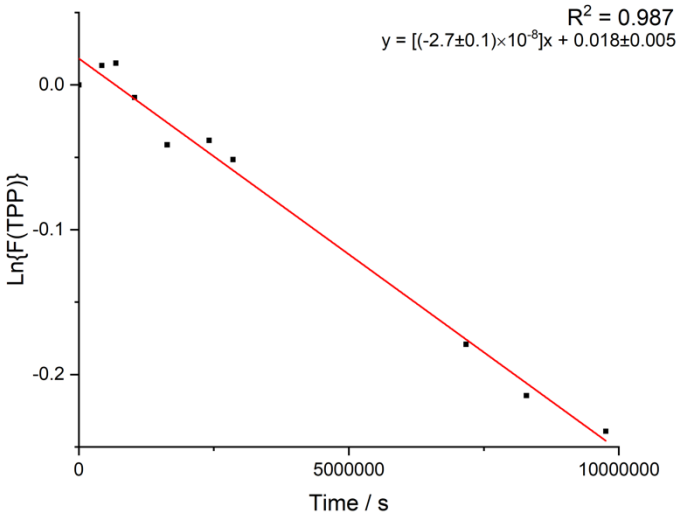

S. Figure 7.2.14. Plot of ln{F(TPP)} against time shows linear behaviour with gradient equal to $-k_{hyd}$ as per Equation 3.3.3, as shown here for hydrolysis at p*D* 4.43.

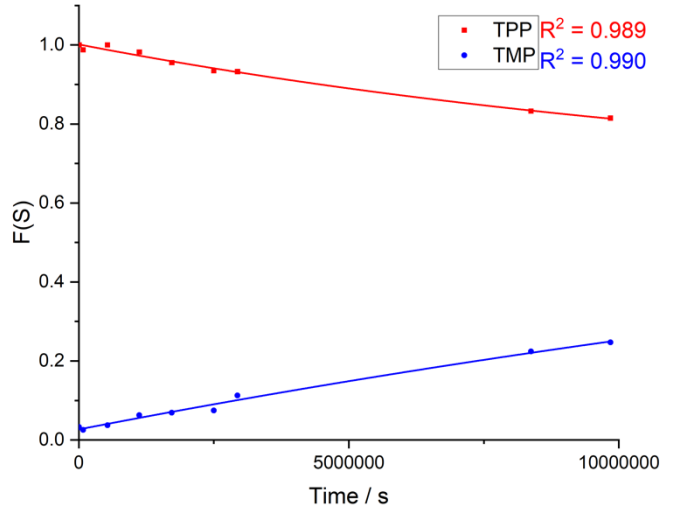

S. Figure 7.2.15. Plot of F(S) (S=TPP or TMP) over time for the hydrolysis of TPP (**5{PP}**) at p*D* 4.90, monitored by ^{31}P NMR spectroscopy. Solid lines show a first order fit (Equation 3.3.2) with excellent R^2 values.

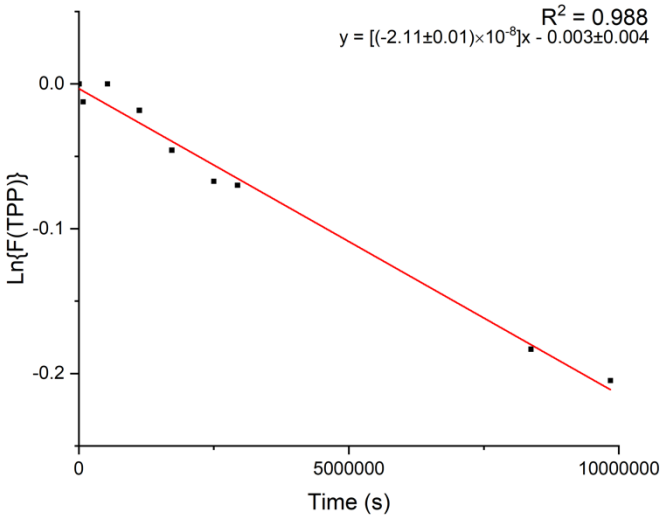

S. Figure 7.2.16. Plot of ln{F(TPP)} against time shows linear behaviour with gradient equal to $-k_{hyd}$ as per Equation 3.3.3, as shown here for hydrolysis at p*D* 4.90

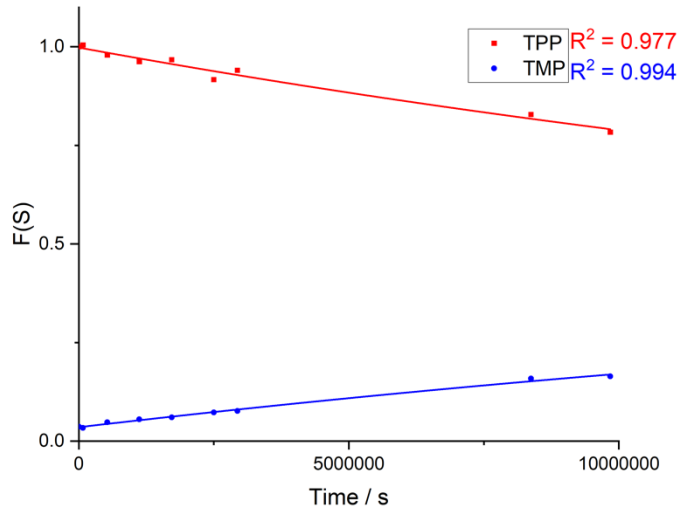

S. Figure 7.2.17. Plot of F(S) (S=TPP or TMP) over time for the hydrolysis of TPP (**5{PP}**) at p*D* 5.51, monitored by ^{31}P NMR spectroscopy. Solid lines show a first order fit (Equation 3.3.2) with excellent R^2 values.

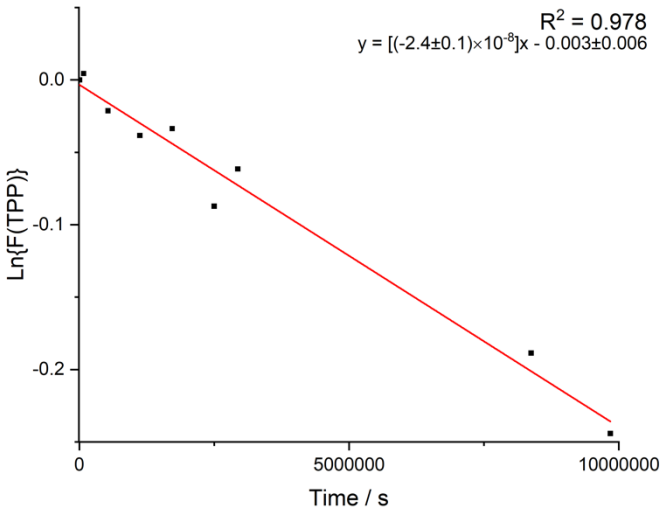

S. Figure 7.2.18. Plot of ln{F(TPP)} against time shows linear behaviour with gradient equal to $-k_{hyd}$ as per Equation 3.3.3, as shown here for hydrolysis at p*D* 5.51.

pD 6.90

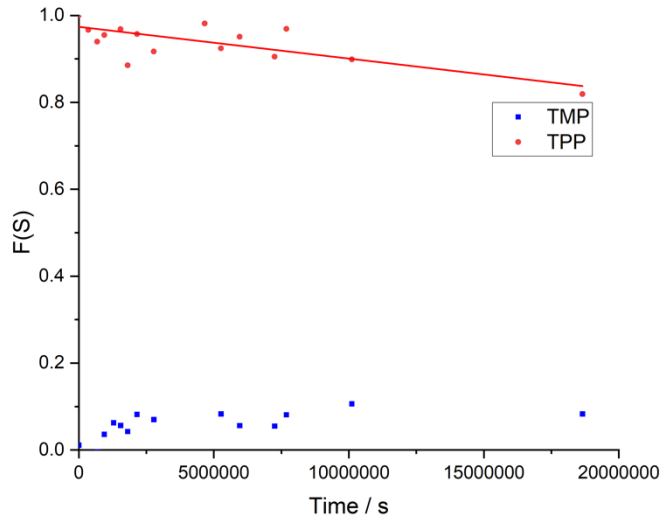

S. Figure 7.2.19. Plot of F(S) (S=TPP or TMP) over time for the hydrolysis of TPP (**5{PP}**) at p*D* 6.90, monitored by ^{31}P NMR spectroscopy. Solid lines show a first order fit (Equation 3.3.2).

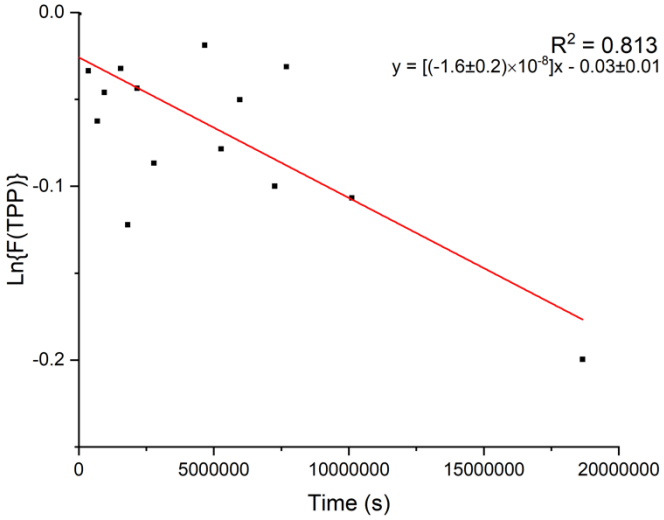

S. Figure 7.2.20. Plot of ln{F(TPP)} against time shows linear behaviour with gradient equal to $-k_{hyd}$ as per Equation 3.3.3, as shown here for hydrolysis at p*D* 6.90.

7.3. H/D Exchange Studies

7.3.1. Thiamine Pyrophosphate (5{PP})

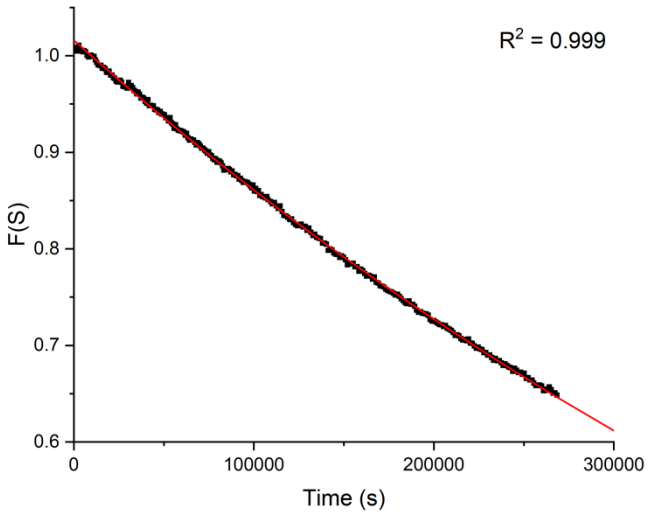

S. Figure 7.3.1. A plot of F(S) against time for the C(2)-H/D exchange for TPP (**5{PP}**) in potassium formate buffer (p*D* 2.37, I = 1 M (KCl)) at 25 °C.

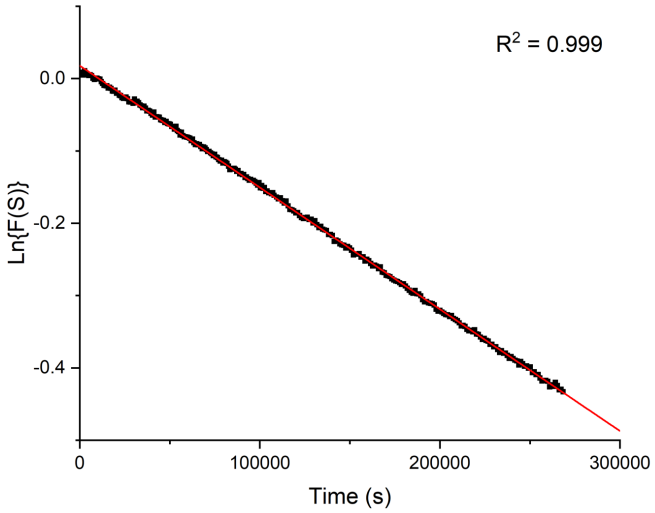

S. Figure 7.3.2. Semilogarithmic plot of fraction of substrate against time for H/D-exchange of TPP (**5{PP}**) in potassium formate buffer (p*D* 2.37, I = 1 M (KCl)) at 25 °C.

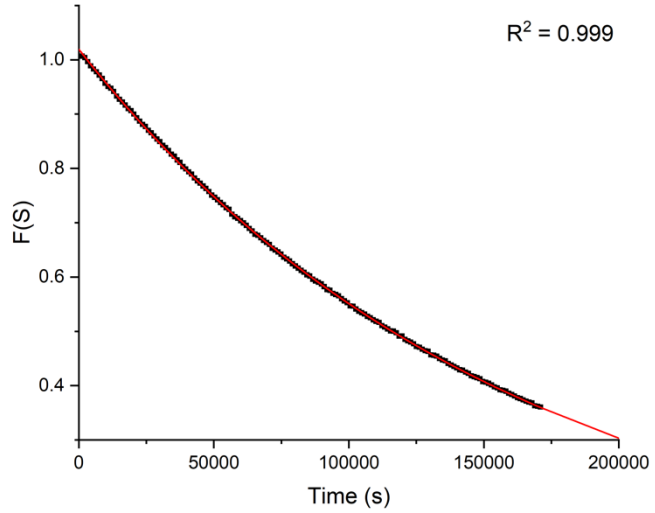

S. Figure 7.3.3. A plot of F(S) against time for the C(2)-H/D exchange for TPP (**5{PP}**) in potassium formate buffer (p*D* 2.90, I = 1 M (KCl)) at 25 °C.

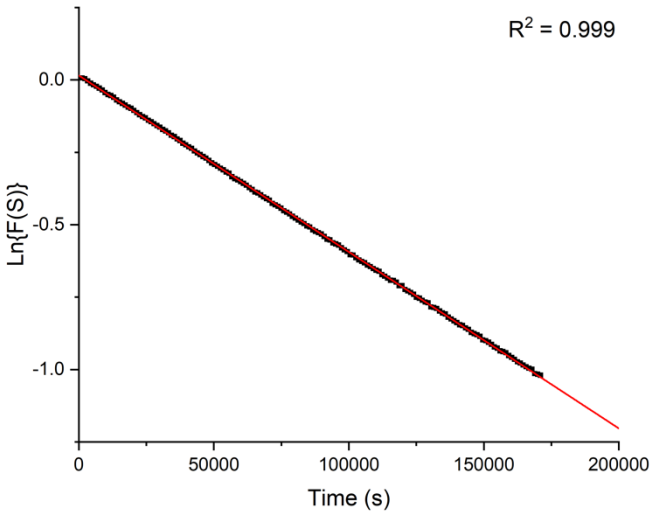

S. Figure 7.3.4. Semilogarithmic plot of fraction of substrate against time for H/D-exchange of TPP (**5{PP}**) in potassium formate buffer (p*D* 2.90, I = 1 M (KCl)) at 25 °C.

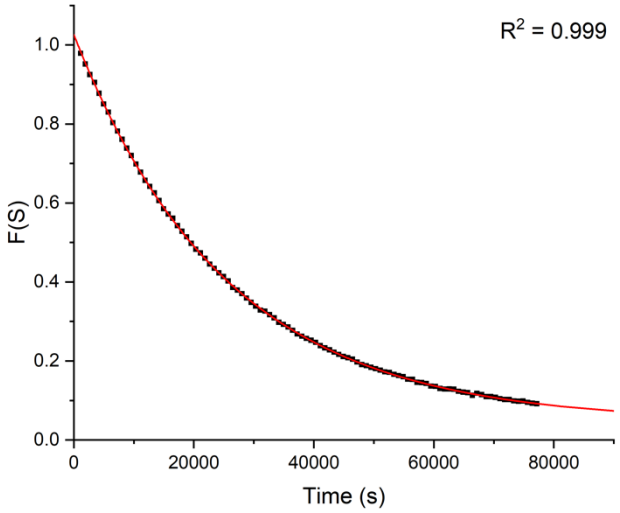

S. Figure 7.3.5. A representative plot of F(S) against time for the C(2)-H/D exchange for TPP (**5{PP}**) in potassium acetate buffer (p*D* 3.73, I = 1 M (KCl)) at 25 °C.

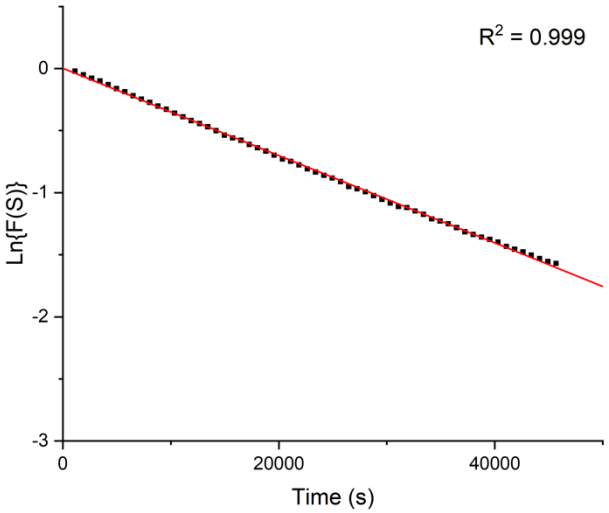

S. Figure 7.3.6. Semilogarithmic plot of fraction of substrate against time for H/D-exchange of TPP (**5{PP}**) in potassium formate buffer (p*D* 2.73, I = 1 M (KCl)) at 25 °C.

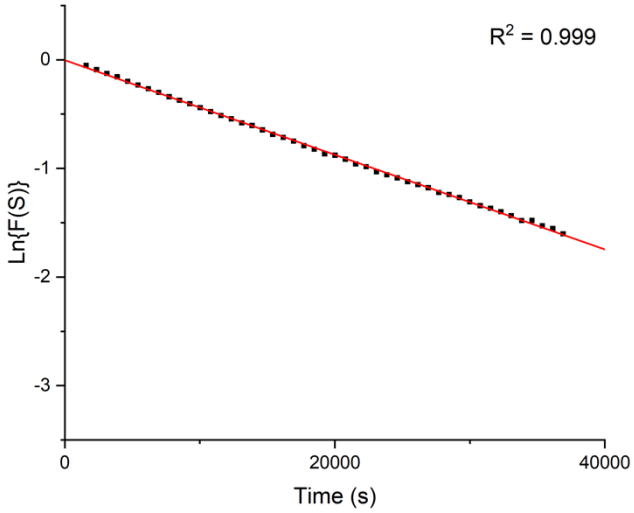

S. Figure 7.3.7. Semilogarithmic plot of fraction of substrate against time for H/D-exchange of TPP (**5{PP}**) in potassium formate buffer (p*D* 3.81, I = 1 M (KCl)) at 25 °C.

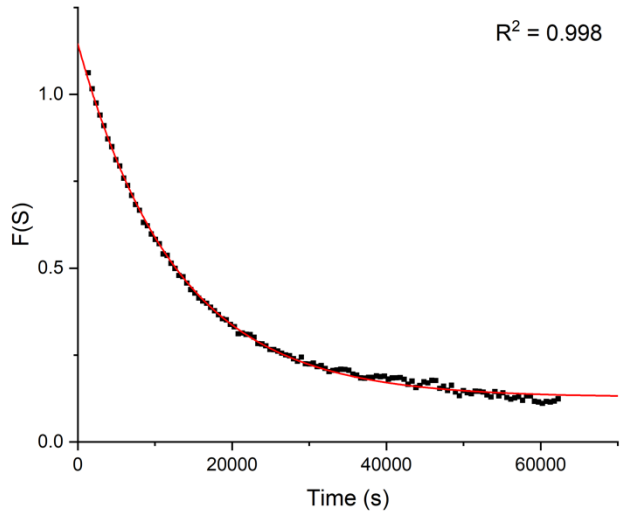

S. Figure 7.3.8. A representative plot of F(S) against time for the C(2)-H/D exchange for TPP (**5{PP}**) in potassium acetate buffer (p*D* 3.89, I = 1 M (KCl)) at 25 °C.

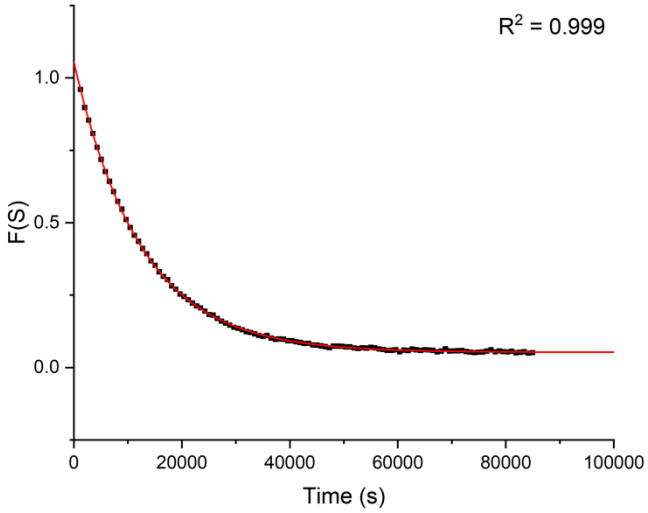

S. Figure 7.3.9. A representative plot of F(S) against time for the C(2)-H/D exchange for TPP (**5{PP}**) in potassium acetate buffer (p*D* 4.06, I = 1 M (KCl)) at 25 °C.

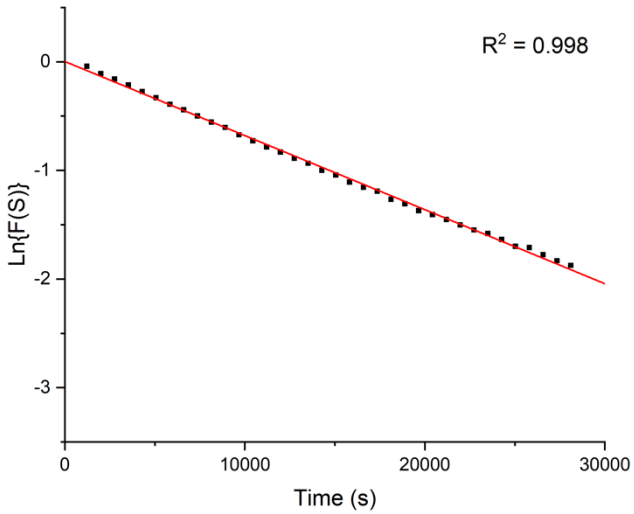

S. Figure 7.3.10. Semilogarithmic plot of fraction of substrate against time for H/D-exchange of TPP (**5{PP}**) in potassium acetate buffer (p*D* 4.06, I = 1 M (KCl)) at 25 °C.

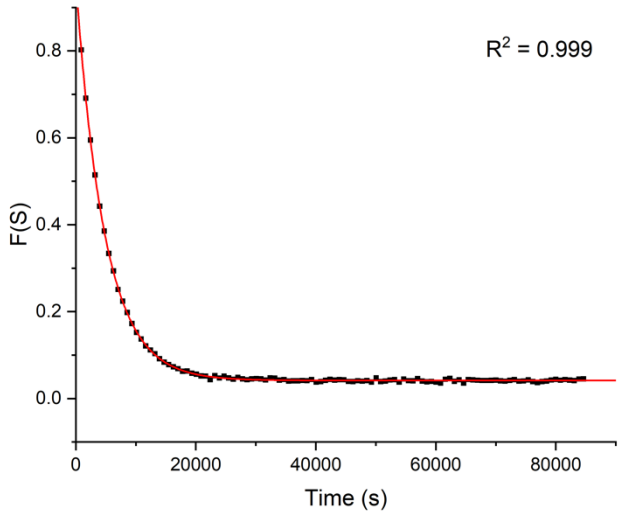

S. Figure 7.3.11. A representative plot of F(S) against time for the C(2)-H/D exchange for TPP (**5{PP}**) in potassium acetate buffer (p*D* 4.39, I = 1 M (KCl)) at 25 °C.

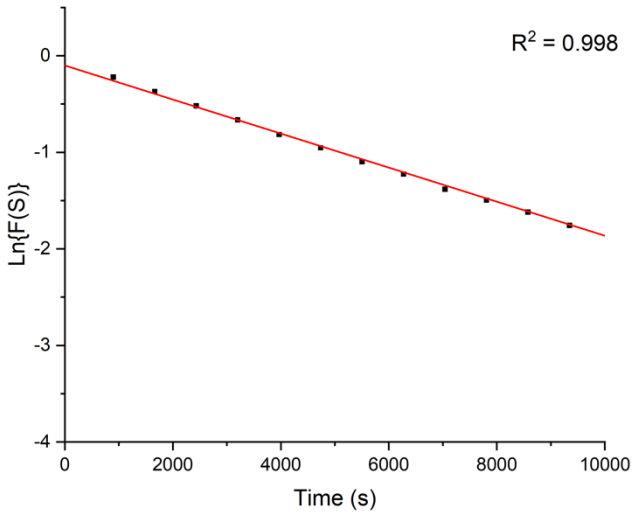

S. Figure 7.3.12. Semilogarithmic plot of fraction of substrate against time for H/D-exchange of TPP (**5{PP}**) in potassium acetate buffer (p*D* 4.39, I = 1 M (KCl)) at 25 °C.

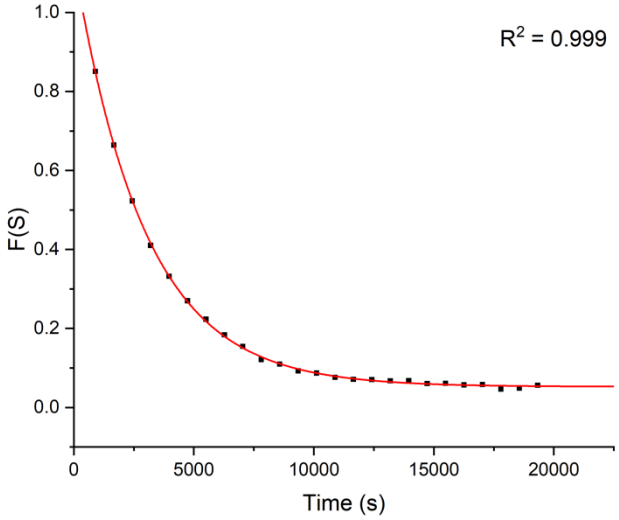

S. Figure 7.3.13. A representative plot of F(S) against time for the C(2)-H/D exchange for TPP (**5{PP}**) in potassium acetate buffer (p*D* 4.74, I = 1 M (KCl)) at 25 °C.

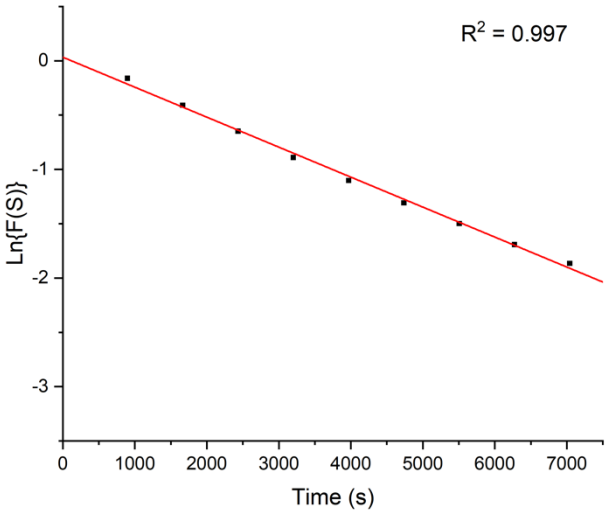

S. Figure 7.3.14. Semilogarithmic plot of fraction of substrate against time for H/D-exchange of TPP (**5{PP}**) in potassium acetate buffer (p*D* 4.74, I = 1 M (KCl)) at 25 °C.

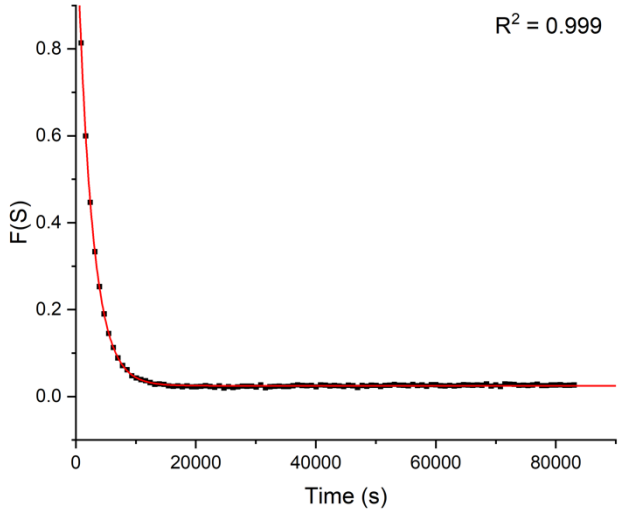

S. Figure 7.3.15. A representative plot of F(S) against time for the C(2)-H/D exchange for TPP (**5{PP}**) in potassium acetate buffer (p*D* 4.77, I = 1 M (KCl)) at 25 °C.

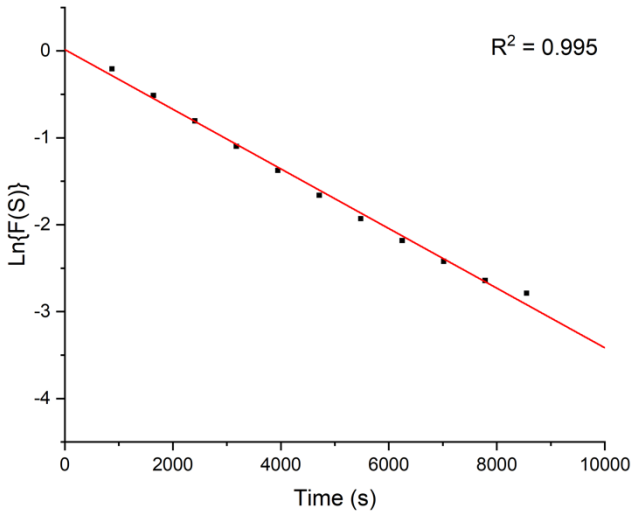

S. Figure 7.3.16. Semilogarithmic plot of fraction of substrate against time for H/D-exchange of TPP (**5{PP}**) in potassium acetate buffer (p*D* 4.89, I = 1 M (KCl)) at 25 °C.

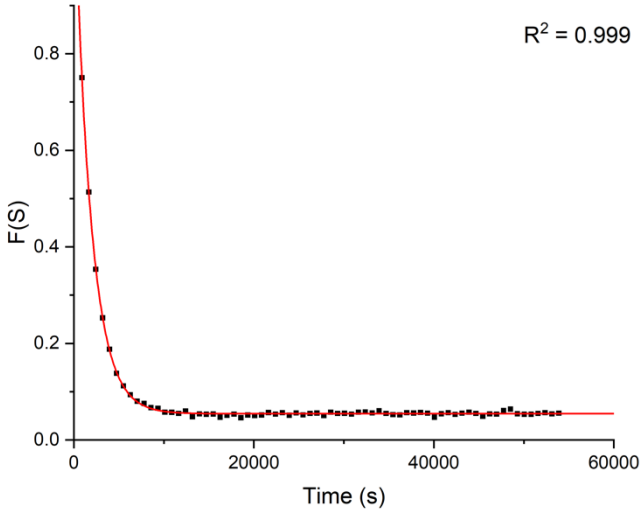

S. Figure 7.3.17. A representative plot of F(S) against time for the C(2)-H/D exchange for TPP (**5{PP}**) in potassium acetate buffer (p*D* 4.99, I = 1 M (KCl)) at 25 °C.

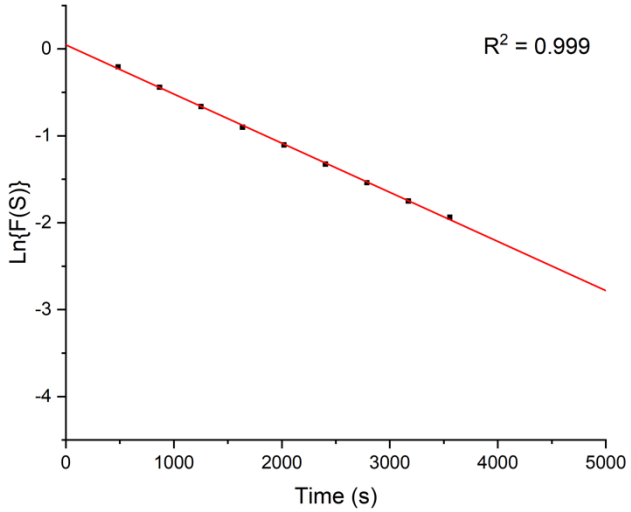

S. Figure 7.3.18. Semilogarithmic plot of fraction of substrate against time for H/D-exchange of TPP (**5{PP}**) in potassium acetate buffer (p*D* 4.9, I = 1 M (KCl)) at 25 °C.

7.3.2. 1,2,4-Triazolium Mimic (26{PP})

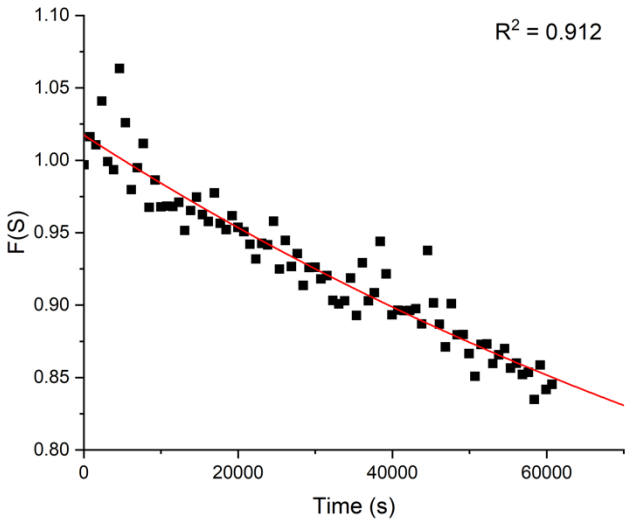

S. Figure 7.3.19. A plot of F(S) against time for the C(3)-H/D exchange for (**26{PP}**) in 0.1 M DCl (p*D* 1.18, I = 1 M (KCl)) at 25 °C.

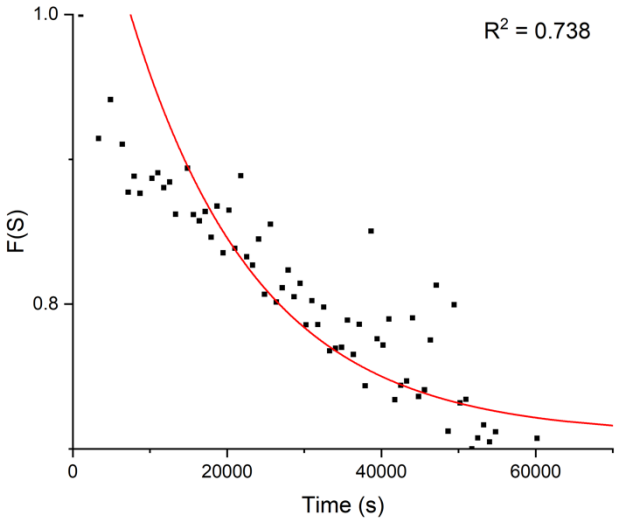

S. Figure 7.3.20. A plot of F(S) against time for the C(3)-H/D exchange for (**26{PP}**) in 0.05 M DCl (p*D* 1.55, I = 1 M (KCl)) at 25 °C.

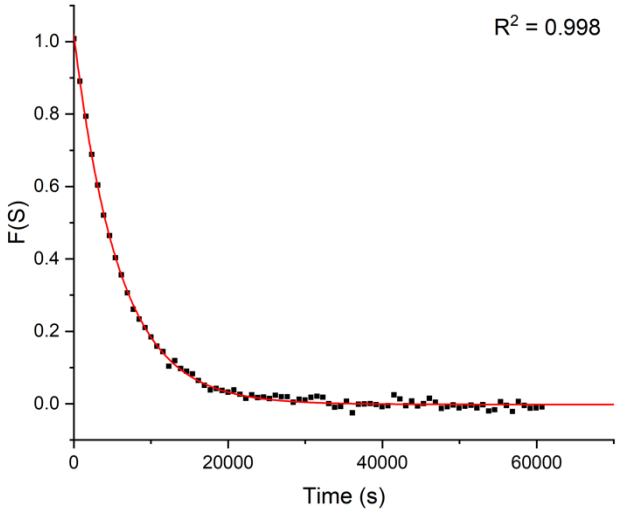

S. Figure 7.3.21. A plot of F(S) against time for the C(3)-H/D exchange for (**26{PP}**) in potassium acetate buffer (p*D* 3.10, I = 1 M (KCl)) at 25 °C.

7.3.3. Lactone Triazolium (27b)

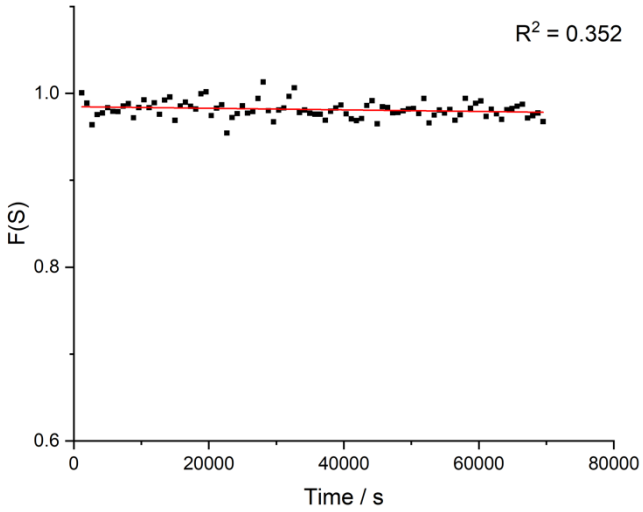

S. Figure 7.3.22. A plot of F(S) against time for the C(3)-H/D exchange for (**27b**) in 0.1 M DCl (p*D* 1.00, I = 1 M (KCl)) at 25 °C.

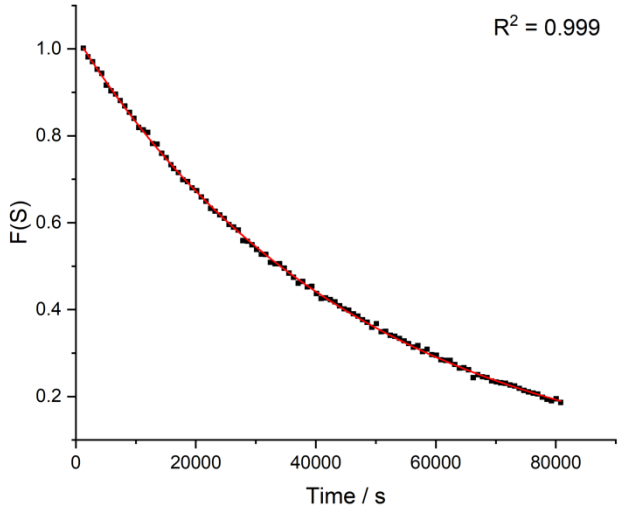

S. Figure 7.3.23. A plot of F(S) against time for the C(3)-H/D exchange for (**27b**) in potassium formate buffer (p*D* 2.37, I = 1 M (KCl)) at 25 °C.

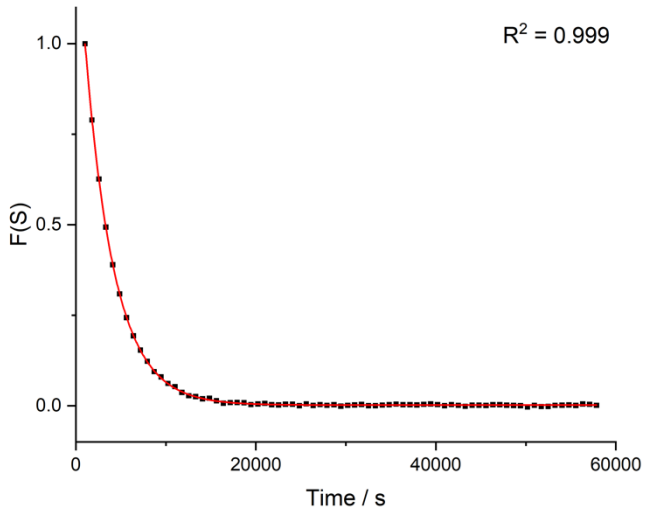

S. Figure 7.3.24. A representative plot of F(S) against time for the C(3)-H/D exchange for (**27b**) in potassium formate buffer (p*D* 3.26, I = 1 M (KCl)) at 25 °C.

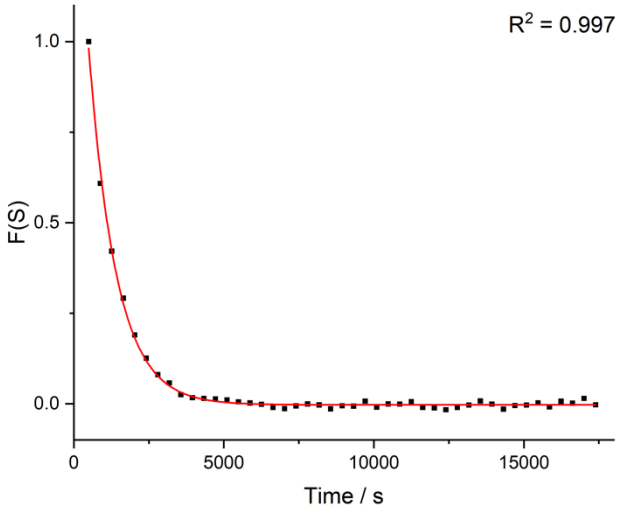

S. Figure 7.3.25. A plot of F(S) against time for the C(3)-H/D exchange for (**27b**) in potassium acetate buffer (p*D* 4.06, I = 1 M (KCl)) at 25 °C.

7.4. Cofactor Catalysis

7.4.1. Spectrophotometric Assays

Pyruvate Decarboxylase

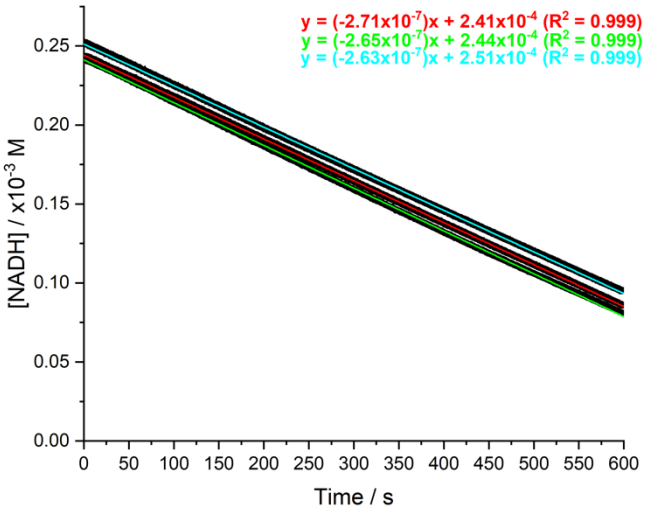

S. Figure 7.4.1. Plot of NADH (**80{H}**) consumption in the coupled assay shown in Scheme 3.4.7. Concentration of pyruvate in this case was 2 mM.

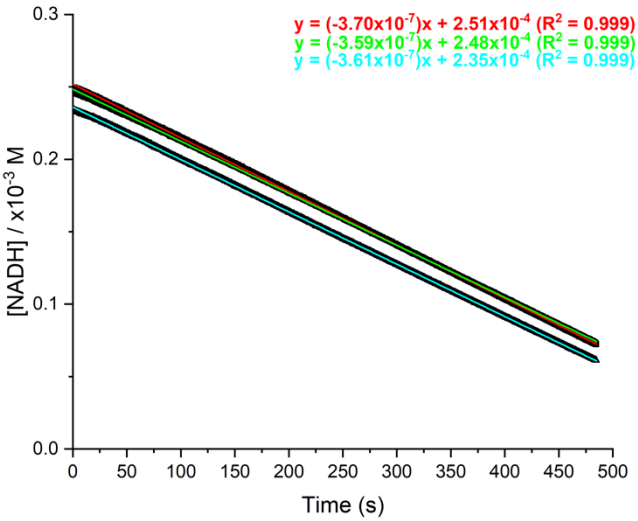

S. Figure 7.4.2. Plot of NADH (**80{H}**) consumption in the coupled assay shown in Scheme 3.4.7. Concentration of pyruvate in this case was 5 mM.

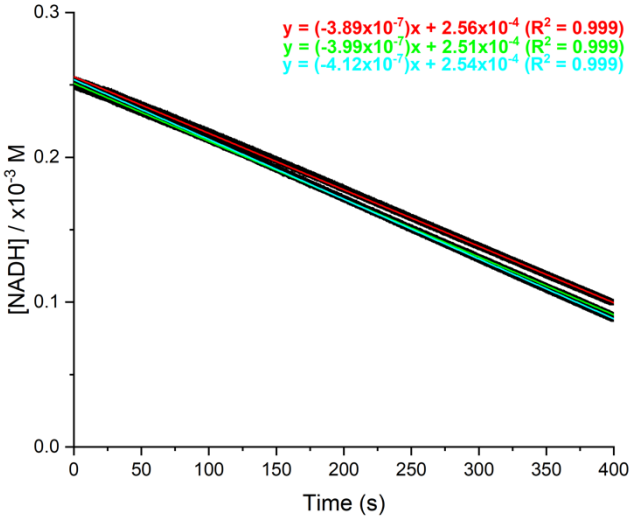

S. Figure 7.4.3. Plot of NADH (**80{H}**) consumption in the coupled assay shown in Scheme 3.4.7. Concentration of pyruvate in this case was 10 mM.

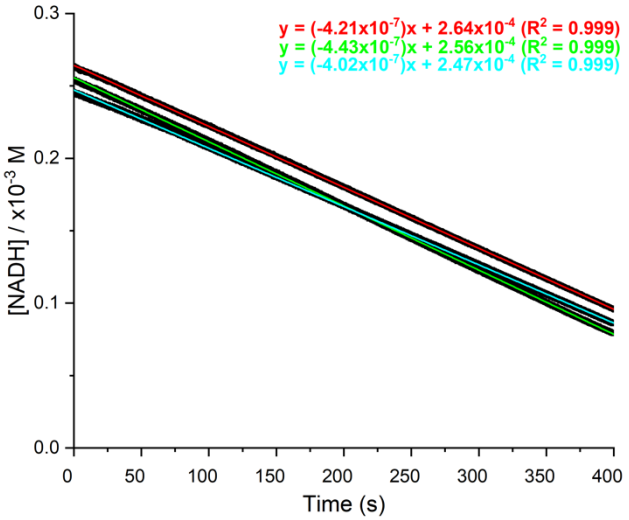

S. Figure 7.4.4. Plot of NADH (**80{H}**) consumption in the coupled assay shown in Scheme 3.4.7. Concentration of pyruvate in this case was 15 mM.

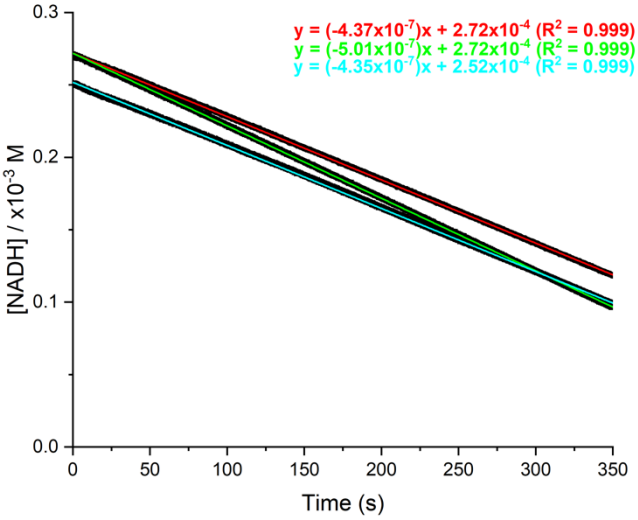

S. Figure 7.4.5. Plot of NADH (**80{H}**) consumption in the coupled assay shown in Scheme 3.4.7. Concentration of pyruvate in this case was 20 mM.

7.4.2. Pyruvate Oxidase

0.1 mM Pyruvate

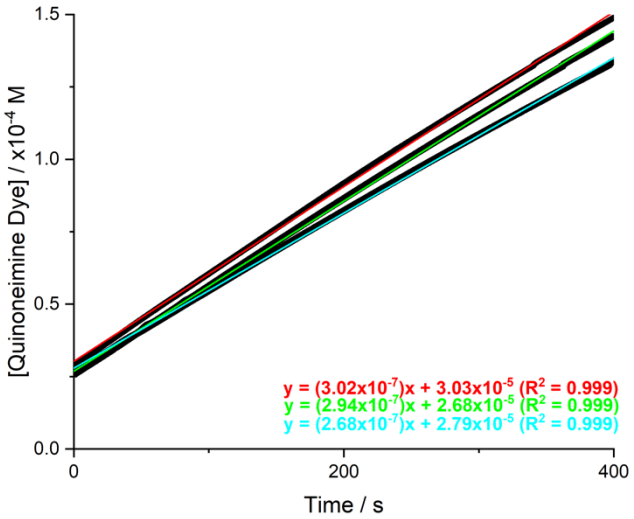

S. Figure 7.4.6. Plot of quinoneimine dye formation in the coupled assay shown in Scheme 3.4.8. Concentration of pyruvate in this case was 0.1 mM.

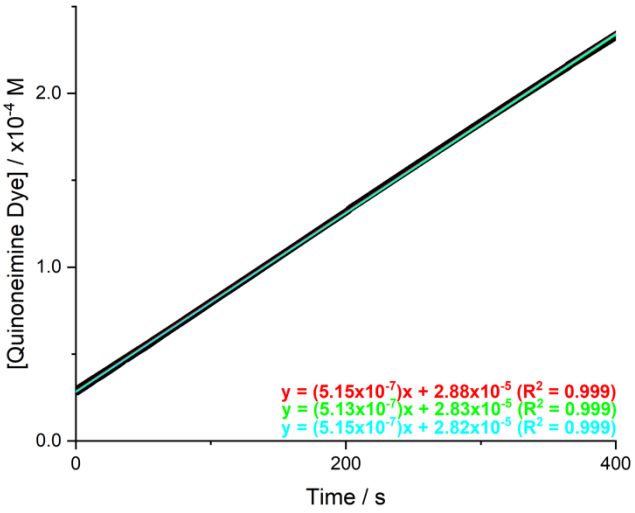

S. Figure 7.4.7. Plot of quinoneimine dye formation in the coupled assay shown in Scheme 3.4.8. Concentration of pyruvate in this case was 0.25 mM.

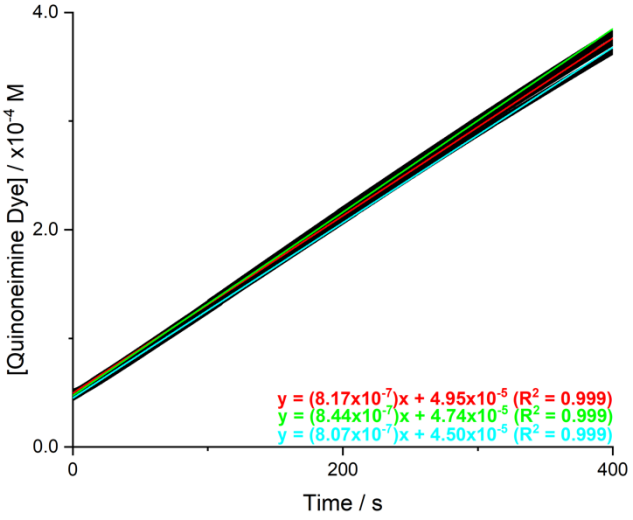

S. Figure 7.4.8. Plot of quinoneimine dye formation in the coupled assay shown in Scheme 3.4.8. Concentration of pyruvate in this case was 0.5 mM.

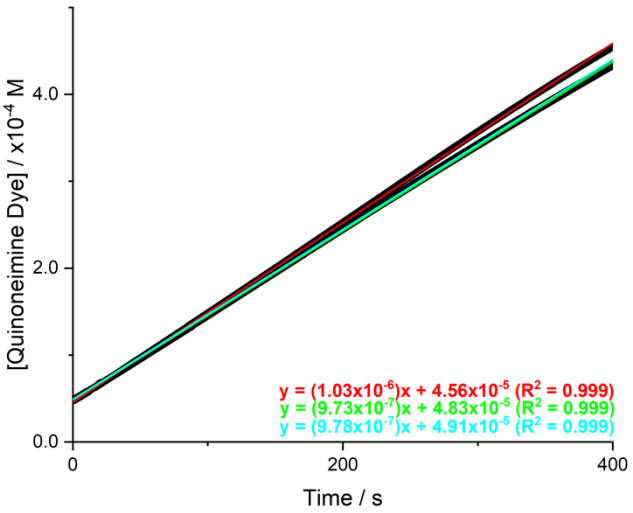

S. Figure 7.4.9. Plot of quinoneimine dye formation in the coupled assay shown in Scheme 3.4.8. Concentration of pyruvate in this case was 1 mM.

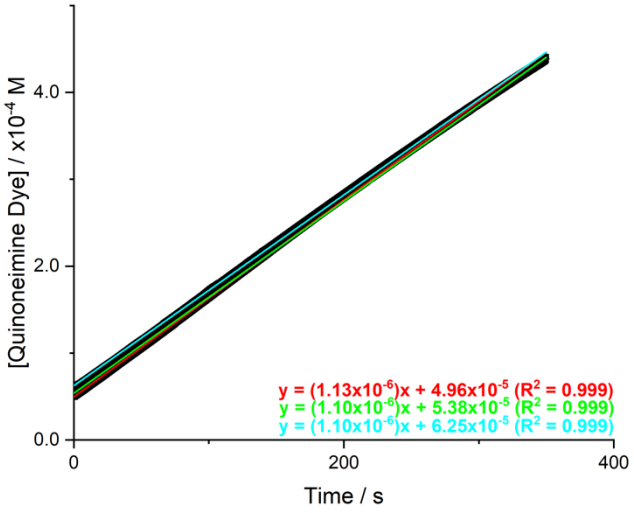

S. Figure 7.4.10. Plot of quinoneimine dye formation in the coupled assay shown in Scheme 3.4.8. Concentration of pyruvate in this case was 2.5 mM.

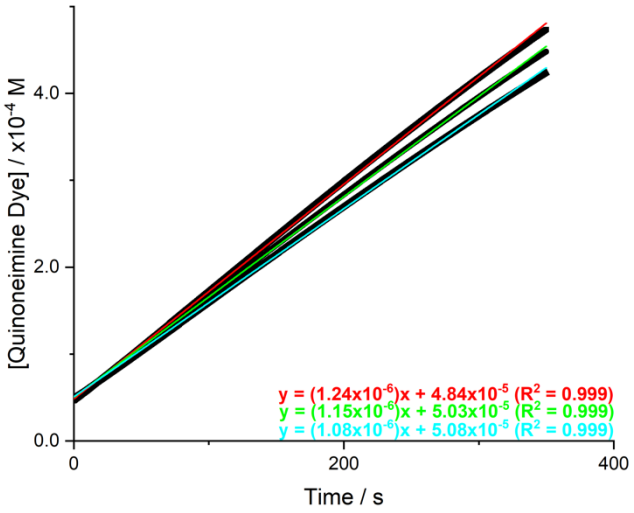

S. Figure 7.4.11. Plot of quinoneimine dye formation in the coupled assay shown in Scheme 3.4.8. Concentration of pyruvate in this case was 5 mM.

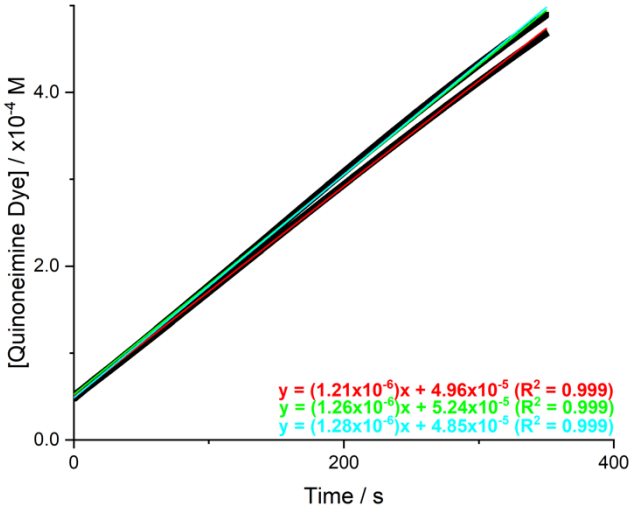

S. Figure 7.4.12. Plot of quinoneimine dye formation in the coupled assay shown in Scheme 3.4.8. Concentration of pyruvate in this case was 20 mM.

7.4.3. NMR Spectroscopy Studies

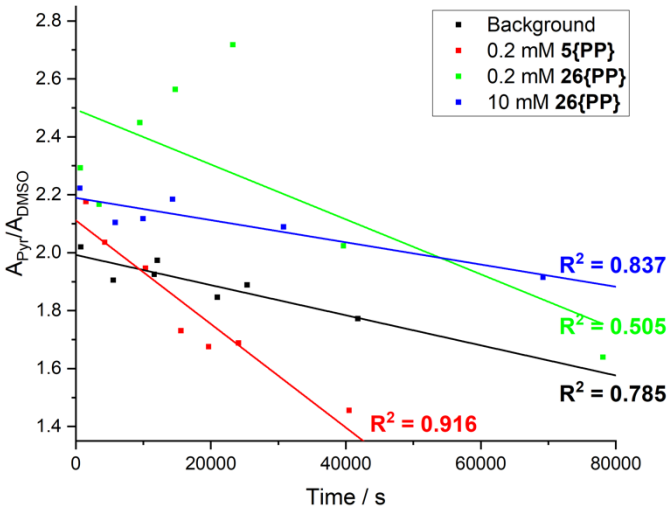

S. Figure 7.4.13. Plots of ^{13}C pyruvate integral (**153**) integral divided by the integral for d_6-DMSO for a selection of the biocatalytic carbinol syntheses (Scheme 3.4.9). Straight lines were fitted to the 'initial rate' regime, before plateauing, and compared to the gradient of the background reaction (no cofactor) (Table 3.4.10).